DOE/ER-0313/8

Fusion Reactor Materials

Semiannual Progress Report for Period Ending March 31, 1990

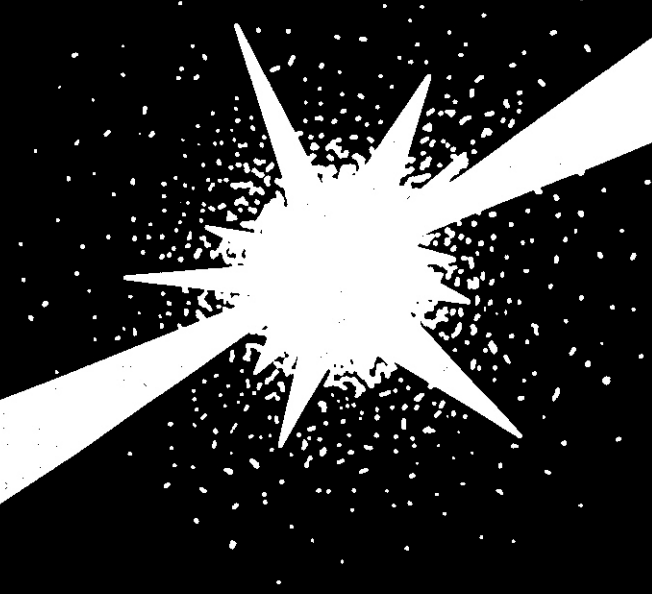

U. S. Department of Energy
Office of Fusion Energy

DOE/ER-0313/8
Distribution
Categories
UC-423, -424

FUSION REACTOR MATERIALS SEMIANNUAL PROGRESS REPORT FOR THE PERIOD ENDING MARCH 31, 1990

Date Published: **August** 1990

Prepared for
DOE Office of Fusion Energy
(AT 15 02 03 A)

Prepared by
OAK RIDGE NATIONAL LABORATORY
Oak Ridge, Tennessee 37831
operated by
MARTIN MARIETTA ENERGY SYSTEMS, INC.
for the
U.S. DEPARTMENT **OF** ENERGY
under Contract DE-AC05-840R21400

FOREWORD

This is the eighth in a series of semiannual technical progress reports on fusion reactor materials. This report combines research and development activities which were previously reported separately in the following technical progress reports:

- Alloy Development for Irradiation Performance
- Damage Analysis and Fundamental Studies
- Special Purpose Materials

These activities are concerned principally with the effects of the neutronic and chemical environment on the properties and performance of reactor materials; together they form one element of the overall materials program being conducted in support of the Magnetic Fusion Energy Program of the U.S. Department of Energy. The other major element of the program is concerned with the interactions between reactor materials and the plasma and is reported separately.

The Fusion Reactor Materials Program is a national effort involving several national laboratories,, universities, and industries. The purpose of this series of reports is to provide a working technical record for the use of the program participants, and to provide a means of comnunicating the efforts of materials scientists to the rest of the fusion community, both nationally and worldwide.

This report has been compiled and edited under the guidance of A. F. Rowcliffe and Frances Scarboro, Oak Ridge National Laboratory. Their efforts, and the efforts of the many persons who made technical contributions, are gratefully acknowledged.
F. W. Wiffen, Reactor Technologies Branch, has responsibility within DOE for the programs reported on in this document.

R. Price, Chief
Reactor Technologies Branch
Office of Fusion Energy

Reports previously listed in this series are as follows:

DOE/ER-0313/1	Period Ending September 30, 1986
DOE/ER-0313/2	Period Ending March 31, 1987
DOE/ER-0313/3	Period Ending September 30, 1987
DOE/ER-0313/4	Period Ending March 31, 1988
DOE/ER-0313/5	Period Ending September 30, 1988
DOE/ER-0313/6	Period Ending March 31, 1989
DOE/ER-0313-7	Period Ending September 30, 1989

TABLE OF CONTENTS

Annealed 316SS was irradiated at 90°C and 290°C in RTNS-II and in CWR. Radiation induced microstructures were examined by transmission electron microscopy. Very small dislocation loops of extremely high density were observed in dark field images. In the case of irradiations at 90°C and 290°C in RTNS-II and 90°C in OWR, the loop density increased moderately with dpa, roughly proportional to the square rwt of dpa, while that of 290°C irradiation at OWR showed stronger dpa dependence about 0.003 dpa, where the yield stress change also Increased strongly. The yield stress change was roughly proportional to the square root of the defect density, independent of irradiation temperature and neutron energy spectrum. The observed small dislocation loops are the origin of the yield stress change, with a Strength parameter estimated to be 0.2.

Micro-bulge testing was conducted on several Fe-Ni-Cr alloys irradiated as 0.3 mm thick disks to 10 dpa at 603 and 773 K in the Oak Ridge Research Reactor. Miniature tensile tests were performed on specimens of tha same alloys irradiated concurrently. Good correlation between the tensile yield strength and the bulge yield load was observed in unirradiated specimens; however, the correlation was not simple for irradiated specimens. Good correlation was also observed between the ultimate tensile strength and the maximum bulge load. While irradiation produced a significant reduction in total elongation in the tensile test, irradiation caused only a small decrease in the deflection corresponding to the maximum bulge load compared to that observed on thinner disks used in earlier experiments. The results suggest that the thinner disk is better suited for ductility evaluations than the thicker disk. The area bounded by the load-deflection traces of the bulge tests shows a systematic variation with both alloy composition and Irradiation condition which is not observed in the tensile data. It is anticipated that this parameter nay prove useful in the evaluation of material toughness.

The influence of helium on the microstructural evolution of irradiated metals is reviered. The review encompasses data from past work involving charged particle irradiations and neutron Irradiations in fission reactors, but emphasizes more recent results. Thls latter data was obtained from experiments in which either the reactor neutron spectrum or the isotopic content of the nickel in the irradiated alloys was tailored to yield a ratio of helium to displacement production (He/dpa ratio) that is near the value that will be obtained in a DT fusion reactor. Both the absolute level of helium present and the He/dpa ratio are shown to be important parameters. All major components of the irradiated microstructure — cavities, precipitates. and dislocations — are shown to be sensitive to helium as a result of either its direct influence on cavity formation, or its indirect effect on point defect and solute partitioning. The results emphasize the importance of careful experimental and theoretical analysis if data from fission reactor experiments are to be used in fusion reactor design. In particular, the effects of helium appear to be greatest during the swelling incubation period, the time of most practical interest for fusion reactor designers.

New concepts are reviewed which replace the conventional separation of microstructure evolution analysis into nucleation and growth. Classical nucleation theory is inadequate under fusion conditions (high helium-to-dpa ratios) and the usual "mean field" approximation of microstructural growth cannot account for cascade effects. A comprehensive theory of microstructure evolution Under fusion conditions is formulated based on non-equilibrium statistical mechanics. Dynamic re-solution of helium gas in cavities is shown to result in continuous nucleation of helium-filled cavities. Microstructure evolution (e.g., dislocation loops and cavities) is modeled by kinetic rate equations for small size features and Fakker-Planck (F-P) equations for sizes larger than fed atomic dimensions. Semi-analytical and numerical methods are developed for the analysis of microstructure evolution and the results are compared to experiments. The problem of spatial self-organization of microstructures under irradiation is described in terms of a nwly developed Ginzburg-Landau-type equation and the results are also conpared to experiments.

Point-defect generation by energetic displacment events is known to take place when a lattice atom requires an energy several tines its lattice binding value. In this energy range, many-body effects are important and interatomic pair potentials generally give poor representations of atomic interactions. By applying our nerly developed molecular-dynamics code, CASC-MD, we investigate the influence of aany-body interatomic interactions on the generation Characteristics of p i n t defects. We use a composite interatomic potential Which assumes the pair-potential nature at high energles and the many-body nature, based on the embedded-atom formalism, at low energies. It is shown that many-body effects lead to lower directional sensitivity of the displacenent threshold surface. For a 60-eV collision cascade in Cu, it is shown that the length of the replacement collision sequence decreases from 6 lattice constants at low temperature [near 0 K) to 1.5 lattice constants near the melting point.

The degree of sensitization of 25% cold-worked PCA irradiated at 60, 200, 330, and 400°C up to 7 dpa under spectrally tailored conditions in the ORR-MFE-6J/7J experiments was evaluated by the electrochemical potentiokinetic reactivation (EPR) test technique on miniaturized TEM disk-type specimens. Irradiation at 60°C to 7 dpa did not affect the reactivation behavior of PCA. The reactivation charge of PCA was increased by the Irradiation at 200, 330, and 400°C, as conpared with unirradiated Control specimens. and increased with increasing irradiation tenperature. Post-EPR examination of the specimen surfaces showed grain boundary etching for the specimen irradiated at 400°C, but not for the specimens irradiated at 330°C and below. This indicates that the intergranular stress corrosion cracking (IGSCC) susceptibility associated with chromium depletion along grain boundaries was not increased by the irradiation at temperatures below 330°C to this damage level. Localized attack across the grain faces was observed for all the specimens irradiated at 200, 330, and 400°C, which suggests the Occurrence of localized sensitization in the grain interior. The Investigation of the possibility of the localized sensitization in grain interiors and its effects on the corrosion behavior is in progress.

The FUBR-1B irradiation experiment in EBR-II has provided important information on the irradiation behavior of candidate lithium solid breeder materials in a high energy neutron Spectrum. The solid breeder materials include Li_2O, $LiAlO_2$, Li_2ZrO_3, Li_8ZrO_6 and Li_4SiO_4 pallets and $LiAlO_2$ spheres. The irradiation behavior of the materials was characterized for the temperature range from 400 to 900°C. The amount of tritium retained by the solid breeder materials, as well as swelling and physical stability, was detemined for specimens removed after the first period of irradlatlon.

LiAlO,. Li_2ZrO_3, and Li_8ZrO_6 exhibited excellent dimensional stability during irradiation while the dimensional stability of Li_2O was found to be dependent on the microstructure. The amount of retained tritium is compared to similar closed capsule experiments and extends the data to burnups as high as 1.6×10^{21} at/cc.

Temperature programmed desorption (TPD) measurements have started on the $LiAlO_2$-H_2 system. The sensitivity of the mass spectrometer that will detect the peaks was shown to be adequate for the measurements. Blank experiments to Characterize the behavior of the stainless steel sample tube in the measurements have revealed the evolution of N from the steel, a process facilitated by H_2. It is necessary to stabilize the sample tube so that it does not augment or distort the TPD peaks. The behavior of an unstabilized tube was demonstrated by means of a simulated TPD run. Stabilization consists of treating the tube with 990 ppm H_2 in helium at high temperature until undistorted simulated TPD runs are obtained. A $LiAlO_2$ sample was loaded in the apparatus: it came from the same batch of material that was used in an EXOTIC test. Prolonged drying of the sample in a He-H_2 stream is necessary, a finding that has important implications for many earlier reports on measurements of tritium release from irradiated samples where it was not demonstrated that the sample was adequately dry or that the apparatus did not affect the data.

Polycrystalline specimens of spinel ($MgAl_2O_4$) and alumina (Al_2O_3) were irradiated at room temperature and 650°C with either dual- or triple-ion beams in order to investigate the effects of simultaneous displacement damage and helium implantation on cavity formation. The cavities in alumina were aligned along the direction of the c-axis, with diameters ranging from <2 to 10 nm. The cavities in spinel were preferentially associated with dislocation loops and were of similar size as the cavities in alumina. Catastrophic amounts of Cavitation were observed at the grain boundaries in spinel when the displacement damage level exceeded a critical value (~20 dpa) in the presence of a fusion-relevant (~60 appm/dpa) helium environment.

A series of experiments have been planned to measure the dielectric properties of alumina in the presence of ionizing and displacive irradiation.

A stock of commercial, polycrystalline alumina with four different levels of purity (0.94, 0.976, 0.995, and 0.998) has been added to the Fusion Reactor Materials inventory. The material is in the form of 3/4 in. (0.998) and 1 in. (0.94) diameter rods and 2 in. by 2 in. bars (0.976 and 0.995).

1. IRRADIATION FACILITIES, TEST MATRICES, AND EXPERIMENTAL METHODS

PREPARATION AND IRRADIATION OF THE FUSION MOTA **(2A) -** M. L. Hamilton and R. M. Ermi (Pacific Northwest Laboratory)[a]

OBJECTIVE

The purpose of this effort is to document the loading of the Fusion Materials Open Test Assembly (MOTA 2A) into the Fast Flux Test Facility (FFTF) for irradiation in cycle 11.

SUMMARY

MOTA 2A was developed on the basis of prior breeder program MOTAs to support the research and development efforts of three fusion materials programs: the U.S. DOE Neutron Interactive Materials (NIMs) program, the Japanese university fusion materials program, and the IEA-sponsored BEATRIX-II experiment. The MOTA was designed and fabricated to support the specimen loading desired by each of the three partners and was inserted into the FFTF for irradiation beginning in cycle 11. Cycle 118.1 has been completed successfully. Both the specimen loading and the history of cycle 116.1 are documented here.

PROGRESS AND STATUS

Introduction

The MOTA type of irradiation vehicle provides the U.S. and international materials community with the unique capability of performing instrumented, temperature controlled, fast neutron irradiation experiments in the FFTF. The first such vehicle devoted exclusively to the needs of the fusion materials community is referred to as MOTA 2A. Three partners are participating in the irradiation of MOTA 2A: the U.S. NIMs program, the Japanese university fusion materials community, and the IEA-sponsored BEATRIX-II experiment. The loading of the Fusion MOTA was tailored to meet the needs of each partner. The goal of the NIMs and Japanese programs is to develop improved materials for use in many different components of proposed fusion devices and to facilitate the prediction of their performance limits in a fusion environment. These programs focus on metallic or ceramic specimens for post-irradiation determination of swelling, mechanical properties and microstructure. The goal of BEATRIX-II is to characterize the tritium release behavior of fusion-relevant solid breeder materials during fast neutron irradiation. It is primarily an in-situ tritium recovery experiment which focuses on the irradiation behavior of Li_2O under a variety of temperature and purge gas conditions.

MOTA Loading

Canister Allocation. The U.S. NIMs program required that a number of specimens be reconstituted from the previous irradiation cycle after having been irradiated in the breeder MOTA (IF). If these specimens had been reconstituted into the Fusion MOTA (2A), comprised largely of new specimens, then hot cell reconstitution would have been required for both the new Fusion MOTA (2A) and the continuing breeder MOTA (1G). As a cost saving measure, the NIMs program exchanged space with the breeder program such that all radioactive specimens would continue irradiation in the breeder MOTA (1G). Thus the breeder program inserted new, unirradiated specimens in the Fusion MOTA (2A) in exchange for insertion of radioactive NIMs specimens in the continuing breeder MOTA (16).

The canister matrix for both MOTAs is shown in Table 1. The numbers given vertically indicate the axial level of the canister (below core through row 8), while the alphabetic designations refer to the radial position around the MOTA stalk (A through F). The box for each occupied canister indicates the irradiation temperature and the program using the canister. A "W" in the lower left corner of the box indicates that the canister is a weeper without temperature control; the absence of a "W" indicates that the canister is gas gapped to control temperature. Information relevant to the thermocouples, such as their absence or their offset location, is given in brackets.

Dosimetry Specimen Matrix. Up to three types of dosimetry were used: spectral sets, gradient sets, and U^{236} spectral sets (the latter in MOTA 1G only). Some of the spectral sets contain helium accumulation fluence monitor (HAFM) sensors. The specific dosimetry loaded into MOTA 1G and MOTA 2A is given in Tables 2a and 2b. The relative physical location of the dosimetry in a given canister is indicated by the relative placement of the information in the box corresponding to the canister in these tables.

(a) Pacific Northwest Laboratory is operated for the U.S. Department of Energy by Battelle Memorial Institute under Contract DE-AC06-76RLO 1830.

BEATRIX-II Specimen Matrix. The specimen matrix for BEATRIX-II is summarized in Table 3. The majority of the canisters are weepers and are therefore located near the bottom of the core in order to minimize the irradiation temperatures. The experiment includes the irradiation of two in-situ tritium recovery capsules containing either a ring or a solid specimen of Li_2O. The ring specimen is located in a vented canister (IE) capable of incrementally imposing large temperature changes. It is vented to allow the recovery of tritium via a sweep gas flowing through the canister. This specimen will provide data on both thermal conductivity and the kinetics of tritium release through variations in temperature, burnup and sweep gas flaw rate and composition. The solid pellet specimen is also located in a vented canister (IC), but the latter operates under a large temperature gradient to investigate the thermal stability of Li_2O, the major operating limitation on the potential use of Li_2O as a solid breeder. The solid pellet irradiation is more prototypic of the conditions expected in a fusion blanket, with an initial centerline temperature approaching 1000°C. The nonvented canisters (1B, ID, 5E and 8B) contain Li_2O and beryllium specimens for the evaluation of irradiation damage, thermal conductivity, tritium release kinetics, and beryllium compatibility.

U.S. NIMs Specimen Matrix. The objective of the U.S. NIMs program is to develop improved materials for use in fusion devices and predict their performance limits in a fusion environment. The long term effort focuses on providing an increased understanding of damage mechanisms through experiment, data analysis and modelling. A short term effort is focussed on meeting the near-term materials needs for the International Thermonuclear Experimental Reactor (ITER).

A summary of the U.S. specimen matrix is shown in Table 4. The geometries of the U.S. and Japanese specimens are listed in Table 5. The U.S. specimen matrix contains specimens from three national laboratories: Pacific Northwest Laboratory, Oak Ridge National Laboratory, and Argonne National Laboratory. In addition, there are specimens supplied by European and Japanese scientists engaged in collaborative research with U.S. staff. The emphasis is primarily on (but is not limited to) alloys for firt wall/blanket applications. Major areas include 1) supplying high fluence, engineering data for current or potential fusion candidate heats of ferritic and austenitic steels, 2) exploring reduced activation alloys of several types, and 3) clarifying the role of helium. Smaller efforts are directed toward the development of copper alloys for high heat flux applications and beryllium for neutron multiplier or plasma interactive components.

Monbusho Specimen Matrix. The Japanese university program for the development of fusion reactor materials is using the FFTF/MOTA as part of a larger program to attain an understanding of the various radiation responses that control materials' behavior. Specifically, their program is designed 1) to establish correlations between high and low exposure irradiations in fission and fusion neutrons and 2) to determine the mechanisms governing microstructural and microchemical evolution and their relation to property changes in materials.

Six sub-groups have been designated responsible for such efforts for different classes of materials:

a) Ferrous materials,
b) Refractory metals and alloys, high heat flux materials,
c) Pure metals and model alloys for fundamental studies,
d) Isotopic tailoring experiments,
e) Ceramics and composite materials, and
f) Dosimetry.

A summary of the Japanese specimen matrix is given in Table 6. Their program areas are somewhat similar to those of the U.S. Major areas include the characterization of candidate austenitic and ferritic alloys, the development of low activation alloys of several types, and a consideration of high heat flux materials, as well as a significant fundamental effort to provide a mechanistic understanding of radiation damage in many materials.

Cycle 118.1 Operation[1]

The gas gapped canisters in MOTA 2A and MOTA 1G were brought up to their design temperatures at slightly different times while difficulties associated with the vent lines of the two MOTAs were resolved. Figure 1 shows the reactor power history during cycle 118.1 in the form of a temperature history of the in-core coolant thermocouple c2 in MOTA 2A. Temperature histories for individual canisters mirror the reactor power history. The reactor was operated initially at 95% power because an experimental fuel assembly outlet temperature approached a technical specification limit. A power coefficient test was run early in the period at 95% power, entailing a brief drop to 85% power. Another similar test was run shortly after the ascent to 100% power. Two unanticipated shutdowns occurred durina the cycle. the first due to an ooerator error during a monthly test and the'second to repair a faulty battery cell in a required backup system. The FFTF accumulated 85.5 equivalent full power days during cycle 118.1.

Table 7 gives the time-averaged temperature data for MOTA 2A and the fusion canisters in MOTA 1G. Time-averaged temperatures were calculated using only temperatures greater than or equal to 20°C below the target

temperature. Since temperatures less than this usually indicated a reactor shutdown condition, the calculated values provide the average temperature at or near full power. Both the average temperature and the time at temperature are included for temperatures above (T_{target}-20°C) and below (T_{target}-20°C). The latter is included since significant times can be realized at lower temperatures during startups, etc. Note that these averages do not include temperatures less than 300°C since temperatures below this value indicate a very low power *or* reactor shutdown condition.

CONCLUSIONS

The first fusion MOTA (2A) was successfully prepared and inserted into the FFTF for operation during cycle 11.

FUTURE WORK

Planning will continue for both post-irradiation testing of MOTA 2A specimens and the specimen loading for MOTA 2B.

REFERENCES

1. A. M. Ermi, Annual Progress Report for Monbusho-DOE Collaboration in Fundamental Studies of Irradiation Effects in Fusion Materials Utilizing Fusion Reactors for Fusion Year 1989, in press.

2. G. W. Hollenberg, First Annual Progress Report: BEATRIX-II Program, January 1988 to December 1988, PNL-6818, March 1989.

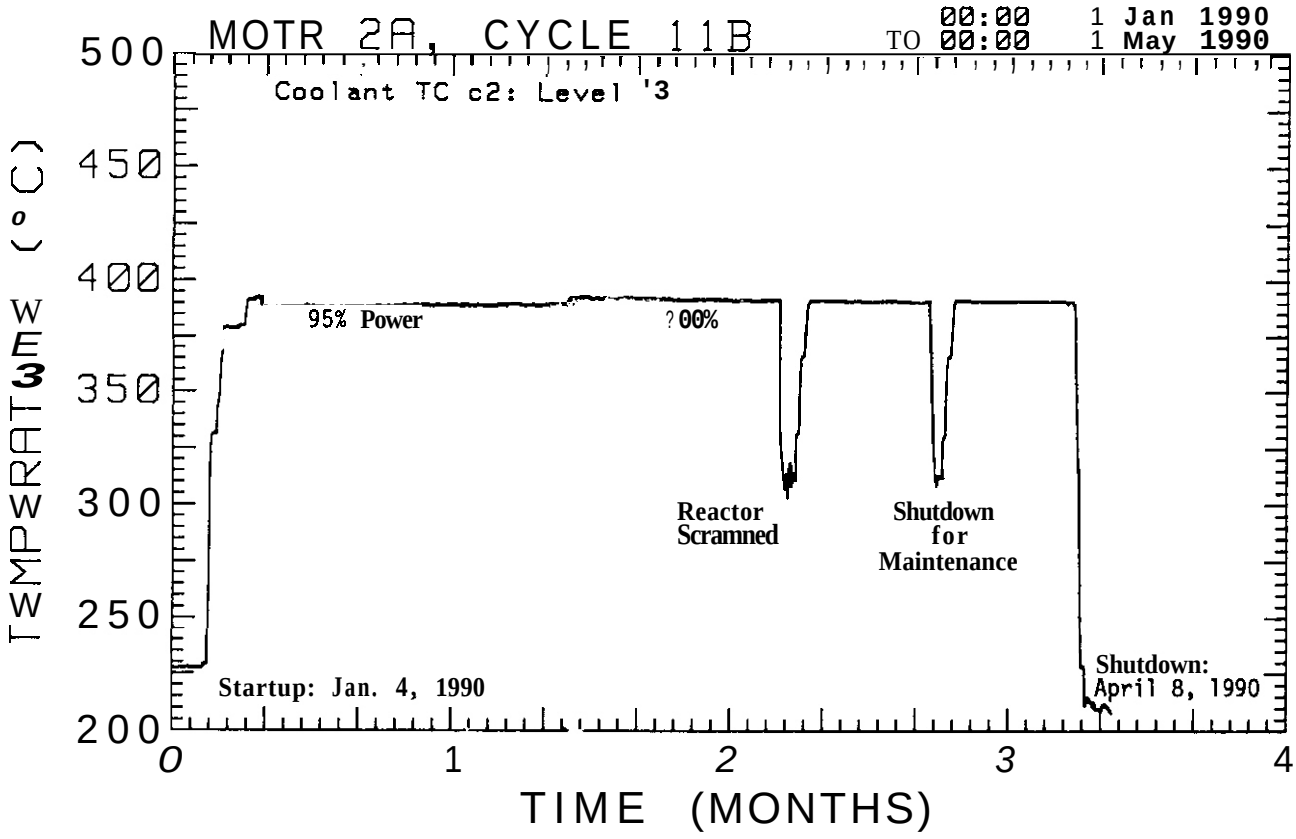

Figure 1. Temperature Plot for Coolant Thermocouple c2 for Entire Cycle 11B.1

MOTA-2A (FUSION MOTA) CANISTER MATRIX

	A	B	C	D	E	F
8	440°C FUSION [offset] W (HHF)	440°C FUS/MONB/ IEA W				
7		435°C FUS/MONB W				
6	430°C FUSION [offset] W (HHF)	430°C FUS/MONB W	430°C MONB [offset] W (HHF)			
5	600°C FUSION [offset] W (HHF)	425°C FUSION [offset] W (HHF)	600°C FUSION [offset] W (HHF)	800°C MONB	425°C IEA/MONB W	600°C MONB
4	425°C LMR W	600°C FUSION	600°C FUSION	425°C MONB W	520°C MONB	600°C MONB
3	605°C LMR	550°C LMR	420°C FUSION W	420°C MONB W	520°C MONB	600°C MONB
2	410°C LMR W	410°C LMR W	520°C FUSION	410°C MONB W	410°C MONB W	520°C MONB
1	390°C MONB W	390°C IEA W	900°C IEA [3 TCs] W	390°C IEA W	450-600°C IEA [3 TCs]	460°C MONB
BC	365°C FUSION W	365°C FUSION W	365°C LMR [no TC] W	365°C LMR [no TC] W	365°C MONB W	410°C MONB

W = Weeper Canisters
FUSION = U.S. Fusion Program
MONB = Japanese MONBUSHO Program
IEA = I.E.A. BEATRIX-II Experiment
LMR = Liquid Metal Reactor Program
HHF = High Heat Flux Capsule
[offset] = Offset Thermocouple

MOTA-1G CANISTER MATRIX

	A	B	C	D	E	F	Nominal Mid-Canister Fast Fluence (10^{22} n/cm^2)
8					440°C FUS/LMR W	440°C LMR [offset] W	0.045
7							0.17
6					490°C LMR	435°C LMR [offset] W	0.54
5	670°C LMR [offset]	550°C LMR	550°C LMR	635°C LMR	670°C LMR [offset]	430°C PNC W	3.5
4	600°C FUSION	635-605°C LMR	750°C LMR	550°C LMR	670°C LMR	670°C LMR	6.3
3	420°C FUSION W	420°C FUSION W	605°C PNC	670°C PNC	550°C LMR	750°C LMR	7.5
2	520°C FUSION	605°C LMR	635°C LMR	550°C PNC	410°C LMR W	520°C FUSION	6.8
1	750°C LMR [offset]	495°C LMR	495°C LMR	495°C PNC	390°C LMR W	390°C LMR W	3.9
BC	365°C LMR [no TC] W	365°C FUSION [no TC] W	365°C LMR [no TC] W	365°C LMR [no TC] W	365°C LMR [no TC] W	365°C FUSION [no TC] W	365°C LMR [no TC] W 0 1.2

W = Weeper Canisters
LMR = Liquid Metal Reactor Program
PNC = Japanese PNC Program
FUSION = U.S. Fusion Program
[offset] = Offset Thermocouple

February 1, 1989

Table 1. Canister distribution in MOTA 2A and MOTA 1G.

Table 2a

Dosimetry Placement in MOTA 1G

	A	B	C	D	E	F
8						G M-78 SH X-37
7						
6						G M-79 S M-6
5						S M-5 G M-80
4	*					G M-83
3	*	S M-4 *	SU M-10	S X-35	SU M-11	SH X-36
2	*					G M-7 *
1						G M-82 S M-3
BC		*				G M-81 S M-1

G = Gradient, S = Spectral, SH = Spectral + HAFM, SU = U^{236} Spectral, M-nn, X-nn = Dosimetry ID Code,
* = U.S. NIMs program canister.

Table 2b

Dosimetry Placement in MOTA 2A

	A	B	C	D	E	F
8		SH X-14 G X-34				
7		G X-33				
6		G X-32 S X-13				
5				G X-30	G X-31	S x-12 S X-11
4	S X-10		G X-28			G X-29
3	G X-25 SH X-08 G X-26			S x-09	G X-27	
2	G X-23	G X-22			G X-24 S X-07	G X-20
1				G X-21 S X-05 SH X-04		S X-06
BC	G X-15 SH X-01 G X-16	G X-17		G X-19	S x-02	G X-18

G = **Gradient,** S = **Spectral,** SH = **Spectral t HAFM, X-nn = Dosimetry ID Code.**

Table 3

BEATRIX-II Specimen Matrix

Canister	Target Temperature (°C)	Vented	Material	Enrichment (%)	Purpose
1E	Variable (gas gapped)	yes	Li_2O ring	61	T release, thermal conductivity
1C	Gradient (weeper)	yes	Li_2O solid	61	T release, thermal stability
1B	390 (weeper)	no	Li_2O single crystal	0.07-61	Irradiation damage
10	390 (weeper)	no	Li_2O: 83.5-93.6% TD	61	Thermal conductivity
			Li_2O single crystal	0.07	Isothermal T release
5E	425 (weeper)	no	Be disks alternating with disks of Li_2O, Li_2ZrO_3, Li_4SiO_4, and $LiAlO_2$	0.2-95	Compatibility of Li ceramics and Be
8B	440 (weeper)	no	Be disks alternating with disks of Li_2O, Li_2ZrO_3, Li_4SiO_4, and $LiAlO_2$	0.2-95	Controls for compatibility study

Table 4

Summary of NIMs Specimens in MOTA 2A and 1G by Laboratory[a]

Type of Specimen	Alloy	T (°C) 365	420	520	600
Tensile	Ferritics:				
	HT9 - High dose	P	P	P	P
	- TMT variations	O	O	O	O
	9Cr1Mo - TMT variations	O	O	O	O
	Fe-Cr binaries	P	P		
	Low activation ferritic:				
	37xx series	O			
	V02xxx series	P	P		
	GA#X series	P	P	P	P
	F82H[b]	P	P	P	P
	Austenitic:				
	316		O	O	O
	Low activation austenitic:				
	PCMA-x		O	O	O
	Vanadium alloys		O	O,A	O,A
	Fe-28Al-4Cr	O			
	JPCA/JFMS (size effects)		P	P	
	Isotopic tailoring[c]	P		P	
	Copper alloys		P		
Charpy[d]	Ferritics:				
	HT9 - High dose	P		P	
	- TMT variations	O	O	O	O
	- Size effects	O			
	9Cr1Mo - High dose	P		P	
	- TMT variations	O	O	O	O
	2-1/4Cr	O			
	Low activation ferritic:				
	37xx series	O			
	V02xxx series	P			
	GA#X series	P	P	P	
	F82H	P	P	P	
	Vanadium alloys		O	O,A	O,A
Compact Tension	Ferritic:				
	HT9 - High dose	P	P	P	P
	Low activation ferritic:				
	GA#X series	P	P	P	P
	F82H	P	P	P	P
Pressurized Tube	Ferritic:				
	HT9	P	P	P	P
	9Cr1Mo		P	P	P
	Austenitic:				
	316		O	O	O
	PCA		O	O	O

Table 4

(contd)

Type of Soecimen	Allov	T_i (°C) 365	420	520	600
TEM	Isotopic tailoring[c]	P		P	
	Copper alloys	P	P		
	Low activation austenitic:				
	PCMA-x		O	O	O
	Fe-Cr-Mn		P	P	P
	Low activation ferritic:				
	V022xxx series	P	P	P	P
	GA#X series	P	P	P	P
	F82H	P	P	P	P
	Ferritic:				
	HT9[b]	P,O	P,O	P,O	P,O
	9Cr1Mo[b]	P,O	P,O	P,O	P,O
	ODS[b]	P	P		P
	Fe-Cr binaries	P	P		
	Misc. Fe-Cr-X	P,O	P,O	P,O	P,O
	Vanadium alloys		O	O,A	O,A
Miscellaneous:					
Compression	Beryllium			P	
Density ring	316, PCA		O	O	O
Punch	Low activation ferritic	P	P	P	P
CCT	HT9, 9Cr1Mo		P		P
Disc	Brazed or coated C, Cu or SS[e]				
Oisc	Graphite or C/C composites[f]				P

(a) P: PNL; O: ORNL; A: ANL
(b) Also at 550, 670, 750°C in MOTA 1G.
(c) Also at 465°C in MOTA 1G.
(d) All specimens are 1/3 size except for those in size effects study, which includes 1/2 size specimens.
(e) High heat flux materials at weeper temperatures (425-440°C) in level 5 and above core.
(f) High heat flux materials.

Tqble 5

U.S. & Japanese Fusion Specimen Geometries in MOTA 2A and 1G

Specimen Type	Geometry	Nominal Mass (gm)	Dimensions (in.)
0.256 in. Swelling Tube	Open tube	0.90	0.256 dia. x 0.375 lg
0.180 in. Creep Tube	Pressurized tube	0.83	0.180 dia. x 0.88 lg
0.230 in. Creep Tube	Pressurized tube	2.05	0.230 dia. x 1.11 lg
SS-3 Tensile	Sheet	0.48	0.195 x 0.030 x 1.00
SS-3 Tensile Modified	Sheet	0.70	0.400 x 0.030 x 1.00
Miniature Tensile	Sheet	0.06	0.100 x 0.010 x 0.5
Japanese Tensile (S)	Sheet	0.098	0.157 x 0.010 x 0.630
Japanese Tensile (W)	Sheet	0.786	0.315 x 0.020 x 1.260
0.630 in. Compact Tension	Disc	3.50	0.630 dia. x 0.10 thk
ANL/PNL 1/3 Size Charpy	Block	2.10	0.131 x 0.121 x 0.930
ORNL 1/3 Size Charpy	Block	2.24	0.131 x 0.131 x 1.0
ORNL 1/2 Size Charpy	Block	5.06	0.197 x 0.197 x 1.0
Japanese 1.5 mm Charpy	Block	0.354	0.059 x 0.059 x 0.787
Japanese 1/3 Size Charpy	Block	1.97	0.130 x 0.130 x 0.906
Miniature CCT Fatigue	Sheet	1.56	0.5 x 1.0 x 0.024
TEM Disc	Disc	0.014	0.118 dia. x 0.01 thk
High Heat Flux	Disc	10.1	0.630 dia. x 0.25 thk
0.72 in. Packet (SS)	Capped weeper tube	1.09	0.144 dia. x 0.72 lg
0.88 in. Packet (SS)	Capped weeper tube	1.25	0.144 dia. x 0.88 lg
1.14 in. Packet (SS)	Capped weeper tube	1.12	0.144 dia. x 1.14 lg
1.14 in. Packet (SS	Sealed tube	1.94	0.144 dia. x 1.14 lg
1.58 in. Packet (SS)	Capped weeper tube	2.59	0.144 dia. x 1.58 lg
Punch Packet (SS)	Capped weeper tube	5.00	0.500 dia. x 0.34 lg
1.75 in. Subcapsule (TZM)	Li-filled tube	14.0	0.375 dia x 1.75 lg
2.05 in. Subcapsule (TZM)	Li-filled tube	2.05	0.375 dia x 2.05 lg
2.25 in. Subcapsule (TZM)	Li-filled tube	17.2	0.375 dia x 2.25 lg
0.71 in. Subcapsule (SS)	He-filled tube	3.6	0.370 dia x 0.70 lg
0.80 in. Subcapsule (SS)	He-filled tube	5.0	0.370 dia x 0.80 lg
1.5 in. Subcapsule (SS)	He-filled tube	6.2	0.370 dia x 1.5 lg
2.05 in. Subcapsule (SS)	He-filled tube	10.9	0.370 dia x 2.05 lg

Table 6

Summary of Japanese Specimens in MOTA 2A

Type of Specimen	Alloy	T (°C) 365[d]	390	410-425	416[d]	460	520	600	800
Tensile	Ferritic:								
	JFMS	S[a]	S	S		S	W,S		
	HT9	S	S			S	W,S		
	ODS					S	S	S	
	Misc. Fe-Cr-X		S	S					
	Misc. Fe alloys	S		S	S	S	S	S	
	Low activation ferritic:								
	ASx series		W,S	W,S			W,S	S	
	JLFx series	S	S	W,S			W,S		
	F82H		W,S	S		S	W,S	S	
	NLFx series	S	S	S			W,S	S	
	Austenitic:								
	PCA/JPCA		W,S	W,S		S	W,S	S	
	Misc.			S		S	S	S	
	Low activation austenitic:								
	Fe-Cr-Mn-X	S		S			S	S	
	HMNx series			S			S		
	JHMx series	S		S			S	S	
	Fe-Cr-Ni-X		S						
	cu	S		S		S	S	S	
	Vanadium alloys			S	S		S	S	S
	Refractories of Mo, W	S		S				S	S
Charpy	Ferritic:								
	HT9		3,5[b]	3		5	5,3	5	
	JFMS	5	5				5		
	ODS			5					
	tow activation ferritic:								
	ASx series		3.5			5	5,3	5	
	JLFx series	5		3,5		5	5,3		
	NLFx series		5,3	5,3		5	5		
	F82H		3,5	3,5		5	5,3	5	
	Low activation austenitic:								
	JHMx series	5		5			5		
	Fe-Cr-Mn-x			5					
Rod/disk/wafer/foil/fiber/block C/ceramic/composites			X	X	X		X	X	X
	Low activation ferritic	X	X	X		X	X	X	
	Misc. ferritic			X	X	X		X	XX
TEM	Low activation austenitic	X	X	X		X	X	X	
	Misc. austenitic			X	X	X		X	XX
	Vanadium alloys			X	X		X	X	X
	Pure metals, model alloys[c]	X	X	X	X	X	X	X	
	Refractories of Mo,W			X			X	X	X

Table 6

(contd)

Type of Specimen		T_i (°C) 365[d]	390	410-425	410[d]	460	520	600	800
Pressurized Tube	Low activation ferritic:								
	ASx series			X		X	X		
	JLFx series			X		X	X		
	F82H		X	X		X	X	X	
	Austenitic:								
	PCA/JPCA		X	X		X	X	X	
	Low activation austenitic:								
	HMNx series			X		X			

(a) Dimenions of "S" and "W" specimens are given in Table 5; W specimens are twice the size of S specimens in each dimension.

(b) "3" refers to 1/3 size charpy specimens and "5" refers to 1.5 mm charpy specimens. Dimensions of both types of charpies are given in Table 5.

(c) Also at 430-440°C above core.

(d) Below core.

Table 1

Time-Averaged Temperature Data for Cycle 118.1

MOTA	Program	Canister (or TC No.)	Canister (or TC) Tvoe	Target Temp. (°C)[b]	Min. Temp	Max. Temp (°C)	Temp. < (T_{targ} -20°C)[a] No. of Days	Temp. < (T_{targ} -20°C)[a] Avg. Temp. (°C)	Temp. ≥ (T_{targ} -20°C) No. of Days	Temp. ≥ (T_{targ} -20°C) Avg. Temp. (°C)
2A	MONB	1a	Weeper	390	207	391	6.6	332	86.1	381
2A	IEA	1b	Weeper	380	206	381	6.2	328	87.1	318
2A	IEA	1c	Weeper	940	208	956	16.0	691	11.4	932
		(1w)	(Outer 1c)	385	206	386	6.4	329	87.0	383
		(1x)	(Upper 1c)	980	207	1000	12.1	638	81.4	971
2A	IEA	1d	Weeper	395	201	395	6.7	333	86.7	392
2A	IEA	1e[c]	Gas gapped		208	613				
2A		(1y)	(Outer 1e)		208	586				
2A		(1z)	(Right 1e)		208	669				
2A	MONB	1f	Gas gapped	460	208	469	1.6	351	85.8	459
1G	US	2a	Gas gapped	520	207	536	1.3	364	86.1	520
2A	US	2c	Gas gapped	520	211	531	1.3	362	86.1	520
2A	MONB	2d	Weeper	405	207	401	6.1	336	86.6	404
2A	MONB	2e	Weeper	405	208	408	6.1	336	86.6	404
2A	MONB	2f	Gas gapped	520	210	530	1.7	363	85.1	519
1G	US	2f	Gas gapped	520	207	534	7.5	363	86.0	520
1G	US	3a	Weeper	430	207	436	9.4	351	84.0	428
1G	US	3b	Weeper	430	207	431	7.2	344	86.2	424
2A	US	3c	Weeper	420	208	428	8.6	353	84.1	420
2A	MONB	3d	Weeper	425	208	429	9.3	356	84.1	422
2A	MONB	3e	Gas gapped	520	211	531	7.8	368	85.6	519
2A	MONB	3f	Gas gapped	600	213	611	7.9	378	85.5	600
1G	US	4a	Gas gapped	600	207	614	1.7	317	85.1	599
2A	US	4b	Gas gapped	600	213	612	7.8	319	85.1	599
2A	US	4c	Gas gapped	600	214	611	7.8	380	85.6	600
2A	MONB	4d	Weeper	425	209	434	9.1	357	84.3	421
2A	MONB	4e	Gas gapped	520	211	530	7.9	311	85.5	520
2A	MONB	4f	Gas gapped	600	213	612	8.0	319	85.4	601
2A	US	5a	Gas gapped	580	213	591	7.8	319	85.6	580
2A	US	5b	Weeper	420	210	422	9.3	355	84.1	411
2A	US	5c	Gas gapped	580	213	592	1.9	315	85.5	580
2A	MONB	5d	Gas gapped	800	219	813	8.4	434	85.1	800
2A	IEA/MONB	5e	Weeper	430	210	430	8.9	351	84.5	421
2A	MONB	5f	Gas gapped	600	214	613	8.2	382	85.3	601
2A	US	6a	Weeper	425	210	421	9.2	351	84.1	424
2A	US/MONB	6b	Weeper	430	211	430	9.3	358	84.1	426
2A	MONB	6c	Weeper	430	210	432	9.3	358	84.1	426
2A	US/MONB	1b	Weeper	435	210	438	9.3	360	84.1	433
2A	US	8a	Weeper	435	211	437	9.4	361	84.0	432
2A	US/MONB/IEA	8b	Weeper	435	211	439	9.3	361	84.1	435
1G	US	8e	Weeper	445	207	456	9.5	364	83.8	442
2A	US	BCA	Weeper	375	206	318	5.5	323	87.9	314
2A	US	BCB	Weeper	375	206	315	5.6	323	87.8	312
2A	MONB	BCE	Weeper	375	206	374	5.6	323	87.8	311
2A	MONB	BCF	Gas gapped	410	207	429	10.2	349	83.2	410
1G	US	BCB	Weeper[d]	365	--	--	--	--	--	--
1G	US	BCF	Weeper[d]	365	--	--	--	--	--	--

Table 7

(contd)

MOTA	Program	Canister (or TC No.)	Canister (or TC) Type	Target Temp. (°C)[b]	Min. Temp. (°C)	Max. Temp. (°C)	Temp. < (T_{targ} -20°C)[a] No. of Days	Temp. < (T_{targ} -20°C)[a] Avg. Temp. (°C)	Temp. ≥ (T_{targ} -20°C) No. of Days	Temp. ≥ (T_{targ} -20°C) Avg. Temp. (°C)
2A	..	c1	Coolant TC	310	206	369	5.4	322	88.0	366
2A	..	c2	Coolant TC	390	208	393	6.5	332	86.8	390
1G	..	c1	Coolant TC	380	201	382	6.2	328	81.2	319
1G	..	c2	Coolant TC	405	201	405	6.9	331	86.5	402
1G	..	c3	Coolant TC	425	201	430	9.4	358	84.0	425

(a) Temperatures less than 300°C not included in calculation.
(b) Weeper and coolant TC target temperatures listed are the values used for the calculations of the average temperatures.
(c) Temperature change canister.
(d) No TC in canister.

ACCURACY OF THE PRECISION IMMERSION DENSITOMETER — H. Kanazawa, T. Sawai (Japan Atomic Energy Research Institute, Assigned to ORNL) and L. J. Turner (Oak Ridge National Laboratory)

OBJECTIVE

The objective of this work is to study the accuracy of the precision imnersion densitometer, and to determine the most important error factors on these measurements.

SUMMARY

To examine the accuracy of immersion density data, an identical control specimen was measured repeatedly. The distribution of the density data obtained shows that the accuracy of this method using an austenitic stainless steel specimen is 0.1% in swelling. Although no direct systematic relationship between the temperature change of the imnersion liquid and the density data was shown, the instability of the microbalance due to such an environmental change was shown to be important.

PROGRESS AND STATUS

Introduction

The precision immersion densitometer' has been employed to quantitatively measure the radiation-induced density changes (including void swelling) using standard transmission electron microscopy (TEM) disks irradiated in various reactors. The TEM disks are small specimens from the standpoint of mass and volume (3 mm diam by 0.254 mm thick) and the densitometer system employs an unadvantageous method to calculate the swelling from the standpoint of accuracy. The density data are obtained by subtracting measured weights of the identical specimens in air and in liquid, and swelling data are calculated by subtracting the calculated density data of irradiated and unirradiated specimens. However, despite those factors, it is an extraordinarily fine apparatus for remote handling of radioactive specimens. These measurements were performed with extensive care and were very effective for obtaining swelling data.' The ultimate accuracy of obtained data, however, has not been fully characterized.

Currently, measurements are under way on specimens irradiated in the MFE-7J capsule in the Oak Ridge Research Reactor (ORR) at 400°C with a low damage level of up to B dpa, as a part of the U.S./Japan collaborative program. This irradiation, along with another series of ORR capsules (MFE-4A, MFE-4B, and MFE-6J) and their successors, the High Flux Isotope Reactor (HFIR) RB* capsules, comprise the only irradiations in the world which employ neutron-spectral tailoring to accurately simulate the correct He:dpa ratio for a fusion environment. Considering the strong effect of He:dpa ratio on the microstructural evolution of austenitic stainless steels,[3] these spectrally tailored experiments are therefore expected to provide a very important set of microstructural data which will reflect the most realistic fusion reactor first-wall materials behavior for design purposes, rather than just a relative comparison of radiation response of differences of various alloys for alloy development.

The specimens now being examined at the damage level of 8 dpa are the first batch of spectrally tailored experiments from the U.S./Japan collaboration. This damage level is much lower than the first eight HFIR target capsules (>30 dpa) in this collaboration and is even lower than the earlier MFE-4A (13 dpa) and MFE-4B (12 dpa) capsules. Moreover, the irradiation temperatures of 60, 200, 330, and 400°C are also low, and at these temperatures void growth rate will be small compared to the temperature range above 500°C. The swelling data being obtained from these specimens will therefore be at or below the detection limit of the densitometer.

An understanding of the accuracy in precision immersion densitometry is essential to make the data obtained meaningful. A program to investigate the accuracy of the precision immersion densitometry has been initiated this reporting period and the purpose of this report is to describe its first result.

Experimental Procedures

The precision densitometer installed at the hot cell (ORNL, Bldg. 3025E) was used in this experiment. This apparatus features a unique specimen transfer system and a modified, ultrasensitive microbalance produced by Metler (Model M3-03) which can measure the weights of an identical TEM specimen in the air and in the liquid (thereafter immersion liquid) successively with the sensitivity of 0.001 mg. This microbalance has been modified to have two buckets set on a string for both the dry and wet weight measurements. A sophisticated control system transfers the TEM specimen from the dry bucket to the wet bucket. The imnersion liquid is FC-43 (freon), produced by 3M Corp., which is kept in a column surrounded by temperature-controlled water supplied from a constant temperature circulation bath, HAAKE

mdel A81. Although the bath can keep the temperature of the water in the bath within ±0.01°C about target temperature, the long piping (almost 2 m in both supply and return circuits) of the water between the bath and densitometer and the temperature change of the air surrounding the measurement unit could reduce the temperature stability of the imnersion liquid. A typical TEM disk used with this densitometer measures 3 mm in diameter and 0.25 mm in thickness. Further details and operating procedure for this densitometer will be presented elsewhere.'

An identical control (unirradiated) TEM disk of JPCA 20% cold-worked (CW) stainless steel, identification No. F29, was measured ten times between August 17 and 28, 1989. These measurements were interspersed with the ordinary tasks of density measurements. The control program written for the Hewlett Packard 9825T desk-top computer also processes the obtained data, including both dry and wet weights and environmental parameters, to calculate the density values.

Results and Discussion

Table 1 shows the obtained density data of disk F29 along with the environmental conditions in which the measurements were made. The average and the standard deviation of these density data are 7.9140 and 0.0053 g/cm^3, respectively. The standard deviation is 0.07% of the average value. The swelling calculation requires two density measurements — onefor the irradiated specimen and the other for the control disk. Hot (ρ_h) and cold (ρ_c) density values are subtracted in the following equation to calculate swelling.

$$\Delta V = \frac{\rho_c - \rho_h}{\rho_h}$$

The standard deviation of calculated swelling is estimated to be 0.1%, according to the following equation of error estimation.

$$(A \pm a) - (B \pm b) = (A - B) \pm \sqrt{a^2 + b^2} \quad , \qquad (2)$$

where ± represents the accompanied error, and assuming $\rho_c \simeq \rho_h$. It is clear that the accuracy of the swelling calculation depends directly on the accuracy of the density measurement. The control program which also calculates the density values includes many environmental corrections, such as the air temperature, the humidity of the air, the atmospheric pressure, and the temperature of the immersion liquid. In this program, the temperature of the immersion liquid is considered to affect the density calculation through the density change of the immersion liquid. Although the program has a correction formula for the calculated density due to the liquid temperature instability (see Appendix), it was our experience that during these density measurements, the data obtained were much affected by the zero-drift of the microbalance. Sometimes the zero-drift during the measurement procedure for a single disk reaches an unacceptable level, especially when the temperature stability of the liquid is not good.

Table 1. Density data of F29 (control)

Date	Environment Conditions					
	Temperature of Air (°C)	Humidity (%)	Atmosphere (mm•Hg)	Temperature, °C		Density (g/cm^3)
				of Cell	of Liquid	
8/17/89	23.7404	50.8387	742.0961	21.2260	20.8580	7.9162
8/17	23.4327	50.6862	742.4749	21.1950	20.8450	7.9142
8/17	23.7644	50.1298	742.3631	21.2120	20.8600	7.9208
8/23	23.5777	52.3186	742.9489	21.2440	20.8470	7.9079
8/23	23.9764	52.7312	742.2371	21.2600	20.8730	7.9210
8/23	24.0674	54.3017	741.3033	21.2620	20.8470	7.9128
8/25	23.3712	53.2282	742.1456	21.2120	20.8390	7.9159
8/25	24.4551	52.1338	741.2627	21.2980	20.8800	7.9183
8/28	23.9706	52.3387	744.2833	21.3050	20.8740	7.9056
8/28	24.3916	53.5590	743.5362	21.3240	20.8850	7.9068

To examine the effect of the liquid temperature on the obtained density data, the obtained density data were plotted against the liquid temperature in Fig. 1 and both data were processed by the least squares method to determine the relationship between these two sets of data. The resultant approximation

line is also included in Fig. 1. The result, however, shows that there is no relationship beyond their statistical scattering between the temperature of the immersion liquid and the obtained density data.

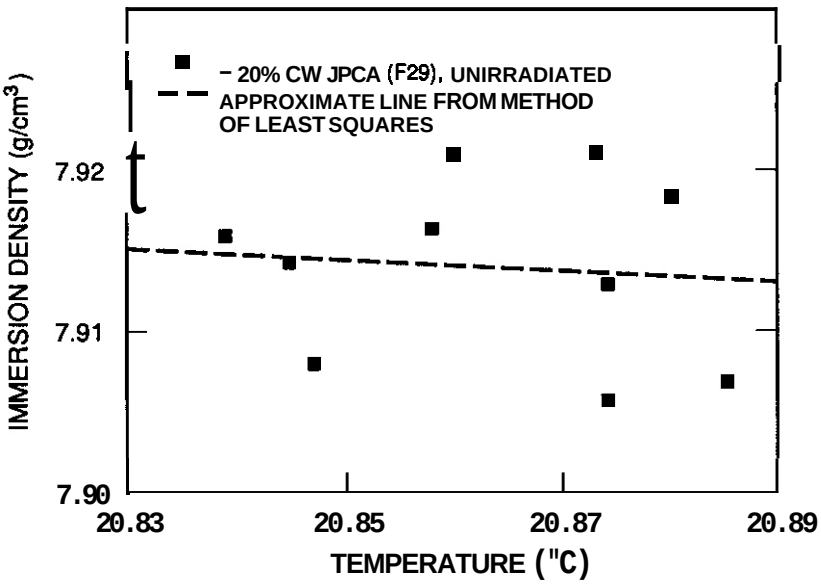

Fig. 1. A plot of F29 density data as a function of liquid temperature.

Nevertheless, the zero-drift experienced by the microbalance during the measurement, whatever the cause, can introduce an appreciable error in density calculation, where the specimen density is determined by the comparison of the wet and dry weights of the specimen. In normal operation, the time period from zero re-set of the microbalance to the dry-weight measurement was 30 s, while 40 s elapsed between the dry-weight and the wet-weight measurements. The recorded zero-drift of the microbalance throughout a single run occasionally exceeded a certain level (currently 0.007 mg), which signals an unsuccessful measurement. The density data obtained under such a large zero-drift is always discarded. It should be noted that there is no way to monitor the zero-drift of the microbalance while the specimen is passing through the two buckets. Although the accepted data are obtained only in more stable conditions of the microbalance, the minimum zero-drift between dry and wet weight measurements causes an appreciable error in density calculation. About 0.001 mg of zero-drift occurring between dry and wet weight measurements will cause a 0.03% error in the density data of stainless steel (*see* Appendix). The precision densitometer has an excellent level of accuracy considering the very tiny size and mass of a TEM disk specimen. Further improvement of accuracy is possible, however, only through further control of the zero-drift of the microbalance.

FUTURE WORK

For improved accuracy of the data and better efficiency of measurement, the following experiments are expected:

1. The zero-drift behavior of the microbalance will be examined. It has been noted that the zero-drift is caused by the environmental instability, but the relationship is not clear. An attempt to characterize and control this instability will be initiated.

2. Zero-drift correction in the density calculation will be attempted. The zero-drift affects the error of density data most severely when it occurs between the dry and wet weight measurement, though it cannot be measured at that point. An effort to derive an equation for quantifying this drift will be made. The equation will then be utilized in the computer data acquisition and analysis program.

REFERENCES

1. R. A. Buhl and L. J. Turner, Remote Controlled Imnersion Densitometer, Oak Ridge National Laboratory Report ORNL/TM-10378 (to be published).

2. P. J. Maziasz, J. L. Scott, L. J. Turner et al., p. 188 in FRM Semiannu. Prog. Rept. March 31, 1987, DOE/ER-0313/2, USDOE Office of Fusion Energy.

3. R. E. Stoller, P. J. Maziasz, A. F. Rowcliffe, and M. P. Tanaka, J. Nucl. Mater. 155-157 (1988) 1328.

APPENDIX

The temperature of the immersion liquid can affect the following equation of density calculation through the density change of the immersion liquid:

$$\rho_t = \frac{\rho_l W_d - \rho_a W_w}{W_d - W_w} \tag{3}$$

where ρ_t is the density of the specimen, W_d and W_w are the dry and the wet weights of the specimen, respectively, ρ_l is the density of the immersion liquid, ρ_a is the density of the air. And ρ_l is calculated by the following equation using the liquid temperature, T, measured by thermistor,

$$\rho_l = \rho_{l0} + a \cdot T \quad , \tag{4}$$

where ρ_{l0} and a are the constants specific to the immersion liquid and the following values are used in this program:

ρ_{l0} = 1.918
a = −0.00218

Assuming ρ_a is close enough to zero, Eq. (3) can be modified in the following equation:

$$\rho_t = \frac{\rho_l W_d}{W_d - W_w} \quad . \tag{5}$$

The density change of the imnersion liquid, ρ_l, in the temperature range from 20.83 to 20.89°C is 0.007% according to Eq. (4). Typical values of W_d and W_w for the TEM disk of austenitic stainless Steel are 14 and 11 mg, respectively. So 0.001 mg error in $(W_d - W_w)$ caused by the zero-drift of the microbalance is 0.03%. According to Eq. (3), this error affects the calculation of the ρ_t proportionally.

2. DOSIMETRY, DAMAGE PARAMETERS, AND ACTIVATION CALCULATIONS

DAMAGE PARAMETERS FOR CANDIDATE FUSION MATERIALS IRRADIATION TEST FACILITIES

D. G. Doran (Pacific Northwest Laboratory), F. M. Mann (Westinghouse Hanford Company), and L. R. Greenwood[a] (Pacific Northwest Laboratory)[b]

OBJECTIVE

The purpose of this work was to begin a consistent comparison of candidate concepts for an International Fusion Materials Irradiation Facility (IFMIF) as recommended by the IFMIF Evaluation Panel. A particular concern is the acceptability for fusion studies of appreciable neutrons above 14 MeV.

SUMMARY

A comparison was made of damage parameters for carbon, iron, and molybdenum trradiated in spectra for d-Li, spallation, and beam-plasma (d-t) neutron sources and a reference DEMO first wall spectrum. The transmutation results emphasize the need to define the neutron spectra at low energies; only the DEMO spectrum was so defined. The spallation spectra were also poorly defined at high neutron energies; they were too soft to produce the desired gas production rates. The treatments of neutron-induced displacement reactions were limited to below 20 MeV and transmutation reactions to below 50 MeV by the limited availability of calculational tools. Recommendations are given for further work to be performed under an international working group.

PROGRESS AND STATUS

Introduction

It is recognized worldwide that an intense source of fusion energy neutrons is needed to evaluate candidate fusion materials. Several concepts for an International Fusion Materials Irradiation Facility (IFMIF) were described and evaluated at a workshop held in San Oiego in Feb. 1989.' This workshop was held at the request of the Executive Committee of the IEA Implementing Agreement on R & D on Radiation Damage to Fusion Reactor Materials. The Evaluation Panel recommended that three neutron source concepts--Beam-Plasma, D-Li, and Spallation--be developed further.*

The Beam-Plasma concept, developed by Lawrence Livermore National Laboratory (LLNL), is based on a mirror-type plasma machine fueled with tritium and subjected to intense deuteron beams injected perpendicular to its axis.[3] The D-Li source, proposed by the Los Alamos National Laboratory (LANL), is an upgrade of the FMIT (Fusion Materials Irradiation Test facility designed at Hanford and Los Alamos but never constructed[4]) design in which neutrons are produced by one or more 35 MeV deuteron beams incident on one or more flowing lithium targets. The conceptual spallation source, EURAC (European Accelerator), proposed at the workshop by the Institute of Nuclear Fusion (INF) of the Polytechnic University of Madrid, generates neutrons with a 600 MeV proton beam incident on a liquid lead target. Both of the accelerator-based sources, D-Li and spallation, produce neutrons above the 15 MeV upper limit of a fusion device, i.e., "high energy tails".

The Evaluation Panel also recommended that the radiation effects community develop descriptions of the radiation environments of these sources "on a consistent basis" as a prelude to a critical examination of how well each source can simulate the environment of a fusion reactor. The Executive Committee subsequently requested one of the authors (DGO) to attempt to implement this recommendation. The objective of this report is to discuss the status of this work.

This study is concerned only with the comparison of damage parameters among the several sources; facility comparisons in terms of test volume, accessibility, reliability, etc. are outside its scope.

Bases for Neutron Source Comparisons

Neutron source comparisons can be made on the basis of neutron fluxes, neutron spectra, primary recoil spectra, damage energy or displacement rates, and transmutation species and rates. However, the Evaluation Panel concluded that each source is capable, in principle, of generating sufficient flux for fusion materials studies, so flux and damage rates, i.e., source strengths, will not be compared in the present study, We will concentrate on spectral comparisons, in terms of the neutron spectra themselves or the following derived spectral-averaged quantities: damage energy or displacement cross sections, transmutation cross sections, and recoil spectra. In addition, the fluence dependence of transmutation production will be examined.

(a) Work performed at Argonne National Laboratory.
(b) Pacific Northwest Laboratory operated for U.S. Department of Energy by Battelle Memorial Institute under Contract DE-AC06-76RLO 1830.

The sources of the neutron spectra used in this study and some of their characteristics are described briefly in Tables la and lb. Some comparisons are given in Figure 1. Neutron spectra were solicited from LLNL for the beam-plasma source, from LANL for the D-Li source, and from the Paul Scherrer Institute (PSI) and the INF for a soallation source.

Table 1A

Neutron Spectra Used in this Work

SPECTRUM	CALC. BY	REFERENCE	CODE USED	NO. OF GROUPS	TOTAL FLUX	PROVIDED BY
DEMO, 1ST WALL	Culham	CLM-R-254 1985	?	100	1.41e+15 n/cm2-s	Ehrlich, KfK
BEAM-PLASMA						
Plasma edge, 8 cm	Kawabe & Sagawa Tsukuba U.	none	ANISN	27		Coensgen, LLNL
Al, 21.5-22.3 cm					8.8e+14 n/cm2-s?	
Al, 21.5-51.5 cm					14.9e+14 n/cm2-s?	
0-Li, 2-250 mA beams at 90 deg.	Varsamis, LANL	IFMIF rept. TBP Nucl. Sci. Eng.	FMITSP (Mann)	50 (1 MeV)		Lawrence, LANL
8.5 cm from vertex					5.45e+14 n/cm2-s	
14 cm from vertex					5.27e+14 n/cm2-s	
T-H (21 MeV tritons)	Cierjacks, KfK	IFMIF rept. TBP Nucl. Sci. Eng.	?	28	1.04e+13 n/cm2-s	Ehrlich, KfK
SPALLATION						
520 MeV p on Pb, 90 deg at targ. face	Pepin, 1982	ANL-82-80 1982	HET, 05R	28	0.846 n/sr-p	Victoria, PSI
600 MeV p on Pb w/ Pb reflector Z=3.75, R=1.3 cm	Atchison & Fischer, PSI	none	HETC	35	0.127 n/cm2-p	Perlado, Madrid

Table 1B

Characteristics of Neutron Spectra Used in this Work

SPECTRUM	FRACTION OF FLUX ABOVE: 100 MeV	20 MeV	15 MeV	13.5 MeV	1.0 MeV	0.1 MeV	LOWEST ENERGY GROUP
DEMO	0	0	0	0.126	0.28	0.56	0 - 0.41 eV
BEAM-PLASMA							
w/o reflector	0	0	0	0.95	0.98	0.997	0 - 0.02 MeV
wlreflector	0	0	0	0.56	0.66	0.84	0 - 0.02 MeV
0-Li							
14.0 cm from vertex	0	0.12	0.49	-	.94	?	0 - 1 MeV
8.5 cm from vertex	0	*0.10*	0.37	-	.90	?	0 - 1 MeV
T-H	0	0	0	0.23	0.90	?	0 - 1 MeV
SPALLATION							
520 MeV (Pepin)	.004	0.04	0.05	-	0.52	0.95	0.001 - .01 MeV
600 MeV (Perlado) R = 1.3 cm	<.003	0.008	0.014	-	0.42	?	0.4 - 0.6 MeV

Two beam-plasma spectra at the edge of the plasma (8 cm radius), with and without an aluminum reflector (inner radius 21.5 cm, outer radius 51.5 cm) were received from Livermore; they were calculated at Tsukuba University.

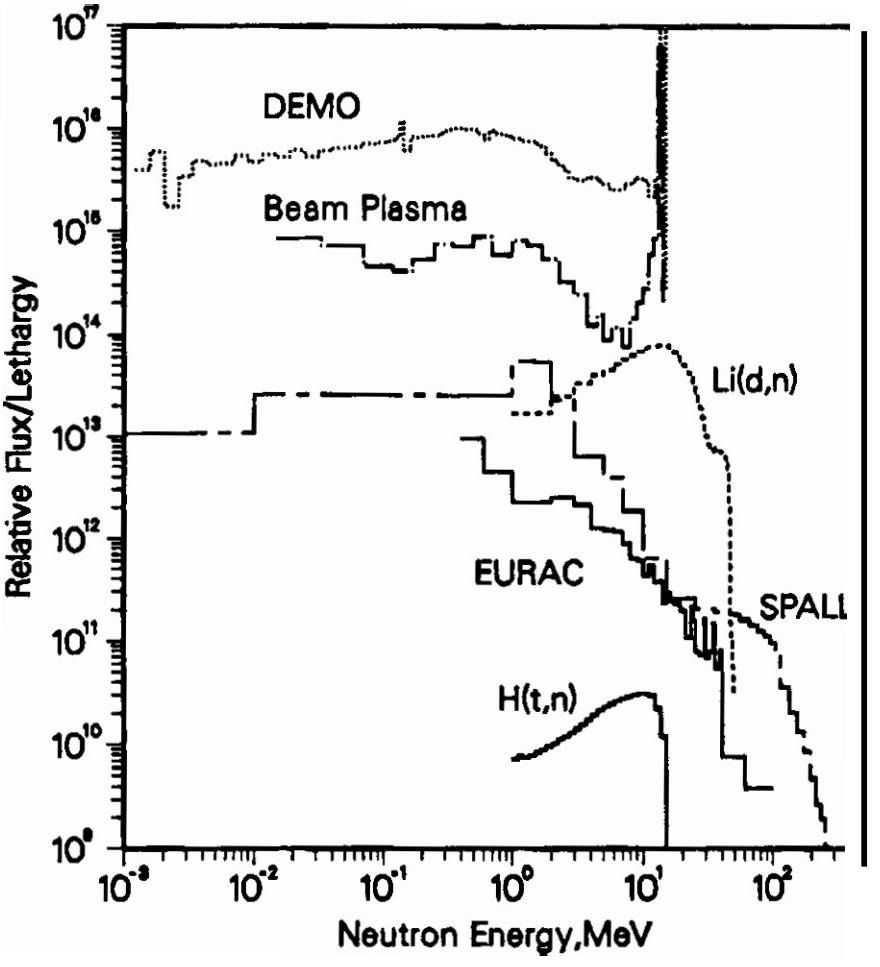

FIGURE 1. Comparison of Neutron Spectra; Curves have been Shifted Arbitrary Amounts for Clarity.

Two D-Li spectra, both uncollided but for different locations in a configuration featuring two accelerator/target systems at 90 deg, were received from Los Alamos. The locations are in the plane of the two beams and along the axis of symmetry between the two targets. Point 1 is 14 cm from the vertex, which is at the virtual intersection of the two beams, Since the highest energy neutrons are emitted in the forward direction, this location illustrates a hard spectrum. Point 2 is 8.5 cm from the vertex, illustrating a somewhat softer, higher flux location.

Two spallation spectra have been examined to date. One, provided by M. Victoria, PSI, is from a published calculation by Pepin (using the HET and 05R codes)[5] for an experimentally realizable configuration. It is for the neutron spectrum at, and 90 degrees to, the curved face of a 15 cm diameter cylindrical lead target bombarded by 520 MeV protons. The other, one of several provided by J. M. Perlado, INF, is from a calculation with HETC for the proposed EURAC in which a finely focused beam of 600 MeV protons is incidenton a one cm wide lead target surrounded by a lead reflector. It corresponds to a specimen located within a centimeter of the liquid lead target. The spectrum is quite soft as shown in Table Ib.

At the IFMIF workshop, the suggestion (attributed to S. Cierjacks) was made that a facility based on a triton beam impinging on a hydrogenous target should be considered, referred to hereafter as a T-H source. A triton energy of 21 MeV would produce a neutron spectrum with a maximum energy of 14 MeV. A T-H source spectrum provided by Kernforschungszentrum Karlsruhe (KfK) has been included in this study.

KfK also provided a first wall spectrum for the conceptual Culham DEMO reactor [6] to be used as a reference case.

None of the spectra received, other than DEMO, provide spectral definition below a few tenths MeV. None of the calculations take account of spectral perturbations by test assemblies. Because each spectrum (or set of spectra) was provided by a different source, no uniformity of accuracy can be assumed.

A primary source of difficulty in making the desired source comparisons is that the neutron energy range covered by the sources extends from thermal to hundreds of MeV. It is convenient here to identify three energy regions: thermal to a few tens of keV, less than 20 MeV, and greater than 20 MeV. The lowest energy range is of interest because neutron absorption cross sections can become very large with decreasing neutron energy, leading to high transmutation rates. Furthermore, this region produces low energy displacement cascades for which residual defect production efficiencies are high.

Twenty Mev is the upper limit of the Evaluated Nuclear Data Files (ENDF/B) used in the U.S. and many other countries (major data files developed in other countries are also limited to 20 MeV or lower). Evaluated cross sections above 20 MeV are rare, so most high energy applications require the use of calculated nuclear data. This introduces uncertainties in both the calculation of neutron spectra at high energies, and the calculation of derived damage parameters at high energies.

More importantly, the nuclear interaction processes change in character as the energy is increased above 20 MeV to hundreds of MeV. Neutron reactions in the MeV range are dominated by elastic and inelastic events that produce neutrons or nuclei of hydrogen and helium. A wealth of nuclear data in this range means most uncertainties are relatively small. At 100 MeV, on the other hand, spallation and fission reactions occur that produce many more atomic species, ranging up to the atomic number of the target nucleus. Few data exist in this region and model calculations are computer intensive, hence expensive.

The planned approach for this study was to combine the various spectra with appropriate cross sections to determine spectral-averaged cross sections for the production of primary recoil spectra, displacement damage, and transmutations. Recent nuclear model calculations at Los Alamos to 100 MeV for iron, molybdenum, and carbon were originally thought to be available for this study. However, we found that the complete data needed to calculate displacement damage was not available. Therefore, it was necessary to estimate the displacement damage energy due to neutrons above 20 MeV.

Transmutation files, on the other hand, are available to 50 MeV in the transmutation and activation code REAC*2,[7] developed originally for FMIT applications. The high energy data for Fe have been subject to evaluation so are probably more accurate than those for Mo and C.

Calculations

Displacement Damage. The codes NJOY[8] and SPECTER', both well known, were used to calculate displacement damage and primary recoil spectra, respectively. For the former, the displacement cross section above 20 MeV, the upper limit of the evaluated nuclear data files, was assumed constant leading to a small underestimate. Better approximations could be made, but this is the least serious computational limitation at present. In calculating recoil spectra, the neutron spectra were truncated at 20 MeV. This distorts the shape of the recoil spectrum somewhat and, of course, fails to indicate the highest energy recoils. Although the number of neutrons above 20 MeV is small (see Table 1b), this calculation should be redone with a different code as suggested below. However, it is of interest to note that the consensus of the present workshop was that the major concern regarding high energy tails is transmutations, not effects of high energy recoils.

Transmutations. The code REAC*2 was used to calculate transmutations for iron, molybdenum, and carbon. The few neutrons above 50 MeV (see Table 1b) in the spallation spectra were ignored. Because transmutation production may be nonlinear due to the production of daughter nuclides, the calculations were carried out to 1000 days for the DEMO case, with output at 100 day intervals. The other spectra were run to the same total damage energy, corresponding to 80 displacements per atom (dpa) in iron.

Recoil Spectra. Recoil spectra files (based on ENDF/B-V nuclear data" and the DISCS code") are contained in SPECTER for neutrons below 20 MeV. SPECTER was used here to calculate complete recoil spectra in Fe, Mo, and C for the DEMO, Beam-Plasma, and H-T cases, i.e., those having no neutrons above 20 MeV . It was also used to estimate recoil spectra for one D-Li and one spallation spectrum, ignoring neutrons above 20 MeV. The authors did not have access, in the time available, to an operating version of a code incorporating intranuclear cascade and fission models that in principle is capable of calculating recoil spectra (and transmutation production) at high neutron energies. (Both recoil and transmutation results are included in published descriptions of EURAC, but documentation of the calculations has not been available to the authors.)

RESULTS AND DISCUSSION

Displacement Damage

Spectral-averaged damage energy cross sections are summarized in Table 2. At low Z (carbon), the cross section increases with decreasing energy below a few MeV which keeps the variation among neutron sources

Table 2

Spectral-Averaged Damage Energy Cross Sections (keV-barns)

SPECTRUM	C	Fe	Mo
DEMO	31	66	67
B-P	41	271	245
B-P w/refl	40	188	171
D-Li, Pt.1	44	240	241
D-Li, Pt.2	45	220	223
Spall (Pepin)	51	81	89
Spal1 (Perlado)	49	55	63
T-H	41	182	182
14 MeV (monoenergetic)	41	293	265
20 MeV (monoenergetic)	49	319	351

Table 3A

Transmutations (APPM) in Iron for 1000 Day Demo Equivalent Exposure (ip dpa iron)

ELEMENT	DEMO 1st WALL	BEAM-PLASMA W/O REFL.	BEAM-PLASMA WIREFL.	0-Li 14 cm	D-Li 8.5 cm	T-H	SPALL. PEPIN	SPALL. PERLAOO
OPA	80	80	80	80	80	80	80	80
H	4880	7520	6060	6980	5840	2260	2180	1390
H/DPA	61	94	76	87	73	28	27	17
He	700	1150	930	1210	1040	473	455	232
He/DPA	8.8	14.4	11.6	15.1	13	5.9	5.7	2.9
Ti	0.3	0.6	0.4	3.4	4.1	0.1	1.4	0.4
V	70	109	86	110	110	56	76	27
Cr	932	1300	1020	1565	1410	1140	494	300
Mn	4620	5430	3570	6420	5270	1180	1710	995
Fe								
co	10	0.7	0.9	0.6	0.6	0.3	0.5	1.2
Ni	0.1		-	-	-	-		

Table 3B

Transmutations (appm) for Molybdenum for 1000 Day Demo Equivalent Exposure (80 dpa iron)

ELEMENT	DEMO 1st WALL	BEAM-PLASMA W/O REFL.	BEAM-PLASMA W/REFL.	D-Li 14 cm	0-Li 8.5 cm	T-H	SPALL. PEPIN	SPALL. PERLAOO
OPA	54	48	49	54	54	53	59	61
H	7440	3170	2540	4400	3840	780	1830	760
H/DPA	138	66	52	82	71	15	31	12
He	2100	888	711	809	706	192	296	130
He/DPA	39	18	15	15	13	4	5	2
Sr	118	29	19	55	50	8	3.8	2.7
Y	1360	569	450	370	320	95	133	53
Zr	2100	900	729	1010	909	302	480	200
Nb	7510	3230	2590	4510	3870	534	1820	760
Mo								
Tc	14900	6310	5740	2950	2540	1890	1680	3100
Ru	15	6.6	150	16	24	32	200	480

Table 3C

Transmutations (appm) in Carbon for 1000 Day Demo Equivalent Exposirue (EO dpa iron)

ELEMENT	DEMO 1st WALL	BEAM-PLASMA W/O REFL.	BEAM-PLASMA W/REFL.	D-Li 14 cm	D-Li 8.5 cm	T-H	SPALL. PEPIN	SPALL. PERLADO
DPA	50	16	23	20	22	24	67	95
H	8.4	9.3	7.3	1700	1520	0.6	920	310
H/DPA	0.2	0.6	0.3	87	70	0.02	14	3.3
He	12100	21100	17000	16700	14000	5720	439	2580
He/DPA	243	1300	743	854	642	236	7	27
Li	0.8	1	0.8	4	4.2	1.6	8.9	6.7
Be	1630	2590	2130	2110	1940	2000	660	510
B	-	-	-	1600	1460	-	910	300
C								

small. The cross sections for Fe and Mo are essentially the same, leading to one-third fewer displacements for Mo at a given fluence if effective displacement threshold values of 40 eV and 60 eV are used for Fe and Mo, respectively.

Transmutations

The results of transmutation calculations, carried to a level of damage energy equivalent to 1000 days in DEMO (8 keV-barn or 80 dpa for Fe) for each spectrum, are summarized in Table 3. The ratios of appm He/dpa and appm H/dpa are included. For Mo, all sources are lower than DEMO by as much as a factor of 11. This unexpected result is apparently caused by the production of Mo-93 which has an anomalously high (n,alpha) cross section.

Hydrogen and helium production show similar trends for Fe and Mo; again the higher hydrogen production in Mo is unexpected and is traced to Mo-93. In carbon, however, we find a large increase in hydrogen production in the higher energy spectra where (n,px) reaction thresholds are exceeded. Such spectral effects are, of course, element specific.

The major solid transmutation products in iron are Mn and Cr, which reflect the dominance of (n,p) and (n,alpha) threshold reactions and the softness of several of the spectra. The production of Ti is anomalously high in the D-Li spectra. The production of Co is unexpectedly high in DEMO because of neutron capture in the low energy tail (although the quantity is negligible). A similar effect is seen with the production of rather large concentrations of Tc in Mo exposed to the DEMO spectrum. This illustrates the importance of careful definition of the low energy portion of the source spectra. Furthermore, this region will be sensitive to the configuration of material in and near the test volume. (When such characterization is done, a further problem may be revealed with spallation spectra that range from hundreds of MeV down to eV. This is the production of nuclides by the high energy neutrons for which thermal and epithermal absorption cross sections are unknown and extremely difficult to calculate. This would create further uncertainties in transmutation rates.)

In this work, only the DEMO first wall spectrum is well characterized at low energies. No spectral detail below a few tenths MeV was provided for most of the other cases (see Table 1b).

In carbon, the high production of boron in the high energy spectra corresponds to the high production of hydrogen mentioned earlier by above-threshold neutrons.

Recoil Spectra

Some examples of calculated recoil spectra for various neutron spectra are compared in Figs. 2-6. Only the energy dependence, i.e., the shapes of the curves, is relevant; the magnitudes are auite arbitrary. The Beam-Plasma w/Reflector case (Figure 2) agrees well with DEMO above a few tenths MeV for all three elements, as would be expected. A modification of the reflector could probably increase the low energy tail to give better agreement at lower energies.

The shape of the D-Li (Point *2)* recoil spectra also agree rather well with DEMO from a few tenths MeV to the upper limit of DEMO (see Figure 3 for Fe), except for a high energy deviation for carbon (Figure 4). A proper calculation for the 0-Li spectrum would extend the high energy tail to perhaps 6 MeV, but at very low magnitude. The corresponding neutron spectrum has 11%neutrons above 20 MeV, only 2% above 30 Mev.

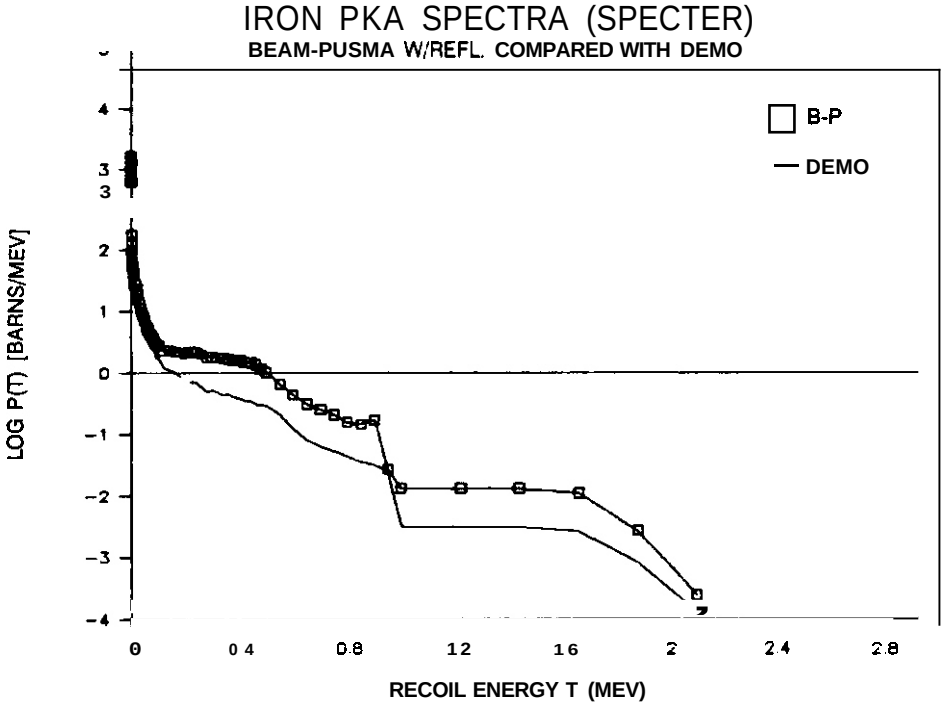

FIGURE 2. **Comparison of the Iron PKA Spectrum for the Beam-Plasma Source (with Al reflector) with that for the DEMO First Wall.**

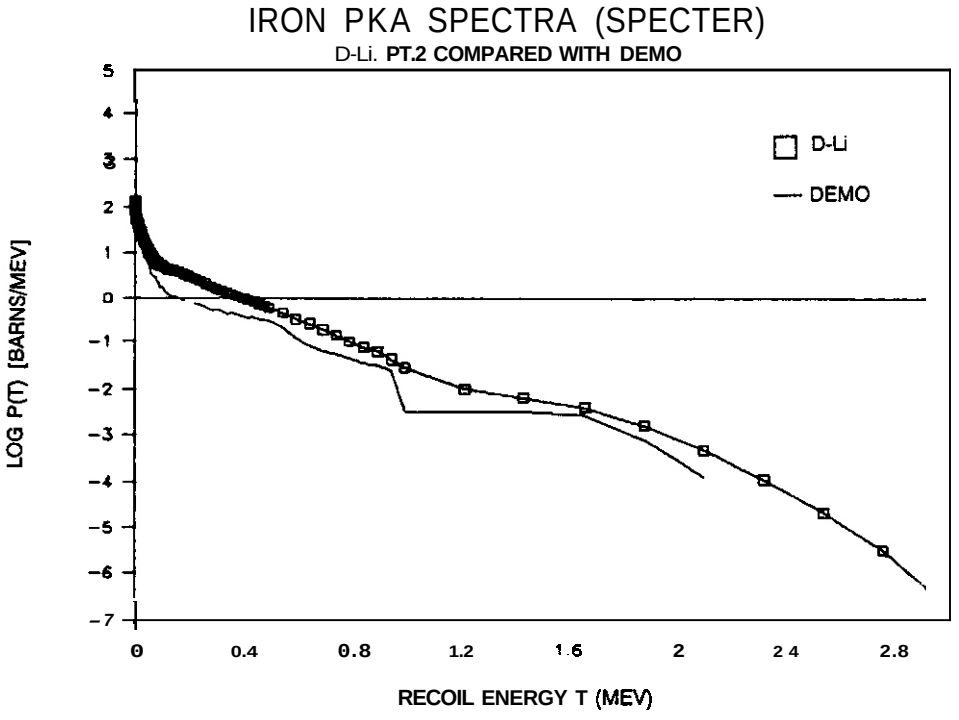

FIGURE 3. **Comparison of the Iron PKA Spectrum for the D-Li Source (pt. 2 at 8.5 cm) with that for the DEMO First Wall.**

To help illustrate the energy dependence, recoil spectra for monoenergetic neutrons at 14 and 20 MeV are compared in Figure 5. From a damage simulation perspective, the main difference is the 2-3 MeV recoils that are present only in the 20 MeV case. But these constitute less than 0.1% of the total number of recoils and account for only a few tenths percent of the displacements.

We are unable to make good comparisons of spallation recoil spectra at this time, as explained above. The result of a SPECTER calculation for Fe for Pepin's spectrum, ignoring neutrons above 20 MeV, is shown in Figure 6. The recoil spectra for Fe and Mo decrease more rapidly with energy than the DEMO spectra. The agreement is somewhat better for C.

The T-H case also agrees well with DEMO above 0.4 MeV. At lower energies, it decreases with decreasing energy much faster than DEMO.

INTERIM CONCLUSIONS

It is no surprise to find that the beam-plasma source promises the best simulation of a D-T reactor. Large discrepancies with certain DEMO transmutation rates may exist, however, depending on the shape of the very low energy end of the neutron spectrum. Of course, first wall spectra vary also, depending on the choice of coolant and blanket materials, which suggests that a range of reference spectra might be appropriate for future calculations.

All candidate spectra need better definition at low energies.

While only three elements have been examined (the transmutation calculations are presently being extended to other elements), some interesting discrepancies among transmutation rates in the various sources have been revealed, emphasizing that these comparisons may be very element specific.

For this comparative study, it is important to determine which region of the neutron spectrum is producing a particular transmutation product.

Both of the specific spallation spectra studied are too soft to provide the high gas production rates required of an IFMIF; harder spectra can be obtained, however, from a spallation source.

RECOMMENDATIONS

1. It is important to determine whether either of the spallation spectra used here are representative of those expected from a well-defined spallation neutron irradiation facility. It remains to be seen whether an appropriate compromise exists between an overly hard spectrum, producing unwanted spallation products, and an overly soft spectrum that produces too little of the desired transmutation products.

2. The inadequate treatment of neutrons above 20 MeV, including the lack of evaluated nuclear data in this region, is the most obvious shortcoming of the present calculations. If a spallation source is to be evaluated, calculations with the HETC code[12] (or equivalent) are needed. Transmutation calculations need to be tested. Some relevant experiments at LAMPF have been performed by a PSI/Risø/LAMPF collaboration and analyses are in progress. These results, and earlier results obtained in an ANL/LAMPF collaboration, should be compared with concentrations predicted by a state-of-the-art code.

3. While such a code would be applied to D-Li spectra also, it is not considered essential. More important is to make sure that current knowledge of cross sections in the 20 to 40 MeV range is incorporated into NJOY (or equivalent), and any important missing data is supplied by calculation or experiment.

4. Better definition of candidate IFMIF neutron source spectra is needed in the thermal and epithermal region if meaningful transmutation calculations are to be made.

5. More realistic beam-plasma spectra are needed, although it seems clear that such a source can satisfactorily mimic neutron environments in a D-T reactor.

6. A decision on the feasibility of a T-H source is needed to justify continued inclusion of this interesting concept in these comparative studies. If positive, more rigorous spectra are needed.

7. A range of reference fusion reactor spectra should be considered to allow for different cooling and blanket materials.

8. A small international working group should be established to pursue source characterizations/comparisons. This group would be concerned with the spectral definition phase through the calculation of various damage parameters. It should include those responsible for neutronics calculations for each candidate squrce, and specialists on nuclear data, damage parameters, code verification, and reactor experimentation.

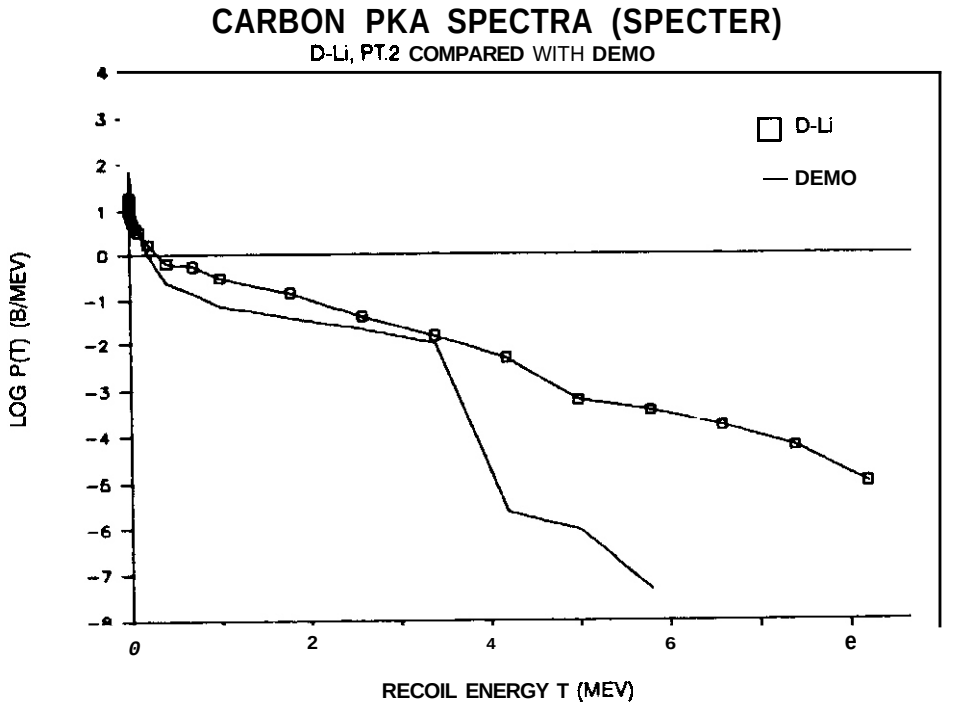

FIGURE 4. Comparison of the Carbon PKA Spectrum for the D-Li Source (pt. 2 at 8.5 cm) with that for the DEMO First Wall.

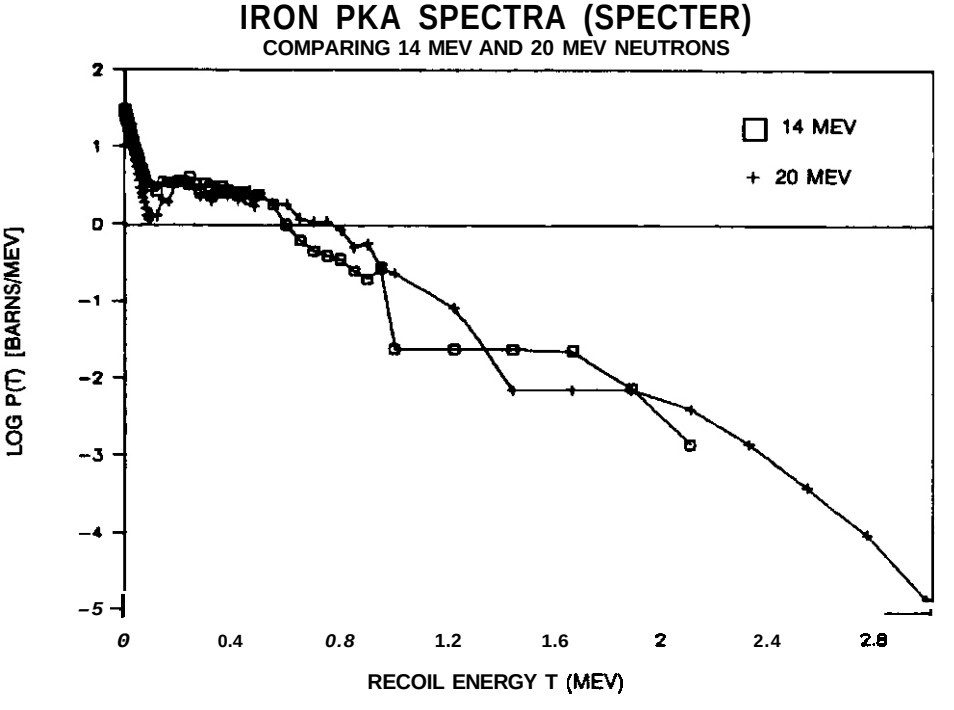

FIGURE 5. Comparison of Iron PKA Spectra for 14 and 20 MeV Monoenergetic Neutrons

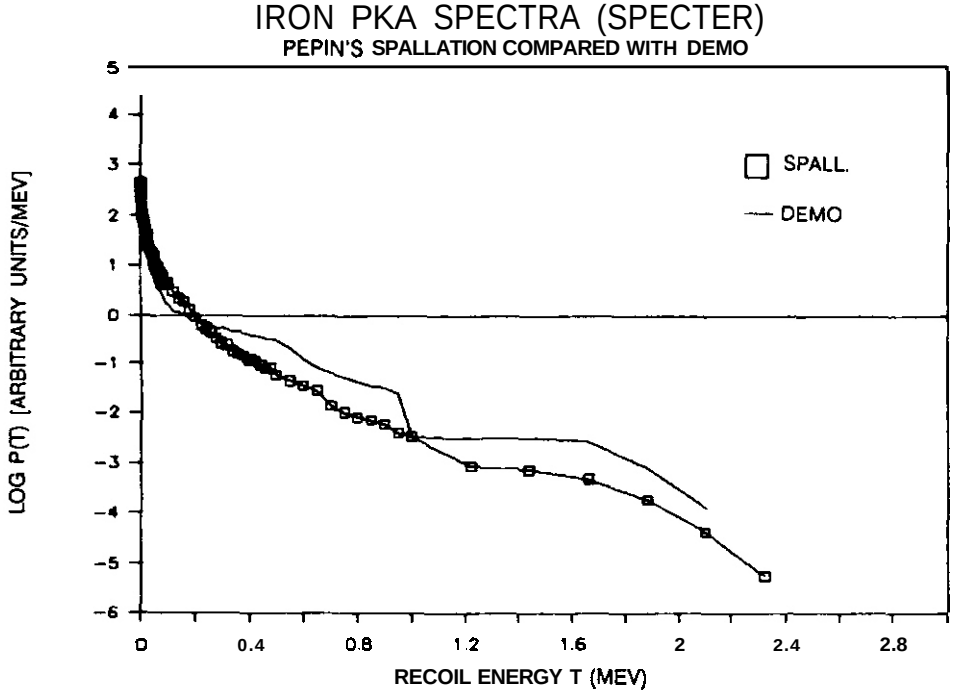

FIGURE 6. Comparison of the Iron PKA Spectrum for Pepin's Spallation Source with that for the DEMO First Wall.

FUTURE WORK

The IEA is currently establishing an international working group to continue this work. The scope will include the definition of potential IMFIF experiments and specimen matrices to aid in the further development of IFMIF concepts.

REFERENCES

1. The technical portion of the International Fusion Materials Irradiation Facility (IFMIF) Workshop is to be published in a special issue of the J. Fusion Energy.

2. Evaluation Panel Report, Vol. 1 of the report of the International Fusion Materials Irradiation Facility (IFMIF) Workshop, can be obtained from R. Verbeek, CEC, DG XII/Fusion, 200 Rue de la Loi, 8-1049 Bruxelles, Belgium.

3. See detailed descriptions of all the neutron sources in Ref. 1 and a special issue of Nucl. Sci. and Eng., to be published.

4. A. L. Trego, et al., "Fusion Materials Irradiation Test Facility: A Facility for Fusion Materials Qualification", Proc. of 5th Top. Mtg. on Tech. Fusion Energy, Knoxville, TN, April 1983.

5. M. Pepin, "Monte Carlo Study of the Energy Deposition of a Flux of Spallation Neutrons in Various Samples", in ICANS-VI, Proceedings of the Sixth Meeting of the International Collaboration on Advanced Neutron Sources, Argonne National Lab., June 28-July 2, 1982, ANL Report ANL-82-80, Jan. 1983.

6. L. J. Baker, et al., Culham Report CLM-R-254, 1985.

7. F. M. Mann, et al., "REAC Nuclear Data Libraries," Proc. International Conference on Nuclear Data for Basic and Applied Science, Sante Fe, NM, May 1985.

8. R. E. Macfarlane, D. W. Muir, and F. M. Mann, J. Nucl. Mat. 122 & 123 (1984) 1041.

9. L. R. Greenwood, ibid., p. 1011.

10. R. Kinsey, Compiler, "ENDF/B Summary documentation (ENDF-210), 3rd ed. (ENDF/B-V), BNL-NCS-17451, Brookhaven National Laboratory, Upton, NY, 1979.

11. G. R. Odette and D. R. Dorian, Nucl. Tech. 29 (1976) 346.

12. T. W. Armstrong and K. C. Chandler, Nucl. Sci. Eng. 49 (1972) 110.

NEUTRON WSIMETRY AND DAMAGE CALCULATIONS FOR THE ORR-MFE6J EXPERIMENT - L. R. Greenwood and D. V. Steidl (Argonne National Laboratory)

OBJECTIVE

To provide dosimetry and damage analysis for fusion reactor materials irradiation experiments.

SUMMARY

Neutron fluence measurements and damage calculations have been competed for the joint U.S.-Japanese MFE 65 experiment in the Oak Ridge Research Reactor. Specimens were irradiated from June 28, 1983 to March 26, 1987 (475 full power days) in position C7 at temperatures of 60 and 200°C,. The average neutron fluence was 2.40×10^{22} n/cm^2 (8.8×10^{21} >0.1 MeV) resulting in 6.9 dpa and 75 appm helium in 316 stainless steel. Radial fluence and damage gradients of ±10% were determined across the assembly.

PROGRESS AND STATUS

The MFE-6J and 7J[1,2] experiments were designed to use the spectral tailoring technique developed for the MFE-4A/4B[3] irradiations in ORR. The dual irradiations were designed to test structural alloys and a wide variety of research alloys at temperatures of 60 and 200°C in 6J and at 300 and 400°C in 7J. The spectral tailoring technique was designed to start with a water filled core piece, switch to a solid aluminum core piece, and finally to add a hafnium liner. This procedure is designed to produce the desired fusion ratio of helium to displacement damage in stainless steel. Only the first phase of the experiment was completed due to the closure of ORR in March 1987. The net exposure was 341,806 MWD or 475 full power days at 30 MW.

Six dosimetry tubes were included in the assembly, four in the outer 60°C region and two in the north and south sides of the inner 200°C region. Each stainless steel dosimetry tube measured 8.5" long by 1/16" O.D. and contained wires of Fe (9 mil), Ti (10 mil), and 0.1% Co-A1 alloy (20 mil). The 60°C tubes were analyzed in March 1989; however, the 200°C tubes were not received until later. Each dosimetry tube was opened and the wires removed in a hot cell. Each wire was then segmented into nine pieces each measuring about 7/8" in length. These segments were then weighed and gama counted.

Due to the long decay times before receipt of the samples, we were only able to detect ^{46}Sc, ^{54}Mn, and ^{60}Co activities. For the 200°C samples, even the ^{46}Sc was difficult to detect resulting in unusually large statistical uncertainties between 2 and 5%. The activation rates were calculated by correcting the counting data for decay during and after irradiation and for gamma self absorption and neutron burnup (<5%). The corrected activation rates are listed in Table I. The results are typically accurate to 2%, except for the 200°C ^{46}Sc results, as noted.

The ^{54}Fe(n,p)^{54}Mn results are plotted as a function of height in figure 1. As can be seen, all of the wires show a similar dependence of activity on the height with the maximum flux position at about -7 cm below midplane, as expected due to the fuel distribution in ORR. These longitudinal flux gradients are rather small with a maximum difference of about 15% between midplane and the bottom ends of the wires. These gradients are well-described by the equation:

$$A(x) = A(0)\ (1. + bx + cx^2) \qquad (1)$$

where A is the activity at height x (cm), b = -1.02×10^{-2}, and c = 7.61×10^{-4}. However, there is also a radial flux gradient, as noted by the compass directions on figure 1. The maximum radial flux difference is about 20%, decreasing from north to south across the assembly. The measured activities are similar to those measured for the MFE 7S experiment[2] as well as for the previous test of the 6J design4 in position C7.

Average, midplane activation rates were used to determine the average neutron fluences, as listed in Table II. The SPECTER[5] computer code was then used to determine the damage parameters listed in Table III. Equation (1) can be used to determine the fluence and damage levels at other heights in the assembly. However, the radial gradients must also be considered. There is no radial effect in the east-west direction across the assembly: however, the fluence and damage rates increase up to 10% going towards the north and decrease up to 10% going towards the south. Since the helium production in nickel is not linear with the fluence, Table IV lists average damage and helium production in 316 stainless steel separately.

The CTR 53 and 54 irradiations were initiated only one month before the suspension of HFIR operations on November 14, 1986. The net exposure was thus only one 22 day cycle resulting in 2026 MWD or 20.26 full power days. The assemblies were irradiated in positions A1 and A4 of the Peripheral Target Position. Similar irradiations in the PTP have been reported previously[1,2].

Work supported by the U.S. Department of Energy, Office of Fusion Energy, under contract W-31-109-Eng-38.

Table I. - Measured Activation Rates for ORR-MFE 6J
(Values normalized to 30 MW: accuracy ±2%, unless noted)

Height, cm[a]	Activation Rate (atom/atom-s) $^{59}Co(n,\gamma)^{60}Co$ (x10-9)	$^{54}Fe(n,p)^{54}Mn$ (x10-11)	$^{46}Ti(n,p)^{46}Sc$ (x10-12)
60°C-West:			
+0.8	6.14	1.28	1.69
-1.4	6.38	1.30	1.74
-3.6	6.37	1.30	1.73
-5.9	6.49	1.32	1.77
-8.1	6.32	1.33	1.74
-10.3	6.39	1.32	1.73
-12.5	6.08	1.29	1.63
-14.8	5.75	1.25	1.62
-17.0	5.37	1.16	1.51
60°C-South:			
+0.8	5.20	1.13	1.48
-1.4	5.37	1.14	1.50
-3.6	5.33	1.17	1.50
-5.9	5.44	1.16	1.50
-8.1	5.45	1.17	1.52
-10.3	5.39	1.17	1.48
-12.5	5.16	1.14	1.44
-14.8	4.98	1.09	1.41
-17.0	4.66	1.04	1.32
60°C-North:			
+0.8	5.75	1.33	1.74
-1.4	5.91	1.38	1.81
-3.6	5.78	1.40	1.84
-5.9	5.98	1.40	1.84
-8.1	5.99	1.40	1.84
-10.3	5.92	1.37	1.82
-12.5	5.63	1.34	1.78
-14.8	5.39	1.27	1.69
-17.0	5.15	1.24	1.66
60°C-East:			
+0.8	5.63	1.27	
-1.4	5.82	1.30	1.67
-3.6	5.87	1.33	1.73
-5.9	5.94	1.31	1.70
-8.1	5.82	1.30	1.71
-10.3	5.86	1.27	1.66
-12.5	5.53	1.24	1.65
-14.8		1.21	1.53
-17.0	4.85	1.14	1.46

Table I. Measured Activation Rates for ORR-MFE 6J (Continued)
(Values normalized to 30 MW: accuracy ±2%, unless noted)

Height, cm[a]	Activation Rate (atom/atom-s) $^{59}Co(n,\gamma)^{60}Co$ (x10-9)	$^{54}Fe(n,p)^{54}Mn$ (x10^{-11})	$^{46}Ti(n,p)^{46}Sc$ (x10^{-12})	
200°C-North:				
+0.8		1.26	1.55	2.5
-1.4	5.51	1.30	1.75	3.4
-3.6	5.61	1.30	1.70	2.8
-5.9	5.71	1.33	1.63	5.0
-8.1	5.74	1.31	1.75	5.9
-10.3	5.68	1.32	1.66	2.6
-12.5	5.64	1.32	1.71	3.1
-14.8	5.41	1.26	1.73	3.8
-17.0	5.10	1.20	1.53	2.8
200°C-South:				
+0.8	5.21	1.16	1.48	3.3
-1.4	5.23	1.20	1.54	4.8
-3.6	5.05	1.20	1.54	2.5
-5.9	5.37	1.24	1.56	2.1
-8.1	5.33	1.24	1.58	2.4
-10.3	5.19	1.21	1.56	2.4
-12.5	5.03	1.18	1.46	4.3
-14.8	4.82	1.13	1.48	3.0
-17.0	4.46	1.07	1.40	4.3

Table II. Neutron Fluences for ORR-MFE 6J
(Radial average of maximum at -7 cm below midplane)

Energy, MeV	Fluence (x10^{21} n/cm^2)	Uncertainty (%)
Total	24.0	8.
Thermal (<.5 eV)	6.71	7.
0.5 eV - 0.1 MeV	8.55	12.
>0.1 MeV	8.76	11.
>1.0 MeV	4.84	12.

Table III. Damage Parameters for ORR-MFE 65
(Radial average of maximum at -7 cm below midplane)

Element		DPA	Helium, appm
Al		11.8	5.3
Ti		7.5	4.1
V		8.3	0.19
Cr		7.5	1.3
Mn		7.9	1.1
Fe		6.6	2.3
co		7.5	1.1
Ni	Fast	7.0	33.
	Thermal	0.9	534.
	Total	7.9	567.
cu		6.4	2.0
Nb		6.4	0.43
Mo		4.7	-
316SS[a]		6.9	75.

[a]316SS: Fe(.645), Ni(.13), Co(.18), Mn(.019), Mo(.026)

Table IV. Average Damage Gradients for 316 SS for ORR-MFE 6J
(DPA includes both fast and thermal effects)

Heiaht.cm	DPA	Helium.appm
0	6.7	71.
-4	6.9	75.
-8	6.9	75.
-12	6.8	73.
-16	6.5	67.
-20	6.0	59.
-24	5.4	49.

Dosimetry packages were inserted at eight heights in each assembly, as listed in Table V. Each aluminum package measured 6.4 mm long by 1.3 mm o.d. and contained small wires of Fe, Ti, Nb, 0.1%Co-Al, and 80.2%Mn-Cu. Each wire was separately gamma counted and the measured activities are listed in Table V. The net uncertainties are typically ±2% except for ^{46}Sc, due to the unusually long decay time prior to receipt of the samples.

These runs were the first where we included Nb dosimeters. The $^{93}Nb(n,\gamma)^{94}Nb$ (20,300 y) reaction results are included in Table V. Work is in progress to measure the $^{93}Nb(n,n')^{93m}Nb$ (16 y) reaction, which is of special interest due to the low energy threshold and long half-life. Thin samples are being prepared for x-ray counting. Absolute counting efficiencies have been determined using the NIST standard reference material (SRM-4267). The data will be used to help adjust the neutron cross sections so that this reaction can be used for routine dosimetry applications.

As can be seen from Table V, the activity results for runs 53 and 54 are nearly identical. The activity gradients with height are very nearly centered at midplane and are well-described by the equation:

$$F(x) = F(0)\ (1. - 1.02 \times 10^{-4}\ x^2) \qquad (1)$$

where F is the activity at height x (cm) and F(0) is the maximum value at midplane. This equation also describes fluence and damage parameter gradients (except for the non-linear reactions with nickel) using midplane values which are given in later tables.

Table V. Activity Measurements for HFIR-CTR-53/54 Experiments
(Values in atom/atom-s at 100 MW; ±2% unless noted)

Height (cm)	$^{59}Co(n,\gamma)^{60}Co$ (x10^{-8})	$^{54}Fe(n,p)^{54}Mn$ (x10^{-11})	$^{55}Mn(n,2n)^{54}Mn$ (x10^{-13})	$^{46}Ti(n,p)^{46}Sc$ (x10^{-12})(±%)	$^{93}Nb(n,\gamma)^{94}Nb$ (x10^{-})
18.8	4.28	5.14	1.55	6.94(8)	1.85
	4.51	4.79	1.40	5.78(6)	1.94
12.5	5.23	6.67	1.96	9.54 (6)	
	5.44	6.20	1.87	8.46(4)	2.44
6.3	6.14	7.34	2.10	9.48 (6)	2.76
	6.67	7.06	2.04	9.75 (6)	2.88
0.0	6.45	7.87	2.34	10.24(8)	2.85
	6.54	7.61	2.22	11.05(7)	2.90
-3.1	6.83	7.17	2.15	9.56(7)	2.91
	6.81	7.30	2.18	9.78(5)	2.84
-9.4	6.02	6.45	1.92	8.28(6)	2.59
	5.75	7.00	2.05	9.93(5)	2.51
-15.6	4.78	5.71	1.71	7.62 (9)	2.03
	4.86	5.48	1.59	7.39 (6)	2.16
-21.9	3.48	4.07	1.19	5.28(11)	1.46
	3.76	3.50	1.15	4.85(9)	1.54

Since the two runs were nearly identical, the activity results were averaged and then used to adjust the neutron spectrum and to calculate damage parameters, using the SPECTER computer code.[3] Neutron fluence values are listed in Table VI and damage parameters in Table VII. Due to the non-linear behavior of damage in nickel and 316 stainless steel, these gradients are listed separately in Table VIII.

Table VI. Neutron Fluences for HFIR-CTR-53/54 Experiments
($\times 10^{21}$ n/cm^2 at midplane: for gradients use Eq. 1)

Energy Range, MeV	Fluence	Uncertainty, %
Total	8.35	6
Thermal, <0.5 eV	3.37	6
0.5 eV - 0.11 MeV	2.69	10
>0.11 MeV	2.30	9

Table VII. Damage Parameters for HFIR-CTR 53/54
(Values at midplane: for gradients use Eq. 1)

Element		DPA	Helium. appm
Al		3.04	1.49
Ti		1.94	1.01
V		2.17	0.05
Cr		1.92	0.34
Mn[a]		2.10	0.30
Fe		1.70	0.61
Co[a]		2.10	0.30
Ni	Fast	1.82	8.17
	Thermal	0.26	145.
	Total	2.08	153.
Cu		1.65	0.54
Nb		1.64	0.11
Mo		1.21	-
316SS[b]		1.78	20.4

[a]Thermal neutron self-shielding may reduce damage.
[b]316SS: Fe(0.645), Ni(0.13), Cr(0.18), Mn(0.019), Mo(0.026).

Table VIII. 316 Damage Parameters for HFIR-CTR 53/54
(Helium values include fast and thermal effect)
(dpa values include extra thermal effect (He/567))

Height, cm	Helium, appm	dpa
0	20.4	1.78
3	20.1	1.77
6	19.1	1.72
9	17.5	1.64
12	15.5	1.53
15	12.9	1.39
18	10.2	1.21
21	7.3	1.01
24	4.5	0.78

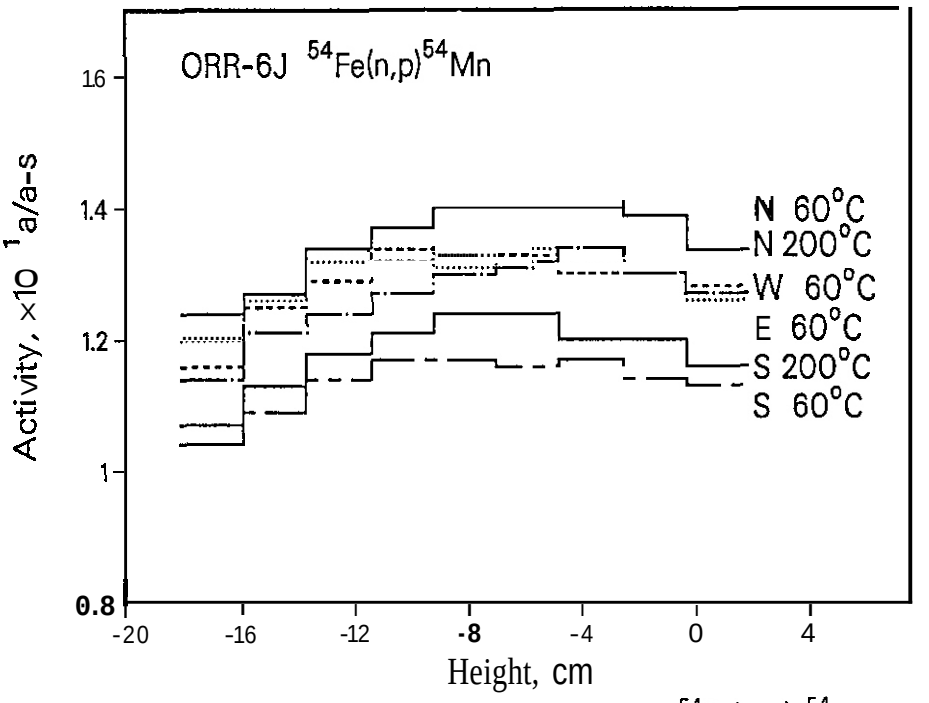

Figure 1. Activity gradients for the $^{54}Fe(n,p)\ ^{54}Mn$ reaction the six positions in the MFE6J experiment.

REFERENCES

1. Neutron Dosimetry and Damage Calculations for the HFIR-CTR-30, 36. and 46 Experiments, L. R. Greenwood, Alloy Development for Irradiation Performance Semiannual Progress Report, DOE/ER-0045/14, pp. 22-26, March 1985.

2. Dosimetry and Damage Analysis for HFIR-CTR-47/48, L. R. Greenwood, Fusion Reactor Materials Semiannual Progress Report, DOE/ER-0313/2, pp. 38-40. March 1987.

3. SPECTER: Neutron Damage Calculations for Materials Irradiations. L. R. Greenwood and R. K. Smither, ANLIFPP-TM-197. January 1985.

4. Neutron Dosimetry and Damage Calculations for the ORR-6J-Test, L. R. Greenwood, Alloy Development for Irradiation Performance Semiannual Progress Report, DOE/ER-0045/15, pp. 4-7, Sept. 1985.

5. L. R. Greenwood and R. K. Smither, ANLIFPPITM-197, SPECTER: Neutron Damage Calculations for Materials Irradiations, January 1985.

6. Neutron Dosimetry and Damage Calculations for the HFIR-CTR-30. 36, and 46 Experiments, L. R. Greenwood, Alloy Development for Irradiation Performance Semiannual Progress Report, DOE/ER-0045/14, pp. 22-26, March 1985.

7. Dosimetry and Damage Analysis for HFIR-CTR-47/48, L. R. Greenwood, Fusion Reactor Materials Semiannual Progress Report, DOE/ER-0313/2, pp. 38-40. March 1987.

8. SPECTER: Neutron Damage Calculations for Materials Irradiations, L. R. Greenwood and R. K. Smither. ANL/FPP-TM-197, January 1985.

DOSIMETRY FOR THE HFIR-CTR 53/54 EXPERIMENTS - L.R. Greenwood and D.V. Steidl (Argonne National Laboratory)

OBJECTIVE

To provide dosimetry and damage analysis for fusion reactor materials irradiation experiments.

SUMMARY

Neutron fluence measurements and radiation damage calculations have been completed for the CTR 53 and 54 experiments in the High Flux Isotopes Reactor at Oak Ridge National Laboratory. Both irradiations were started on October 25, 1986 and only lasted one cycle due to the suspension of HFIR operations. The net exposure was 2026 MWD resulting in a neutron fluence of 8.4 $x10^{21}$ n/cm^2 (2.3 x 10^{21} above 0.1 MeV) with damage production of only 1.8 dpa and 20 appm helium in 316 stainless steel.

PROGRESS AND STATUS

The CTR 53 and 54 irradiations were initiated only one month before the suspension of HFIR operations on November 14, 1986. The net exposure was thus only one 22 day cycle resulting in 2026 MWD or 20.26 full power days. The assemblies were irradiated in positions A1 and A4 of the Peripheral Target Position. Similar irradiations in the PTP have been reported previously[1,2]. Dosimetry packages were inserted at eight heights in each assembly, as listed in Table 1. Each aluminum package measured 6.4 mm long by 1.3 mm o.d. and contained small wires of Fe, Ti, Nb, 0.1%Co-Al, and 80.2%Mn-Cu. Each wire was separately gamma counted and the measured activities are listed in Table 1. The net uncertainties are typically ±2% except for ^{46}Sc, due to the unusually long decay time prior to receipt of the samples.

These runs were the first where we included Nb dosimeters. The $^{93}Nb(n,1)^{94}Nb$ (20,300 y) reaction results are included in Table 1. Work is in progress to measure the $^{93}Nb(n,n')^{93m}Nb$ (16 y) reaction, which is of special interest due to the low energy threshold and long halflife. Thin samples are being prepared for x-ray counting. Absolute counting efficiencies have been determined using the NIST standard reference material (SRM-4267). The data will be used to help adjust the neutron cross sections so that this reaction can be used for routine dosimetry applications.

Table 1. Activity Measurements for HFIR-CTR-53/54 Experiments
(Values in atom/atom-s at 100 MW; ±2% unless noted)

Height	$^{59}Co(n,\gamma)^{60}Co$	$^{54}Fe(n,p)^{54}Mn$	$^{55}Mn(n,2n)^{54}Mn$	$^{46}Ti(n,p)^{46}Sc$	$^{93}Nb(n,\gamma)^{94}Nb$
(cm)	($x10^{-8}$)	($x10^{-11}$)	($x10^{-13}$)	($x10^{-12}$) (±%)	($x10^{-9}$)
18.8	4.28	5.14	1.55	6.94(8)	1.85
	4.51	4.79	1.40	5.78(6)	1.94
12.5	5.23	6.67	1.96	9.54(6)	
	5.44	6.20	1.87	8.46 (4)	2.44
6.3	6.14	7.34	2.10	9.48(6)	2.76
	6.67	7.06	2.04	9.75(6)	2.88
0.0	6.45	7.87	2.34	10.24(8)	2.85
	6.54	7.61	2.22	11.05(7)	2.90
-3.1	6.83	7.17	2.15	9.56(7)	2.91
	6.81	7.30	2.18	9.78(5)	2.84
-9.4	6.02	6.45	1.92	8.28(6)	2.59
	5.75	7.00	2.05	9.93(5)	2.51
-15.6	4.78	5.71	1.71	7.62 (9)	2.03
	4.86	5.48	1.59	7.39(6)	2.16
-21.9	3.48	4.07	1.19	5.28(11)	1.46
	3.76	3.50	1.15	4.85(9)	1.54

Work supported by the U.S. Department of Energy,
Office of Fusion Energy, under contract W-31-109-Eng-38.

As can be seen from Table 1, the activity results for runs 53 and 54 are nearly identical. The activity gradients with height are very nearly centered at midplane and are well-described by the equation:

$$F(x) = F(0)\ (1. - 1.02 \times 10^{-4} x^2) \quad (1)$$

where F is the activity at height x (cm) and F(0) is the maximum value at midplane. This equation also describes fluence and damage parameter gradients (except for the non-linear reactions with nickel) using midplane values which are given in later tables. Since the two runs were nearly identical, the activity results were averaged and then used to adjust the neutron spectrum and to calculate damage parameters, using the SPECTER computer code.[3] Neutron fluence values are listed in Table 2 and damage parameters in Table 3. Due to the non-linear behavior of damage in nickel and 316 stainless steel, these gradients are listed separately in Table 4.

FUTURE WORK

All dosimetry has now been completed for irradiations in HFIR prior to suspension of operations in November 1986. New dosimeters are being fabricated for the CTR 60/61 irradiations and the JP 9-16, 605, and 3305 experiments are expected to begin when HFIR resumes operations at 85 MW by April 1990.

Table 2. Neutron Fluences for HFIR-CTR-53/54 Experiments ($\times 10^{21}$ n/cm^2 at midplane: for gradients use equation 1)

Energy Range, MeV	Fluence	Uncertainty, %
Total	8.35	6
Thermal, <0.5 eV	3.37	6
0.5 eV - 0.11 MeV	2.69	10
>0.11 MeV	2.30	9

Table 3. Damage Parameters for HFIR-CTR 53/54 (Values at midplane: for gradients use equation 1)

Element		dpa	Helium, appm
Al		3.04	1.49
Ti		1.94	1.01
V		2.17	0.05
Cr		1.92	0.34
Mn[a]		2.10	0.30
Fe		1.70	0.61
Co[a]		2.10	0.30
Ni	Fast	1.82	8.17
	Thermal	0.26	145.
	Total	2.08	153.
cu		1.65	0.54
Nb		1.64	0.11
Mo		1.21	-
316SS[b]		1.78	20.4

[a] Thermal neutron self-shielding may reduce damage.
[b] 316SS: Fe(0.645), Ni(0.13), Cr(0.18), Mn(0.019), Mo (0.026).

Table 4. 316 Damage Parameters for HFIR-CTR 53/54
(Helium values include fast and thermal effect)
(dpa values include extra thermal effect (He/567))

Height, cm	Helium, appm	dpa
0	20.4	1.78
3	20.1	1.77
6	19.1	1.72
9	17.5	1.64
12	15.5	1.53
15	12.9	1.39
18	10.2	1.21
21	7.3	1.01
24	4.5	0.78

REFERENCES

1. Neutron Dosimetry and Damage Calculations for the HFIR-CTR-30, 36, and 46 Experiments, L.R. Greenwood, Alloy Development for Irradiation Performance Semiannual Progress Report, DOEIER-0045114, pp. 22-26, March 1985.

2. Dosimetry and Damage Analysis for HFIR-CTR-47/48, L.R. Greenwood, Fusion Reactor Materials Semiannual Progress Report, DOE/ER-0313/2, pp. 38-40, March 1987.

3. SPECTER: Neutron Damage Calculations for Materials Irradiations. L.R. Greenwood and R.K. Smither, ANLIFPP-TM-197, January 1985.

3. MATERIALS ENGINEERING AND DESIGN REQUIREMENTS

No contributions.

4. FUNDAMENTAL MECHANICAL BEHAVIOR

RADIATION HARDENING IN NEUTRON-IRRADIATED POLYCRYSTALLINE COPPER: BARRIER STRENGTH OF DEFECT CLUSTERS — S. Kojima, Present address: Dept. Nuclear Engineering, Nagoya University, Nagoya, Japan, S. J. Zinkle (Oak Ridge National Laboratory), and H. L. Heinisch (Pacific Northwest Laboratory)

OBJECTIVE

To obtain fundamental information on the interaction between dislocations and defect clusters in neutron-irradiated metals.

SUMMARY

Defect cluster formation in 14-MeV neutron-irradiated polycrystalline copper has been observed by transmission electron microscopy (TEM) and correlated with the increase in yield stress. The measurements indicate that the radiation hardening component of the yield strength in polycrystals is not directly additive to the unirradiated yield strength. A transitional behavior was observed for radiation hardening at low fluences, which produces an anomalous variation of the defect cluster barrier strength with fluence. The behavior is attributed to the effect of grain boundaries on slip band transmission. An upper limit for the room temperature barrier strength of defect clusters in neutron-irradiated copper was determined to be $a = 0.23$.

PROGRESS AND STATUS

Introduction

The study of neutron irradiation damage at a very low fluence provides useful insight into the formation and properties of defect clusters. Recent studies of 14-MeV neutron irradiated metals such as copper have shown that the number density of point defect clusters changes from a linear dependence on neutron fluence to a one-half power dependence as the fluence increases.[1-4] Mitchell[5] has shown that the yield stress change in 14-MeV neutron-irradiated copper abruptly increased at about 3×10^{20} n/m^2. This implies that an abrupt change occurred in the microstructure and/or in the interaction between dislocations and defect clusters at this fluence.

According to conventional theory based on dispersed barrier hardening,[6] the change in critical resolved shear stress ($\Delta\tau$) due to defect clusters is given by

$$\Delta\tau = a\mu b\sqrt{Nd} \quad , \tag{1}$$

where a is a constant related to the strength of defect clusters as obstacles to dislocation motion (barrier strength), μ is the shear modulus (46 GPa for copper), $b = a_0/\sqrt{2}$ is the line dislocation Burgers vector, N is the defect cluster density, and d is the mean defect diameter. For tensile tests on polycrystals, the right-hand side of Eq. (1) must be multiplied by the Taylor factor to convert from shear to tensile stress, which is $\bar{M} = 3.06$ for fcc polycrystals.[7] The general validity of Eq. (1) at 2.5×10^{22} n/m^2 ($E > 1$ MeV) was confirmed for neutron-irradiated copper by Makin et al.[8]

The value of the barrier strength coefficient a was recently[3] calculated at several fluences by combining Mitchell's[5] tensile results with TEM[3] and electrical resistivity[10] measurements of the defect cluster size and density in 14-MeV neutron-irradiated polycrystalline copper. The results are shown in Fig. 1. The apparent value of a (calculated from the individual yield stress change data points) increased steadily from 0.04 to 0.18 as the neutron fluence increased from 1×10^{20} to 3×10^{21} n/m^2. On the other hand, a similar analysis of radiation hardening data obtained on single crystal copper" using an extrapolation of the TEM results given in ref. 3 produces a constant hardening coefficient of $a = 0.22$. These results suggest that there is some intrinsic difference between the deformation behavior of single and polycrystals following neutron irradiation. Unfortunately, this comparison suffers the serious drawback that different heats of copper were used for the tensile and defect cluster measurements. In the present study, TEM observations have been made on polycrystalline specimens prepared and irradiated at the same time as the tensile test specimens[12,13] to avoid the ambiguity arising from specimen differences.

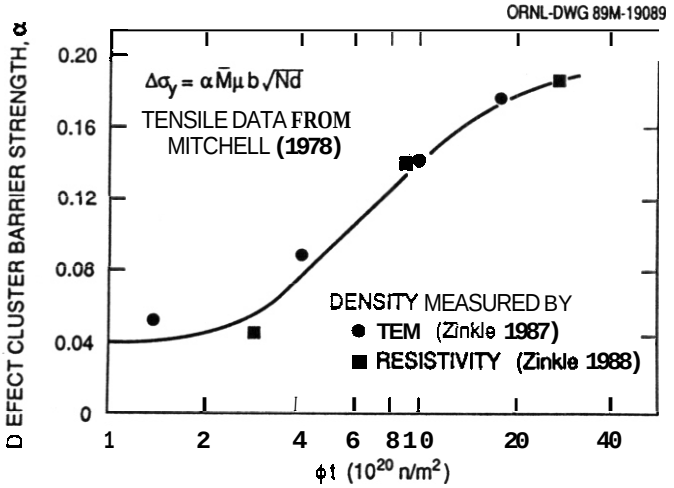

Fig. 1. Apparent barrier strength of defect clusters in 14-MeV neutron-irradiated polycrystalline copper (55 μm grain size). Calculations[9] performed using the data from refs. 3,5,10.

Experimental Procedure

Miniature sheet-type tensile specimens were prepared from pure (Marz grade) copper. The specinens were punched from 0.25 mm cold-rolled sheet, de-burred, and annealed at 723 K for 15 min in argon. The resultant grain diameter was 36 μm. The specimens were irradiated with 14-MeV neutrons at 363 K in the RTNS-II facility to fluences of 0.62 to 20.0 × 10^{21} n/m^2.

Tensile tests[12,13] were performed at room temperature at a strain rate of 4.9 × 10^{-4}/s. Electron microscopy specimens were prepared from several tensile specimens that had not been used for the tensile tests. They were examined in a JEOL 2000FX electron microscope using weak beam dark field imaging conditions with a beam direction of [110] and the 200 reflection. In order to achieve the minimal uncertainty in the number density, analysis was performed on several areas with foil thickness 0 to 100 nm, and the volume number density was determined from the slope of the line through plotted data points of areal number density vs. foil thickness. No correction was made for invisible small defects, which have the same image intensity as the background.

Results

Figure 2 shows the typical microstructure of specimens irradiated to fluences of 6 × 10^{20} and 1 × 10^{21} n/m^2. Dislocation loops and stacking fault tetrahedra (SFT) were uniformly distributed in the matrix, with some evidence of grouped subcascades visible. In these specimens, about 70% of the defects were SFT and the rest were dislocation loops.

The measured number densities and man sizes of the defect clusters are listed in Table 1. The mean size was approximately the same for all three fluences, ranging from 2.4 to 2.7 nm. Although only three different fluences were available for microstructural observation in the present study, the data are consistent with the established interpretation[3,14] that the increase in the number density of defect clusters in copper is linear with the 14-MeV neutron fluence up to approximately 2 × 10^{21} n/m^2 after which it changes to a square root dependence on fluence.

The fluence-dependent increases in the 0.2% offset yield stress are shown in Fig. 3. The masured yield stress of unirradiated copper was 49 MPa. The slope of the log-log curve drawn through the two lowest fluence data points was about 0.75, which is shown as tan θ in the figure. From this figure, the increases in yield stress of the specimens used for electron microscopy were determined as 43, 67 and 91 MPa, respectively.

Figure 4 shows a plot of the yield stress change vs. the square root of the product of number density and mean size of defect clusters, which can be used to examine the validity of Eq. (1) for polycrystalline copper. The three

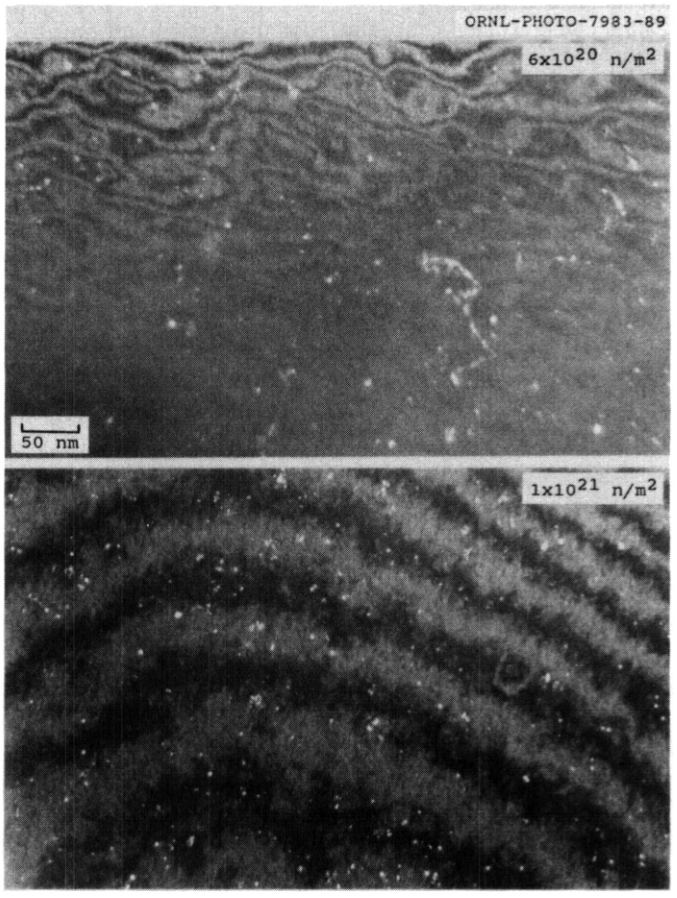

Fig. 2. Defect structures developed at 363 K in 14-MeV neutron-irradiated copper at 6 × 10^{20} and 1 × 10^{21} n/m^2. Weak beam dark field condition (g,6g), g = 200.

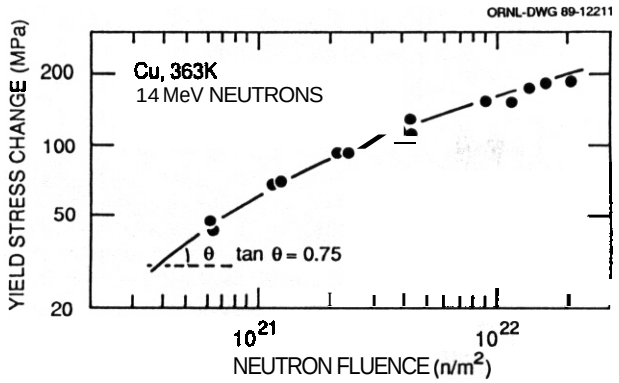

Fig. 3. Variation of the yield stress change with neutron fluence. The slope of the curve at the two lowest fluence data points is about 0.75.

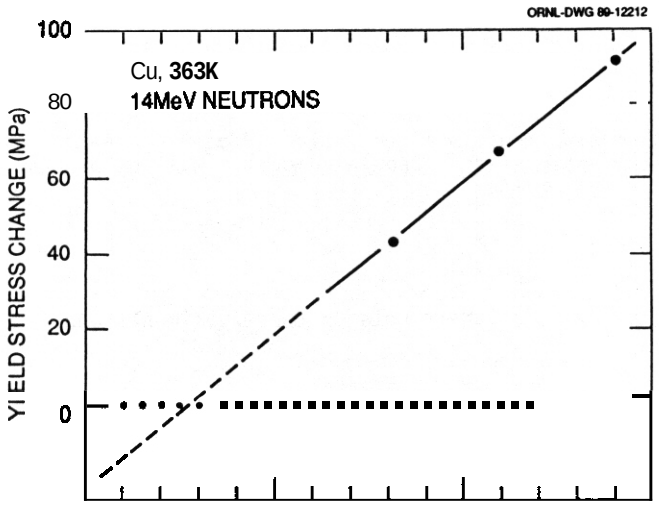

Table 1. Number density and mean size of defect clusters

Fluence ($\times 10^{21}$/m^2)	Number density ($\times 10^{22}$/m^3)	Mean size (nm)
0.62	**2.5**	2.7
1.21	4.7	2.5
2.36	8.1	**2.4**

data points indicate a linear relation between the yield stress change and $(Nd)^{1/2}$. However, the line connecting the points does not intersect the origin of the coordinates but shows a negative value of yield stress change, −22 MPa, at $(Nd)^{1/2} = 0$.

Discussion

Two unexpected observations were found in the present results. First, the slope of the lower fluence hardening data in Fig. 3 was 0.75. The expected slope from Eq. (1) is 0.5 since the number density of defect clusters was linear with neutron fluence (at $\phi t < 2 \times 10^{21}$ n/m^2) and the mean size of defects was almost constant. Second, when the data in Fig. 4 was extrapolated to $(Nd)^{1/2} = 0$, a negative intercept (−22 MPa) was obtained instead of zero. This difference is too large to be attributable to an error in the unirradiated yield stress, where the uncertainty in the measurement was less than 3 MPa. It can be seen immediately that the non-zero intercept of the $\Delta\sigma$ vs. $\sqrt{Nd}$ data (Fig. 4) causes the value of a (calculated from the individual yield stress increases) to show an apparent dependence on fluence. From Fig. 4, the apparent barrier strength increased with fluence from $\alpha = 0.15$ to 0.18. This anomalous fluence dependence follows the same trend as the estimates for α from the previous study (Fig. 1).

The apparent variation with fluence of the defect cluster barrier strength is not expected from a theoretical basis. It might be possible to interpret that the value of α in Eq. (1) could be changing over this fluence range due to a nonuniform defect distribution in the grouped subcascades that becomes more uniform with increasing fluence. However, a comparison of defect groupings for the three different fluences of this study (e.g., Fig. 2) shows this interpretation is unlikely. Instead, it is worthwhile to consider the effects of grain boundaries and deformation mechanisms on the yield strength of irradiated metals.

The yield stress of unirradiated polycrystals is known to be described by the Hall-Petch relation,[15] where the yield strength is inversely proportional to the square root of grain diameter D. Several experimental investigations of grain size effects on radiation hardening in copper[16,17] have found that the Hall-Petch relation is also obeyed following irradiation for fluences $>10^{21}$ n/m^2,

$$\sigma_{irr} = \sigma_i + k_i/\sqrt{D} \ . \qquad (2)$$

Radiation hardening studies have found that both σ_i and k_i increase with increasing fluence.[7,16,17]

There is experimental evidence that the rather abrupt change in yield stress with increasing fluence typically observed in low fluence tensile studies of irradiated polycrystals[3,5,17] is due to a change in the deformation mode. The change from a cellular to a slip band-intensive deformation mode at fluences $>10^{21}$ n/m^2 (refs. 18–21) may produce a change in the radiation hardening behavior of polycrystals. The

post-transition ($>10^{21}$ n/m^2) hardening rate in polycrystals should be higher than that observed for single crystals [Eq. (2)] since the grain boundaries limit the propagation of the slip bands. This oroduces a higher hardening rate of the yield stress and causes the extrapolated yield stress change at zero fluence to have a negative value (Fig. 4).

An estimate of the true barrier strength of defect clusters in neutron-irradiated copper can be obtained from the slope of the line drawn through the data points in Fig. 4. This method of analysis eliminates the transient error associated with the nonzero intercept of the extrapolated data. The calculated value obtained from the slope of the plotted data points is $a = 0.23$. This value is in general agreement with previous theoretical estimates[6,22,23] although it is significantly lower than the value proposed by Makin.[24] A similar slope analysis of the data used to obtain Fig. 1 yields a comparable value of $a = 0.25$, although this value cannot be considered as reliable due to the use of different copper specimens for the tensile and number density measurements. The polycrystal values for a obtained from the slope of the radiation hardening data are an upper limit for the matrix radiation hardening since the grain size-dependent hardening rate in polycrystals is higher than that for single crystals due to the Hall-Petch effect [Eq. (2)].

Conclusions

A simple application of the dispersed barrier model to analyze the radiation hardening behavior of polycrystals produces an anomalous fluence-dependent barrier strength, which is attributed to grain boundary effects. The radiation hardening component of the yield strength is not linearly additive to the unirradiated strength due to a change in the deformation mode at ~10^{21} n/m^2 and the existence of a radiation-modified Hall-Petch grain size effect. The room temperature barrier strength of defect clusters produced in copper irradiated at 363 K with 14-MeV neutrons is a = 0.23.

FUTURE WORK

Transmission electron microscopy and yield strength measurements will be performed on neutron-irradiated polycrystalline copper specimens with different grain sizes. Special emphasis will be placed on analysis of the deformation structure at fluences near 10^{21} n/m^2.

ACKNOWLEDGMENTS

The authors would like to thank N. H. Rouse and E. L. Ryan for their help in the experiments and Frances Scarboro for manuscript preparation.

REFERENCES

1. N. Yoshida. Y. Akashi, K. Kitajima and M. Kiritani, J. Nucl. Mater. 133&134 (1985) 405.
2. M. Kiritani, T. Yoshiie and S. Kojima, J. Nucl. Mater. 141-143 (1986) 625.
3. S. J. Zinkle, J. Nucl. Mater. 150 (1987) 140.
4. M. Kiritani, Materials Science Forum 15-18 (1987) 1023.
5. J. B. Mitchell, Lawrence Livermore Laboratory Report, UCRL52388 (January 1978); also J. B. Mitchell et al., in Radiation Effects and Tritium Technology for Fusion Reactors, Vol. II, eds., J. S. Watson and F. W. Wiffen, CONF 750989 (1975), p. 172
6. A. L. Bement, Jr., in: 2nd Int. Conf. on Strength of Metals and Alloys (ASM, Metals Park, OH, 19701, p. 693.
7. U. F. Kocks, Met. Trans 1 (1970) 1121.
8. M. J. Makin et al.. Phil. Mag. 13 119661 729.
9. S. J. Zinkle, Fusion Reactor-Materials Semiann. Prog. Rep. March 31, 1987. DOE/ER-0313/2 (1987) 99.
10. S. J. Zinkle, J. Phys. F, 18 (1988) 377.
11. K. Shinohara and S. Kitajima, J. Nucl. Mater. 133&134 (1985) 690.
12. H. L. Heinisch. S. D. Atkin and C. Martinez, J. Nucl. Mater. 141-143 (1986) 807.
13. H. L. Heinisch and C. Martinez, J. Nucl. Mater. 141-143 (1986) 883.
14. Y. Satoh, H. Ishida, T. Voshiie and M. Kiritani, J. Nucl. Mater. 155-157 (1988) 443.
15. T. L. Johnston and C. E. Feltner, Met. Trans. 1 (1970) 1161.
16. M. A. Adams and P. R. B. Higgins, Phil. Mag. 4 (1959) 777.
17. M. J. Makin, in: Radiation Effects, Ed. W. F. Sheely (Gordon and Breach. New York, 1967) p. 627.
18. A. Rukwied, Z. Metallk. 55 (1964) 146.
19. U. Essmann and M. Rapp, Acta Met: 21 (1973) 1305.
20. L. M. Howe, Rad. Effects 23 (1974) 181.
21. A. Okada et al., Bull. Fac. Eng. Hokkaido Univ., No. 141 (1988) 93.
22. R. L. Fleischer, J. Appl. Phys. 33 (1962) 3504.
23. T. J. Koppenaal and R. J. Arsenault, Met. Rev. 16 (1971) 175.
24. M. J. Makin, Phil. Mag. 18 (1968) 1245.

MICROSTRUCTURE-TENSILE PROPERTY CORRELATION OF 316SS IN LOW DOSE NEUTRON IRRADIATIONS - N. Yoshida (Kyushu University), H. L. Heinisch (Pacific Northwest Laboratory),(a) T. Muroga (Kyushu University), K. Araki (Kyushu University), and M. Kiritani (Nagoya University)

OBJECTIVE

The objective of this work is to determine the effects of the neutron spectrum on radiation-induced changes in mechanical properties for metals irradiated with fission and fusion neutrons.

SUMMARY

Annealed 316SS was irradiated at 90°C and 290°C in RTNS-II and in DWR. Radiation induced microstructures were examined by transmission electron microscopy. Very small dislocation loops of extremely high density were observed in dark field images. In the case of irradiations at 90°C and 290°C in RTNS-II and 90°C in OWR, the loop density increased moderately with dpa, roughly proportional to the square root of dpa, while that of 290°C irradiation at OWR showed stronger dpa dependence above 0.003 dpa, where the yield stress change also increased strongly. The yield stress change was roughly proportional to the square root of the defect density, independent of irradiation temperature and neutron energy spectrum. The observed small dislocation loops are the origin of the yield stress change, with a strength parameter estimated to be 0.2.

PROGRESS AND STATUS

Introduction

The change in mechanical properties, such as yield stress, is caused by radiation induced lattice defects, which act as obstacles for dislocation motion. Therefore, in order to understand the physical background of radiation effects on mechanical properties, comparative studies of mechanical properties and microstructures are essential.

Many studies have focused on microstructure-tensile property correlations of neutron irradiated materials. At higher temperatures, where defect size is reasonably large, the correlation is quite good.[1,2] At lower temperatures the density of observable defects is too low to account for mechanical property changes.[3,4] It has been hypothesized that submicroscopic invisible defects act as obstacles of dislocation motion in these cases. Improvements in resolution and observation techniques are necessary to promote studies in this field.

Recently, Heinisch reported that tensile property changes of 316SS irradiated at 90°C with D-T fusion neutrons (RTNS-II) and fission neutrons (OWR) correspond well by using dpa as a correlation parameter.[5] In the case of 290°C irradiations, however, the yield stress changes of OWR specimens behaved oddly, and dpa does not account for the neutron spectral differences. In order to understand these temperature and neutron energy dependencies of mechanical properties of 316SS, the role of defects in tensile property changes and their formation mechanism were studied in the present work by means of transmission electron microscopy.

ExDerimental

Annealed 316SS specimens of 0.2 mm thickness were irradiated at 90 and 290°C by fusion and fission neutrons by using RTNS-II at LLNL and OWR at LANL, respectively. The specimens are identical to those used in reference 5. Neutron fluence of RTNS-II irradiation ranged from 1.89 x 10^{21} to 4.11 x 10^{22} n/m^2, and corresponding dpa was 0.003-0.0114. That of OWR irradiation ranged from 4.49 x 10^{22} to 1.39 x 10^{24} n/m^2 (total neutrons), and corresponding dpa was 0.001-0.0319.

After electro-polishing, these specimens were observed very carefully by transmission electron microscope. In order to get optimum resolution and contrast, weak beam dark field images at the diffraction conditions of g = (200) and (g, 6g) were observed. To separate images of very small oxide grains formed on the specimen surfaces, which have a diffraction spot near (200) of 316SS, a small angle (2 to 3 degrees) stereo observation technique was used. Details of the technique will be described elsewhere.[6] Some of the specimens were annealed isochronally (10 minutes at every 50 or 100°C) in a microscope, and the change of microstructure was observed at room temperature.

Annealed 316SS specimens were irradiated at 90 and 290°C by 1 MeV electrons in a high voltage electron microscope at the HVEM Laboratory in Kyushu University to introduce interstitial type dislocation loops.

(a) Pacific Northwest Laboratory is operated for the U.S. Department of Energy by Battelle Memorial Institute under Contract DE-AC06-76RLO 1830.

Exoerimental Results and Discussion

The micrographs in Figure 1 show dark field images of OWR and RTNS-II specimens irradiated at 290°C. A tremendous number of small white images are observed. A part of them, especially with faint contrast, are small oxides formed on the surfaces. In both cases, the density of defects increases with increasing dpa, but that of RTNS-II specimens is much lower than that of OWR specimens. On the other hand, the average size of the defect images is about 1 nm, and it increases slightly with dpa but does not depend strongly on it.

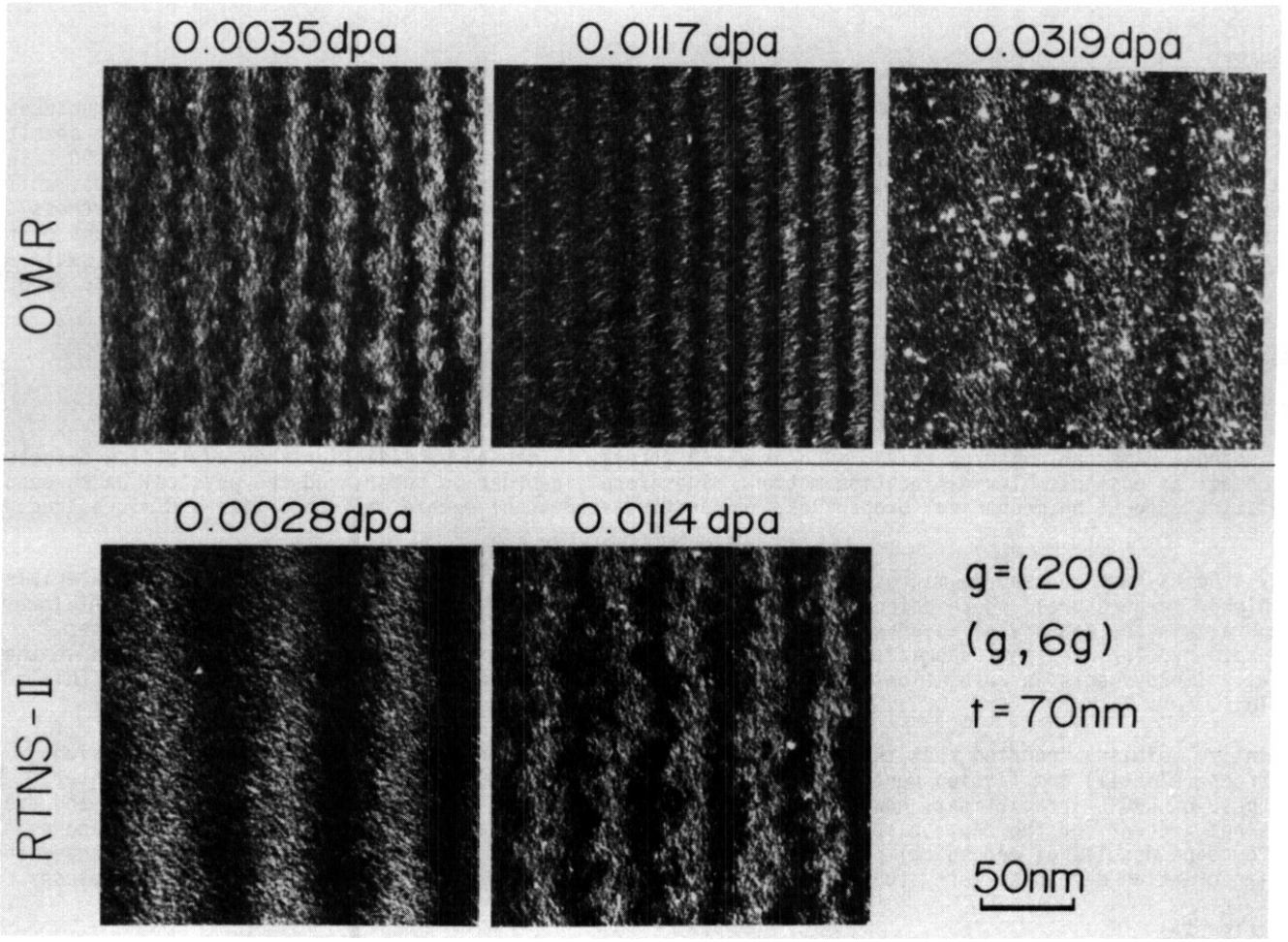

FIGURE 1. Dark Field Image of Defects Formed in 316SS by the Irradiation at 290°C with OWR (above) and RTNS-II (below) to Several dpa. Average thickness of the observed area is 70 nm. Diffraction conditions; g = (200), (g, 6g).

Judging from the results of Cu and Ni irradiated by D-T neutrons'.' the observed defects are probably dislocation loops or stacking fault tetrahedra (SFT). Their image sizes, however, are too small to determine their type only from the characteristics of the image. It is possible to infer the type of the defects from the thermal stability, because the annealing temperature of SFT is in general higher than that of dislocation loops. In Figure 2 the thermal stability of defects formed in an OWR specimen irradiated at 290°C is compared with that of interstitial loops formed by HVEM irradiation at 290°C. In both cases small defects start to coalesce above 400°C, and then most of them disappear between 500 and 600°C. Judging from the identical recovery behavior and similar image character, the observable defects formed at 290°C by neutron irradiation should be dislocation loops.

Figure 3 shows dark field images of OWR specimens at 90°C. The number of defects increases with dpa. Their sizes range from 0.6 nm to 2 nm and do not depend strongly on dpa. Because the defects show similar thermal stability to those formed at 290°C by OWR or HVEM irradiation, they must be dislocation loops. Defects in RTNS-II specimens formed at 90°C showed similar thermal stability.

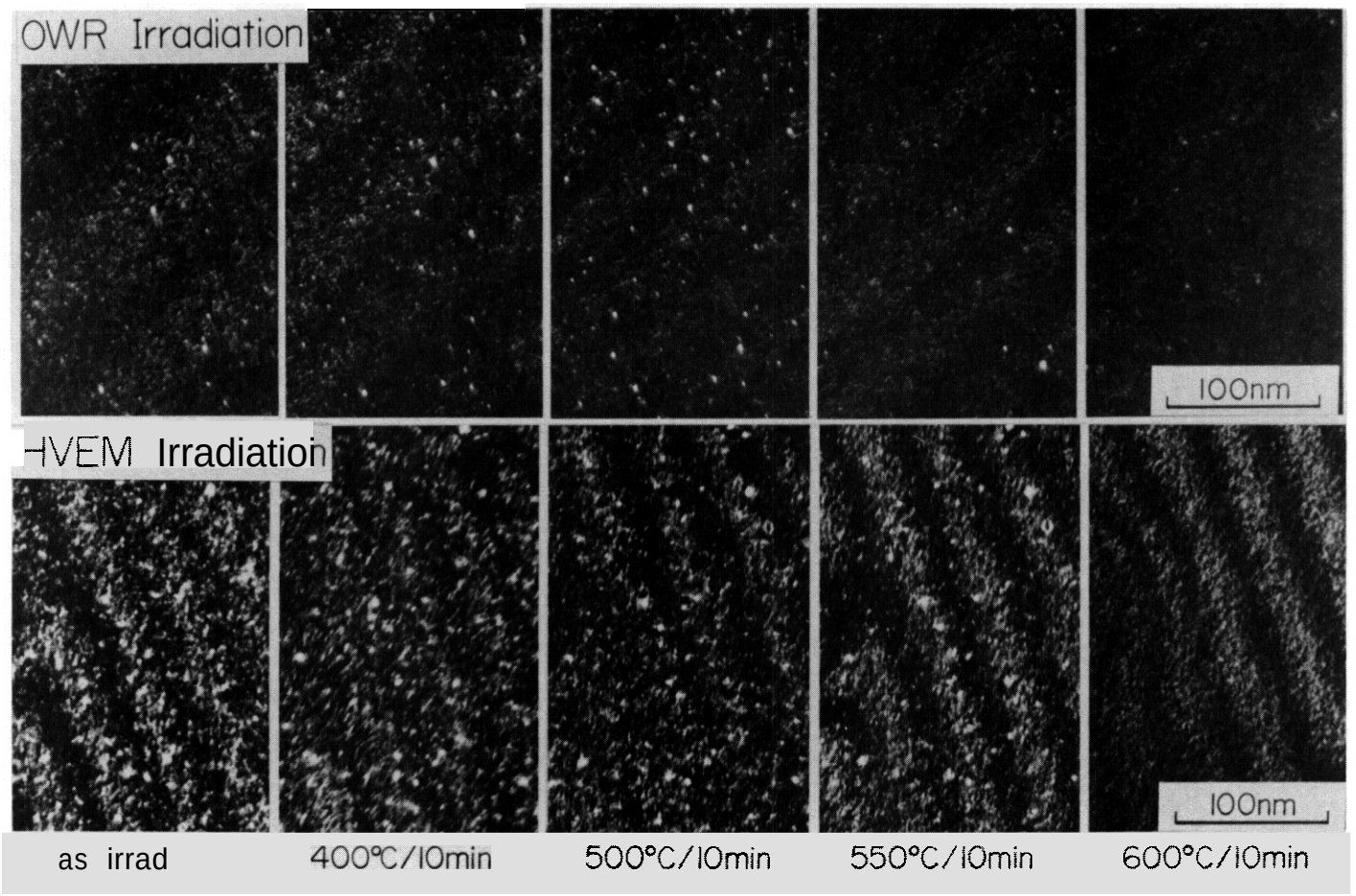

FIGURE 2. Recovery of Defects Formed by Neutron Irradiation at 290°C with OWR (0.0117 dpa) and Interstitial Loops Formed by 1 MeV Electron Irradiation in HVEM at 290°C (0.68 dpa)

From the careful electron microscopic observation mentioned above, we can conclude that the very small defects formed by fission and fusion neutrons at 90°C and 290°C are dislocation loops. Judging from the mobility of interstitials and vacancies, they are probably interstitial type. Strong contrast of images even at weak beam conditions suggests that the loops have a stacking fault; namely, that they are Frank loops with b = a/3<111>.

Density of dislocation loops is plotted against dpa in Figure 4. At 90°C, defect densities in both OWR specimens and RTNS-II specimens increase gradually. The increase is roughly proportional to the square root of dpa or fluence. Note that, regardless of the energy spectrum of neutrons, the nucleation of dislocation loops depends simply on dpa, or somethinq proportional to dpa. Since a siqnificant fraction of the dpa in OWR comes from lower energy events, cascade damage may not play an important role on the formation of dislocation loops at 90°C.

Increasing the irradiation temperature from 90°C to 290°C, loop density decreases about 10 times. The increase of loop density of both RTNS-II specimens and OWR specimens at lower dose is moderate. It is worth noting that loop density of OWR specimens increases drastically above the critical dpa, 0.003 dpa, where yield stress also changed.[5]

In order to clarify correlation between observed small dislocation loops and yield stress change reported in reference 5, yield stress change is plotted against defect density in Figure 5. All of the data points lie on one line within the experimental error, independent of neutron energy and irradiation temperature. This fact suggests that the observed loops are obstacles that increase yield stress.

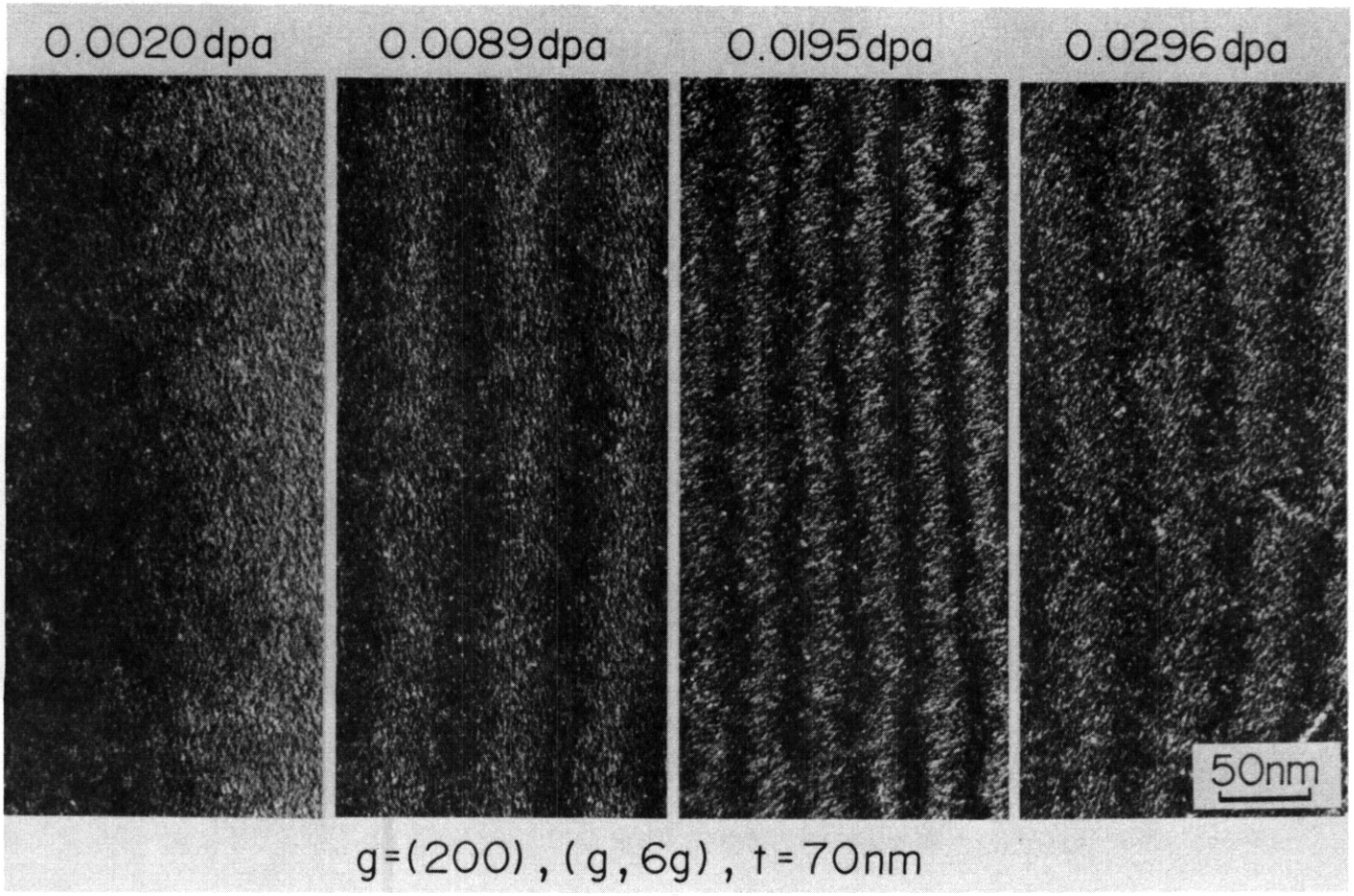

FIGURE 3. Defects Formed by OWR Irradiation at 90°C. Average thickness of the area is 70 nm. Diffraction conditions: g = (200), (g, 6g).

According to the theory of hardening, yield stress change due to dislocation loops, $\Delta\sigma_y$, is expressed by the following equation:

$$\Delta\sigma_y = 2\ \alpha\mu b(Nd)^{1/2},$$

where α, μ, b, N, and d are the mean strength parameter for the obstacles, the shear modulus, the Burgers vector, the density of dislocation loops and the average diameter of dislocation loops, respectively. Because d is almost independent of dpa, temperature, and neutron energy in the present case, $\Delta\sigma_y$ should be proportional to $N^{1/2}$ if the observed loops determine the yield stress change.

Figure 6 shows $\Delta\sigma_y$ as a function of $N^{1/2}$. It is clear that $\Delta\sigma_y$ is proportional to $N^{1/2}$. From the slope of the line, α is estimated to be 0.2, assuming that all of the loops are visible. This value agrees well with theoretical predictions[1] and experimental data on 304SS.[9] From these results it can be concluded that yield stress in 316SS irradiated by neutrons at 90°C and 290°C is mainly determined by the very small dislocation loops.

At 290°C both loop density and yield stress change of OWR specimens separate from those of RTNS-II specimens above a certain dpa. It is not easy to explain this odd phenomenon from present knowledge. One possible explanation is an effect of irradiation temperature control.

In the case of RTNS-II irradiation, irradiation was performed only at the desired temperature. Irradiation was started after the specimens reached the temperature and they were cooled down after stopping irradiation. In OWR irradiation, however, heating up and cooling down of the specimens was repeated every day under irradiation. Though total irradiation time below 290°C was relatively short (20 to 30 minutes a day), it is impossible to deny the possibility that active nucleation of dislocation loops at lower temperatures increased the density of loops in OWR specimens during repeated heating and cooling. The

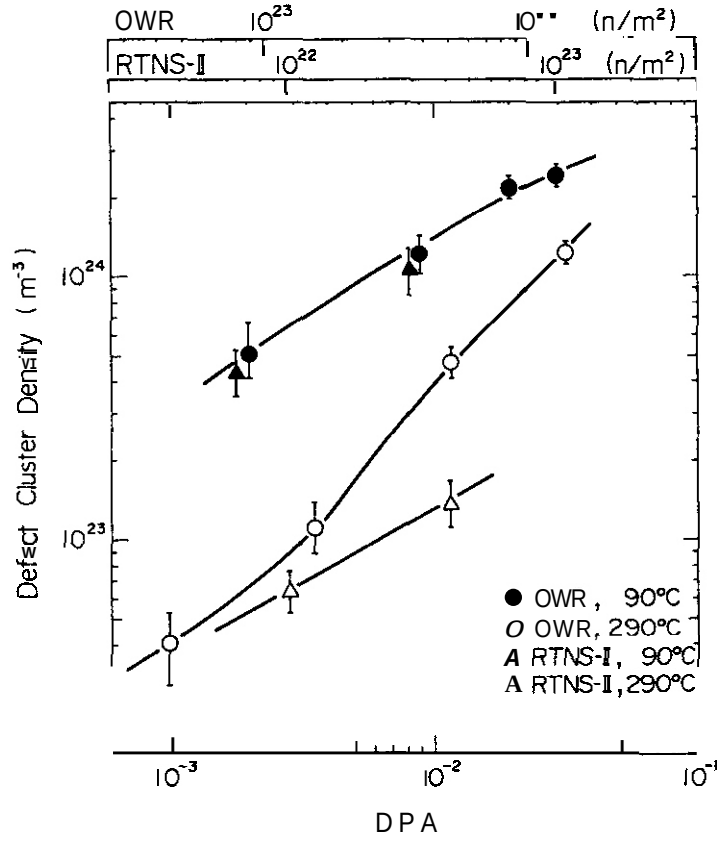

FIGURE 4. Defect Cluster Density as a Function of dpa. The corresponding neutron fluences are also indicated.

deviation of OWR data from those of RTNS-II started after two or three repetitions of the irradiation. It was demonstrated that large changes in irradiation temperature, even if the period was short, had a strong effect of microstructure evolution."

SUMMARY

1) Microstructures of 316SS irradiated by fission and fusion neutrons at 90°C and 290°C were observed by weak beam dark field stereo technique and compared with Heinisch's yield stress data.

2) In all cases, very small (about 1 nm on average) interstitial type dislocation loops were formed.

3) At 90°C, the density of dislocation loops was extremely high and those of fission and fusion irradiations agreed very well. Judging from the mobility of point defects, the loops were probably formed by radiation induced migration of accumulated interstitials. Therefore, dpa was a good fission-fusion correlation parameter at this temperature.

4) At 290°C, both loop density and yield stress change of fission neutron irradiation increased drastically above 0.003 dpa. This odd behavior might be caused by lower temperature irradiation during heating-up and cooling-down.

5) The major defects responsible for increasing the yield stress were observed to be very small interstitial dislocation loops. The strength parameter for the loops was estimated to be 0.2.

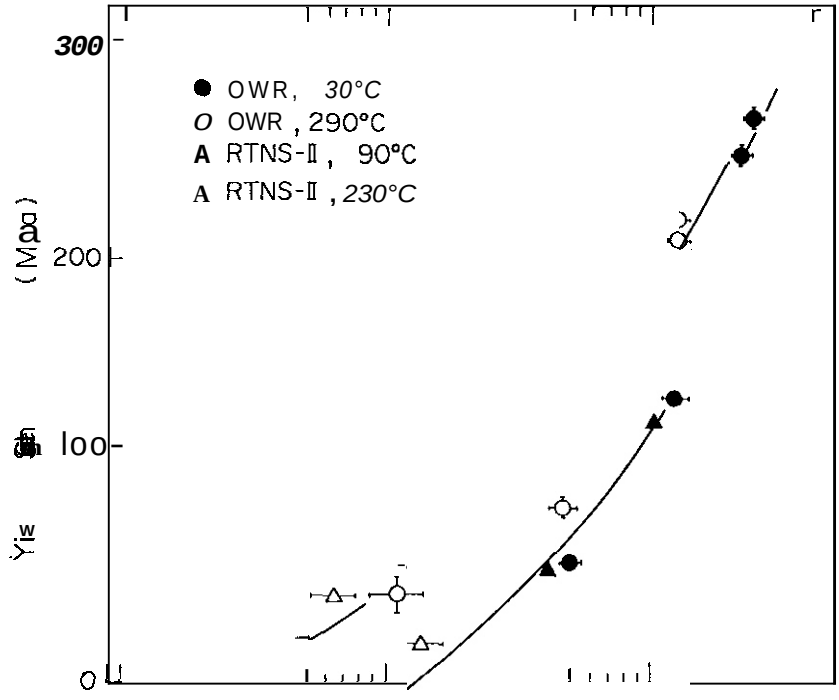

REFERENCES

1. J. J. Holmes, R. E. Robbins, J. L. Brimhall and B. Mastel, Acta Met. 16 (1968) 955.

2. R. L. Simons and L. A. Hulbert, in: ASTM STP 870, Eds. F. A. Garner et al. (ASTM, Philadelphia, 1985) p. 820.

3. R. R. Vandervoort, E. L. Raymond and C. J. Echer, Rad. Effects 45 (1980) 191.

4. N. F. Panayotou, J. Nucl. Mater. 108 & 109 (1982) 456.

5. H. L. Heinisch, J. Nucl. Mater. 155-157 (1988) 121.

6. N. Yoshida, to be published.

7. N. Yoshida, Y. Akashi, K. Kitajima and M. Kiritani, J. Nucl. Mater. 133 & 134 (1985) 405.

8. N. Yoshida, T. Muroga, H. Watanabe, K. Araki and Y. Miyamoto, J. Nucl. Mater. 155-157 (1988) 1222.

9. J. Moteff, D. J. Michel and V. K. Sikka, In: Proc. Int. Conf. Defects and Defect Clusters in B.C.C. Metals and Other Alloys (Gatlinburg 1973) p. 198.

10. M. Matsuda, N. Yoshida, T. Muroga and M. Kiritani, In: Proc. Fourth International Conference on Fusion Reactor Materials, Dec. 4-8, 1989, Kyoto (to be published in J. Nucl. Mater.).

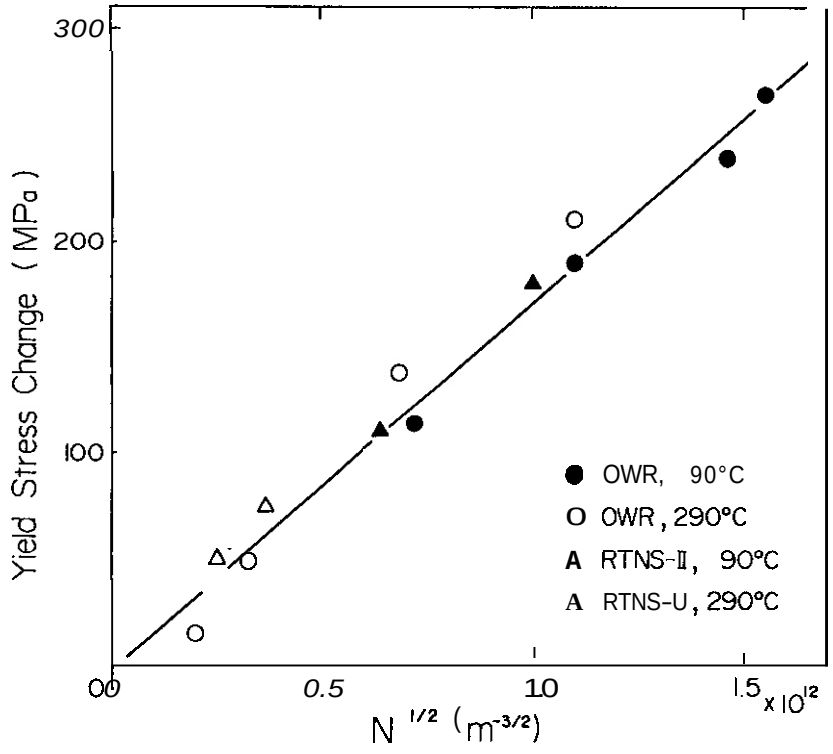

FIGURE 6. **Yield Stress Changes as a Function** of **the Square Root** of **Defect Density,** $N^{1/2}$

MICRO-BULGE TESTING APPLIED TO NEUTRON IRRADIATED MATERIALS - A. Dkada (Hokkaido University), M. L. Hamilton (Pacific Northwest Laboratory)(a) and F. A. Garner (Pacific Northwest Laboratory)

OBJECTIVE

This work was performed in an effort to extend the applicability of micro-bulge tests to standard electron microscopy disks.

SUMMARY

Micro-bulge testing was conducted on several Fe-Ni-Cr alloys irradiated as 0.3 mm thick disks to 10 dpa at 603 and 773 K in the Oak Ridge Research Reactor. Miniature tensile tests were performed on specimens of the same alloys irradiated concurrently. Good correlation between the tensile yield strength and the bulge yield load was observed in unirradiated specimens, however, the correlation was not simple for irradiated specimens. Good correlation was also observed between the ultimate tensile strength and the maximum bulge load. While irradiation produced a significant reduction in total elongation in the tensile test, irradiation caused only a small decrease in the deflection corresponding to the maximum bulge load compared to that observed on thinner disks used in earlier experiments. The results suggest that the thinner disk is better suited for ductility evaluations than the thicker disk. The area bounded by the load-deflection traces of the bulge tests shows a systematic variation with both alloy composition and irradiation condition which is not observed in the tensile data. It is anticipated that this parameter may prove useful in the evaluation of material toughness.

PROGRESS AND STATUS

Introduction

Among the various types of miniaturized mechanical testing developed for reactor materials research,' test techniques using transmission electron microscopy (TEM) disks 3 mm in diameter have a great advantage in reducing the radioactivity of the irradiated materials and in the occupation of a smaller fraction of the limited irradiation volume available. TEM disks have been utilized in the micro-bulge,[2-4] bend,[5-7] shear punch' and small punch[9] tests. In the micro-bulge test, a spherical punch (usually a tiny steel ball) is pressed into a disk, generally ~0.1 mm in thickness, whose periphery is held by a pair of dies. The load for the bulge deformation is recorded against the deflection of the punch. One of the present authors published a correlation between micro-bulge and tensile data for several metals and alloys in both the irradiated and unirradiated conditions, as well as the dependence on die geometry.[8] Very little data are available for materials irradiated to doses as high as 10 dpa or for specimens as thick as 0.3 mm. In the present work, micro-bulge tests were conducted on several Fe-base ternary austenitic alloys irradiated as 0.3 mm thick disks to 10 dpa. The validity of the micro-bulge test results is discussed vis-a-vis their correlation with the tensile data.

Exoerimental Procedures

TEM disks 0.3 mm in thickness and miniature tensile specimens of seven Fe-Ni-Cr ternary austenitic alloys were irradiated concurrently to 12-14 dpa at 603 and 773 K in the MFE-4 experiment in the Oak Ridge Research Reactor.[10] The compositions are shown in Table 1. The miniature tensile specimens were 0.25 mm thick with a gauge length and width of 12.7 and 1.0 mm, respectively. A hardened steel ball 1 mm in diameter was employed for the tip of the punch. The diameter of the lower die hole was 1.7 mm (clearance between ball and die hole was 0.35 mm) to accommodate disks up to 0.3 mm in thickness, and its shoulder radius was 0.4 mm.

Figure 1 shows typical examples of micro-bulge test curves and the parameters extracted from them for the evaluation of irradiation hardening and ductility loss. The parameters are determined as follows: a) bulge yield load (L_y: the load at t/10 offset from the tangent of the initial slope of the curve, where t is the disk thickness), b) maximum bulge load (L_{max}), c) bulge depth (D_{max}) and d) bulge energy (E_B: the area bounded by the load-deflection curve). These parameters were normalized to account for the variation in disk thickness, t, by dividing by t^2, dt, d and d^2t_o/d^2t, respectively, where d is the ball diameter and t_o is 0.3 mm, the nominal disk thickness. Normalizing parameters were chosen on the basis of earlier micro-bulge tests on other materials. The bulge energy is normalized to the equivalent value expected for disks 0.3 mm thick.

(a) Pacific Northwest Laboratory is operated for the U.S. Department of Energy by Battelle Memorial Institute under Contract DE-AC06-76RLO 1830.

Results and Discussion

The normalized results are given in Table 2 and summarized below according to various parameters of interest. Note that the normalized yield load is larger than the normalized maximum bulge load due to the choice of normalizing parameter (t^2 versus dt). The tensile data on the same materials were reported in Reference 11.

Comparison of Bulge and Tensile Tests. The tensile test traces for the same materials as in Figure 1 are shown in Figure 2.[11] The irradiated specimens show a very large ductility loss in the tensile curve while the bulge test curves still show a considerable amount of deflection. The ball displacement for both the maximum bulge load and the load drop at the point of disk fracture are not too different for the unirradiated and irradiated specimens. The difference between the irradiated and unirradiated conditions in the tensile and bulge tests is due to the difference in the deformation mode, viz., the uniaxial stress condition in the tensile test and the essentially biaxial condition in the bulge deformation. This demonstrates the potential for using the bulge test technique for material property evaluations by virtue of the larger deformations that are unobtainable in a uniaxial tensile test due to the necking that results from the larger instability of deformation.

Yield load. The bulge yield load and yield strength are shown in Figure 3 as a function of the alloy composition. In the unirradiated specimens, both sets of data show a similar dependence on composition, while the irradiated specimens show an opposite dependence on nickel level at 15 Cr. The origin of this result may be described as follows. The shoulder of the bulge curve corresponds to a change in the deformation mode from indentation to plastic bending. This transition may be controlled by both the hardness and the rigidity of the specimen, particularly in the case of irradiation hardened, relatively thick disks such as were used in this experiment. If the hardness of the disk exceeds a certain level, the transition to plastic bending will take place earlier than in a less hardened material; therefore, the load L_y at the shoulder of the curve may be smaller. To avoid unnecessary complexity in analyzing test data, disks thin enough to avoid the situation discussed above may be better suited for the bulge test.

Maximum Bulge load. A straight line through the origin can be drawn as shown in Figure 4 for the correlation between the maximum bulge load and the ultimate tensile strength regardless of composition. The slope of this line is different than that drawn for 0.1 mm thick disks. In the case of thinner disks, as thin as 0.1 mm, the correlations for the fully annealed and the fully hardened materials were separated into two groups independent of material type and different correlation lines could be drawn for each of them.[4] The separation between the lines for annealed and cold worked materials will decrease with thickness. The ductility loss and the hardening induced by irradiation are clearly observed in such a plot. The less distinct results obtained in the present experiment on thicker disks suggest that the thinner disks are better suited for the evaluation of strength and ductility using the micro-bulge test.

The maximum bulge load depends on the bulge depth, corresponding to the load at the necking of the bulged disk. If the material is soft, the punch presses deeper into the disk and conversely presses less deeply if the material is hard, so the radius of the contacting circle between the specimen and the punch is larger in the former case and smaller in the latter. Therefore, ductility loss and an increase in material hardness tend to occur concurrently.

Bulge Depth. Irradiation caused only a small decrease in the deflection corresponding to the maximum bulge load (Figure 5), especially when compared to the decrease observed in thinner disks.[4] The bulge depth of the specimens irradiated at 773 K was almost the same as that of specimens irradiated at 603 K. The uniform elongation of the irradiated specimens, however, was very small. It was almost zero for the 603 K irradiation, suggesting that localized deformation may control the tensile test. The tensile test may therefore more correctly provide only fracture-related information rather than true ductility data in the embrittled materials. The bulqe test may Drovide truer ductility data on these specimens, although the test does not seem to be sensitive enough for the specimen thickness considered. The results suggest that the materials retained considerable ductility for biaxial deformation even after irradiation at 603 K.

Relationship Between Maximum Bulge load and Bulge Depth. As mentioned above, the bulge depth must be taken into consideration for evaluating the maximum bulge load, because the load is a function of bulge deflection. The maximum bulge loads are plotted against the bulge depth in Figure 6 for the solution annealed specimens. Ductility loss and irradiation hardening are easily observed in the figure as an overall shift to the left and upward, respectively. Unirradiated cold worked specimens exhibit lower bulge depths and higher maximum bulge loads. After irradiation, they exhibit less hardening than the solution annealed specimens with no distinct change in the bulge depth.

Bulge Fracture Energy. The area bounded by the load-deflection curve gives the work done throughout the bulge deformation process and is defined as the bulge fracture energy. The bulge energy is plotted against alloy composition in Figure 7. A clear variation is evident in the bulge fracture energy as a function of nickel level, decreasing as Ni increased from 20 to 35% and increasing again at 45 Ni. Such a variation was not present in the tensile data. This should reflect the microstructural evolution of the alloy, and is

considered to correspond to the observation by Sekimura[12] that a larger variation in microstructure was seen at 45 Ni in this alloy system. The bulge energy may therefore be a useful parameter for mechanical property evaluation, regardless of disk thickness.

Scatter. The scatter in the present experiment was a little larger than in similar experiments performed on the thinner 0.1 mm disks, but it is still only on the order of 10%. Some of the scatter may be due to the difficulty of holding the thicker disk firmly against the die as well as the fact that the deformation mode was not constant.

CONCLUSIONS

It appears that the bulge test data may be used in two ways in the present experiment for the evaluation of mechanical properties. The tensile properties can be estimated from the bulge data by correlation of the bulge yield load, maximum bulge load and bulge depth with the yield strength, tensile strength and uniform elongation, respectively. Alternatively, the bulge fracture energy may be of potential use in the absence of tensile data.

FUTURE WORK

Micro-bulge tests will be performed on ferritic alloys irradiated in FFTF/MOTA, JOYO and JMTR for comparisons between different neutron spectra and irradiation temperatures.

REFERENCES

1. W. R. Corwin and G. E. Lucas, Ed., The Use of Small-Scale Specimens for Testing Irradiated Material, ASTM-STP-888, Philadelphia, PA. (1986).
2. G. E. Lucas, J. Nucl. Mater., 117 (1983) 327
3. M. Dooley, G. E. Lucas and J. W. Sheckherd, J. Nucl. Mater., 103 and 104 (1981) 1533.
4. G. E. Lucas, A. Okada and M. Kiritani, J. Nucl. Mater., 141-143 (1986) 532.
5. F. H. Huang, M. L. Hamilton and G. L. Wire, Nuclear Technology, 57 (1982) 234.
6. K. Abe, Kinzoku, 55 (1985) 24.
7. M. P. Manahan, A. S. Argon and O. K. Harling, J. Nucl. Mater., 103 and 104 (1981) 1545
8. G. E. Lucas, J. W. Sheckherd and G. R. Odette, ASTM-STP-888, Philadelphia, PA (1986).
9. J. M. Baik, J. Kameda and O. Buck, Scripta Met., 17 (1983) 1443.
10. A. Okada, G. E. Lucas and M. Kiritani, Trans. JIM, 29 (1989) 99.
11. M. L. Hamilton, A. Okada and F. A. Garner, Fusion Reactor Materials Semiannual Progress Report for Period Ending March 31, 1989, DOE/ER-0313/6, pp. 59-71.
12. N. Sekimura, private communication.

Table 1

Alloys Used in the MFE-4 Experiment[a]

Alloy	Comoosition, wt%	TEM Disk	Tensile
F19	Fe-19.7Ni-14.7Cr	SA	--
E20	Fe-24.4Ni-14.9Cr	SA,CW	SA
E21	Fe-30.1Ni-15.1Cr	SA	--
E22	Fe-34.5Ni-15.1Cr	SA,CW	SA
E23	Fe-45.3Ni-15.0Cr	SA	SA
E37	Fe-35.5Ni-7.5Cr	SA	--
E38	Fe-35.1Ni-21.7Cr	SA	SA

(a) SA - solution annealed.
CW - 30% cold worked.

Table 2

Normalized Micro-Bulge Data on Fe-Ni-Cr Alloys

	Yield load/t^2 (MPa)			Max. Bulge Load/dt (MPa)			Bulge Depth/d (unitless)			Average Normalized Bulge Fracture Energy (Nm)		
Alloy	Unirr.	603 K	773 K	Unirr.	603 K	773 K	Unirr.	603 K	773 K	Unirr.	603 K	773 K
E19-SA	368 398	1561 1398	1356 1334	1209 1095	1423 1346	903 840	0.952 0.927	0.775 0.787	0.419 0.356	0.228	0.281	0.065
E20-SA	345 315	1374	1286	1113 1095	1470	1337	0.927 0.902	0.838	0.787	0.216	0.254	0.239
E20-CW	1471 1430	1601	1717	1430 1425	1540	1383	0.762 0.737	0.762	0.813	0.256	0.261	0.244
E21-SA	420 445	1357 1151	1334	1065 1187	1319 1394	1334	0.876 0.902	0.762 0.775	0.787	0.202	0.274	0.261
E22-SA	420 435	1587	1470 1536	1157 1084	1329	1326 1308	0.889 0.851	0.749	0.775 0.762	0.191	0.268	0.261
E22-CW	1366 1639	1465 1480	1519	1278 1366	1377 1400	1360	0.724 0.724	0.762 0.762	0.801	0.259	0.265	0.266
E23-SA	524 517	1774	1465	1189 1237	1405	1350	0.876 0.876	0.762	0.762	0.205	0.272	0.283
E37-SA	403 420	1420 1315	1334 1351	1034 1067	1278 1238	1148 1167	0.864 0.876	0.787 0.775	0.762 0.749	0.173	0.358	0.233
€38-SA	467 459	1420	1379	1223 1189	1465	1406	0.889 0.851	0.775	0.778	0.222	0.284	0.311

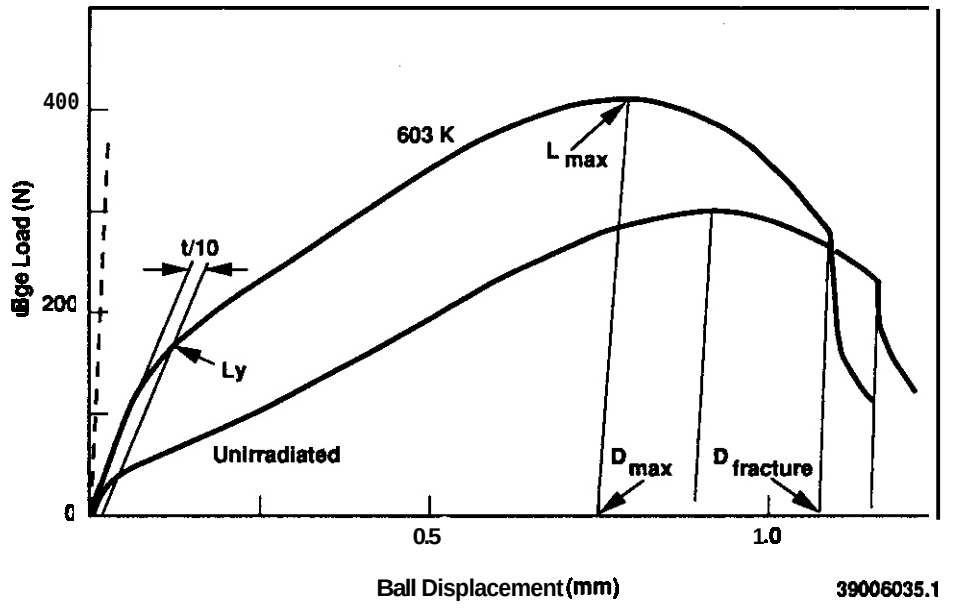

Figure 1. Examples of the bulge test curves and the parameters determined from bulge testing. Dashed line denotes the elastic deformation of the fixture, L is the bulge yield load, L_{max} is the maximum bulge load, D_{max} is the bulge depth, E is the bulge fracture energy, and t is the disk thickness. Curves shown for 25Ni-15Cr.

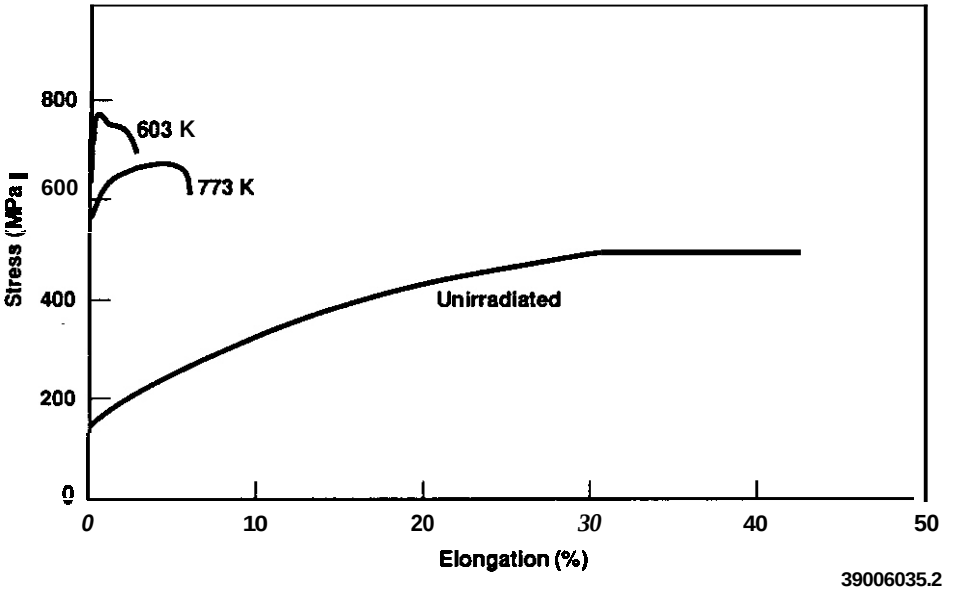

Figure 2. Tensile test curves for the same materials whose bulge test curves are shown in Figure 1.

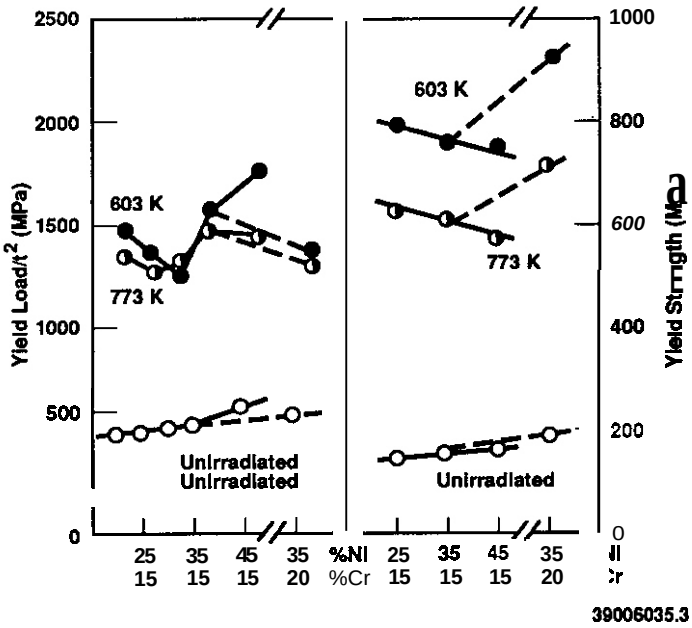

Figure 3. The bulge yield load (a) and yield strength (b) plotted against alloy composition. The bulge yield load is normalized by t^2, where t is the disk thickness. The solid lines denote Ni variations for a constant Cr level (15%). and the dotted lines denote Cr variations for a constant Ni level (35%).

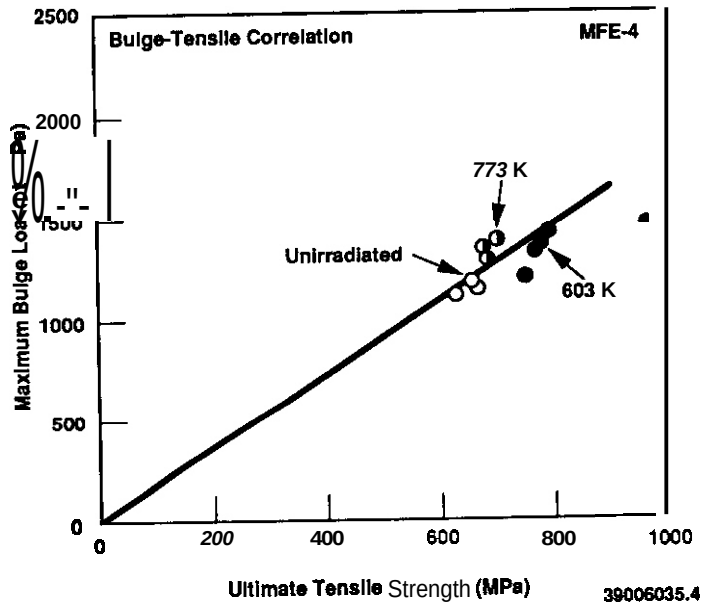

Figure 4. Maximum bulge load versus ultimate tensile strength. The maximum bulge load is normalized by the product dt, where d is the ball diameter and t is the specimen thickness.

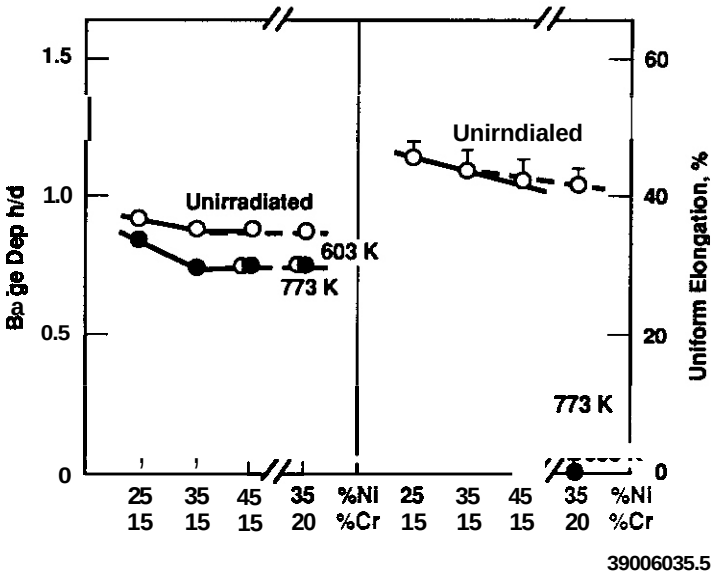

Figure 5. The bulge depth (a) and uniform elongation (b) plotted against alloy composition. The bulge depth is normalized by the ball diameter, d. The solid lines denote Ni variations for a constant Cr level (15%). and the dotted lines denote Cr variations for a constant Ni level (35%).

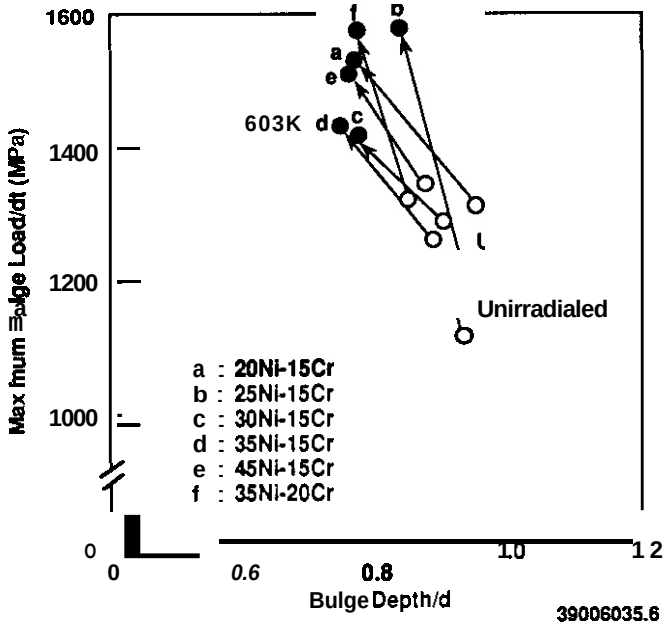

Figure 6. Shift in the maximum bulge load and in the bulge depth induced by irradiation in solution-annealed specimens.

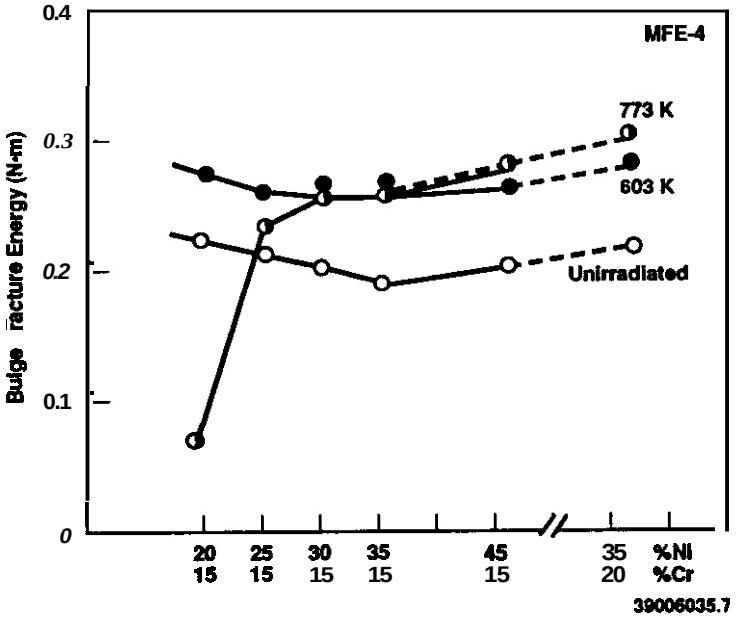

Figure 7. Bulge fracture energy as a function of alloy composition. The solid lines denote Ni variations for a constant Cr level (15%), and the dotted lines denote Cr variations for a constant Ni level (35%).

5. RADIATION EFFECTS: MECHANISTIC STUDIES, THEORY, AND MODELING

THE INFLUENCE OF HELIUM ON MICROSTRUCTURAL EVOLUTION: IMPLICATIONS FOR DT FUSION REACTORS

— Roger E. Stoller (Oak Ridge National Laboratory)

OBJECTIVE

This analysis is intended to help provide direction for future planning of experiments by the Fusion Reactor Materials Program and to support fusion reactor design teams.

SUMMARY

The influence of helium on the microstructural evolution of irradiated metals is reviewed. The review encompasses data from past work involving charged particle irradiations and neutron irradiations in fission reactors, but emphasizes more recent results. This latter data was obtained from experiments in which either the reactor neutron spectrum or the isotopic content of the nickel in the irradiated alloys was tailored to yield a ratio of helium to displacement production (He/dpa ratio) that is near the value that will be obtained in a DT fusion reactor. Both the absolute level of helium present and the He/dpa ratio are shown to be important parameters. All major components of the irradiated microstructure — cavities, precipitates, and dislocations — are shown to be sensitive to helium as a result of either its direct influence on cavity formation, or its indirect effect on point defect and solute partitioning. The results emphasize the importance of careful experimental and theoretical analysis if data from fission reactor experiments are to be used in fusion reactor design. In particular, the effects of helium appear to be greatest during the swelling incubation period, the time of most practical interest for fusion reactor designers.

PROGRESS AND STATUS

Introduction

When materials are irradiated by high energy neutrons, the displacement damage is accompanied by the production of impurity atoms due to nuclear transmutation reactions. The inert gas helium is the transmutation product that has received the most attention by those researchers concerned with fusion reactor materials. This interest is a result of the significant impact that helium is known to have on the microstructure of irradiated materials and the fact that the differences between the neutron spectra obtained in a fast fission reactor and in a deuterium-fusion (DT) fusion reactor result in much higher helium production rates in the latter. For example, the structural first wall nearest the plasma in a DT fusion reactor will be exposed to a neutron spectrum that leads to atomic displacement rates between 10^{-7} and 10^{-6} displacements per atom (dpa) per second. The ratio of transmutant helium to displacement production (He/dpa ratio) will be on the order of 10 to 20 appm He/dpa. The displacement rate in a typical fast fission test reactor such as the Experimental Breeder Reactor-I1 (EBR-II) or the Fast Flux Test Facility (FFTF) is similar to the fusion reactor, but the He/dpa ratio is about 0.3 to 0.5 appm He/dpa. As a result, data extrapolation from fast reactor to fusion conditions is not straightforward for any phenomena that are sensitive to the level of helium present.

The issue of which microstructural phenomena are helium-sensitive. and to what degree, has been discussed in detail since the mid-1970s. Odette addressed many of the broad issues in a 1979 review.[1] More recently, there have been several thorough reviews of this topic.[2-6] This report does not contain a detailed re-examination of such data as discussed in refs. 2 to 6; rather, the focus is on the results of more recent experiments that were designed specifically to address the uncertainty that remained after the earlier work. Some of the phenomena of interest here are sensitive to experimental variables that are not always well controlled and, in any single experiment, specimen-to-specimen variations can give rise to considerable data scatter. Therefore, the intent is to examine the earlier, broad data field to look for consistent trends and then to see if these trends are followed in the most recent experiments. This data analysis is supplemented by examining the results of theoretical investigations of radiation-induced microstructural evolution.

The fact that the microstructure of a material changes during irradiation can be viewed primarily as a result of incomplete recombination of the vacancies and interstitials that are produced. This simple view neglects any chemical influence of impurities produced by nuclear transmutation, but it provides a helpful basis for discussing microstructural evolution. In particular, the way in which transmutant helium influences microstructural evolution can most easily be understood by examining the way it influences point defect recombination. This perspective provides a common thread in the discussion that follows. The influence of helium on the radiation-induced or radiation-enhanced evolution of the three primary components of the microstructure of irradiated materials — cavities, dislocations, and precipitates — is examined in turn. Relevant experimental data and theoretical insights into the mechanisms involved will be discussed for each of the components. Finally, some inferences are drawn from our present understanding of helium effects relative to the issue of extrapolating data from fission reactor irradiation experiments to DT fusion reactor conditions.

Radiation-Induced Microstructural Evolution

Microstructural evolution in irradiated materials is a complex phenomenon, driven by a number of processes that lead to the evolution of the various components of the microstructure. Some of these processes are nearly independent of the others, while some interact in a synergistic or competitive way. The time-dependent evolution of the microstructure is primarily driven by the radiation-induced point defect fluxes. The point defect concentrations are in turn determined by the displacement rate, the rate of recombination, and the sink structure. The fact that mast point defects recombine with an anti-defect can be illustrated by noting that at a dose of 100 dpa, swelling in conventional AISI 316 stainless steel can be on the order of 50% (ref. 7). While such swelling sounds severe, it implies that a fraction of only 5.0×10^{-3} of the originally-produced vacancies avoided recombining with interstitials. The relative fraction of the defects that are lost to recombination in the matrix compared to those that recombine at sinks (e.g., due to interstitial absorption by a void) varies with the irradiation temperature and damage rate, but mast defects do recombine. Therefore, small changes in the defect survival fraction can have a large influence on microstructural evolution. Most of the discussion that follows is drawn from experience with austenitic stainless steels, but the general concepts apply to ferritic or martensitic steels* and other metallic alloys[9] as well. However, before turning to the discussion of microstructural evolution, some of the relevant differences between fission and fusion neutron spectra will be described.

Neutron Spectrum Effects — Collisions between high energy neutrons and the constituent atoms of a crystalline solid lead to the displacement of these atoms from their lattice sites. Each of these initially-displaced atoms are called primary knock-on atoms (PKAs) and they typically produce a large number of subsequent displacements. The energy spectrum of the PKAs is sensitive to the neutron spectrum as shown in Fig. 1.[10] Well-accepted procedures for calculating the total number of atoms displaced by a given PKA have been developed, one of the most common being that of Norgett, Robinson and Torrens (the so-called NRT model).[10,11] The dpa has proven to be a relatively robust damage correlation parameter, in part because it provides a basis for comparing the results of charged particle irradiation experiments with those from neutron irradiations.

In recent years, the general utility of the dpa has been questioned as additional research has indicated that only a relatively small fraction of the initially-produced defects survive intracascade annealing and contribute to the long-range diffusion of vacancies and interstitials.[12,13] In particular, the observation that the net displacement efficiency is a strong function of PKA energy[13] has raised new questions about data correlation from experiments in which the neutron (and hence PKA) spectrum vary. While the focus of much of the fusion materials research has been on the component of the neutron spectrum with energies above 10 MeV, this recent work implies that mare attention should be given to the area below about 10 to 50 keV. Figure 2 compares neutron spectra from several commonly used test reactors and a DT fusion spectrum.[14] The figure indicates that the DT fusion spectrum differs sianificantly from fission test reactors *in* the' low energy regime-as well as the high. If the lower energy neutrons prove to be as significant as it now appears they are, material performance in the first wall may also prove to be sensitive to the details of blanket design. For example, the use of water as a coolant will lead to a much higher flux of low energy neutrons than if a liquid metal coolant is used.

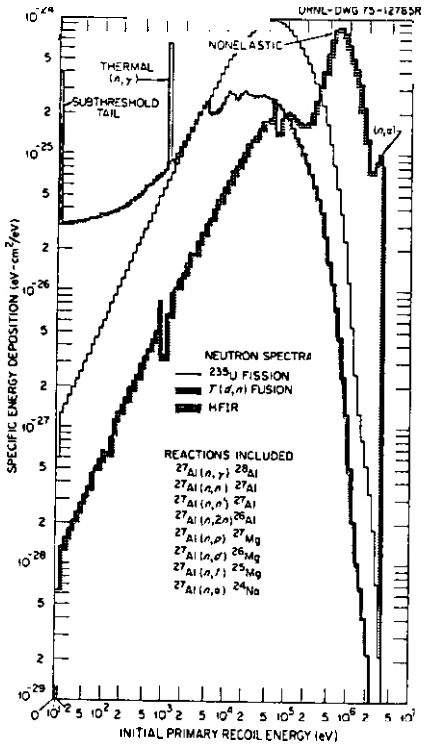

Fig. 1. Calculated primary recoil spectra in aluminum for various neutron spectra.[10] The curve marked ^{235}U is similar to a fast reactor spectrum.

Because of the spectral differences just mentioned, all attempts to correlate radiation effects data for the purpose of extrapolating from fission to fusion irradiation conditions must be based on the broadest possible data base, and be supplemented by a sound theoretical understanding of the mechanisms responsible for the observed behavior. However, with these caveats in mind, the discussion here will use the dpa as the best correlation parameter that is currently available. A second spectrum-dependent irradiation parameter that will be used is the He/dpa ratio. While it is not thought of as a correlation parameter, it does provide a convenient way of characterizing different irradiation environments. For similar damage rates, differences in the Heldpa ratio are known to lead to consistent changes in the irradiated microstructure. Thus, the information on helium effects which is obtained by varying the He/dpa ratio in high-dose-rate charged particle irradiations can be helpful for anticipating the effects of helium at low dose rates. Such information is needed to extrapolate fission reactor data to fusion reactor conditions.

Table 1 compares damage rates and He/dpa ratios from several facilities that have been used by fusion materials researchers in the United States[15,16] with those calculated

Table 1. Displacement and helium generation rates in AISI 316 stainless steel in various irradiation facilities', [15-17]

Facility	Damage Rate (dpa/s)	He/dpa Ratio (appm He/dpa)
Typical charged particle irradiation	1.0×10^{-3}	0.0 to 50
EBR-II	1.2×10^{-6}	0.4
FFTF	1.8×10^{-6}	0.2
HFIR	1.0×10^{-6}	0.8 to 65*
ORR	2.3×10^{-7}	0.2 to 8.3*
DT fusion at 1.0 MW/m^2	3.7×10^{-7}	13.8

'Nonlinear due to buildup of ^{59}Ni.

for a typical DT fusion reactor.[5] Helium generation in the High Flux Isotope Reactor (HFIR) and the Oak Ridge Research Reactor (ORR) is shown as a range in Table 1. Since these reactors are water cooled, they have a large thermal neutron flux as shown in Fig. 2. In nickel-bearing alloys, thermal neutron absorption by ^{58}Ni leads to a helium generation rate that increases in a non-linear fashion from the low number in Table 1 to a maximum given by the greater number via the two-ste reaction ^{58}Ni(n,γ)^{59}Ni(n,α)^{56}Fe. The recoiling ^{5} Fe atom from this reaction generates significant number of additional displacements as well.[17] This additional increment in displacements is also non-linear. For AISI 316 stainless steel with 13% nickel, the contribution of the ^{56}Fe recoils is about 1% of the total dose at 1 dpa. increasing to a maximum of 13% when the total dose is 65 dpa. The contribution declines at higher doses.[17]

As Table 1 shows, the fusion displacement rate *is* easily achieved, but the fission reactor helium generation rates are either too low or too high. Two techniques that have been developed to improve the fusion simulation are spectral and isotopic tailoring. In the first, selective shielding of thermal neutrons in the ORR was used in several experiments to obtain a nearly constant He/dpa ratio at near the damage rate as shown in Table 2.[18,19] The data obtained from these experiments will be discussed below. The second technique involves tailoring the isotopic abundance of one or more of the atomic species in the composition of an alloy in order to take advantage of the fact that the different isotopes have have different (n,α) cross-sections. This method was apparently first suggested by De Raedt[20] in 1982 and developed in mare detail by Simons[21] in 1983 and Mansur et al.[22] in 1986. Experiments have been planned by several groups to irradiate nickel-bearing alloys in which the nickel content was isotopically tailored by selective additions of ^{58}Ni, ^{59}Ni, and/or ^{60}Ni to obtain nearly the fusion He/dpa ratio in both the HFIR and the FFTF.[22-24] The initial results from one of these isotopic tailoring experiments will also be discussed below.[25]

Table 2. Displacement and helium generation rates in AISI 316 stainless steel in ORR experiments MFE-4A, 4B, 6J, and 7J (refs. 18,19)

Experiment	Irradiation Temperature (°C)	Final Dose (dpa)	Damage Rate (dpa/s)	He/dpa Ratio (appm He/dpa)
MFE-4A	400	5.35	1.4×10^{-7}	15.3
MFE-4B	500, 600	5.35	1.4×10^{-7}	14.8
MFE-6J	60, 200, 300, 400	6.88	1.7×10^{-7}	8.95
MFE-7J	60, 200, 300, 400	7.92	1.9×10^{-7}	12.2

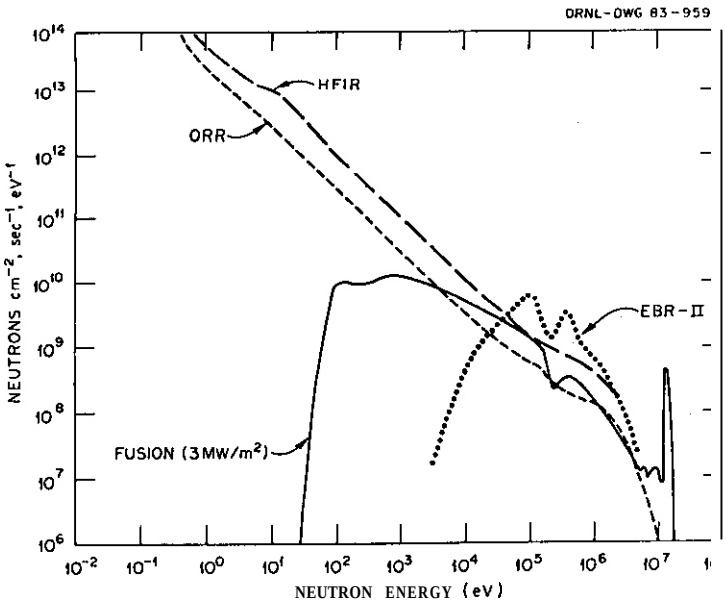

Fig. 2. Neutron energy spectra for three fission test reactors and a typical DT fusion spectrum.

Cavity and Dislocation Evolution — The terms cavity, bubble and void have sometimes been used in an ambiguous way when discussing irradiated metals. For purposes of this report, the term cavity denotes any hollow inclusion in the material. Bubble will be used to denote a cavity that is primarily stabilized by its internal gas pressure (i.e., the internal gas pressure P is nearly equal to $2\gamma/r$, where γ is the surface free energy and r is the radius). The term void is used for cavities which are not gas stabilized (i.e., $P<<2\gamma/r$). Only those cavities induced by irradiation are of interest here.

Although it is possible for voids to form via classical nucleation, it has been shown that this mechanism cannot account for void formation at the level commonly observed in irradiated metals.[26] The generally accepted sequence of events which lead to void swelling is that gas bubbles nucleate and slowly grow by accumulating both vacancies and helium until they reach a critical radius, r_c^*. The critical radius is determined by the effective vacancy supersaturation, Φ, the irradiation temperature, T, the surface free energy and the atomic volume, Ω.

$$r_c^* = f(\ell n\Phi)\,\frac{\gamma\Omega}{kT\ell n\Phi} \qquad (1)$$

The constant k in Eq. (1) is Boltzman's constant and the function $f(\ell n\Phi)$ is a non-ideal gas correction factor;[27] for an ideal gas, f = 413. An analogous expression can

be derived for the critical number of gas atoms, n_g^*, that corresponds to the critical radius.[27] After reaching the critical radius, the bubbles convert to voids and begin to grow primarily by vacancy accumulation. The pivotal role of transmutant helium in this method of void formation in charged particle and fast neutron irradiated stainless steels has been confirmed by a number of workers.[4,26,28,29] The importance of gas accumulation is shown in Fig. 3 where the calculated ratio of the void nucleation time due to the gas accumulation mechanism to that by classical nucleation is plotted as a function of the helium content of a test cavity.[26] These results indicate that the classical nucleation mechanism begins to be significant only when the gas content of the cavity is near the critical number of gas atoms.

The effective vacancy supersaturation provides a measure of a material's deviation from thermal equilibrium during irradiation:

$$\Phi = \frac{z_v^c D_v C_v - z_i^c D_i C_i}{z_v^c D_v C_v^e} \qquad (2)$$

where the interstitial and vacancy concentrations and diffusivities are given by $C_{i,v}$ and $D_{i,v}$; C_v^e is the thermal equilibrium vacancy concentration, and the $z_{i,v}^c$ are the cavity capture efficientles for interstitials and vacancies. In the absence of radiation, $\Phi = 1.0$ The supersaturation, and hence the critical radius, can be calculated from the point defect generation rate and the sink strengths of the extended defects in the material.[27] For example, when bulk recombination is negligible and dislocations are the major point defect sink, the vacancy supersaturation takes the following simple form.[30]

$$\Phi = \frac{G}{S_d D_v C_v^e} (z_i^d - 1)$$

where G is the effective damage rate, S_d is the dislocation sink strength, and z_i^d is the dislocation capture efficiency for interstitials. Similar, but more complex expressions are obtained when the effects of recombination or other sinks are included. Equations **(1)** and (3) reflect the importance of the radiation-produced microstructure. The alloy chemistry determines such parameters as the surface energy and diffusivities. However, for a given chemistry, the microstructure determines the void swelling incubation time. The important point is that changes in the point defect sink strengths or the rate of point defect recombination are directly reflected in the vacancy supersaturation and in the critical bubble radius. Changes in the critical radius lead to changes in the void swelling incubation time.

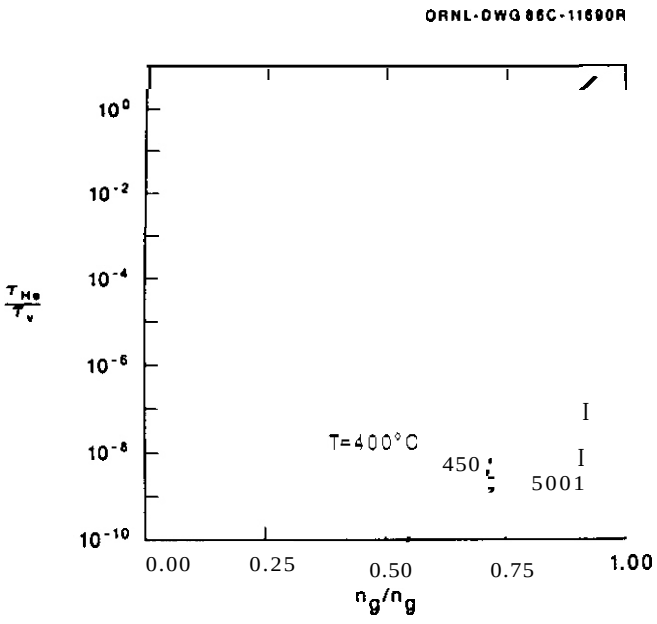

Fig. 3. Calculated ratio of the void nucleation time due to the gas accumulation process to that by classical nucleation as a function of the helium content of a test cavity.[26]

In addition to the absolute level of the various sink strengths, the ratio of the interstitial-biased dislocation sink strength to the other sinks is also of importance.[30-32] The influence of the sink strength ratio is shown in Fig. 4 where the effective vacancy supersaturation is plotted as a function of the dislocation density with typical cavity densities at 400 and 550°C. The results shown in Fig. 4 were obtained from a detailed theoretical analysis of microstructural evolution[30,32] and show that changes in the dislocation density can lead to either increases or decreases in the supersaturation. This effect is due to the balance of point defect partitioning between the network dislocations and the other microstructural sinks, particularly the small highly pressurized bubbles that are present early in the irradiation. When dislocations are the dominant sink, Eq. (3) indicates that increases in the dislocation density reduce the vacancy supersaturation. This increases the critical bubble size and extends the incubation time for void swelling. The influence of the dislocation/interstitial bias is mitigated by the presence of a nearly equal vacancy flux, leading *to* the recombination of most point defects absorbed at dislocations. When dislocations are not the dominant sink, an increased dislocation density will result in an increased supersaturation and reduce the swelling incubation time.

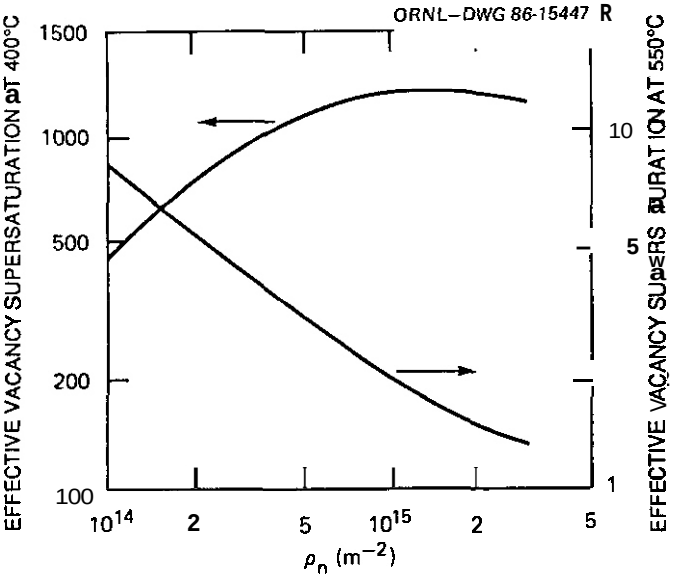

Fig. 4. Influence of the network dislocation density on the effective vacancy supersaturation at 400 and 550°C. Calculations reflect the use of a value for the cavity sink strength that is representative of the temperature.

This dependence of the vacancy supersaturation on the dislocation and cavity components of the irradiated microstructure is further illustrated in Figs. 5 to 7 with results obtained from the model described in refs. 26 and 30. Figure 5 shows the predicted network dislocation density, Frank faulted loop density, and void swelling as a function of dose for 20% cold-worked material irradiated at 500°C. These predictions are consistent with a broad set of experimental observations.[30] After an initial transient that lasts for several dpa, the microstructure reaches an apparent steady state which lasts until void swelling begins at about 40 dpa. During this "steady state" period, the cavity sink strength is slowly increasing while bubbles grow below the critical size. The corresponding cavity volume is too small to be seen on the scale of Fig. 5. The incubation time for swelling is not primarily associated with the microstructural transient but rather with the time required for the bubbles to accumulate the critical number of helium atoms. Following the initiation of void swelling, some additional dislocation recovery occurs as the cavity sink strength begins to increase. This recovery is due to an increase in dislocation climb as the dislocations absorb a greater excess of interstitials now that the vacancies are being absorbed by the voids. A regime in which the swelling rate is approximately constant and fairly high occurs when the cavity and dislocation sink strengths have similar values. When such parity occurs, the most efficient differential partitioning of the point defects takes place and the maximum theoretical swelling rate is observed.[31,33] This effect is shown in Fig. 6 where both the swelling rate and the ratio of the dislocation sink strength to the cavity sink strength are plotted as a function of dose. The swelling rate passes through a maximum value of about 1%per dpa when the sink strength ratio is about 1.0 and then begins to slowly decrease.

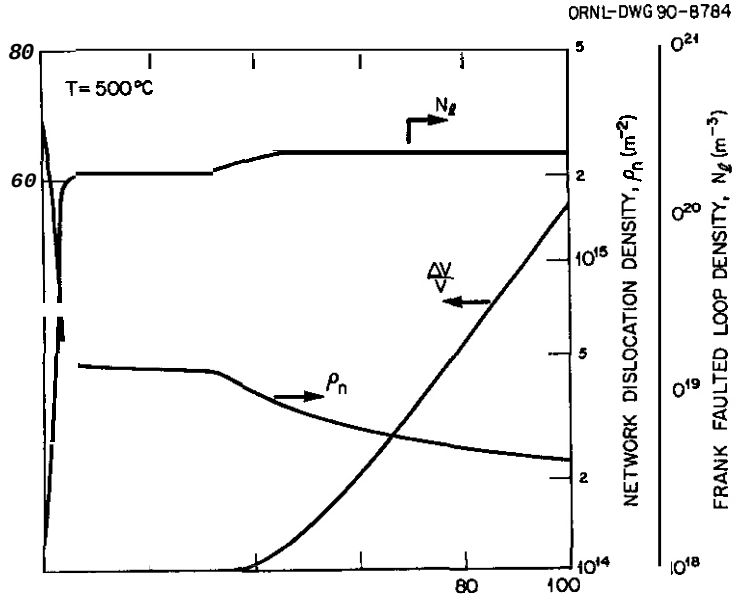

Fig. 5. Dose dependence of the calculated swelling, network dislocation density, and Frank faulted loop density for 20% cold-worked material irradiated at 500°C.

Once swelling begins, the evolution of the microstructure can suppress further void formation by reducing the vacancy supersaturation as shown in Fig. 7. The void swelling curve from Fig. 5 is repeated in Fig. 7, along with the vacancy supersaturation and the critical number of gas atoms. The reduction in the vacancy supersaturation leads to an increase in the critical number of gas atoms. Thus bubbles that are formed after the initial population can be effectively trapped below the critical size. This contributes to the formation of the bi-modal cavity distributions that are commonly reported.[34]

Precipitation and Solute Segregation – Altnough precipitate evolution and solute segregation during irradiation have been extensively studied for many years, the research has not yielded a theoretical description of the phenomena that can be broadly applied. However, there is a reasonably large body of data from which a number of general observations can be drawn. In austenitic stainless steels, undersized solutes such as nickel and silicon have been shown to segregate to internal defect sinks, such as loops and grain boundaries, and to free surfaces during irradiation.[35-37] Oversized solutes are

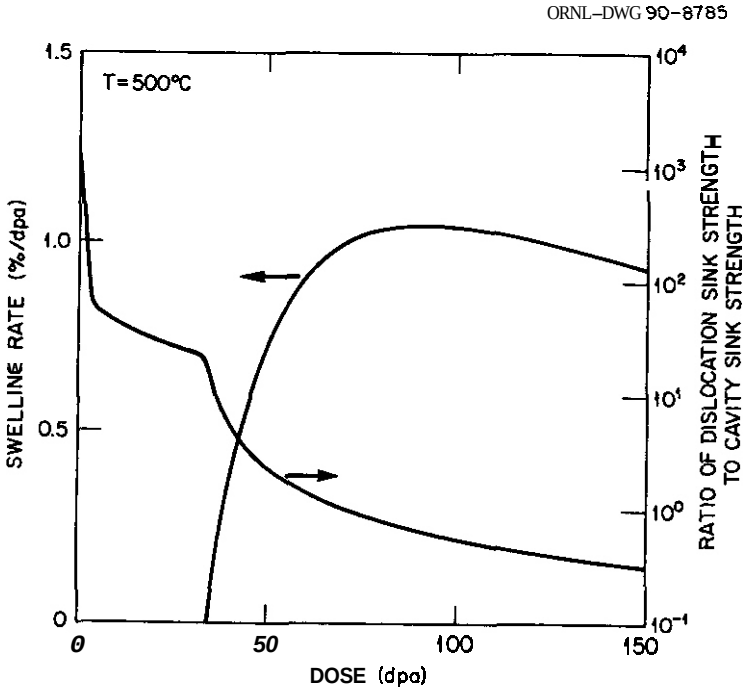

Fig. 6. Dose dependence of the swelling rate and the ratio of the dislocation sink strength to the cavity sink strength for 20% cold-worked material irradiated at 500°C.

correspondingly depleted from these regions. In extreme cases, solute segregation can lead to ferrite formation due to the breakdown of austenite.[38]

More generally, radiation-induced solute segregation (RIS) can lead to the formation of phases that are not observed during thermal aging. It can also alter the composition of phases that are stable under thermal aging, and it can change the time and temperature regimes in which thermally-stable phases are observed. These three types of phases have been referred to as radiation-induced, radiation-modified and radiation-enhanced phases, respectively.[38] In austenitic stainless steels, the primary radiation-induced phases are γ' and G phase, while eta and Laves phases are radiation-enhanced. Laves is also radiation-modified.

In many cases, void swelling has been shown to correlate with the extensive formation of radiation-induced phases.[39-42] This is not surprising since both of these phenomena reflect the non-equilibrium, radiation-induced point defect supersaturations. The fact that void swelling occurs due to differential partitioning of vacancies and interstitials has already been mentioned. In an analogous way, differential solute segregation that results from the dependence of the dislocation bias on the interstitial relaxation volume has been proposed as a mechanism that could be responsible for some radiation-induced phase formation.[6,42]

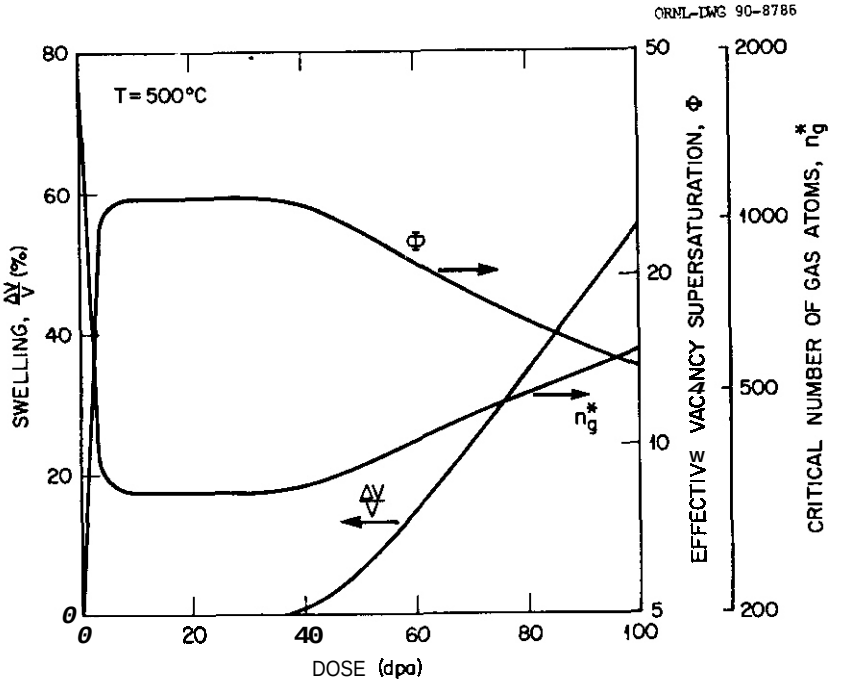

Fig. 7. Dose dependence of swelling, the effective vacancy supersaturation, and the critical number of gas atoms for 20% cold-worked material irradiated at 500°C.

Since the solute fluxes responsible for RIS are due to the radiation-induced point defect fluxes,[36,43] RIS and radiation-induced phase formation should be sensitive to any parameter that alters the flow and fate of point defects. For example, if the point defect supersaturations are reduced as a result of changes in the microstructure that increase recombination, thermal phase evolution should be favored. At the same time, less void swelling should occur. The irradiation of advanced austenitic alloys has confirmed this ex ectation; alloy modifications that reduce the formation of radiation-induced phases also reduce swelling.[e4]

Effects of Helium on Microstructural Evolution

Helium can exert a strong influence on microstructural evolution by changing the fraction of point defects that recombine. There are at least two ways that this can be accomplished. First, helium can alter bulk recombination rates by trapping either vacancies or interstitials. Mansur has shown that the effect of point defect trapping can be modeled using an effective recombination coefficient.[45] According to the theory, trapping of either interstitials or vacancies should lead to increased recombination. However, because it is a gaseous impurity, helium could also act to stabilize vacancies by inhibiting recombination with metallic interstitials. Since the long-term survival of point defects requires the presence of both a biased sink and a second sink for partitioning, a second way that helium can affect the surviving defect fraction is by changing the relative fraction of the different sinks that are formed under irradiation. As pointed out above, if the microstructure is dominated by any one sink, increases in the density of that sink will reduce the effective vacancy supersaturation. The first of these two phenomena cannot be directly observed, but the second is regularly reported. In the next few sections, evidence for both will be presented.

Helium Effects on Dislocation Structure — The amount of data from which to infer the effects of helium on dislocation evolution is limited since the attention of most researchers investigating helium effects has been focused on cavity evolution. The interest in observing voids has also directed attention to relatively high doses that are beyond the dislocation transient that is shown in Fig. 5. Most of the data that is available involves the use of an accelerator to implant helium prior to irradiation with either neutrons or heavy charged particles, or experiments that involve simultaneous helium implantation and ion irradiation. References 2 and 3 discuss a number of examples of such experiments. Only a summary will be given here.

The data shown in Fig. 8 were obtained by Ayrault et al.[46] after simultaneous helium implantation and nickel ion irradiation. These data illustrate a common observation, namely, that high levels of helium tend to increase the dislocation density at low to moderate doses. At higher doses, the effect appears to diminish. They also reported that loop evolution proceeded at a faster rate in the specimens irradiated at the highest He/dpa ratio (i.e. the dislocation structure passed from being primarily composed of loops to a dislocation network at a lower dose). In contrast, Choyke et al.[47] found little effect of helium on the total dislocation density in AISI 304 stainless steel that was irradiated with silicon ions followins pre-implantation of helium at room temperature. However, they found that the loop fraction of the dislocation structure increased strongly with the level of helium that was implanted.

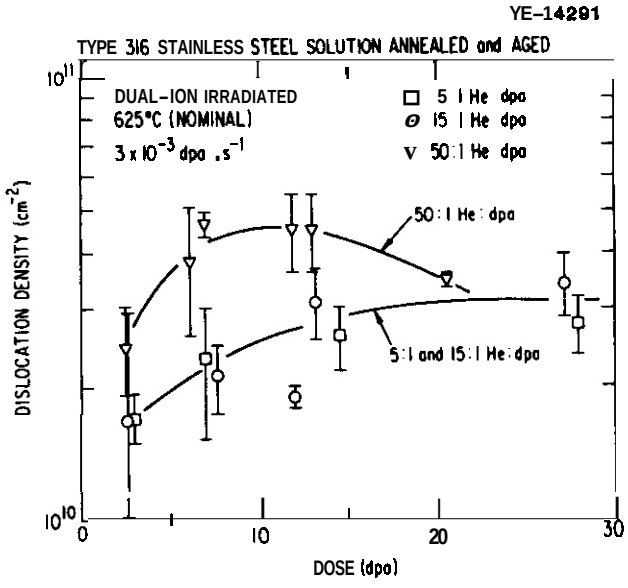

Fig. 8. Influence of He/dpa ratio on dislocation evolution in solution-annealed and aged AISI 316 stainless steel under nickel ion irradiation.[46]

In an another experiment that involved helium pre-implanted specimens, Farrell et al.[9] also observed an enhancement of dislocation formation. They imolanted 4 appm He in aluminum specimens at about 100°C, subjected them to several post-implantation heat treatments, and then irradiated them in the HFIR to a peak dose of 2.6 dpa. In order to separate the influence of the implanted helium from that of the displacement damage that the implantation produced, they also irradiated specimens that were exposed to an a-particle beam of high enough energy that the helium atoms passed completely through. Unimplanted specimens were also irradiated. A portion of their results pertaining to dislocations is summarized in Fig. 9 which shows a clear influence of helium. No difference is observed between the specimens that received no helium and those specimens that had the helium pass completely through. At the lowest doses, the loop density is roughly a factor of 10 higher in the helium implanted specimens. Since loops provide the major source of dislocations, this leads to a similar enhancement of the network dislocation density at intermediate doses. The explanation offered by Farrell et al. for their observations

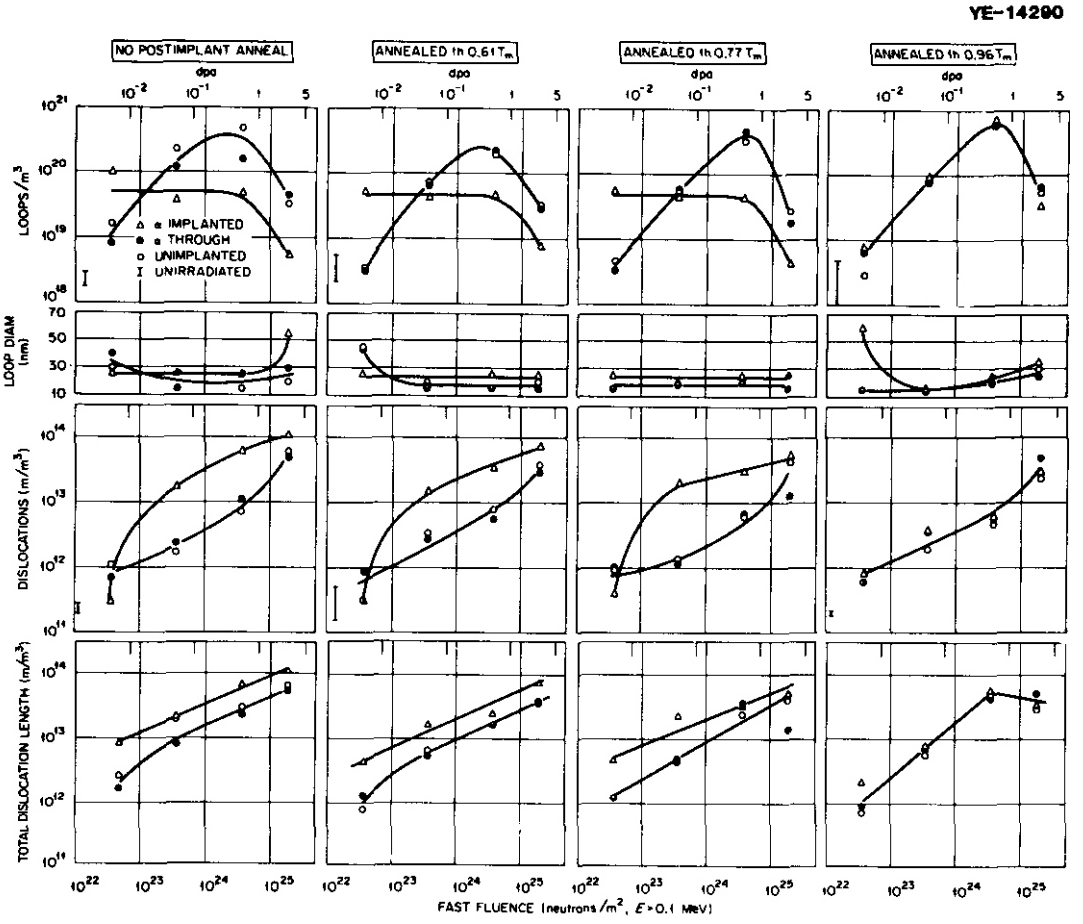

Fig. 9. Fluence dependence of the dislocation structure in aluminum irradiated in the HFIR at 60°C following helium implantation and post-implantation annealing at the indicated temperature.[9]

was that a greater fraction of the interstitials were able to escape recombination and form loops because the corresponding vacancies were trapped by the implanted helium.[9]

A third type of experiment that provides some insight into the mechanism by which helium influences dislocation evolution is to characterize the microstructure that evolves during thermal annealing following helium implantation. There have been a number of such studies,[14,48-52] with the earliest being that of Barnes and Mazey in 1960 (ref. 48). Beginning from an as-implanted microstructure that consists of only "black spot" damage, isochronal annealing experiments consistently show the correlated evolution of faulted interstitial loops and helium bubbles. A typical result from Stoller and Odette[52] is shown in Fig. 10. They implanted the model austenitic alloy, P7, with 40 appm helium at room temperature and then annealed the specimens for 1 h at various temperatures. The average radii of faulted loops and helium bubbles that they observed are shown. At thermal equilibrium, the loops would be expected to shrink during annealing, not grow. Two reasonable explanations for the unexpected growth of interstitial loops in these annealing experiments can be presented. One is that the high gas pressure in small helium/vacancy clusters leads them to emit self-interstitials that can drive loop growth.[53] A second is that this same high pressure can reduce vacancy emission from the clusters to such an extent that the matrix becomes subsaturated with vacancies. In this case, uncompensated thermal vacancy emission by the interstitial loops leads to their growth. Calculations simulating the annealing experiment have demonstrated the feasibility of this second mechanism.[54]

The dislocation data just discussed is consistent with helium having an indirect effect on dislocation evolution by changing the partitioning of the point defects. Interstitial loop nucleation and growth is enhanced because helium strongly traps vacancies and inhibits recombination. Although the evidence of a helium effect on the dislocation structure appears to be erased at higher doses, this same mechanism could continue to influence cavity evolution. The most direct effect could be on void nucleation since the critical bubble radius is a function of the other microstructural components as discussed above [see Eq. (3)].

The question of concern for fusion reactor designers is whether or not the behavior observed in these experiments indicates that the higher fusion He/dpa ratio will lead to comparable changes relative to the results of fission reactor irradiations. There is only a limited amount of microstructural information that is directly applicable to this question. Figure 11 compares the dislocation structure

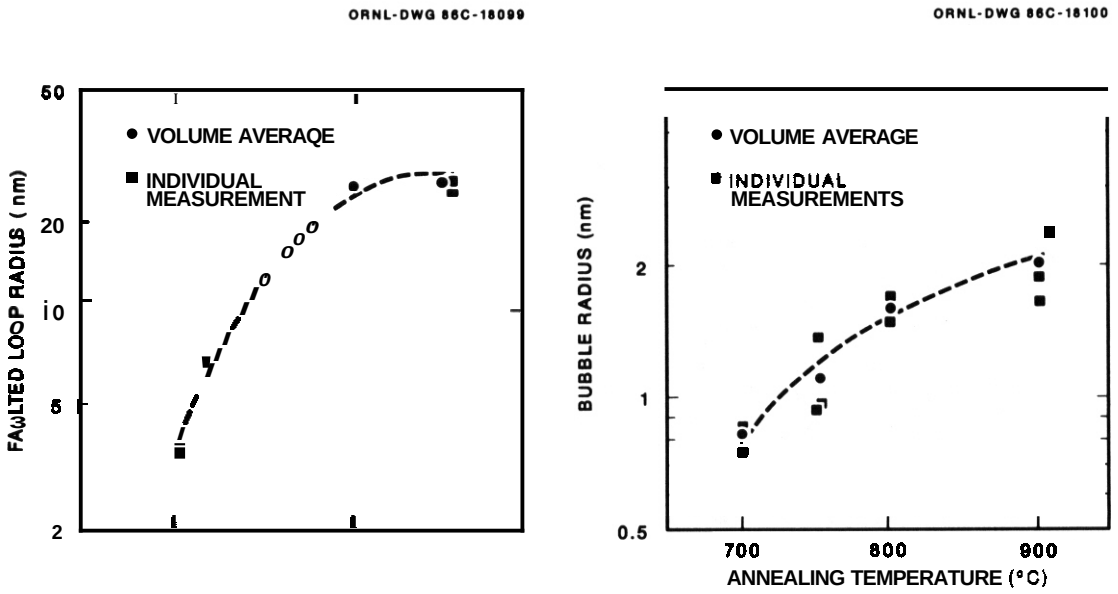

Fig. 10. Evolution of: (a) faulted loops and (b) helium bubbles observed in alloy P7 during isochronal annealing for 1 h at the indicated temperature following room temperature implantation of 40 appm helium.[52]

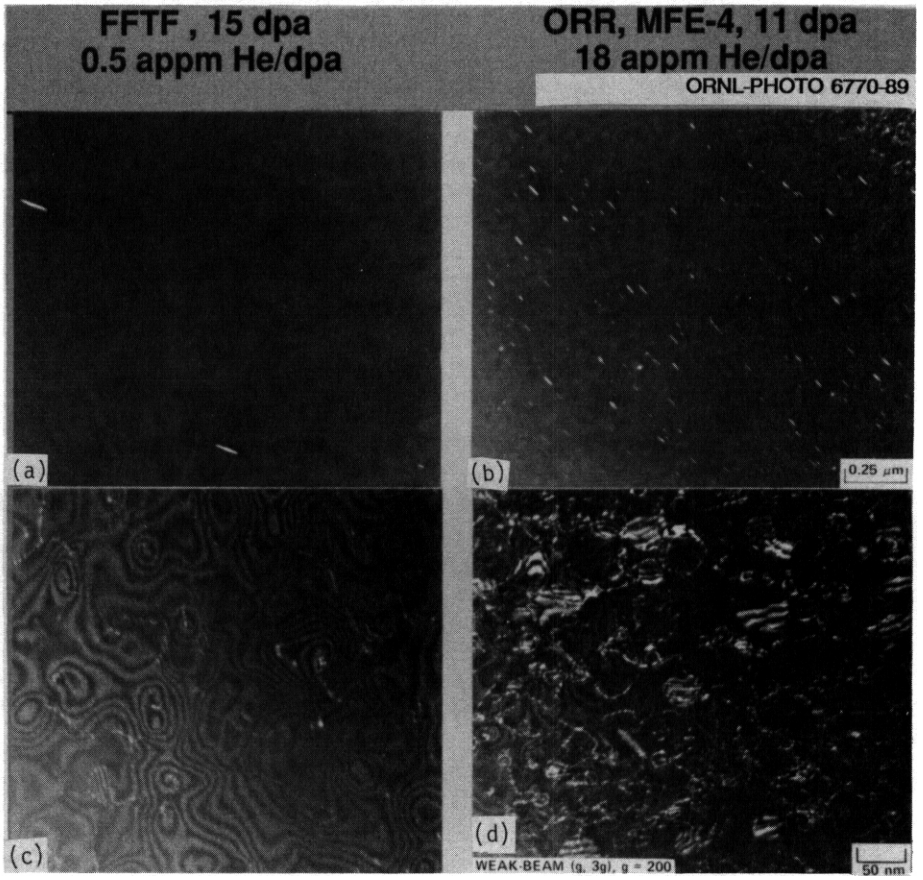

Fig. 11. Comparison of dislocation structure observed in 25% cold-worked PCA after irradiation to 10 to 15 dpa in the FFTF (a,c) and MFE-4 spectral tailoring experiment in the ORR (b,d) (ref. 55).

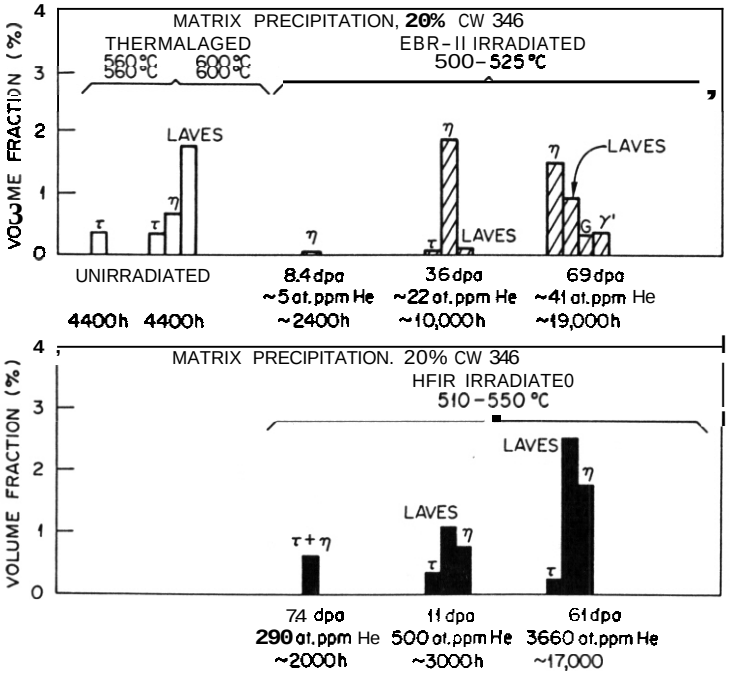

Fig. 12. Comparison of the phases formed in AISI 316 stainless steel during thermal annealing (a) with those formed during irradiation in the EBR-II (a) and the HFIR (b) (refs. 3, 60).

much greater swelling was observed in the specimens that exhibited greater RIS and radiation-induced precipitation.

Because the data field from neutron irradiations is sparse, it is difficult to draw any firm conclusions regarding the effects of helium on RIS and radiation-induced precipitation. In fact, the interpretation of the data from the EBR-II/ HFIR inter-reactor comparison that was just mentioned has generated some controversy.[61,62] However, the bulk of the ion data and the EBR-II/HFIR comparison support the conclusion that high levels of helium can reduce RIS. Two mechanisms are believed to be responsible for this suppression, and both are due to the higher densities of cavities and loops that are obtained at higher helium levels. One is that a high sink density dilutes RIS by partitioning the solutes to more sites. The second is increased point defect recombination at sinks. The increased recombination means that the point defect fluxes that drive RIS are reduced. This increase in recombination at sinks is not inconsistent with the reduced recombination in the matrix that was proposed to account for higher loop densities above because the doses of interest are different. In the case of loop formation, the effect of helium is at very low doses and reduced bulk recombination

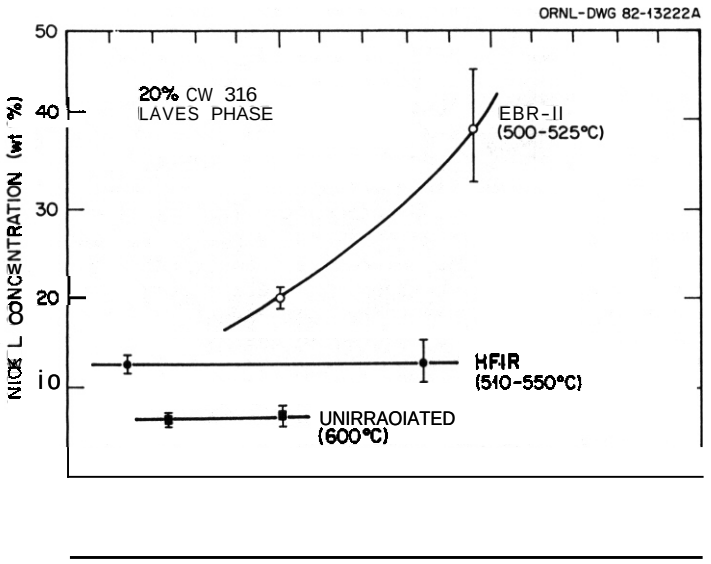

leads to higher loop (and cavity) nucleation rates. Then, at higher doses, recombination at sinks is increased because of the higher sink density.

The implications of this observed suppression of RIS for fusion are not clear since the suppression may be only a transient effect, delaying, but not eliminating RIS.[2] Because of the coupling of RIS and void formation, delaying RIS should extend the swelling incubation tine. Experience with advanced alloys developed in the U.S. Fusion Materials Program support this expectation.[**] However, since the degree of RIS suppression varies with the helium level, additional experiments need to be done to verify the behavior at the fusion He/dpa ratio. The limited results obtained in the MFE-4 spectral tailoring experiment indicate that the correlation between radiation-induced phase formation and swelling is maintained at the fusion He/dpa ratio. The cavity and precipitate microstructures that were observed in 25% cold-worked PCA after irradiation at 400, 500, and 600°C in this experiment are shown in Fig. 14 (ref. 55). However, the rapid dissolution of the thermally-stable MC phase and the loss of swelling resistance at only

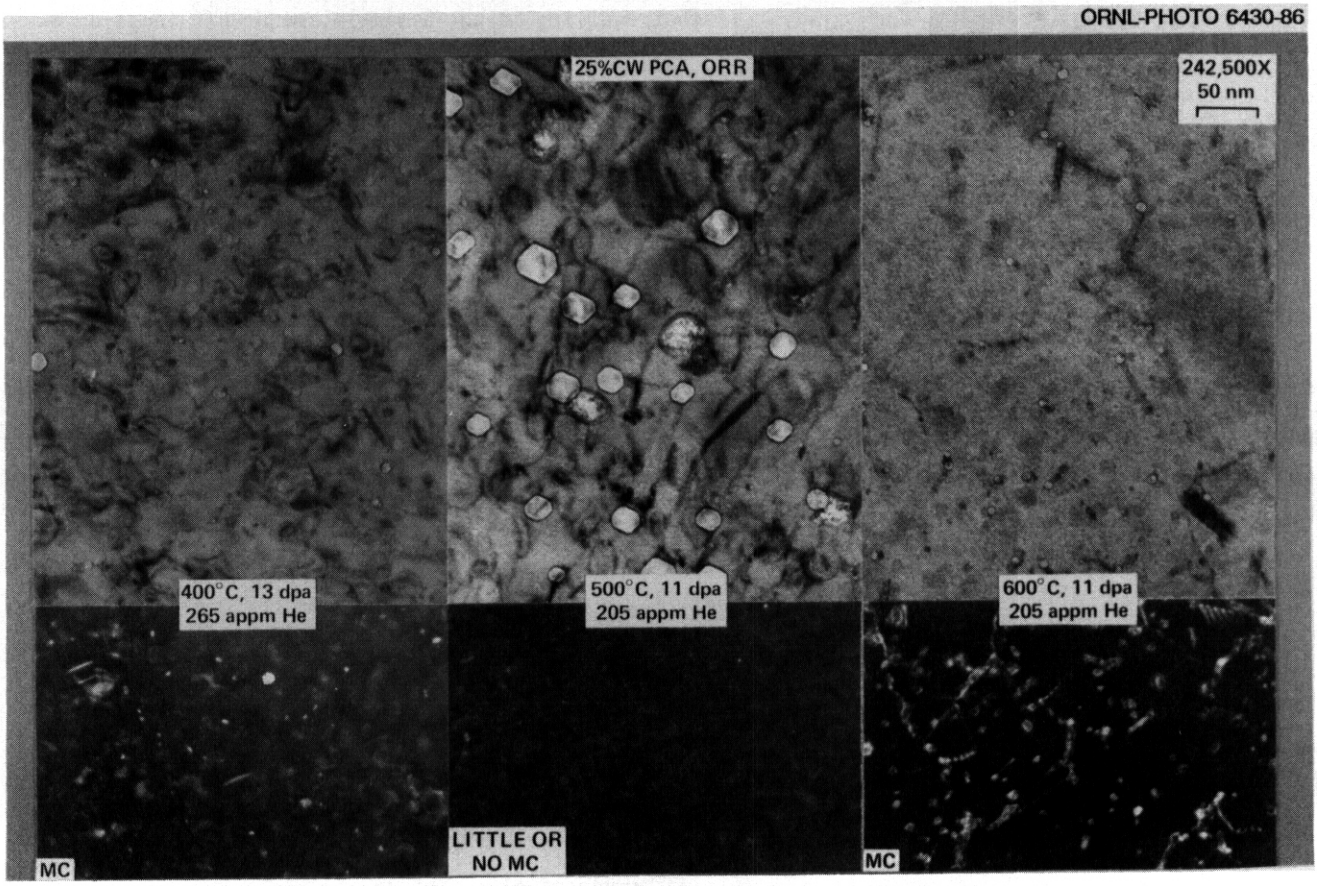

Fig. 14. The cavity and precipitate microstructures observed in 25% cold-worked PCA after irradiation at 400, 500, and 600°C in the MFE-4 spectral tailoring experiment in the ORR.[55]

11 dpa at 500°C serve to emphasize the importance of doing alloy development in an environment that is representative of the ultimate application. This alloy does not exhibit such behavior until much higher doses in experiments in which the He/dpa ratio is either much lower (EBR-II) or much higher (HFIR).[44]

Helium Effects on Cavity Formation and Void Swelling — A fairly extensive data base on the effects of helium has been generated over the last 15 to 20 years by researchers at many universities and laboratories. Most of this work has involved either helium implantation followed by neutron or charged particle irradiation, or helium implantation with simultaneous charged particle irradiation. This work is supplemented by a limited amount of data from several reactor irradiation experiments. The EBR-II/HFIR inter-reactor comparison that has already been mentioned provides swelling results at very low and very high helium levels. Another reactor experiment investigated the influence of cavity sink strength on void swelling in the FFTF. In order to produce a high bubble density, the specimens were initially irradiated in the HFIR and the irradiation was then continued in the FFTF.[63,64] The most recent, and most relevant swelling data, is that from the spectral tailoring experiments conducted in the ORR[55] and an isotopic tailoring experiment that was conducted in the FFTF.[25]

The ion irradiation data has been extensively reviewed.[2-6,65] The major conclusion that can be drawn from that work is that higher levels of helium (or other implanted gases) lead to a higher cavity density. In an early investigation that was concerned with fission gas bubble formation in fuels, Greenwood et al. used a simple kinetic mdel to show that the bubble density should be proportional to the gas generation rate to the one-half power.[66] Later theoretical work by Singh and Foreman demonstrated this same power law dependence.[67] A review of the ion data indicates that the experimentally observed dependence varies between about $G_{He}^{0.25}$ and $G_{He}^{1.0}$ (ref. 65). where G_{He} is the helium implantation rate if co-implanted or the helium concentration if the helium is pre-implanted. This same dependence is observed in 20% cold-worked AISI 316 stainless steel irradiated in both the EBR-II and the HFIR as shown in Fig. 15 (refs. 3.14) where the peak bubble density in the HFIR-irradiated specimens is 25 to 30 times greater than in those irradiated in the EBR-II. Since the ratio of the peak helium generation rate in the HFIR to that in the EBR-II is about 200, the cavity densities shown in Fig. 15 correspond to an exponent of about 0.6.

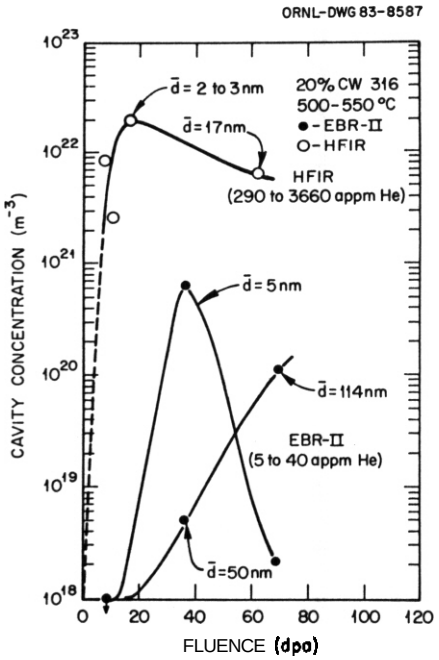

Fig. 15. Dose dependence of cavity formation observed in 20% cold-worked AISI 316 stainless steel[3,14] irradiated in the EBR-II and HFIR at 500-550°C. Separate curves are shown for small and large cavities in the EBR-II.

A second significant observation from the ion data is that swelling is not a simple, monotonic function of the helium level or cavity density. Kenik and Lee irradiated a titanium-modified AISI 316 stainless steel with 4 MeV nickel ions at 625°C while co-implanting helium at the rates of 0, 0.2, and 20 appm/dpa (ref. 68). The microstructures they observed at 70 dpa are shown in Fig. 16. Although the cavity density is higher at 20 appm Heldpa, the swelling is greater at 0.2 appm Heldpa. Part of the explanation for this swelling behavior is the same as that which was proposed to account for the suppression of RIS by high helium levels (i.e., enhanced point defect recombination leading to lower defect supersaturations). At relatively low levels of helium, the primary impact of increasing the helium implantation (or generation) rate is to reduce the time required for the bubbles to obtain the critical number of gas atoms, while simultaneously increasing the cavity density. This leads to increased swelling. However, for higher Heldpa ratios, a regime can be reached in which the cavity density becomes high enough that a significant number of the point defects are recombining at the cavities. This reduces the vacancy supersaturation, leading to a greater critical number of gas atoms and therefore extended void swelling incubation time. A second obvious effect that comes into play is that as the bubble density increases, the available helium must be partitioned to more bubbles. This can prolong the incubation time even more strongly. The physical basis for this effect of helium on swelling was first described by Odette and Langley[69] and it has been discussed in more detail by Mansur et al.[70] Additional verification of this mchanism is provided by many experiments. Three will be mntioned here. The first is the comparison of 20% cold-worked AISI 316 stainless steel irradiated in the EBR-II and the HFIR at 500-550°C to 69 and 61 dpa, respectively. The cavity microstructures observed for these two irradiation conditions are shown in Fig. 17 (refs. 3,14,65). The cavity densities plotted in Fig. 15 correspond to these microstructures. In this case, the high bubble density induced by the helium in the HFIR has resulted in much lower swelling. Another significant experiment was designed by Lee and Mansur to explore the influence of a high cavity sink strength on helium partitioning.[71] They

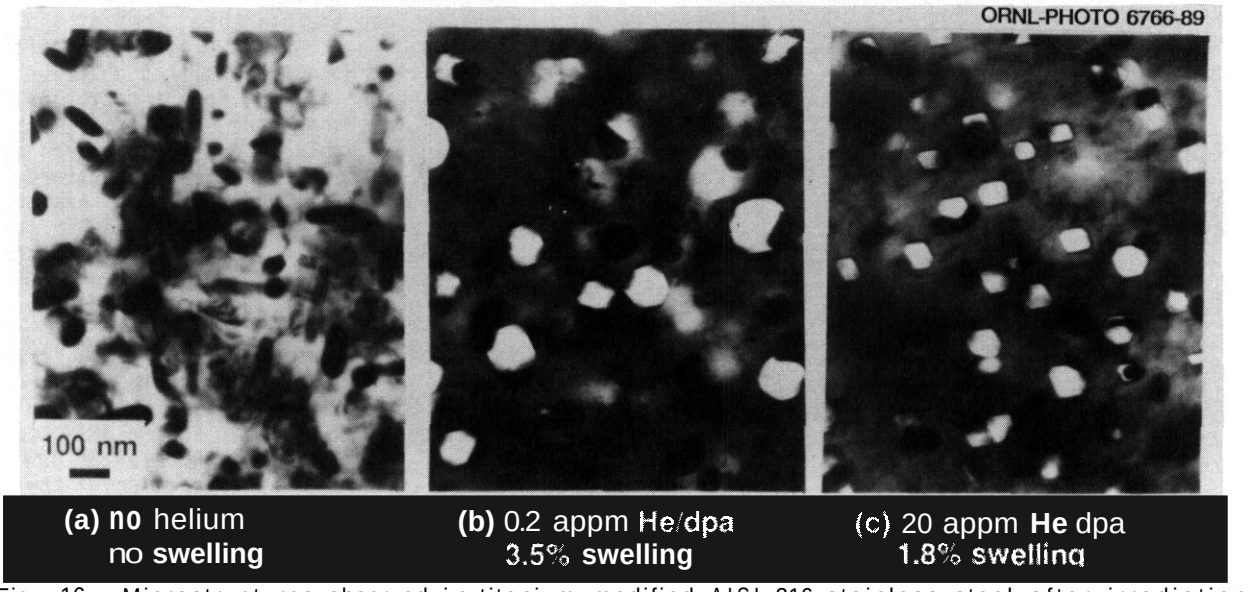

Fig. 16. Microstructures observed in titanium-modified AISI 316 stainless steel after irradiation with 4 MeV nickel ions to 70 dpa at 625°C. Helium implantation rate and observed swelling were: (a) no helium, no swelling; (b) 0.2 appm He/dpa, 3.5% swelling, and (c) 20 appm He/dpa, 1.8% (ref. 68).

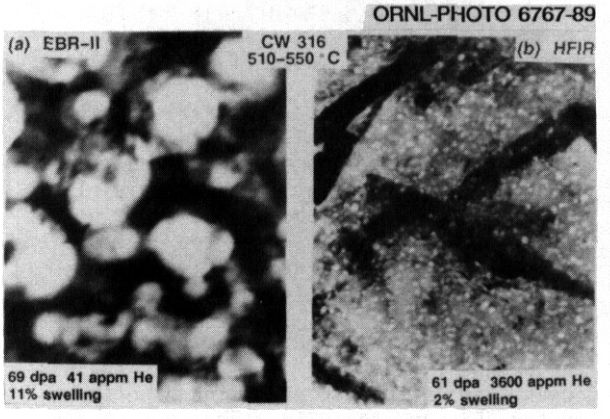

Fig. 17. Cavity microstructures observed in 20% cold-worked AISI 316 stainless steel irradiated in the EBR-II and the HFIR at 500 to 550°C (refs. 3, 14, 65).

irradiated several austenitic alloys with nickel ions and co-implanted helium at the rate of 20 appm/dpa. They obtained a very high bubble density in some of the alloys by inducing extensive bubble nucleation on a fine dispersion of phosphide precipitates. The resultant dilution of the implanted helium prevented void formation up to 109 dpa.

A third relevant experiment is one that was planned to help verify the inference that a high cavity sink strength could extend the incubation time.[63,64] Specimens were irradiated in the HFIR at 400. 500 and 600°C to a dose of about 20 dpa to establish a high bubble density.[63] These specimens were subsequently irradiated in the FFTF for another 38 dpa along with identical specimens that had not been previously irradiated. Unfortunately, during the FFTF irradiation, an operational error led to a short (~60 min) excursion during which the temperature of the specimens irradiated at 500 and 600°C increased by up to 200°C. This makes the interpretation of the results at these temperatures somewhat ambiguous. The 400°C data from the sequential irradiation experiment are not clouded by this uncertainty and some of this data is shown in Fig. 18(a) (ref. 72). The specimen irradiated in only the FFTF appears to be exhibiting the behavior that one would expect based on earlier EBR-II data. as shown. The swelling incubation time does appear to be somewhat longer for the PCA alloy than for n-lot. This is to be expected since PCA was developed to yield improved swelling behavior. However, the specimen that was irradiated in the HFIR prior to the FFTF irradiation has not followed the expected behavior. The swelling observed in this specimen at a total dose of 58 dpa is much less than that observed after only 38 dpa in the FFTF. The swelling data for 20% cold-worked material (n-lot) at 500 and 600°C from this same experiment are shown in Fig. 18(b) (ref. 73). The expected behavior is again represented by a data band from EBR-II irradiations. The specimens that were pre-irradiated in the HFIR at these temperatures appear to be demonstrating a much longer swelling incubation time also. Since the material that was irradiated only in the FFTF appears to be following the expected behavior, it appears that the short over-temperature transient did not have a significant impact on the observed swelling. Therefore, the extended incubation time at these temperatures can also be attributed to the high bubble density formed during the HFIR component of the irradiation.[63,72]

The MFE-4 spectral tailoring experiment provided the first swelling data that were generated by neutron irradiation at the fusion Hefdpa ratio. Furthermore, comparing the values in Tables 1 and 2 shows that the damage rate in this experiment was near that which will be obtained in a DT fusion reactor with a modest wall loading. In higher powered fusion reactors, the MFE-4 damage rate would be reached some short

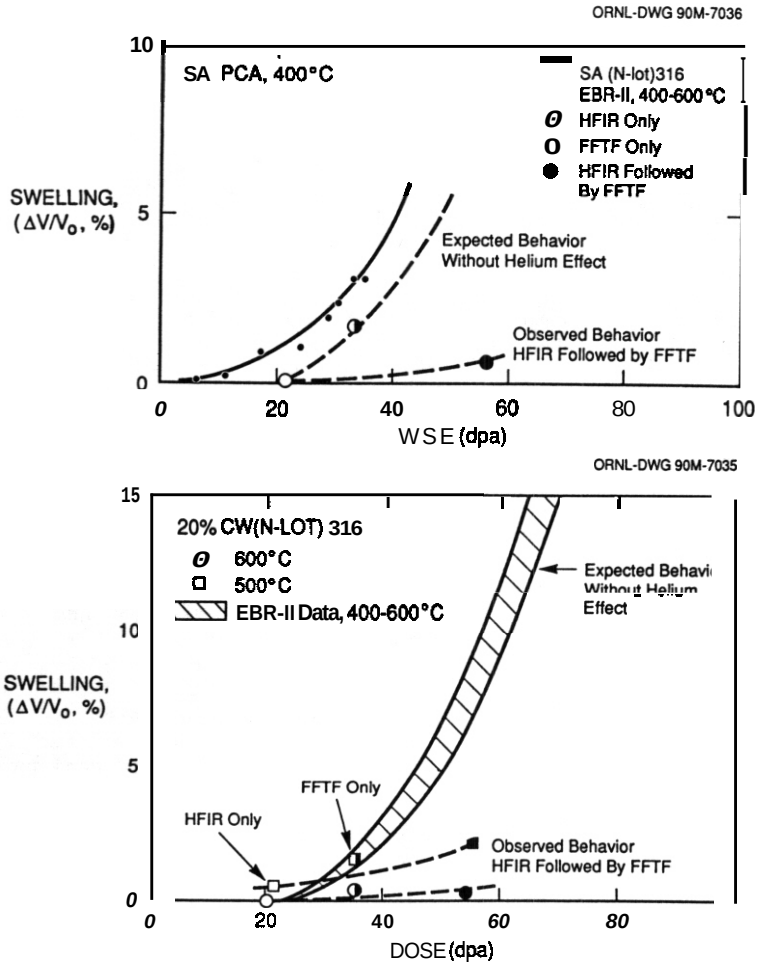

Fig. 18. Swelling observed in HFIR/FFTF sequential irradiation experiment: (a) solution-annealed PCA at 400°C and (b) 20% cold-worked n-lot at 500 and 600°C. "Expected behavior" is characteristic of fast-reactor irradiation.

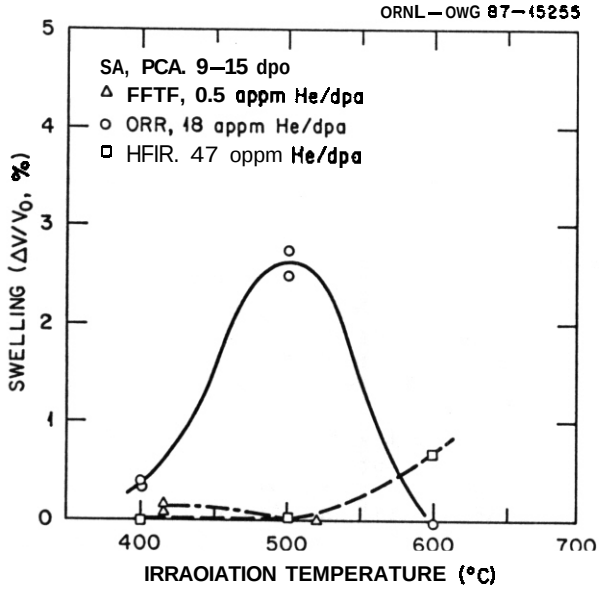

Fig. 19. Temperature dependence of swelling observed in solution-annealed PCA after irradiation to 9 to 15 dpa in the FFTF, HFIR and MFE-4 spectral tailoring experiment in the ORR.[55]

distance into the blanket. Some of the swelling data from this experiment are shown in Fig. 19. Here the swelling observed in solution-annealed PCA after irradiation in the FFTF. HFIR, and the MFE-4 experiment in the ORR to roughly 10 dpa are compared as a function of the irradiation temperature.55 Clearly, the swelling below 600°C has been greatly accelerated by irradiation at the fusion He/dpa ratio. The cavity microstructures that correspond to the 400 and 500°C data points in Fig. 19 are shown in Fig. 20 (ref. 55). The expected influence of helium on the cavity density is observed. Irradiation at the fusion He/dpa ratio has produced a lower total cavity density (bubbles plus voids) than was obtained in the HFIR. However, the swelling is greater at 400 and 500°C because a greater fraction of the bubbles have converted to voids at the intermediate (fusion) He/dpa ratio. Compared to irradiation in the FFTF, irradiation at the fusion He/dpa ratio has led to both a higher total cavity density and higher void density. The swelling of 25% cold-worked material in the MFE-4 experiment was similarly increased.[55] The dependence of swelling on the He/dpa ratio observed in this comparison is consistent with the ion irradiation data, the earlier EBR-II/HFIR comparisons and the simple theoretical arguments mentioned above. Using a rate-theory-based model of void swelling that incorporated the concepts discussed in Sect. 2, Stoller and Odette predicted that such non-monotonic swelling behavior could occur.[74] A comparison of their predictions with the 500°C swelling data from Fig. 19 is shown in Fig. 21. Although the model predictions were at a higher dose, the expectation of increased swelling at an intermediate He/dpa ratio has been realized in the data.

It should once again be mentioned that the damage rate in the MFE-4 experiment was lower than in the corresponding experiments in the FFTF and the HFIR. French fuel pin data[56,57] has been used to suggest that the lower damage rate is the variable responsible for the higher swelling.[75] However, a closer examination of the fuel pin swelling data finds that the correlation between the two data sets is only superficial. It is true that in both the inter-reactor comparison just described and in the fuel pin data that the swelling incubation time appears to be shorter at the lower damage rates. But, it has already been pointed out that the dislocation structures obtained in the MFE-4 experiment were not consistent with a damage rate effect on the microstructure. In addition, the temperature dependence of the effect is different in the two data sets. In the fuel pin data, a lower damage rate shortens the incubation time most for temperatures above 500-550°C. Below about 450°C, it appears that a lower damage rate has little effect on the incubation time, or may actually increase it.[76] Contrary to the proposed damage rate effect, the present FFTF-ORR-HFIR comparison shown in Figs. 19 and 20 indicate that at 600°C the higher damage rate environment (HFIR) has the shorter incubation

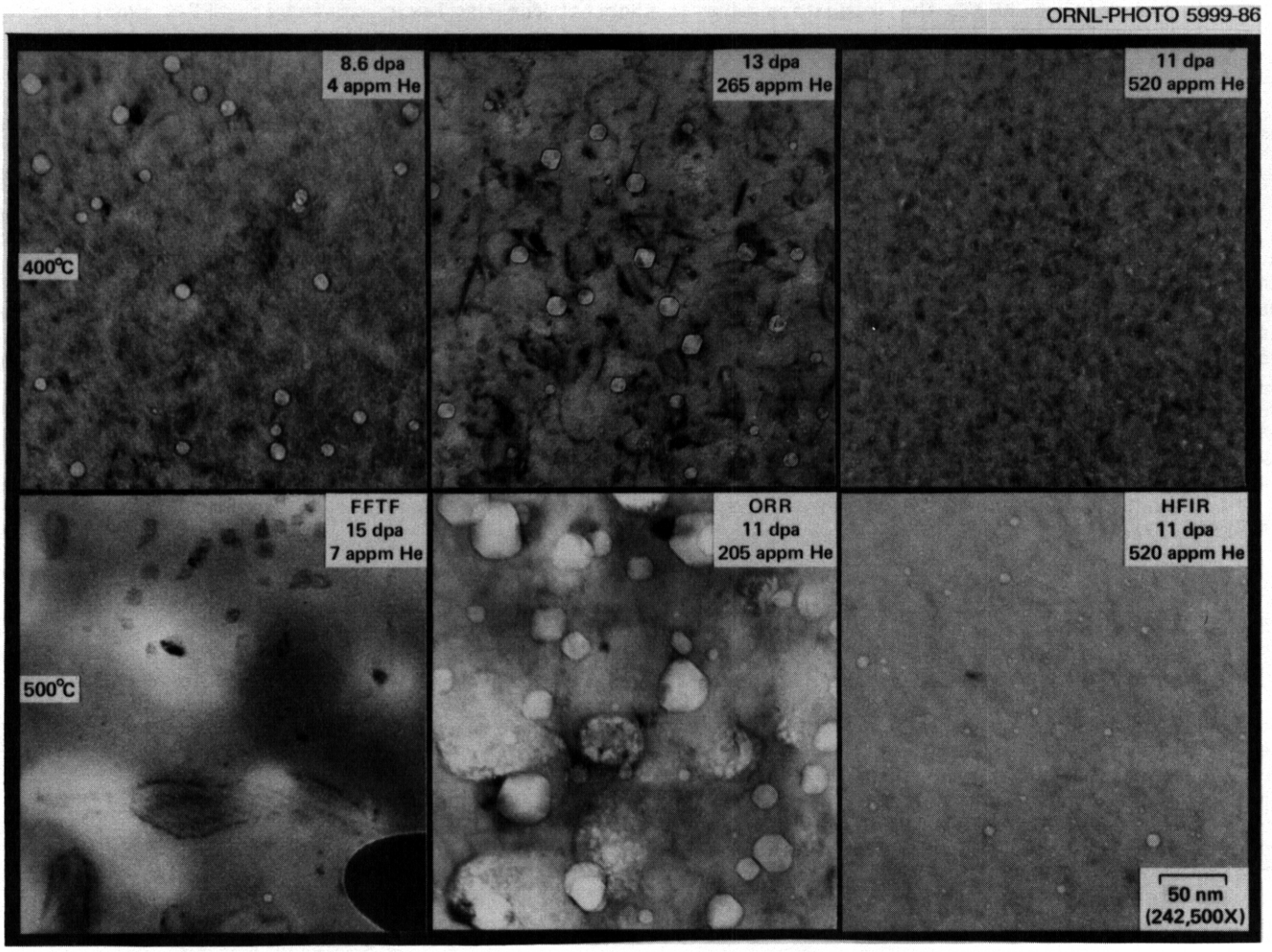

Fig. 20. Cavity microstructures observed in solution-annealed PCA after irradiation at 400 and 500°C to 9 to 15 dpa in the FFTF, HFIR, and MFE-4 spectral tailoring experiment in the ORR.[55]

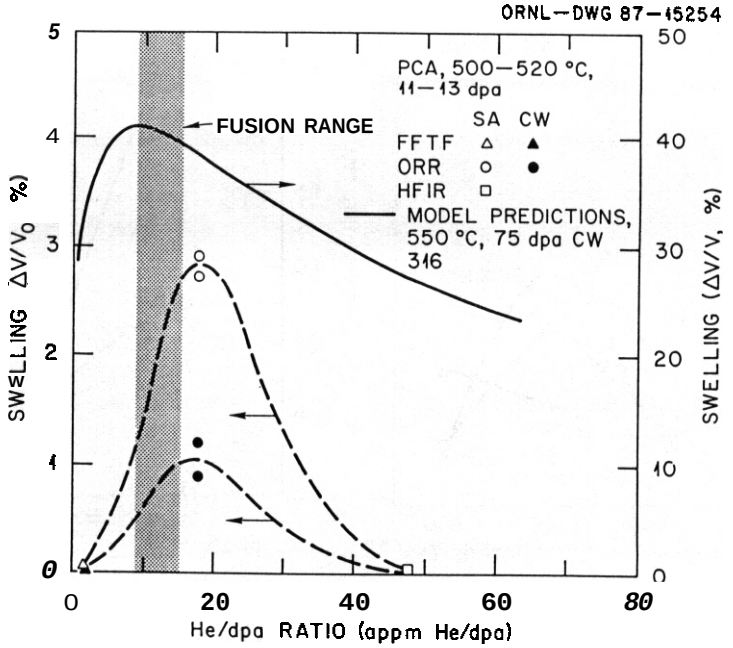

Fig. 21. Comparison of observed and predicted swelling as a function of He/dpa ratio. ORR data from MFE-4 spectral tailoring experiment and model predictions from Stoller and Odette.[74]

time. In the data at 500°C, the incubation time is shortest for the lower damage rate MFE-4 experiment and this same behavior persists down to 400°C. In a relevant experiment, Kimoto et al. investigated the influence of damage rate on swelling in Japanese PCA (J-PCA) and Type 316 stainless steel.[77] Their specimens were implanted with 10 appm helium at room temperature prior to proton irradiation at 550°C to 20 dpa at damage rates of 1.5×10^{-5} and 2.0×10^{-4} dpa/s. They observed that damage rate did not influence the swelling of the Type 316 stainless steel specimens and that swelling was lower in J-PCA after irradiation at the lower damage rate.

There is additional data that indicates that it is the He/dpa ratio, rather than the damage rate, that is responsible for the higher swelling observed in the spectral tailoring experiment. Hamilton et al. have reported swelling data for several Fe-Ni-Cr ternary alloys that were irradiated in the MFE-4 experiment in the ORR and in the AD-1 experiment in the EBR-II.[78] The damage rate in the EBR-II is similar to that in the FFTF and the HFIR. The swelling data from ref. 78 have been re-plotted as a function of temperature in Fig. 22. In this case, it is clear that the lower damage rate in the ORR did not lead to a shortened incubation time. Instead. in spite of the fact that the dose is higher, somewhat lower swelling is observed in the ternary alloys after irradiation in the MFE-4 experiment. Irradiation at the fusion He/dpa ratio has also altered the temperature dependence of swelling observed at 10 dpa. This is consistent with the data shown in Fig. 19. In their analysis of the specimens irradiated in the MFE-4 experiment, these authors report an "unanticipated non-monotonic' dependence of swelling on nickel at a nickel content of about 30% (ref. 78). Since helium generation in this experiment is roughly proportional to nickel content, this observation may be due to the non-monotonic dependence of swelling on helium discussed above.

Finally, the results of a recently-completed isotopic tailoring experiment should be discussed.[25,79] In this experiment. a number of Fe-Ni-Cr ternary alloys were fabricated with the nickel enriched in the isotope ^{59}Ni. Specimens were then irradiated in the FFTF to 12, 14, and 9 dpa at 365, 495, and 600°C, respectively. Helium generation in the ^{59}Ni bearing alloys led to a He/dpa ratio of 5-8 appm/dpa, while in control specimens the He/dpa ratio was less than 0.5. Immersion density data for specimens irradiated at 495°C from refs. 25 and 79 are reproduced in Fig. 23. The immersion density data at the other temperatures are similar.[79] It is difficult to draw broad conclusions from this data since the total swelling is small at this low dose. However, higher helium has produced more swelling for all conditions except the solution-annealed Fe-25Ni-15Cr alloy. This is consistent with the observations from the earlier experiments that have already been discussed in that the effect of helium is not always in the same direction. The reported microstructural information[25,79] is also similar to the results of earlier experiments. Higher helium levels tended to lead to higher cavity densities. The magnitude of the increase in cavity density was a function of alloy composition and whether the material was cold-worked or solution-annealed. The largest increase was by more than an order of magnitude. Consistent with the ion data, the specimens with the higher cavity densities tended to have a smaller average cavity size.

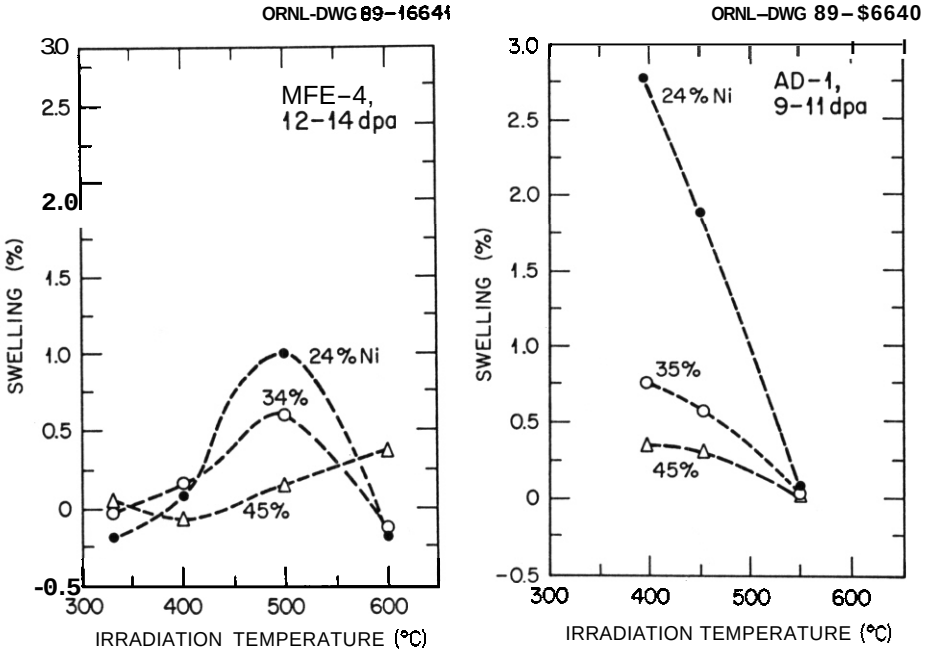

Fig. 22. Swelling behavior of Fe-Ni-Cr ternary alloys observed after irradiation in the MFE-4 experiment in the ORR and in the AD-1 experiment in the EBR-II.[78] The He/dpa ratio in the MFE-4 experiment was about 33. 45, and 56 appm He/dpa in the alloys containing 24, 34, and 45% nickel, respectively. In the AD-1 experiment, the He/dpa ratio was about 0.5 appm He/dpa for all alloys.

While additional data are needed to determine the degree of helium effects in this experiment, the small differences in swelling observed here may be significant because the swelling rate is low near the end of the swelling incubation time. Differences of 1% in swelling would correspond to a shift of at least 5 to 10 dpa in dose at 500°C.

Overall, the effects of helium on cavity formation and void swelling are complex. However, a few things can be distilled from the broad data base and our present understanding of the mechanisms involved. First, the total cavity density is consistently increased if the helium generation (or implantation) rate is increased. The swelling observed as a result of this higher cavity density may be either increased or decreased. If the cavity density has crossed a threshold value such that the cavities act as a major recombination site for point defects, the incubation time can be extended since the critical number of gas atoms for void formation will increase. At the same time, the higher cavity density will reduce the gas accumulation rate for all cavities. For very high cavity densities, this helium dilution can extend the incubation time considerably. Since the dominant mechanism for void formation requires that bubbles obtain a critical number of gas atoms, swelling incubation times will primarily be determined by the effects of helium on the microstructure. Alloy chemistry and factors such as cavity-precipitate association only alter the critical number of gas atoms, they do not change the nucleation mechanism.

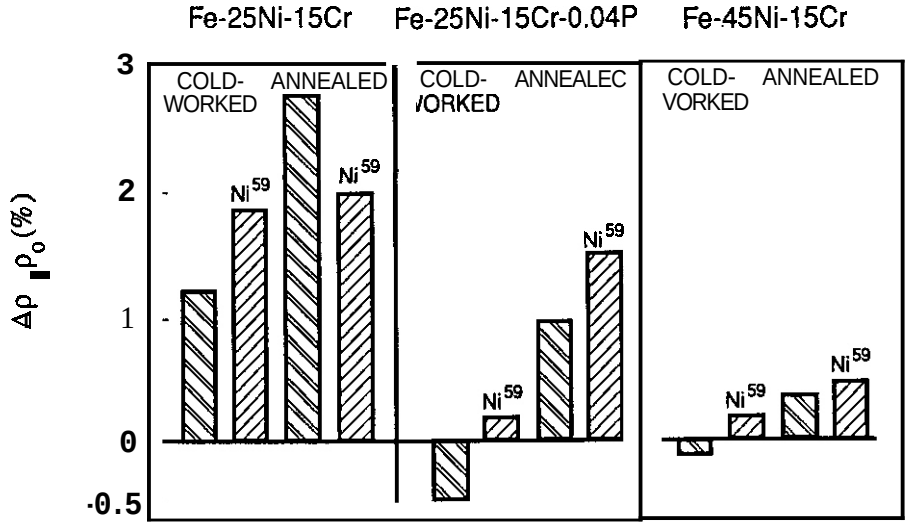

Fig. 23. Density changes observed in several model alloys after irradiation at 495°C to 14 dpa in the FFTF isotopic tailoring experiment.[25] The Hefdpa ratio is about 0.5 appm Hefdpa for the alloys without ^{59}Ni and 5 appm Hefdpa in the alloys containing ^{59}Ni.

CONCLUSIONS

Helium has been shown to have a strong impact on all the major components of the microstructure of irradiated materials, with the degree and the duration of the effect depending on the level of helium present. Consistent data trends have been demonstrated across a broad range of irradiation conditions, from ion irradiations with helium either pre-implanted or co-implanted, to the more recent spectral and isotopic tailoring experiments. A major practical implication of this work is that swelling exhibits a complex dependence on helium, particularly at low to intermediate doses. Once swelling begins, it accelerates rapidly in most materials. This suggests that the swelling incubation time probably represents an effective component lifetime in a fusion reactor. Attempts to extend the incubation time by alloy design must not ignore helium because it is during this critical period that the effects of helium appear to be strongest.

A simple way to understand some of the observed effects of helium is to consider its influence on point defect recombination. At low doses, helium acts as a powerful vacancy trap. This reduces the rate of bulk recombination and helps promote both bubble and interstitial loop formation. This in turn leads to greater sink densities at higher doses. The microstructure that evolves at higher doses depends on how much the cavity density is increased. If it is only modestly increased, the microstructure will evolve in a manner very similar to that observed under fast reactor irradiation. The only expected difference would be a somewhat shorter swelling incubation time due to the greater helium being available. However, if the cavity density is increased to a sufficient degree that the cavities become a major sink for point defects, another path of microstructural evolution becomes possible. In this case, the high cavity sink strength leads to greater recombination of point defects at the cavities. This reduces the point defect supersaturations and inhibits bubble-to-void conversion because the critical number of gas atoms is increased. This effect is compounded because the available helium has to be partitioned to more cavities. At the same time, RIS and radiation-induced precipitation are reduced because the point defect fluxes that drive RIS have been reduced. Any solute segregation that does take place is also diluted by the higher sink densities. If very high sink densities are maintained, the dilution effect can strongly limit both RIS and void formation.

One purpose of this review was to provide some guidance for those who need to use existing fission reactor data to design early fusion reactors. Such an extrapolation is necessary because of the lack of a high-flux, high-energy neutron source. The available data indicates that this extrapolation is not straightforward. In particular, both the data and well-established theoretical mechanisms that have been used to describe and predict the effects of helium on swelling indicate that swelling is not a monotonic function of the helium generation rate. This means that simple extrapolations of fast reactor swelling data or interpolations between data obtained from low and high helium environments may give results that prove to be nonconservative. Moreover, the results of the MFE-4 experiment emphasize the importance of doing alloy development in an environment typical of the ultimate application. Alloys that were optimized for good swelling resistance based on experiments in the EBR-II, FFTF, and HFIR appeared to swell much more rapidly at the fusion Heldpa ratio. This demonstrated potential for a reduced incubation time at an intermediate helium generation rate emphasizes the need for a proper fusion materials test facility. In the absence of such a facility, the isotopic tailoring experiments that are planned and in progress provide the best available opportunity for obtaining design data that can be used with confidence.

REFERENCES

1. G. R. Odette, J. Nucl. Mater. 85 & 86 (1979) 533-545.
2. K. Farrell, Rad. Eff. 53 (1980) 175-194.
3. K. Farrell, P. J. Maziasz, E. H. Lee and L. K. Mansur, Rad. Eff. 78 (1983) 277-295.
4. L. K. Mansur and W. A. Coghlan, J. Nucl. Mater. 119 (1983) 1-25.
5. H. Ullmaier, Nucl. Fusion 24 (1984) 1039-1083.
6. D. F. Pedraza, P. J. Maziasz and R. L. Kleuh, Rad. Eff. and Defects in Solids 113 (1990) 213-228.
7. F. A. Garner, "Overview of the Swelling Behavior of 316 Stainless Steel," Optimizing Materials for Nuclear Applications, Symp. Proc., F. A. Garner, D. S. Gelles, and F. W. Wiffen, Eds., American Institute of Mining, Metallurgical, and Petroleum Engineers, New York, 1984, pp. 111-139.
8. P. J. Maziasz and R. L. Klueh, "Void Formation and Helium Effects in 9Cr-1MoVNb and 12Cr-1MoVW Steels Irradiated in HFIR and FFTF at 400°C," Effects of Radiation on Materials: Fourteenth Int. Symp., ASTM STP 1046, N. H. Packan, R. E. Stoller, and A. S. Kumar, Eds., American Society of Testing and Materials, Philadelphia (1989), pp. 35-60.
9. K. Farrell, R. W. Chickering, and L. K. Mansur, Phil. Mag. A 53 (1986) 1-26.
10. M. T. Robinson, "The Theory of Radiation Induced Defect Production," Fundamental Aspects of Radiation Damage in Solids, Proc. of Int. Conf., CONF-751006-P1 , Vol. 1, M. T. Robinson and F. W. Young, Eds., U.S. National Technical Information Center, Springfield, VA, 1976, pp. 1-20.
11. M. J. Norgett, M. T. Robinson, and I. M. Torrens, Nucl. Engr. and Des. 33 (1975) 50-54.
12. H. L. Heinsch and F. W. Mann, J. Nucl. Mater. 122 & 123 (1984) 1023-1027.
13. L. E. Rehn and P. R. Okamoto, Materials Science Forum 15-18 (1987) 985-1002.
14. P. J. Maziasz, Effects of Helium Content on Microstructural Development in Type-316 Stainless Steel Under Neutron Irradiation, ORNL-6121, Oak Ridge National Laboratory, 1985.
15. T. A. Gabriel, B. L. Bishop and F. W. Wiffen, Calculated Irradiation Response of Materials Using Fission Reactor (HFIR, ORR, EBR-II) Neutron Spectra, ORNL/TM-6361, Oak Ridge National Laboratory, 1979.
16. R. L. Simons, "Analysis of Damage Exposure Rates in Materials Open Test Assembly of the Fast Flux Test Facility," DAFS Quart. Prog. Rept., January-March, 1985, DOE/ER-0046/21, USDOE Office of Fusion Energy, 1985, pp. 10-14.
17. L. R. Greenwood, J. Nucl. Mater. 115 (1983) 137-142.
18. R. A. Lillie, "Neutronics Calculations in Support of the ORR-MFE-4A and -48 Spectral Tailoring Experiments," ADIP Semiannu. Prog. Rept., April—September 1985, DOE/ER-0045/15, USDOE Office of Fusion Energy, 1986, pp. 45-46.
19. R. A. Lillie, "Neutronics Analysis in Support of the U.S./Japan Spectral Tailoring Capsules," Fusion Reactor Materials Semiannu. Prog. Rept., March 31, 1987, DOE/ER-0313/2, USDOE Office of Fusion Energy, 1987, p. 25.

20. C. De Raedt, "Neutronic Aspects of the Utilization of Nickel Enriched in ^{59}Ni in Samples for In-pile Testing of Fusion Reactor First Wall Candidate Materials," Fast, Thermal and Fusion Reactor Experiments, Proc. of Int. Conf., Vol. II, American Nuclear Society, LaGrange Park, IL, 1982, pp. 336-341.

21. R. L. Simons, "^{59}Ni Isotopic Enrichment as a Means of Simulating the He/dpa Ratio of a Fusion Environment," DAFS Quart. Prog. Rept., October-December, 1982, DOE/ER-0046/12, USDOE Office of Fusion Energy, 1983, pp. 37-48.

22. L. K. Mansur, A. F. Rowcliffe, M. L. Grossbeck and R. E. Stoller, J. Nucl. Mater. 139 (1986) 228-236.

23. R. L. Simons, H. R. Brager and W. Y. Matsumoto, J. Nucl. Mater. 141-143 (1986) 1057-1060.

24. G. R. Odette, J. Nucl. Mater. 141-143 (1986) 1011-1017.

25. J. F. Stubbins, J. E. Nevling, F. A. Garner and R. L. Simons, "Microstructural Evolution in Neutron Irradiated Fe-Cr-Ni Alloys at 495°C in Response to Changes in He/dpa Ratio," Effects of Radiation on Materials: Fourteenth Int. Symp., ASTM STP 1046, N. H. Packan, R. E. Stoller, and A. S. Kumar, Eds., American Society of Testing and Materials, Philadelphia (1989), pp. 147-159

26. R. E. Stoller and G. R. Odette, "A Comparison of the Relative Importance of Helium and Vacancy Accumulation in Void Nucleation," Effects of Radiation on Materials: Thirteenth Int. Symp., ASTM STP 955, F. A. Garner, N. H. Packan and A. S. Kumar, Eds., American Society for Testing and Materials, Philadelphia, 1987, pp. 358-370.

27. R. E. Stoller and G. R. Odette, J. Nucl. Mater. 131 (1985) 118-125.

28. M. R. Hayns, The Transition From Gas Bubble to Void Growth, AERE-R8806, U.K.A.E.A., 1977.

29. C. A. Parker and K. C. Russell, Scripta Met. 15 (1981) 643-647.

30. R. E. Stoller and G. R. Odette, "A Composite Model of Microstructural Evolution in Austenitic Stainless Steel Under Fast Neutron Irradiation," Effects of Radiation on Materials: Thirteenth Int. Symp., ASTM STP 955, F. A. Garner, N. H. Packan and A. S. Kumar, Eds., American Society for Testing and Materials, Philadelphia, 1987, pp. 371-392.

31. E. H. Lee and L. K. Mansur, "Unified Theoretical Analysis of Experimental Swelling Data for Irradiated Austenitic and Ferritic/Martensitic Alloys," Met. Trans. 21A (1990) in press.

32. R. E. Stoller, "Modeling Dislocation Evolution in Irradiated Alloys," Met. Trans. 21A (1990) in press.

33. L. K. Mansur, Nucl. Tech. 40 (1978) 5-34.

34. L. K. Mansur, E. H. Lee, P. J. Maziasz, and A. F. Rowcliffe, J. Nucl. Mater. 131-143 (1986) 633-646.

35. P. R. Okamoto and H. Weidersich, J. Nucl. Mater. 53 (1974) 336-345.

36. P. R. Okamoto and L. E. Rehn, J. Nucl. Mater. 83 (1979) 2-23.

37. H. R. Brager and F. A. Garner, "Radiation-Induced Evolution of the Austenite in Silicon-Modified AISI 316 Alloys," Phase Stability During Irradiation, Symp. Proc., J. R. Holland, L. K. Mansur, and D. I. Potter, Eds.. American Institute of Mining, Metallurgical, and Petroleum Engineers, New York, 1981, pp. 219-235.

38. E. H. Lee, P. J. Maziasz, and A. F. Rowcliffe, "The Structure and Composition of Phases Occurring in Austenitic Stainless Steel in Thermal and Irradiation Environments," Phase Stability During Irradiation, Symp. Proc., J. R. Holland, L. K. Mansur, and D. I. Potter, Eds., American Institute of Mining, Metallurgical, and Petroleum Engineers, New York, 1981, pp. 191-218.

39. L. K. Mansur, M. R. Hayns, and E. H. Lee, "Mechanisms Affecting Swelling in Alloys with Precipitates," Phase Stability During Irradiation, Symp. Proc., J. R. Holland, L. K. Mansur, and D. I. Potter, Eds., American Institute of Mining, Metallurgical, and Petroleum Engineers, New York, 1981, pp. 350-382.

40. W. J. S. Yang, "Precipitate Evolution in Type 316 Stainless Steels Irradiated in EBR-II," Effects of Radiation on Materials: Thirteenth Int. Symp., ASTM STP 955, F. A. Garner, N. H. Packan and A. S. Kumar, Eds., American Society for Testing and Materials, Philadelphia, 1987, pp. 628-646.

41. P. J. Maziasz and C. J. McHargue, International Materials Reviews 32 (1987) 190-219.

42. D. F. Pedraza and P. J. Maziasz, "void-Precipitate Association During Neutron Irradiation of Austenitic Stainless Steel," Effects of Radiation on Materials: Thirteenth Int. Symp., ASTM STP 955, F. A. Garner. N. H. Packan and A. S. Kumar, Eds, American Society for Testing and Materials, Philadelphia, 1987, pp. 161-194.

43. A. D. Marwick, J. Phys. F: Metal. Phys. *8* (1978) 1849-1861.

44. P. J. Maziasz, "Microstructural Stability and Control for Improved Irradiation Resistance and for High-Temperature Strength of Austenitic Stainless Steels," MiCon 86: Optimization of Processing, Properties, and Service Performance Through Microstructural Control, Symp. Proc., ASTM STP 979, B. L. Bramfitt. R. C. Benn, C. R. Brinkman, and G. F. Vander Voort, Eds., American Society for Testing and Materials, Philadelphia, 1988, pp. 116-161.

45. L. K. Mansur, J. Nucl. Mater. 83 (1979) 109-127.

46. G. Ayrault, H. A. Hoff, F. V. Nolfi, Jr., and A.P.L. Turner, J. Nucl. Mater. 103 8 104 (1981) 1035-1040.

47. W. J. Choyke, J. N. McGruer, J. R. Townsend, J. A. Spitznagel, N. J. Doyle, and F. J. Venskytis, J. Nucl. Mater. 85 E 87 (1979) 647-651.

48. R. S. Barnes and D. J. Mazey, Phil. Mag. 5 (1960) 1247-1253.

49. O. J. Mazey and S. Francis, 'Observations of Dislocation Structure and Cavities Formed by Annealing in Type 316 Stainless Steel after Ion Irradiation at Ambient Temperature," The Physics of Irradiation Produced Voids, Consultants Symp., AERE R-7934, AERE Harwell, 1975, pp. 257-262.

50. D. J. Mazey and R. S. Nelson, "The Influence of Pre-Injected Helium on Void Swelling in Ion-Irradiated Stainless Steels," Radiation Effects and Tritium Technology for Fusion Reactors, Proc. of Int. Conf., CONF-750989, Vol. I, U.S. EROA, Washington, DC, 1976, pp. 240-258.

51. F. A. Smidt and A. G. Pieper, "Observations of Helium Bubble Formation in 316 Stainless Steel Implanted by Alpha Bombardment," Radiation Effects and Tritium Technology for Fusion Reactors, Proc. of Int. Conf., CONF-750989, Vol. II, U.S. ERDA, Washington, DC, 1976, pp. 250-279.
52. R. E. Stoller and G. R. Odette, J. Nucl. Mater. 154 (1988) 286-304.
53. 8. 8. Glascow and W. G. Wolfer, J. Nucl. Mater. 122 E 123 (1984) 503-508.
54. R. E. Stoller, Oak Ridge National Laboratory, unpublished research.
55. R. E. Stoller, P. J. Maziasz, A. F. Rowcliffe, and M. P. Tanaka, J. Nucl. Mater. 155-157 (1988) 1328-1334.
56. J. L. Seran and J. M. Dupouy, "The Swelling of Solution Annealed 316 Cladding in Rapsodie and Phenix," Effects of Radiation on Materials: Eleventh Int. Symp., ASTM STP 782, H. R. Brager and J. S. Perrin, Eds, American Society for Testing and Materials, Philadelphia, 1982, pp. 5-16.
51. L. LeNaour, N. Vouillon, and V. Levy, "Influence of Dose and Dose Rate on the Microstructure of Solution Annealed 316 Steel Irradiated Around 600°C," Effects of Radiation on Materials: Eleventh Int. Symp., ASTM STP 782, H. R. Brager and J. S. Perrin, Eds. American Society for Testing and Materials, Philadelphia, 1982, pp. 310-324.
58. E. A. Kenik, J. Nucl. Mater. 85 E 87 (1979) 659-663.
59. A. F. Rowcliffe and E. H. Lee, J. Nucl. Mater. 108 & 109 (1982) 306-318.
60. P. J. Maziasz, J. Nucl. Mater. 122 & 123 (1984) 472-486.
61. H. R. Brager and F. A. Garner, J. Nucl. Mater. 117 (1983) 159-176.
62. P. J. Maziasz, J. Nucl. Mater. 108 & 109 (1982) 359-384.
63. P. J. Maziasz, "Re-irradiation in FFTF of Swelling-Resistant Path A Alloys Previously Irradiated in HFIR," ADIP Semiannu. Prog. Rept., April-September, 1984, DOE/ER-0045/13, USDOE Office of Fusion Energy, pp. 45-49.
64. P. J. Maziasz, F. A. Garner and H. R. Brager, "An Assessment of Helium Effects on Swelling by Re-irradiation in FFTF of Path A Alloys Previously Irradiated in HFIR," ADIP Semiannu. Prog. Rept. April-September, 1984, DOE/ER-0045/13, USDOE Office of Fusion Energy, pp. 50-51.
65. G. R. Odette, P. J. Maziasz, and J. A. Spitznagel, J. Nucl. Mater. 103 E 104 (1981) 1289-1304.
66. G. W. Greenwood, A.J.E. Foreman, and D. E. Rimer, J. Nucl. Mater. 1 (1959) 305-324.
67. 8. N. Singh and A.J.E. Foreman, J. Nucl. Mater. 103 E 104 (1981) 1469-1474.
68. E. A. Kenik and E. H. Lee. "Influence of Injected Helium on the Phase Stability of Ion-Irradiated Stainless Steel." Phase Stability During Irradiation, Symp. Proc., J. R. Holland, L. K. Mansur, and D. I. Potter, Eds., American Institute of Mining, Metallurgical, and Petroleum Engineers, New York, 1981, pp. 493-503.
69. G. R. Odette and S. C. Langley, "Modeling of Synergistic Effects of Displaced Atom and Transmutant Damage in Fission and Fusion Environments," Radiation Effects and Tritium Technology for Fusion Reactors, Proc. of Int. Conf., CONF-750989, Vol. I, U.S. ERDA. Washington, DC, 1976, pp. 395-416.
70. L. K. Mansur, P. J. Maziasz, E. H. Lee, and A. F. Rowcliffe, J. Nucl. Mater. 141-143 (1986) 633-646.
71. E. H. Lee and L. K. Mansur, J. Nucl. Mater. 141-143 (1986) 695-702.
72. P. J. Maziasz, Oak Ridge National Laboratory and H. R. Brager, Hanford Engineering Oevelopment Laboratory, unpublished data presented at the Second International Conference on Fusion Reactor Materials, Chicago, 1986.
73. P. J. Maziasz, Oak Ridge National Laboratory, unpublished data presented at the Second International Conference on Fusion Reactor Materials, Chicago, 1986.
74. R. E. Stoller and G. R. Odette, "The Effect of Helium on Swelling in Stainless Steel: Influence of Cavity Density and Morphology," Effects of Radiation on Materials: Eleventh Int. Symp., ASTM STP 782, H. R. Brager and J. S. Perrin, Eds., American Society for Testing and Materials, Philadelphia, 1982, pp. 275-294.
75. F. A. Garner, H. L. Heinisch, R. L. Simons, and F. M. Mann, Rad. Eff. and Defects in Solids 113 (1990) 229-255.

76. F. A. Garner, J. Nucl. Mater. 122 &123 (1984) 459-471.
77. T. Kimoto, H. Shiraishi, and A. Hishinuma, J. Nucl. Mater. 133 & 134 (1985) 540-543.
78. M. L. Hamilton, A. Okada, and F. A. Garner, "Tensile Behavior and Swelling of Ternary Austenitic Alloys Irradiated in Different Neutron Spectra," Fusion Reactor Materials, Semiannu. Proq. Rept. March 31, 1989, DOE/ER-0313/6, USDOE Office of Fusion Energy, pp. 59-69; also presented at the Fourth International Conference on Fusion Reactor Materials, Kyoto, December 4-8, 1989, to be published in J. Nucl. Mater.
79. H. Kawanishi, F. A. Garner. and J. F. Stubbins. "Results of Microstructural Examination of Ni-59 Experiment Irradiated in FFTF,' Fundamental Studies of irraaiation Effects in Fusion Materials utilizing Fission Reactors, Annual Progress Report on Mond.sno-DOE Collaooration, June 1989, pp. 132-138, also oresented at the Fourth International Conference on Fusion Reactor Materials, Kyoto. December 4-8. 1989. to be published in J. Nucl. Mater.

THEORY OF MICROSTRUCTURE EVOLUTION UNDER FUSION NEUTRON IRRADIATION - N. M. Ghoniem, (University of California, Los Angeles)

OBJECTIVE

The work is intended to give a concise review of the recent developments in the theory of microstructure evolution under fusion conditions. The review focuses on the usefulness of the Fokker-Planck theory to describe the stochastic effects of cascades on microstructures. Recent theoretical insights into the physical origins of spatial instabilities of microstructures are reviewed.

SUMMARY

New concepts are reviewed which replace the conventional separation of microstructure evolution analysis into nucleation and growth. Classical nucleation theory is inadequate under fusion conditions (high helium-to-dpa ratios) and the usual "mean field" approximation of microstructural growth cannot account for cascade effects. A comprehensive theory of microstructure evolution under fusion conditions is formulated based on non-equilibrium statistical mechanics. Dynamic re-solution of helium gas in cavities is shown to result in continuous nucleation of helium-filled cavities. Microstructure evolution (e.g., dislocation loops and cavities) is modeled by kinetic rate equations for small size features and Fokker-Planck (F-P) equations for sizes larger than few atomic dimensions. Semi-analytical and numerical methods are developed for the analysis of microstructure evolution and the results are compared to experiments. The problem of spatial self-organization of microstructures under irradiation is described in terms of a newly developed Ginzburg-Landau-type equation and the results are also compared to experiments.

PROGRESS AND STATUS

Introduction

Understanding the relationships between microstructures and material properties is central to the development of new alloys. This is particularly significant for improving the radiation resistance of structural alloys for fusion reactors. Under the intense neutron radiation environment, large amounts of point defects and gases are generated, driving the solid far from thermodynamic equilibrium. Restoration of the equilibrium state is achieved by a slow evolutionary process of the solid's microstructure. In this respect, point-defect generation by atomic displacements can be viewed as the main driving force for microstructure evolution and, hence, for all property changes in a fusion irradiation environment.

The problem of cavity swelling under irradiation has occupied a central position in the theory of microstructure evolution because of the impact of volumetric swelling on the lifetime of structural components under irradiation. Traditionally, cavity formation in irradiated metals has been theoretically analyzed in two distinct phases: nucleation and growth. It has been implicitly assumed that the nucleation of cavities is a fairly rapid process which is followed by the growth phase. Cavity nucleation theories, as formulated by Katz and Wiedersich [1,2] and equivalently by Russell [3,4], have been motivated by the classical nucleation theory of droplet formation, developed earlier by Becker and Doring [5] and by Zeldovich [6]. Cavity growth, however, has been treated in the "mean field" approximation of identical spherical sinks which grow in the diffusion fields of point defects. The rate theory of "average" cavity growth has been contributed to by many investigators (e.g., Refs. [7-13]), and many features of experimentally observed cavity growth behavior were explained or predicted. However, theoretical inconsistencies within this framework have persisted until recently and they are summarized below.

(1) The continuous production of gas atoms and point defects is in contradiction with the termination of nucleation by a sudden decrease in the vacancy supersaturation. (This is a requesite in classical nucleation theory.)

(2) Classical nucleation theory predicts nucleation rates which are extremely sensitive to parametric variations, such as surface energy, supersaturation ratio, and number of gas atoms in a cavity. It also does not give quantitative information on cavity densities.

(3) Rate theory of cavity growth is unable to explain variations in the size distribution of cavities, their spatial inhomogenieties, and the effects of collision cascades. Coalescence, which can lead to a broadening of the size distribution, is not included in the present analysis. The migration of dislocation loops or cavities is normally a very slow process, relevant only at high temperatures.

Another recent approach to the theory of microstructure evolution has been developed which is based on extending the concepts of nonequilibrium statistical mechanics to describe microstructure evolution, particularly dislocation loops [14-19] and gas-filled cavities [20-25]. This approach overcomes problems associated with the artificial separation of nucleation and growth of microstructural components and the extreme parametric sensitivity of nucleation theory. Additionally, the approach allows for a detailed description of the size distribution of evolving microstructural features (e.g., dislocation loops and cavities), and for the influence of collision cascades.

Certain aspects of the spatial self-organization of microstructures (i.e., void and bubble lattices, and dislocation loop walls and 3-D cubic arrangements) can be explained as dynamical instabilities resulting from the interaction of the spatio-temporal diffusion fields of mobile point defects and the immobile microstructures. Recent progress in this area can be found in Refs. [26-32].

In this paper, we present a review of a statistical theory of cavity and loop evolution under fusion neutron-irradiation conditions. We also show that spatial instabilities in the point-defect diffusion fields can lead to an explanation of experimentally observed features of dislocation-loop self-organization. In Section 2, we give the main equations which define, in a unified way, the nucleation and growth aspects of microstructures in the framework of statistical mechanics. This is followed by the theory of self-organization in Section 3. The results of example computations are given in Section 4, and conclusions are stated in Section 5.

Statistical Theory of Microstructure Evolution

Helium migration under irradiation is determined by a competition between the rate of transport through the lattice until it is trapped, and the detrapping rate from helium-vacancy (He-V) clusters. Near steady state, however, the most effective traps are single vacancies, and the dominant detrapping mechanism has been shown to be by thermal dissociation at high temperatures, by self-interstitial replacement at intermediate temperatures, and by displacement reactions at lower temperatures [33].

The starting point of the theory of microstructure evolution is the Smoluchowsky-Chapman-Kolmogorov (SCK) equation for a Markovian process [34], i.e.,

$$\frac{\partial f}{\partial t} = \int [\omega(\bar{x}',\bar{x},t')f(\bar{x}',t) - \omega(\bar{x},\bar{x}',t')f(\bar{x},t)]d\bar{x}' \quad , \tag{1}$$

where $f(\bar{x},t)$ is the probability distributio? for the stochastic variable $\bar{x}$ at time t. The transition probability per unit time from state x to state x′ at time t′ is $\omega(\bar{x},x',t')$. Equation (1) can be reduced to a deterministic rate eauation for the concentration of a specific defect cluster (e.g., di-interstitials, di-vacancies, tri-vacancies and two helium atoms, etc.) if the transition probabilities, u, are replaced by reaction rates. This mean-field approximation does not take into account the statistical nature of defect production, cascade effects, and the arrival and absorption of single and multiple defects at defect clusters.

Since defect clustering is driven by the concentration of three types of monomers (vacancies, interstitials, and helium), we would have a coupled heirarchy of discrete equations for the probability distribution, f, using rate or master equations of the form given by Eq. (1). One unique feature of microstructure evolution under irradiation, however, is that the size of atomic transitions (x - x′) is generally smaller than the defect-cluster size, x. The mobility of large defect clusters (≥ 3) is negligible and, hence, one can derive a F-P equation as an approximation to the master equation [Eq. (1)].

The transition probability from a defect-cluster size $\bar{x}'$ to size $\bar{x}$, $\omega(\bar{x}',\bar{x},t')$, can be redefined in the following way:

$$\omega(\bar{x}',\bar{x},t') = W(\bar{x}',\bar{x} - \bar{x}',t') = W(\bar{x} - \bar{r}, \bar{r},t,\tau) \quad . \tag{2}$$

In Eq. (2), we distinguish between slow $(\bar{x},t)$ and fast $(\bar{r} = \bar{x} - \bar{x}'\tau)$ variables. By expanding the function $W(\bar{x} - \bar{r},\bar{r},t,\tau)f(\bar{x} - \bar{r},t)$ in a Taylor series for the slow variable $(\bar{x})$, truncating to second order, and integrating over an appropriate correlation time, T, we obtain the F-P equation:

$$\frac{\partial f(\bar{x},t)}{\partial t} = \frac{1}{2}\sum_{i,j}\frac{\partial^2}{\partial x_i \partial x_j}(\langle r_i r_j\rangle f) - \sum_i \frac{\partial}{\partial x_i}(\langle r_i\rangle f) \quad , \tag{3}$$

where $$\langle r_i\rangle(\bar{x},t) = \frac{1}{T}\int_0^T \int_1^\infty r_i\, w(\bar{x},r,t,\tau)d\bar{r}d\tau \quad , \tag{4}$$

and $$\langle r_i r_j\rangle(\bar{x},t) = \frac{1}{T}\int_0^T \int_1^\infty r_i r_j\, w(\bar{x},\bar{r},t,\tau)d\bar{r}d\tau \tag{5}$$

The indexes i or j represent the dimension in cluster size space (1-D for interstitial loops and 2-D for a He-V cluster). Equations (4) and (5) give the first and second moments of the transition. probabilities. The correlation time, T, is chosen to represent the appropriate physics of the relevant transition (e.g., inverse of arrival frequency for single-atom transitions or cascade-production frequency for cascade-induced transitions). Equation (4) represents the elements of a drift vector, while Eq. (5) is used to derive the elements of a dispersion tensor. A schematic representation of this model is shown in Fig. 1.

The following is a summary of the general procedure for the implementation of the theory. A set of rate equations for the concentrations of single defects and small defect aggregates is formulated to represent time-dependent nucleation. Larger-size defect clusters are treated by the F-P approximation given by Eq. (3), with the transition moments obtained via Eqs. (4) and (5). The rate equations are coupled to the F-P equation through a current boundary condition, and the solution is obtained semi-analytically as in Ref. [19], or numerically as in Ref. [25].

Interstitial loop evolution

The diffusion coefficient of self-interstitials is generally several orders of magnitude higher than that of vacancies. As a result, all clustering transition probabilities driven by self-interstitials have much faster time variations than those driven by vacancies. Moreover, an interstitial loop cluster containing 2 to 3 atoms is stable against thermal dissociation. As a consequence, several investigators [14 - 18] have shown that the time scale for interstitial loop evolution is much shorter than that for cavity evolution. This observation simplifies the analysis and the loop evolution can be approximately separated from that of cavities.

Equation (3) can be written in the 1-D form for interstitial loops:

$$\frac{\partial f}{\partial t} = - \frac{\partial}{\partial x} (Ff) + \frac{\partial^2}{\partial x^2} (Df) \quad , \tag{6}$$

where x is the number of atoms in a loop, $F(x,t)$ is a scalar drift coefficient defined by Eq. (4) and $D(x,t)$ is a scalar dispersion coefficient defined by Eq. (5). Analytical moment equations have been developed from Eq. (6) in the form of evolution equations for the average size, $\langle x \rangle$, and higher order moments, M_r, $r = 2,3, \ldots, \infty$. These are given by:

$$\frac{d}{dt} \langle x \rangle = \langle F \rangle + \xi_1 \quad , \qquad \frac{d}{dt} M_r = \psi_r + \Phi_r + \xi_r \quad , \qquad r = 2,3, \ldots, \infty \quad . \tag{7}$$

The symbol $\langle\rangle$ is used for averages over the loop distribution function. The dispersion functions, ψ_r, the distortion functions, Φ_r, and the nucleation functions, ξ_r, are defined in Ref. [19]. They are also dependent upon the average size $\langle x \rangle$ and the moments, M_r, which couple the system of evolution equations (7).

This system of equations (7) is usually solved numerically, except in special cases where simplifying assumptions can be invoked. Once the moments are determined, the loop size-distribution function, f, can be reconstructed as:

$$f(x,t) = \frac{1}{\sqrt{2\pi M_2}} \exp\left[- \frac{y^2}{2}\right] \left\{ 1 + \frac{M_3}{6M_2^{3/2}} H_3(y) + \frac{1}{24} \left[\frac{M_4}{M_2^2} - 3\right] H_4(y) \right.$$
$$\left. + \frac{1}{120} \left[\frac{M_5}{M_2^{5/2}} - 10 \frac{M_3}{M_2^{3/2}}\right] H_5(y) + \frac{1}{720} \left[\frac{M_6}{M_2^3} - 15 \frac{M_4}{M_2^2} + 30\right] H_6(y) \right\} \quad , \tag{8}$$

where $y = [(x - \langle x \rangle)/\sqrt{M_2}]$ and H_j, $j = 1,2, \ldots, 6$ are the Hermite polynomials.

Application of the theory to interstitial loops, as outlined in this section, has shown that the probability distribution function given by Eq. (8) is consistent with ion-irradiation experiments [16]. The comparison revealed that under cascade-irradiation conditions, cascade-induced fluctuations of loop sizes are the main contributors to the dispersion coefficient, D.

Cavity evolution

For the case where cascade-induced transitions are not dominant, the six elements in an F-P model of He-V cavity evolution are given by:

$$\langle r^v \rangle = k^{vc} - (k^{ic+ve} + k^{hr}) \quad , \qquad \langle rh \rangle = k^{hc} - (k^{he} + k^{hr}) \quad ,$$

$$\langle r_v r_v \rangle = \frac{1}{2!} (k^{ic+ve} + k^{hr} + k^{vc}) \quad , \qquad \langle r_h r_h \rangle = \frac{1}{2!} (k^{he} + k^{hr} + k^{hc}) \quad ,$$

$$\langle r_v r_h \rangle = \langle r_h r_v \rangle = k^{hr} \quad , \tag{9}$$

where the subscript/superscript notation is as follows: i ≡ interstitial, v ≡ vacancy, h ≡ helium, c ≡ capture, e ≡ emission, r ≡ replacements, and k ≡ reaction rates. In a 2-D size space, He-V clusters would

have trajectories which depend on their initial conditions and the moments of the transition probabilities, given by Eq. (9). Clusters would propagate by a Brownian-like motion in a drift field. The dispersion coefficients are given by the second moments while the drift coefficients are described by the first moments of Eq. (9).

Figure 2 shows the results of computations for the cavity size distribution in stainless steel for HFIR irradiation conditions at 450°C. It is to be noted that the majority of He-V clusters deviate from the state of thermodynamic equilibrium (gas pressure = surface tension stress), and tend to contain more vacancies than necessary for equilibrium. A comparison between computations and HFIR experimental data [35] is shown in Fig. 3. The moments of atomic transition probabilities are computed on the basis of single-atom transitions determined by Eq. (9) The comparison with experimental data indicates that without cascade effects, the width of the computed cavity-distribution function is smaller than that observed experimentally.

Spatial Instabilities and Self-Organization

Many experimental observations have shown striking spatial regularities in microstructures (e.g., void and bubble lattices, dislocation loop walls, etc.). To illustrate the origins of this self-orgnaization, we include the spatial diffusion operators for vacancies and interstitials, while larger clusters are considered to be immobile. A minimal model is proposed by Murphy [28] in which linear stability analysis is performed on the vacancy and interstitial concentrations and the vacancy dislocation-loop density, p. The wavelength predicted from the dispersion relationship by Walgraef and Ghoniem [32] is in good agreement with experiments on loop self-organization. The critical wavelength, λ_c, is given by the equation

$$\lambda_c = 2\pi\left[\frac{D_v(\bar{C}_{VL} - \bar{C}_{VN})}{(1 + B)\epsilon K \rho_N}\right]^{1/4} , \qquad (10)$$

where D_v is the vacancy diffusion coefficient, ϵ is the cascade collapse efficiency, (1 t B) is the dislocation bias factor, K the displacement rate, ρ_N the network density, $\bar{C}_{VL}$ the average thermodynamic vacancy concentration at vacancy loops, and $\bar{C}_{VN}$ the average thermodynamic vacancy concentration at dislocations. The wavelength predicted by Eq. (10) decreases with increasing network dislocation density, cascade collapse efficiency, and damage rate. These predictions are consistent with experimental observations [32]. Physically, the strength of point-defect fluctuations is increased by an increase in ϵ or K, while a shorter distance to absorption at sinks tends to damp these fluctuations.

In the weakly nonlinear regime, point-defect concentrations can be expanded as a power series in the vacancy-loop density which leads to a Ginzburg-Landau equation for ρ of the form

$$\dot{\rho} = \left[\left(\frac{b - b_c}{b_c}\right) - \xi_0^2(q_c^2 + \nabla^2)^2\right]\rho + v\rho^2 - u\rho^3 , \qquad (11)$$

where $b = B/\epsilon$, $\xi_0^2 \alpha (\rho_N/\rho_0)$, $v = 2/(x_0)^{3/2}$, $u = 2/(x_0)^{5/2}$, and $x_0 = \rho_0/\rho_N$. The homogeneous solution for the loop density is ρ_0, b_c is the critical value of the bifurcation parameter at the instability, and q_c is the critical wave vector. The density in Eq. (11) can be expressed in terms of a slowly varying amplitude and the critical wave vector, giving rise to a bifurcation diagram for the amplitude versus the bifurcation parameter. The details of the theory developed by Walgraef and Ghoniem are given in Ref. [32]. A comparison between this theory and experimental observations is shown in Fig. 4. Microstructural self-organization can be explained as a phase transition in analogy to the Landau-Ginzburg analysis.

Conclusions and Outlook

The theory of microstructure evolution under irradiation conditions typical of fusion reactor environments (i.e., continuous helium generationand cascade damage) combines nucleation and growth of microstructural features in a unified way. Concepts of non-equilibrium statistical mechanics are used to combine these two phases of microstructure evolution. Applications of the theory to fusion conditions show the following features.

(1) Nucleation of interstitial loops is very rapid and has little effect on the evolution of the size distribution function.

(2) Cascade-induced fluctuations dominate the dispersion of the loop and cavity distribution functions under fusion conditions.

(3) Nucleation of helium-filled cavities will likely be continuous because of the re-solutioning of helium atoms trapped in He-V clusters. The size distribution function will be asymmetric with a long tail towards smaller sizes.

(4) Spatially organized microstructures are expected to exist under a wide range of irradiation conditions. They result from spatial instabilities in point-defect concentrations in the presence of cascades.

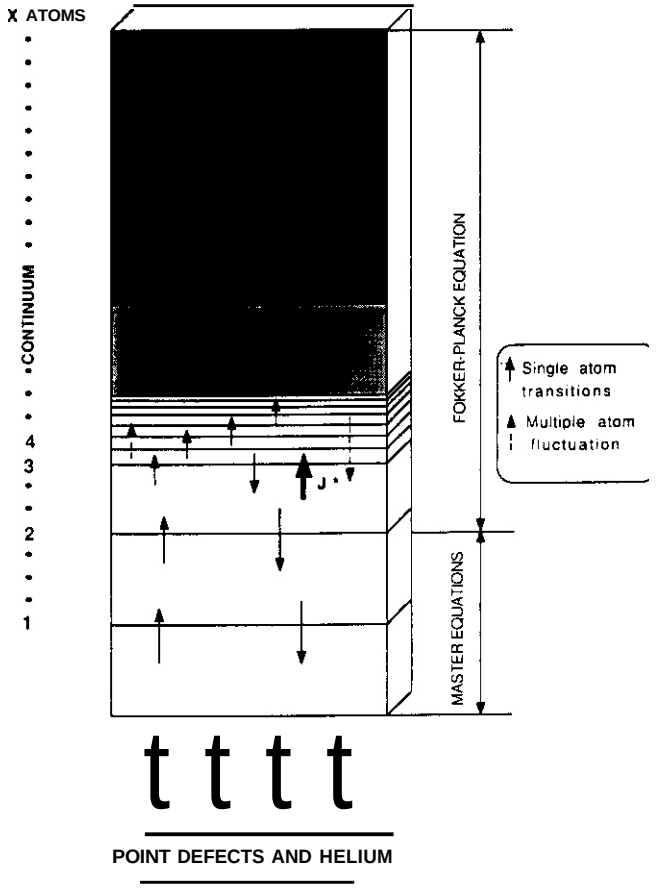

Fig. 1. Schematic representation of the clustering model. The number of interstitials, vacancies, or helium atoms in a cluster are represented by X.

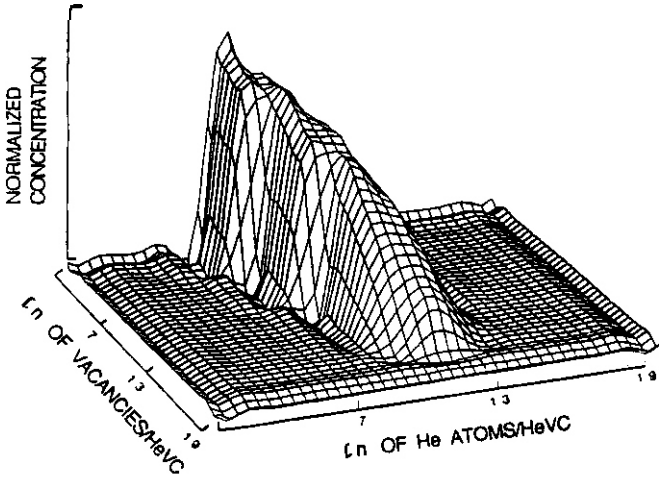

Fig. 2. Evolution of cavity size distribution HFIR irradiation conditions at 450°C.

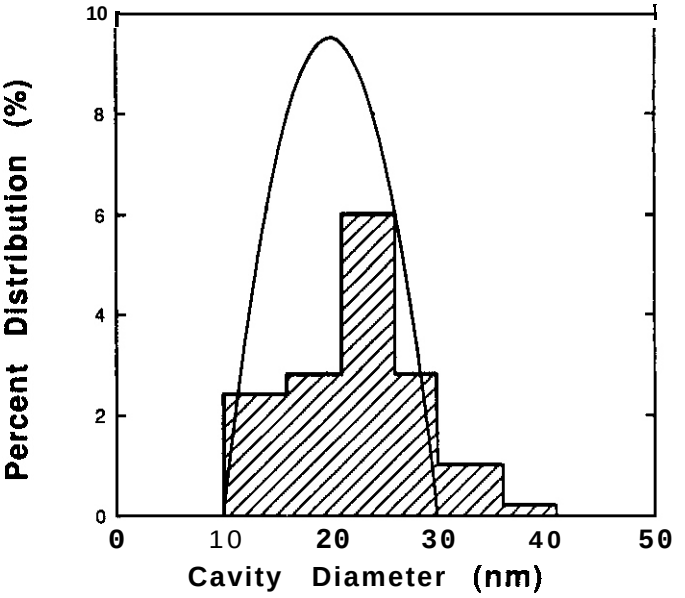

Fig. 3. Comparison of computed and experimentally measured cavity size distribution (histogram) at 14.3 dpa for HFIR irradiation conditions at 450°C (experimental data [35]).

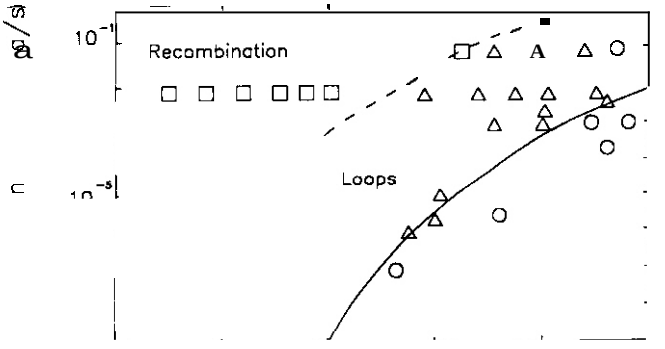

Detailed and careful experiments are needed to measure the effects of continuous cavity nucleation and of cascade fluctuations on the size distribution functions of microstructural features. Specific experiments can also be devised to directly measure the moments of the transition probabilities as defined by Eqs. (4) and (5). Such experimental details, when correlated to theory, can enhance our understanding of the underlying physics of microstructure evolution under irradiation and, hence, our extrapolation of current data to anticipated fusion conditions.

Acknowledgement

This work was supported by the U. S. Department of Energy, Office of Fusion Energy, Grant No. DE-FG03-84ER52110, with UCLA.

References

[1] J. L. Katz and H. Wiedersich, J. Chem. Phys. 55 (1971) 1753.
[2] J. L. Katz and H. Wiedersich, J. Nucl. Mater. 46 (1973) 41.
[3] K. C. Russell, Acta Metall. 19 (1971) 753.
[4] K. C. Russell, Acta Metall. 20 (1972) 899.
[5] R. Becker and W. Daring, Ann. Phys. 24 (1935) 719.
[6] J. B. Zeldovich, Acta. Phys.-Chim. URSS 18 (1943) 7.
[7] S. D. Harkness, J. A. Tesk, and Che-Yu Li, Nucl. Appl. Technol. 9 (1970) 24.
[8] R. Bullough and R. C. Perrin, in: Proc. of the Symposium on Radiation Damage in Reactor Materials, Vol. II (IAEA, Vienna, 1969) p. 233.
[9] A. D. Brailsford and R. Bullough, J. Nucl. Mater. 44 (1972) 121.
[10] R. Bullough, B. L. Eyre, and K. Krishan, Proc. R. Soc. London A346 (1975) 81.
[11] N. M. Ghoniem and G. L. Kulcinski, Radiat. Eff. 39 (1978) 47.
[12] L. K. Mansur and W. G. Wolfer, J. Nucl. Mater. 69&70 (1978) 825.
[13] L. K. Mansur, Nucl. Technol. 40 (1978) 5.
[14] L. M. Brown, A. Kelly, and R. M. Mayer, Philos. Mag. 19 (1969) 721.
[15] M. Kiritani, J. Phys. Soc. Jpn. 35 (1973) 95.
[16] B. O. Hall and D. I. Potter, in: Proc. of the 9th International Symposium on Effects of Radiation on Structural Mqterials, ASTM-STP-683 (American Society for Testing Materials, Richland, WA, 1978) p. 789.
[17] N. M. Ghoniem and O. D. Cho, Phys. Status Solidi A54 (1979) 1971.
[18] N. M. Ghoniem and S. Sharafat, J. Nucl. Mater. 92 (1980) 121.
[19] N. M. Ghoniem, Phys. Rev. B39 (1989) 11810.
[20] W. G. Wolfer, L. K. Mansur, and J. A. Sprague, in: Proc. of the International Conference on Radiation Effects in Breeder Reactor Structural Materials, Eds. M. Bleiberg and T. W. Bennet (American Institute of Mining, Metallurgical, and Petroleum Engineers, Scotsdale, AZ, 1977) p. 84.
[21] K. Kitajima, N. Yoshida, and E. Kuramoto, J. Nucl. Mater. 103&104 (1981) 1355.
[22] K. Kitajima, E. Kuramoto, and N. Yoshida, J. Nucl. Mater. 108&109 (1982) 267.
[23] M. F. Wehner and W. G. Wolfer, Phys. Rev. A28 (1983) 3003; also Philos. Mag. A52 (1985) 189.
[24] H. Trinkaus, J. Nucl. Mater. 113&114 (1985) 105.
[25] S. Sharafat and N. M. Ghoniem, Radiat. Eff. and Def. in Solids, to be published.
[26] G. Martin, Phys. Rev. B30 (1984) 1424.
[27] K. Krishan, Radiat. Eff. 66 (1982) 121.
[28] S. M. Murphy, Europhys. Lett. 3 (1987) 1267.
[29] E. A Koptelov and A. A. Semenov, Phys. Status Solidi A89 (1985) 117.
[30] E. A Koptelov and A. A. Semenov, Phys. Status Solidi A93 (1986) K33.
[31] C. Abromeit and H. Wollenberger, J. Mater. Res. 3 (1988) 640.
[32] D. Walgraef and N. M. Ghoniem, Phys. Rev. B39 (1989) 8867.
[33] N. M. Ghoniem, S. Sharafat, J. M. Williams, and L. K. Mansur, J. Nucl. Mater. 117 (1983) 96.
[34] I. Oppenheim, K. E. Schuler, and G. H. Weis, Adv. Mol. Relaxation Processes 1 (1967) 13.
[35] P. J. Maziasz, "Effects of Helium Content on Microstructural Development in Type-316 Satinless Steel Under Neutron Irradiation," Ph.D. thesis, University of Tennessee, Knoxville (December 1984).
[36] P. Ehrhart, W. Jager, W. Schilling, F. Dworschak, A. A. Gadalla, and W. Tsukuda, Mater. Res. Soc. Symp. Proc. 82 (1987) 265.
[37] W. Jager, P. Ehrhart, and W. Schilling, in: Non-Linear Phenomena in Materials Science, Eds. L. Kubin and G. Martin, Solid State Phenomena 3&4 (1988).

FUTURE WORK

No future work on reviewing microstructure evolution theory is planned.

THE EFFECTS OF MANY-BODY INTERACTIONS ON POINT-DEFECT GENERATION

S. P. Chou and N. M. Ghoniem
(University of California, Los Angeles)

OBJECTIVE

The displacement damage threshold and the size of point-defect recombination volume are two important parameters for a fundamental understanding of radiation effects. The work is aimed at developing a new composite pair/many-body interatomic potential for low-energy ion collisions in solids. This potential is used in molecular dynamics simulations of collision cascades in copper. Good agreement is obtained with experimental data at 10 K.

SUMMARY

Point-defect generation by energetic displacement events is known to take place when a lattice atom requires an energy several times its lattice binding value. In this energy range, many-body effects are important and interatomic pair potentials generally give poor representations of atomic interactions. By applying our newly developed molecular-dynamics code, CASC-MD, we investigate the influence of many-body interatomic interactions on the generation characteristics of point defects. We use a composite interatomic potential which assumes the pair-potential nature at high energies and the many-body nature, based on the embedded-atom formalism, at low energies. It is shown that many-body effects lead to lower directional sensitivity of the displacement threshold surface. For a 60-eV collision cascade in Cu, it is shown that the length of the replacement collision sequence decreases from 6 lattice constants at low temperature (near 0 K) to 1.5 lattice constants near the melting point.

PROGRESS AND STATUS

Introduction

The generation of point defects has been studied theoretically by using both the Monte Carlo and the molecular dynamics (MD) methods with pair potentials for high energies [1-14]. Theoretical and experimental results both indicate that atomic displacements occur with a threshold energy on the order of a few times the lattice binding energy. Because pair potentials are generally inaccurate near the displacement threshold energy, the use of pair potentials to study this energy range is questionable. Daw and Baskes [15-16], using the embedded atom method (EAM), formulated the basis for a many-body potential by incorporating the embedding-function contribution to the atomic pair interaction. With a Taylor-series expansion about the equilibrium local electron density, Foiles [17] derived a many-body-type potential which accounts for the contribution of volume-dependent electron interactions. The EAM potential derived in this way is a good representation of atomic interactions in the sub- and low-eV energy range. Therefore, the cascade interaction is expected to be more precisely described by using a pure pair potential at high energies and the EAM many-body potential in the sub- and low-eV range.

In this work, the incorporation of both pair and many-body potentials into MD simulations is realized through the use of a composite spline technique. A brief discussion of the main features of a newly developed MD code, CASC-MD, is given. The collision-cascade interaction dynamics and calculations of the displacement threshold surface in copper are studied by using the Born-Mayer pair potential and comparing the results to the newly developed composite potential. Comparisons with earlier computer simulations by King and Benedek [12-14] are then made. The effects of temperature on the length of the replacement collision sequence are also studied.

Development of CASC-MD

Spline potential

A molecular dynamics code, CASC-MD, has been developed to study low-energy collision cascades. The unique features of this code are the use of a more realistic potential for the description of atomic interactions and the incorporation of viscoelastic boundary conditions. A cubic-spline scheme is used to bridge the gap between the low-energy EAM many-body potential and the high-energy pair potential. The low-energy many-body potential for a solid at or near equilibrium is derived from the total energy of a system of atoms by using the EAM which is based on local density approximation. This many-body potential is derived by Daw, et al. [15-17] and has the form

$$\phi_{EAM} = \phi_{ij}(R_{ij}) + 2\,\frac{\partial F_i(\bar{\rho}^a)}{\partial \rho}\rho^a_{ij}(R_{ij}) + \frac{\partial^2 F_i(\bar{\rho}^a)}{\partial \rho^2}\,[\rho^a_{ij}(R_{ij})]^2 \qquad (1)$$

where i and j are indice of interacting atoms, $\bar{\rho}^a$ is the local average background electron density on atom i, $\rho^a_{ij}(R_{ij})$ is the local average electron density contribution from atom j to atom i at a separation distance of

R_{ij}, and ϕ_{ij} is the core-core repulsive potential between atoms **i** and **j**. The range of this potential extends to the third nearest neighbors.

The high-energy pair-interaction potential is well represented by the Ziegler potential [18]. The transition from high- to low-energy interactions is represented by a cubic-spline potential function which is adjusted to guarantee continuity of potential and force at two spline points, r_1 and r_2, located along the interatomic separation distance. Details of the method are given in Ref. [19]. Figure 1 shows a 3-D plot of the composite potential as a function of the distance between interacting atoms and the total local electron density for nickel atoms. The transition region is taken to be from 1.5 to 2.0 Å. It is worth mentioning that the selection of r_1 and r_2 is achieved by requiring smooth force variation over the transition region. Improper choices of spline boundaries can artificially introduce high potential minima and maxima which locally trap recoils.

Wolecular dynamics scheme and boundary conditions

In MD simulations, the motion of a system of particles can be fully described by the solutions of a system of Newtonian equations of motion. Equations of motion (EOMs) are integrated using an explicit leapfrog technique (see Ref. [19]).

In equilibrium MD simulations, it has been established that the dynamic behavior of a small number of atoms can be a valid statistical representation of the solid as long as periodic boundary conditions and velocity renormalization are used [10]. In equilibrium phase-transition problems, sample sizes up to 250,000 atoms have been used. However, in our cascade simulations, we are not interested in simulating a global phenomenon (e.g., phase transitions) for which an increase in the size of the computational box is likely to give more accurate results. Rather, the size of the computational box is determined solely by the energy dissipation rate at the boundary. Ideally, and in an infinite solid, the excess kinetic energy of the primary knock-on atom (PKA) must eventually be dissipated to the outside world or else it will lead to a uniform temperature rise. Practically, however, we are more interested in the study of energy dissipation in the generation of point defects. We introduce an arbitrary cutoff kinetic energy per atom (say, 1 eV), below which cascade simulation for the purpose of point-defect generation is no longer suitable. The number of atoms for a particular cascade simulation is chosen to guarantee that no energy reflection occurs at the boundary in a way which alters atomic rearrangements inside the computational box. We also introduce two atomic planes of special "boundary atoms" which have viscoelastic EOMs in order to simulate cascade energy dissipation into the surrounding solid. Details are given in Ref. [19].

Low-Energy Collision-Cascade Simulations

The dynamics of a collision cascade by a 60-eV (speed = 135 Å Cu PKA initially along [100] direction on a (001) plane in Cu at 300 K is illustrated in Fig. 2. The X-axis is the particle ID number. It is arranged so that the particle ID number increases along the X direction in the computational cell (boundary atoms are not included). It is clearly shown that the collision cascade subsides quickly in less than 0.15 ps, which is the collisional phase of the cascade evolution. None of the atoms has energy greater than 1 eV (17 Å/ps) at the end of this phase. It is observed that the energy propagation speed is greater than the speed of recoils and far exceeds the speed of sound. This is because the collective interaction is the dominant mode of energy transfer. Figure 3 shows a linear replacement-collision sequence (RCS) generated by the same 60-eV Cu PKA in a layer, which has a thickness of 0.5 lattice constant, with the major interaction plane (001) in the middle. The linear RCS has a length of 5.5 lattice constants. The energy dissipation is preferred along special crystallographic directions (e.g., [100] and [110]). This is clearly shown by the larger-than-thermal vibration movement of the lattice atoms along these directions. Figure 4 shows the effect of temperature on the RCS length by the same 60-eV PKA along the [100] direction. Cascade de-focusing at high temperatures is clearly caused by variations of the impact parameter along the primary focusing direction which results in a shortening of the RCS length. In some cases, no displacement is generated at all. This suggests that the directional displacement threshold energy varies depending on the irradiation temperature. Figure 5 shows CASC-MD calculations of the threshold displacement energy along selected crystallographic directions compared with the numerical results of King and Benedek [14]. For their numerical calculations, King and Benedek used the Born-Mayer pair potential. It appears that the use of the present composite potential results in less sensitive directional variations of the displacement threshold when compared with'the results of a pure pair potential. However, our computational results are more consistent with their experimental data on Cu [12-14].

Conclusions and Future Directions

In this work, a molecular dynamics code, CASC-MD, is developed. A composite potential (comprising pair- and many-body-interaction types for high and low energies, respectively) is used and yields good agreement with experimental values for the displacement threshold energy surface. Our results clearly show the influence of temperature on the dynamics of collision cascades and displacement generation. It is also shown that many-body effects are important to consider in the sub- and low-eV energy ranges.

Because of the complicated EAM potential at low energy and its long-range interactions, our analyses have been limited to small computational cells and sub-keV collision cascades. The computational overhead is a major concern for the use of such potentials: 15 minutes of CRAY-2 time for simulations of a computational cell size of 1271 particles with a duration of 1 ps. To extend our calculations to higher cascade energies and larger computational cells requires further development of the present code.

Acknowl edaement

This work was supported by the U. S. Department of Energy, Office of Fusion Energy, Grant #DE-FG03-84ER52110, with UCLA.

References

[1] M. Yoshida, J. Phys. Soc. Jpn. 16 (1961) 44.
[2] 0. Oen and M. T. Robinson, J. Appl. Phys. 34 (1964) 2515.
[3] T. Ishitani, R. Shimuzu and K. Murata, Jpn. J. Appl. Phys. 11 (1972) 125.
[4] H. L. Heinisch, J. Nucl. Mater. 103/104 (1981) 1325; also J. Nucl. Mater. 117 (1983) 46.
[5] S. P. Chou and N. M. Ghoniem, J. Nucl. Mater. 117 (1983) 55.
[6] J. B. Gibson, A. N. Goland, M. Milgram, and G. H. Vineyard, Phys. Rev. 120 (1960) 1229.
[7] J. R. Beeler, Jr., Phys. Rev. 150 (1966) 470.
[8] R. N. Stuart, N. W. Guinan and 8. J. Borg, Radiat. Eff. 30 (1976) 129.
[9] J. D. Schiffgen and R. D. Bourquin, J. Nucl. Mater. 69/70 (1978) 790.
[10] A. Tenenbaum and N. V. Doan, J. Nucl. Mater. 69/70 (1978) 775.
[11] T. Diaz de la Rubia, R. S. Averbeck, and H. Hsieh, J. Mater. Res. 4 (1989) 579.
[12] W. E. King and R. Benedek, Phys. Rev. 823 (1981) 6335.
[13] W. E. King and R. Benedek, in: Point Defects and Defect Interactions in Metals, Eds. J. Takamura, M. Ooyama, and M. Kiritini (University of Tokyo Press, Tokyo, 1982) p. 807.
[14] W. E. King and R. Benedek, J. Nucl. Mater. 117 (1983) 26.
[15] M. S. Daw and M. I. Baskes, Phys. Rev. Lett. 50 (1983) 1285.
[16] M. S. Daw and M. I. Baskes, Phys. Rev. 829 (1984) 6443.
[17] S. M. Foiles, Phys. Rev. 832 (1985) 7685.
[18] J. F. Ziegler, J. P. Biersack, and U. Littmark, The Stopping and Range of Ions in Solids (Pergamon Press, New York, 1985) p. 48.
[19] S. P. Chou and N. M. Ghoniem, submitted to Phys. Rev. Lett. (1989).
[20] F. F. Abraham, Adv. Phys. 35 (1986) 1.

FUTURE WORK

The Molecular Dvnamics code will be modified to study the displacement damage process in SiC for fusion applications.

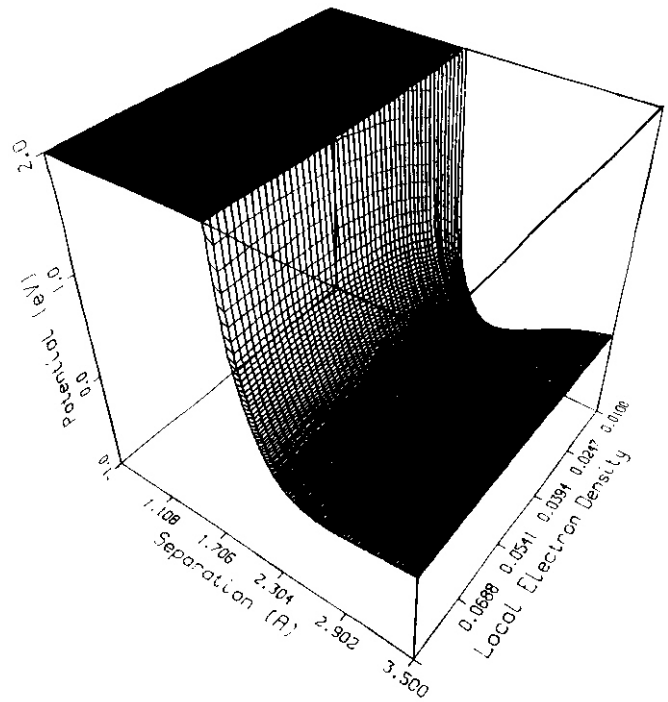

Fig. 1. Dependence of the composite potential on the interatomic separation distance and the local electron density.

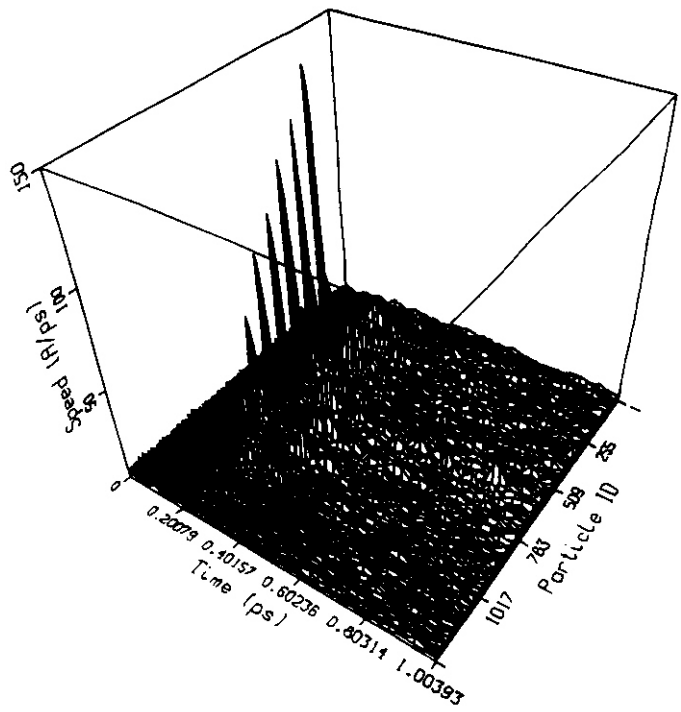

Fig. 2. Cascade dynamics of a 60-eV Cu PKA incident along the [100] direction in a (001) plane. The particle (recoil) ID increases along the X-axis.

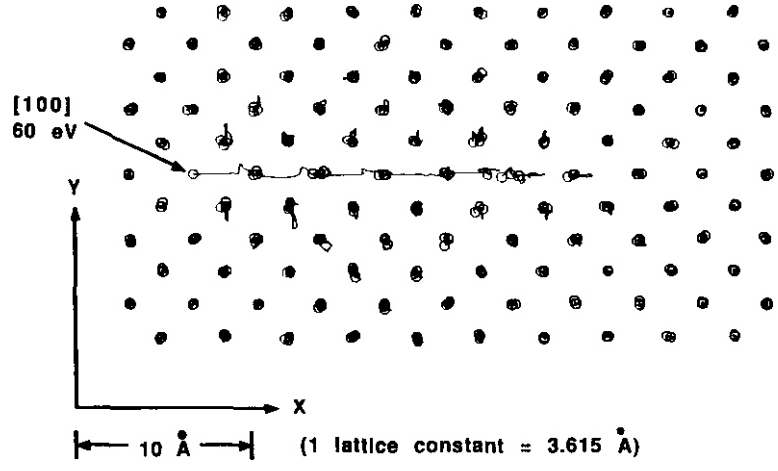

Fig. 3. Cascade trajectories for a 60-eV Cu PKA incident along the [100] direction in a (001) plane at 300 K. A linear RCS with a length of 5.5 lattice constants is produced.

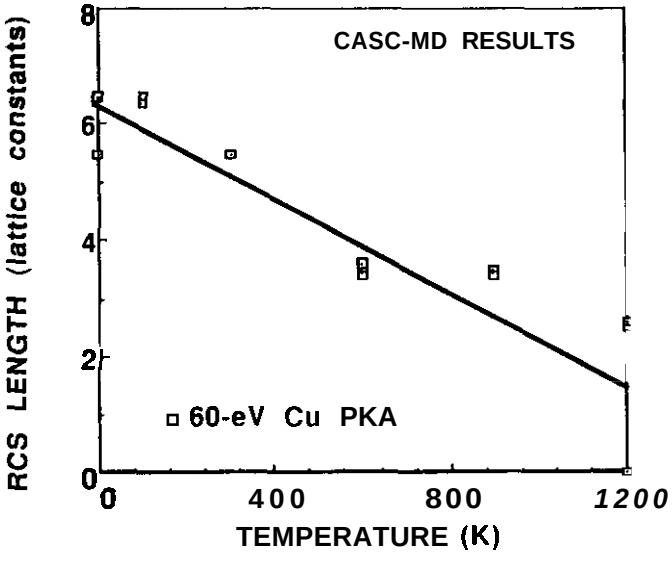

Fig. 4. The dependence of the linear RCS length on temperature.

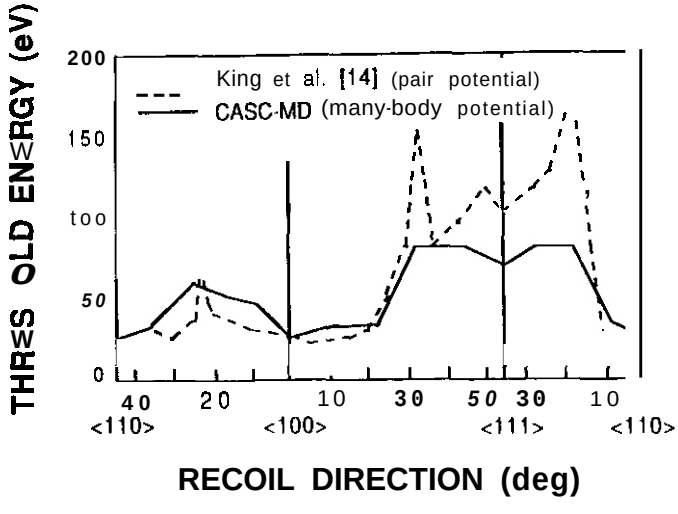

Fig. 5. A comparison between the displacement threshold energies along selected crystallographic directions evaluated by CASC-MD simulations and those of King and Benedek [14].

NUCLEATION AND GROWTH THEORY OF CAVITY EVOLUTION UNDER CONDITIONS OF CASCADE DAMAGE AND HIGH HELIUM GENERATION

N. M. Ghoniem (University of California Los Angeles)

OBJECTIVE

Radiation effects on the microstructure are dependent upon the irradiation environment. For fusion machines, it is useful to develop correlations from existing irradiation data. This research is aimed at developing a physical framework which can allow for investigating the effects of collision cascades and helium generation on the evolution of cavities in irradiated steels.

SUMMARY

The evolution of helium-filled cavities during neutron irradiation is analyzed in terms of the stochastic theory of atomic clustering. The conventional separation of nucleation and growth is replaced by a self-consistent evolution model. Starting from kinetic rate (master) equations for the clustering of helium and vacancies, helium mobility, helium-vacancy cluster stability, and cavity nucleation and growth are all included in the model. Under typical fusion irradiation conditions (cascade damage and high helium-to-dpa ratios), the following is suggested: (1) Helium mobility decreases with the evolution of the microstructure. At quasi-steady-state, it is mainly controlled by interstitial replacement or thermal desorption. (2) Gas re-solution from cavities by cascades increases nucleation at high fluences. (3) The cavity size distribution is broadened because of cascade-induced fluctuations. (4) The majority of helium-filled cavities are in a nonequilibrium thermodynamic state.

PROGRESS AND STATUS

Introduction

Under neutron irradiation conditions expected in fusion reactor structural materials, the evolution of microstructures can not be easily described by the conventional separation into sequential nucleation and growth phases. In particular, helium-filled cavity formation proceeds via competitive reaction mechanisms which render the conventional viewpoint inapplicable. For example, the mobility of helium atoms is dictated by the evolving cavity microstructure. Since helium mobility is controlled by the rates of trapping and detrapping from various helium-vacancy (HV) clusters, it would be inappropriate to assume that it is a constant value. Because cavity nucleation is determined by helium mobility, the two processes are therefore interdependent. Collision cascades interact directly with helium atoms inside cavities and can result in their displacement back into the matrix. This process, called gas re-solution, is dynamic and continuous, resulting in re-nucleation of smaller size cavities, provided that a significant amount of helium has already been introduced into the solid. Nucleation is therefore not terminated, as assumed in classical nucleation theories, but is continuously supplying freshly formed small cavities. Nucleation and growth of cavities are strongly coupled under these circumstances, and the "mean field" approximation used in the rate theory of cavity growth is poor.

Classical nucleation theory was originally applied to the nucleation of voids with no gas assistance. When the theory is used to predict the conditions for condensation of water vapor in air, liquid droplets are found to form at a critical value of the supersaturation ratio (about 5 to 6). As soon as the liquid droplets form, the supersaturation ratio abruptly drops and thereby terminates nucleation. The success of classical nucleation theory critically depends on this aspect. However, these conditions are not met under irradiation because of the continuous production of point defects and gas atoms. The theory (developed independently by Katz and Wiedersich [1] and Russell [2]), and its extensions, displayed several unsettling characteristics. First, nucleation rates and not cavity densities can be predicted. Second, computed nucleation rates are extremely sensitive to the physical parameters (e.g., the interstitial/vacancy arrival ratio, surface energy, and gas pressure). When gas production is predominant, however, as in nuclear fuels or in fusion structural materials, terminal cavity densities can be obtained. The work of Greenwood [3] and of Trinkaus [4,5] are examples of this approach.

Growth of gas-filled cavities has been treated within the framework of the mean field approximation where statistical variations in time and space are averaged. The original developments of Brailsford and Bullough [6], Bullough, Eyre, and Krishan [7], and many others (e.g., Refs. [8 - 11]) have been successful in explaining the gross features of many experimental observations on cavity growth. However, under fusion conditions, the high helium-generation rates and the presence of collision cascades require consideration of additional physical mechanisms which influence the details of cavity growth.

In this paper we give a concise description of our work on HV-cluster evolution under irradiation, as applied to fusion reactor conditions. Analysis of helium transport and its coupling with the transient nucleation of small HV clusters is provided in Section 2. A stochastic approach to the coupled nucleation/growth problem is given in Section 3. The effects of single- and multiple-atom absorption and loss from an HV cluster are incorporated into the framework of Fokker-Planck theory given in Section 4. The resulting equation which describes the evolution of the size distribution is solved bv a two-moment approximation in Section 5. Results for the effects of high helium-generation rates and coliision cascades are discussed in Section 6, and conclusions are given in Section 7.

Transient Helium Transport and Nucleation

Helium migration and transport is a time-dependent process controlled by the density and distribution of helium traps and by the trapping/detrapping rate of each. Since most helium traps are in the form of single vacancies or small vacancy clusters, it is obvious that helium transport is intrinsically coupled with the nucleation of small HV clusters. As an interstitial atom, helium mobility is very high. Unless helium is migrating between traps, it will be transported quickly to grain boundaries causing severe embrittlement. Therefore, any mechanism that enhances the speed of matrix trapping will be advantageous in preventing grain boundary absorption of helium. To determine the transport and nucleation rates of helium, a model was developed for the reactions between the three primary species (i.e., vacancies, interstitials, and helium) [12].

Rate equations are developed for the concentrations of the following species: (1) free vacancies, C_v; (2) self-interstitial atoms, C_i; (3) interstitial helium atoms, C_g; (4) substitutional helium atoms, C_{gv}; (5) di-interstitial helium atom clusters, C_{2g}; (6) di-helium, single vacency clusters, C_{2gv}; (7) and bubble nuclei containing three helium atoms, C^*. These are given by:

$$\frac{dC_v}{dt} = fG + (\beta e_1 + 6)C_{gv} - \left[\alpha C_i + \beta C_g + \gamma(C_s^v + C_{gv} + 2C_{2g} + 2C_{2gv} + 3C^*)\right]C_v \quad , \tag{1}$$

$$\frac{dC_i}{dt} = fG - (C_v + C_{gv} + 2C_{2gv} + 3C^* + C_s^i)\alpha C_i \quad , \tag{2}$$

$$\frac{dC_g}{dt} = G_H + (\beta e_1 + 6 + \alpha C_i)C_{gv} + (\beta e_2 + 2\delta)C_{2gv} + 3(\delta + \alpha C_i)C^* + 4\delta C_{2g} + 4\alpha C_i C_{2gv} + m\delta C_{tot}$$
$$+ \delta M_{gb} + \delta M_{ppt} - \left[\epsilon C_{tot} + C_v + 4C_g + C_{gv} + 2C_{2g} + 2C_{2gv} + C_{gb} + \epsilon_{ppt}C_{ppt}\right]\beta C_g \quad , \tag{3}$$

$$\frac{dC_{gv}}{dt} = \beta C_g C_v + (e_2 + 2\delta)C_{2gv} - (e_1 + \beta C_g + 6 + \delta C_v + \alpha C_i)C_{gv} \quad , \tag{4}$$

$$\frac{dC_{2g}}{dt} = 2\beta C_g^2 + 3\alpha C_i C^* - (2\gamma C_v + 2\beta C_g + 2\delta)C_{2g} \quad , \tag{5}$$

$$\frac{dC_{2gv}}{dt} = \beta C_g C_{gv} + 3\delta C^* + 2\gamma C_v C_{2g} - (2\beta C_g + 2\delta + \beta e_2 + 2\delta C_v + 2\alpha C_i)C_{2gv} \quad , \tag{6}$$

$$\frac{dC^*}{dt} = 2(C_{2g} + C_{2gv})\beta C_g - 3(\beta C_g + \gamma C_v + \alpha C_i + \delta)C^* \quad , \tag{7}$$

$$\frac{dM_{ppt}}{dt} = \epsilon_{ppt}\beta C_{ppt} C_g - \delta M_{ppt} \quad , \tag{8}$$

$$\frac{dM_{gb}}{dt} = \beta C_{gb} C_g - \delta M_{gb} \quad . \tag{9}$$

The definitions of various reaction rates are given in Appendix A. Four basic reaction frequencies are used in our analysis:

$\alpha = 48\,\nu_i \exp(-E_i^m/kT)$, s^{-1} (self-interstitial rf); $\beta = 48\,\nu_g \exp(-E_g^m/kT)$, s^{-1} (helium rf);

$\gamma = 48\,\nu_v \exp(-E_v^m/kT)$, s^{-1} (vacancy rf); $\delta = bG$, s^{-1}, (radiation re-solution frequency);

where the atomic jump frequencies are denoted by $\nu_{i,g,v}$ and the migration frequencies by $E_{i,g,v}^m$. The re-solution parameter, b, is defined as the probability per displacement for dissolving a helium atom back into the matrix. The emission probabilities, e_1 through e_5, are computed from binding energies, as outlined in ref. 12.

Numerical solutions to the reaction rate equations have been developed, and the concentrations were computed as functions of irradiation time. Two major quantities can be obtained from this analysis: (1) the "effective" helium diffusion coefficient and (2) the time-dependent cavity nucleation current. We will show results for the helium diffusion coefficient in this section and will then proceed to describe nucleation and growth of HV clusters.

Helium transport in an irradiated material occurs by one of several mechanisms or channels. A convenient way of defining the effective diffusion coefficient, D^e_{He}, is to take the weighted mean of all channels:

$$D^e_{He} = \frac{\sum_i D^i_{He} C^i_{He}}{\sum_i C^i_{He}}, \qquad (10)$$

where D^i_{He} and C^i_{He} are, respectively, the diffusion coefficient of helium and its concentration in channel i. Obviously, the dominant channel will be the one with the highest helium concentration and the highest mobility. This turned out to be a complicated situation during transients, since clustering must be taken into account. Under typical reactor conditions, the length of the transient is strongly dependent upon the temperature and initial sink structure (see refs. 12 and 13). During steady state, however, the effective diffusion coefficient can be obtained by simple analysis (see refs. 4, 13, 14). Fig. 1 shows the effective helium migration energy as a function of temperature for nickel at a displacement damage rate of 10^{-6} dpa/s. The results are shown after an initial transient (i.e., at quasi steady state), and are shown for both numerical solutions of the equations and approximate analytical solutions. The mobility of helium is determined (a) at low temperatures by radiation displacement from atomic-size traps, (b) at intermediate temperatures by the interstitial replacement mechanism, and (c) at higher temperatures by the thermal detrapping mechanism. The abrupt jumps in the migration energy are the result of analytical approximations. They indicate the approximate temoerature boundaries for the various dominant mechanisms in nickel under reactor irradiation'conditions. Helium mobility by the vacancy mechanism has also been considered by Trinkaus [4] and by Forman and Singh [14].

Stochastic Description of Nucleation/Growth

Following Russell [15], we represent an HV cluster as a point in a two-dimensional (2-D) HV phase space. The dynamical equations of motion of this point (h,v) can be written as a set of two Langevin-type equations for the velocity components as:

$$\dot{h} = \frac{dh}{dt} = R^c_h - R^{gr}_h - R^r_h + \xi_h(t) \quad , \qquad (11)$$

$$\dot{v} = \frac{dv}{dt} = R^c_v - R^e_v - R^c_i \, t \, \xi_v(t) \quad . \qquad (12)$$

Here, the time-averaged (non-fluctuating) rates can be cpmputed from the rate equations (1)-(9): R^c_h = rate of helium capture, R^{gr}_h = rate of helium replacement, R^r_h = rate of helium re-solution, R^e_v = rate of vacancy emission, and R^c_i = rate of interstitial capture. Stochastic fluctuations are represented by the random "forces" $\xi_h(t)$ and $\xi_v(t)$. These random components have a zero time-average, but are characterized by an amplitude and a spectrum. Cascade-induced fluctuations in point-defect concentrations have been studied by Mansur, Coghlan, and Brailsford [16], Marwick [17], and Chou and Ghoniem [18]. Fig. 2 shows the relative value of the root-mean-square (RMS) fluctuation in vacancy concentrations as a function of the cascade radius [18]. It is to be noted that the amplitude of the fluctuation is quite significant, and this will be reflected in the random function, $\xi_v(t)$. It is interesting to see that as the cascade size increases, the fluctuation amplitude decreases for cascades with a radius greater than ~400 Å. Cascades initiated by 14-MeV neutrons can be several thousand angstroms in size and may, therefore, result in a lower fluctuation amplitude, as compared with fission neutrons. Since the frequency range of the fluctuation spectrum is much higher than inverse relaxation times in cluster phase space, the average value of the phase-space vector can be described by trajectories, each being determined by the initial conditions. Those trajectories are solutions of eqs. (11) and (12), with the fluctuating functions $\xi_h(t)$ and $\xi_v(t)$ set to their time-averaged value of zero.

Stability of the HV cluster can be investigated by examining the phase-plane representation of the nodal lines given by dh/dt = dv/dt = 0. The critical points of the solution are obtained by the intersection of the line dh/dt = 0 with the line dv/dt = 0.

Numerical solutions of eqs. (11) and (12) have been implemented for the conditions of stainless steel irradiated in EBR-II (appm He/dpa = 0.1) and HFIR (appm He/dpa = 57). The results are shown in fig. 3, where the flow field in the HV phase space is represented by arrows. Fig. 3a illustrates that stochastic fluctuations (e.g., by cascades) are necessary to drive nucleation past the second critical point. On the other hand, it is shown that under high He-to-dpa conditions (fig. 3b), there are no critical points and the flow field propagates smoothly from any small cluster size (e.g., two helium atoms and a few vacancies) to larger ones. Nucleation is expected, therefore, to proceed without the need for stochastic fluctuations.

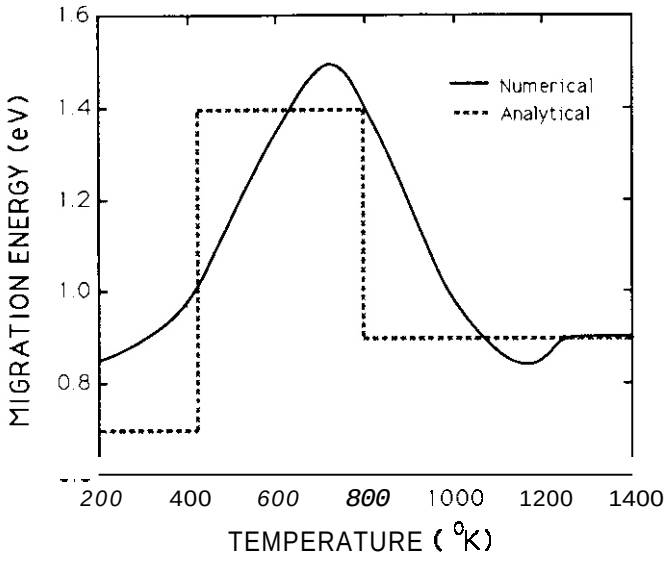

Fig. 1. Effective helium migration energy for Ni under reactor irradiation as a function of temperature.

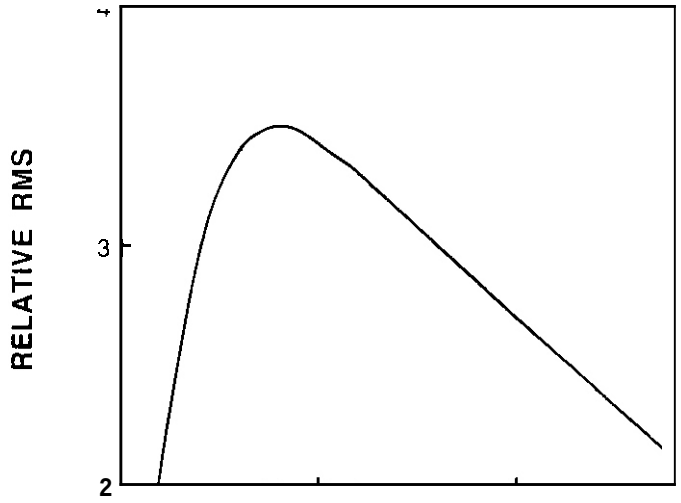

Fig. 2. Dependence of the relative root-mean-square (RMS) for vacancy concentration of the fluctuation amplitude on cascade size.

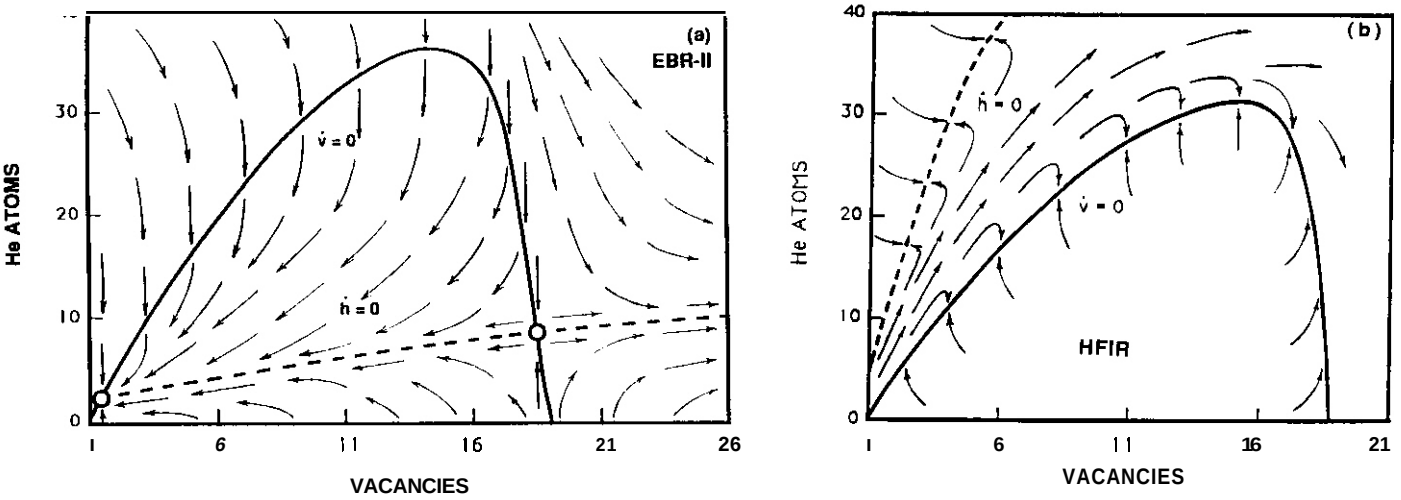

Fig. 3. Phase space representation of the flow field for (a) EBR-II and (b) HFIR conditions. Computations were made for a total sink density of 10^{10} cm^{-2} and at 500°C.

This phase-space analysis is useful in damage correlation studies. It can be used to determine if a given damage simulation experiment will lead to the same nucleation and cluster stability conditions as in a fusion reactor.

If the critical HV-cluster size is assumed to contain three helium atoms and one vacancy (see fig. 3b), the nucleation rate can be calculated from the forward reaction rates of eq. (7):

$$\frac{dC_{tot}}{dt} = |\vec{J}|^* = 3(\beta C_g + \gamma C_v)C^* \qquad (13)$$

The critical nucleus concentration is denoted by C^*. In eq. (13), it is assumed that nucleation is driven by further absorption of helium atoms and vacancies at existing clusters which contain three helium atoms. This is a simplified form of the nucleation current, but this simplification is possible because of the high He-to-dpa ratio.

In the present development, the nucleation current $\vec{J}^*$ has two components which represent-one of the boundary conditions to the flow field (shown in fig. 3). The helium- and vacancy-driven components can be represented by, respectively, J_h and J_v. Thus

$$\vec{J} = J_h \vec{i} + J_v \vec{j} \quad , \tag{14}$$

where $\vec{i}$ and $\vec{j}$ are unit vectors in the helium and vacancy directions, respectively.

Fig. 4 shows results of calculations for the total density of HV clusters for the conditions of dual ion-beam irradiation of steel at 625°C [19]. The He-to-dpa ratio is 5 appm He/dpa and the displacement damage rate is 3×10^{-3} dpa/s. Continuous nucleation is clearly evident in the experimental results. Our study of the re-solution parameter, b (the probability of gas re-solution into the matrix per dpa) shows that an average value of b on the order of unity is consistent with these experiments. The exact value of b should be determined from theoretical comparisons with experiments under the specific damage conditions. This value represents an average over the cavity size distribution and is quite important in explaining the continuous nucleation of cavities.

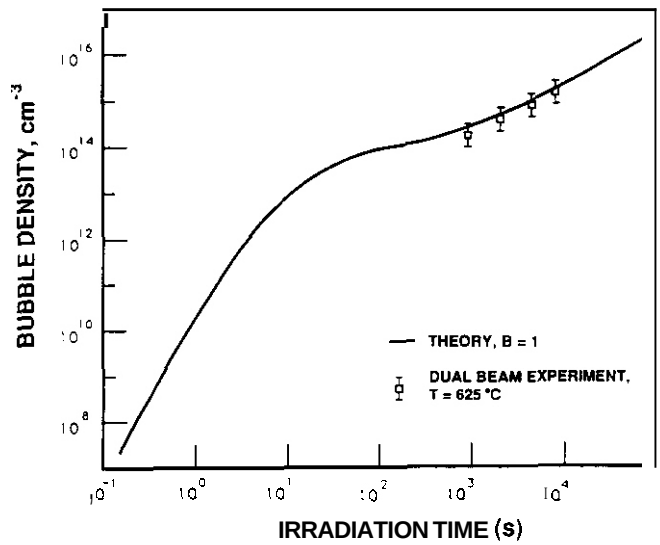

Fig. 4. Comparison between calculations and experiments on the total HV-cluster density for steel irradiated at 625°C and 3×10^{-3} dpa/s.

The Fokker-Planck Description of Cavity Evolution

The concentration of clusters containing h helium atoms and v vacancies at time t is given by

$$C(h,v,t)dhdv = C_{tot}(t)P(h,v,t)dhdv \quad , \tag{15}$$

where $P(h,v,t)dhdv$ is the probability of finding a cluster in the size interval $(h,v \rightarrow h+dh, v+dv)$. The time evolution of the probability function in terms of all possible transitions in the HV phase space is given by the master equation

$$\frac{dP(h,v,t)}{dt} = \sum_k W[[(h - \Delta h_k),(v - \Delta v_k)] \rightarrow (h,v)]P[(h - \Delta h_k),(v - \Delta v_k),t]$$

$$- \sum_k W\{(h,v) \rightarrow [(h + \Delta h_k),(v + \Delta v_k)]\}P(h,v,t) \quad . \tag{16}$$

Here Δh_k and Δv_k are fluctuations in the helium and vacancy contents, respectively, which are caused by a stochastic process, k. We have shown that when the transition probability, W, and the cluster probability density, P, are both expanded around the point (h,v), one obtains the 2-D Fokker-Planck equation given by

$$\frac{\partial P}{\partial t} + \vec{\nabla} \cdot \vec{J} = 0 \quad , \tag{17}$$

where

$$\vec{J} = \vec{F}P - \vec{\nabla}(\vec{\vec{D}}P) \quad , \tag{18}$$

$$\vec{F} = \begin{bmatrix} a_{1h} \\ a_{1v} \end{bmatrix} \tag{19}$$

is a drift vector and

$$\vec{\vec{D}} = \begin{bmatrix} a_{2hv} & a_{2hh} \\ a_{2vv} & a_{2vh} \end{bmatrix} \tag{20}$$

is a diffusion tensor. The components in eqs. (19) and ('LO) represent first and second moments of the transition probability. Details of the derivation of eqs. (17)-(20) can be found in ref. 20. It is noted, however, that while cascade-induced fluctuations do not affect the magnitude of the first moments (a_{1h} and a_{1v}), they increase the magnitudes of the second moments (a_{2hh} and a_{2hv}). This can be seen by referring back to fig. 3.

Numerical solution of eq. (17) on an infinite quarter phase plane is given in ref. 20. In this paper, a two-moment solution is presented for simplicity. Under these conditions, the rates of helium (k^{gc}), vacancy (k^{vc}), and interstitial (k^{ic}) capture, helium replacement (k^{gr}), and vacancy emission (k^{ve}) can be used to compute the elements of $\vec{F}$ and $\vec{D}$. These are given by

$$a_{1h} = k^{gc} - (k^{ge} + k^{gr}) \quad , \tag{21}$$

$$a_{1v} = k^{vc} - (k^{ic+ve} + k^{gr}) \quad , \tag{22}$$

$$a_{2hh} = \frac{1}{2}\left[k^{ge} + k^{gr} + k^{gc}\right] \quad , \tag{23}$$

$$a_{2vv} = \frac{1}{2}\left[k^{ic+ve} + k^{gr} + k^{vc}\right] \quad , \tag{24}$$

$$a_{2hv} = a_{2vh} = k^{gr} \quad . \tag{25}$$

Approximate Two-Moment Solution to the Fokker-Planck Eauation

The Fokker-Planck equation (eq. (17)) must be solved for the evolution of the probability density, P, in order to determine the nature of the evolving HV clusters. A numerical solution, which is coupled with the transient nucleation condition (eq. (13)), has been developed by Sharafat and Ghoniem [20] for eq. (17). Denoting the cluster size by the vector $\vec{x}$, such that

$$\vec{x} = h\vec{i} + v\vec{j} \quad , \tag{26}$$

and taking the first moment of eq. (17), we obtain

$$\frac{d\langle\vec{x}\rangle}{dt} = \langle\vec{F}(\vec{x})\rangle \quad , \tag{27}$$

where the right-hand side represents the drift vector averaged over the probability distribution function. The symbol $\langle\ \rangle$ is used to denote this average. Eq. (27) is not a closed equation because of the non-linearity of $\vec{F}$. Howeuer, to lowest order, one can approximate this equation by

$$\frac{d\langle\vec{x}\rangle}{dt} = \vec{F}(\langle\vec{x}\rangle) \quad . \tag{28}$$

The integration of eq. (28) gives the trajectory of the average cluster in the growth regime of the flow field shown in fig. 3.

Let us define the variance matrix by

$$\langle\delta X_i \delta X_j\rangle = \langle X_i X_j\rangle - \langle X_i\rangle\langle X_j\rangle \quad , \quad i,j = h,v \quad . \tag{29}$$

Kinetic equations for the variance matrix can be shown to be given by [17]:

$$\frac{d}{dt}\langle\delta X_i \delta X_j\rangle = \langle X_i a_{ij}\rangle - \langle X_i\rangle\langle a_{ij}\rangle + \langle X_j a_{1i}\rangle - \langle X_j\rangle\langle a_{1i}\rangle + \langle a_{2,ij}\rangle \quad . \tag{30}$$

Eq. (30) is again not closed, and expansions of the parameters around their values at the average trajectory, $\langle\vec{x}\rangle$, would result in an open-ended set of moment equations. Although it is possible to develop coupled equations for higher order moments (see ref. 22), it is sufficient here to develop a lowest order expansion of eq. (30):

$$\frac{d}{dt}\langle\delta X_i \delta X_j\rangle = a_{2,ij}(\langle\vec{x}\rangle) \quad . \tag{31}$$

Eq. (31) is the lowest order evolution equation for the variance matrix. The second moments of the transition probabilities, $a_{2,ij}$, are the components of the diffusion tensor (eq. (20)), and are to be evaluated at the average trajectory, $\vec{x}$.

We will proceed here by reconstructing the probability density function from its zeroth, first, and second moments. The simplest reconstruction procedure can be based on Gaussian functions, i.e.,

$$P(h,v,t) \simeq (\delta X_h \delta X_v \sqrt{2\pi})^{-1} \exp(-y^2/2) \quad , \tag{32}$$

where

$$y = \sqrt{\left(\frac{h - \langle h \rangle}{\delta X_h}\right)^2 + \left(\frac{v - \langle v \rangle}{\delta X_v}\right)^2} \tag{33}$$

The Effects of Helium and Collision Cascades on Cavity Evolution

The formulation presented in the previous section permits study of the effects of simultaneous helium generation and cascade-induced point-defect fluctuations on cavity evolution. This is certainly useful for extrapolating existing radiation damage data to anticipated fusion conditions where the primary differences in damage parameters are the helium generation rate and the cascade size. Fig. 5 illustrates the propagation of the probability distribution function in size space under typical HFIR and EBR-11-type irradiation conditions for stainless steel at 500°C. The He-to-dpa ratio plays an important role in determining the character of the distribution function. Both the HFIR and EBR-II reactors have similar displacement damage rates of $\sim 10^{-6}$ dpa/s, but differ in the He-to-dpa ratio (i.e., 57 for HFIR and 0.1 for EBR-II). The effects of this large difference between the ratios on the spread of the size distribution can be seen clearly in fig. 5. The low He-to-dpa ratio, characteristic of EBR-II, results in a smaller spread in helium content, and helium plays a small role in cavity evolution. (Notice the different scales between figs. 5a and 5b.) In both cases, however, most of the cavities are not in thermodynamic equilibrium where the gas pressure is balanced by surface tension force [20].

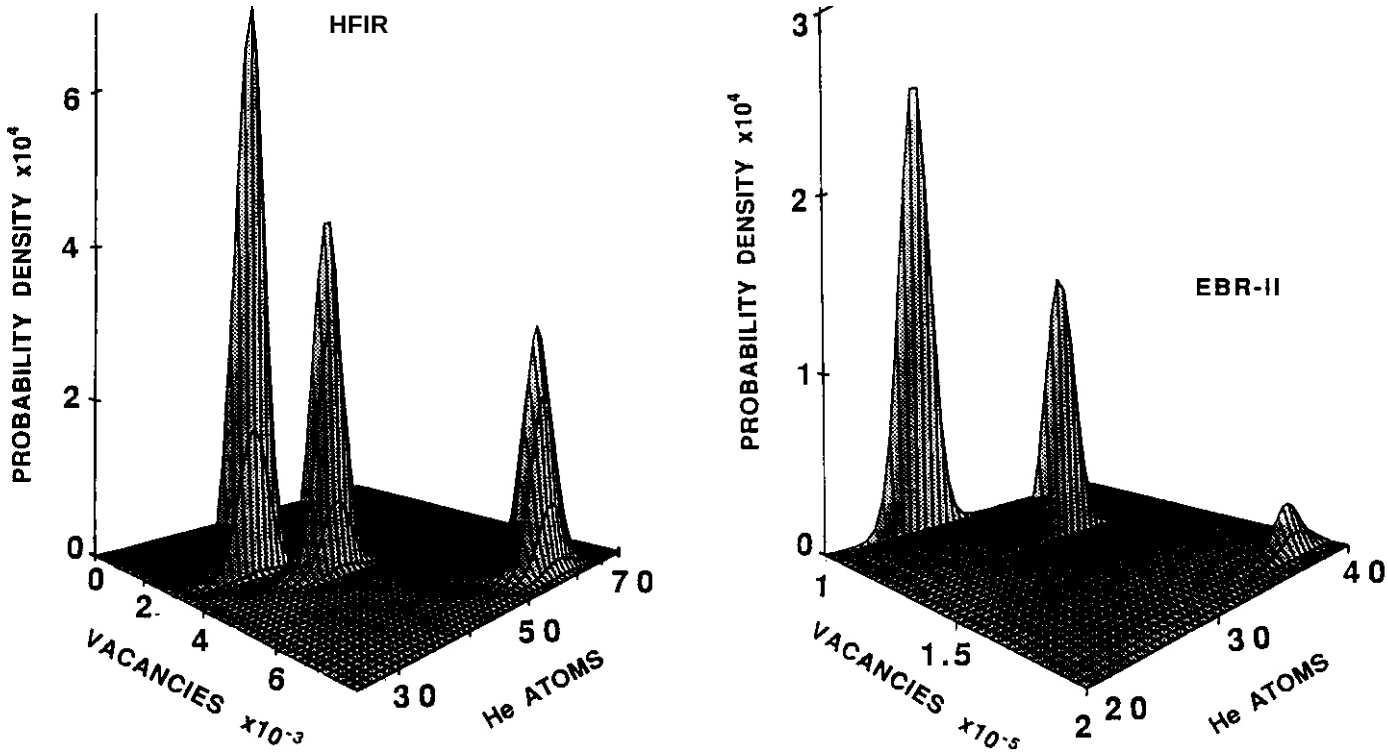

Fig. 5. Probability distribution function for HV clusters under irradiation of stainless steel at 500°C.

Cascade effects on the cavity size distribution are included through the second moments of the transition probabilities in the Fokker-Planck equation. Cascades induce fluctuations in point-defect concentrations, as previously shown in fig. 2. Since the RMS value of the fluctuation depends on the cascade size, we must determine a spectrally averaged value for the variances δX_h and δX_v. We will treat this problem parametrically here, where we assume that cascades do not change the value of δX_h but simply increase δX_v. Fig. 6 shows the anticipated effects of cascades on the spread of the same size distribution as shown for HFIR conditions in fig. 5. Cascades were assumed to result in a fourfold increase in the magnitude of δX_v. The point to be made here is that a "broad" size distribution is indicative of an important effect of cascades. Without a systematic experimental/theoretical study, it is difficult to be more quantitative about the effects of cascades on cavity evolution.

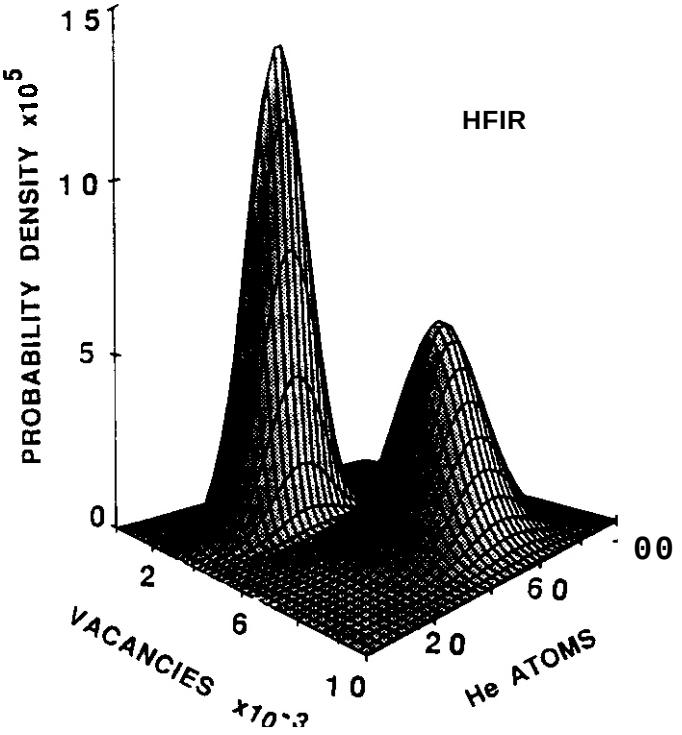

Fig. 6. The effects of a fourfold increase in the point-defect fluctuation amplitude on the probability distribution function for HV clusters under irradiation of stainless steel at 500°C.

Conclusions

Cavity evolution under conditions of cascade damage and high helium generation, which are typical of fusion reactor conditions, is shown to be a continuous process which cannot be easily separated into the classical nucleation and growth regimes. It is also emphasized that the rate of helium transport, which is described as an effective helium mobility, has a strong dependence on HV-cluster evolution. The long transient, associated with high helium mobility, is a result of the concentration build-up of small HV clusters which act as the primary traps for migrating helium. However, the quasi steady-state mobility can be understood in terms of three simple mechanisms: radiation displacement at low temperatures, interstitial replacement at intermediate temperatures, and thermal desorption at high temperatures.

The displacement of helium by cascades from HV clusters results in significant effects on cavity evolution. First, this displacement process provides for an internal source of helium production which, in turn, causes continuous cavity nucleation. Second, the resulting fine distribution of helium nuclei in the matrix is associated with slower growth rates for helium-filled cavities.

The stochastic framework represented by Fokker-Planck theory is shown to be a convenient approach to the analysis of cavity evolution under fusion and simulation conditions. Although the major features of cavity evolution are included in this framework, its utility can be fully exploited by a systematic experimental approach where the basic parameters of the model can be clearly determined.

Acknowledgments

This work was supported by the U. S. Department of Energy, Office of Fusion Energy, Grant No. DE-FG03 84ER52110, with UCLA. The author wishes to acknowledge Drs. B. Singh, M. Victoria, and W. V. Green, for their efforts on behalf of the Workshop on Radiation Damage Correlation for Fusion Conditions.

References

[1] J. L. Katz and H. Wiedersich, J. Chem. Phys. 55 (1971) 1414.
[2] K. C. Russell, Acta Metall. 19 (1971) 753.
[3] G. W. Greenwood, J. Nucl. Mater. 4 (1959) 305.
[4] H. Trinkaus, J. Nucl. Mater. 118 (1983) 39.
[5] H. Trinkaus, Radiat. Eff. 101 (1986) 91.
[6] A. D. Brailsford and R. Bullouqh, J. Nucl. Mater. 48 (1973) 87.
[7] R. Bullough, B. Eyre and K. Krishan, Philos. Trans. R. Soc. London. Ser. A346 (1975) 81.
[8] W. F. Wolfer and M. Ashkin, J. Appl. Phys. 46 (1975) 547.
[9] L. K. Mansur. Nucl. Technol. 40 (1978) 5.
[10] N. M. Ghoniem and G. L. Kulcinski, Radiat. Eff. 39 (1978) 47.
[11] K. Krishan, Radiat. Eff. 66 (1982) 121.
[12] N. M. Ghoniem, J. Alhajji and D. Kaletta, J. Nucl. Mater. 136 (1985) 192.
[13] N. M. Ghoniem, S. Sharafat, J. M. Williams, and L. K. Mansur, J. Nucl. Mater. 117 (1983) 96.
[14] A. Forman and 8. Singh, J. Nucl. Mater. 141-143 (1986) 672.
[15] K. C. Russell, Acta Metall. 26 (1978) 1615.

[16] L. K. Mansur, W. A. Coghlan and A. D. Erailsford, J. Nucl. Mater. 85 & 86 (1979) 591.
[17] A. O. Marwick, J. Nucl. Mater. 116 (1983) 40.
[18] P. Chou and N. M. Ghoniem, J. Nucl. Mater. 137 (1985) 63.
[19] G. Ayrault, H. A. Hoff, F. V. Nolfi, Jr. and A. P. L. Turner, J. Nucl. Mater. 103 & 104 (1981) 1035.
[20] S. Sharafat and N. M. Ghoniem, "Non-Equilibrium Agglomeration of helium-Vacancy Clusters in Irradiated Materials," Radiat. Eff. and Def. in Solids, to be published 1990.
[21] G. Nicolis and I. Prigogine, Self-Organization in Non-Equilibrium Systems (John Wiley and Sons, New York, 1977) p. 254.
[22] N. M. Ghoniem, Phys. Rev. E39 (1989) 11810.

Appendix A

Notation	Variable
f	Fraction of point defects surviving in-cascade recombination
G	Displacement damage rate
$C_s^{v,i}$	Equivalent matrix distributed point-defect sink density (i.e., for dislocations. cavities. and grain boundaries)
G_H	Helium generation rate
m	Average number of helium atoms in a cavity
C_{tot}	Total cavity density
Mg_b	Helium concentration at grain boundaries
M_{ppt}	Helium concentration at precipitate interfaces
ϵ	Matrix cavity combinatorial number
ϵ_{ppt}	Precipitate cavity combinatorial number
C_{ppt}	Precipitate concentration
C_{gb}	Equivalent distributed sink for grain boundaries

FUTURE WORK

The theory will be further developed to investigate helium and hydrogen cavity formation in SiC composites. The importance of coalescence mechanisms and helium diffusion to matrix/fiber interface will be emphasized.

ISOTOPIC TAILORING WITH ^{59}Ni TO STUDY THE INFLUENCE OF HELIUM/DPA RATIO ON TENSILE PROPERTY CHANGES

F. A. Garner and M. L. Hamilton, Pacific Northwest Laboratory;(a) R. L. Simons, Westinghouse Hanford Company; M. K. Maxon, Northwest College and University Association for Science, Washington State University

OBJECTIVE

The object of this effort is to study the separate and interactive effects of helium and other important variables on evolution of microstructure and macroscopic properties during irradiation of structural metals.

SUMMARY

Irradiation of miniature tensile specimens of simple model Fe-Cr-Ni alloys is proceeding in the Fast Flux Test Facility to study the interactive effects of alloy composition, cold work level, helium/dpa ratio and irradiation temperature on the evolution of microstructure and associated changes in mechanical properties. The addition of ^{59}Ni to these alloys allows side-by-side irradiation of otherwise identical specimens, differing only in helium/dpa ratio. In the absence of differences in displacement rate and temperature history, it is shown that helium in this experiment exerts a rather small influence on tensile properties at 365 and 600°C. While the saturation level of yield stress in Fe-25Ni-15Cr is strongly dependent on irradiation temperature, it is relatively insensitive to cold work level and helium/dpa ratio. At 365°C, the yield strength of Fe-25Ni-15Cr is increased slightly by addition of 0.04 wt% phosphorus.

PROGRESS AND STATUS

Introduction

In a recent review article it was demonstrated that some important early perceptions of the radiation damage community, concerning the influence of neutron spectra on microstructural evolution and its associated changes in mechanical properties, needed significant revision in light of recent insights.[1] Fission-fusion correlation experiments directed toward the influence of helium/dpa ratio and PKA recoil spectra were often difficult to interpret due to the strong influences of displacement rate, temperature history, low energy recoils from softer components of neutron spectra and, in some cases, solid transmutants. It was also shown that materials data published in earlier decades concerning the effects of helium must be reevaluated in light of recent advances in defining and controlling irradiation parameters. In the case of helium effects on mechanical properties, such reevaluation can lead to reversal of the original conclusions.[1,2]

Until recently it has been impossible to conduct experiments in which spectral-related parameters were varied without also accepting variations in important parameters such as displacement rate and temperature history. However, a technique currently being used allows the study of the influence of helium alone on density change, microstructural evolution and mechanical properties. This technique utilizes isotopic tailoring to vary the helium production rate without introducing changes in neutron spectrum or displacement rate.[3,4] By producing alloys whose only difference is the presence or absence of ^{59}Ni, an isotope which does not occur naturally, and irradiating doped and undoped specimens side-by-side in the appropriate reactor spectra, it is possible to generate substantial variations in He/dpa ratio without varying any other important parameter.

A particular advantage of isotopic doping experiments is that one need not be concerned with the details of temperature history, now known to influence heavily the outcome of some fission-fusion correlation experiments.[1] Since both doped and undoped specimens are irradiated side-by-side, the primary variable is still that of helium/dpa ratio only. The production rate of helium is also nearly constant throughout the experiment.

This report addresses a limited subset of tensile specimens irradiated in a larger experiment currently being conducted in the Fast Flux Test Facility (FFTF) utilizing the Materials Open Test Assembly (MOTA).[5]

Experimental Details

The alloys employed in this study were nominally Fe-15Cr-25Ni, Fe-15Cr-25Ni-0.04P and Fe-15Cr-45Ni (wt%) in both the cold worked and annealed conditions. The experimental matrix is shown in Figure 1. These alloys were chosen to complement those in several earlier studies, one in the Experimental Breeder Reactor-II (EBR-II), designated the AD-I experiment,[6] and another conducted in the Oak Ridge Research (ORR) Reactor, designated MFE-4.[7] The acquisition of the ^{59}Ni, the production of the ^{59}Ni-doped tensile specimens and their

(a) Pacific Northwest Laboratory is operated for the U.S. Department of Energy by Battelle Memorial Institute under Contract DE-AC06-76RLO 1830.

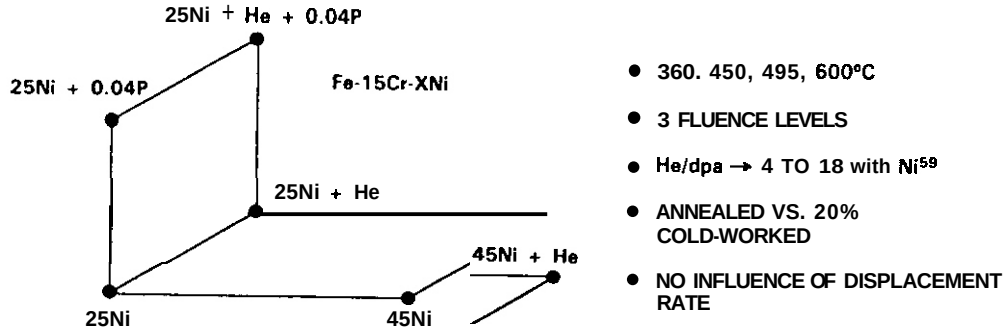

Figure 1. Schematic Representation of the ^{59}Ni Isotopic Tailoring Experiment

irradiation conditions are described in Reference 3. Microscopy disks were also prepared and irradiated; the results of the examination of these specimens are described in detail in References 8 and 9. The miniature tensile specimens measured 5.1, 1.0 mm and 0.25 mm in gauge length, width and thickness, respectively. They were tested at room temperature at a strain rate of 4.7×10^{-4} sec^{-1} in a horizontal test frame described in Reference 10. Yield strengths were determined at 0.2% offset.

This report will describe only the results of irradiations conducted at 365°C to 6.1 dpa and at 600°C to 8.7 dpa. Testing of specimens irradiated at other temperatures and dpa levels is still in progress. Irradiation proceeded in the FFTF/MOTA with active temperature control to ±5°C, with one varying but upward excursion, reaching a maximum of ~200°C for ≤50 minutes for the 600°C irradiation. While the impact of the excursion is difficult to assess, it was the same for both doped and undoped specimens.

Some specimens were sacrificed to make measurements of the accumulated helium by mass spectrometry, conducted by B. Oliver of Rockwell International. The helium levels attained in the doped specimens were somewhat lower than originally anticipated, reflecting some uncertainty in the softer components of the neutron spectrum. The helium levels measured in the ^{59}Ni-doped specimens were still representative of the intermediate helium/dpa ratios expected in fusion-relevant neutron spectra, however.

Results

Three tensile tests were conducted for each undoped alloy in both the cold worked and the annealed conditions. Since the availability of doped specimens was rather limited, only one was tested for each combination of doped alloy and thermomechanical starting condition. Figure 2 shows that the range of yield strengths in the undoped specimens is not large and that the single doped specimen in each condition did not exhibit any significant difference in behavior. Also shown in Figure 2 are the yield strengths exhibifed by the larger unirradiated specimens of the annealed alloys irradiated in the AD-1 and MFE-4 experiments, demonstrating excellent agreement among the three experiments.

Figures 3 and 4 show comparisons of the results of tensile tests conducted on both irradiated and unirradiated specimens. Only one irradiated specimen was available at each condition. Note that the differences observed between specimens with and without ^{59}Ni are usually very small, on the order of the variability observed in the unirradiated specimens. The only case where the helium-induced change may be larger than the variability is in the annealed phosphorus-free alloy at 365°C. There also appears to be a tendency for the irradiated strengths of the single doped specimens to be just above that of the single undoped specimens, indicating the possibility that some small increment of the strengthening may be related to the extra helium. There is only one specimen at each condition, however, and this possibility cannot be confirmed.

The data generated using unirradiated miniature specimens in this experiment upholds the claim that the yield strength determined from miniature specimens is representative of similar data from larger specimens, while the ultimate strength and ductility may not be representative. Relative property values for a given specimen type can provide, however, some insight as to the relative effects of experimental variables.

Annealed specimens in the unirradiated condition exhibit elongations of ~30 and ~40% for the Fe-15Cr-25Ni and Fe-15Cr-25Ni-0.04P alloys, respectively, and ~1% for both alloys in the cold worked condition. Irradiation reduces the elongation to ~0.5% at 365% and ~20% at 600°C, with no obvious dependence on either cold work level or helium content.

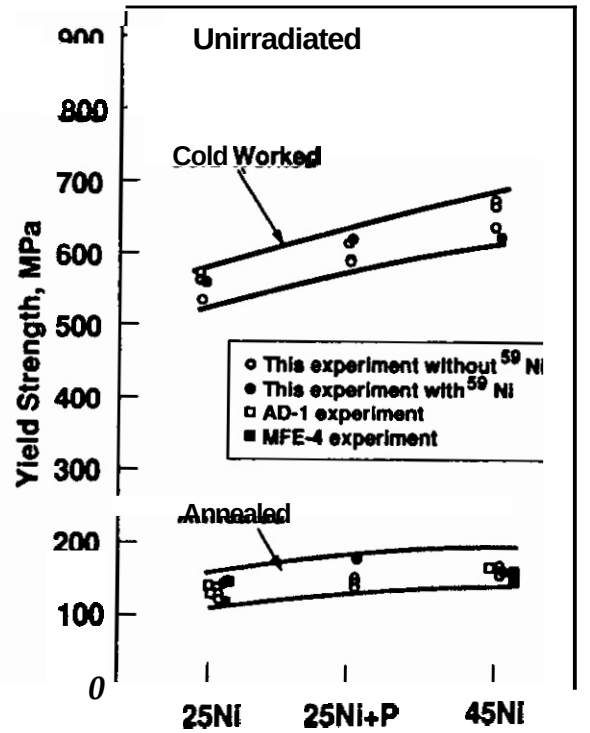

Figure 2. Compilation of Yield Strength Data on Unirradiated Specimens in the ^{59}Ni Isotopic Tailoring Experiment in FFTF-MOTA and Also Several Related Experiments Conducted in Other Reactors

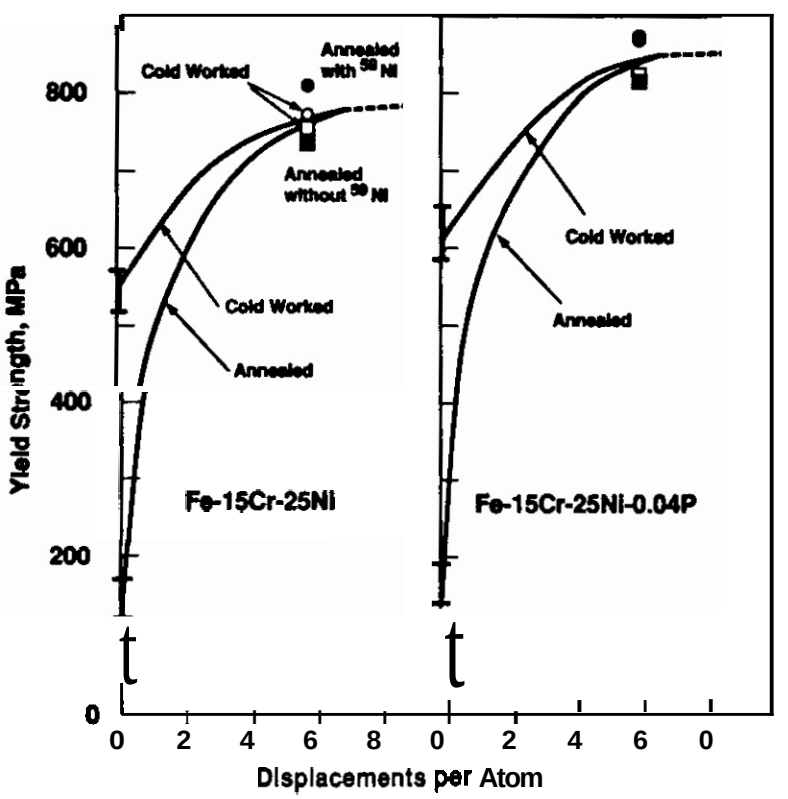

Figure 3. Influence of Phosphorus, Thermomechanical Starting State and He/dpa Ratio on Yield Strength Changes of Irradiated Fe-15Cr-25Ni at 365°C and 6.1 dpa (He/dpa ratios of 0.3 and 13.9).

Discussion

It is obvious that irradiation at 365°C leads to large increases in strength for both the annealed and cold worked conditions of Fe-15Cr-25Ni and Fe-15Cr-25Ni-0.04P. As shown in Figure 3, saturation appears to be occurring with the saturation levels of both alloys independent of the starting state, with cold worked and annealed steels converging within 6.1 dpa. Phosphorus additions increase the strength of both unirradiated and irradiated alloys, although the strengthening increment is somewhat larger for the irradiated condition.

Figure 4 shows that convergence of the yield strength of annealed and cold worked Fe-15Cr-25Ni also appears to be occurring during irradiation at 600°C, but at a level intermediate to the two original starting states, reflecting a net softening of the cold worked alloy. Once again, the difference between the presence or absence of ^{59}Ni is very small compared to the scatter observed in the data obtained using unirradiated specimens.

The convergence of strength at a level dependent on irradiation temperature but not starting state is consistent with the results of earlier studies on *316* stainless steel" and arises primarily from a convergence of dislocation and loop microstructure,[11-13] which is also known to be independent of helium/dpa ratio at sufficiently high displacement levels.[13] Kawanishi, Garner and Simons[3] and Stubbins and Garner[8] confirm that the large difference in initial dislocation density indeed disappears in these experiments, although at 600°C there is still a sufficiently large difference in both network and loop densities to account for the residual difference in strength seen at 600°C and 8.7 dpa. 'Phosphide precipitates form in both the annealed and cold worked conditions at 600°C and contribute to the strengthening.[9]

Kawanishi et. al.[3] notes that no phosphide precipitates occur at 365°C and Stubbins and Garner' note that a similar situation occurs at 495°C, in agreement with another study conducted by Muroga, Garner and McCarthy on a larger series of phosphorus-modified Fe-15Cr-25Ni alloys irradiated in EBR-II at eight different temperatures." The role of phosphorus in strengthening of irradiated alloys in the absence of precipitation lies in its ability to influence the evolution of dislocation, loop and void microstructure while in solution, in agreement with the results of other studies.[14-18] The major conclusion of microscopy studies[8,9] conducted on these three alloys is that helium can influence the details of the microstructure somewhat, sometimes increasing or decreasing the densities of each component at a given fluence level and alloy condition, but the net macroscopic effect is small, not only on void swelling but also on other macroscopic properties such as yield strength.

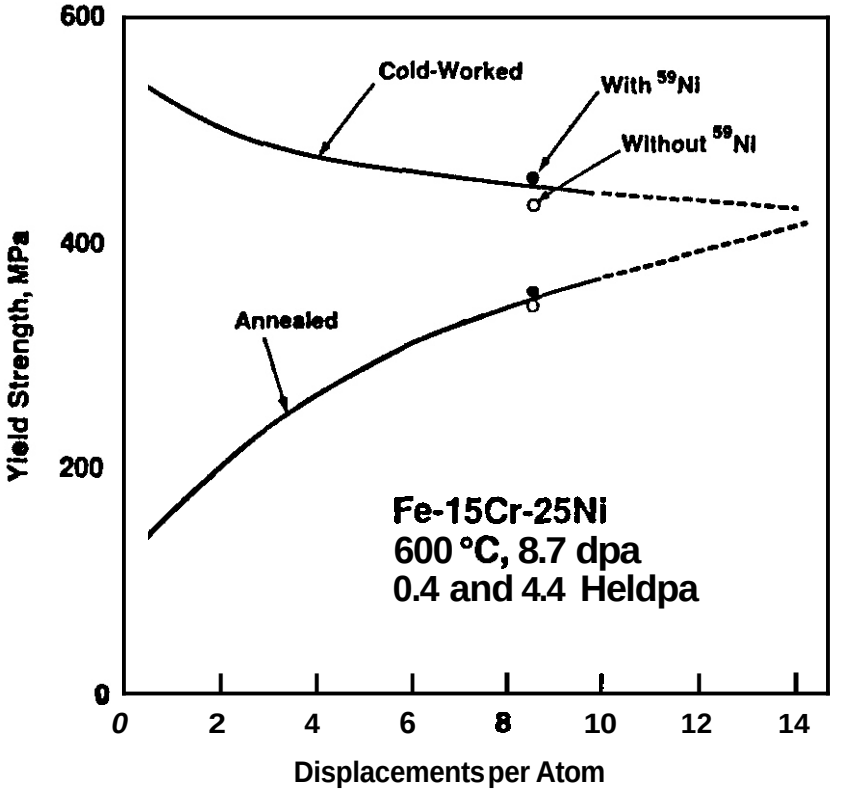

Figure 4. Influence of Thermomechanical Starting State and He/dpa Ratio on Yield Strength Changes of Irradiated Fe-15Cr-25Ni at 600°C and 8.7 dpa.

In the MFE-4 and AD-1 experiments on which the ^{59}Ni experiment was based, it was noted that a significantly higher level of strengthening occurred in the MFE-4 experiment for all compositions and irradiation temperatures studied. The MFE-4 experiment was conducted to somewhat higher dose levels, however, and proceeded at an order of magnitude lower displacement rate. It appears from the results of the present study that differences in these parameters may have determined the differences in tensile behavior much more than differences in helium/dpa ratio.

CONCLUSIONS

When the effect of helium production rate on microstructure and tensile properties of simple model Fe-Cr-Ni alloys is studied at levels relevant to both fast reactor and fusion reactor applications, it appears that helium sometimes exerts only a second order influence, and its effect can be easily overwhelmed by differences in variables such as displacement rate and temperature history.

REFERENCES

1. F. A. Garner, H. L. Heinisch, R. L. Simons and F. M. Mann, "Implications of Neutron Spectrum and Flux Differences on Fission-Fusion Correlations at High Neutron Fluence," Radiation Effects and Defects in Solids, 1990, in press.

2. F. A. Garner, "New Developments in Fusion Materials Research Using Surrogate Neutron Spectra," elsewhere in this semiannual report.

3. R. L. Simons, H. R. Brager and W. Y. Matsumoto, J. Nucl. Mater. 141-143 (1986) 1057-1060.

4. G. R. Odette, J. Nucl. Mater. 141-143 (1986) 1011-1017.

5. M. Kiritani, J. Nucl. Mater. 160 (1988) 135-141.

6. H. R. Brager, F. A. Garner and M. L. Hamilton, J. Nucl. Mater. 133 & 134 (1985) 594-598.

7. M. L. Hamilton, A. Okada and F. A. Garner, "Tensile Behavior and Swelling of Ternary Austenitic Alloys Irradiated in Different Neutron Spectra." Proceedings 4th International Conference on Fusion Reactor Materials, Kyoto, Japan, Dec 3-8, 1989.

8. J. F. Stubbins and F. A. Garner, "The Relative Influence of Helium/dpa Ratio and Other Variables on Neutron-Induced Swelling at Fe-Ni-Cr Alloys at 495°C and 14 dpa." Proceedings 4th International Conference on Fusion Reactor Materials, Kyoto, Japan, Dec 3-8, 1989.

9. H. Kawanishi, F. A. Garner and R. L. Simons, "Synergistic Effects of Helium and Other Variables on Microstructure Change in Neutron-Irradiated Fe-Ni-Cr Alloys Doped with Nickel-59." Proceedings 4th International Conference on Fusion Reactor Materials, Kyoto, Japan, Dec 3-8, 1989.

10. N. F. Panayotou, S. D. Atkin, R. J. Puigh and B. A. Chin, The Use of Small-Scale Specimens for Testing Irradiated Material, ASTM STP 888, W. R. Comin and G. E. Lucas, Eds., American Society for Testing and Materials, Philadelphia, 1986, 201-219.

11. F. A. Garner, M. L. Hamilton, N. F. Panayotou and G. D. Johnson, J. Nucl. Mater. 103 & 104 (1981) 803-808.

12. H. R. Brager, F. A. Garner, E. R. Gilbert, J. E. Flinn and W. G. Wolfer, in: Radiation Effects in Breeder REactor Structural Materials, M. L. Bleiberg and J. W. Bennett, Eds., The Metals Society of AIME, New York, 1977, 727-755.

13. F. A. Garner and W. G. Wolfer, in: Effects of Radiation on Materials: Eleventh Conference, ASTM STP 782, H. R. Brager and J. S. Perrin, Eds., American Society for Testing and Materials, 1982, 1073-1087.

14. T. Muroga, F. A. Garner and J. M. McCarthy, J. Nucl. Mater. 168 (1989) 109-120.

15. F. A. Garner and H. R. Brager, J. Nucl. Mater. 133 & 134 (1985) 511-514.

16. F. A. Garner and A. S. Kumar in Radiation-Induced Changes in Microstructure: 13th International Symposium (Part I) ASTM STP 955, F. A. Garner, N. H. Packan and A. S. Kumar, Eds., American Society for Testing and Materials, Philadelphia, 1987, 289-314.

17. M. Itoh, S. Onose and S. Yuhara, in Reference **16,** 114-126.

18. **H.** Watanabe, A. Aoki, **H.** Murakami, T. Muroga and N. Yoshida, J. Nucl. Mater. 155-157 (1988) 815-822.

FUTURE WORK

This effort will continue, utilizing specimens irradiated to higher neutron exposures.

ACKNOWLEDGMENTS

This work was supported by the U.S. Department of Energy under Contract DE-AC06-76RLO 1830. The participation of M. Maxson was supported by the Northwest College and University Association for Science (Washington State University) under U.S. DOE Contract DE-AM-06-76-RLO 2225.

THE EFFECT OF HELIUM ON MICROSTRUCTURAL EVOLUTION IN AUSTENITIC STEELS AS DETERMINED BY SPECTRAL TAILORING EXPERIMENTS - N. Sekimura, University of Tokyo, F. A. Garner, Pacific Northwest Laboratory,(a) and R. D. Griffin, University of Wisconsin-Madison

OBJECTIVE

The object of this effort is to determine the separate and synergistic effects of helium/dpa ratio and other important environmental and material variables on the swelling, microstructural evolution and tensile properties of austenitic alloys.

SUMMARY

Fe-15Cr-XNi alloys irradiated at both low (0.66 to 1.2) and very high (27 to 58) helium/dpa levels exhibit significantly different levels of strengthening due to an unprecedented refinement of cavity microstructure at the very high helium levels. When compounded with the nickel dependence of helium generation, the cavity distribution for some irradiation conditions and alloy compositions can be driven below the critical radius for bubble to void conversion, leading to a delay in swelling.

PROGRESS AND STATUS

Introduction

A variety of experiments are underway at Pacific Northwest Laboratory to assess the interactive influence of helium generation rate and other important variables on the radiation-induced evolution of both microstructure and mechanical properties of simple metals and Fe-Cr-Ni austenitic alloys. One of these involves a comparison of the response of a series of Fe-15Cr-XNi and Fe-YCr-35Ni alloys in two reactors, EBR-II and ORR.[1]

The AD-l experiment was conducted to doses of 9.5 to 11.3 dpa in EBR-II at the relatively low helium/dpa ratios typical of fast reactors. The ratios range from 0.66 to 1.2 appm/dpa for nickel levels of 25 to 45%. The MFE-4 experiment was conducted in ORR to doses of 12.2 to 14.3 dpa at helium/dpa ratios ranging from 27 to 58 appm/dpa. For a given irradiation temperature the displacement level was independent of nickel content in EBR-II, but this was not the case in ORR, where the $^{58}Ni(n,\alpha)^{59}Ni(n,\alpha)^{56}Fe$ reaction that produces the large helium levels in this reactor also makes a measurable contribution to the displacement rate (see Table 1).

Table 1

Displacement and Helium Levels(a) in the MFE-4 Experiment in ORR

	330 and 400°C		500 and 600°C	
Comoosition. wt%	dpa	He. appm	dpa	He. appm
Fe-19.7Ni-14.7Cr	13.4	371	12.2	332
Fe-24.4Ni-14.9Cr	13.6	463	12.4	414
Fe-30.1Ni-15.1Cr	13.8	555	12.6	495
Fe-34.5Ni-15.1Cr	14.0	647	12.7	573
Fe-45.3Ni-15.0Cr	14.3	832	13.1	740

(a) These values were calculated using dosimetry calculations and measurements provided in Reference 2 for individual elements. Note that the dpa levels increase with nickel content, reflecting the contributions of the ^{56}Fe recoil atom during helium production.

(a) Pacific Northwest Laboratory is operated for the U.S. Department of Energy by Battelle Memorial Institute under Contract DE-AC06-76RLO 1830.

Another significant difference between the two experiments arises from the roughly order of magnitude difference in displacement rate, with MFE-4/ORR proceeding at a lesser rate than AD-1/EBR-II. Microstructural evolution is known to be sensitive to displacement rate, a consideration which complicates the comparison of the results of these two experiments.

Figure 1 compares the swelling behavior of these two experiments, measured using immersion density. Note that while there is no significant amount of swelling for any nickel level at 400°C in ORR at 13.4-14.3 dpa, measurable amounts of swelling were found at only 9.5 dpa in EBR-II at 395°C, with swelling exhibiting the decreasing dependence on nickel content commonly observed in many other experiments. Figure 2 shows another feature of the results of the EBR-II/ORR comparison. Throughout the temperature range studied the radiation-induced changes in yield strength are larger in ORR than in EBR-II.

The microstructural origins of the behavior shown in Figures 1 and 2 are being sought using transmission electron microscopy. Although the microscopy has been finished, the analysis of the micrographs is still in progress.

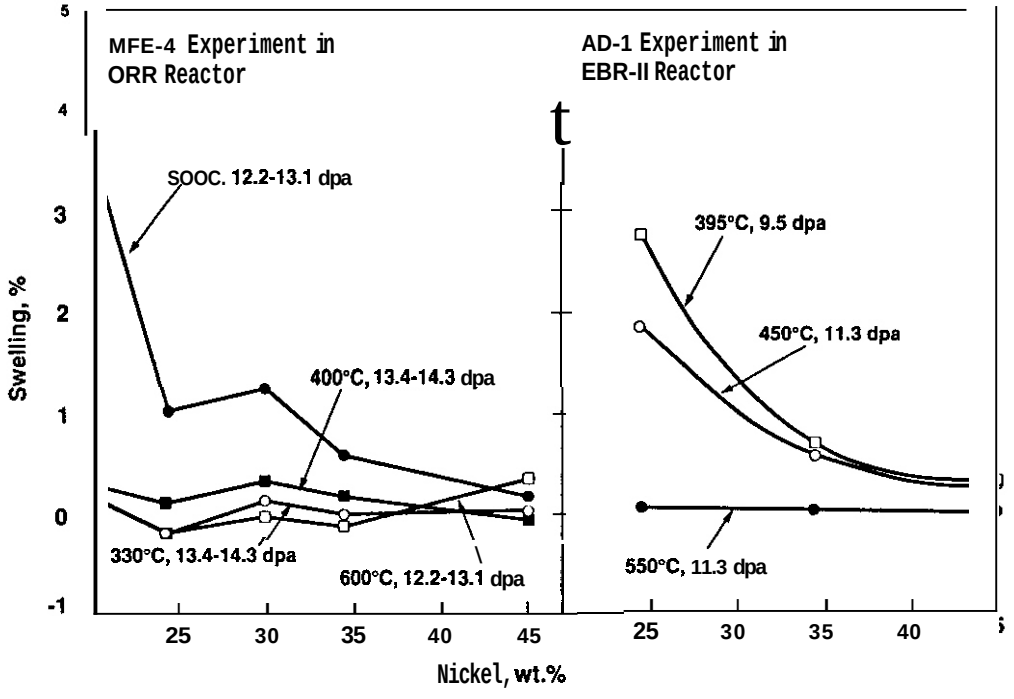

FIGURE 1. Comparison of Swelling Behavior in Fe-15Cr-XNi Alloys in Two Different Reactors'

Results

The analysis effort has concentrated first on Fe-15Cr-XNi irradiations conducted at 400 and 500°C in ORR and at 395 and 450°C in EBR-II. The EBR-II data at 450°C were reported in an earlier paper.[3] A comparison is shown in Figure 3 of the swelling in ORR as determined by both immersion density and microscopy, showing relatively good agreement. No precipitates were observed in any alloy. As can be seen in Figure 4 the major difference between the two sets of irradiations is reflected in the cavity density. Whereas the EBR-II cavity densities exhibit the usual trends, decreasing both with irradiation temperature and nickel content, the densities reached in ORR not only increase with nickel content but reach levels that are two to three orders of magnitude larger than in EBR-II. At 400°C cavity densities in excess of 10^{17} cm^{-3} are some of the largest ever observed in reactor irradiation studies. The cavity densities at 400°C are clearly saturating at levels that increase with nickel, but they are not as sensitive to nickel content as was observed at 500%. In contrast to the behavior observed at 500°C, the cavity sizes at 400°C increase with nickel content as do those at 330°C. as shown in Figure 5. Note that the cavity sizes for the most part do not change significantly between 330 and 400°C.

The width of the size distribution of the voids in the ORR experiment at 500°C was observed to become progressively smaller as the nickel content increased, as shown in Figure 6. This contrasts with the behavior observed in EBR-II, where voids are in general larger but whose sizes are relatively independent of nickel content at a given irradiation temperature.

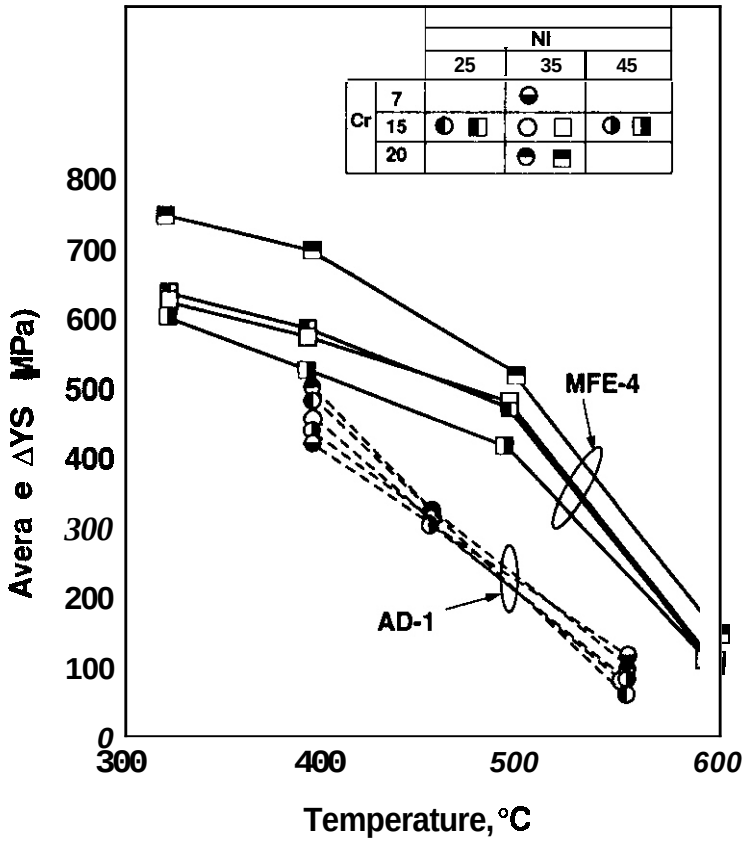

FIGURE 2. Comparison of Radiation-Induced Changes in Yield Strengths of Fe-15Cr-XNi and Fe-YCr-35Ni Alloys Irradiated in the AD-1 Experiment in EBR-II and the MFE-4 Experiment in ORR'

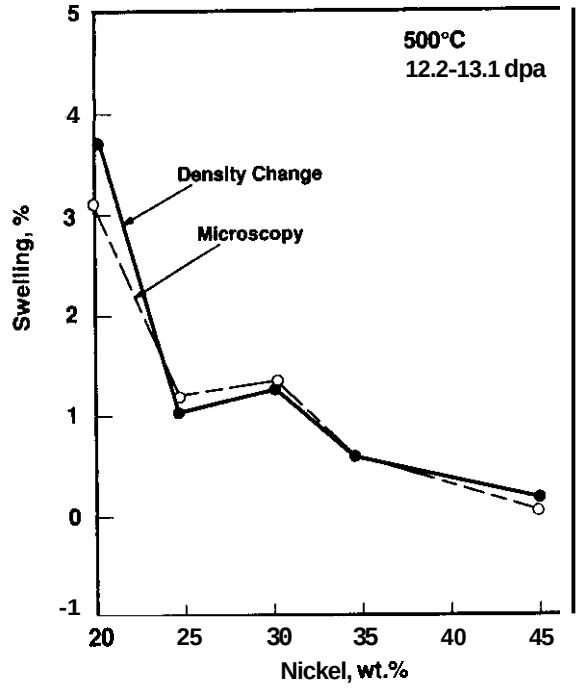

FIGURE 3. Excellent Agreement Between Two Different Measurements of Swelling Observed in Fe-15Cr-XNi Alloys Irradiated in ORR

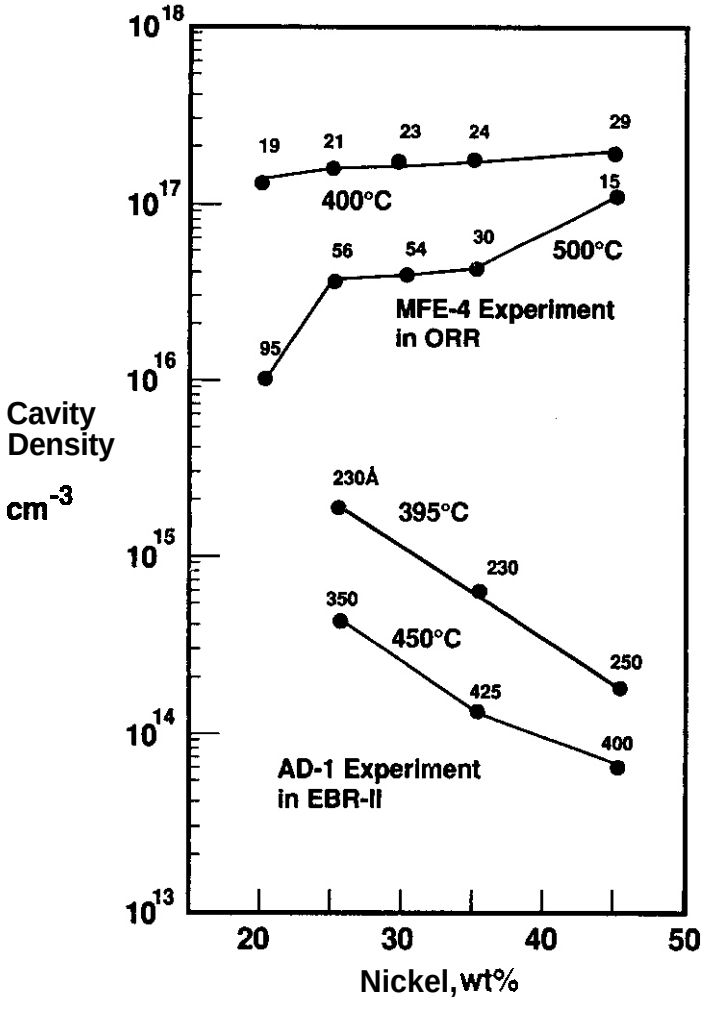

FIGURE 4. Void Densities Observed in the Fe-15Cr-XNi Allays Irradiated in EBR-II and ORR. Voids sizes in A are included in parentheses.

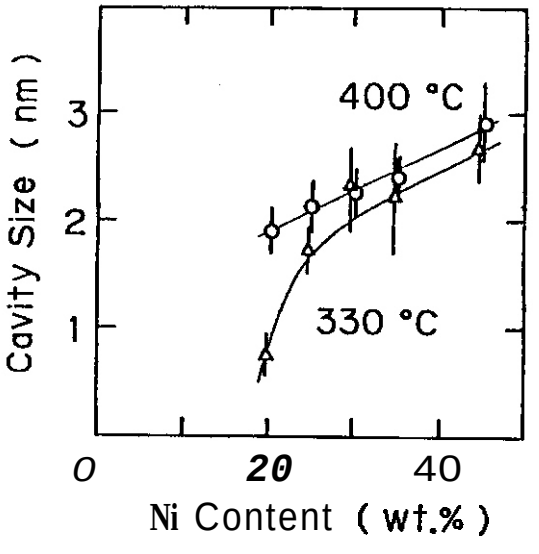

FIGURE 5. Cavity Sizes Observed in Fe-15Cr-XNi Alloys Irradiated in ORR at 330 and 400°C

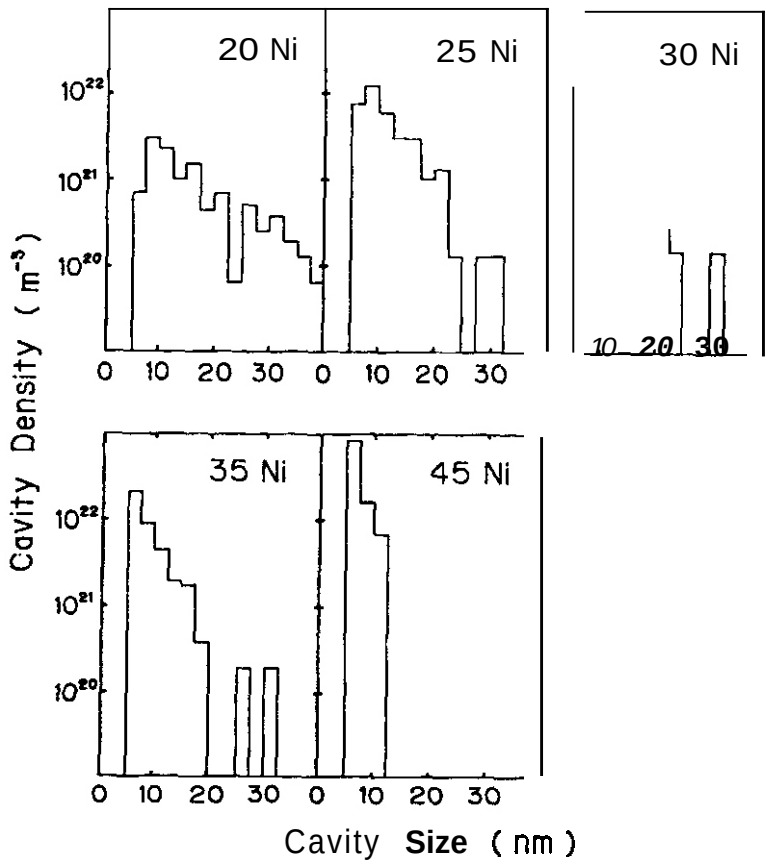

FIGURE 6. Cavity Size Distributions Observed in Fe-15Cr-XNi Alloys Irradiated in ORR at 500°C

Although the data are still being analyzed, it appears that there is some refinement of the dislocation loop microstructure in the higher helium experiment but that the degree of refinement is much smaller, on the order of a factor of two or three in the loop density.

Discussion

In the range 400-500°C the swelling in EBR-II is known to exhibit a transient regime of ~10 dpa prior to swelling at a rate of ~1%/dpa.[4] If this trend also pertains to swelling at the lower displacement rate of ORR then these alloys would have accumulated 280-580 appm helium prior to reaching the 10 dpa level. The large decrease in swelling at 400°C at all nickel levels relative to that of EBR-II may reflect the impact of the very large and almost unprecedented density of cavities.

The swelling in ORR at 500°C increases with declining nickel content as the void density decreases from the 10^{17} to the 10^{16} cm^{-3} level, but at this temperature in EBR-II it is expected that swelling would also increase as the nickel level falls. Thus the behavior observed at 500°C must reflect not only some aspect of the helium-induced refinement but also the earlier defined effect of nickel on swelling via its effect on vacancy diffusivity and dislocation bias at low helium levels.[5-7]

It is significant that the cavity sizes at 45 Ni and 500°C, as well as at all nickel levels at 400°C, are small enough that they are most likely helium bubbles rather than voids. At these sizes, the cavities may have been driven below the critical radius for bubble-to-void conversion.[8] Although the swelling in ORR at 400°C is significantly less than that observed in EBR-II, the extensive refinement of the small amount of swelling present is probably the major reason for the much larger level of strengthening observed in the tensile tests on ORR irradiated specimens. Preliminary analysis of the microstructural results indicates that, at all irradiation temperatures studied, the refinement of swelling (along with a smaller refinement of loop microstructure) is sufficient to account for the higher levels of strengthening observed in the ORR experiment.

It should be cautioned, however, that the helium/dpa ratios employed in the ORR test are much larger than anticipated in proposed fusion neutron spectra. Similar tests conducted using isotopic doping at more appropriate helium/dpa levels do not show such a large effect of helium on microstructure and tensile properties.[9]

CONCLUSIONS

Comparison of microstructures developed in Fe-Cr-XNi alloys irradiated in EBR-II and ORR shows that very large amounts of helium can significantly strengthen alloys via their effect on refinement of cavity microstructure. In addition, this refinement may have as one of its consequences a reduction of individual cavity sizes below the critical radius of bubble-to-void conversion for some alloy and irradiation conditions.

FUTURE WORK

This effort will continue, focusing on extraction of microstructural data from micrographs and on calculation of strength increases expected from the measured microstructural densities.

ACKNOWLEDGMENTS

The ORR portion of this work was sponsored by the Japan/U.S. FFTF-MOTA Collaboration of U.S. DOE and Monbusho. The AD-1 portion was conducted under the auspices of the Northwest College and University Association for Science.

REFERENCES

1. M. L. Hamilton, A. Okada and F. A. Garner, "Tensile Behavior and Swelling of Ternary Austenitic Alloys Irradiated in Different Neutron Spectra," accepted for publication in J. Nucl. Mater. (proceedings of ICFRM-4).

2. L. R. Greenwood, in Fusion Reactor Materials Semiannual Progress Report DOE/ER-0313/6 (1989) pp. 29-35.

3. H. R. Brager, F. A. Garner and M. L. Hamilton, J. Nucl. Mater., 133 and 134 (1985) 594-598.

4. F. A. Garner and H. R. Brager, ASTM STP 870, 1985, pp. 187-201.

5. F. A. Garner and A. S. Kurmar, ASTM STP 955, pp. 289-314.

6. J. J. Hoyt and F. A. Garner, "The Solute Dependence of Bias Factors in Irradiated Fe-Ni Alloys," accepted for publication in J. Nucl. Mater. (proceedings of ICFRM-4); also in this semiannual report.

7. W. A. Coghlan and F. A. Garner, ASTM STP 870 (1985) 289.

8. G. R. Odette, et al., J. Nucl Mater., 85 and 86 (1979) 533-545, also 103 and 104 (1981) 1361-1366 and 122 and 123 (1984) 514-519.

9. F. A. Garner, M. L. Hamilton, R. L. Simons and M. K. Maxon, "Isotopic Tailoring with ^{59}Ni to Study the Influence of Helium/dpa Ratio on Tensile Property Changes," accepted for publication in J. Nucl. Mater. (Proceedings of ICFRM-4); also in this semiannual report.

THE SOLUTE DEPENDENCE OF BIAS FACTORS IN IRRADIATED Fe-Ni ALLOYS - J. J. Hoyt, Washington State University and F. A. Garner, Pacific Northwest Laboratory[a]

OBJECTIVE

The object of this effort is to determine the origins of radiation induced changes in structural materials.

SUMMARY

The interstitial and vacancy biases for an edge dislocation in a binary alloy were examined, assuming the existence of an equilibrium Cottrell atmosphere around the line defect. The Larche' and Cahn treatment of stress relaxation due to a solute atmosphere was employed with the Wolfer and Ashkin formulation for the bias of an edge dislocation to compute the bias as a function of nickel concentration in the Fe-Ni system. Using the minimum critical void radius concept, the concentration-dependent bias offers a plausible explanation for the minimum in swelling observed at intermediate nickel levels and the gradual increase in swelling at higher nickel levels.

PROGRESS AND STATUS

Introduction

The swelling behavior of irradiated metals is strongly dependent on composition. For example, in Fe-Cr-Ni alloys the swelling at relatively high temperatures decreases strongly with nickel until some intermediate level of 40-60% nickel is reached.[1] Thereafter, increases in nickel result in a more gradual increase in swelling. The strong decreases observed in swelling of austenitic alloys can be partially explained by the effect of various solute additions (Ni, Si, P) on vacancy diffusivity.[2-6] However, at present, no mechanism has been advanced for the slow upturn at higher nickel levels.

Although many studies have investigated the concentration dependence of various material parameters, few have considered the effect of compositional variations on microstructural bias factors. The interaction of a point defect, interstitial or vacancy, with the stress field of a given defect sink determines the bias toward one point defect over the other. Since the stress field is altered in the presence of a solute species, one would intuitively expect the bias to be dependent on its concentration.

Consider a binary alloy in which the solute atoms are oversized; i.e., the lattice parameter of the solute in the pure state is larger than that of the host species in its pure state. To reduce the total strain energy of a dislocation, the solute will tend to segregate on the tensile side and be repelled from the compressive side. In equilibrium a Cottrell atmosphere is established. Although this effect has long been known, it was only recently shown that the change in the stress field around a dislocation could be computed for concentrated solutions. We examine here the effect this change in stress field has on bias factors for edge dislocations in Fe-Ni alloys.

Marwick[7] computed the bias for a free surface due to solute redistribution by numerically solving the diffusion equations for solute, vacancy and interstitial species. The Marwick scheme is the preferred method of computing bias factors but for a general distribution of defect sinks with non-homogeneous stress fields, the numerical solutions to the diffusion equations become quite intractable. We shall take a simpler approach and compute an initial bias by estimating the change in the stress field around an edge dislocation due to a Cottrell atmosphere. The emphasis on the word initial arises from the knowledge that sinks often become further enriched in various solutes via radiation-induced segregation.

Theoretical Background

Larche' and Cahn[8] have developed a general theory for the thermochemical equilibrium of solids under nonhydrostatic stress. A Cottrell atmosphere is one application of the theory and it was shown that the stress field with the solute atmosphere present is given by the stress field for a pure material but with the various elastic constants replaced by the open-field elastic constants. These constants, denoted by *, are given by:

$$E^* = E/(1 \pm \chi\eta^2 E) \quad (1a)$$

$$\nu^* = (\nu - \chi\eta^2 E)/(1 \pm \chi\eta^2 E) \quad (1b)$$

(a) Pacific Northwest Laboratory is operated for the U.S. Department of Energy by Battelle Memorial Institute under Contract DE-AC06-76RLO 1830.

$$(\kappa^{-1})^* = 3\,(1 - 2\nu^*)/E^* \qquad (1c)$$

where linear elasticity has been assumed. The parameters E, κ and ν are respectively the elastic and bulk moduli, and Poisson's ratio. The quantity η is the fractional change in the lattice parameter with composition (c); i.e.,

$$\eta = \frac{1}{a}\left(\frac{da}{dc}\right) \qquad (2)$$

Finally, χ is given as $(f'')^{-1}$ where f" is the second derivative of the free energy with composition. All parameters are evaluated at the average concentration.

To model in an approximate way the Fe-Ni system, the various material parameters need to be evaluated. In general, E, κ and ν are dependent on the average concentration, but for simplicity we assume they are constant. The values employed for the subsequent computations are the same as employed in an earlier study and represent conditions typical of fast reactor irradiation [9]. The fractional change in lattice parameter is found by assuming a linear dependence vs. the concentration of Ni; i.e., Vegard's law. Lattice parameters of pure Ni and pure Fe are readily obtained.

To estimate χ, a model for the free energy of mixing in Fe-Ni must be assumed. (Since we are ultimately concerned with the second derivative, the free energy and free energy of mixing can be used interchangeably.) The simplest nontrivial free energy model is the regular solution approximation with a free energy of mixing of the form:

$$f = \omega c(1 - c) + RT(c \ln c + (1 - c)\ln(1 - c)) \qquad (3)$$

where c is the Ni concentration, R is the gas constant and ω is an interaction parameter. The first term on the right of Equation 3 is the temperature independent enthalpy of mixing, ΔH. By adjusting ω to fit the experimentally measured ΔH, a better approximation to ΔH is established.

Figure 1 shows the enthalpy of mixing data for Fe-Ni measured by Kubaschewski et al.[10] and the assumed model used in the calculations (ω = 8510 J/mol). The assumed ΔH vs. c model is a reasonable approximation up to the Invar concentration but is rather poor at higher Ni levels. Nevertheless, for the first evaluation we expect the results to be qualitatively correct.

Using a perturbation technique for non-linear diffusion equations, Wolfer and Ashkin [11] derived the bias of an edge dislocation. In the absence of applied stress the bias is:

$$Z_{i,v} = 1 + \left(\frac{Bo_{i,v}}{kt}\right)^2 / [16a^2 \ln(\frac{R}{a})] \qquad (4)$$

where R and a are outer and inner cutoff radii respectively, measured in units of the Burgers vector and k is the Boltzmann's constant. The subscript i or v refers to interstitial or vacancy. The quantity $Bo_{i,v}$ is given by:

$$Bo_{i,v} = v_{i,v} K\,(1 - 2\nu)/2\pi\,(1 - \nu) \qquad (5)$$

where $v_{i,v}$ is the difference between the defect volume and atomic volume

Equation 5 was derived assuming a stress field around a dislocation in an compositionally homogeneous alloy. We now examine the change in Z when the stress field relaxation is due to a solute atmosphere. Thus, Equations 1-3 are employed in conjunction with Equations 4 and 5 to arrive at the initial bias as a function of average Ni concentration.

Figure 2 shows the ratio of Z_i over Z_v vs. concentration of Ni (C_{Ni}) at various temperatures. The curves are symmetric about C_N = 0.5, a direct consequence of employing the regular solution approximation. The magnitude of the change in Z_i/Z_v is only a few percent but this small change can have a large effect on the swelling behavior.[12-13] Note that the change of Z_i/Z_v is more pronounced at lower temperatures. Recall, however, that the bias is only one factor which controls void nucleation and growth.

The interactive effect of a concentration dependent bias factor and other relevant parameters on swelling behavior can be examined using the concept of a minimum critical radius, R_{mc}. For a void to grow it must nucleate as a vacancy cluster and reach a critical size. Below this critical size, a cavity will spontaneously decrease in size unless stabilized by gas atoms.

The bubble to void conversion idea was first discussed by Sears[**], and later developed by Odette and Stoller[13] and Coghlan and Mansur[14] and employed by Coghlan and Garner[9] to examine the effect of Ni concentration on R_{mc} in simple austenitic alloys. The latter study focused on the effect of compositional

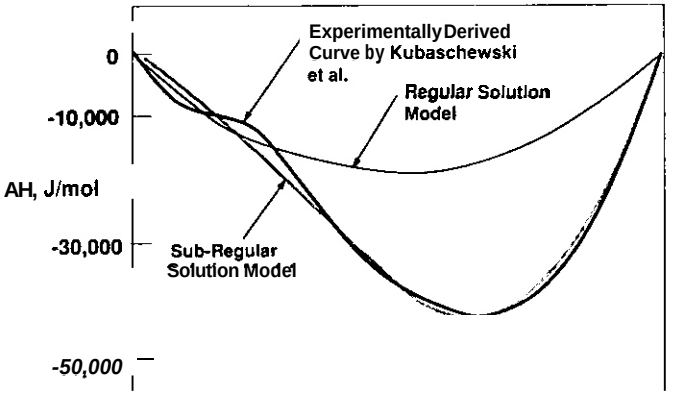

FIGURE 1. Mixing Enthalpies of Solid Fe-Ni Alloys, as Published by Kubaschewski and Coworkers[11] and the Regular and Subregular Models Assumed in This Study for Illustration Purposes.

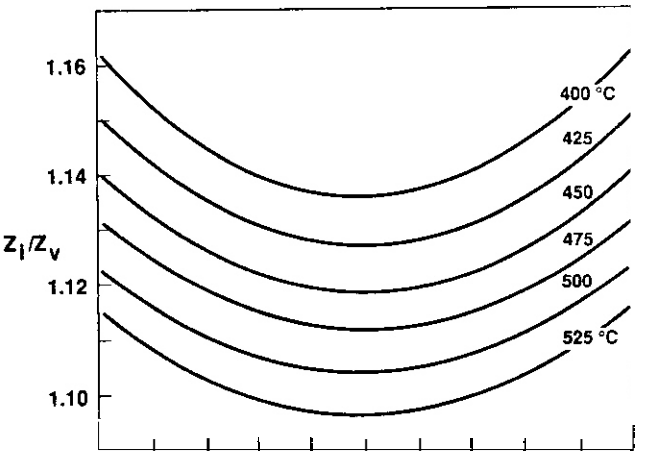

FIGURE 2. Calculated Ratio of Z_i/Z_v vs. Nickel Concentration for Various Irradiation Temperatures

changes in vacancy diffusivity on the minimum critical radius. The equations involved in the computation of R_{mc} are lengthy and the reader is referred to reference 12 for details. The various material and kinetic parameters needed are identical to those of reference 9. In the following it is assumed that the system bias is equal to the bias of an edge dislocation; i.e., that the ratio of void bias for an interstitial to that of a vacancy is unity. This may not be completely accurate but it is a common assumption and simplifies the calculation.

Figure 3 shows the critical radius of Fe-Ni alloys vs. C_{Ni} at 475°C. Again due to the symmetric form chosen for the free energy, a peak is observed at C_{Ni} = 0.5 with an approximately 10% increase in R_{mc} over that of the pure metals. Figure 3 suggests that the swelling behavior of Fe-Ni would also be symmetric. However, this conclusion neglects changes in vacancy diffusivity, the importance of which has been stressed in earlier papers.[1-6] In particular, it was shown that changes in the pre-exponential factor D_v^o with Ni content are very important.

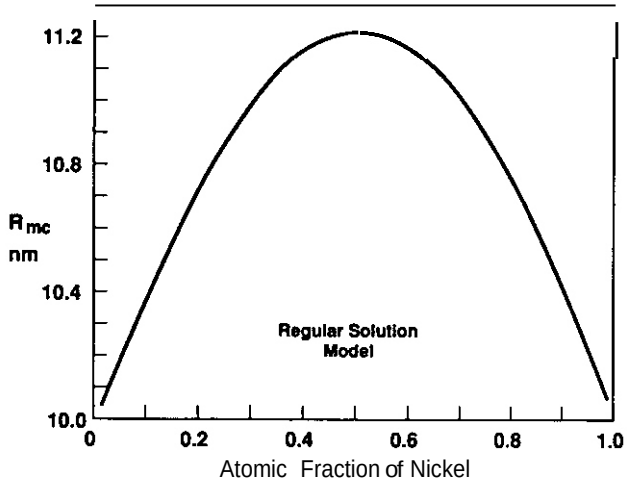

FIGURE 3. Calculated Values of Minimum Critical Radius of FeNi Alloys at 475°C

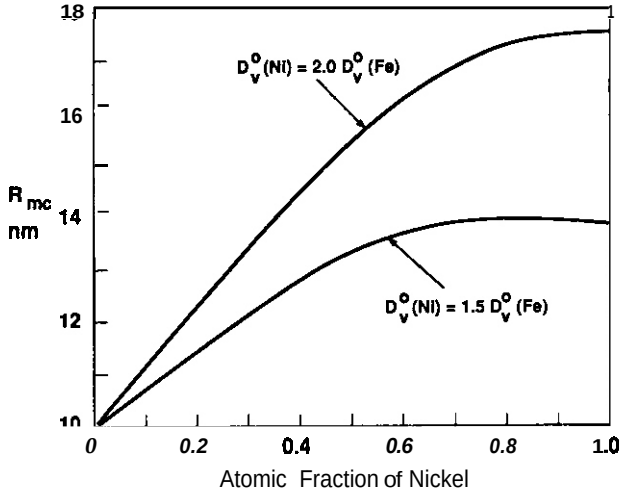

FIGURE 4. Calculated Values of Minimum Critical Radius at 475°C Assuming D_v^o to be a Function of Nickel Concentration

We will examine two qualitatively correct scenarios. We assume D_v^p increases linearly with Ni such that D_v^p for pure Ni is either a factor of 2 or a factor of 1.5 greater than that of pure Fe. The results of these assumptions are shown in Figure 4. For the 1.5 factor change in D_v^p, R_{mc} changes by ~40% from low to high Ni. The change in R_{mc} is a function of temperature and increases at higher temperatures. Figure 4 offers a plausible explanation for the observed gradual upturn in swelling at high Ni levels. A similar conclusion cannot be drawn by considering solely the impact of changes in D_v^p.

Figure 5 shows a plot of R_{mc} vs. temperature for various nickel levels. These curves show that R_{mc} is not very sensitive to nickel or temperature at relatively low temperatures, but is a steep function of temperature at higher temgeratures while being moderately sensitive to nickel. all in agreement with experimental observations.

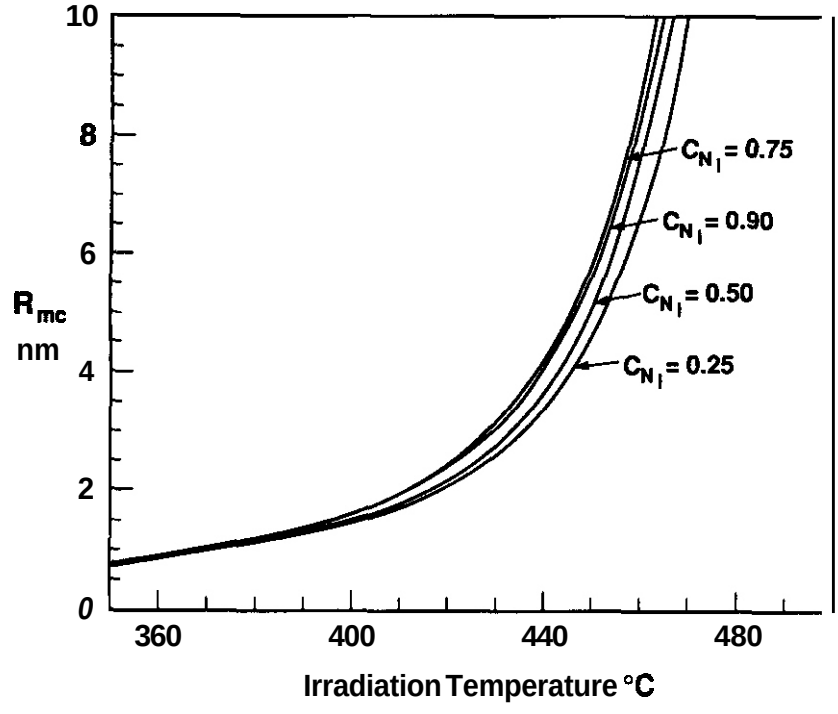

FIGURE 5. Minimum Critical Radius as a Function of Irradiation Temperature and Composition

Figure 1 shows that the regular solution model is a poor approximation to the free energy of mixing in Fe-Ni. If the interaction parameter ω is itself assumed to be concentration dependent, the so-called sub-regular solution model results. A fit, using this more accurate model, to the Kubaschewski et al. ΔH data is shown in Figure 1 where it was assumed that ω varied linearly with C_{Ni}. It was found that with the improved ΔH function the dependence of Z and R_{mc} with Ni concentration changed somewhat in detail but was not significantly different in overall conclusions.

It must be stressed that the composition-dependent bias presented in this work refers to an initial bias. The Larche' and Cahn formalism for the solute atmosphere around an edge dislocation refers to a system in thermal equilibrium. During irradiation, a material cannot be considered in equilibrium and dynamic factors such as the inverse Kirkendall effect or solute drag become important. In the Fe-Ni-Cr system, nickel always segregates at microstructural sinks. It would be unjustified to extend the above ideas to the steady state swelling behavior at late times without incorporating the time dependence of C_i at the sinks. Wolfer and coworkers have shown that segregation of nickel at sinks changes their bias.[15,16]

CONCLUSIONS

Changes with composition of the pre-exponential coefficient for vacancy diffusion have previously been invoked to explain the rapid decrease in swelling with Ni additions in irradiated steels. However, this factor alone cannot explain the gradual increase in swelling with Ni content for $C_{Ni} \geq 0.5$. It has been

shown that the combined effect of a concentration dependent bias factor and changes in D_v^o offers one possible explanation for the swelling behavior in Fe-Ni. The change in bias was assumed to arise from the existence of a Cottrell atmosphere of nickel atoms around the dislocations.

FUTURE WORK

This effort will continue, exploring the interaction between the Cottrell atmosphere effect and other composition-dependent operating mechanisms.

ACKNOWLEDGMENTS

J. J. Hoyt thanks the Northwest College and University Association for Science for financial support under U.S. Department of Energy Contract DE-AM-06-76-RL02225. F. A. Garner's participation was sponsored by the U.S. Department of Energy under Contract DE-AC06-76RLO 1830.

REFERENCES

1. F. A. Garner and A. S. Kumar, ASTM STP 955 (1987) 289.

2. F. A. Garner and W. G. Wolfer, J. Nucl. Mater. 102 (1981) 143.

3. F. A. Garner and W. G. Wolfer, J. Nucl. Mater. 122 & 123 (1984) 201.

4. 8. Esmailzadeh and A. Kumar, ASTM STP 870, (1985), 468.

5. B. Esmailzadeh, A, Kumar and F. A. Garner, J. Nucl. Mater. 133 & 134 (1985) 590.

6. F. A. Garner and H. R. Brager, J. Nucl. Mater. 133 & 134 (1985) 511.

7. A. D. Marwick, J. Nucl. Mater. 135 (1985) 68.

8. F. C. Larche' and J. W. Cahn, Acta Metall. 21 (1973) 1051; 26 (1978) 53; 30 (1982) 1835; 33 (1985) 331

9. W. A. Coghlan and F. A. Garner, in Reference 4, 289.

10. O. Kubaschewski, K. H. Geiger and K. Hack, Z. Metallk. 68 (1977) 337.

11. W. G. Wolfer and M. Ashkin, J. Appl. Phvs. 47 (1976) 791.

12. V. F. Sears, J. Nucl. Mater. 39 (1971) 18-26.

13. G. R. Odette et al., J. Nucl. Mater. 85 & 86 (1979) 533-545, also 103 & 104 (1981) 1361-1366 and 122 & 123 (1984) 514-519.

14. W. A. Coghlan and L. K. Mansur, J. Nucl. Mater. 122 & 123 (1984) 495.

15. A. Si-Ahmed and W. G. Wolfer, ASTM STP 782 (1982) 1008.

16. W. G. Wolfer, F. A. Garner and L. E. Thomas in Reference 14, 1023-1041

INFLUENCE OF MATERIAL AND ENVIRONMENTAL VARIABLES ON THE NEUTRON-INDUCED SWELLING OF NICKEL, F. A. Garner, Pacific Northwest Laboratory[a]

OBJECTIVE

The object of this effort is to provide an understanding of the fundamental response of metals and alloys to irradiation, and to use this understanding as a basis for interpreting the perturbations that arise due to differences in neutron spectra, especially with respect to the influence of PKA recoil spectra and helium/dpa ratio.

SUMMARY

Nickel has been employed in a number of efforts directed toward the development of fission-fusion correlations. Unlike iron-base alloys, nickel's swelling behavior is dominated not by its tendency to swell initially at a rate comparable to that of Fe-Cr-Ni austenitic alloys, but by its persistent tendency to later saturate in swelling, a behavior not observed in other metals and alloys. The saturation level of swelling in neutron irradiation studies in nickel is usually less than 10%, but the rate of approach to saturation is very sensitive to many environmental and material variables. Fission-fusion correlation efforts involving nickel are difficult to interpret unless great care is taken to conduct single variable experiments which take into account the unique swelling behavior of this metal.

PROGRESS AND STATUS

Introduction

A series of parallel and joint activities are in progress in the U.S., Japan and Europe to study the impact of helium/dpa ratio and PKA recoil spectra on the microstructural evolution of metals and alloys. Some of these are directed toward simple metals of little technological relevance and others toward more complex alloys which are candidates for direct application to fusion environments. The simple metals and model alloys are used in studies directed toward the identification of individual mechanisms which might not be easily isolated and studied in more complex systems where numerous mechanisms are in competition.

Whereas most of the model alloy efforts at PNL focus on iron-base alloys, simple copper alloys (for high heat flux applications) and vanadium binary alloys, the efforts of several joint studies conducted in MOTA with colleagues from Japan and Denmark focus on nickel and other pure metals. Nickel, in particular, is often used in fission-fusion correlation efforts. Operating on the principle that one cannot clearly define the effect of a perturbing variable associated with the simulated environment until the parametric response in the surrogate environment is understood, analyses are in progress to define the baseline behavior of several simple metals: nickel, copper and vanadium.

This report focuses on the behavior of nickel in EBR-II and other fast reactors as observed in a series of fusion and breeder program studies. Some of the data reported here have not been previously published-and, in one important case (the AA-14 experiment), the measurements of swelling were performed just recently and are reported here for the first time.

Results and Discussion

There are a rather limited number of high exposure neutron irradiation experiments conducted on nickel that are relevant to current fusion-oriented studies and an equally limited number of charged particle experiments. There are even fewer studies in which the influence of helium was studied. There are sufficient data, however, to extract the overall features of nickel's response to irradiation.

Figure 1 shows that at very low neutron exposures and temperatures in the range 380-450°C, Harbottle and Dickerson' found that, after a small incubation period, the swelling of 99.995% nickel was linear with exposure at ~1%/dpa. A similar linearity was observed by Holmes' in EBR-II at 399-455°C, but he found the swelling rate to be dependent on the purity of the nickel as shown in Figure 2. Both of these figures imply that swelling is relatively insensitive to both irradiation temperature and displacement rate at these lower temperatures. Holmes also demonstrated that swelling was not sensitive to cold-work level at these low temperatures. Yoshida and coworkers demonstrated that the onset of swelling in nickel was sensitive to the impurity content, with voids nucleating earlier in very pure nickel, and stacking fault tetrahedra forming as the early dominant sink in less pure material.[3]

(a) Pacific Northwest Laboratory is operated for the U.S. Department of Energy by Battelle Memorial Institute under Contract DE-AC06-76RLO 1830.

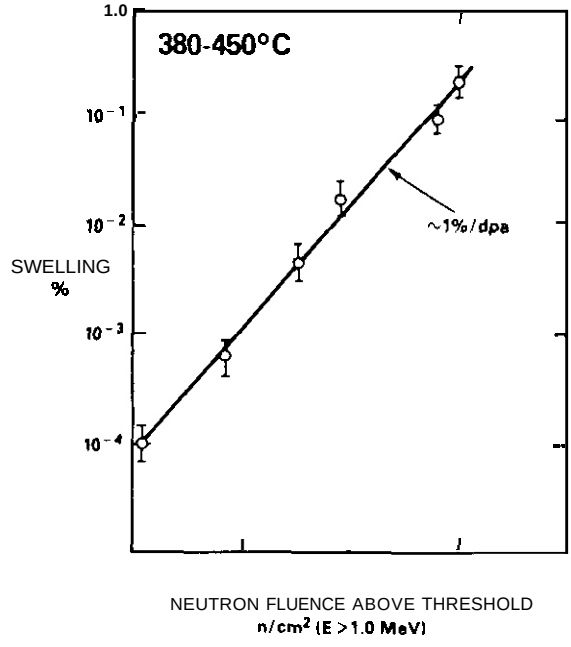

FIGURE 1. Swelling Observed in Thermal Reactor Irradiation of Annealed 99.995% Pure Nickel at 380-450°C.' An observed incubation or threshold fluence of 4 x 10^{17} n/cm^2 has been subtracted from each fluence level. The swelling rate shown is estimated using knowledge of reactors with comparable spectra.

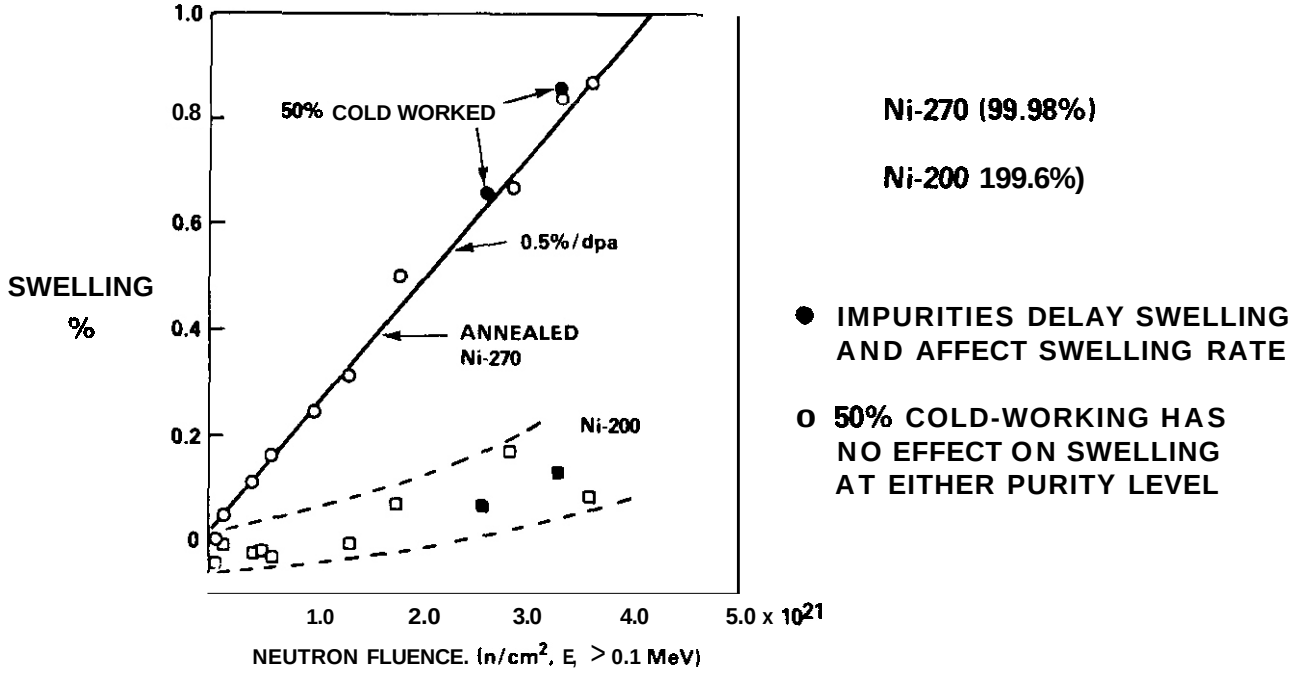

FIGURE 2. Swelling Observed in Nickel-200 and Nickel-270 in both the annealed and the 50% Cold Worked Conditions at 399-455°C in EBR-II.[2] Each datum was measured from specimens which had the same residence time in reactor but which were irradiated at different displacement rates. There is a substantial uncertainty in the fluence levels quoted for this experiment.

It was shown by Garner that nickel behaves rather differently from Fe-Cr-Ni alloys in one very important aspect.' Whereas both swell at a rate of ~1%/dpa in the range 400-450°C, nickel exhibits a tendency toward saturation after reaching several percent swelling. The origin of the saturation response is not clear and nickel's behavior contrasts with that of pure copper, which does not exhibit saturation at these

temperatures.[5] Figure 3 shows this behavior as observed in three different fast reactors for a variety of purity levels and starting conditions.[6-10] Harbottle also observed a decreasing rate of swelling in 99.995% nickel during irradiation in the SILOE reactor at 350°C.[11] Note in Figure 4 that the initial steady state swelling rate is ~1%/dpa, but that it falls very quickly at this purity level.

One consequence of this saturation phenomenon is that neutron-induced swelling levels in excess of 10% have not been reported for nickel even when irradiated to displacement levels of 50-60 dpa. This limitation has also been observed in heavy ion and electron irradiation studies.[12-19] Most interesting, however, is the observation that within a given irradiation environment the saturation level is not very sensitive to irradiation temperature, as shown in Figures 5-8. This is somewhat surprising in that irradiations conducted at temperatures above 450°C appear to approach saturation at lower initial rates,[20,21] as shown in Figures 9 and 10. It should be noted, however, that the effect of irradiation temperature on the transient regime manifests itself primarily at higher displacement rates and not at lower displacement rates, as shown in Figure 10. As we shall see later, there appears to be strong interactions between displacement rate, temperature, dislocation density and alloy purity in the early stages of microstructural evolution in nickel.

The effect of displacement rate on swelling is well known. As shown in Figure 11, an early ion irradiation experiment showed that in nickel the regime of swelling shifts upward in temperature for relatively large increases in displacement rate.[23] Thus, at relatively low temperatures a large decrease in displacement rate leads to a relatively large increase in swelling. When solutes are present in amounts sufficient to significantly delay the onset of swelling, however, the effect of differences in displacement rate can be much larger. Figure 12a shows some early swelling data on 99.6% nickel rings irradiated in EBR-II.[24] These relatively high fluence data were interpreted at that time according to the conventional wisdom that steady-state swelling rate of all metals and alloys exhibits a strong dependence on temperature. The significance of the low fluence data shown in Figure 12b was not really addressed at that time. Note that the low fluence and high fluence data were derived from opposite sides of rings that spanned a substantial flux gradient but not much of a temperature gradient. Therefore it is best to utilize both low and high fluence data together and reassess the effects of both displacement rate and temperature. Figures 12b and 12c show two alternate interpretations of the data using this approach. One interpretation assumes that all variations arise from differences in irradiation temperature and the other assumes all variations arise from differences in displacement rate, which varies only a factor of three across each ring. On the basis of the temperature insensitivity demonstrated in previous studies for this temperature range, it appears that the flux sensitivity of swelling (Figure 12c) is the most plausible interpretation. This leads to the conclusion that for relatively impure nickel, fission-fusion correlation experiments spanning even a small range of displacement rates will be difficult to interpret.

A recent measurement of void swelling in 99.999% pure nickel irradiated in EBR-II in the AA-14 fusion materials experiment yields some particularly revealing results, as shown in Figure 13. The swelling of annealed nickel at 14 dpa is a moderately strong function of temperature, but when irradiated in the 30% cold-worked condition, the swelling is relatively insensitive to temperature. After aging, the swelling actually increases somewhat but retains the relative independence of irradiation temperature. This suggests that annealed specimens experience more difficulty at higher temperatures in generating a stable dislocation network, a problem which is easily overcome in the presence of a preexisting network. The slight increase in swelling with preirradiation aging suggests that there is an optimum initial dislocation density for void swelling that is somewhat lower than that obtained by cold-working. Microscopy examination will be used to confirm this hypothesis,

The data shown in Figure 13 are consistent with the behavior shown in Figure 2, both of which show little dependence on starting state for relatively pure nickel at relatively low irradiation temperature. For relatively impure nickel, however, the effect of cold work is to suppress swelling somewhat at temperatures in the range of 400-500°C, as shown in Figure 6.

The effect of helium/dpa ratio on neutron-induced swelling of nickel has not previously been investigated, although this is now the focus of joint studies with other laboratories. It appears that we can anticipate that earlier void nucleation due to higher helium generation rates may lead to different levels of swelling saturation. Ryan[25] has shown in ion irradiation studies that helium preinjection at higher irradiation temperatures (where void nucleation is presumably more difficult) leads to larger levels of swelling in nickel early in the irradiation, followed by a higher level of saturation, as shown in Figure 14. Note in this figure that a swelling level in excess of 10% was reached in this experiment. Ryan[23], Pinizotto[26] and Delaplace[27] all reached levels between 10 and 20% in some of their irradiation experiments. Ryan attributed this to the possible influence of the ion-incident surface as a sink for interstitials, producing higher levels of swelling than observed for similar levels of neutron-induced displacements.

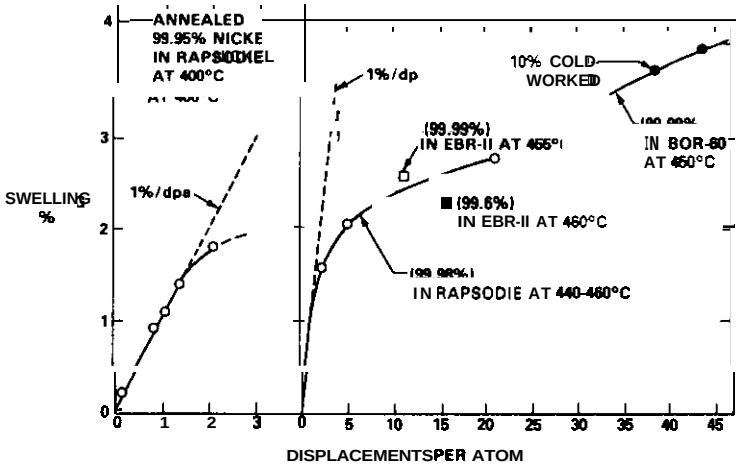

FIGURE 3. Swelling Observed in Annealed Nickel of Various Purity Levels in Three Fast Reactors at Quoted Temperatures of 400° and 440-460°C.[4] Some cold-worked nickel data are also shown.

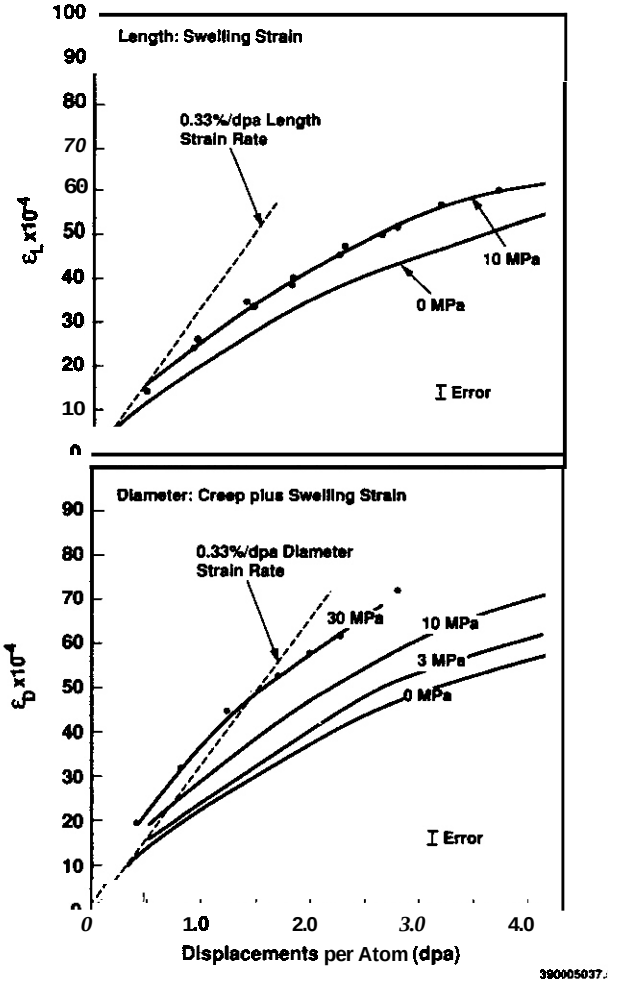

FIGURE 4. Length and Diameter Changes at 350°C Observed in the SILOE Reactor Using Pressurized Tubes of 99.995% Nickel.[11] The length changes arise only from swelling and are affected by stress. The diameter changes incorporate both creep and swelling strains. The stress-free diameter and length changes are identical, showing that swelling is isotropic. Swelling initially begins at a linear rate of ~0.33%/dpa (a volumetric rate of ~1%/dpa) but tends to saturate quickly thereafter.

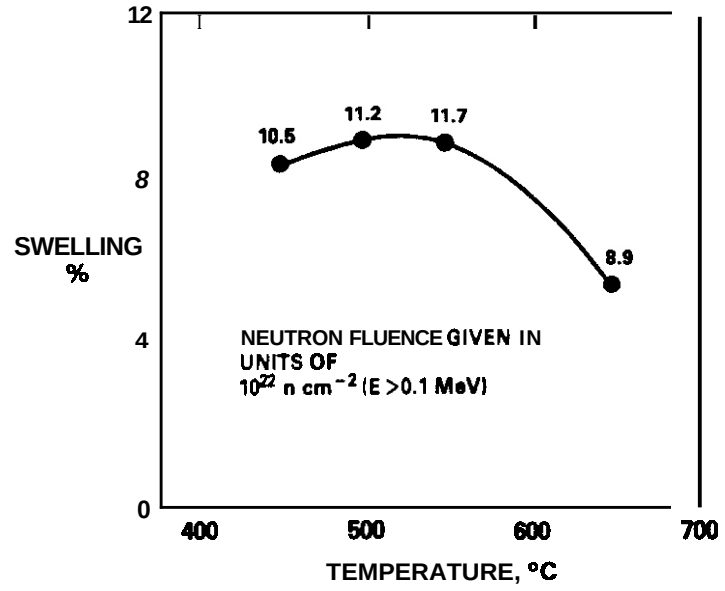

FIGURE 5. Neutron-Induced Swelling Observed in Annealed 99.99% Nickel Irradiated in the BOR-60 Fast Reactor.[20] The authors indicate that for this spectrum 5.6 dpa results from 1.0 x 10^{22} n cm^{-2} (E>0.1 MeV). Swelling appears to have saturated at rather low values that are not very sensitive to irradiation temperature.

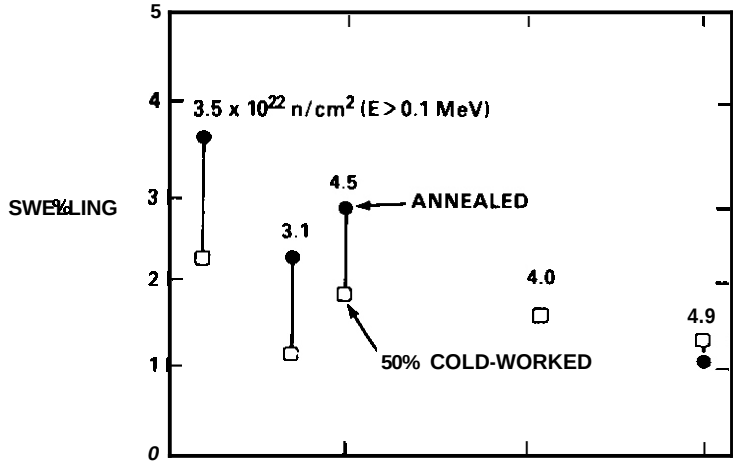

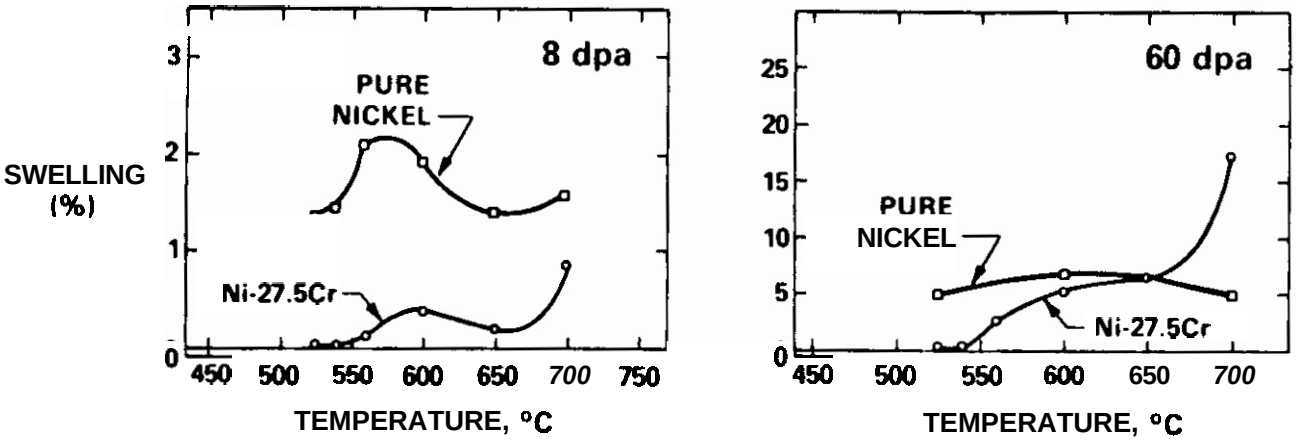

FIGURE 7. Swelling Observed in Comparative Irradiations of Pure Nickel and Ni-27.5Cr at 8 and 60 dpa with 46.5 MeV Ni^+ Ions.[17] Note scale change between graphs.

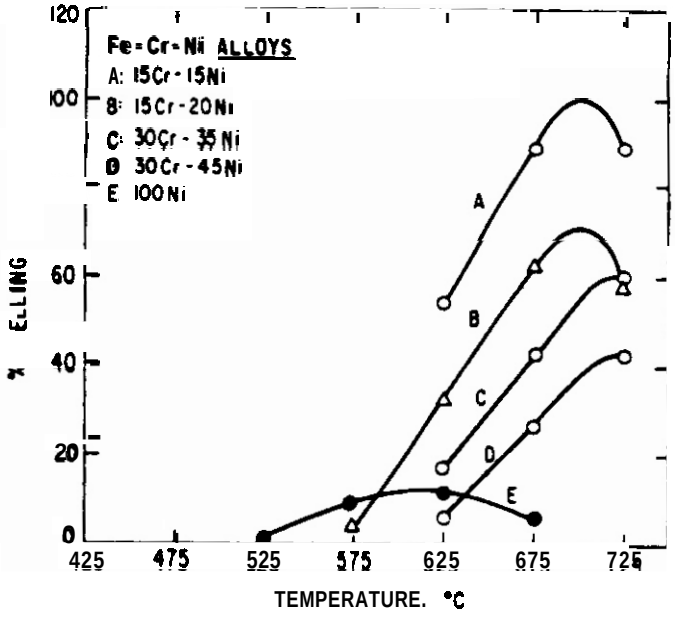

FIGURE 8. Relatively Low Levels and Temperature-Sensitive Behavior of Swelling in Pure Nickel Compared to that of Various Fe-Cr-Ni Alloys at 117 dpa After Irradiation with 5 MeV Ni^+ Ions.[19]

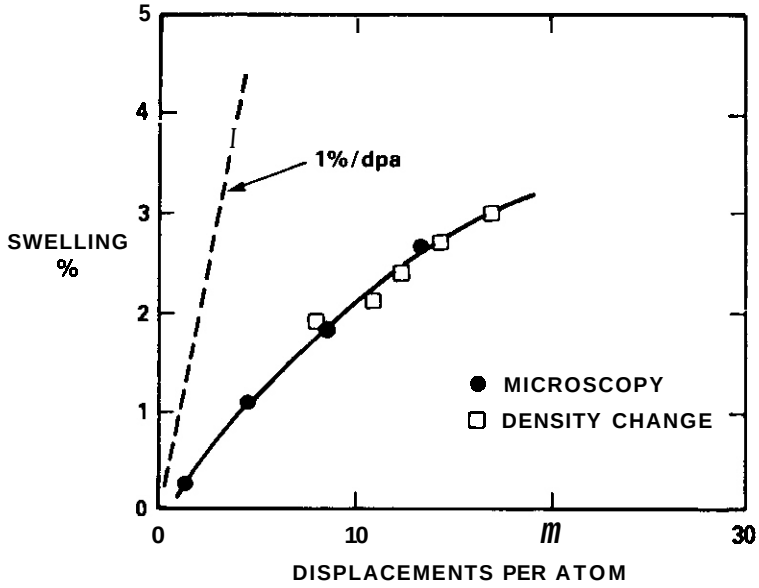

FIGURE 9. Neutron-Induced Swelling of 99.99% Nickel at 500°C as Observed in the BOR-10 Reactor[22]

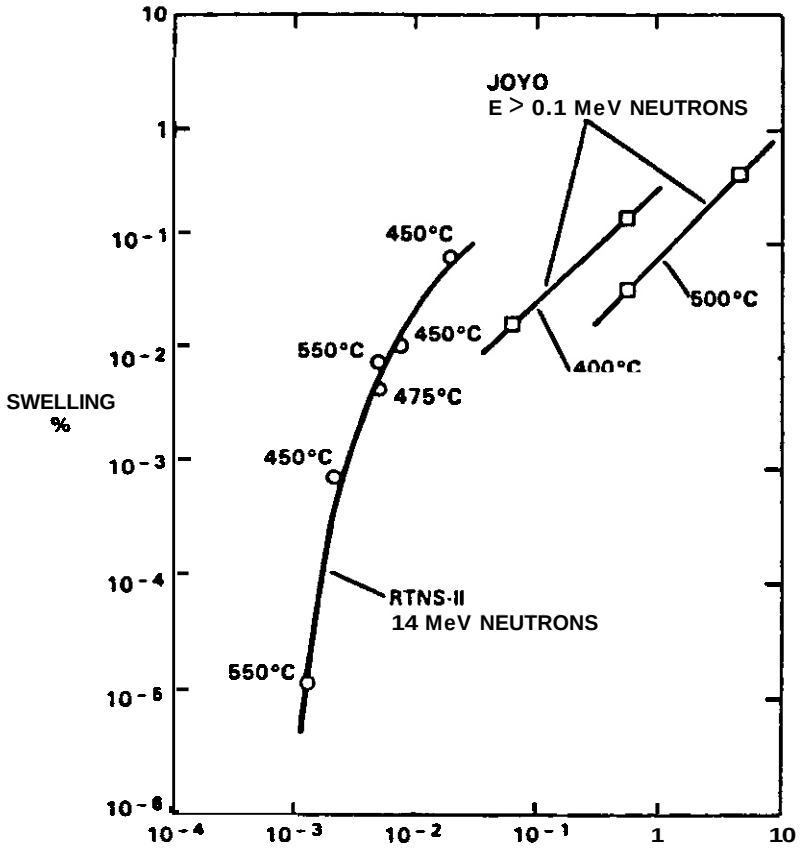

FIGURE 10. Swellin Observed in Nickel During a Correlation Experiment Conducted at Very Different Displacement Rates." Swelling is seen to be dependent on temperature at the higher displacement rate of the Japanese JOYO reactor but not at the lower displacement rate of RTNS-II. Flux effects are thought to have dominated over PKA recoil spectra considerations in this experiment.

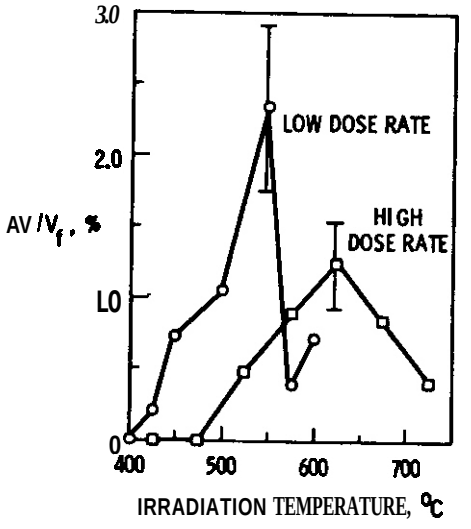

FIGURE 11. Temperature Shift of Swelling Observed in 2.8 MeV Ni^{+} Ion Irradiations *of* Pure Nickel at 13 dpa.[23] The low dose rate is 7 x 10^{-4} dpa/sec and the high dose rate *is* 7 x 10^{-2} dpa/sec.

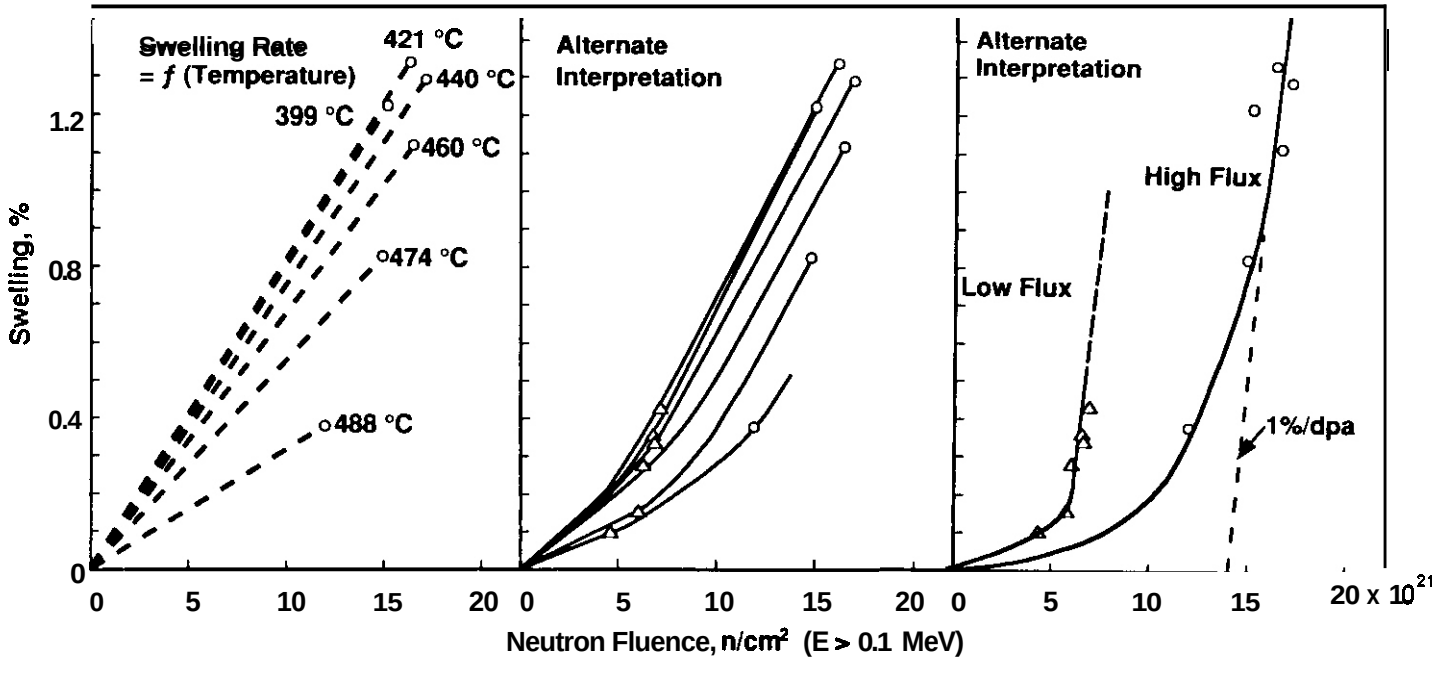

FIGURE 12. Swelling Observed on Both Sides *of* 99.6% Nickel Rings Irradiated in a Flux Gradient in EBR-II.[24] The initial intepretation is shown in (a) and two alternate interpretations are shown in (b) and (c).

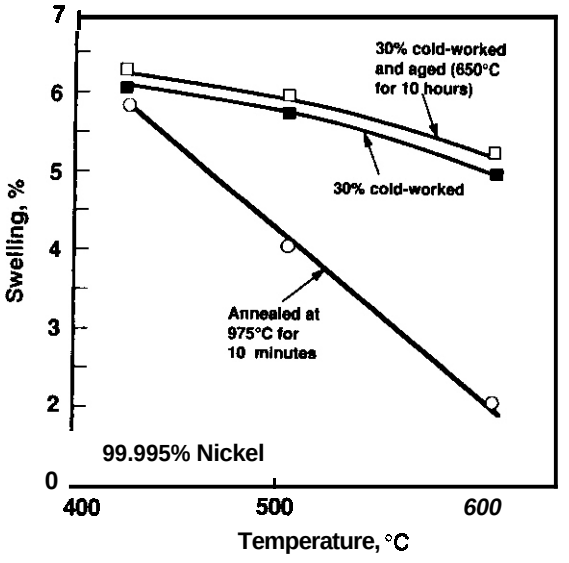

FIGURE 13. Swelling of 99.99% Nickel Irradiated to 14 dpa in the EBR-II Fusion Materials Experiment Designated AA-14. Three irradiation temperatures and three starting conditions were employed.

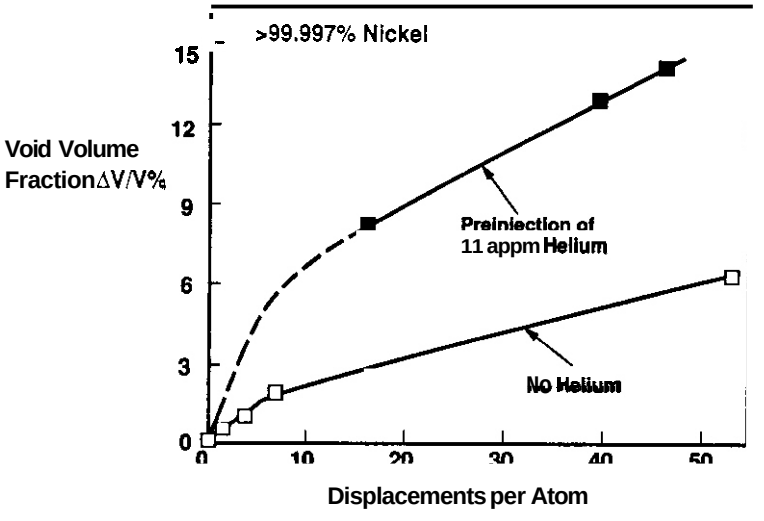

FIGURE 14. Influence of Helium Preinjection on Swelling of 99.997% Nickel Irradiated at 750°C by 4.5 MeV Ni^{+} Ions.[25]

When experiments are analyzed involving nickel in reactors which produce a large amount of helium, an additional complication arises in that the same reaction which produces the helium also leads to a sizable increase in displacement rate. Greenwood has shown that the displacement rate of pure nickel irradiated in the mixed spectrum reactor HFIR can be increased as much as 90%.[8] This important consideration must be factored into the comparative analysis of irradiations conducted on nickel in different reactor spectra.

Conclusions

In comparative irradiations of nickel at low and high He/dpa ratios, one must be careful to fully characterize the parametric dependence of swelling in the low helium environment before drawing conclusions concerning the perturbing influence of helium. It appears that nickel in the relatively pure state swells at a temperature-independent and possibly flux-independent rate of ~1%/dpa at low temperatures but that swelling quickly begins to saturate thereafter. The tendency to saturate appears to occur earlier with increasing purity levels. As the temperature increases more difficulty is encountered in generating a

sufficiently high density of dislocations and the saturation process dominates from almost the beginning of the irradiation. Introduction of a preexisting dislocation network counteracts this difficulty and the temperature dependence of swelling becomes rather small as a result. As impurities are added to nickel there is a tendency to extend the incubation period that precedes both the development of a high swelling rate and the saturation process. When solutes exert a strong effect on swelling behavior, an enhanced sensitivity to both displacement rate and cold work is observed.

The saturation process appears to be a ubiquitous feature of nickel irradiations but the approach to and magnitude of the satura'tion level appears to be very sensitive to variables such as helium, purity and dislocation density. Fission-fusion correlations utilizing nickel should be careful to minimize the number of variables operating in the experiment. Otherwise differences in environmental and material variables may overwhelm the effects of helium/dpa ratio or PKA recoil spectra.

REFERENCES

1. J. E. Harbottle and S. M. Oickerson, J. Nucl. Mater., 44 (1972) 313.

2. J. J. Holmes, Trans. ANS, 12 (1969) 701.

3. N. Yoshida, T. Muroga, H. Watanabe, K. Araki and Y. Miyamoto, J. Nucl. Mater., 155-157 (1988) 1222.

4. F. A. Garner, J. Nucl. Mater., 122 and 123 (1984) 459.

5. F. A. Garner, H. R. Brager and K. R. Anderson in Fusion Reactor Materials Semiannual Prowess Report for Period Endina Seotember 30, 1989, DOE/ER-0313/7, pp. 223-231.

6. Y. Adda, in Proc. Int. Conf. on Radiation-Induced Voids in Metals. CONF-710601, Albany, NY (1971) p. 31.

7. G. Silvester, A. Silvent, C. Regnard and G. Sainfort, J. Nucl. Mater., 57 (1975) 125.

8. N. P. Agapova et al., Atomnava Eneraiva, 45 (1978) 433.

9. K. B. Roarty, J. A. Sprague, R. A. Johnson and F. A. Smidt, J. Nucl. Mater., 97 (1981) 67.

10. H. R. Brager and J. L. Straalsund, Irradiation Swelling Resistance of Inconel 600, unpublished data contained in HEDL-SA-322 S (Hanford Engineering Development Laboratory, Richland, WA, 1972).

11. J. E. Harbottle, J. Nucl. Mater., 66 (1977) 258.

12. J. B. Whitley, G. L. Kulcinsky, P. Wilkes and J. Billen, J. Nucl. Mater., 85 and 86 (1979) 701.

13. G. L. Kulcinsky, J. L. Brimhall and H. E. Kissinger, in ref. [6], 449.

14. R. S. Nelson, J. A. Hudson, D. J. Mazey, G. P. Walters and T. M. Williams, in ref. [6], 430.

15. J. A. Hudson, S. Frances, O. J. Mazey and R. S. Nelson, in: Effects of Radiation on Substructure and Mechanical Properties of Metals and Alloys, ASTM STP 529 (1973) 326.

16. D. 1. R. Norris, J. Nucl. Mater., 40 (1971) 66.

17. J. A. Hudson and S. J. Ashby, in: The Physics of Irradiation Produced Voids, AERE-R-7934, Ed. R. S. Nelson, 1974, 140.

18. T. D. Ryan and A. Taylor, in Application of Ion Beams to Metals, S. T. Pieraux, E. P. EerNisse and F. L. Vook, Eds., Plenum Press, 1975, 675.

19. W. G. Johnston, T. Lauritzen, J. H. Rosolowski and A. M. Turkalo in Radiation Damage in Metals, N. L Peterson and S. O. Harkness, Eds., American Society for Metals, 1976, 227.

20. N. K. Vasina, I. P. Kursevich, O. A. Kozhevmikov, V. K. Shamardin and V. N. Golovanov, Atomnaya Eneraiva, 59 (1985) 265.

21. T. Muroga, H. Watanabe, K. Araki and N. Yoshida, J. Nucl. Mater., 155-157 (1988) 1290.

22. V. I. Scherbak, Fiz. Metal. Metalloved., 50 (1980) 1314.

23. J. E. Westmoreland, J. A. Sprague, F. A. Smidt, Jr. and P. R. Okamoto, Radiation Effects, 26 (1975) 1.

24. R. V. Strain and W. E. Ruther, Results of Irradiation of Nickel Reflector Test Assemblies. ANL/EBR-044, August 1971.

25. T. D. Ryan, Heavy Ion-Induced Void Formation in Nickel, Doctoral Dissertation, University of Michigan, 1975.

26. R. F. Pinizotto, Jr., J. L. Chen and A. J. Ardell, Met. Trans. 9A (1978) 1715.

27. J. Delaplace, N. Azam, L. LeNaour, M. Lott and C. Fiche, Journal de Phvsiaue, Colloaue C5, Tome 34:C5-11 (1973) 11.

28. L. R. Greenwood, J. Nucl. Mater., 115 (1983) 137.

A TEST OF THE CREEP-SWELLING RELATIONSHIP DEVELOPED FOR AUSTENITIC STEELS - F. A. Garner, Pacific Northwest Laboratory[a]

OBJECTIVE

The object of this effort is to develop an understanding of the creep-swelling relationship and to apply this relationship to the development of creep equations for new materials without the necessity of conducting extensive and therefore expensive irradiation creep studies.

SUMMARY

Pure nickel at 350°C swells with almost no incubation period and with a continuously declining instantaneous swelling rate, in contrast to the large incubation periods and increasing swelling rates observed in austenitic steels. Both types of metals appear to obey the same creep-swelling relationship, however, in which the major component of the irradiation creep rate is directly proportional to the instantaneous swelling rate. The creep-swelling coupling coefficient appears to be -0.6 x 10^{-2} MPa^{-1} in both systems. The coefficient is remarkably insensitive to a variety of environmental and material variables.

PROGRESS AND STATUS

Introduction

The creep-swelling relationship of annealed AISI 304[1] and various thermomechanical treatments of AISI 316 stainless steel[2-6] has recently been investigated in EBR-II. Another similar study has also been conducted on the Fusion Prime Candidate Alloy (PCA) in FFTF.[7] In each alloy, it was shown that irradiation creep at most temperatures of interest consists of several minor contributions (precipitation-related dimensional changes and relaxation of cold work-induced dislocations) and two major contributions. The major contributions are the creep compliance B_o, a quantity unrelated to void swelling, and a swelling-related creep component. Swelling is known to be very sensitive to many material and environmental variables, but the instantaneous creep rate appears to be governed only by the applied stress and the instantaneous swelling rate. The instantaneous creep rate B can be written $B = \dot{\varepsilon}/\sigma = B_o + DS$, providing that the material is annealed and does not develop any phase-related strains. The quantity $\dot{\varepsilon}/\sigma$ is the effective strain rate per unit effective stress, $\dot{\varepsilon}$ is $2/\sqrt{3}\ \dot{\varepsilon}_{hoop}$, σ is the effective stress ($\sqrt{3}/2\ \sigma_{hoop}$), σ_{hoop} and $\dot{\varepsilon}_{hoop}$ are the hoop stress and strain rate, respectively, D is the creep-swelling coupling coefficient and S is the instantaneous swelling rate.

It was found in the previous studies that B_o was ~2.0 x 10^{-6} MPa^{-1} dpa^{-1} and that the creep-swelling coupling coefficient was -0.6 x 10^{-2} MPa, a value refatively independent of variables which affect swelling, such as cold work level, composition and irradiation temperature. It was shown in another related study that the fusion heats of the ferritic/martensitic alloys HT9 and 9Cr1Mo also obeyed the same relationship with a coupling coefficient estimated to be ≤1.0 x 10^{-2} MPa^{-1}, in remarkable agreement with the values observed in the austenitic alloy system.[7] This rather surprising result leads to the question "How generally valid is the application of the B_o and D values determined from these earlier studies to other alloys and metals?"

To test the general validity of these parameters requires simultaneous data on simultaneous creep and swelling covering a range of dpa levels where swelling is in progress. For most materials of interest this requires relatively high exposure levels. Most data fields meeting these criteria have already been analyzed in the earlier studies.

There is one data set, however, that not only meets these criteria but offers some unique features not available in other experiments. Harbottle studied the swelling and creep of 99.995% nickel at 350°C using pressurized tubes irradiated to ~4 dpa in the SILOE reactor.[9,10] These tubes were examined following each cycle of irradiation (500 hours) for a total of nine cycles.

Pure nickel is unique in that it swells initially at ~1%/dpa at temperatures below ~450°C with almost no incubation period, and then declines continuously thereafter in swelling rate with accumulated exposure.[11] This is in sharp contrast to the behavior of austenitic steels, which increase in swelling rate (to a maximum of ~1%/dpa) after a frequently extensive incubation period. Harbottle's data on creep in nickel

---

(a) Pacific Northwest Laboratory is operated for the U.S. Department of Energy by Battelle Memorial Institute under Contract DE-AC06-76RLO 1830.

pose a unique test for the validity of the B_o t $\dot{D}S$ relationship, which to date has been tested only on austenitic steels. Unlike such steels, nickel does not undergo any phase instabilities or the phase-related strains that accompany them.

RESULTS AND DISCUSSION

It is well known that thin walled pressurized tubes extend axially only in response to swelling and not creep.[12] Harbottle irradiated tubes at four hoop stress levels (0, 3, 10 and 30 MPa) and measured both axial and diametral strains. Examination of the axial strains showed that stress caused enhancement of void swelling (designated by Harbottle as volumetric creep) at the intermediate stress levels but did not enhance it significantly at 30 MPa. The small stress effect on swelling observed at 30 MPa peaked at ~1 dpa and was zero at 2.6 dpa. The tube was punctured at 3.0 dpa and returned for irradiation in the unpressurized condition.

The diameter strain data are shown in Figure 1. Note, that as the stress-free swelling rate decreased, the total deformation rate (including irradiation creep) in the stressed tubes also decreased. This is what one would expect from a metal obeying the B_o t $\dot{D}S$ model. The instantaneous stress-free swelling rate at 2.5 dpa was calculated from Figure l by this author to be 41.1×10^{-4} dpa^{-1}, three times the measured linear rate, or 13.7×10^{-4} dpa^{-1}. Figure 2 shows the true creep strain calculated by Harbottle after subtracting the swelling contribution represented by the axial strain. The instantaneous creep strain rate at 2.5 dpa was measured on Figure 2 by this author to be 5.71×10^{-4} dpa^{-1}. When divided by the hoop stress and converted to effective stress and strain, this yields an instantaneous creep rate of 2.53×10^{-3} MPa^{-1} dpa^{-1}.

When the instantaneous creep rate is divided by the instantaneous swelling rate, a creep-swelling coupling coefficient of 0.62×10^{-2} MPa^{-1} is obtained, in remarkable agreement with the coupling coefficient found in various austenitic steels. Since the swelling rate was declining rather than increasing, the general validity of the B_o + $\dot{S}$ model is therefore confirmed.

This procedure was repeated at ~0.5 dpa where the creep curve is much steeper and exhibits more curvature. It is therefore much more difficult to define an instantaneous creep rate. However, the coupling coefficient was determined to lie in the range 0.7 to 0.8×10^{-2} MPa^{-1}, confirming once again the general validity of this approach.

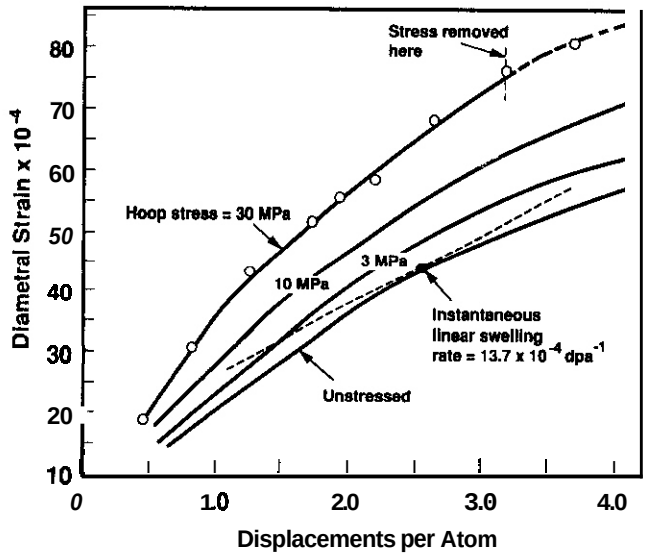

FIGURE 1. Total Diametral Strain (swelling + volumetric creep + irradiation creep) Observed for Four Stress Levels in 99.995% Nickel Pressurized Tubes Irradiated in SILOE at 350°C[9,10]

CONCLUSIONS

It appears that the simple B_o t $\dot{D}S$ relationship describing irradiation-induced creep is a generally valid relationship for a wider variety of materials than previously believed. It also appears that the

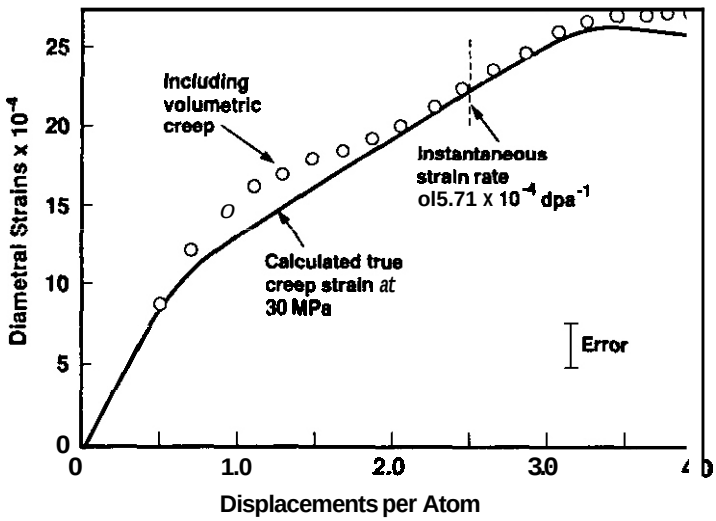

FIGURE 2. Diametral Creep Strains Calculated by Harbottle for 30 MPa Tube Shown in Figure 1.

creep-swelling coupling coefficient is -0.6×10^{-2} MPa^{-1}, a value relatively insensitive to metal or alloy composition and also to other environmental and material variables.

FUTURE WORK

This effort will continue, focusing on examination of the B_o term using data from U.S. mixed spectrum reactors and fast reactor data from other countries.

REFERENCES

1. D. L. Porter, F. A. Garner and G. O. Hudman, accepted for J. Nucl. Mater. (Proceedings of ICFRM-4) and also published in DOE/ER-0313/7, 133.

2. F. A. Garner, D. L. Porter and B. J. Makenas, J. Nucl. Mater., 148 (1987) 279.

3. D. L. Porter and F. A. Garner, ASTM STP 956 (1987) 11.

4. F. A. Garner and D. L. Porter, J. Nucl. Mater., 155-157 (1988) 1006.

5. D. L. Porter and F. A. Garner, J. Nucl. Mater., 159 (1988) 114.

6. R. W. Clark, A. S. Kumar and F. A. Garner, J. Nucl. Mater., 155-157 (1988) 845.

7. F. A. Garner and R. J. Puigh, accepted for J. Nucl. Mater., (Proceedings of ICFRM-4) and also published in DOE/ER-0313/7, 140.

8. F. A. Garner and R. J. Puigh, DOE/ER-0313/7, 114.

9. J. E. Harbottle, in Radiation Effects in Breeder Reactor Structural Materials, M. L. Bleiberg and J. W. Bennett, Eds., The Metallurgical Society, 1977, 455.

10. J. E. Harbottle, J. Nucl. Mater., 66 (1977) 258.

11. F. A. Garner, "Influence of Material and Environmental Variables on the Neutron-Induced Swelling of Nickel," this semiannual report.

12. C. R. Soderberg, Trans. ASME 58 (1936) 733.

VOID FORMATION AND PHASE STABILITY OF Fe-15Cr-15Mn-Ni ALLOYS IRRADIATED IN FFTF - S. Ohnuki, Hokkaido University, F. A. Garner, Pacific Northwest Laboratory,(a) H. Takahashi, Hokkaido University, J. M. McCarthy, Pacific Northwest Laboratory

SUMMARY

A series of Fe-15Cr-15Mn-XNi alloys (X = 0, 5, 10, 15) have been examined by transmission electron microscopy and X-ray microanalysis following irradiation in the FFTF/MOTA to 17-25 dpa at 420-550°C. All specimens were found to have developed features typical of radiation damage; i.e., voids, dislocations, and precipitates. Both void formation and radiation-induced phase instability were found to be strongly dependent on nickel content. Ferrite formed on grain boundaries in alloys with zero or low Ni content. Sigma phase often formed on the boundary between ferrite and austenite. With increasing nickel, both ferrite and sigma formation were suppressed. The density change was also found to be sensitive to nickel content. The phase instability and density change behavior are explained in terms of radiation-induced solute segregation and formation of lower swelling phases.

PROGRESS AND STATUS

Introduction

Austenitic stainless steels based on the Fe-Cr-Mn system are candidate materials for first wall fusion reactor applications due to their low induced long-term radioactivity compared to that of austenitic steels which contain nickel.[1,2] However, recent studies on simple Fe-Cr-Mn alloys have indicated that neutron irradiation at high temperatures leads to phase instabilities not encountered in nickel-stabilized steels.[3-6] Commercial Fe-Cr-Mn steels which are used for low temperature non-nuclear structural materials have also been examined after neutron irradiation and have been found to exhibit additional phase instabilities, especially at grain boundaries.[7] The aim of this study is to examine a number of simple Fe-15Cr-15Mn-XNi quaternary alloys irradiated in the Materials Open Test Assembly of the Fast Flux Test Facility (FFTF/MOTA), and to clarify the effect of nickel additions on void formation, phase instability and radiation-induced segregation. Nickel was chosen as the fourth element because it is usually contained in commercial alloys and because its segregation behavior is usually opposite that of manganese, possibly providing a way to reduce radiation-induced phase instabilities.

ExDerimental Procedure

Four alloys irradiated at three temperatures were examined by transmission electron microscopy. Nominal compositions of the alloys were Fe-15Cr-15Mn, Fe-15Cr-15Mn-5Ni, Fe-15Cr-15Mn-10Ni and Fe-15Cr-15Mn-15Ni in wt%. After solution annealing at 1000°C for 30 min these specimens were found to possess a fully austenitic structure. They were irradiated in the form of 3 mm disks in cycle 9 of FFTF/MOTA at temperatures of 420, 470 and 550°C, to damage levels of 25, 17 and 20 dpa, respectively. The temperatures were actively controlled within ±5°C.

Following irradiation, one or two specimens of each alloy were assigned for density change measurement and the others were provided for conventional transmission electron microscopy. Electropolishing proceeded using a conventional method employing an electrolyte solution of 5% $HClO_4$ in CH_3COOH. Microstructural examinations were performed on a 200 keV TEM, and compositional analysis (EDS) employed a STEM operating at 120 keV. Examination also proceeded on identical specimens of Fe-15Cr-15Mn which were thermally aged at the irradiation temperature. No aged specimens were available for the nickel-containing alloys.

RESULTS

Density Changes

Figure 1a shows the density changes observed after irradiation in these alloys.[6] There was a peak swelling value at ~10% Ni at each irradiation temperature. The maximum swelling occurred at 550°C even though the dose at 420°C was higher. A similar trend was also observed in Fe-30Mn-10Cr-XNi alloys as shown in Figure 1b.

(a) Pacific Northwest Laboratory is operated for the U.S. Department of Energy by Battelle Memorial Institute under Contract DE-AC06-76RLO 1830.

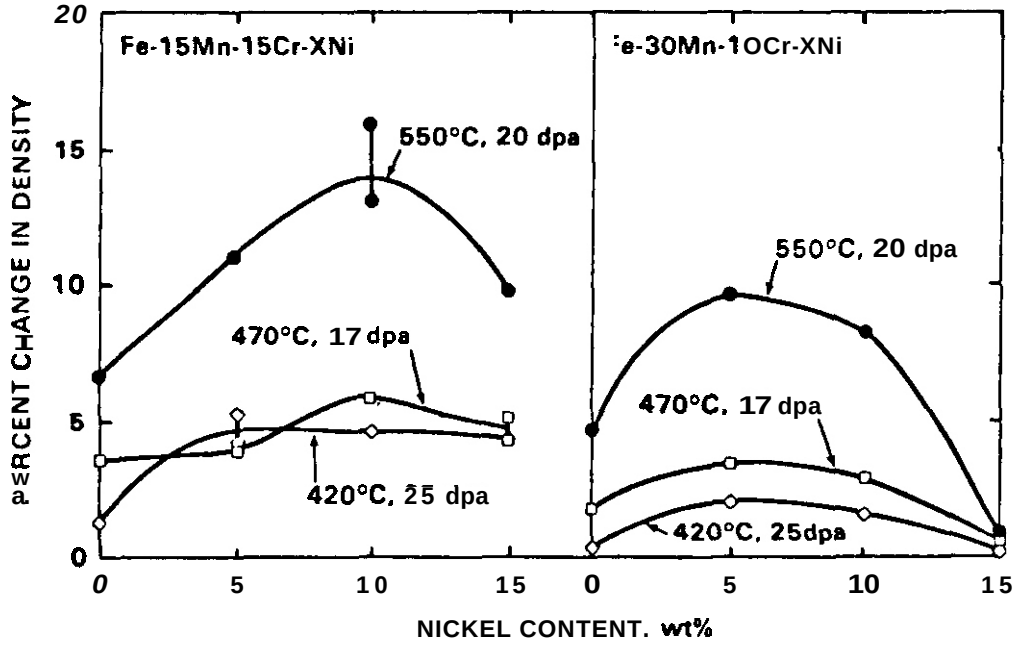

FIGURE 1. Density Changes Caused by Irradiation of Fe-15Cr-15Mn-XNi and Fe-10Cr-30Mn-XNi Alloys in FFTF/MOTA

Microstructures

Figures 2a-c show relatively low magnification microstructures including grain boundaries in Fe-15Cr-15Mn, Fe-15Cr-15Mn-5Ni and Fe-15Cr-15Mn-15Ni, following irradiation at 550°C. Three phases were found in low nickel alloys. The first and major phase contained large voids, stacking fault-like structures and dislocation line segments, and was identified as an austenite structure by using selected area diffraction patterns. The second phase was a ferritic structure which contained only dislocation loops and dislocations. The third phase was a blocky form of sigma, which was usually located at the boundary between austenite and ferrite. The ferrite was probably induced by the irradiation, since only epsilon martensite was observed in thermally aged specimens of Fe-15Cr-15Mn. Most importantly, the fractions of ferrite and sigma were reduced with increasing nickel content. The total ferrite and sigma content ranged as high as ~60% in some areas of both the nickel-free and low nickel alloys at the higher irradiation temperatures.

In all Fe-15Cr-15Mn-XNi alloys, voids on the order of 100 nm in diameter were distributed uniformly within austenite grains. The voids were clearly faceted, and their surfaces were often surrounded with ferrite precipitates at lower temperatures and strain contrasts at higher temperatures. Such contrast is generally ascribed to solute segregation and was observed even in the 15% Ni alloy. The size and number density of voids in the austenite phase of all four alloys were in the range of 50-100 nm and 1-2 x 10^{19} m^{-3}, respectively. Thus nickel additions did not change swelling very much in austenitic areas.

At lower irradiation temperatures, the microstructures were qualitatively the same as those at higher temperature. Figures 3a-c show grain boundary structures in Fe-15Cr-15Mn irradiated at different temperatures. At 470 and 550°C the structure was composed of austenite, ferrite and sigma phases. At 420°C a ferrite precipitate has just formed on a grain boundary triple point in austenite.

Microchemical Change

EDS analysis was performed at several kinds of areas, such as phase boundaries, grain boundaries and voids. Figure 4 shows the concentration changes observed near an austenite/ferrite boundary in Fe-15Cr-15Mn irradiated at 550°C. The manganese level is significantly reduced in the ferrite phase and chromium is slightly reduced.

Figure 5 shows compositions observed at a ferrite/ferrite boundary formed in Fe-15Cr-15Mn at 550°C. Both chromium and manganese contents were slightly depleted at the boundary, indicating that segregation at grain boundaries still proceeds in the ferrite phase after its formation. Measurements of composition at voids formed in austenite areas showed that both chromium and manganese were also depleted at voids.

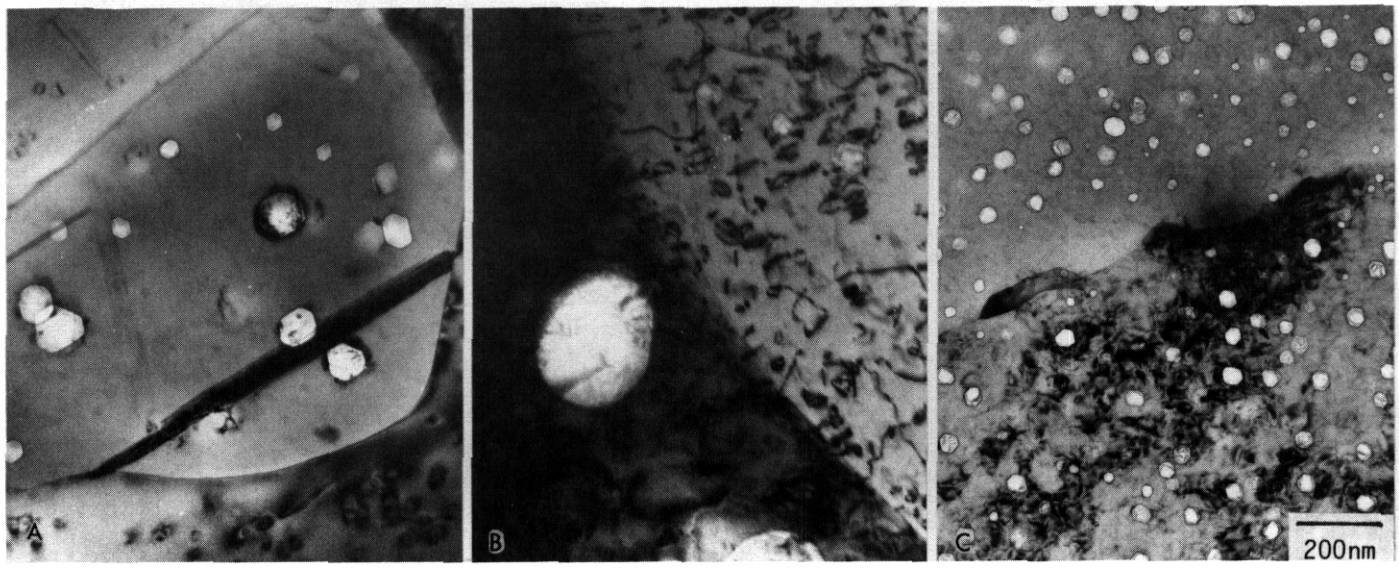

FIGURE 2. Typical Microstructures Observed in Fe-15Cr-XNi Irradiated to 20 dpa at 550°C. (a) 0% Ni, (b) 5% Ni and (c) 15% Ni

Figure 6 shows the concentration changes near an austenite/ferrite grain boundary in Fe-15Cr-15Mn-15Ni irradiated at 550°C, where a austenite boundary without any precipitate was selected for analysis. Chromium and manganese were depleted on the boundary, as expected. Nickel was enriched on the boundary, however, and the amount of segregation almost balanced that of chromium and manganese depletion. As a consequence of this balanced flaw, no second phases formed at this boundary.

Discussion

Garner and coworkers have shown that the swelling of Fe-Cr-Mn alloys is not very sensitive to composition compared to that of Fe-Cr-Ni alloys, but that manganese-stabilized steels are much more likely to develop phase instabilities.[2-5] The reason presented for the latter phenomenon was that nickel is a slow-diffusing element that accumulates at sinks while manganese is a fast-diffusing element that depletes at sinks. The resultant enrichment of iron, coupled with manganese depletion, leads to the tendency toward ferrite formation at all microstructural sinks.

The addition of nickel to Fe-Cr-Mn alloys apparently does not have much influence on void formation within the austenite but it affects the total amount of swelling by controlling the ratio of ferrite to austenite, since ferrite is well known to swell at a lower rate than austenite. In Fe-15Cr-15Mn the alloy resides close to the borders of austenite t ferrite and austenite t sigma regions. Segregation can easily drive portions of the matrix near grain boundaries into the ferrite and sigma regimes. This has been demonstrated in electron irradiations of Fe-Cr-Mn alloys.'

In general, the observed phase instabilities result from radiation-induced segregation and can be explained by the inverse Kirkendall effect' and/or size effects.[9,10] These effects are different in the details of the operating mechanism, but operate similarly in aggregate, and can be sumnarized as follows: a) slower diffusing and/or undersized solutes are enriched at defect sinks, and b) faster diffusing and/or oversized solutes are depleted at sinks. Elements in the Fe-Cr-Mn-Ni system are consistent with both mechanisms without contradiction. Since chromium and manganese are slightly oversized and faster diffusing solutes, they deplete from grain boundaries and void surfaces. Conversely, nickel is both an undersized and slower diffusing solute, and therefore segregates at sinks.

The segregation and phase change process operating in the Fe-Cr-Mn-Ni system can be explained by the simple model shown in Figure 7. Before irradiation, the concentrations of chromium and manganese are high enough to stabilize the austenite. Early during irradiation, depletion of chromium and manganese occurs on grain boundaries with increases of these elements occurring at some distance from the boundary. Ferrite

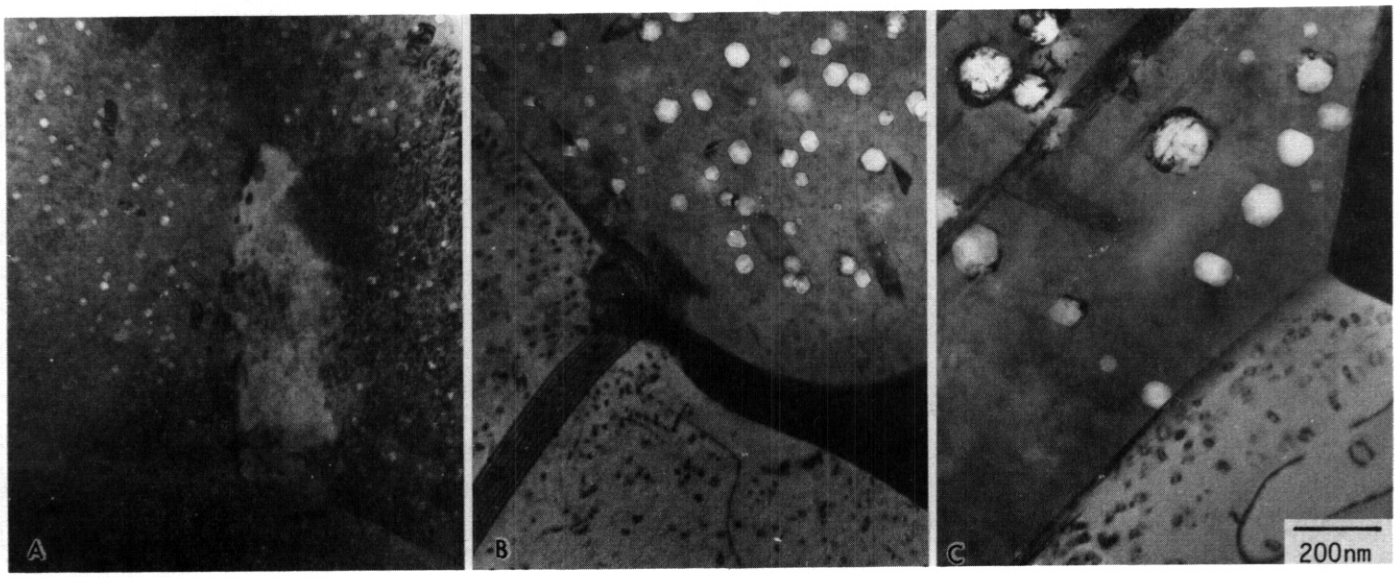

FIGURE 3. Typical Microstructures Observed in Fe-15Cr-15Mn Irradiated at Different Conditions. (a) 420°C, 25 dpa, (b) 470°C, 17 dpa and (c) 550°C, 20 dpa

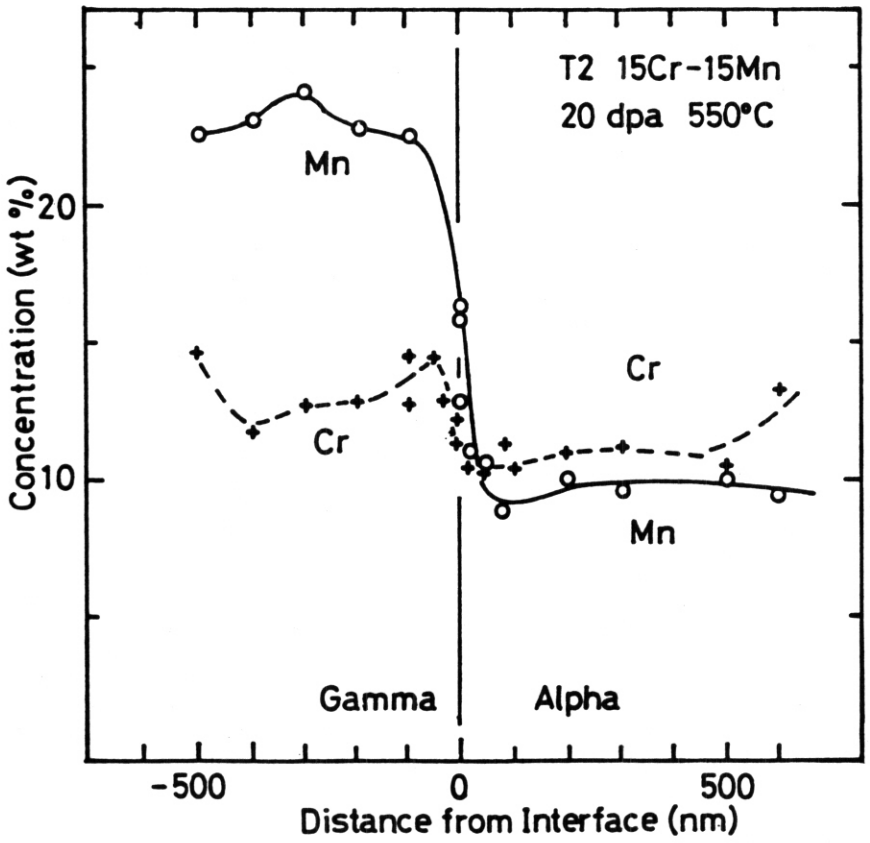

FIGURE 4. Microchemical Profiles Observed on an Austenite/Ferrite Boundary in Fe-15Cr-15Mn Irradiated to 20 dpa at 550°C

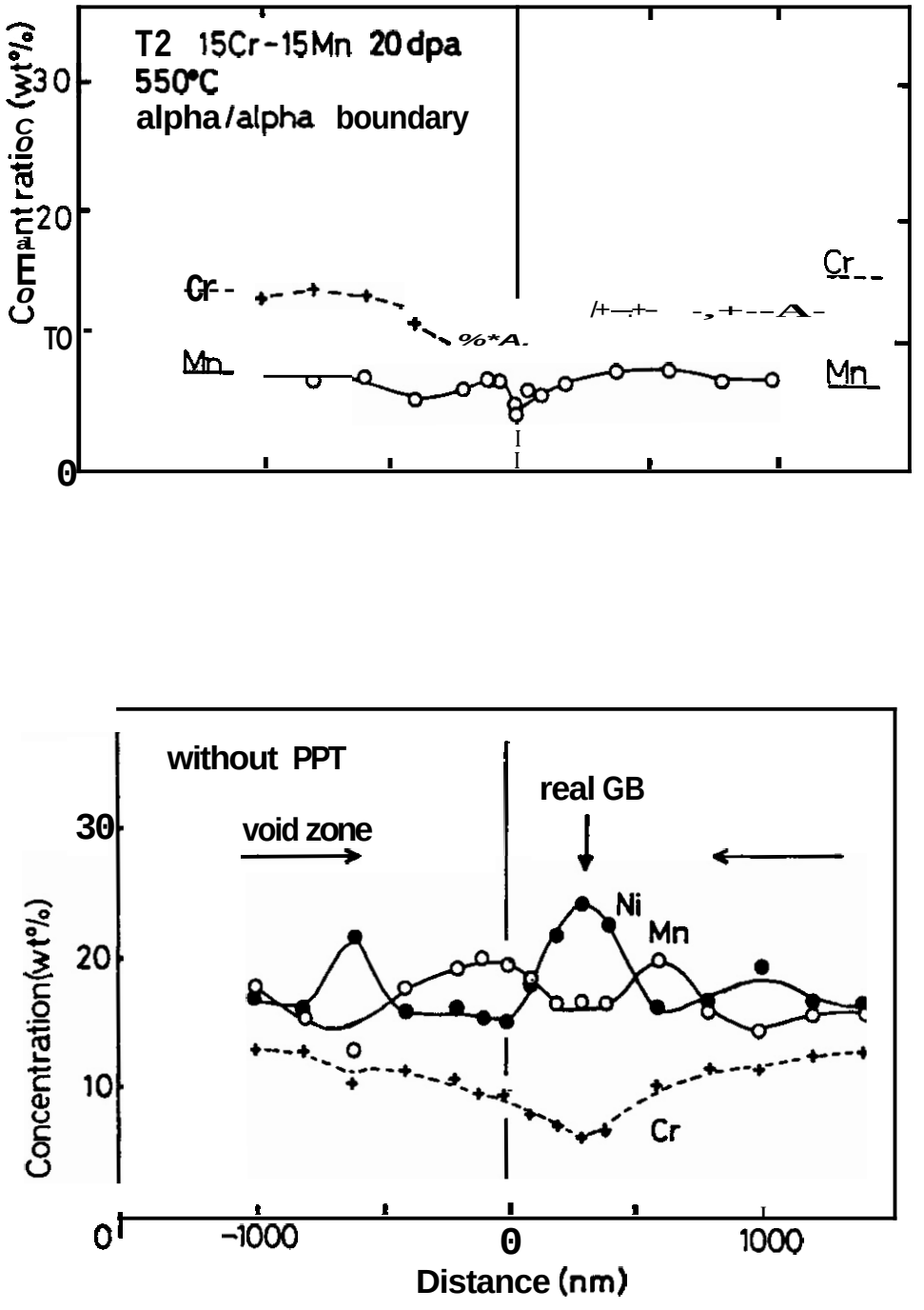

FIGURE 6. Microchemical Profiles Observed on an Austenite/Ferrite Boundary in Fe-15Cr-15Mn-15Ni Irradiated to 20 dpa at 550°C

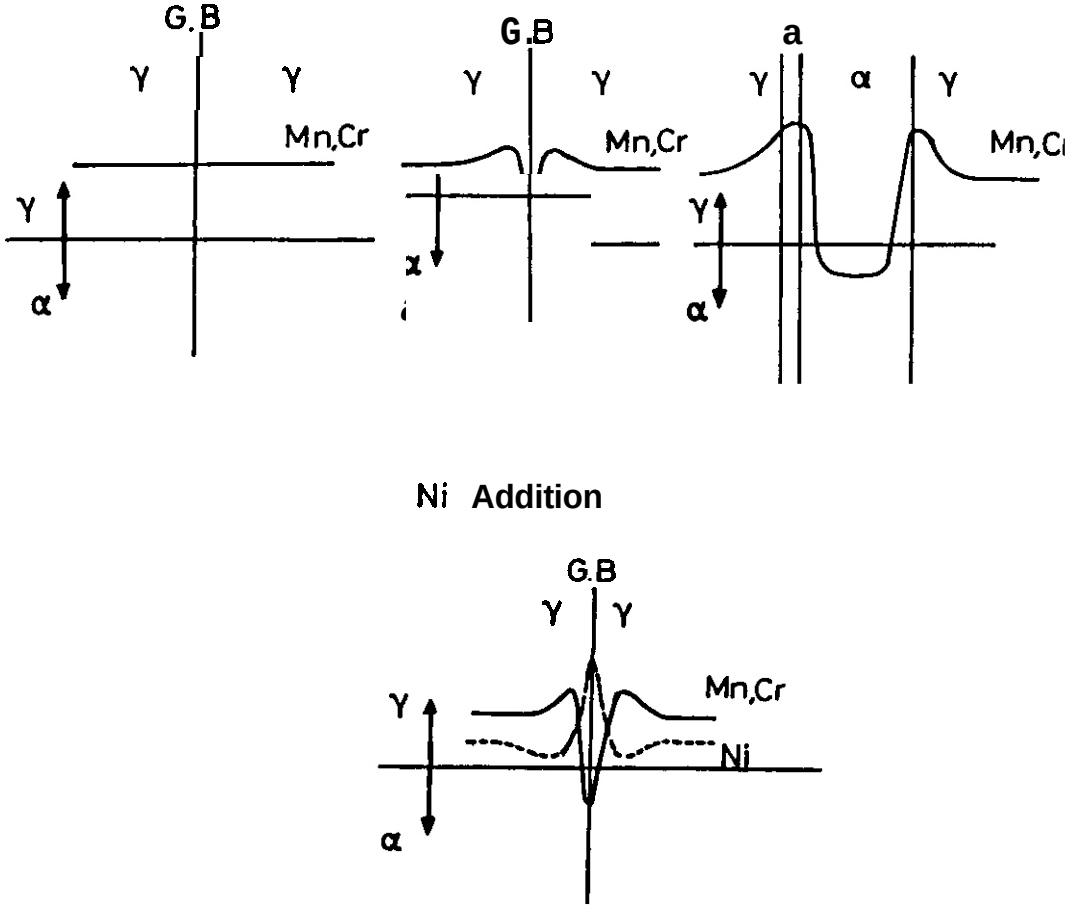

FIGURE 7. Schematic Illustration of the Transformation Process in Simple Fe-Cr-Mn and Fe-Cr-Mn-Ni Alloys During Radiation-Induced Segregation

precipitates then develop on the boundaries. In areas outside the ferrite, the local concentration of chromium and manganese may have increased sufficiently to form the sigma phase. Sigma formation has been shown in aqed Fe-Cr-Mn alloys to require the increased vacancy mobility associated with grain boundary migration. Thus less sigma is usually observed in annealed specimens than in cold worked specimens. Under irradiation, however, the formation of ferrite and the outward movement of its boundary may remove the necessity for cold working in order to form sigma. It is known, however, that formation of sigma and other intermetallic phases is also sensitive to manganese, nickel, solutes, thermomechanical starting state and temperature.[2,11-13]

If nickel is added to an Fe-Cr-Mn alloy, chromium and manganese still deplete from grain boundaries, but nickel is concurrently enriched on the boundaries. Nickel is a austenite-stabilizing element, stronger in its effect than that of manganese. Therefore, the effects of nickel segregation and outflow of chromium and manganese balance each other to retain phase stability.

CONCLUSION

Although nickel is not perceived as a low activation element, it may be prudent to retain some nickel in Fe-Cr-Mn base alloys to avert radiation-induced phase instabilities peculiar to manganese-stabilized alloys. It does not appear that such additions will have an adverse impact on the swelling behavior.

ACKNOWLEDGMENT

This work was conducted under the sponsorship of the Japan/U.S. collaboration for FFTF/MOTA irradiation The authors wish to acknowledge E. M. Dieffenbacher for specimen preparation, R. M. Ermi for density measurement and A. M. Ermi for FFTF/MOTA irradiation.

FUTURE WORK

This effort will continue, including a more detailed analysis of the effect of aging on the stability of these alloys.

REFERENCES

1. D. G. Doran, H. L. Heinisch and F. M. Mann, J. Nucl. Mater., 133-134 (1985) 892.

2. F. A. Garner, F. Abe and T. Noda, J. Nucl. Mater., 155-157 (1988) 870.

3. J. M. McCarthy and F. A. Garner, J. Nucl. Mater., 155-157 (1988) 877.

4. J. M. McCarthy, Fusion Reactor Materials Semiannual Progress Report, DOE-ER-0313/7.

5. F. A. Garner and J. M. McCarthy, ASTM STP 1047 (1990) 19-29.

6. F. A. Garner, H. R. Brager and H. Takahashi, accepted for publication in J. Nucl. Mater., also in this semiannual report.

7. H. Takahashi, K. Shiba, S. Nakahigashi, S. Ohnuki, H. Kinoshita and F. A. Garner in reference 5, pp. 93-102.

8. P. R. Okamoto and L. E. Rehn, J. Nucl. Mater., 83 (1979) 2.

9. H. Takahashi, S. Ohnuki and T. Takeyama, J. Nucl. Mater., 103-104 (1981) 1415.

10. J. F. Bates and J. L. Straalsund, Met. Trans., 5 (1974) 493.

11. Y. Okazaki, M. Mochizuki, K. Miyahara and Y. Hosoi, in reference 5, pp. 80-92.

12. N. Yukawa, M. Morinaga, K. Nishiyama, Y. Matsumoto, Y. Murata and H. Ezaki, in reference 5, pp. 30-46

13. W. Schüle, E. Lang and A. Panzarasa, Report EUR 11756 EN, 1988.

RADIATION-INDUCED MICROSTRUCTURAL DEVELOPMENT AND MICROCHEMICAL CHANGES IN Fe-Cr-Mn-Ni SOLUTE-BEARING ALLOYS — H. Takahashi and S. Ohnuki, Hokkaido University and F. A. Garner, Pacific Northwest Laboratory(a)

OBJECTIVE

The object of this effort is to determine the nature of the driving forces which tend to destabilize the austenite and to promote changes in dimensions in the Fe-Cr-Mn austenitic alloy system during irradiation.

SUMMARY

The density changes measured in three Fe-Cr-Mn-Ni solute-bearing austenitic alloys irradiated in FFTF-MOTA indicate that nickel additions do not decrease swelling as had been anticipated, but actually increase swelling initially. These data were confirmed by microscopy examination but are contrary to the behavior observed during electron irradiation of these same alloys. Nickel and commercially relevant solute additions also appear to suppress the formation of ferrite and sigma phases, which were observed in solute-free Fe-Cr-Mn ternary alloys irradiated in the same experiment.

PROGRESS AND STATUS

Introduction

The irradiation-induced swelling and phase stability of simple Fe-Cr-Mn austenitic alloys has been reported in earlier publications.[1,2] In general, it has been shown that the swelling of these alloys is less sensitive to comoosition than are comoarable Fe-Cr-Ni alloys. It was also shown that a areater dearee of phase instability exists in the Fe-Cr-Mn system. The differences in these two facets of-alloy behavior are thought to arise partially from the different influence of nickel and manganese on vacancy diffusion and also from their different impact on austenite stabilization. In particular, it was shown that relatively slow-diffusing nickel segregates at sinks while faster-diffusing manganese migrates away from microstructural sinks. The out-migration of manganese from sinks leads to nucleation of ferritic phases while nickel segregation keeps the various microstructural sinks safely within the austenite regime.

Nickel additions are known to delay void nucleation in the Fe-Cr-Ni system.[3] As shown in Figure 1, electron irradiation studies of Fe-17Cr-19Mn-XNi alloys with Si, P, C, Ni additions have exhibited similar behavior.[6] In order to study the interactive effects of nickel and manganese, a number of Fe-Cr-Mn-Ni austenitic alloys were irradiated in FFTF-MOTA. The motivation for studying these alloy systems was not only to see if nickel additions reduce swelling but also to ascertain whether the simultaneous segregation of nickel and the out-migration of manganese at sinks would balance, thereby promoting an increased level of phase stability. This paper addresses a subset of three Fe-Cr-Mn-Ni alloys, designated 813, 814 and B17, which incorporate solute levels typical of commercial manganese-stabilized alloys.

ExDerimental Oetai1s

The alloys in this study were chosen from those irradiated earlier with electrons,[6] being Fe-17Cr-19Mn-XNi with solute levels of roughly 0.5 Si, 0.02 P, 0.10 C and 0.16 N. These alloys contained relatively low nickel levels (55.9 wt%) and were irradiated in the annealed condition (1030°C for 0.5 hr and air cooled). The exact compositions of these alloys are shown in Table 1.

All alloys were prepared in the form of microscopy disks 3 mm in diameter by 0.25 mm thick and irradiated in static sodium in the Fast Flux Test Facility (FFTF) at ~ 3 x 10^{-6} dpa sec^{-1}. The specimens were placed in the Materials Open Test Assembly (MOTA-IO) which nominally controls the temperature to ±5°C. There was one abnormal temperature event of approximately one hour duration during the irradiation, the details of which are shown in Table 2. The range of neutron spectra over this assembly produces approximately 5 dpa for each 1.0 x 10^{22} n cm^{-2} (E>0.1 MeV); the dpa levels attained are also included in Table 2. The bulk swelling levels were measured using an immersion density technique which is accurate to ±0.16% change in density.

The microstructures of these alloys were observed using a 200 kV transmission electron microscope; compositional analysis was conducted using an energy dispersive X-ray analyzer.

(a) Pacific Northwest Laboratory is operated for the U.S. Department of Energy by Battelle Memorial Institute under Contract DE-AC06-76RLO 1830.

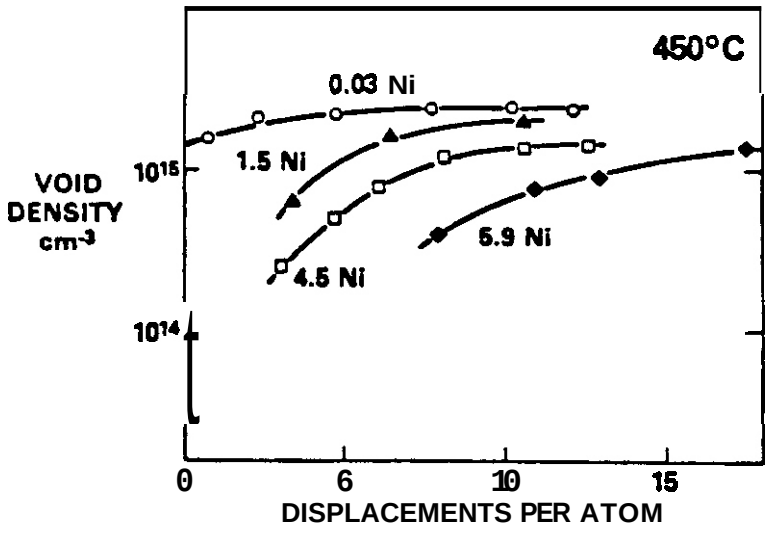

FIGURE 1. Effect of Nickel Level on Void Nucleation in 1.3 MeV Electron Irradiation of Fe-17Cr-19Mn-XNi Alloys series at 450°C.[6] The primary effect of nickel is to delay void nucleation and extend the transient regime of swelling.

Table 1

Composition of Alloys (wt%)

Designation	Cr	Mn	Ni	Si	C	P	N	Fe
813	16.83	19.49	0.03	0.54	0.10	0.020	0.162	bal
814	16.59	18.87	1.47	0.55	0.10	0.019	0.164	bal
B17	16.95	19.08	5.90	0.52	0.10	0.022	0.099	bal

Table 2

Temperature and Displacement Levels for MOTA-IO

Nominal Temperature (°C)	Displacement Exposure (dpa)	Off-Normal Events[a]
420	25	None
470	17	657°C for 70 rnin
550	20	749°C for 50 min
650	18	928°C for 50 min

(a) These events occurred at displacement levels which were -53% of the total exposures quoted above.

Results

The swelling as calculated from density change is shown in Figure 2. Contrary to our expectations, the effect of nickel additions is not to delay swelling but to increase it initially. While further nickel increases were sometimes found to decrease swelling, this happened only at relatively high nickel levels.

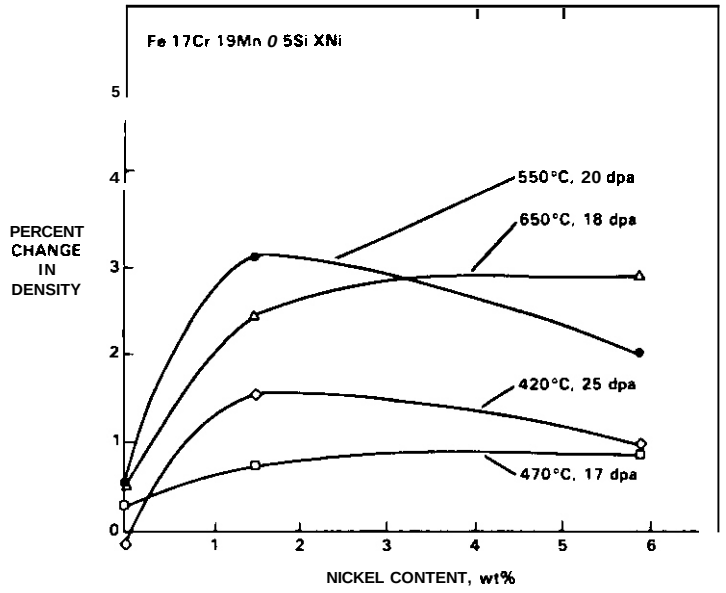

FIGURE 2. Neutron-Induced Swelling of Fe-17Cr-19Mn-XNi Alloy Series Irradiated in FFTF-MOTA as Measured by Density Change

Figure 3 shows that with minor exceptions the trends observed in the density change are mirrored in the swelling determined by electron microscopy. The void densities shown in Figures 4 and 5 decrease with temperature as expected and are relatively insensitive to nickel content at the higher nickel levels.

The void sizes are also relatively insensitive to nickel content, as shown in Figure 6. Unfortunately three of the specimens at the lowest nickel level did not survive electropolishing, and we assume from the bulk density behavior that the void densities at the lowest nickel level are lower for all temperatures. Typical microstructures of the two higher nickel alloys are shown in Figure 7 for each irradiation temperature. Some precipitates, mostly small carbides, are seen in the matrix.

Analysis of precipitation and segregation is in progress, with particular emphasis on the resultant modification of the matrix composition. Precipitation was often observed on the grain boundaries at higher irradiation temperatures. As shown in Figure 8, a compositional trace through a $M_{23}C_6$ grain boundary precipitate in the 1.5 Ni alloy (814) at 550°C showed it to be enriched in chromium as expected. The observed decrease in nickel and manganese levels is only a reflection of their displacement by chromium. Figure 9 shows that in a grain boundary area without precipitation, nickel segregates at the boundary and manganese and chromium are depleted, in agreement with the behavior expected as a consequence of their respective diffusivities and atomic sizes. Similar behavior has been previously observed in electron irradiation.' At 470°C the 1.5 Ni alloy also produced chromium-rich $M_{23}C_6$ precipitates, and a typical compositional profile across a precipitate is shown in Figure 10. Other phases such as ferrite and sigma were not observed to form at any temperature in the 1.5 Ni alloy, however.

Voids also are sites for segregation as shown in Figure 11. As expected, nickel segregates at voids at the expense of manganese and chromium.

Discussion

The lower swelling in these alloys compared to that of solute-free alloys' is thought to reflect primarily the presence of silicon and other solutes. Silicon is known to be a potent suppressor of void nucleation in many alloys.

Solute-free Fe-15Cr-15Mn has recently been shown to decompose during irradiation into ferrite and sigma phases, particularly at grain boundaries.' The addition of nickel to Fe-15Cr-15Mn tended to suppress the formation of these phases and it appears that the combined action of nickel, silicon and other austenite-stabilizing solutes in the current alloy series serves the same purpose. This may be the reason the low nickel alloy swelled less than alloys with higher nickel levels. If the low nickel alloy developed ferrite phases during irradiation it would not only have swelled less on the average, but its unanticipated presence may have caused a much more irregular electropolishing behavior, leading to the destruction of the specimens.

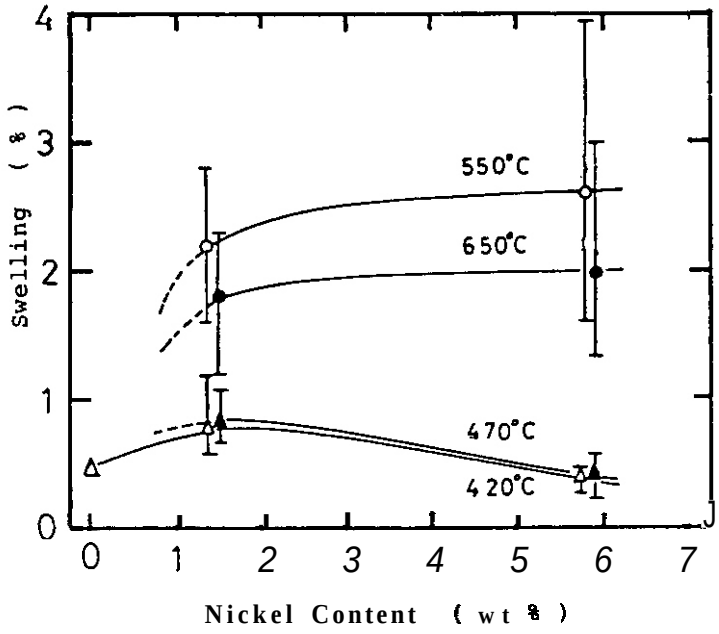

FIGURE 3. Effect of Nickel Level on Void Swelling in FFTF-MOTA Irradiation of Fe-17Cr-19Mn-XNi Alloy Series, as Determined by Microscopy Examination

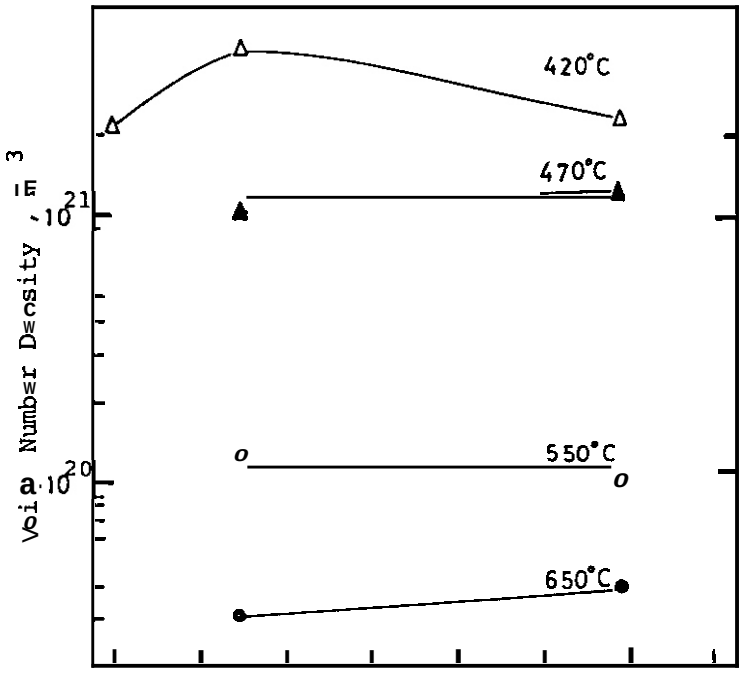

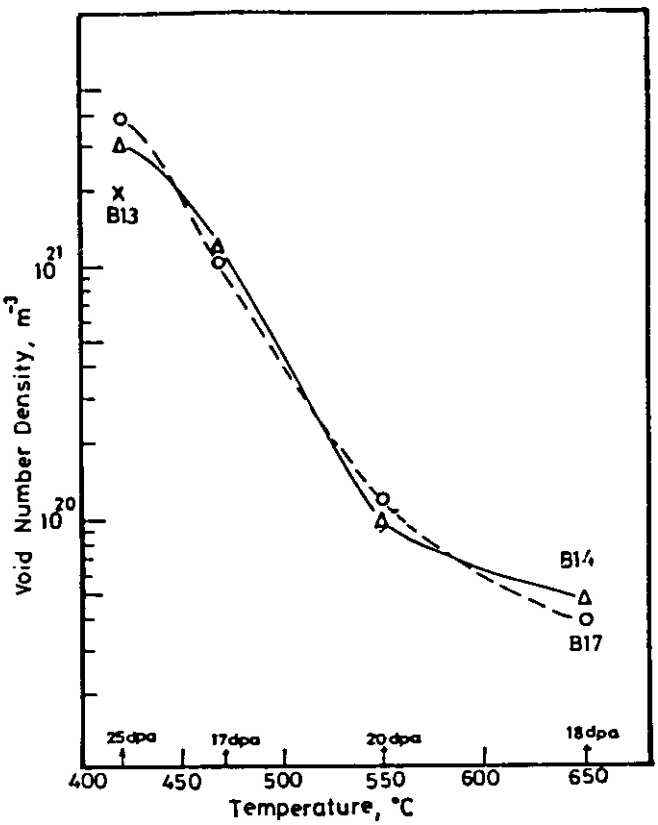

FIGURE 5. Void Densities Plotted vs. Irradiation Temperature

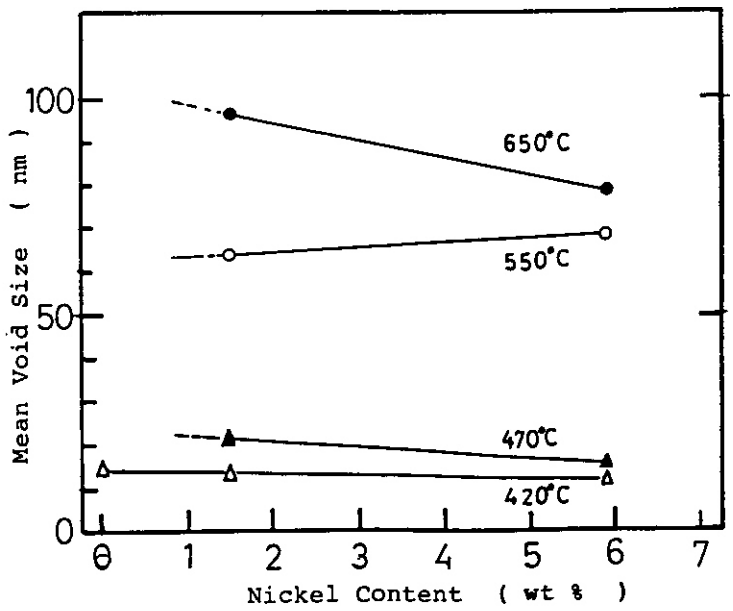

FIGURE 6. Mean Void Sizes Corresponding to Swelling Shown in Figure 3

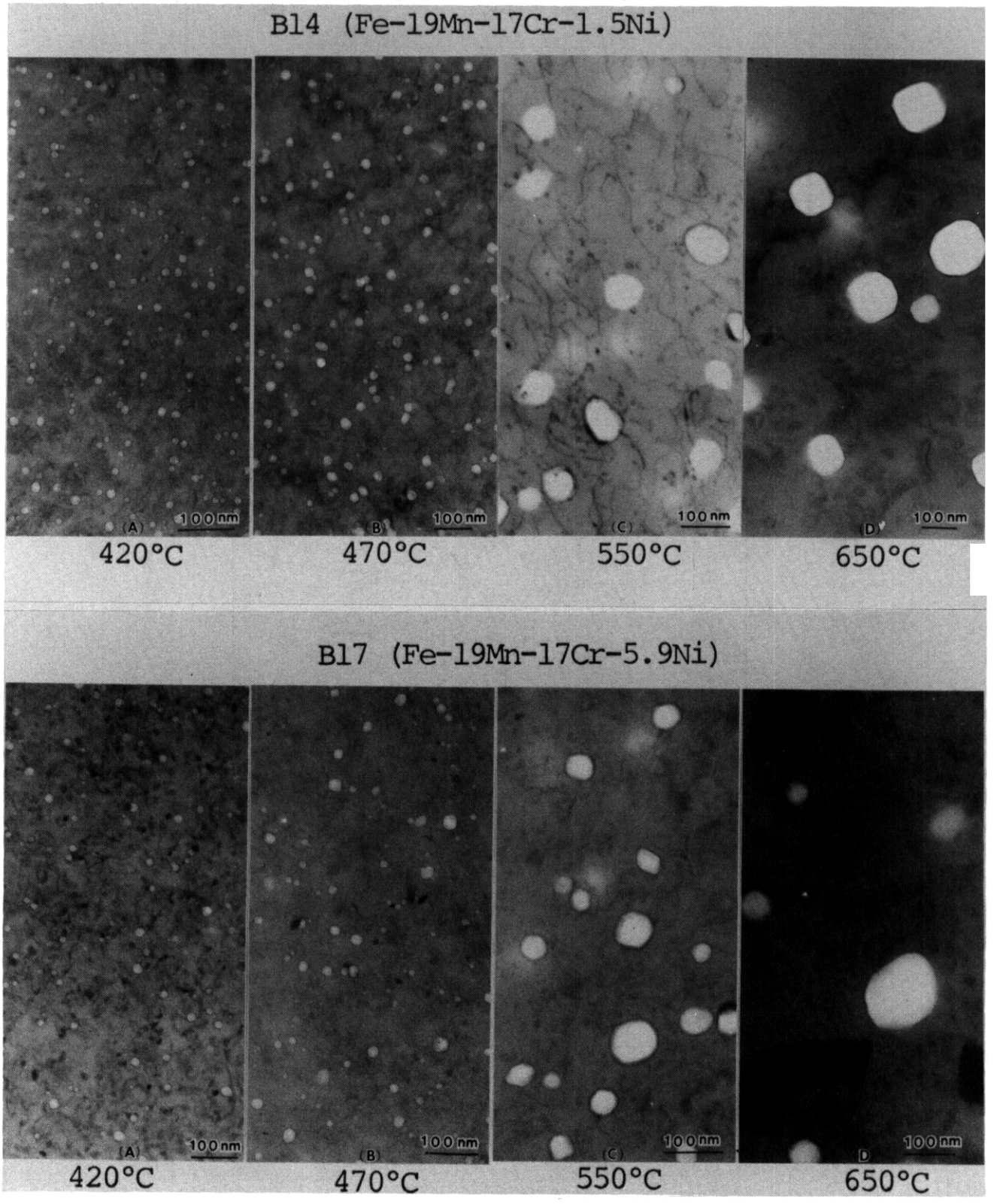

FIGURE 7. Microstructures Observed in Alloys 814 and B17 at Each Irradiation Temperature

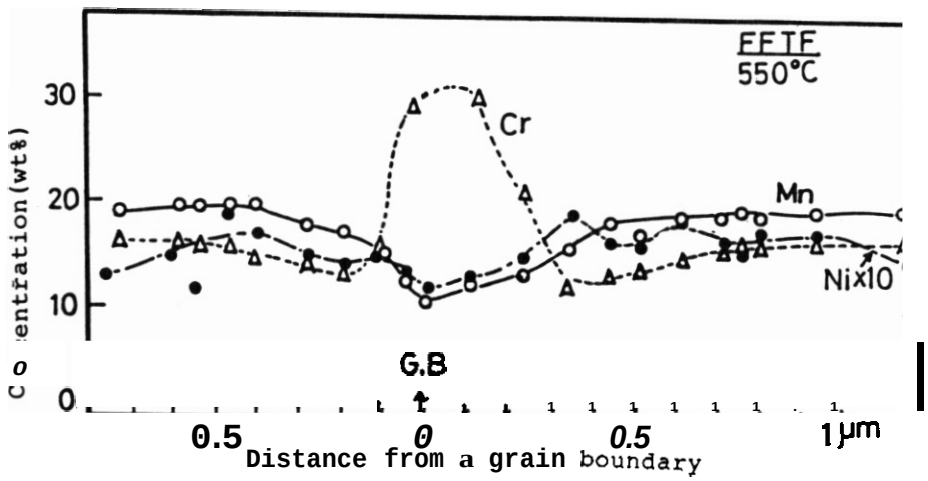

FIGURE 6. Concentration Profile Across a Grain Boundary $M_{23}C_6$ Precipitate After Neutron Irradiation of Alloy B14 at 550°C

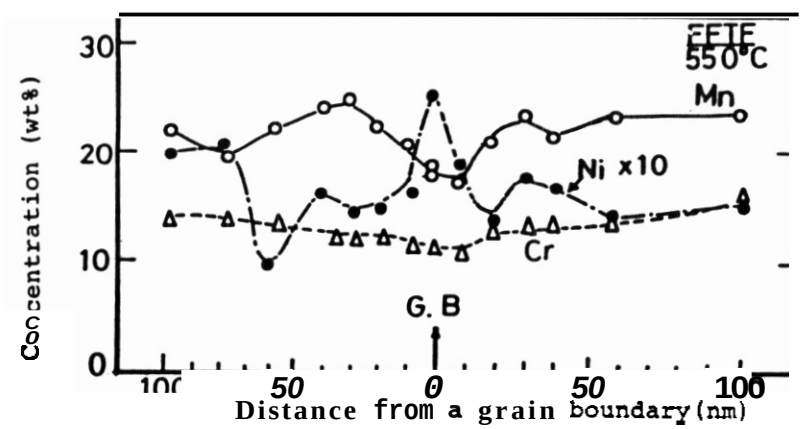

FIGURE 9. Concentration Profile Across a Grain Boundary Without Precipitation After Neutron Irradiation of Alloy B14 at 550°C

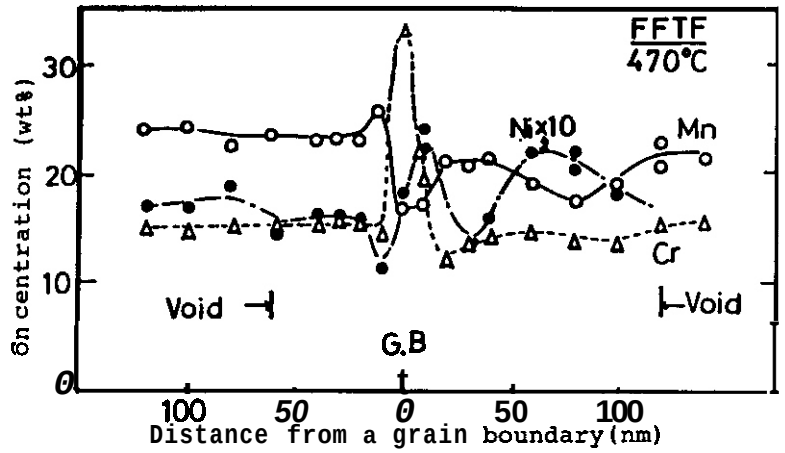

FIGURE 10. Concentration Profile Across a Grain Boundary $M_{23}C_6$ Precipitate in Alloy B14 After Neutron Irradiation at 470°C

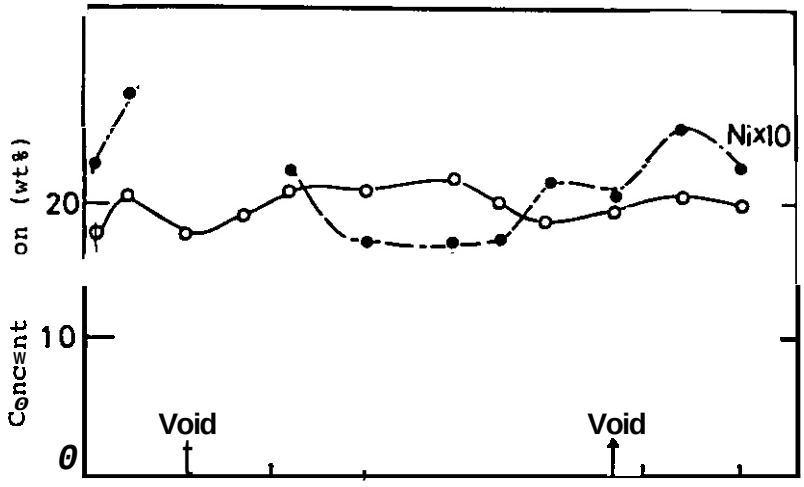

These results may not actually be in conflict with results from electron irradiation studies which showed nickel additions to decrease swelling. Note that the electron irradiation experiment was conducted at 450°C and at a displacement rate of 2 x 10^{-3} dpa/sec. If one assumes that a "temperature shift" arising from differences in displacement rate is necessary to correlate the neutron and electron irradiation data, these two experiments may not have been operating at comparable temperatures.

The lack of agreement of the swelling data with our expectation derived from electron irradiation studies signals that once again this alloy system is different from that of the simple Fe-Cr-Ni system and requires further study prior to development of a low-activation alloy based on the Fe-Cr-Mn austenitic system. While nickel per se must be reduced or removed to meet current low-activation guidelines, the interplay between nickel and manganese may teach us much about the nature of the driving forces tending to destabilize the Fe-Cr-Mn alloy system during irradiation.

The 1 hr temperature increase experienced halfway through this experiment is not thought to have affected these results very much. First, the trends observed with nickel content were the same for all four irradiation temperatures, even though the over-temperature event did not affect the 420°C capsule. Second, the over-temperature event also occurred to other subcapsules which experienced irradiation in MOTAs 1B, 1C and 1D. When data on Fe-Cr-Mn alloys from those capsules were plotted, there were no discontinuities observed.' Third, the trends with nickel and chromium content observed in solute-free quaternary alloys

irradiated in the same capsules' are consistent with those observed in Fe-Cr-Mn alloys at 16 dpa without an over-temperature event, probably reflecting the fact that the temperature-sensitive void nucleation stage occurs very early in these simple alloys.' The impact of the overtemperature event on phase stability cannot be so easily assessed, however.

CONCLUSION

The addition of nickel and silicon, as well as other austenite-stabilizing solutes to Fe-19Mn-17Cr changes not only its phase stability but also the swelling behavior. While silicon addition leads to depression of swelling, the addition of nickel leads to increased swelling, a behavior that is somewhat surprising and probably reflects nickel's role in phase stability more than its role in void nucleation. The suppression of ferrite and sigma formation during irradiation by nickel and other solutes is encouraging for development of reduced activation manganese-stabilized steels.

FUTURE WORK

Examination of the microchemistry and segregation of these alloys will continue.

REFERENCES

1. F. A. Garner, H. R. Brager, D. S. Gelles and J. M. McCarthy, J. Nucl. Mater., 148 (1987) 294-301

2. F. A. Garner, F. Abe and T. Noda, J. Nucl Mater., 155-157 (1988) 870-876.

3. J. M. McCarthy and F. A. Garner, J. Nucl. Mater., 155-157 (1988), 877-882.

4. F. A. Garner and H. R. Brager, pp. 195-206 in Radiation-Induced Changes in Microstructure. 13th International Symposium, ASTM STP 955, F. A. Garner, N. H. Packan and A. S. Kumar, Eds., American Society for Testing and Materials, Philadelphia, 1987.

5. F. A. Garner and J. M. McCarthy, pp. 19-29 in Reduced Activation Materials for Fusion Reactors, ASTM STP 1047. R. L. Kleuh. D. S. Gelles., M. Okada and N. H. Packan. Eds.. American Societv for Testing and Material;, Philadelphia, PA, 1990.

6. F. A. Garner and A. S. Kumar, pp. 289-314 in reference 4.

7. H. Takahashi, T. Takeyama, K. Tanikawa and R. Miura, J. Nucl. Mater., 133-134 (1985) 566-570.

8. S. Ohnuki, F. A. Garner, H. Takahashi and J. M. McCarthy, "Void Formation and Phase Stability of Fe-15Cr-15Mn-Ni Alloys Irradiated in FFTF," accepted for publication in J. Nucl. Mater.; also in this semiannual report.

NEW DEVELOPMENTS IN FUSION MATERIALS RESEARCH USING SURROGATE NEUTRON SPECTRA

F. A. Garner, Pacific Northwest Laboratory[a]

OBJECTIVE

The object of this effort is to determine the environmental and materials factors relevant to the use of data generated in fission reactors for application to fusion environments.

SUMMARY

The use of surrogate irradiation facilities to conduct fusion-relevant materials research requires that fission-fusion correlations be developed to account for the differences between the surrogate and fusion spectra. It is shown that with the exception of ^{59}Ni isotopic doping of nickel-containing alloys and irradiation in a temperature-controlled environment, it is almost impossible to study the effects of helium without introducing other important variables such as displacement rate, temperature history and solid transmutants. When helium effects are studied in the absence of differences in these variables, helium's impact on macroscopic properties is shown to sometimes be second order in magnitude. Differences in displacement rate and temperature history, however, can completely dominate experiments directed toward the study of PKA recoil spectra and helium/dpa ratio.

PROGRESS AND STATUS

Introduction

The absence of irradiation facilities possessing fusion-relevant neutron spectra at appropriate displacement rates requires that current fusion materials research proceed in surrogate facilities possessing nonrepresentative spectra and sometimes nonrepresentative displacement rates. Additional limitations arise in that some facilities have constraints placed on irradiation temperature by either the gamma heating level or coolant inlet temperature.

Data from surrogate neutron environments cannot in general be applied directly to fusion conditions without some type of translation that accounts for the differences between the surrogate and fusion spectra.[1] "Intercorrelation" or fission-fusion correlation experiments are under way to determine the nature of such translations.[2] These experiments fall into two broad classes, low fluence studies directed primarily toward PKA recoil spectra considerations and high fluence experiments concerned with transmutation and other factors.[1] These experiments can also be divided into two other categories, those involving comparative irradiations in two different neutron environments and those which involve side-by-side comparison of slightly modified materials in the same environment.

As these studies proceed it has become increasingly clear that in general most fission-fusion correlation experiments are not single-variable experiments. The sometimes inadvertent and even unrecognized introduction of unavoidable second variables can distort or even dominate the experiment, possibly yielding misleading or invalid conclusions about PKA recoil spectra or transmutation effects. This paper first explores the influence of such second variables on the interpretation of intercorrelation experiments. Second, a comparison of the early results of a series of related on-going experiments is presented to demonstrate the combined influence of several of these variables on the intercorrelation process.

TemDerature and TemDerature History

There are a variety of ways in which differences in temperature history can complicate the interpretation of comparative irradiation experiments. Kiritani has shown that low fluence intercorrelation studies conducted in the early stages of transient microstructural development are particularly vulnerable to the details of how different reactor facilities are brought to power.[3] This is particularly important when the irradiation temperature is determined by the power level of the reactor, a situation where the early stages of the irradiation are conducted at lower than desired temperatures.

Another example was recently provided by Yoshida and coworkers who compared the very different microstructures developed in irradiation of AISI 316 at the Omega West Reactor and the RTNS-II 14 MeV neutron source.[4] While the RTNS-II experiment was essentially a continuous irradiation with independent temperature control, the Omega West Reactor was operated for a single E-hour shift each day and the temperature of the irradiation vehicle during the daily ascent to full power was somewhat dependent on the power level. This introduced repeated transients in displacement rate and, more importantly, temperature. Whereas the spectral effects comparison of Heinisch[1] on these same specimens (see Figure 1) was originally interpreted in terms of recoil spectra and the possible influence of displacement rate at higher temperatures, it now appears that temperature history also played a strong role.

(a) Pacific Northwest Laboratory is operated for the U.S. Department of Energy by Battelle Memorial Institute under Contract DE-AC06-76RLO 1830.

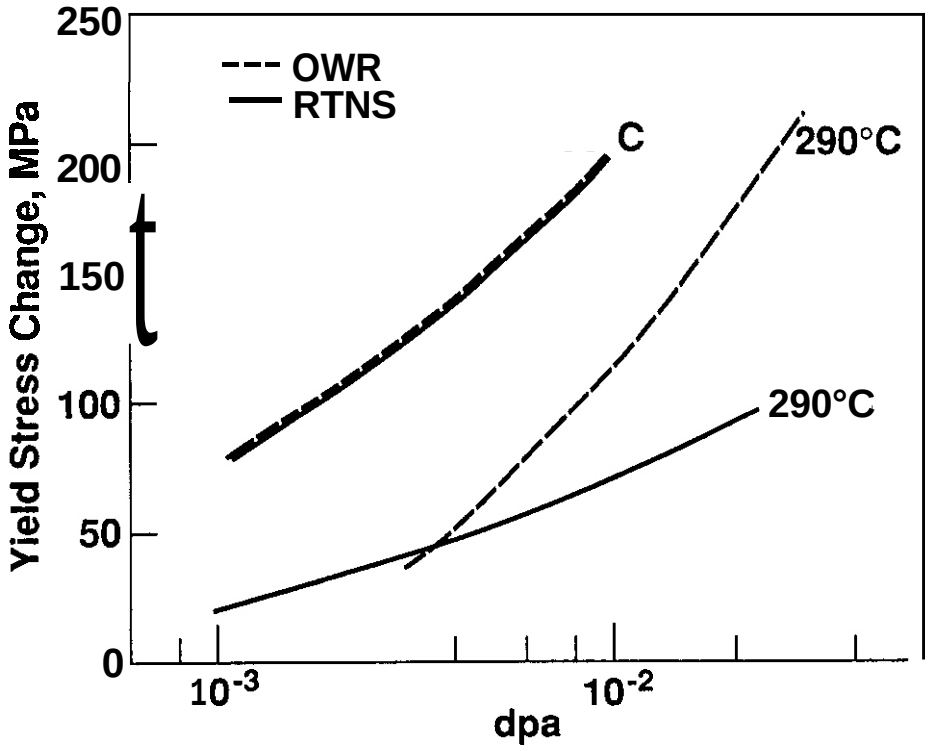

Figure 1. Yield Strength Changes Observed in Annealed AISI 316 After Irradiation Either in the Omega West Fission Reactor or in the 14 MeV neutron spectrum of RTNS-II. Heinisch' originally interpreted these results as showing a good correlation based on PKA recoil spectra at 90°C, with displacement rate differences exerting their influence at higher temperature. It now appears that temperature history effects were strongly involved in producing the divergent behavior at 290°C.

High flux mixed-spectrum reactors have very large gamma heating rates. It is ~54 watts per gram for steel in the central portion of the High Flux Isotope Reactor (HFIR) at Oak Ridge National Laboratory. The temperature is thus determined solely by the gamma heating rate and the thermal resistances selected to control the local environment. This is a very unforgiving thermal environment, often leading to substantial and time-dependent changes in temperature in response to perturbations in neutron flux or small changes caused by swelling and irradiation creep in the thermal resistances. Data from such reactors usually exhibit a much larger amount of scatter when compared to experiments involving active temperature control. In addition, gama heating levels of this magnitude are sensitive to many design variables and are difficult to calculate and measure. Referring to the often cited work by Bloom and Wiffen[6] shown in Figure 2, Garner' has shown that early comparisons of HFIR and fast reactor data are inconclusive with respect to the influence of helium. This is due primarily to the original substantial underestimate (33 watts per gram) of gamma heating in HFIR and secondarily to changes required in the quoted dpa levels.

More recent studies involving comparison of HFIR and fast reactor data show that the influence of large differences in helium on mechanical properties is not very significant,[7] although the reason for the nonresponsiveness compared to the behavior shown in Figure 2 were attributed by the authors to improvements in the steel (cold working and solute modification) rather than better determination of irradiation temperatures and dpa levels.

An additional consideration lies in the fact that gamma heating arises from a number of sources; prompt gamnas from the fission event, delayed gamma's from fission products and inelastic scattering events. The latter contribution is most pronounced in water cooled reactors. The delayed contribution requires some time after start-up to reach its equilibrium value. Thus the gamma heating rate is time-dependent and the temperature is likewise time-dependent.

In high fluence intercorrelation experiments the impact of temperature uncertainties and temperature variations depends somewhat on the property being examined. Tensile properties exhibit saturation levels that are relatively sensitive to temperature.' While the incubation period of void swelling is also very sensitive to flux temperature, and temperature history, the steady-state swelling rate is not very responsive to differences in temperature or displacement rate.[9] It has been shown that while deliberate or unavoidable changes in temperature can affect the transient regime of swelling, changes in temperature

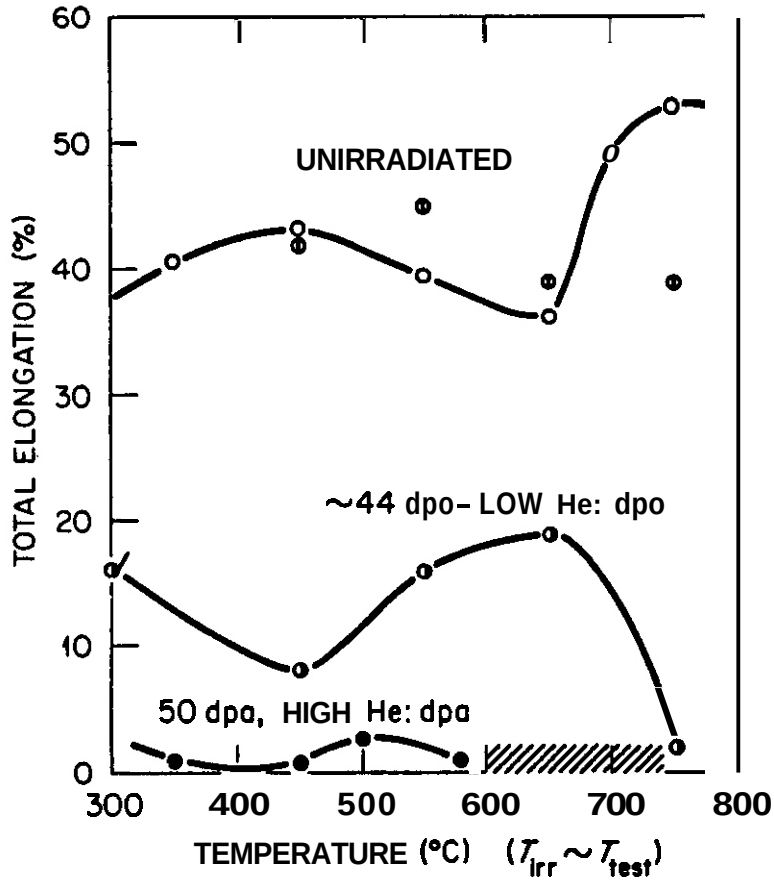

Figure 2. An Early Estimate of the Effect of Helium/dpa Ratio on Irradiation-Induced Changes in Tensile Properties of Annealed AISI 316 Irradiated in the DFR Fast Reactor and HFIR.[6] The temperatures for the HFIR data and the displacement levels for both reactors require significant revision, thus invalidating the conclusion drawn in the original paper concerning the strong influence of helium/dpa ratio. The revised dpa levels are 37 and 57 dpa for DFR and HFIR, respectively.

introduced in the post-transient regime have little effect, even though the microstructures developed in isothermal and temperature-change irradiations can be quite different."."

Flux Effects

Many fission-fusion correlation studies directed toward helium or spectral effects are conducted by necessity at different displacement rates. In a recent review article by Garner and coworkers, however, it as shown that even relatively modest differences in displacement rate can exert pronounced influence on the swelling, irradiation creep and tensile properties of stainless steels at high neutron exposure.' The transient regime of these properties is particularly sensitive to differences in displacement rate.

Kiritani has shown that low fluence spectral effects experiments are also flux-sensitive.'* Figure 3 shows the results of low fluence swelling comparisons of pure nickel by Muroga and coworkers,[13] who concluded that their results could not be interpreted solely in terms of spectral differences because the experiment was dominated by the large difference in displacement rates. Even relatively small differences (factors of 2 or 3) in neutron flux can lead to pronounced effects in pure nickel,[14] however, as shown in Figure 4.

Disolacement Considerations

Recently, several previously unrecognized contributions to the displacement process have been examined. The recoil of the iron atom in the $^{58}Ni(n,\gamma)$ $^{59}Ni(n,\alpha)$ ^{56}Fe reaction used to produce helium in many studies can cause a time-dependent increase of as much as 90-100% in the displacement level of pure nickel when irradiated in a mixed spectrum reactor.[15] Thus studies of the separate and synergistic effects of helium and nickel content necessarily involve nickel-dependent differences in displacement rate. This may be a small or large contribution, depending on the design of the experiment. It is small in the studies shown in Figures 3 and 4 and most pronounced in mixed spectrum reactors. For instance, the displacement level quoted for the HFIR data in Figure 2 must be increased -13% to account for the ^{59}Ni contribution.

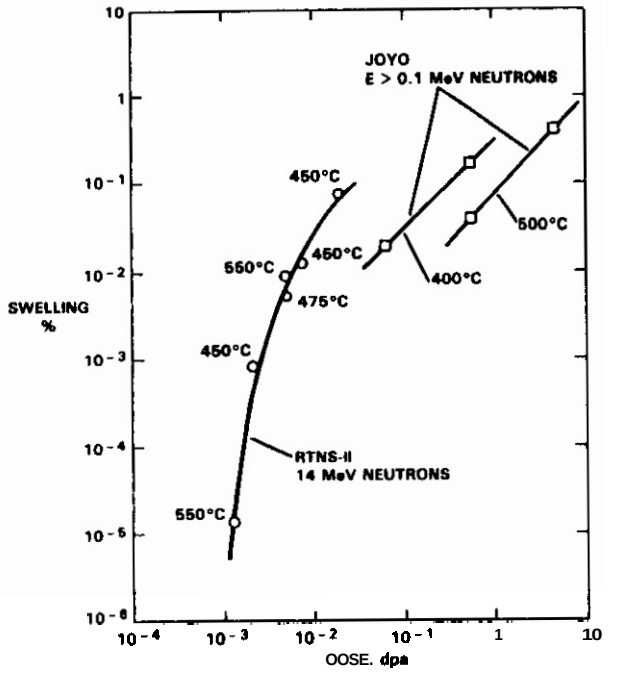

Figure 3. Swelling Observed in Nickel During a Correlation Experiment Conducted at Vastly Different Displacement Rates.[13] Swelling is seen to be dependent on temperature at the higher displacement rate of the JOYO reactor but not at the lower displacement rate of RTNS-II. Flux effects are thought to have dominated over PKA recoil spectra considerations in this experiment.

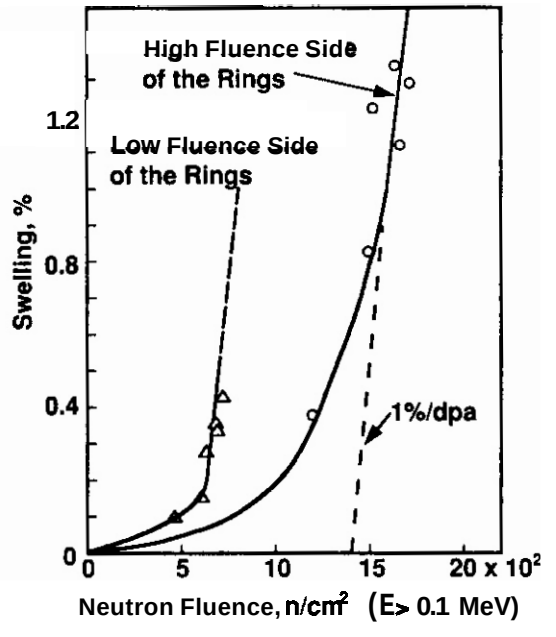

Figure 4. Swelling Observed in Ni-200 (99.6% Ni) Across a Series of Stacked Ring Samples Lying in a Neutron Flux Gradient.[14] The temperatures do not vary significantly across the rings. While the steady state swelling rate is relatively insensitive to temperature (399-488°C) and displacement rate, the incubation period is very flux-sensitive.

Another potentially more significant contribution to the displacement process arises from the realization that displacements associated with (n,γ) events induced by thermal neutron capture may influence damage production disproportionately due to their greatly reduced levels of point defect recombination.[1,16,17] Thus, irradiation in mixed spectrum reactors may appear to involve only 1 or 2% thermal neutron contributions to calculated displacement levels, but may actually involve much greater levels of survivable point defects compared to those produced in high energy cascades.

Transmutation Effects

Most transmutation studies are directed toward the influence of the gaseous transmutants helium and hydrogen. However, the impact of solid transmutants is sometimes strongly involved in comparative irradiations directed toward the evolution of microstructure or macroscopic properties. A recent review article presented three examples where solid transmutant differences influenced experiments in either a minor, moderate or major manner.' These were studies on AISI 316 stainless steel, copper alloys and aluminum alloys, respectively.

The solid transmutants produced in copper and aluminum can in some spectra dominate the response of these metals more than any other variable, thus rendering these metals unsuitable for helium or PKA recoil spectra effects studies where different reactor spectra are employed. A similar situation exists for manganese-based reduced activation alloys and to some extent for alloys containing vanadium and chromium.[18]

Some helium effects studies involve the side-by-side irradiation of ferritic steels with and without low levels of nickel in mixed spectrum reactors to produce different helium/dpa ratios by transmutation of nickel.[19] This approach assumes that nickel does not itself alter the behavior of the steel. Two ion bombardment studies have shown, however, that nickel does influence the microstructural evolution and swelling of ferritic alloys.[20,21] Helium and nickel effects therefore compete in these experiments.

A more subtle solid transmutant problem exists in the use of ^{10}B to generate helium within an alloy.' Since both lithium and helium are light elements, this technique does not introduce significant amounts of additional displacements and thus involves no differences in displacement rate. Unfortunately, while one can adjust the $^{10}B/^{11}B$ ratio to avoid differences due to the chemical effect *of* boron, one cannot avoid the influence of the lithium transmutant that accompanies the helium. Various studies have shown that lithium exerts a strong effect on microstructural evolution of stainless steels and various pure metals.[22-28] The lithium effect is particularly obvious when the helium and lithium influences are separated by use of the "halo effect" around small precipitates.[25] In recent studies, Zinkle and coworkers employed ^{10}B to study in side-by-side irradiations the effects of helium on microstructure and swelling in pure copper.[29,30] While the details of the microstructure were found to be quite sensitive to the ~100 appm helium formed early in the irradiation, the overall swelling over a wide temperature range was remarkably similar to that of copper irradiated without boron. While it is tempting to conclude that helium's macroscopic influence on swelling in copper is small, one cannot ignore the unknown, concurrent and possibly synergistic influence of ~100 appm lithium.

Spectral Comparisons and Isotopic Tailorina Experiments

A number of comparative irradiation experiments involving mixed spectrum and fast reactors have been conducted at relatively high fluence levels, primarily to study the effect of helium. The result of most of these were discussed in a recent review paper by Mansur and Grossbeck. Two of these experiments on various austenitic stainless steels are of particular interest[31,32] and show that there is an apparent increase in swelling and creep rate that occurs at the intermediate helium/dpa ratios found in the Oak Ridge Research Reactor (ORR) compared to the lower and higher ratios found in FFTF (Fast Flux Test Facility) and HFIR. Unfortunately, ORR operates at a displacement rate that is almost an order of magnitude smaller than that of the other two reactors. The increase in swelling observed in ORR is consistent with the observed effect of displacement rate on swelling,[1] and creep is known to accelerate in the presence of swelling.[9] Each of these three reactors also exhibit different temperature histories. How do we separate the various contributions of spectrum, helium/dpa ratio, displacement rate and temperature in such experiments?

In a comprehensive effort to study the separate and synergistic effects of helium and other variables involved in comparative irradiations of austenitic alloys, a series of closely related experiments on simple Fe-Cr-Ni alloys is in progress. The approach of these studies is to first determine in some detail the major compositional and environmental sensitivities of Fe-Cr-Ni model alloys irradiated in the EBR-II (Experimental Breeder Reactor-11) and FFTF fast reactors. The roles of phosphorus, silicon and titanium are also included in these studies since precipitates formed by these elements are often invoked to play a role in the distribution and action of helium.[7] Some early results of these continuing studies are documented in other papers.[33-37] These fast reactor results are then being compared with the behavior of subsets of these alloys which were irradiated in spectrally tailored experiments in ORR,[38-39] companion nontailored experiments in EBR-II[38,39] and in ^{59}Ni isotopic-doping experiments in FFTF.[40-42]

When first comparing the results of the AD-1 and MFE-4 irradiations in EBR-II and ORR it appears that there may be some possiblity that the higher helium/dpa ratio in ORR alters both the swelling and mechanical

behavior, as shown in Figures 5 and 6. However, a direct helium-based comparison ignores the differences in total dose and dose rate encountered in the two reactors. It also ignores the impact of the ^{59}Ni dpa contribution on the experiment. Given the demonstrated influence of these variables it is unwise to ignore their potential dominance of the experiment. The complexity of this type of comparative experiment is further illustrated in Table 1, which shows that these "comparable" irradiations were actually conducted at a variety of dose levels, even within each experiment. This is a consequence of the operating characteristics and limitations associated with reactor use.

The most promising approach currently available to explore the separate and synergistic effects of helium and other variables involves the use of nickel isotopic tailoring, which allows side-by-side comparisons of helium effects at fusion-relevant generation rates. This technique can be used in a variety of reactor spectra by employing ^{59}Ni additions or by making adjustments in the $^{58}Ni/^{60}Ni$ ratio.[44,45]

Isotopic doping with ^{59}Ni combined with the on-line temperature control (±5°C) available in the FFTF Materials Open Test Assembly is an approach which can unambiguously separate the contributions of various important variables.[45] Even in the event of nonisothermal irradiation, the doped and undoped specimens experience exactly the same temperature, spectrum and flux history. For a doped 25% nickel alloy producing 10 appm/dpa in FFTF, the ^{59}Ni contribution contributes only a 0.4% increase in dose rate, producing essentially a one-variable experiment designed to study helium effects in competition with other important variables.

In the first series of microstructural studies the interactive effects of helium, temperature, nickel level, phosphorus addition and cold-working were investigated.[40-43,45] While higher helium generation rates were shown to influence somewhat the details of the microstructure, the effect of helium was in general small and secondary to that of all other variables studied. In mechanical property measurements it was clearly shown that in the absence of other perturbing variables, the influence of helium was rather minor as shown in Figures 7 and 8. This conclusion is in sharp contrast to the conclusion one could draw in an uncritical assessment of Figure 6. Further studies now in progress will test the validity of this conclusion at higher fluence levels.

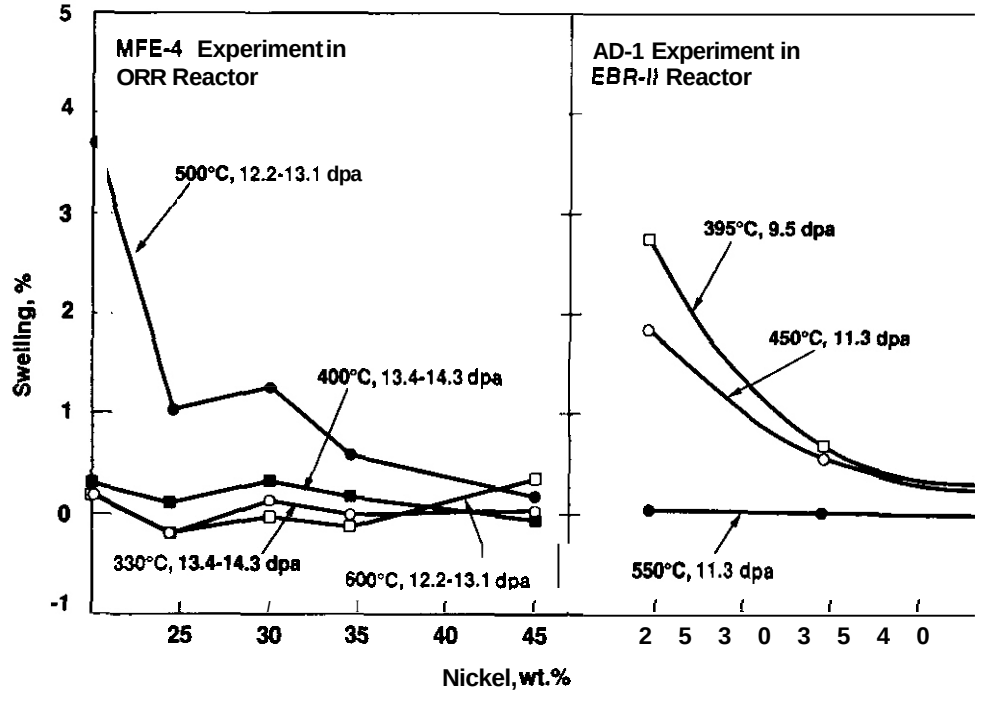

Figure 5. Comparison of the Swelling Behavior of Fe-15Cr-XNi Alloys In ORR and EBR-II as a Function of Temperature and Nickel Content.[38] The ORR dpa levels vary with nickel content due to the ^{56}Fe-induced contribution. At ~400°C there is an apparent suppression of ORR-induced swelling relative to that in EBR-II. The helium/dpa ratios are rather large, ranging from 27 to 58 as the nickel level inceases.

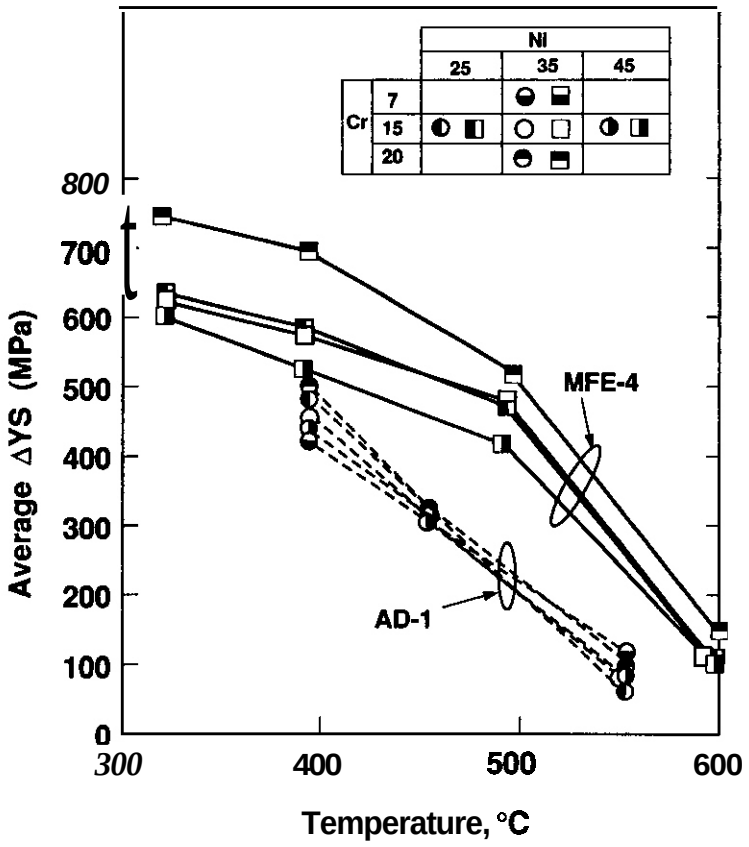

Figure 6. Comparison of Yield Strength Changes of Fe-15Cr-XNi Alloys Observed in ORR and EBR-II as a Function of Temperature and Nickel Content.[38] The ORR data are at higher dpa levels and were generated at lower calculated displacement rates.

TABLE I. Displacement and Helium Levels in MFE-4 and AD-1 Experiments

Composition (wt%)	330 and 400°C		500 and 600°C	
	dpa	He, appm	dpa	He, appm
Fe-19.7Ni-14.7Cr	13.4	371	12.2	332
Fe-24.4Ni-14.9Cr	13.6	463	12.4	414
Fe-30.1Ni-15.1Cr	13.8	555	12.6	495
Fe-34.5Ni-15.1Cr	14.0	647	12.7	573
Fe-45.3Ni-15.0Cr	14.3	832	13.1	140

The two displacement levels in AD-I experiment were relatively independent of composition: 9.5 dpa at 394°C, 11.3 dpa at 450 and 550°C. The helium/dpa ratios, however, ranged from 0.5 to 0.9, dependent on nickel content.

CONCLUSIONS

It is very difficult to determine the influence of either PKA recoil spectra or helium/dpa ratio when other perturbing variables also operate in the experiment. The most persistant problem appears to be that of differences in displacement rate, which have been shown to totally dominate the results of many fission-fusion correlation experiments. When differences in displacement rate, temperature history and other variables are removed, helium is shown to sometimes exert only a secondary effect on macroscopic property changes. Isotopic tailoring and irradiation in temperature controlled experiments offers the most promise for further sucessful fission-fusion correlation efforts. Isotopic tailoring experiments conducted in mixed spectrum reactors with high gamma heating rates may not be quite as successful unless the temperature is actively controlled.

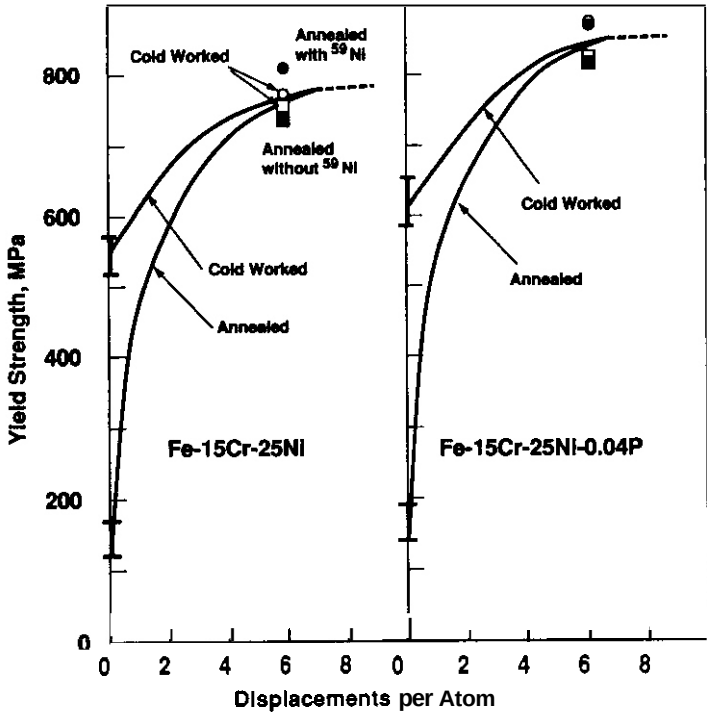

Figure 7. Influence of Cold-Work Level, dpa, Helium/dpa Ratio and Phosphorus on the Tensile Strength of Fe-15Cr-25Ni Irradiated in FFTF at 375°C Using ^{59}Ni Isotopic Tailoring.[40] The convergence of yield strengths at a saturation value independent of cold-work level has been observed in other studies.[41]

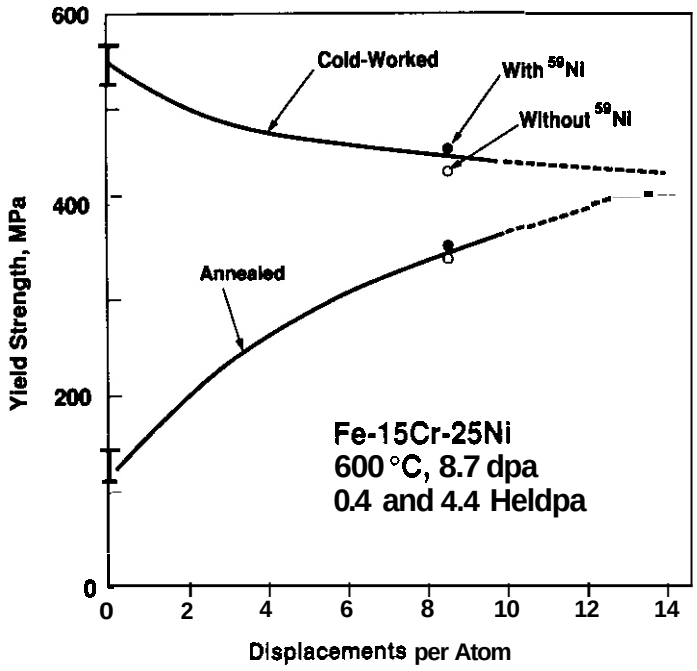

Figure 8. Influence of Cold Work Level, dpa and Helium/dpa Ratio in ^{59}Ni Doping Experiments Conducted in FFTF at 600°C[40]

REFERENCES

1. F. A. Garner, H. L. Heinisch, R. L. Simons and F. M. Mann, Radiation Effects and Defects in Solids (1990) in press.

2. Proceeding of Workshop on Effects of Recoil Energy Spectrum and Nuclear Transmutations on the Evolution of Microstructure, March 24-29, 1988, Lugano, Switzerland (in press).

3. M. Kiritani, J. Nucl. Mater. 160 (1988) 135-141.

4. N. Voshida, H. L. Heinisch, T. Muroga, and K. Araki and M. Kiritani, to be published in proceedings of the 4th International Conference on Fusion Reactor Materials, Kyoto, Japan, Dec 3-8, 1989.

5. H. L. Heinisch, J. Nucl. Mater. 155-157 (1988) 121-129.

6. E. E. Bloom and F. W. Wiffen, J. Nucl. Mater. 58 (1975) 171.

7. L. K. Mansur and M. L. Grossbeck, J. Nucl. Mater. (1988) 130-147.

8. F. A. Garner, M. L. Hamilton, N. F. Panayotou and G. D. Johnson, J. Nucl. Mater. 103 and 104 (1981) 803-808.

9. F. A. Garner, J. Nucl. Mater. 122 and 123 (1984) 459-471.

10. F. A. Garner, E. R. Gilbert, D. S. Gelles and J. P. Foster, ASTM STP 725 (1981), 698-712.

11. W. J. S. Yang and F. A. Garner, ASTM STP 782, (1982), 186-206.

12. M. Kiritani, J. Nucl. Mater. 169 (1989) 89-94.

13. T. Muroga, H. Watanabe, M. Araki and N. Yoshida, J. Nucl. Mater. 155-157 (1988) 1290-1295.

14. R. V. Strain and W. E. Ruther, ANL/EBR-044, August 1971.

15. L. R. Greenwood, J. Nucl. Mater. 115 (1983) 137-142.

16. H. L. Heinisch, DOE/ER-0313/6 (1989) 51-56.

17. L. K. Mansur and K. Farrell, J. Nucl. Mater. (1989) in press.

18. J. F. Bates, F. A. Garner and F. M. Mann, J. Nucl. Mater. 103 and 104 (1981) 347-351.

19. R. L. Kleuh et al., J. Nucl. Mater. 103 and 104 (1981) 887-892; 150 (1987) 272-280.

20. G. Ayrault, DOE/ER-0046/8 (Vol. 1) 182-190.

21. W. G. Johnston et al., ASTM STP 782 (1982) 809-823.

22. O. S. Gelles and F. A. Garner, J. Nucl. Mater. 85 and 86 (1979) 689-693.

23. W. J. S. Yang, F. A. Garner and A. Kumar, J. Nucl. Mater. 122 and 123 (1984) 659-663.

24. A. S. Kumar and F. A. Garner, Rad. Effects 82 (1984) 61-72.

25. L. L. Horton, J. Bentley and K. Farrell, J. Nucl. Mater. 108 and 109 (1982) 222-233.

26. D. A. Woodford, J. P. Smith and J. Moteff, J. Nucl. Mater. 24 (1967) 118.

27. R. C. Rau and R. L. Ladd, J. Nucl. Mater. 30 (1969) 297-302.

28. P. Vela, J. Hardy and B. Russel, J. Nucl. Mater. 26 (1968) 129-131.

29. S. J. Zinkle and K. Farrell, J. Nucl. Mater. 168 (1989) 262-267

30. S. J. Zinkle, K. Farrell and H. Kanazawa, to be published in proceedings of the 4th International Conference on Fusion Reactor Materials, Kyoto, Japan, Dec 3-8, 1989.

31. M. L. Grossbeck and J. A. Horak, J. Nucl. Mater. 155-157 (1988) 1001-1005.

32. R. E. Stoller, P. J. Maziasz, A. F. Rowcliffe and M. Tanaka, J. Nucl. Mater. 155-157 (1988) 1328-1334.

33. F. A. Garner and A. Kumar, ASTM STP 956 (1987) 289-314.

34. H. R. Brager, F. A. Garner and M. L. Hamilton, J. Nucl. Mater. 133 and 134 (1985) 594-598.

35. F. A. Garner and J. M. McCarthy, Proceedings of Symposium on Physical Metallurgy of Controlled Expansion Alloys, Las Vegas, NV, Feb 27-Mar 3, 1989, The Metals Society, 187-206.

36. T. Muroga, F. A. Garner and S. Ohnuki, to be published in proceedings of the 4th International Conference on Fusion Reactor Materials, Kyoto, Japan, Dec 3-8, 1989.

37. T. Muroga, F. A. Garner and J. M. McCarthy, J. Nucl. Mater. 168 (1989) 109-120.

38. M. L. Hamilton, A. Okada and F. A. Garner, to be published in proceedings of the 4th International Conference on Fusion Reactor Materials, Kyoto, Japan, Dec 3-8, 1989.

39. A. Okada, M. L. Hamilton, and F. A. Garner, to be published in proceedings of the 4th International Conference on Fusion Reactor Materials, Kyoto, Japan, Oec 3-8, 1989.

40. F. A. Garner, R. L. Simons, M. L. Hamilton and M. F. Maxon, to be published in proceedings of the 4th International Conference on Fusion Reactor Materials, Kyoto, Japan, Dec 3-8, 1989; also this report.

41. J. F. Stubbins and F. A. Garner, to be published in proceedings of the 4th International Conference on Fusion Reactor Materials, Kyoto, Japan, Dec 3-8, 1989.

42. H. Kawanishi, F. A. Garner and R. L. Simons, to be published in proceedings of the 4th International Conference on Fusion Reactor Materials, Kyoto, Japan, Dec 3-8, 1989.

43. J. F. Stubbins, J. E. Nevling, F. A. Garner and R. L. Simons, ASTM STP 1046, (1990) 147-159.

44. G. R. Odette, J. Nucl. Mater. 141-143 (1986) 1011-1012.

45. R. L. Simons, H. R. Brager and W. Y. Matsumoto, J. Nucl. Mater 141-143 (1986) 1057-1060

FUTURE WORK

This effort will continue as additional relevant data become available.

LOW EXPOSURE SPECTRAL EFFECTS EXPERIMENTS UTILIZING IRRADIATIONS WITH LAMP! SPALLATION NEUTRONS -
H. L. Heinisch, M. L. Hamilton, F. A. Garner, Pacific Northwest Laboratory[a]' and W. F. Sommer, Los Alamos National Laboratory

PURPOSE

The purpose of this work is to determine the effect of the neutron spectrum on radiation-induced changes in mechanical properties of metals.

SUMMARY

An irradiation program is in progress at the Los Alamos Spallation Radiation Effects Facility (LASREF) that will complement earlier low exposure spectral effects experiments (LESEX) performed using RTNS-II and the Omega West Reactor. As in RTNS-II, the specimens in LASREF will be brought to temperature prior to irradiation so as to avoid temperature history effects apparently present in some materials in the OWR irradiations. LASREF irradiations will include specific experiments to look for and quantify temperature history effects. Damage rate effects will also be investigated. A trial LESEX irradiation has been completed at LASREF using an abreviated specimen matrix, and the specimens are being shipped to PNL for tensi1e testing.

PROGRESS AND STATUS

Direct comparison of fusion and fission neutron radiation damage effects has been investigated in experiments using miniature tensile specimens irradiated to low fluences in RTNS-II and the Omega West Reactor (OWR)'. For the most part, tensile property changes due to irradiation in the two neutron spectra correlate when compared on the basis of displacements per atom (dpa). For one of the exceptions, AISI 316 stainless steel, it appears that temperature history effects in the OWR irradiations might account for the increased hardening per dpa^2. Defects nucleated at lower temperatures during the daily ascent to power could be the source of the increased hardening. The temperature-controlled irradiation vehicle at OWR has been decommissioned, so investigation of temperature history effects there is not possible.

LASREF utilizes the neutron irradiation facilities available in the beam stop area of the Los Alamos Meson Physics Facility (LAMPF), where conditions exist for irradiations at doses and temperatures in the ranges of those done at RTNS-II and OWR. Direct comparisons of spallation neutron irradiations with fusion and fission neutron irradiations can be made with the same materials, temperatures and dose range. Effects of displacement damage due to the "high energy tail" of the spallation neutron spectrum will be assessed at low doses, where transmutations are expected to be too small to have any effect. Experiments to examine the effects of temperature history and damage rate will also be included.

Trial Run

From August 16 to September 29, 1989, a trial irradiation was performed with spallation neutrons in a rabbit tube at LAMPF. The purpose of the trial run was to determine the temperature characteristics of the rabbit capsules and to provide an early indication of tensile property changes to be expected in the full experiment. Materials in the trial run included Marz grade copper, solution annealed 316 SS and two copper alloys. The specimens were encapsulated in four capsules (sealed while flowing helium through them) and were irradiated without active temperature control at the relatively constant ambient temperatures in the rabbit tube. The capsules were placed at four distances radially from the beam center, and they received estimated doses ranging from 0.02-0.2 dpa. Analysis of dosimetry foils in the capsules will proceed shortly. Thermocouples attached to the capsules recorded temperatures ranging from 36-55°C, depending on the position of the capsule. The specimen temperatures are estimated to be up to 10 degrees higher than the capsule because of nuclear heating, assuming a worst case helium gas gap between specimens and capsules. It is anticipated that temperatures from 90 to 290°C can be maintained in the rabbit capsules with a flowing heated gas system.

Spectral Effects Experiments

The primary LASREF irradiations for LESEX will match the temperatures and dose ranges of the primary RTNS-II and OWR irradiations: to doses from 0.0003 to 0.03 dpa at 90°C and to doses from 0.001 to 0.1 dpa at 290°C. The material matrix for LESEX is listed in Table 1.

(a) Pacific Northwest Laboratory is operated for the U.S. Department of Energy by Battelle Memorial Institute under Contract DE-AC06-76RLO 1830.

Table 1

Materials for Low Exposure Spectral Effects Experiment in LASREF

Material	Composition (wt%)	Condition
cu	cu (99.999)	annealed 450°C, 15 min
Cu5%Al	Cu - 5.0 Al	annealed 450°C, 15 min
Cu5%Mn	Cu - 5.0 Mn	annealed 450°C, 15 min
Cu5%Ni	Cu - 5.0 Ni	annealed 450°C, 15 min
CuAl25	Cu - 0.25 Al as Al_2O_3	annealed 982°C, 1 h
316 SS	N-lot	annealed 1000°C, 10 m
A302B	pressure vessel steel	service condition

The first LESEX irradiation in temperature-controlled capsules will be done at 90°C, with four capsules placed to obtain doses varying over an order of magnitude. Measurements show the neutron spectrum does not vary significantly over this range of capsule positions.

Temperature History and Damage Rate Effects

With active temperature control in the rabbit capsules, experiments will be done to measure the sensitivity of temperature history effects to both the value and duration of the initial lower temperature. Specimens will be brought to the lower temperature, irradiated for a time interval, then raised to the higher nominal irradiation temperature. The initial experiment will investigate 316 SS at 290°C with 2 lower temperatures of 2 durations each. Additional experiments will be done as deemed necessary. These experiments will provide information that can be used to judge the potential for (or magnitude of] temperature history effects in previous irradiation experiments, as well as for planning future experiments.

As in RTNS-II, the doses will be achieved at different damage rates (the damage rates in LAMPF are about ten times higher than in RTNS-II). Damage rate effects in LAMPF will be investigated by doing additional irradiations at the same positions and temperature, but to smaller total doses.

Post-irradiation testing will include tensile tests on miniature tensile specimens and examination of the microstructures by TEM. Additional specimens will be available for other destructive analyses.

FUTURE WORK

The trial run specimens have been removed from the rabbit capsules and will be shipped to PNL shortly. Tensile testing will proceed soon after arrival. The first temperature-controlled irradiation is now planned to begin in late August, 1990.

REFERENCES

1. H. L. Heinisch, J. Nucl. Mater., 155-157 (1988) 121

2. N. Yoshida, H. L. Heinisch, T. Muroga, K. Araki and M. Kiritani, J. Nucl. Mater., in press, and this Fusion Reactor Materials Semiannual Report DOE/ER-0313/8.

6. DEVELOPMENT OF STRUCTURAL ALLOYS

6.1 Ferritic Stainless Steels

IRRADIATION EFFECTS ON IMPACT BEHAVIOR OF 12Cr-1MoVW AND 2¼Cr-1Mo STEELS — R. L. Klueh and D. J. Alexander (Oak Ridge National Laboratory)

OBJECTIVE

The goal of this study is to evaluate the impact behavior of irradiated ferritic steels and relate the change in properties to the irradiation damage.

SUMMARY

Charpy impact tests were conducted on 12Cr-1MoVW steel after irradiation in the Fast Flux Test Facility (FFTF) and the Oak Ridge Research Reactor (ORR). One-half-size and one-third-size Charpy specimens were irradiated in FFTF at 365°C. After irradiating half-size specimens to ~10 and 17 dpa, a shift in ductile-brittle-transition temperature (DBTT) of 160°C was observed for both fluences, indicating a saturation in the shift. A shift in DBTT of 151°C was observed for the third-size specimens after irradiation to 10 dpa. Third-size specimens of 12Cr-1MoVW steel irradiated to ~7 dpa in the ORR at 330 and 400°C developed shifts in DBTT of 200 and 120°C, respectively, somewhat above and below the shifts observed after irradiation at 365°C in FFTF. This correspondence of results in the mixed-spectrum ORR and the fast-spectrum FFTF is in marked contrast to large differences observed between specimens irradiated in the mixed-spectrum High Flux Isotope Reactor and the fast spectrum Experimental Breeder Reactor.

The first data on the effect of fast reactor irradiation on the impact behavior of 2¼Cr-1Mo steel were obtained. Third-size specimens were irradiated in FFTF to ~10 dpa at 365°C. An increase in DBTT of 170°C was observed, similar to the shift observed for 12Cr-1MoVW steel following comparable irradiation. The reduction in the upper-shelf energy for the 2¼Cr-1Mo steel was less than that observed for 12Cr-1MoVW steel. Because of the low DBTT of unirradiated 2¼Cr-1Mo steel, the DBTT after irradiation remained below that for 12Cr-1MoVW steel.

PROGRESS AND STATUS

Introduction

Ferritic steels are being considered as possible structural materials for the first wall and blanket structure of future fusion reactors. A major problem with the use of ferritic steels for this application involves the large increase in the ductile-brittle transition temperature (DBTT) and large decrease in the upper-shelf energy (USE) that can be caused by irradiation. After neutron irradiation, DBTT values well above room temperature have been observed.[1-7]

Irradiation effects on impact behavior have been studied by irradiating materials in fission test reactors. Due to the limited irradiation space available in most of these reactors, miniature Charpy V-notch (CVN) Specimens one-half and one-third the standard size have been developed and used.[2-5,8-11] Such miniature specimens show a transition from ductile to brittle fracture similar to that found in the standard full-size CVN specimens, although over a different temperature range.[8,10,11] Because of the small size, the energy absorbed during fracture is considerably less for miniature specimens than for full-size specimens.

In comparing Charpy curves for different-size specimens, it has been found that the DBTT for a given material is lower for a subsize specimen than for a full-size specimen.[9-11] Attempts have been made to normalize the impact data for the different-size specimens so that curves obtained from the different specimens can be compared.[2,8,10-12] Normalization by volume and by area have been attempted. Volume normalization has been found to give the best correlation for USE, and area normalization the best correlation for lower-shelf energy.[2,8,10,11] In addition to using just the physical dimensions and ligament size for normalization, as is the case for volume and area normalizations, Louden et al. incorporated the notch geometry into their normalization calculations.[12] None of these attempts have been successful over the entire temperature range of the Charpy test.

Of most interest in alloy development programs for steels for fusion reactor applications is the determination of the shift in DBTT and how this shift is related for specimens of different size. Louden et al. calculated a normalized DBTT that allowed the shifts in DBTT (ADBTT) due to irradiation to be compared for specimens of different sizes.[12] Their approach implies that different shifts will occur for the different specimen sizes. In this report, data obtained from half-size and third-size specimens irradiated simultaneously will be compared to determine how the shift in DBTT depends on specimen size.

Investigations of 9Cr-1MoVNb and 12Cr-1MoVW steels irradiated in the Experimental Breeder Reactor (EBR-II) have indicated that the shift in DBTT saturates with increasing fluence.[3] This report will examine saturation for 12Cr-1MoVW steel irradiated in FFTF. The saturation values for ADBTT obtained for

the 9Cr-1MoVNb and 12Cr-1MoVW steels in EBR-II[3,6] did not correspond to the values measured for these same steels after they were irradiated in the mixed-spectrum High Flux Isotope Reactor (HFIR).[4,13] The difference may have been caused by the larger amount of helium generated during irradiation in HFIR.[4,13] Only small amounts of helium form during irradiation in a fast reactor, whereas relatively large quantities can be generated in nickel-containing materials in the mixed-neutron spectrum of HFIR. Helium is produced by the following two-step reaction of ^{58}Ni with thermal neutrons in the spectrum: $^{58}Ni(n,\gamma)^{59}Ni$ followed by $^{59}Ni(n,\alpha)^{56}Fe$. The nominal concentration of nickel in 12Cr-1MoVW steel is 0.5 wt %, of which about 68% is ^{58}Ni. The effect of transmutation helium on mechanical properties is important for fusion reactor first-wall materials, because the high-energy neutrons generated by the fusion reaction will produce large amounts of transmutation helium, typically 10 to 15 appm/dpa for iron-base alloys.

Specimens of the same heat of 12Cr-1MoVW steel irradiated in FFTF have also been irradiated in the Oak Ridge Research Reactor (ORR), which, like HFIR, is a mixed spectrum reactor. The results from the two reactors will be compared, and those results will be compared with material previously irradiated in HFIR.

The 9Cr-1MoVNb and 12Cr-1MoVW steels are of most interest as possible ferritic steel candidate materials for the first wall of a fusion reactor. However, there is some interest in 2¼Cr-1Mo steel, and in this paper, the first Charpy impact data for this steel after irradiation in a fast reactor will be presented.

Experimental Procedure

The 12Cr-1MoVW steel specimens irradiated in FFTF and ORR were taken from hot-rolled plate from an electroslag-remelted (ESR) heat (National Fusion Heat 9607-R2). This steel was normalized and tempered as follows: 0.5 h at 1050°C, air cooled; 2.5 h at 780°C. The microstructure after this heat treatment was a tempered martensite (Fig. 1). The 2¼Cr-1Mo steel specimens were taken from 25.4-mm thick plate (heat 56447) that was normalized and tempered as follows: 1 h at 900°C, air cooled; 1 h at 700°C, air cooled. The microstructure contained polygonal ferrite and tempered bainite (Fig. 2). The chemical compositions for both steels are given in Table 1.

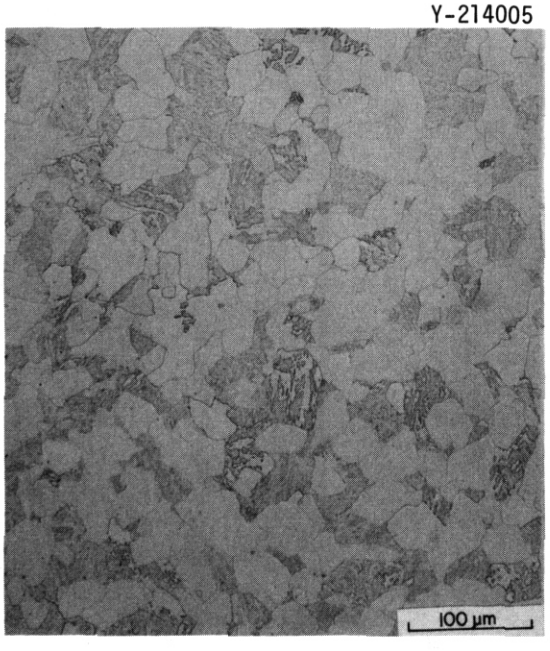

Fig. 1 Tempered martensite microstructure of normalized-and-tempered 12Cr-1MoVW steel.

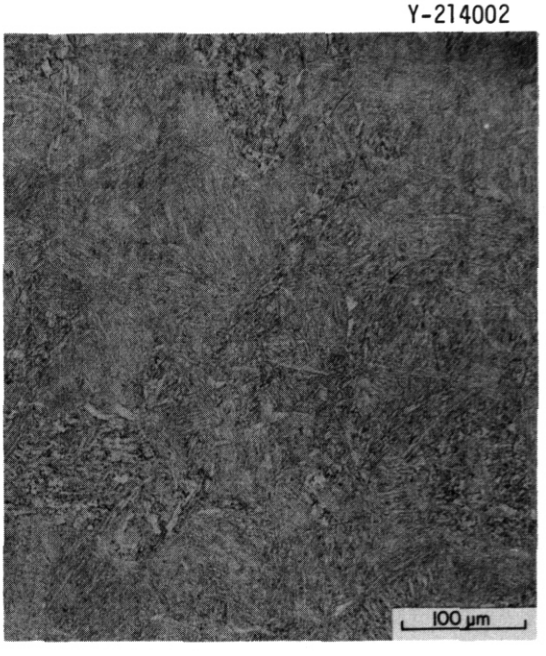

Fig. 2 Polygonal ferrite and tempered bainite microstructure of normalized-and-tempered 2¼Cr-1Mo steel.

Miniature CVN specimens. essentially one-half and one-third standard size specimens, were machined from the heat-treated plates in the longitudinal (LT) orientation. Half-size specimens measured 5 mn by 5 mn by 25.4 mm and contained a 0.76-mn-deep 30° V-notch with a 0.05- to 0.08-mm-root radius. Third-size specimens measured 3.3 by 3.3 by 25.4 mm with a 0.51-mn-deep 30° V-notch that had a 0.05- to 0.08-mn-root radius.

	12Cr-1MoVW (Heat 9607-R2)	2¼Cr-1Mo (Heat 56447)		12Cr-1MoVW (Heat 9607-R2)	2¼Cr-1Mo (Heat 56447)
C	0.20	0.10	Ni	0.51	0.14
Si	0.17	0.23	V	0.28	0.01
Mn	0.67	0.40	W	0.45	--
P	0.016	0.009	N	0.027	--
S	0.003	0.006	Al	0.006	--
Cr	12.1	2.16	Ti	0.001	0.01
Mo	1.04	1.03	Cu	--	0.03

The 12Cr-1MoVW and 2¼Cr-1Mo specimens irradiated in the FFTF were in the below-core specimen canister of the Materials Open Test Rssembly (MOTA). This is a sodium "weeper" that operates at ~365°C, which is slightly above the coolant ambient temperature. Third-size and half-size specimens of 12Cr-1MoVW steel and the third-size specimens of 2¼Cr-1Mo steel were exposed simultaneously. Specimens were irradiated to fluences of ~2.7 × 10^{26} and 4.7 × 10^{26} n/m^2 (E > 0.1 MeV), which produced displacement-damage levels of ~10 and 17 dpa, respectively. Very low helium levels (<1 appm) were present in these specimens.

The third-size 12Cr-1MoVW steel specimens irradiated in the ORR were in the joint U.S.-Japan experiment ORR-MFE-7J. Details on the experiment have been presented elsewhere.[7] Specimens were irradiated to a maximum thermal fluence (E > 0.5 eV) of ~8.1 × 10^{25} n/m^2 and a maximum fast fluence (E > 0.1 MeV) of 9.5 × 10^{25} n/m^2. An average displacement damage of ~7 dpa was obtained, and the helium level, which was primarily determined by the transmutation reaction of thermal neutrons with ^{58}Ni, was <5 appm.

Charpy tests were carried out in a pendulum-type impact machine specially modified to accommodate subsize specimens.[8] To obtain the DBTT and upper-shelf energy (USE), impact energy-temperature curves were generated by fitting the data with a hyperbolic tangent function. The DBTT was determined at the energy corresponding to one-half of the USE.

Results

Table 2 gives the experimentally determined DBTT and USE values for all tests, as obtained from the calculated best-fit curves. These results are presented below according to the reactors in which the specimens were irradiated.

Table 2. Results of Charpy Impact Tests on Normalized-and-Tempered Steels

Alloy	Irradiation Temperature (°C)	Displacement Damage (dpa)	DBTT[a] (°C)	ΔDBTT (°C)	Upper Shelf Energy (J)
		Irradiated in FFTF -- 1/2 Size Specimens			
12Cr-1MoVW	Control	D	-19		20.8
	365	10	142	161	11.4
	365	17	142	161	10.0
		Irradiated in FFTF -- 1/3 Size Specimens			
12Cr-1MoVW	Control	0	-46		6.0
	365	10	105	151	3.2
2 1/4Cr-1Mo	Control	0	-107		10.5
	365	10	66	173	7.6
		Irradiated in ORR -- 1/3 Size Specimens			
12Cr-1MoVW	Control	0	-46		6.0
	330	7	153	199	3.9
	400	7	76	122	4.7

[a]Determined at one-half upper-shelf energy.

FFTF Irradiation

Figure 3 shows the Charpy curves for the half-size 12Cr-1MoVW steel specimens irradiated in FFTF to 10 and 17 dpa. Also shown is the curve for this heat of steel in the normalized-and-tempered condition. Irradiation caused a substantial increase in the DBTT and a decrease in the USE. However, for all practical purposes, there was no difference between specimens irradiated to 10 or 17 dpa, suggesting that the magnitude of the DBTT shift saturates with fluence, and that saturation is reached by 10 dpa.

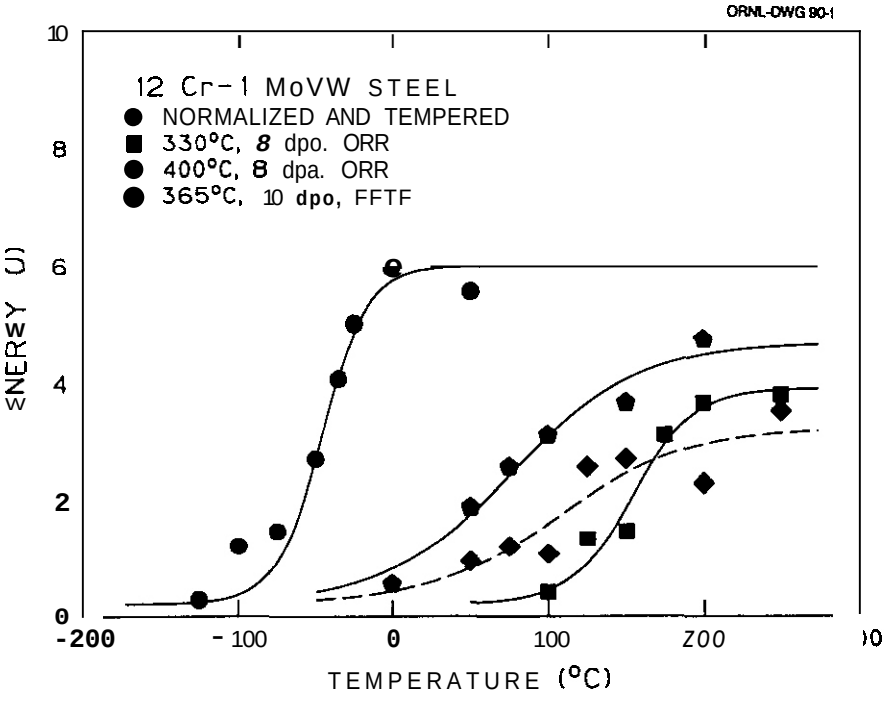

Fig. 3. Charpy curves for half-size specimens of 12Cr-1MoVW steel in the normalized-and-tempered condition and after irradiation to 10 and 17 dpa at 365°C in FFTF.

Third-size specimens irradiated in FFTF to 10 dpa showed a behavior similar to that obtained for the half-size specimens irradiated to the same fluence (Table 2). Although the unirradiated DBTT of the third-size specimens is lower than that of the half-size specimens, the ADBTT is similar. A 151°C change was observed for the third-size specimens and 161°C for the half-size specimens. There was also a difference in the USE of the unirradiated specimens, but again, similar decreases in USE for the two types of specimens were observed after irradiation. A 47% decrease was observed for the half-size specimens, and a 45% decrease was observed for the third-size specimens.

Figure 4 shows Charpy curves for 2¼Cr-1Mo steel in the unirradiated and irradiated conditions. A ADBTT comparable to that observed for the third-size 12Cr-1MoVW steel was observed for this low-chromium steel (Table 2).

ORR Irradiation

Irradiation of the third-size specimens of 12Cr-1MoVW steel at 330 and 400°C to ~7 dpa in the ORR resulted in a shift in DBTT with a magnitude similar to that measured after irradiation to 10 dpa at 365°C in FFTF. This is shown in Fig. 5, where the curves for the specimens irradiated to 10 dpa at 365°C in FFTF are compared with those irradiated at 330 and 400°C in ORR. Specimens irradiated at 330°C showed a slightly larger shift and those irradiated at 400°C showed a slightly smaller shift than observed for the specimens irradiated at 365°C in FFTF. The decrease in USE at 365°C in FFTF was slightly larger than that for the specimens irradiated in ORR at 330°C.

Discussion

Irradiation Effects on Impact Properties

Previous studies on the effect of irradiation on toughness include work by Hu and Gelles[2,3] who irradiated half-size specimens of 12Cr-1MoVW steel in EBR-II to 13 and 26 dpa at 390°C. They reported ADBTT values of 124 and 144°C. respectively. These observations were taken to indicate a saturation in ADBTT

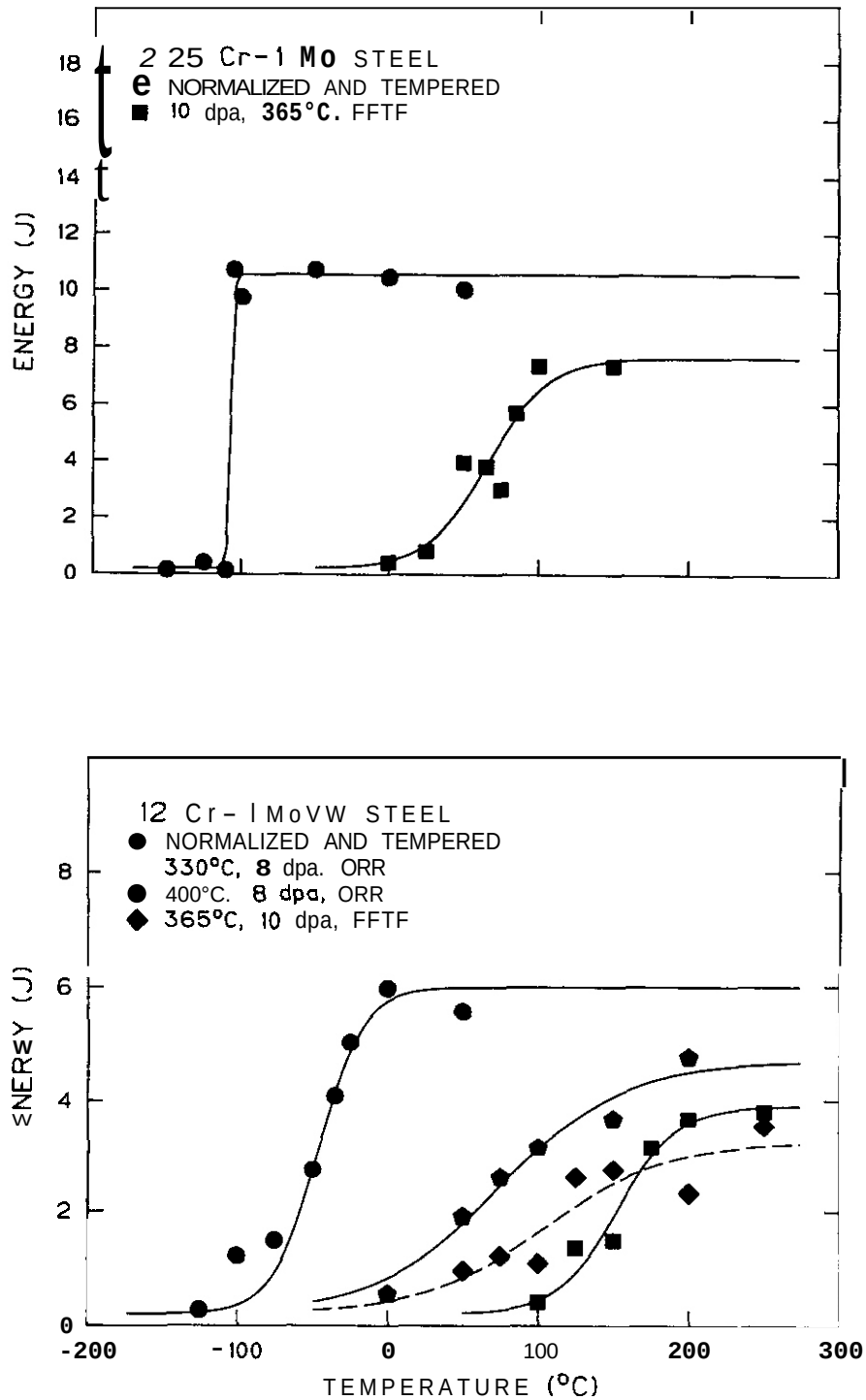

Fig. 5. A comparison of Charpy curves for third-size 12Cr-1MoVW steel specimens irradiated to 7 dpa at 330 and 400°C in ORR and specimens irradiated to 10 dpa at 365°C in FFTF. Also shown is the curve for the normalized-and-tempered steel.

with fluence.[4] Corwin, Vitek, and Klueh[6] irradiated half-size specimens of 12Cr-1MoVW steel to ~11 dpa in EBR-II and found a ADETT of 122°C, which agrees with the Hu and Gelles observation. Smidt et al.[1] irradiated full-size specimens of 12Cr-1MoVW steel at a somewhat higher temperature (419°C) to about 6 dpa. They observed a ADBTT of ~108°C, a slightly lower change, but of similar magnitude to the results at 390°C. Finally, Hu and Gelles irradiated half-size specimens of 12Cr-1MoVW steel at 450°C and found a significantly lower ADETT after 26 dpa (59°C) than was observed at 390°C. These results indicate that the ADETT saturates with fluence and decreases with irradiation temperature in fast reactors.'

The present observations fall into the pattern of the previous results in that a saturation in ADBTT occurred after irradiation at 365°C. Further, the magnitude of change was similar to the previous changes, and the change at 365°C exceeded that at 390°C, in agreement with the observation that ADBTT increases with decreasing temperature. The agreement between all the different experiments conducted to date is excellent, considering the different experiments used different heats of steel,[3,6] and Hu and Gelles[3] used precracked Charpy specimens.

Results of ADBTT on the third-size specimens of 12Cr-1MoVW steel irradiated in the ORR agreed quite well with the results from FFTF. Shifts of 199 and 122°C were observed after irradiation to ~7 dpa at 330 and 400°C, respectively. This compares with a shift of 151°C for the third-size specimens irradiated to 10 dpa in FFTF at 365°C. The results at 400°C also agree with the results for steels irradiated in EBR-II at 390°C.[3,6]

These observations on 12Cr-1MoVW steel indicate that under the conditions of irradiation in ORR and FFTF, the shift in DBTT increases with decreasing irradiation temperature. This is contrary to results for the same heat of 12Cr-1MoVW steel irradiated in HFIR to an average of ~6 dpa (the fluence varied from 4 to 9 dpa, depending upon the location of the specimens in the reactor) where ~25 appm He formed in the steel during irradiation.[4,13] In those experiments, the ADBTT at 400°C exceeded that at 300°C. Furthermore, it was observed that the saturation for ADBTT of ~144°C found for 12Cr-1MoVW steel irradiated in EBR-II at 390°C[3] did not apply for irradiation in HFIR. When irradiated in HFIR at 400°C to 4 to 9 dpa, a ADBTT of 195°C was observed.[4] Irradiation of a different heat of 12Cr-1MoVW to ~40 dpa (≈110 appm He) in HFIR resulted in a ADBTT of 242°C.[13] This difference in behavior between HFIR and EBR-II was tentatively attributed to the larger amount of helium that is formed in the steel when irradiated in HFIR.[4,13]

Like HFIR, OUR is a mixed-spectrum reactor. However, little helium (<5 appm) formed during the ORR irradiation to 7 dpa because of the much lower ratio of thermal to fast neutron fluxes in ORR than in HFIR. The HFIR and ORR experiments had the common temperature of 400°C. After irradiation in HFIR, a ADBTT of 195°C was observed, compared with the 122°C shift observed after irradiation in ORR. Although the same heat of steel was irradiated in HFIR as in ORR, half-size specimens were irradiated in HFIR. As discussed below, specimen size should not affect the comparison.

It appears, therefore, that despite the differences in the spectra of ORR and EBR-II, the same saturation ADBTT is obtained in both reactors. In ORR, it occurred after 7 dpa. Results from both ORR and EBR-II display significant differences from those obtained with HFIR. At present, it appears that the effect of helium offers the best explanation for those differences. It has been suggested that displacement rate may have an effect on mechanical properties.[15] The displacement rate is almost an order of magnitude higher in EBR-II than ORR (~1.2 × 10^{-6} dpa/s for EBR-II and ~1.4 × 10^{-7} dpa/s for ORR for austenitic stainless steel), but there appeared to be no difference in the effect on ADBTT. The displacement rate in HFIR (~1.1 × 10^{-6} dpa/s) is comparable to that of EBR-II, as is the value for FFTF. Therefore, displacement rate would not appear to be a factor in these comparisons.

The 2¼Cr-1Mo steel has received much less attention as a potential candidate for fusion applications than the 9Cr-1MoVNb and 12Cr-1MoVW steels. No studies on the effect of irradiation on toughness appear to have been reported. The present results indicate that the ΔDBTT for 2¼Cr-1Mo steel behaves like that of 12Cr-1MoVW steel when the two steels are irradiated under similar conditions in FFTF. Although the 2¼Cr-1Mo steel showed a slightly larger shift in DBTT than 12Cr-1MoVW steel (170 vs. 151°C), the DBTT for 2¼Cr-1Mo after irradiation was about 40°C lower than that for 12Cr-1MoVW. This is because the 2¼Cr-1Mo steel had a much lower DBTT before irradiation. The percent decrease in USE for the 2¼Cr-1Mo Steel was less than that for the 12Cr-1MoVW steel (29% vs. 47%); the magnitude of the USE for the 2¼Cr-1Mo after irradiation was substantially greater than that for the 12Cr-1MoVW. In fact, because the 2¼Cr-1Mo Steel had a higher USE in the unirradiated condition, its value after irradiation remained higher than the USE of the 12Cr-1MoVW steel prior to irradiation.

It should be noted that the microstructure of the 2¼Cr-1Mo steel was primarily polygonal ferrite (Fig. 2), because of the thick plate that was heat treated. If this steel were heat treated to obtain a tempered bainite microstructure, a similar low DBTT relative to that of 12Cr-1MoVW steel would still be expected.

Effect of Specimen Size on Shift in DBTT

Although there was but one set of third-size and half-size specimens for comparison, the excellent agreement between the shift in DBTT (151 and 160°C) and the percent reduction of USE (45 and 47%) after similar irradiation leads to the tentative conclusion that the value of these changes are the same for the two types of specimens. When specimen miniaturization for determining irradiated properties first began, half-size specimens were irradiated in HFIR[4,5,13] and EBR-II.[2,3,10] With the advent of MOTA in FFTF, a still smaller specimen was required, and the third-size specimen was introduced. These limited data obtained in the present experiment for the half- and third-size specimens indicate that a direct comparison of ADBTT data obtained from the two types of irradiated specimens may be appropriate. In the future, third-size specimens of the 12Cr-1MoVW steel irradiated to 17 dpa will be tested to determine if the agreement noted at 10 dpa still applies.

The only previous published comparison of ADBTT for different-size specimens irradiated under similar conditions are apparently those of Vitek et al.[4] Those observations involved the changes observed in subsize specimens and standard specimens, which is of most importance, because it is of interest to relate changes back to a full-size specimen. Full- and half-size CVN specimens of 12Cr-1MoVW were simultaneously irradiated in the University of Buffalo Reactor (UBR) to 8.6 × 10^{23} n/m^2. The standard specimens reported by Hawthorne, Reed, and Sprague[7] developed a ADBTT of 47°C, and the half-size specimens tested by Vitek et al.' developed a ADBTT of 36°C. This was concluded to be goad agreement, considering the experimental error inherent in such measurements.[4*] After irradiation, identical drops in the USE of 13% were found for both the standard and half-size specimens.[4]

An unpublished set of data for half-size specimens is also available for 9Cr-1MoVNb irradiated in UBR to ~9 × 10^{23} n/m^2 at 150°C. The Charpy curves for unirradiated and irradiated specimens are shown in Fig. 6. These data can be compared to previously published data by Hawthorne, Reed, and Sprague for similarly irradiated full-size specimens.' A ADBTT (at 41 J) of 83°C was observed for the standard specimens,' compared to a shift (at 9.2 J) of 87°C for the half-size specimen, again an indication that the ADBTT for the different-size specimens is equal (excellent agreement is also obtained if the DBTT is determined at one-half the upper shelf energy). Good agreement was again observed for the change in USE: a decrease of 5% was observed for the full-size specimen, compared to 8% for the half-size specimen.

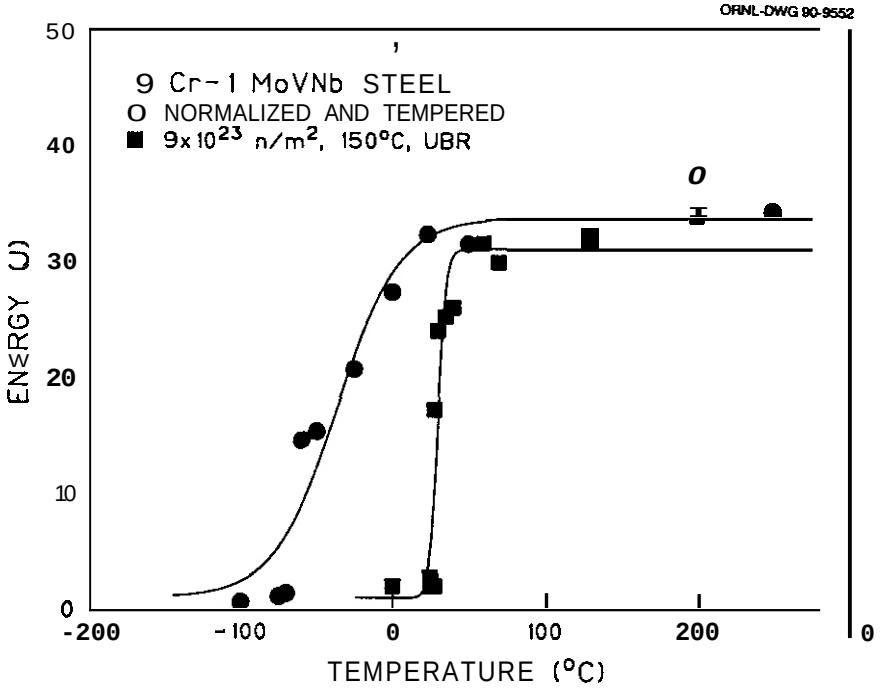

Fig. 6. Charpy curves for half-size specimens of 9Cr-1MoVNb steel in the normalized-and-tempered condition and after irradiation to 9 × 10^{23} n/m^2 at 150°C in the University of Buffalo Reactor.

Loudon et al. attempted to develop a normalized DBTT to allow for a comparison of the ADBTT for full-size and subsize specimens.[12] Their treatment can be carried further than the authors originally carried it, and when this is done, it can be shown that the ADBTT for a full-size specimen should be approximately 72% of a half-size specimen and 58% of a third-size specimen. The ADBTT for half-size specimens is expected to be about 81% of the shift observed for a third-size specimen. Such calculated values for the present studies would not agree with observations. Therefore, from the limited data obtained here, it is concluded that a one-to-one correspondence results for the ADBTT for the different-size specimens irradiated similarly.

Summary and Conclusions

Charpy specimens of 12Cr-1MoVW and 2¼Cr-1Mo steels were irradiated in the FFTF at 365°C, and specimens of 12Cr-1MoVW steel were irradiated in the ORR at 330 and 400°C. The following summarizes the observations and conclusions.

'Vitek et al.[4] compared the ADBTT determined at 9.2 J for the half-size specimens with that determined at 41 J by Hawthorne, et al.[7] for the full-size specimens.

(1) The increase in OBTT and decrease in USE were the same after irradiating 12Cr-1MoVW steel to 10 and 17 dpa at 365°C in FFTF, in agreement with previous work that showed a saturation in the effect of irradiation on toughness when irradiated in a fast reactor. An increase in DBTT of 160°C was observed.

(2) Irradiation of half- and third-size specimens of 12Cr-1MoVW steel to 10 dpa at 365°C in FFTF resulted in comparable shifts in DBTT and similar percentage reductions in USE. Comparable shifts in DBTT and USE for full-size and subsize specimens irradiated similarly have also been observed under conditions where such irradiations have been made.

(3) Shifts in DBTT for the 12Cr-1MoVW steel irradiated in the mixed-spectrum ORR to 7 dpa at 330 and 400°C were comparable to those observed in the fast-spectrum FFTF and EBR-II. However, the changes were considerably smaller than those observed for irradiation in the mixed-spectrum HFIR. The difference was attributed to the larger amount of helium formed by irradiation in HFIR.

(4) The increase in DBTT for 2¼Cr-1Mo steel irradiated in FFTF to 10 dpa at 365°C was similar in magnitude to the increase observed for 12Cr-1MoVW steel. However, the final DBTT for the 2¼Cr-1Mo was lower than that For 12Cr-1MoVW because of the lower starting DBTT for the 2¼Cr-1Mo. Even after the reduction due to irradiation, the USE for 2¼Cr-1Mo steel remained higher than that for the 12Cr-1MoVW steel before irradiation.

Acknowledgment

We wish to thank the following people who helped in the completion of this work: T. N. Jones carried out the Charpy tests; C. W. Houck did the optical metallography; J. M. Vitek, D. N. Braski, and A. F. Rowcliffe reviewed the manuscript; and Frances Scarboro prepared the manuscript.

References

1. F. A. Smidt, Jr., J. R. Hawthorne, and V. Provenzano, "Fracture Resistance of HT-9 After Irradiation at Elevated Temperature," Effects of Radiation on Materials, STP 725. Eds. D. Kramer, H. R. Brager, and J. S. Perrin (American Society for Testing and Materials, Philadelphia, 1981), pp. 269-284.

2. W. L. Hu and D. S. Gelles, "Miniature Charpy Impact Test Results for The Irradiated Ferritic Alloys HT-9 and Modified 9Cr-1Mo," Ferritic Alloys for use in Nuclear Energy Technologies, J. W. Davis and O. J. Michel, Eds. (Metallurgical Society of AIME, Warrendale. PA. 1984). pp. 631-645.

3. W. L. Hu and D. S. Gelles, "The Ductile-to-Brittle Transition Behavior of Martensitic Steels Neutron Irradiated to 26 dpa," Influence of Radiation on Material Properties: 13th International Symposium (Part II), ASTM STP 956. F. A. Garner, C. H. Henager, Jr., and N. Igata, Eds. (American Society for Testing and Materials, Philadelphia, 1987), p. 83.

4. J. M. Vitek, W. R. Corwin, R. L. Klueh, and J. R. Hawthorne, "On the Saturation of the DBTT Shift of Irradiated 12Cr-1MoVW With Increasing Fluence," J. Nucl. Mater. 141-143 (1986) 948-953.

5. R. L. Klueh, J. M. Vitek, W. R. Corwin, and D. J. Alexander, "Impact Behavior of 9-Cr and 12-Cr Ferritic Steels After Low-Temperature Irradiation," J. Nucl. Mater. 155-157 (1988) 973-977.

6. W. R. Corwin, J. M. Vitek, and R. L. Klueh, "Effect of Nickel Content of 9Cr-1MoVNb and 12Cr-1MoVW Steels on the Aging and Irradiation Response of Impact Properties," J. Nucl. Mater. 149 (1987) 312-320.

7. J. R. Hawthorne, J. R., Reed, and J. A. Sprague, Fracture Resistance of Two Ferritic Stainless Steels After Intermediate Temperature Irradiation," Effect of Radiation on Materials: Twelfth International Symposium, ASTM STP 870, F. A Garner and J. S. Perrin, Eds. (American Society for Testing Materials, Philadelphia, 1985), pp. 580-604.

8. W. R. Corwin and A. M. Hougland, "Effect of Soecimen Size and Material Condition on the Charpy Impact Properties of 9Cr-1MoVNb Steel," The Use of Smail-Scale Specimens for Testing Irradiated Material, ASTM STP 888, W. R. Corwin and G. E. Lucas, Eds., (American Society for Testing and Materials, Philadelohia. 1986), pp. 325-338.

9. 'G. E. Lucas G. R. Odette, J. W. Sheckherd, P. McConnell, and J. Perrin, "Subsized Bend and Charpy V-Notch Specimens for Irradiated Testing," Ibid, pp. 305-324.

10. W. R. Corwin, R. L. Klueh, and J. M. Vitek, "Effect of Specimen Size and Nickel Content on the Impact Properties of 12Cr-1MoVW Ferritic Steel," J. Nucl. Mater. 122 & 123 (1984) 343-348.

11. F. Abe, T. Noda, H. Araki, M. Okada, M. Narui, and H. Kayano, "Effect of Specimen Size on the Ductile-Brittle Transition Behavior and the Fracture Sequence of 9Cr-W Steels," J. Nucl. Mater. 150 (1987) 292-301.

12. B. S. Louden, A. S. Kumar, F. A. Garner, M. L. Hamilton, and W. L. Hu, "The Influence of Specimen Size on Charpy Impact Testing of Unirradiated HT-9," J. Nucl. Mater. 155-157 (1988) 662-667.

13. R. L. Klueh, and D. J. and Alexander, "Impact Behavior of 9Cr-1MoVNb and 12Cr-1MoVW Steels," Journal of Nuclear Materials, to be published.

14. J. L. Scott et al., "Second Annual Progress Report on United States-Japan Collaborative Testing in the High Flux Isotope Reactor and the Oak Ridge Research Reactor for the Period Ending September 30, 1985," ORNL/TM-10102, Oak Ridge National Laboratory, Oak Ridge, TN, 1986.

15. M. L. Hamilton, A. Okada, and F. A. Garner, "Tensile Behavior and Swelling of Ternary Austenitic Alloys Irradiated in Different Neutron Spectra," Journal of Nuclear Materials, to be published.

IMPROVED PROCESSING FOR TWO FERRITIC LOW ACTIVATION OXIDE DISPERSION STRENGTHENED STEELS - A. N. Niemi, M. G. McKimpson (Michigan Technology Institute) and D. S. Gelles (Pacific Northwest Laboratory)[a]

OBJECTIVE

The objective of this effort is to determine if oxide dispersion strengthened alloys produced by mechanical alloying are suitable for first wall applications.

SUMMARY

Two oxide dispersion strengthened low activation ferritic alloys have been manufactured into extruded bar using improved mechanical alloying and extrusion procedures. The alloy compositions are, in weight percent, Fe-13Cr-0.7Ti-0.8W-0.2Y_2O_3 and Fe-9Cr-0.8W-0.04C-0.2Y_2O_3.

PROGRESS AND STATUS

Introduction

An effort has been initiated to consider the use of mechanically alloyed oxide dispersion strengthened (ODS) alloys for fusion. The first attempts to produce a low activation ferritic ODS alloy were made by the Institute of Materials Processing (IMP), Michigan Technology University.' Two extrusions were prepared from mechanically alloyed powder, of compositions (in weight percent) Fe-14Cr-1.0Ti-0.5W-0.25Y O_3 and Fe-9Cr-2.0W-0.3V-0.08C-0.25Y_2O_3. The alloy compositions and method of processing were defined so that the 14Cr alloy was a low activation variant of the commercial alloy MA957 and the 9Cr alloy was a mechanically alloyed version of the low activation martensitic alloy GA3X. The results of that effort were significant for two reasons. First, they demonstrated that bar stock could be made of OOS low activation ferritic alloys, but improvements were required for extrusion processing because the as-extruded bars contained radial cracks. Second, intentional carbon additions to promote both martensite formation and oxide dispersion strengthening did not work because a carbide-yttria reaction occurred during aging. Also, examples of second phase particles were found in hot isostatic pressed (HIP) coupons. Based on the facts that improvements in processing procedure could be made to exclude the second phase particles and that carbon contents needed to be kept low, new bars of both compositions were ordered with carbon levels as low as possible. This report describes the production of these new bars.

ExDerimental Procedure

The intended alloy compositions were Fe-14Cr-1.0Ti-0.5W-0.25Y_2O_3 and Fe-9Cr-1.0Ti-0.5W-0.25Y_2O_3. The starting powders and the maximum mesh sizes are given in Table 1. In the previous attempt to mechanically alloy similar materials, master alloy powders were used, where possible, in an attempt to minimize inhomogeneity in the final product. Due to the presence of what appeared to be residual Fe-Ti master alloy particles in those extrusions, Ti powder was substituted in this phase of the program on the assumption that the Ti particles would be more easily deformed than the master alloy particles during mechanical alloying. Additionally, it was found that the major source of carbon contamination in the previous mechanically alloyed powders came from wear debris associated with the polymeric packing in the attritor shaft seal. Although it was not possible to eliminate the packing, it was possible to operate the attritor in a way that minimized the accumulation of wear debris. Moreover, carbon analyses were performed on each batch of mechanically alloyed powder immediately after removal from the mill and the batch was discarded if the carbon content exceeded 0.05% by weight.

Table 1.

Composition and Mesh Size or Mean Particle Size of Precursor Powders Used in Mechanical Alloy Processing of the Two Extrusion Alloy Compositions.

Powder	ComDosition	Mesh Size
Fe	99.5%	-100
Fe-Cr	Fe-74Cr	-200
Ti	99.9%	-270
W	99.9%	6 micron
Y_2O_3	99.9%	<40 nm

(a) Pacific Northwest Laboratory is operated for the U.S. Department of Energy by Battelle Memorial Institute under Contract DE-AC06-76RLO 1830.

A 1S Szegvari attritor with a tank capacity of 9.5 liters (2.5 gal.) was used for the mechanical alloying. The tank was charged with 27.3 kilograms (60 lb) of 9.53 mm (3/8 in.) 440C stainless steel balls and 1.36 kilograms (3 lb) of powder. Three batches of each composition were required. The attritor was operated at 350 rpm with a positive pressure high purity argon purge rate of 100 cc per minute. Each batch was attrited for 12 hours, held overnight under argon, and attrited for 12 hours the'next day. During attrition, the agitator drive torque and tank lid temperature were monitored. The torque ran between 556 and 570 n-m (410 - 420 in.-lb) while the lid temperature ran between 363 and 380 K. The tank and discharge valve were wiped clean after each batch. The three batches of each composition were combined in a v-cone blender for 15 minutes before consolidation. Powder for the extrusion billets was poured through the evacuation stem of a 80 mm diameter by 100 mm long copper can with intermittent vibration to ensure a maximum packing density. After filling, the cans were outgassed at 10^{-6} torr vacuum and 873 K for 24 hours, removed from the vacuum furnace into an argon-filled glove box, evacuated to 30 millitorr, and sealed. Following evacuation and sealing, the billets were HIPed at 1223 K for 4 hours at 200 MPa. The billets were then machined to dimension (50.8 mm diameter by 63 mm long) for extrusion. As-HIPed densities were determined for one billet of each composition using the Archimedes method. The density of the 5% Cr billet was found to be 1.70 g/cc and that of the 14% Cr billet was 7.66 g/cc. These values are 99% of the calculated theoretical densities. In an attempt to minimize or eliminate the radial cracking that occurred during extrusion of the billets produced in the previous phase of this program, the HIPed billets were placed in evacuated mild steel cans prior to extrusion during this phase. The primary function of the steel can was to prevent oxidation of the billet surface during the extrusion preheat soak and to act as a lubricant during extrusion.

Three billets were sent to RMI Company of Ashtabula, Ohio, for extrusion. One of the billets was made from powder with a higher carbon content (0.075% by weight) than the other two (0.04% and 0.046%) and was intended as a trial billet to evaluate the extrusion parameters. An extrusion ratio of 2.63:1 and an extrusion temperature of 1255 K were used on the Fe-14Cr trial billet with the high carbon content. This billet could not be extruded and had to be removed from the die. The temperature was increased to 1422 K for the remaining two billets. Both of the remaining billets, an Fe-14Cr billet with 0.046% C and an Fe-9Cr billet with 0.04% C, were successfully extruded.

Results

The as-extruded bars encased in mild steel are shown in Figure 1. The upper bar, labeled 078, is the Fe-9Cr alloy; the lower bar, labeled 086, is the Fe-14Cr alloy. Each bar measured approximately 44 cm long by 2.5 cm in diameter, with an internal core of ODS steel of about 1.9 cm. Extrusion produced no obvious defects on the mild steel surface, indicating that, in comparison with previous extrusions,' the quality was much better.

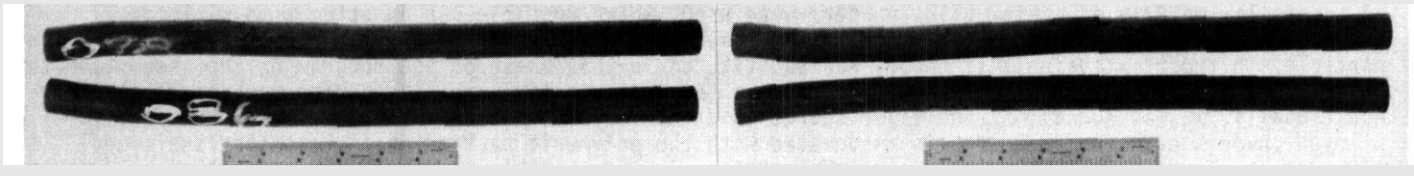

FIGURE 1. Extruded Bars of OOS Fe-9Cr Alloy, Upper Bar Labeled 078, and Fe-14Cr Alloy, Lower Bar Labeled 086, Shwoing Both Sides of Each Bar, As-Received

Chemical analyses for Cr, Ti, W, Y (converted to equivalent Y_2O_3), and C were performed at IHP on samples from the two successful extrusions and the results are sumnarized in Table 2. The carbon was determined by fusion analysis and the other concentrations were determined by atomic absorption. It should be noted that the carbon values in Table 2 are not the same measurements quoted earlier, which were measured on the powder prior to HIP consolidation.

Metallographic sections in both transverse and longitudinal directions were prepared and the results are provided in Figures 2 through 5. The etchant was Vilella's etch. Figure 2a shows a the transverse section of bar 078, the Fe-9Cr alloy, at low magnification. The mild steel canning is easily identified by its coarsergrain size. A region adjacent to the canning is shown in an etched condition at intermediate magnifications in Figures 2b and c. These micrographs reveal the presence of black features uniformly distributed across the bar, and Figure 2d shows the structure at higher magnification. In Figure 2d, a fine background precipitate on the order of 0.5 μm, which is typical of carbide, can be identified. Careful through-focus examination revealed that the larger black features were cavities or pores in the material.

Table 2

Results of Chemical Analysis on Extrusion Samples. All values are given in weight percent.

	Fe - 14Cr		Fe - 9Cr	
Element	Measured	Stated	Measured	Stated
Cr	12.96	14	9.58	9
Ti	0.73	1	0.80	1
W	0.76	0.5	0.80	0.5
Y_2O_3	0.18	0.25	0.21	0.25
C	0.047		0.036	

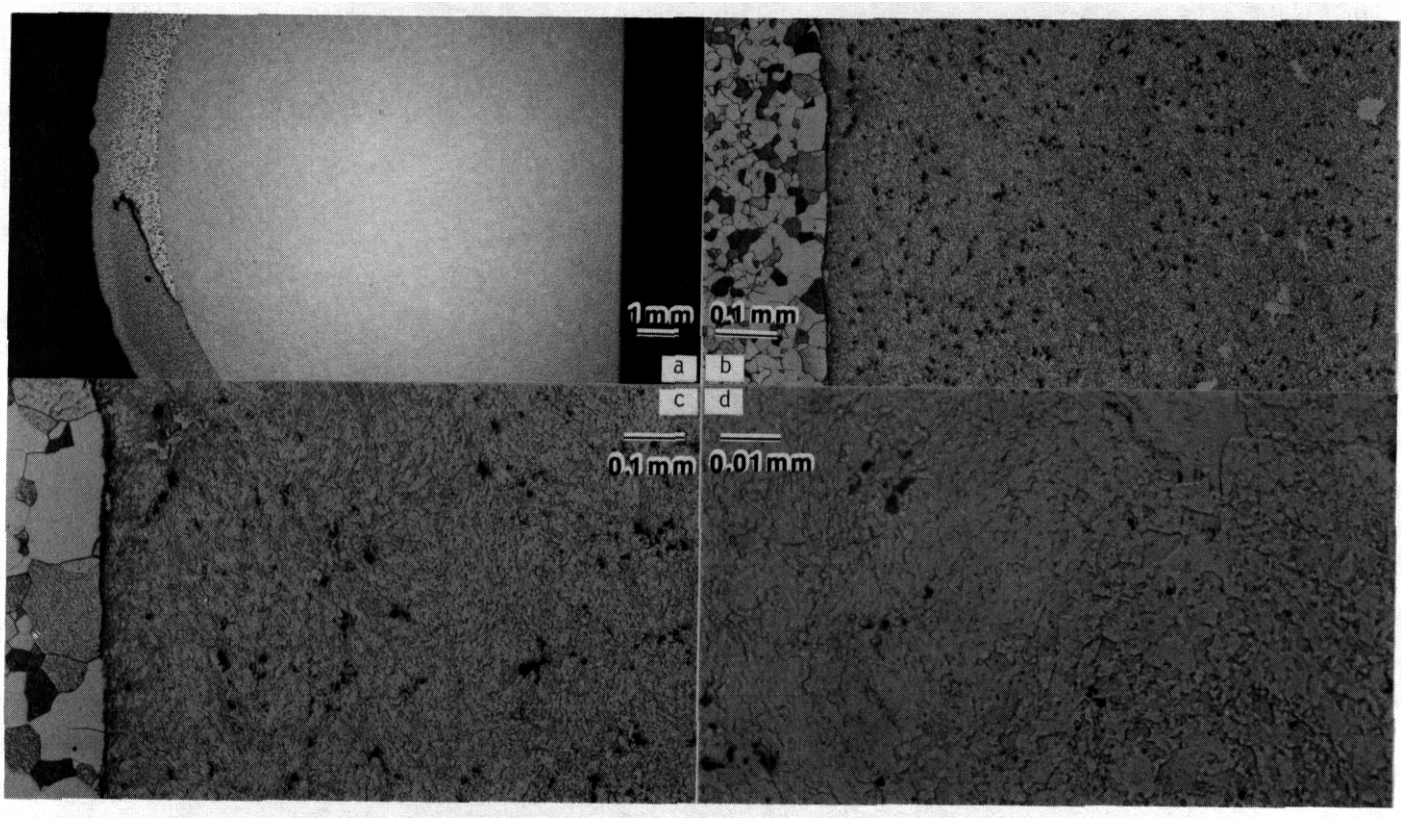

FIGURE 2. Optical Metallography of a Transverse Section of Bar 078, Showing Alloy Fe-9Cr at Various Magnifications

Therefore, porosity on the order of 4 μm in diameter is present at fairly high density throughout the as-extruded Fe-9Cr bar.

Figure 3a gives an as-polished example of the pores in a longitudinal section of the Fe-9Cr alloy bar. The pores were not uniformly distributed, with groups of pores formed into strings often parallel to the extrusion (horizontal) direction. Figure 3b shows a similar view for the etched microstructure and Figures 3c and d give the etched microstructure at higher magnifications. Again, carbide precipitate can be identified in Figure 3d. Also of note is the elongated grain structure, with an aspect ratio of about three to one.

Figures 4 and 5 give equivalent metallographic conditions for bar 086, the Fe-14Cr alloy. In this case, porosity was found to be significantly reduced, but carbide precipitation appears at higher number density. The aspect ratio for elongated grains in the longitudinal section is approximately four to one. The Fe-14Cr alloy is expected to have superior properties because it has reduced porosity.

FIGURE 3. Optical Metallography for a Longitudinal Section of Bar 078, Showing Alloy Fe-9Cr at Various Magnifications. Figure 3a is in the as-polished condition.

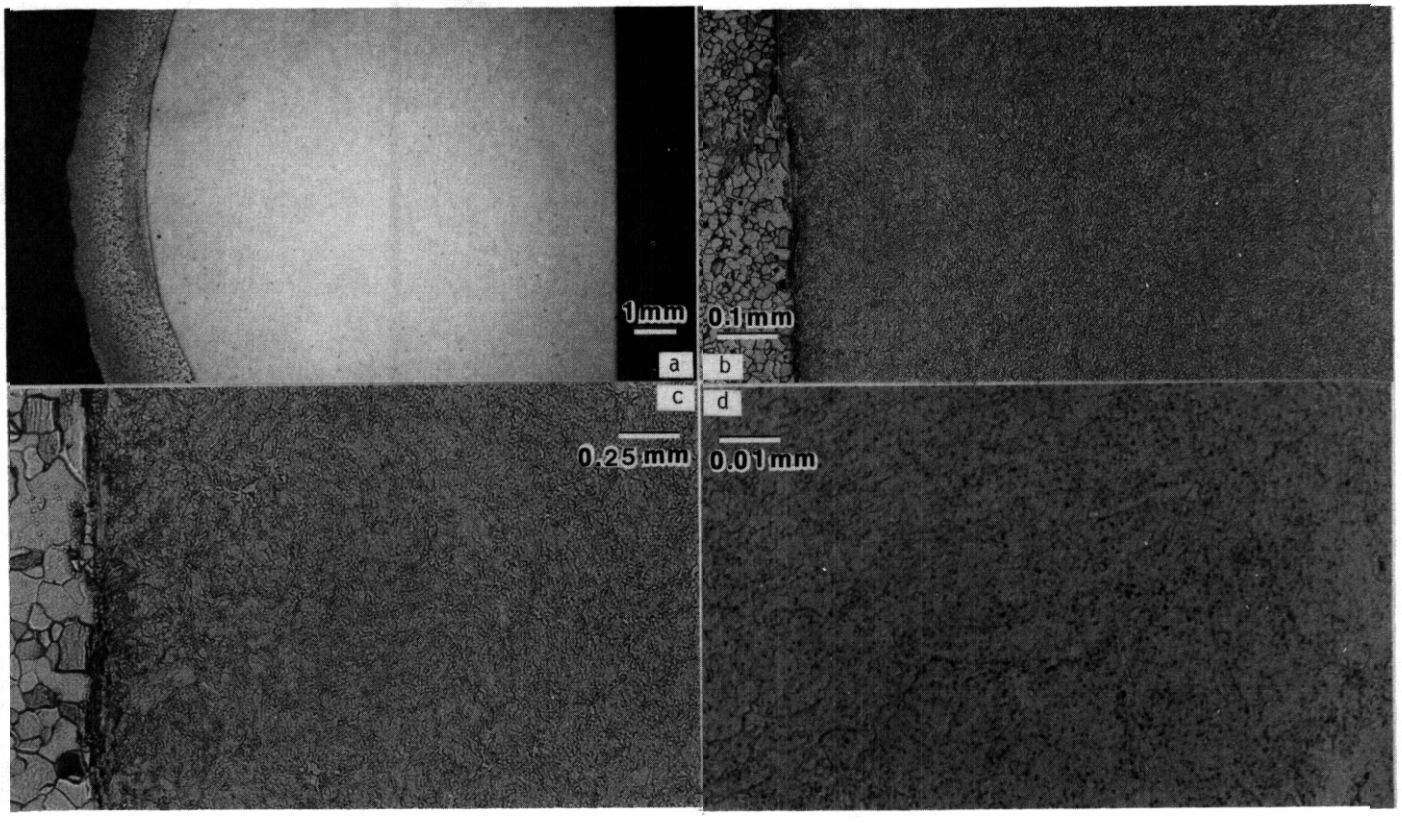

FIGURE 4. Optical Metallography of a Transverse Section of Bar 086, Showing Alloy Fe-14Cr at Various Magnifications

FIGURE 5. Optical Metallography of a Longitudinal Section of Bar 086, Showing Alloy Fe-14Cr at Various Magnifications. Figure 5a is in the as-polished condition

Discussion

The outgassing procedure employed prior to HIP is critical in minimizing residual porosity due to gas entrapment. Ideally, outgassing should be done at a temperature higher than the highest exposure temperature of the material subsequent to HIPing. However, because of practical problems associated with evacuation and sealing of the HIP can, it is not always possible to outgas at such high temperatures. The outgassing temperature used in this program was chosen on the basis of Thennogravimetric Analysis (TGA) of samples taken from the milled powders. A typical TGA plot showing the sample weight as a function of temperature as the specimen is heated is shown in Figure 6. It is apparent in this figure that a substantial weight loss occurs just under 600°C, or 873 K. It is also apparent that little weight loss occurs above 873 K, so this was chosen as the outgassing temperature. The 24 hour hold time during outgassing was chosen based on experience. It is believed that the major species removed during the outgassing cycle is Teflon" from the attritor shaft packing, as wear debris was observed to accumulate near the packing during operation. Residual gas analysis of powders outgassed using this method in a subsequent study, however, has shown that the brief exposure to the glove box atmosphere for even the short time necessary to connect the vacuum hose to the evacuation stem may be sufficient to allow moisture adsorption to occur. This moisture may not be adequately removed during evacuation prior to sealing the can. Hence, the powders canned in this program may have had excessive adsorbed moisture levels that could lead to gas porosity during extrusion.

CONCLUSIONS

Two low activation ODS ferritic alloys have been successfully manufactured using mechanical alloying processes and extruded into bar encased in mild steel.

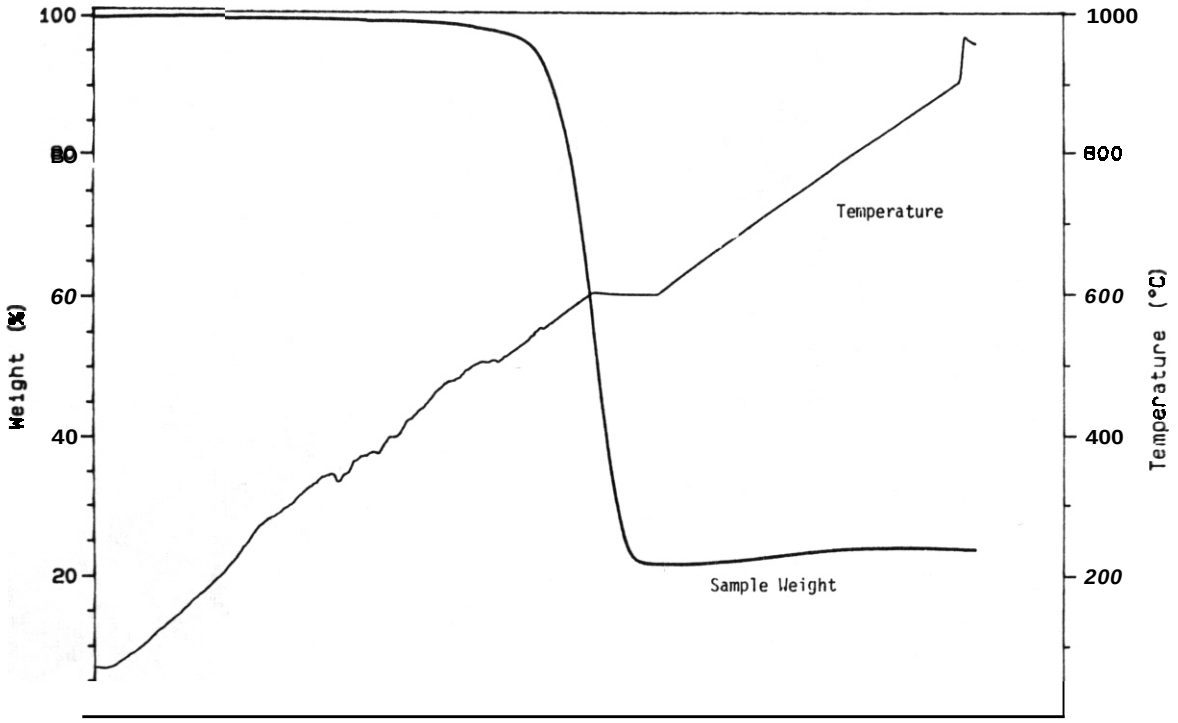

FUTURE WORK

Fabrication of tubing from the 14Cr oxide dispersion strengthened alloy will be attempted during the next reporting period in order to provide pressurized tube specimens for thermal and irradiation creep measurements.

REFERENCES

1. A. N. Niemi, M. G. McKimpson and D. S. Gelles, "Processing of Two Iron-Chromium Oxide Dispersion Strengthened Steels by Mechanical Alloying," DOE/ER-0313/6, (1989) 187.

RESEARCH AND DEVELOPMENT OF IRON-BASE0 ALLOYS FOR NUCLEAR TECHNOLOGY · O. S. Gelles, (Pacific Northwest Laboratory)[a]

OBJECTIVE

The objective of this effort is to document progress on materials development for nuclear technology for the international community. This report is to be submitted for publication as an invited review paper in ISIJ International, a journal of the Iron and Steel Institute of Japan.

SUMMARY

This paper describes several of the nuclear materials research and development programs that have involved ferrous metallurgy. The research programs highlighted are as follows: For light water reactors, corrections have been made for stress corrosion of coolant piping and irradiation embrittlement of pressure vessel steels. Gas-cooled reactor concerns have included breakaway oxidation of mild steel components, nitride strengthened cladding materials development, breakaway oxidation in martensitic steel and structural materials specifications for very high temperature. Programs for liquid metal reactors have included efforts on void swelling resistance, piping alloy optimization, and application of mechanically alloyed oxide dispersion strengthened steels. Fusion alloy development has considered first wall materials optimization and low activation materials development. Descriptions of the causes and needed corrections are given for each of these research and development programs.

PROGRESS AND STATUS

Introduction

A nuclear energy option has only been available to mankind for one generation; therefore, materials development for nuclear energy applications has been a modern effort. Nuclear energy involves large investments of resources for individual plants and is politically controlled for nuclear non-proliferation reasons, thereby assuring major government involvement, so that sufficient funding has been available to optimize the materials used in these systems within large research and development programs. Many programs have been operated to develop new or improved materials for nuclear reactor systems. In several cases, the materials are of direct interest to the Iron and Steel Institute of Japan. Thus, the objective of this paper is to describe several of those programs that have been concerned with ferrous metallurgy. The author has been directly involved with two of the programs, liquid metal fast breeder reactor cladding and duct materials development, and fusion reactor structural materials development. Apologies are made in advance for omissions in descriptions of programs that are not so familiar to the author.

Reactor Systems

The nuclear reactor systems that have been developed based on fission technology can be classified as a function of cooling system parameters. Coolants have included water, liquid metal, and gas as heat transfer media so that restrictions on operating temperatures were 100 to 250°C, 350 to 700°C, and up to 900°C, respectively. Consequently, ferrous metals were often the materials of choice for water and liquid metal technology, but nickel-based metals and high temperature materials were often required for high temperature gas-cooled reactors. Fusion reactor systems cannot be classified so straightforwardly. System designs are not yet well defined, but several design studies have recommended ferrous metals for structural components based on either water or liquid metal coolant systems, so ferrous metals are also being developed for fusion applications. Therefore, steels have found application in most nuclear reactor systems, and as problems or concerns developed, alloy research and development programs became necessary and were instituted.

To provide the basis for discussion of the ferrous alloy development programs associated with nuclear reactor systems, the various reactor systems will first be described with particular emphasis on application of ferrous metallurgy.

Water-cooled Systems

Three water-cooled reactor systems have been developed: light water reactors (LWRs) using either boiling water (BWR), or using pressurized water (PWR) systems, and heavy water reactors or reactors using deuteriated rather than hydrogenated water, of which the leading proponent is the Canadian deuterium uranium (CANDU) reactor. Each reactor system uses a reactor core of fissile fuel pellets in non-ferrous metal cladding, but piping, heat exchanger materials, and confinement systems are ferrous based. Piping and heat exchanger materials are generally austenitic stainless steels (304SS) or ferritic stainless steels

---

(a) Pacific Northwest Labortory is operated for the U.S. Department of Energy by Battelle Memorial Institute under Contract DE-AC06-76RLO 1830.

(2¼Cr-1Mo) to minimize corrosion. The confinement systems (some of the largest steel structures fabricated in the world) are generally welded structures made from low alloy steels. The major ferrous metallurgy concerns that arose in these systems involved either corrosion-related problems for piping or irradiation embrittlement of the pressure vessels. As pressure vessel degradation was a life-limiting factor, significant effort on a global scale has been spent on research and allay development solutions to the problem.

Gas-Cooled Systems

Several very different types of gas-cooled reactors have been developed because the limits on heat transfer can vary greatly as a function of cooling gas and reactor design. The designs can be compared as a function of operating temperature. An example of a low temperature design is the Magnox reactor, an early design developed in the United Kingdom (UK). It is graphite moderated, CO_2-cooled, and uses natural uranium with either steel or steel-reinforced concrete pressure vessels and internal boilers. Reactor gas outlet temperatures vary from 336 to 412°C and are kept low because a magnesium alloy is used as fuel cladding. Breakaway oxidation in mild steel components proved to be an unexpected problem.

The Advanced Gas Reactor (AGR), also of UK design, was designed for greater efficiency. It used a cooling gas mixture of CO_2, methane and water that provided operating gas temperatures over 600°C. This was possible because a niobium-stabilized austenitic stainless steel was used for fuel cladding. But, significant improvement in reactor operation was possible by development of 20/25 titanium nitride strengthened cladding materials. For the heat transfer system, a martensitic steel, 9Cr-1Mo, has been used for primary systems, and 300 series austenitic stainless steels have been used for secondary systems. However, breakaway oxidation was encountered in this system as well.

The high temperature gas-cooled reactor (HTGR) employs a very different fuel system because operating temperatures are usually considered too high for standard cladding designs. The coolant gas is helium and, in general, the fuel is provided as balls or pellets and cooling is accomplished using fluidized bed designs. Therefore, structural materials requirements are reduced by careful design to allow the use of high temperature nickel-based alloys. Steam generators use 2¼Cr-1Mo ferritic steel and superheaters are made from Alloy 800H, a nickel-based alloy. However, a Japanese approach to HGTR materials specification was development of very high temperature structural materials to operate at 1000°C.

Liquid Metal-Cooled Systems

Several liquid metal-cooled reactors (LMRs) have been built primarily as breeder reactor prototypes, but no commercial design is yet in full-scale production. Reactor systems are generally sodium cooled and use stainless steel fuel cladding, piping, and welded reactor pressure vessels. Some components are fabricated from high nickel alloys for neutronic considerations. However, early operation showed that stainless steels were susceptible to a form of radiation damage called swelling that resulted in gross dimensional instability in in-core structural components that could limit the life of those components. Also, an effort to optimize piping alloy compositions was undertaken to reduce plant construction costs. Finally, attempts to increase high temperature design limits have relied on the use of oxide dispersion strengthening by application of advanced mechanical alloying processing procedures.

Fusion Reactors

Control of a fusion reaction for power generation is not yet possible. Several design concepts have been proposed, but the physics of controlled fusion power have yet to be demonstrated. Most systems involve control of a high temperature plasma using magnetic fields, so that designs have generally required a structural barrier or first wall to contain the plasma. Most designs have considered either austenitic or martensitic steels for first wall applications, although alternate materials such as vanadium alloys are also under consideration. Materials development for fusion systems has been a world-wide effort. It has been noted that one inherent advantage of fusion in comparison with fission is the relatively short radioactive lifetimes of the reaction products, and an effort has begun to develop low activation structural materials so that, after reactor decommissioning, waste storage is minimized, and the reactor and its site can be returned to other uses.

Tooics of Interest

The above description of reactor types has highlighted several ferrous alloy research and development efforts:

corrosion-related problems
irradiation embrittlement of the pressure vessels
breakaway oxidation in mild steel components
nitride strengthened cladding materials
breakaway oxidation in martensitic steel
very high temperature structural materials
swelling

optimized piping alloy compositions
oxide dispersion-strengthened mechanical alloying
materials development for fusion
low activation structural materials

The remainder of this review will consider each of these programs in turn and describe them in more detail.

Intergranular Stress Corrosion Cracking

By far the most important materials issue in the BWR nuclear steam supply system is intergranular stress corrosion cracking (IGSCC) of stainless steel coolant piping.' The problem was first identified in 1974 in 0.10 m diameter recirculation bypass piping of Dresden Unit 2 made from Type 304 stainless steel. Subsequent basic research on the phenomenon of IGSCC in welded type-304 steel that was conducted on a world-wide scale[2-3] has resulted in an accepted model to describe the operating mechanism, which requires the coexistence of three factors for its operation: a weld-sensitized microstructure, tensile stresses above 75% of yield, and an environment that supports IGSSC.[4] Reducing the severity of any one or a combination of these factors will alleviate the problem. Two potential sensitization-related remedies have been developed and evaluated: heat treatment of pipe welds and corrosion-resistant clad, and a third remedy resulted in the qualification of a commercially available alternative piping alloy that is immune to IGSCC over the lifetime of the plant.' This so-called nuclear grade (NG) stainless steel, typically Type 316, in seamless or welded pipe forms, is being installed in most of the plants where it has been decided to replace recirculation piping.[5] Table 1 compares the compositions of austenitic alloys 304, 316, and 316NG.

Table 1.

Compositions for BWR Steam System Piping Alloys

	Chemical ComDosition in w/o						
Alloy	C	Mn	N	Si	Mo	Cr	Ni
304	0.08 (max)	2.00 (max)	ns	1.00 (max)	ns	18.00-20.00	8.00-12.00
316	0.08 (max)	2.00 (max)	ns	1.00 (max)	2.00-3.00	17.00-19.00	12.00-14.00
316NG	0.02 (max)	2.00 (max)	0.01 (max)	1.00 (max)	2.00-3.00	16.00-18.00	10.00-14.00

ns = not specified

Irradiation Embrittlement of Pressure Vessel Steels

When the first commercial PWRs were being designed and built, changes in pressure vessel steel properties were anticipated arising from exposure to neutron irradiation, and programs were implemented to monitor behavior over plant lifetimes. Differences in toughness reduction with neutron fluence were found from heat to heat of the same steel, but these differences were not initially understood. Weldments exhibited the greatest shifts in response to irradiation, greater than the parent plate stock. Early pressure vessels were fabricated from plate stock using ASTM A 302 B low alloy ferritic steel. A change took place around 1968 to A533B CL1 material to improve unirradiated toughness properties.[6] Compositions for these steels are given in Table 2; the difference lies in nickel additions to A533B.

Table 2.

Compositions for LWR Pressure Vessel Steels

	Chemical ComDosition in w/o						
Alloy	C	Mn	P	S	Si	Mo	Ni
A302B	0.25 (max)	1.07-1.62	0.035 (max)	0.040 (max)	0.13-0.32	0.41-0.64	--
A533B CL1	0.25 (max)	1.07-1.62	0.035 (max)	0.040 (max)	0.13-0.32	0.41-0.64	0.37-0.73

The accumulation of irradiation embrittlement results on pressure vessel steels has continued on an international scale,'' and statistical analysis of the data base has shown in several studies that this embrittlement is due to the presence of minor element additions.[9-11] In particular, copper additions arising from welding practices, phosphorus and tin impurities and, ironically, nickel impurities in conjunction with copper, are all found to correlate with degradation in Charpy impact property behavior due to irradiation.

The mechanism that is responsible for embrittlement in pressure vessel steels, at least for the copper impurity case, has been shown by field ion microscopy/atom probe to be due to ultra-fine copper precipitates.[12-13] By inference, it is thought that other minor element effects are similarly due to precipitation and defect clustering. This understanding has led to the recommendation that pressure vessel life extension is possible by reactor vessel annealing such that the irradiation damage is removed, with a concomitant increase in toughness properties.

Ereakawav Oxidation in Mild Steel Components

Breakaway oxidation was found to be an unexpected problem in Magnox gas-cooled reactors.[14] Mild steel is used for structural steel work in the reactor and for associated boilers. Extensive laboratory studies had shown that a protective oxide would form on steel components exposed to the carbon dioxide transfer gas. However, after a few years of reactor operation, it was discovered that a more aggressive breakaway form of oxidation could occur under service conditions. The oxide that formed was porous and thus continued to form even after interstitial gaps were filled. The phenomenon of breakaway oxidation is peculiar to high pressure CO_2, and the explanatory mechanism requires that metal ions diffuse through the protective oxide, leaving vacancies behind which coalesce to form pores. Carbon monoxide produced by the oxidation reaction fills the pores and promotes the formation of carbon dioxide and free carbon. The carbon thus formed diffuses into the steel and produces cementite, which acts as a catalyst for further carbon monoxide reaction. The research program on breakaway oxidation sufficiently defined the necessary operating conditions so that reactor operating parameters could be altered to alleviate the problem and no materials specifications were affected.

Nitride Strengthened Cladding Materials Development

With the development of the AGR reactor design, stronger fuel cladding was necessary to allow load following, or non-steady state operation. As a result, an effort was made to improve the strength of niobium-stabilized stainless steel containing 20 w/o Cr and 25 w/o Ni.[15] The base composition was retained for its excellent oxidation resistance and strength was improved by the introduction of a dispersed second phase of TiN by nitriding processes. Nitride strengthening was chosen over oxide strengthening to allow greater control over chemical potential and therefore the precipitation process, and over carbide strengthening for precipitate thermal stability reasons. Titanium was chosen over zirconium to allow formation of a larger volume fraction of precipitate. Processing was optimized using non-standard nitriding procedures: an atmosphere of 95 vol% N_2 and 5 vol% H_2 at 1423 K for Ih followed by outgassing for 2.5 h at the nitriding temperature in pure hydrogen. This reduced excess nitrogen content and the tendency for Cr_2N formation. This procedure produces TiN particles in dendrite shapes resembling a cruciform about 0.5 μm in width. For levels of 2.0 w/o Ti, approximately 4% volume fraction of TiN is produced.[16] Optimization of both creep and oxidation behavior has resulted in the nominal composition given in Table 3.[17] The titanium level chosen maximizes the amount of titanium in solid solution prior to nitriding and the level of silicon was set to avoid "globular attack" or voidage formation during oxidation, a phenomenon believed to arise from non-uniform chromium distribution and peculiar to the nitrided alloys.

Table 3.

AGR Stainless Steel Cladding Compositions

	Nominal Chemical Composition in w/o							
Alloy	C	Mn	Si	Ti	Cr	Ni	Nb	N
20Cr/25Ni[15]	0.05	0.6	0.6	t0.05	20	25	0.7	0.02
20/25 TiN	0.01	0.6	0.9	2.0	20	25	--	--

Application of the nitrided cladding has been very successful. In all fueled tests completed through 1982, no cladding failures had been reported, and full deployment was awaiting two final test programs.'' In summary, the development of this high strength alloy was an all-British effort that took ten years from conception to completion of extensive testing.

Breakaway Oxidation in Martensitic Stainless Steel

Breakaway oxidation was also found to plague components made of 9Cr-1Mo in AGR systems.[18] It was decided to specify the martensitic stainless steel 9Cr-1Mo in evaporation/boiling zones of the British carbon dioxide cooled AGR system because greater corrosion resistance was needed than that obtained from 2¼Cr-1Mo, and because an austenitic steel specification for higher corrosion resistance would have required use of austenitic steel on the secondary water/steam side under conditions where its use was largely unproven. However, early testing showed that 9Cr-1Mo was prone to breakaway oxidation over the temperature range 450 to 600°C, and the behavior was sensitive both to alloy composition and component geometry. Higher levels of silicon were found to be beneficial in lowering oxidation rates at all temperatures from 450 to 550°C, and to reduce the tendency for breakaway oxidation at the higher temperatures. As a result, it was possible to tighten the silicon specification for AGR components from 0.25 · 1.0% to 0.45 · 0.75% to avoid breakaway oxidation due to low silicon levels, and to employ heats with higher silicon in the more corrosive hotter end of the boiler zone. A unique aspect of breakaway oxidation in 9Cr-1Mo was a pronounced tendency to favor edges and corners as initiation sites rather that flat surfaces. The controlling mechanism was ascribed to accelerated carbon accumulation at corners. Substitution of a plain tube design for the original finned design in the hottest areas effectively controlled the problem. Predictions for oxidation response can now be obtained based on a statistical model.[19]

Very High Temoerature Structural Materials

Structural materials research for HTGR applications began in the early 1970s and was initially concerned with generation of a properties data base for alloys such as Hastelloy X, Inconel 718, and Alloy 800H. However, by 1976, a nuclear grade of Hastelloy X, designated alloy XR, had been developed in Japan that required high levels of manganese and silicon and reduced levels (as low as possible) for phosphorus, sulfur, cobalt, aluminum, and titanium." Compositions of Hastelloy X and XR are given in Table 4.

Table 4.

Specifications in w/o for the Chemical Composition of Hastelloy XR Relative to That for Hastelloy X

		C	Mn	Si	P	S	Cr	Co	Mo	W	Fe	B	Ni	Al	Ti
HASTELLOY XR	Max.	0.15	1.0	0.5	0.040	0.030	23.00	0.5	10.00	1.00	20.00	0.01	Bal	0.10	0.03
	Min.	0.05	0.6	0.3	LAP	LAP	20.50	LAP	8.00	0.20	17.00	LAP	Bal	LAP	LAP
HASTELLOY X	Max.	0.15	1.0	1.0	0.040	0.030	23.00	2.5	10.00	1.00	20.00	0.01	Bal	--	--
	Min.	0.05	--	--	--	--	20.50	0.5	8.00	0.20	17.00	--	Bal	--	--

LAP: Lowest possible; -: Not specified

Void Swelling Resistance

Prior to 1974, the undisputed materials choice for LMR structural components was AISI 316, an austenitic stainless steel in the 17% Cr range with 13% Ni and 2% Mo. (compositional details are given in Table 1.) The choice was based on good high temperature properties, excellent corrosion resistance and ease of fabrication and welding. That choice was first challenged following the observation that AISI 316 developed cavities during neutron irradiation, indicating a volumetric expansion of the material, now called swelling." Swelling and its associated phenomenon, irradiation creep, proved to be the life-limiting factors in the application of AISI 316 for LMR fuel cladding. The discovery that cold working to the level of about 20% delayed the development of swelling[22] allowed interim use of AISI 316. In about 1974, an international effort was begun to find a replacement alloy in order to permit optimization of fast breeder reactor systems.[23]

These programs took as their missions the testing of alternative alloys for fast breeder reactor structural applications. The major goal was to reduce the tendency for irradiation induced swelling, but, at the same time, other materials properties such as creep, rupture strength, and postirradiation tensile strength were measured. A wide range of alloys was investigated including austenitic, ferritic and martensitic steels, nickel-based superalloys, and molybdenum- and niobium-based alloys. The primary candidates were titanium-stabilized austenitic steels and precipitation-strengthened superalloys. Martensitic steels were included initially as a low priority option based on observations of swelling inhibition in the ferrite phase of a ferritic/austenitic dual phase steel.[24] As it became apparent that titanium stabilization only delayed the onset of swelling[25-27] and precipitation strengthening led to severe postirradiation embrittlement,[28-29] the suitability of ferritic/martensitic alloys became more apparent.

However, development of titanium-stabilized stainless steels has proven to be beneficial for other applications. In the course of improving the swelling resistance of austenitic steels, it was learned that

phosphorus and boron additions at low levels were beneficial.[30] Not only did such additions increase swelling resistance, but they also improved the high temperature creep properties of titanium-stabilized steels.[31]

Ferritic/martensitic alloys are now finding expanded application in nuclear reactor systems as substitutes for austenitic steels. Two martensitic alloys are of greatest interest in the United States. Sandvik HT-9 is a 12% Cr, 1% Mo, 0.2% C alloy containing intentional additions of W and V. ASTM designation T91 is a modified 9% Cr alloy with 1% Mo, 0.1% C, 0.25% V, 0.1% Nb, 0.05% N. More complete compositional information is given in Table 5. Both alloys were developed for high temperature applications where the corrosion resistance inherent in austenitic stainless steels was not required, The high temperature mechanical properties of these alloys are similar, with the higher carbon and chromium additions of HT-9 balanced by careful control of vanadium, niobium, and carbon additions in T91. However, T91 has inherently better resistance to irradiation embrittlement at about 350°C, whereas HT-9 has better corrosion and swelling resistance and provides better resistance to irradiation embrittlement at 60°C.

The most significant consequence of these alloy development programs has been the application of HT-9 to most of the internal components in the U.S. experimental liquid metal-cooled test reactor, Fast Flux Test Facility (FFTF) located in Richland, WA,[34] and the expected application of similar steels in European plants.[35] For FFTF, both fuel cladding and duct work which contains the cladded fuel have been manufactured from HT-9 by cold tube drawing operations. As the duct geometry requires a hexagonal cross section, manufacture required development of hexagonal drawing operations for a martensitic steel with a ductile-brittle transition temperature (DBTT) at about room temperature. The transition from austenitic to martensitic stainless steel has dictated reduced operating temperatures in FFTF and consequential lowering of the power of the reactor from 400 to 300 MW in return for more efficient fuel cycle performance.

Table 5.

Chemical Analysis of Martensitic Steels Used for Nuclear Systems

Element	HT-9[32]	T91[33]
Carbon	0.20	0.08-0.12
Chromium	11.5	8.00-9.50
Molybdenum	1.0	0.85-1.05
Manganese	0.6	0.30-0.60
Silicon	0.4	0.20-0.50
Nickel	0.5	0.40 max
Tungsten	0.5	not spec.
Vanadium	0.3	0.18-0.25
Niobium	not spec.	0.06-0.10
Phosphorus	0.030 max	0.020 max
Sulfur	0.020 max	0.010 max
Aluminum	not spec.	0.04 max
Nitrogen	not spec.	0.030-0.070

More recently, independent design efforts for the Power Reactor Inherently Safe Module (PRISM) and Sodium Advanced Fast Reactor (SAFR) systems have also recommended the use of HT-9 for in-core structural components.[36,37] In both cases, HT-9 was chosen for in-core structural applications to improve fuel cycle economy. Fuel recycling is anticipated only every 4 years to doses as high as 3.4×10^{23} n/cm^2 E>0.1MeV or 160 dpa for PRISM and 3.5×10^{23} n/cm^2 or 175 dpa for SAFR. Austenitic steels are not expected to remain serviceable to such high doses.

Piping Alloy Optimization

A major alloy development success story concerns the alloy T91, mentioned earlier (see Table 4). T91 is a modified 9Cr-1Mo alloy containing carefully controlled ratios of additions of carbon, vanadium, niobium, and nitrogen. The alloy development work was initiated by Combustion Engineering, Inc. of Chattanooga, TN,[38] but was assimilated into a U.S. Department of Energy program for the development of an advanced alloy for out-of-core fast reactor structural applications. Programmatic responsibility resided at Oak Ridge National Laboratory.[31] The program not only provided a properties data base for T91 but also arranged for fabrication of several big heats of the alloy, at both U.S. and Japanese steel production facilities. The end product of that effort is a code-qualified steel which provides high temperature properties comparable to HT-9 and only slightly below those of austenitic stainless steel, but which is much less costly to produce than are austenitic steels. A similar steel has been developed independently in Japan using the same ratios of carbon, vanadium, niobium, and nitrogen.[39]

Mechanically Alloyed Oxide Dispersion Strensthening

A final LMR example is provided where private industry, in supporting research on materials development for irradiation environments, has developed a novel alloy. Alloy MA957 is a mechanically alloyed ferritic alloy, dispersion strengthened with yttria, commercially available from Inco Alloys International of Huntington, WV. It was developed specifically for fast reactor fuel cladding applications at a time when Inco was assisting the U.S. LMR materials development program.[40] An alloy with good high temperature strength and high radiation resistance was needed. The mechanical alloying process applies high energy ball milling to produce powders with dissimilar ingredients dispersed on a very fine scale.[41] The powders are then consolidated using powder metallurgy procedures. For MA957, the result is an alloy of base composition, Fe-14Cr-1Ti-0.25Mo, to which has been add $0.25Y_2O_3$ as 5-nm particles uniformly dispersed through the material. The cost of MA357 is significantly higher than material processed by more standard techniques, and component fabrication procedures are much more complicated and expensive. However, a component made from MA957 can be expected to have unsurpassed capability; fast breeder reactor fuel cladding made from MA957 is expected to provide at least a five-year fuel lifetime, with improved high temperature performance in comparison with HT-9.[42] Application of MA957 follows the trend of using metal-matrix composites to solve extremely difficult metallurgical problems.

Materials Development for Fusion

Concurrent with LMR materials development, an effort has evolved to develop materials for fusion reactor applications. There are similarities between the irradiation environments of a fusion first wall and fast reactor in-core components. As a result, development of fusion first wall materials has closely parallelled the LMR effort. Materials development for fusion was initiated in the U.S. in 1978, with similar efforts in Europe and Japan. As originally defined for the U.S. program, materials development concentrated on four classes of materials: austenitic alloys, higher strength Fe-Ni-Cr alloys, refractory/reactive alloys, and innovative concepts.[43] However, in part based on the encouraging results being obtained by the fast reactor effort, a fifth class of ferritic steels was added by late 1979.[44]

Over the last ten years, the attractiveness of ferritic steels for first wall applications has steadily increased. A major concern, the effect of extremely high electromagnetic fields on a ferromagnetic structure, was alleviated when it was realized that a ferromagnetic material would behave paramagnetically in an extremely strong electromagnetic field.[45-46] The status of martensitic steels for fusion applications can best be measured based on the recommendations of fusion design studies. The five most recent design studies all seriously consider HT-9,[47-51] ranking it second in comparison either with an austenitic steel or with a vanadium alloy for water-cooled Tokamak designs and, in the case of Tandem Mirror designs, ranking HT-9 first[00] or on a par with a vanadium alloy.[50] These design studies are particularly notable because, for the water-cooled designs (a very inefficient concept), martensitic steels must be operated at temperatures where very little data is available and where the material is not expected to behave well, whereas higher temperature designs will be more efficient and operate in a regime where martensitic steels can be expected to out-perform austenitic steels.

Therefore, martensitic steels have become or are becoming the materials of choice for high neutron damage irradiation environments. In order to reach this status, it has been necessary to compile materials property data bases, including irradiation response. This has been done both for LMRs[52] and for fusion systems[53] applications.

Low Activation Structural Materials

Laboratories in Japan, Europe, the USSR, and the U.S. are each designing, fabricating, and testing low activation alloys for fusion reactor structural materials that would satisfy regulations for near surface disposal of radioactive waste. A call for development of such alloys in the U.S. originated with the U.S. Department of Energy (DOE) Panel on Low Activation Materials for Fusion Applications.[54] The panel noted that "lower activation materials for fusion reactors are technically possible, may be important to the public acceptance of fusion energy, and should be a main goal of the fusion program." The element additions that must be carefully controlled are Cu, Ni, Mo, Nb, and N, with Nb representing the most severe restriction.[55-58] For near surface disposal of ferritic or martensitic steels, only minor changes in composition appear to be required, whereas for austenitic steels a substitute for nickel must be found. Alternately, isotopic tailoring could provide equivalent performance. For example, HT-9, a 12Cr martensitic steel under study for fusion applications, could be made acceptable if Mo additions were isotopically tailored to remove the unwanted isotope ^{92}Mo.[59]

The alloy compositions being considered for low activation austenitic steels all use manganese additions in substitution for nickel to maintain austenite stability. A compilation of the alloy compositions that are being studied is given in Table 6. Research and development programs for low activation austenitic alloys have been primarily concerned either with phase stability and properties of Fe-Cr-Mn alloys or with the swelling resistance of the alloy class. As a result, many of the alloys of interest have been made in small quantities, and the data base for a given composition may be very limited. Also, several commercial manganese-containing steels have been studied.

Table 6.

Compositions of Heats of Low Activation Austenitic Alloys

Alloy Designation		Composition in w/o (balance Fe) C	Si	Mn	Cr	W	P	S	Other	Ref.
A-25MN		0.25	0.2	25.7	13.6	--	0.018	0.004	0.15Ti, 0.023N	[60]
316T	nom	0.045	lmax	12.2	17	5				[61]
316T	melt	0.038	0.17	14.5	16.3	4.1				
320T	nom	0.06max	lmax	12.2	17.5	5				
320T	melt	0.050	0.18	14.8	17.7	4.22				
321T	nom	0.08max	lmax	9.7	18	0.9				
321T	melt	0.060	0.16	11.9	17.6	1.0				
FV548T	nom	0.075	0.6max	12	16.5	2.7				
FV548T	melt	0.053	0.17	i2.3	16.4	2.2				
OPTSTAB	nom	0.08max	lmax	11	15	2				
OPTSTAB	melt	0.070	0.19	11.9	14.2	2.15				
PCMA-0		0.069	0.04	13.4	15.0				0.01V, 0.01Mo, 0.03Cu, 0.001N	[62]
PCMA-1		0.014	0.02	14.2	14.8				0.01V, 0.01Mo, 0.03Cu, 0.001N	
PCMA-2		0.056	0.04	17.1	15.2				<0.01V, 0.01Mo, 0.03Cu, 0.001N	
PCMA-3		0.089	0.02	13.9	10.0				<0.01V, 0.01Mo, 0.03Cu, 0.002N	
PCMA-4		0.093	0.02	18.9	9.9				<0.01V, <0.01Mo, 0.02Cu, 0.002N	
PCMA-5		0.18	0.02	13.9	15.3				<0.01V, 0.01Mo, 0.04Cu, 0.002N	
PCMA-6		0.18	0.02	14.3	16.0				<0.01V, 0.01Mo, 0.03Cu, 0.003N	
PCMA-7		0.38	0.02	19.1	14.8				<0.01V, 0.01Mo, 0.05Cu, 0.005N	
PCMA-8		0.13	0.02	17.7	20.1				<0.01V, 0.01Mo, 0.03Cu, 0.003N	
PCMA-9		0.26	0.03	17.6	20.2				<0.01V, 0.01Mo, 0.03Cu, 0.006N	
PCMA-10		0.081	0.04	19.9	10.0				0.01V, 0.01Mo, 0.02Cu, 0.005N	
PCMA-11		0.084	0.03	19.9	11.9				0.01V, 0.01Mo, 0.02Cu, 0.009N	
PCMA-12		0.18	0.02	20.0	12.0				0.01V, 0.01Mo, 0.02Cu, 0.008N	
PCMA-13		0.088	0.04	19.2	14.0				0.01V, 0.01Mo, 0.04Cu, 0.013N	
PCMA-14		0.17	0.05	19.9	15.9				0.01V, 0.01Mo, 0.02Cu, 0.001N	
x-75		0.10	0.4	30	2				0.5Ni, 0.15N	[63]
R76		0.60	0.4	30	2		0.05		0.5Ni, 0.005B, 0.05N	
R77		0.40	0.4	30	2	1.0	0.05		0.5Ni, 0.005B, 0.15N, 1V	
R78		0.05	0.4	30	5				0.5Ni, 0.15N	
R79		0.05	0.4	30	10				0.5Ni, 0.10N	
R80		0.50	0.4	30	10	2.0			0.5Ni, 0.0056, 0.10N, 2V, 1Al	
R81		0.05	0.4	20	15				0.5Ni, 0.10N	
R82		0.40	0.4	15	5				0.5Ni, 0.10N	
R83		0.05	0.1	15	5		0.05		0.5Ni, 0.005B, 0.05N	
R84		0.70	0.4	15	5				0.5Ni, 0.10N, 2V, 1Al	
R85		0.05	0.4	15	15				0.5Ni, 0.15N	
R86		0.10	0.4	15	15				0.5Ni, 0.35N	
R87		0.10	0.4	15	15		0.05		0.5Ni, 0.0056, 0.10N	
R88		0.30	0.4	15	15	2.0	0.05		0.5Ni, 0.0056, 0.30N, 2V	
R89		0.50	0.4	15	15	2.0			0.5Ni, 0.10N, 2V, 1Al	
Nitronic 32		0.1	0.6	12	18		0.02		1.5Ni, 0.2Mo, 0.2Cu, 0.4N	[63]
18/18 PLUS		0.1	0.6	18	18		0.02		0.5Ni, 1.1Mo. 1.0Cu. 0.4N	
AMCR 0033		0.2	0.6	18	10				0.7Ni, 0.06N	
NMF3		0.6	0.7	19	4		0.02		0.2Ni, 0.09N	
NONMAG 30		0.6	0.3	14	2		0.02		2.0Ni, 0.02N	
81/5289		0.004		40.3	10.2					[64]
81/5288		0.003		30.3	10.2					
81/5286		0.004		20.0	10.5					
AMCR 0033		0.105	0.56	17.5	10.1				<0.1Ni	
AMCR 0034		0.100	0.56	17.5	10.1				<0.1Ni	
81/5287		0.004		11.	10.1					
81/5291		0.004		25.4	13.1					
AMCR 0035		0.029	0.63	19.9	14.1				0.27Ni, 0.06Mo	
81/5290		0.004		16.0	13.1					
81/5292		0.005		15.7	5.3					
81/5285		0.004		14.9	18.2					
81/5284		0.004		10.5	18.0				5.1Ni	

Table 6.
(contd)

Alloy Desianation	ComDosition in w/o (balance Fe) C	Si	Mn	Cr	W	P	S	Other	Ref.
81/5283	0.005		6.9	11.4				4.2Ni	
81/5282	0.003			17.0				l2.lNi	
1	0.4	0.5	14	12		0.04		5Ni, 0.5Mo, 2Al, lB	[65]
2	0.4	0.4	19	12		0.02		2Ni, 0.6Mo, 0.2N	
3	0.04	0.4	17	17		0.02		0.2Mo, 0.2Cu, lB, 0.2Nb, 0.3N	
4	0.03	0.3	1.7	16		0.01		l2Ni, 2.6Mo	
5	0.02	0.9	0.6	18		0.015		9.8Ni	
6	0.8	0.6	0.3	15.6				l4.6Ni, 3.3Mo, 0.5Nb	
12Cr-10Mn	0.004	0.007	10.1	12.4		0.001	0.007	<0.001Ni, 0.002N	[66]
12Cr-15Mn	0.004	t0.05	15.4	11.4		0.002		t0.003 0.035Ni, 0.0013N	
12Cr-20Mn	0.004	t0.05	20.6	11.7		0.002	0.010	0.057Ni, 0.0014N	
12Cr-25Mn	0.004	0.021	23.2	12.6		0.003	0.012	0.036Ni, 0.0014N	
12Cr-30Mn	0.003	0.009	32.2	14.6		t0.003	0.011	0.12Ni, 0.0021N	
12Cr-15Mn-3Ni	0.048	<0.05	15.3	11.8		<0.0005	0.009	2.89Ni, 0.0027N	
12Cr-15Mn-6Ni	0.047	<0.05	15.3	11.7		0.005	0.009	5.97Ni, 0.0017N	
12Cr-15Mn-9Ni	0.048	<0.05	15.1	12.0		<0.0005	0.008	9.09Ni, 0.0021N	
8Cr-15Mn	0.005	0.004	15.3	7.9		t0.003	0.006	<0.005Ni, 0.0016N	
10Cr-15Mn	0.007	0.010	15.3	9.9		t0.003	0.006	<0.005Ni, 0.0016N	
12Cr-15Mn-.05C	0.048	0.006	15.1	8.7		t0.003	0.006	<0.005Ni, 0.0023N	
12Cr-15Mn-.1C	0.088	0.010	14.2	11.2		t0.003	0.005	<0.005Ni, 0.0017N	
12Cr-15Mn-.2C	0.18	0.008	14.4	11.6		<0.003	0.005	<0.005Ni, 0.0021N	
12Cr-15Mn-.3C	0.28	0.007	14.4	11.6		t0.003	0.005	<0.005Ni, 0.0022N	
12Cr-15Mn-.2N	0.005	0.035	14.1	11.3		t0.003	0.008	<0.005Ni, 0.18N	
12Cr-15Mn-.2C-.2N	0.2	<0.05	15.0	11.7		t0.0005	0.009	0.009Ni, 0.17N	
16Cr-15Mn	0.004	0.006	15.2	16.3		0.005	0.006	0.0018N	
20Mn-12Cr	0.25		20	12					[67]
20Mn-12Cr-1W	0.25		20	12	1				
20Mn-12Cr-.3Ti	0.25		20	12				0.3Ti	
20Mn-12Cr-.3Ti-1W	0.25		20	12	1			0.3Ti	
20Mn-12Cr-4Ni	0.25		20	12				4n1	
10Mn-16Cr	0.25		10	16					

The results obtained so far demonstrate that the response to irradiation of low activation Fe-Cr-Mn alloys is similar to Fe-Cr-Ni austenitic stainless steels.[62-69] Simple alloys swell at similar rates and more complex alloys are superior to simple alloys. Cold working reduces swelling but accelerates the formation of carbide and intermetallic phases. Also, a similar tendency for sensitization to stress corrosion cracking has been demonstrated.[67] However, phase stability relationships are more complex, both under irradiation and in thermal environments;[63,62] therefore, care must be taken to develop Fe-Cr-Mn alloys suitable for fusion service.

The alloy compositions being considered for low activation ferritic or martensitic steels are based on two commercially important alloy classes: 2-1/4Cr steels and the super 9 to 12Cr steels. The former is in fact a bainitic class and the latter a martensitic class. Both of these steels contain Mo at levels of about 1%. Therefore, design of low activation alternatives requires substitution for Mo. Leading candidates are W and V, with consideration given for using Ta as a substitute for Nb. In order to obtain a fully martensitic 12Cr steel without additions of Ni, austenite stabilizing additions must be included. Thus far Mn and C have been considered. Therefore, three classes of low activation ferritic/martensitic alloys are possible: low chromium bainitic alloys, 7 to 9Cr martensitic alloys, and 12Cr stabilized martensitic alloys. The alloy compositions which have been considered are given in Table 7, and for comparison, examples of similar commercial alloys are given in Table 8. The alloys in Table 7 have been grouped by composition in order to emphasize the similarities among the approaches taken at different laboratories. Examination of Table 7 shows that the 7 to 9Cr alloy class and the 12Cr alloy class are about equal in size and the smallest group is the 2Cr range. In each class, each of the alloying approaches have been tried: W substituted for Mo, V substituted for Mo, and small additions of Ta substituted for Nb (except for Ta additions to 2Cr alloys). However, in many cases, the higher Cr alloys were found to be duplex martensitic/delta ferritic and therefore further changes in compositional specification were needed.

Table 7.

Compositions of Heats of Low Activation Ferritic/Martensitic Alloys

Alloy Designation	Composition in w/o											Ref.
	Cr	W	V	C	Si	Mn	Ta	B	N	P	S	
2Cr-2W	2.06	1.96	--	0.10	0.29	0.50			0.001	t0.002	0.004	[70]
2CrV	2.36	--	0.25	0.11	0.17	0.40						[71]
2Cr-1WV	2.30	0.93	0.25	0.10	0.13	0.34						
2Cr-2W	2.48	1.99	0.01	0.11	0.15	0.39						
2Cr-2WV	2.42	1.98	0.24	0.11	0.20	0.42						
L1	2.32	<0.01	0.50	0.09	0.08	<0.01			0.004	<0.005	0.003	[71]
L2	2.82	<0.01	1.01	0.09	0.08	t0.01			0.003	<0.005	0.002	
L3	2.46	--	1.50	0.11	0.30	0.30			0.015	t0.005	0.015	
5Cr-2W	4.84	1.98	--	0.10	0.30	0.50			0.002	<0.002	0.004	[70]
5Cr-2WV	5.00	2.07	0.25	0.13	0.25	0.47						[71]
F-82	7.52	2.2	0.19	0.10	0.17	0.49	--	0.0035	0.002	0.003	0.002	[72]
F-82H	7.65	2.0	0.18	0.09	0.09	0.49	0.04	0.0034	0.002	0.005	0.001	
9Cr-2W	8.92	1.92	--	0.10	0.28	0.48			0.002	t0.002	0.003	[70]
9Cr	8.96	--	--	0.10	0.30	0.49			0.001	t0.002	0.003	
9Cr-1W	9.01	0.99	--	0.10	0.29	0.48			0.002	t0.002	0.004	
9Cr-2W	8.92	1.92	--	0.10	0.28	0.48			0.002	t0.002	0.003	
9Cr-4W	9.09	3.93	--	0.10	0.29	0.50			0.002	<0.002	0.002	
9Cr-.25V	8.82	--	0.26	0.13	0.30	0.46			0.019	<0.002	0.002	
9Cr-.5V	8.86	--	0.53	0.11	0.29	0.48			0.020	t0.002	0.003	
9Cr-1V	0.72	--	1.03	0.12	0.31	0.51			0.018	t0.002	0.003	
9Cr-2WV	8.73	2.09	0.24	0.12	0.25	0.51						[71]
9Cr-2WVTa	8.72	2.09	0.23	0.10	0.23	0.43	0.075					
GA3X nom.	9	2.5	0.3	0.15	--	--						[71]
melt	7.5	1.95	0.02	0.17		0.002					0.005	
GA3X	9.00	2.0	0.30	0.15	0.06	0.04			0.002	0.001	0.001	[73]
GA5X	8.92	2.1	0.30	0.15	0.05	0.04			0.002	0.001	0.002	
LA12	9.1	0.68	0.24	0.16								[74]
LA13	9.2	2.90	0.25	0.17								
LA13	9.22	2.90	0.25	0.17	0.42	0.74	--		0.059			[75]
LA13Ta	9.0	2.96	0.25	0.18	0.04	0.70	0.11		0.045			
LA12	9.1	0.68	0.24	0.16	0.37	0.79	--		0.06			
LA12Ta	9.8	0.85	0.27	0.16	0.03	0.80	0.10		0.042			
LA12TaLN	9.1	0.77	0.25	0.17	0.02	0.74	0.10		0.004			
LA12LC	9.0	0.76	0.38	0.09	0.03	1.01	--		0.033			
LA12TaLC	8.9	0.76	0.39	0.09	0.03	1.01	0.09		0.019			
L4	9.13	0.01	0.52	0.10	0.09	0.02			0.003	<0.005	0.003	[71]
L6	9.14	0.02	1.23	0.20	0.09	1.08			0.003	t0.005	0.003	
L5	9.02	0.01	0.51	0.10	0.09	2.68			0.003	t0.005	0.003	
L7	8.82	0.89	0.27	0.10	0.10	2.44			0.002	<0.005	0.004	
LA2	11.4	t0.02	0.26	0.16								[74]
LA3	11.5	0.24	0.25	0.16								
LA4	10.9	0.65	0.25	0.17								
LA5	10.9	1.12	0.24	0.16								
LA6	11.7	1.95	0.24	0.15								
LA7	11.2	3.04	0.23	0.17								
LA8	11.1	0.66	0.46	0.16								
LA9	11.7	0.77	0.80	0.15								
LA10	11.4	0.70	0.25	0.16				0.0083				
LA11	11.2	0.69	0.25	0.16					0.103			
LA14	11.4	2.94	0.25	0.17			0.19		0.04			

Table 7

(contd)

Alloy Designation	Composition in w/o Cr	W	V	C	Si	Mn	Ta	B	N	P	S	Ref.
LA7	11.3	2.94	0.25	0.17	0.26	0.76	--		0.059			[75]
LA7Ta	11.4	2.90	0.25	0.15	0.07	0.76	0.12		0.073			
LA7TaLN	11.1	2.95	0.24	0.18	0.04	0.70	0.10		**0.005**			
L8	12.19	<0.01	1.05	0.09	0.10	6.47			0.003	<0.005	**0.005**	[71]
L9	11.81	0.89	0.28	0.10	0.11	6.47			0.003	**<0.005**	**0.005**	
12Cr1WVTa	11.96	0.82	0.23	0.09	0.10	***6.56***	0.14		0.008	<0.005	0.004	[76]
12Cr1WVTa'	11.95	0.80	0.25	0.10	0.09	6.45	0.20		0.003	t0.005	0.006	
12Cr1VWTa	11.80	0.22	0.97	0.10	0.10	7.84	0.23		**0.005**	<0.005	0.006	
12Cr-2WV	11.49	2.12	0.23	0.10	0.24	**0.46**						[71]
12Cr2WV3Mn	11.23	1.79	0.21	0.08	0.23	2.76						[77]
12Cr2WV6Mn	10.86	1.97	0.21	0.08	0.20	5.57						
1Cr2WV	11.52	1.83	0.22	0.17	0.20	0.40						
GA4X nom.	11	2.5	0.3	0.15								[71]
melt	10.2	1.1	0.2	0.01	--	0.011					<0,003	
GA4X	11.0	2.0	0.30	0.14	0.05	0.04			0.002	0.001	0.001	[73]
GA6X	11.1	2.1	0.30	0.15	0.07	0.04			0.002	0.001	0.002	
12Cr-2W	11.56	1.96	--	0.10	0.32	0.49			0.001	t0.002	0.003	[70]
15Cr-2W	14.72	1.94	--	0.11	0.30	0.49			0.001	t0.002	0.003	

nom. - nominal composition
melt - actual melt composition

Table 8.

Examples of Commercial Alloy Compositions in w/o Similar to Low Activation Ferritic Alloys.

Alloy	Cr	Mo	C	Mn	Ni	V	Si	Nb	W	P	S
2¼Cr-1Mo	2.25	1.0	0.09	0.45	--	t0.03	0.20	--	--	t0.015	t0.015
T91	8.43	0.89	0.09	0.37	0.11	0.24	0.16	0.08	--	0.011	0.004
FV448	11.3	0.66	0.15	--	0.75	0.25	t0.02				
HT-9	11.80	1.02	0.21	0.50	0.58	0.32	0.22	--	0.50	0.007	0.003

Therefore, a broad range of low activation ferritic alloys are possible. Low activation bainitic alloys in the Fe-2Cr composition range, martensitic alloys in the Fe-7 to 9Cr range and stabilized martensitic alloys in the Fe-12Cr range have been successfully fabricated and are undergoing testing on an international level. However, it is found that irradiation significantly degrades the properties of bainitic and stabilized martensitic alloys.[78] Bainitic alloys containing vanadium develop severe hardening due to irradiation-induced precipitation at temperatures below 450°C and extreme softening due to carbide coarsening at temperatures above 500°C. Stabilized martensitic alloys which rely on manganese additions to provide a fully martensitic microstructure are embrittled at grain boundaries following irradiation, leading to severe degradation of impact properties. The most promising composition regime appears to be the 7 to 9Cr range with tungsten additions in the 2% range, where high temperature mechanical properties and microstructural stability are retained and impact properties are relatively unaffected by irradiation. The higher void swelling behavior observed in these alloys is not expected to be a major problem.

CONCLUSIONS

Nuclear energy development is sufficiently costly to require systems optimization on a large scale. As a result, there have been many examples of research and development programs involving ferrous metallurgy for

nuclear energy systems. Those programs have included control of stress corrosion cracking and irradiation embrittlement in water-cooled reactors, breakaway oxidation, nitrided materials development and materials specification for very high temperature applications in gas-cooled reactors, control of swelling resistance, piping alloy optimization and development of oxide dispersion strengthening for liquid metal reactors, and materials development and low activation alloy development for fusion energy systems. Each of these programs has been described in detail.

FUTURE WORK

No further review on this subject is planned.

REFERENCES

1. J. T. A. Roberts, in Materials for Future Energy Systems, American Society for Metals, Metals Park, OH (1985) 51.

2. Seminar on Countermeasures for Pipe Cracking in BWRs, EPRI WS-79-174, Electric Power Research Institute, Palo Alto, CA (1980).

3. Proceedings: Second Seminar on Countermeasures for Pipe Cracking in BWRs, EPRI-NP-3684-SR, Electric Power Research Institute, Palo Alto, CA (1984).

4. F. P. Ford: EPRI NP-2589 (1982).

5. J. C. Danko: Proceedings of the International Symposium on Environmental Degradation of Materials in Nuclear Power Systems -Water Reactors, National Association of Corrosion Engineers, Houston, TX (1984) 209.

6. W. P. Chernock et al., ibid ref. 1, 61.

7. Coordinated Research Programme on Irradiation Embrittlement of Pressure Vessel Steels, Rep. IAEA-176, International Atomic Energy Agency, Vienna (1975).

8. Analysis of the Behavior of Advanced Reactor Pressure Vessel Steels Under Neutron Irradiation, Technical Report Series No. 265, International Atomic Energy Agency, Vienna (1986).

9. J. D. Varsik and S. T. Byrne, in Effects of Radiation on Structural Materials, ASTM STP 683, American Society for Testing and Materials, Philadelphia, PA (1979) 252.

10. C. Guionnet, Y. Robin, C. Flavier, A. Lefort, D. Gros, and R. Perdreau, in Effects of Radiation on Materials, ASTM STP 725, American Society for Testing and Materials, Philadelphia, PA (1981) 20.

11. G. R. Odette and G. E. Lucas, in Radiation Embrittlement of Nuclear Reactor Pressure Vessel Steels, ASTM STP 909, American Society for Testing and Materials, Philadelphia, PA (1986) 207.

12. M. K. Miller and S. S. Brenner, Res. Mechanica 10 (1984) 161.

13. R. G. Lott, in Proceedings of Topical Conference on Ferritic Allovs for Use in Nuclear Energy Technologies, J.W. Davis and O.J. Michel, Eds., Metallurgical Society of AIME, New York, NY (1984) 37.

14. D. W. James, Nuclear Technology 55 (1981) 50.

15. H. E. Evans and D. A. Hilton, Nucl. Energy, 18 (1979) 33.

16. H. E. Evans, I. Beden, and R. C. Ecob, Proc. R. Soc. Lond. A, 404 (1986) 339.

17. H. E. Evans, in Gas-Cooled Reactors Today, Vol. 2, British Nuclear Energy Society, London (1983) 55.

18. J. W. Taylor, ibid, Vol. 4, 183.

19. P. C. Rowlands , D. R. Holmes, A. Whittaker, R. A. Brierley and J. C. P. Garrett, ibid, Vol. 4, 173.

20. M. Shindo and T. Kondo, ibid, Vol 2, 179.

21. C. Cawthorne and E. J. Fulton, Nature, 216 (1967) 515.

22. J. L. Straalsund, H.R. Brager, and J. J. Holmes, in Radiation-Induced Voids in Metals, CONF-710601 (1972) 142.

23. *See* Session 1 in Radiation Effects in Breeder Reactor Structural Materials, M.L. Bleiberg and J.W. Bennett, Eds., Metallurgical Society of AIME, New York, NY (1977).

24. S. D. Harkness, B. J. Kestel and P. Okamoto, ibid ref. 22, 334.

25. F. A. Garner, H. R. Brager, and R. J. Puigh, J. Nucl Mater. 133 & 134 (1985) 535.

26. J. L. Seran, L. LeNaour, P. Grosjean, M. P. Hugon, Y. Carteret, and A. Maillard, in Effects of Radiation on Materials: Twelfth International Symposium, F. A. Garner and J. S. Perrin, Eds., ASTM STP 870, ASTM, Philadelphia, PA (1985) 233.

27. R. J. Puigh and F. A. Garner, in Radiation-Induced Chanaes in Microstructure: 13th International Symposium (Part 1) F. A Garner, N. H. Packan and A. S. Kumar, Eds., ASTM STP 955, ASTM, Philadelphia, PA. (1987) 154.

28. R. Bajaj et al, in Effects of Radiation on Materials: Tenth Conference, ASTM STP 725, D. Kramer, H. R. Brager and J. S. Perrin, Eds., ASTM, Philadelphia, PA. (1981) 326.

29. W. J. S. Yang, D. S. Gelles, J. L. Straalsund and R. Bajaj, J. Nucl. Mater. 132 (1985) 249.

30. M. L. Hamilton, G. D. Johnson, R. J. Puigh, F. A. Garner, P. J. Maziasz, W. J. S. Yang, and N. Abraham, in Residual and Unspecified Elements in Steel, A. S. Melilli and E. G. Nesbett, Eds., ASTM STP 1042, ASTM, Philadelphia, PA (1989) 124.

31. P. J. Maziasz, JOM V41 No. 7 (1989) 14.

32. Sandvik HT-9 data sheet S-1,720-ENG, May 1981.

33. V. K. Sikka, in Proceedinas of Topical Conference on Ferritic Allovs for use in Nuclear Energy Technoloaies, J.W. Davis and D.J. Michel, Eds., Metallurgical Society of AIME, New York, NY (1984) 317.

34. A. J. Lovell, A. L. Fox, W. H. Sutherland, and S. L. Hecht, in International Conference on Reliable Fuels for Liauid Metal Reactors, ANS (1987) 3-25.

35. K. Q. Bagley, E. A. Little, V. Levy, A. Alamo, K. Ehrich, K. Anderko, and A. Calza Bini, in Materials for Nuclear Reactor Core Applications, Vol. 2, British Nuclear Energy Society, London (1988) 37,

36. F. E Tippets, L. N. Salerno, C. E. Boardman, W. Kwant, R. E. Murata, and C. R. Snyder, Proc. Amer. Power Council, 49 (1987) 874-883 or S. Vaidyanathan and R. E. Murata, ibid ref. 32, 1-43.

37. D. S. Bost and L. D. Felten, ibid ref. 32, 1-61.

38. G. C. Bodine and R. E. McDonald, in Ferritic Steels for Hiah-Temperature Applications, A. K. Khare, Ed., American Society for Metals, Metals Park, OH (1983) 9.

39. K. Hashimoto, M Yamanaka, Y. Otoguro, T. Zaizen, M. Omoyama, and T. Fujita, ibid ref. 31, 307

40. J. J. Fischer, US Patent 4,075,010, Feb. 21, 1978.

41. Frontiers of High TemDerature Materials 11, J. S. Benjamin and R. C. Benn, Eds., International Nickel Company, Huntington, WV (1985).

42. R. W. Powell, G. D. Johnson, M. L. Hamilton, and F. A. Garner, ibid ref. 32, 4-17.

43. The Fusion Reactor Materials Program Plan Section 1, Alloy Development for Irradiation Performance, DOE/ET-0032/1, July 1978.

44. Alloy Development for Irradiation Performance Ouarterlv Proaress Reports beginning with the period ending December 31, 1979, DOE/ER-0045/1-16.

45. S. N. Rosenwasser, P. Miller, J. A. Dalessandro, J. M. Rawls, W. E. Toffolo, and W. Chen, J. Nucl. Mater. 85 & 86 (1979) 177.

46. H. Attaya, G. L. Kulcinski, and W. G. Wolfer, J. Nucl. Mater. 122 & 123 (1984) 96.

47. Starfire. A Commercial Tokamak Fusion Power Plant Studv, ANL/FPP-80-1, V1, Sept. 1980, p. 10-232.

48. A Demonstration Tokamak Power Plant Study, ANL/FPP/82-1, Sept. 1982, p. 2-3.

49. MARS Mirror Advanced Reactor Study. Final Report, Volume 1-B, UCRL-53480, July 1984, 12-9.

50. Blanket Comnarison and Selection Study, Final Report, ANL/FPP-84-1, Sept. 1984, 7.3.

51. Modeling, Analysis and Experiments for Fusion Nuclear Technology, FNT Progress Report: Modeling and FINESSE, Jan. 1987, 1021.

52. J. L. Straalsund and D. S. Gelles, oral presentation, ibid ref. 31, HEDL-SA-2771, May 1983

53. D. S. Gelles, J. Nucl. Mater. 149 (1987) 192.

54. Report of the DOE Panel on Low Activation Materials for Fusion Applications, R.W. Conn, Panel Chairman, UCLA/PPG-728, June 1983.

55. D.G. Ooran, A.F. Rowcliffe and F.M. Mann, J. Nucl. Mater., 141-143 (1986) 1074.

56. O.N. Jarvis, Low-Activity Materials Reuse and Disposal, AERE - R 10860, July 1983.

57. C. Ponti, Fusion Tech., 13 (1988) 157.

58. G. J. Butterworth and L. Giancarli, J. Nucl. Mater., ICFRM-3 Conference Proceedings, to be published.

59. J. D. Gordon, J.J. Thomson and S.N. Suchard, Isotopically Tailored HT-9 Steel for Radioactive Waste Management, TRW-FRE-001, December 1983.

60. M. Tamura, H. Hayakawa, M. Tanimura, A. Hishinuma, and T. Kondo, J. Nucl. Mater., 141-143 (1986) 1067.

61. A. H. Bott, F. B. Pickering, and G. J. Butterworth, J. Nucl. Mater., 141-143 (1986) 1088.

62. R. L. Klueh and E. E. Bloom, in Optimizing Materials for Nuclear Annlications, F. A. Garner, O. S. Gelles, and F. W. Wiffen, Eds., The Metallurgical Society, Inc., Warrendale, PA (1985) pp. 73.

63. F. A. Garner and J. M. McCarthy, in Reduced Activation Materials for Fusion Reactors, R. L. Klueh, D. S. Gelles, M. Okada, and N. H. Packan, Eds., ASTM, Philadelphia, PA (1990) 19.

64. W. Schiile, E. Lang, and A. Panzarasa, Study of Phase Transformations in Fe-Mn-Cr Alloys, EUR 11756 EN, Commission of the European Communities, Joint Research Centre, Ispra Establishment (1988).

65. V. K. Shamardin, T. M. Bulanova, V. S. Neustroev, L. I. Ivanov, E. V. Djomina, and Yu. M. Platov, in Reduced Activation Materials for Fusion Reactors, R. L. Klueh, D. S. Gelles, M. Okada, and N. H. Packan, Eds., ASTM, Philadelphia, PA, 1990

66. Y. Hosoi, Y. Okazaki, N. Wade, and K. Miyahare, J. Nucl. Mater., 169 (1989) 257.

67. G. E. C. Bell, P. F. Tortorelli, and E. A. Kenik, in J. Nucl. Mater., ICFRM-4 Conference Proceedings, to be published.

68. F. A. Garner, H. R. Brager, and H. Takahashi, ibid ref. 67.

69. S. Ohnuki, F. A. Garner, H. Takahashi, and J. M. McCarthy, ibid ref. 67.

70. T. Noda, F. Abe, H. Araki, and M. Okada, J. Nucl. Mater., 141-143 (1986) 1102.

71. R. L. Klueh, D. S. Gelles, and T. A. Lechtenberg, J. Nucl. Mater., 141-143 (1986) 1081.

72. M. Tamura, H. Hayakawa, M. Tanimura, A. Hishinuma, and T. Kondo, J. Nucl. Mater., 141-143 (1986) 1067.

73. Letter; C-Y. Hsu to D. S. Gelles, September 29, 1987, providing compositions of alloys manufactured by Mitsubishi Corporation, Japan.

74. D. Dulieu, K. W. Tupholme and G. J. Butterworth, J. Nucl. Mater., 141-143 (1986) 1097.

75. K. W. Tupholme, D. Dulieu and G. J. Butterworth, J. Nucl. Mater., ICFRM-4 Conference Proceedings, to be published.

76. O. S. Gelles, previously unpublished.

77. R. L. Klueh and P. J. Maziasz, ibid ref. 63, 140

78. O. S. Gelles, ibid ref. 63, 113.

6.2 Austenitic Stainless Steels

IRRAOIATION CREEP IN FUSION REACTOR MATERIALS AT LOW TEMPERATURES — M. L. Grossbeck and L. K. Mansur (Oak Ridge National Laboratory)

OBJECTIVE

This study was conducted to evaluate irradiation creep at temperatures relevant to the ITER (International Thermonuclear Experimental Reactor).

SUMMARY

Irradiation creep has been investigated in the Oak Ridge Research Reactor (ORR) at 60 to 400°C in an assembly spectrally tailored to achieve a He:dpa ratio of 12 to 14:1 appm/dpa in austenitic stainless steels. It was found that austenitic alloys, especially PCA, have higher creep rates at 60°C than at 330 and 400°C. A new mechanism was proposed and a corresponding theoretical model developed. Since vacancy migration times can be a few orders of magnitude longer than the irradiation times in this temperature regime, the immobile vacancies do not cancel climb produced by mobile interstitials absorbed at dislocations, resulting in a high climb rate. Preliminary calculations indicate that this mechanism coupled with preferred absorption driven glide predicts a high creep rate at low temperatures and a weak temperature dependence of irradiation creep over the entire temperature range .investigated.

PROGRESS AND STATUS

Introduction

Although irradiation creep has been known to occur below 200°C for the past 20 years,' little attention has been paid to it since most applications for reactor structural materials have been for fission power reactors that operate at higher temperatures. In addition, the effect was believed to be a transient of short duration. Near-term fusion devices such as the International Thermonuclear Experimental Reactor (ITER), will operate with high neutron flux components at temperatures below 100°C (ref. 2). This temperature is below the swelling regime for all structural alloys, but our recent work has shown that irradiation creep can be as large an effect at 100°C as at 500°C. The effects of irradiation creep can be beneficial in a fission reactor in that it relieves stresses induced by swelling and allows fuel to flow into a central void rather than bulge its cladding. It is also possible for irradiation creep to induce plastic flow at the tip of a crack, thus blunting and arresting its propagation. Nonetheless, irradiation creep must be considered in the design of fusion reactor components since, in addition to the beneficial effects noted above, it may also lead to bulging, bowing, or other unacceptable deformation of structural components. The magnitude of the effects of irradiation creep is illustrated in Fig. 1, where the stress in a tightened bolt is shown as a function of displacement level. If a bolt is torqued to a stress of 250 MPa and placed in a neutron flux, irradiation creep will relieve the stress by the time a displacement level of 10 dpa has been attained. Of course, the first wall of a fusion reactor will not be bolted, but the example illustrates that irradiation creep is an important source of deformation and must be considered in the design of fusion devices.

Experimental Procedures

Both austenitic and ferritic/martensitic alloys were investigated. AISI type 316 stainless steel in 20% cold-worked and in annealed conditions as well as the U.S. and Japanese PCA alloys were investigated. Type 316 stainless steel was selected from both U.S. heat X15893 (ref. 3) and Japanese heat J316 (ref. 4). The PCA specimens were from U.S. heat K-280 (ref. 3) and Japanese heat JPCA.[5] Only the Japanese alloys were investigated in annealed as well as cold-worked conditions: the JPCA was 15% cold worked, and the J316 was 20% cold worked. The ferritic alloys Sandvik HT-9, heat 91353 (ref. 6), and a laboratory heat of the pure binary Fe-15Cr were also investigated to study irradiation creep in normally low swelling alloys. Tube specimens 4.57 mm in diameter and 25.4 mm long with a wall thickness of 0.25 mm (0.18 for HT-9) were pressurized with helium to exert desired stresses between 50 and 400 MPa.

The experiments were carried out in the ORR in irradiation vehicles where the neutron flux was tailored to achieve a He:dpa ratio of 12 to 14 appm/dpa, characteristic of that expected in a fusion environment. Atomic displacement levels of 7 to 8 dpa were achieved and helium levels of 60 to 125 appm, depending upon the alloy, were produced.

The tubes were profiled with a non-contacting laser micrometer system with a precision of ~250 nm. A total of 300 measurements were made on each tube and the central three-fifths were used to compute the diameter changes of the tubes. Details of the experiments are given by Grossbeck et al.[7].

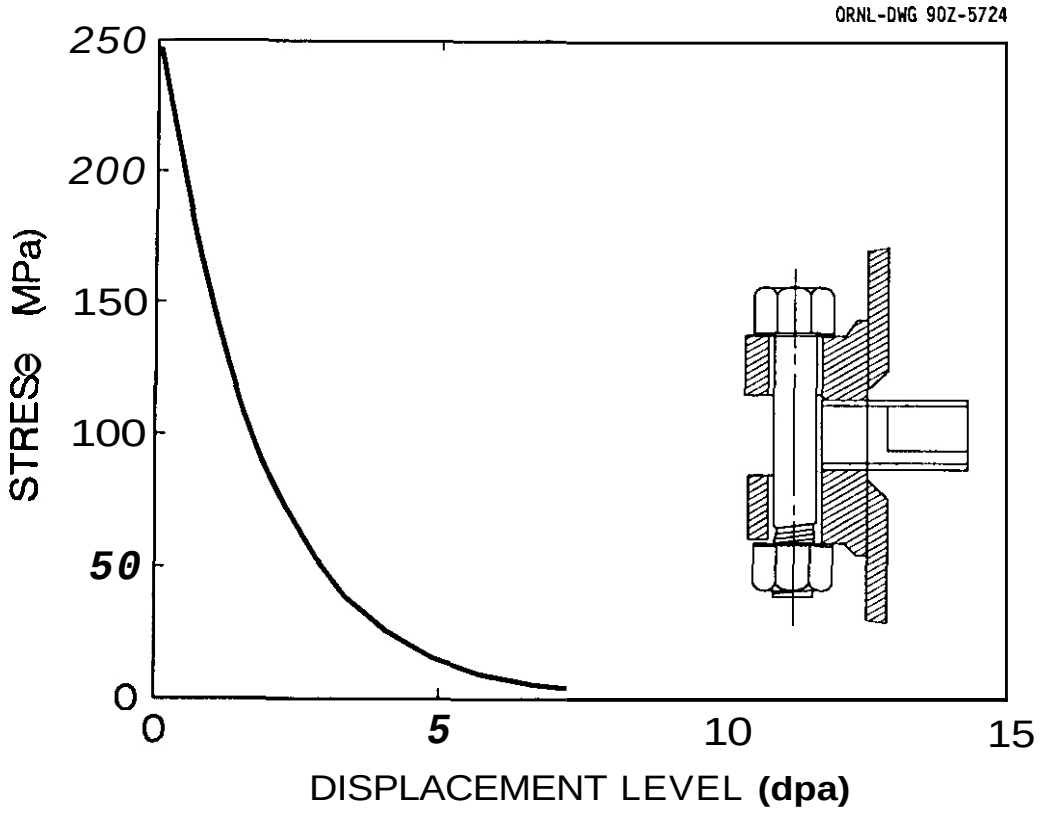

Fig. 1. Relief of stress in a bolt, originally torqued to a stress of 250 MPa, exposed to a neutron flux.

Results and Discussion

Figures 2 and 3 show the measured creep of austenitic stainless and ferritic steels, respectively, as a function of temperature for three temperatures: 60, 330 and 400°C; the creep rates are shown in Table 1. At 330 and 400°C, the creep rates are nearly the same, in agreement with previous similar experiments.[3,8] Experiments on the same austenitic alloys also indicated a small or negligible temperature dependence in the range 330 to 600°C.[3] The creep rates for the ferritic steels are about a factor of 3 to 6 lower than for austenitic alloys at 330 and 400°C. An exception is the binary Fe-15Cr alloy at 400°C. which has a creep rate comparable to the austenitic alloys. Since this alloy is a high-purity laboratory heat, it is likely to be weak in thermal creep which could account for the large deformation at 400°C.

At 60°C, creep rates are higher than at 330 and 400°C for all alloys. The most pronounced differences occur in U.S. PCA and in the two ferritic alloys where creep rates 6 to 18 times higher than at 330 and 400°C are observed at 60°C.

The weak temperature dependence of irradiation creep has been known for many years. Hudson et al.[9] observed a rather abrupt reduction in the temperature dependence of creep between 500 and 550°C in type 321 stainless steel using proton irradiation. The low-temperature portion of the curve obtained for creep rate was weakly temperature dependent and was attributed to the phenomenon of irradiation creep. This temperature insensitivity below the thermal creep regime has been confirmed by Puigh,[10] Grossbeck and Horak,[3] and cited in a review by Straalsund.[11] Since most of the neutron irradiations have been done in relation to liquid metal breeder reactor development programs, temperatures below 400°C were seldom investigated. However, perhaps the first observation of irradiation creep was by Zaimovsky et al.[12,13] in uranium at a temperature of only 200°C (Fig. 4). Hesketh[1] later observed irradiation creep in nickel and Zircaloy at 195°C. In a comprehensive review of irradiation creep, Gilbert[14] suggested that the creep rate increases with decreasing temperature.

Although irradiation creep has been observed at low temperatures, it is not understood in terms of currently accepted theory. Perhaps the most widely accepted mechanisms are stress-induced preferential absorption (SIPA)[15-17] and the climb-enabled-glide mechanism,[18] which is driven by SIPA and other climb processes that enable glide and produce creep. Both of these mechanisms lead to a linear dependence on interstitial concentration and diffusivity. For SIPA, we have

$$\dot{\varepsilon} = 2/9\ \Omega\ \Sigma D_i C_i Z_i\ , \qquad (1)$$

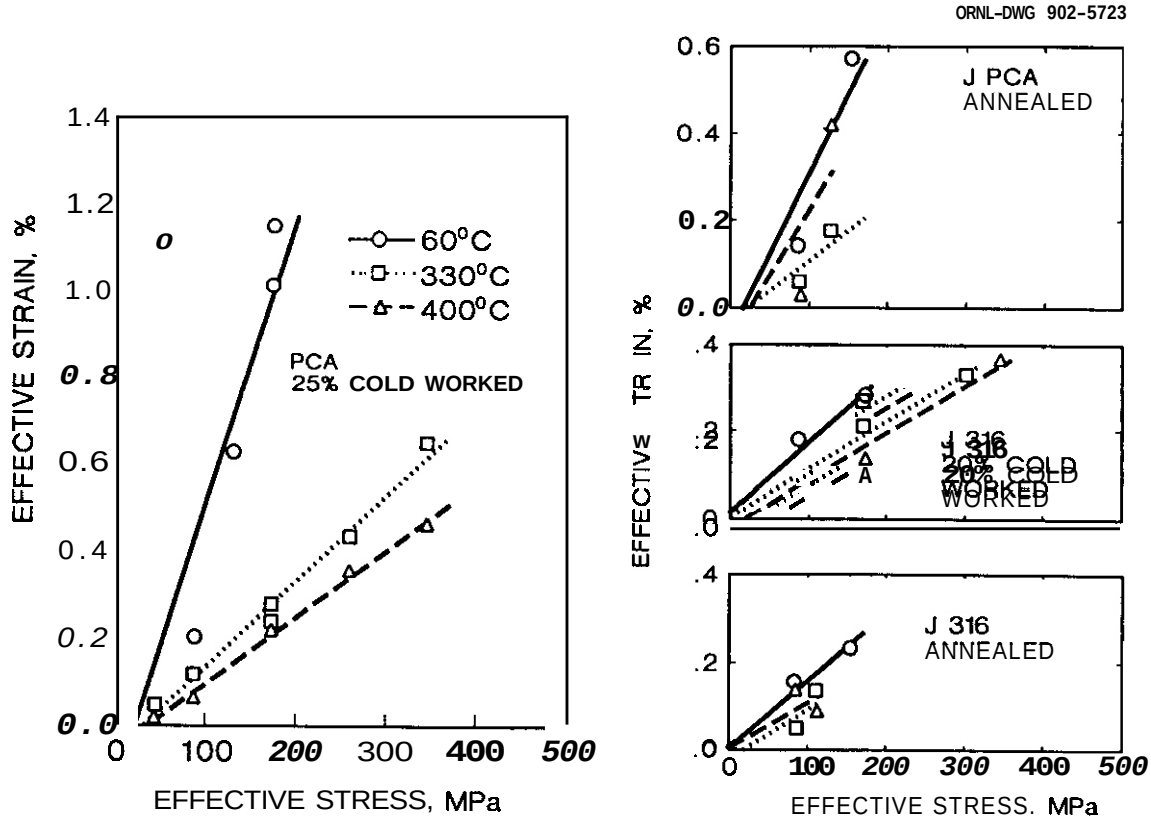

Fig. 2. Total irradiation creep deformation in austenitic alloys irradiated in a spectrally tailored neutron flux in the ORR to a displacement level of 8 dpa.

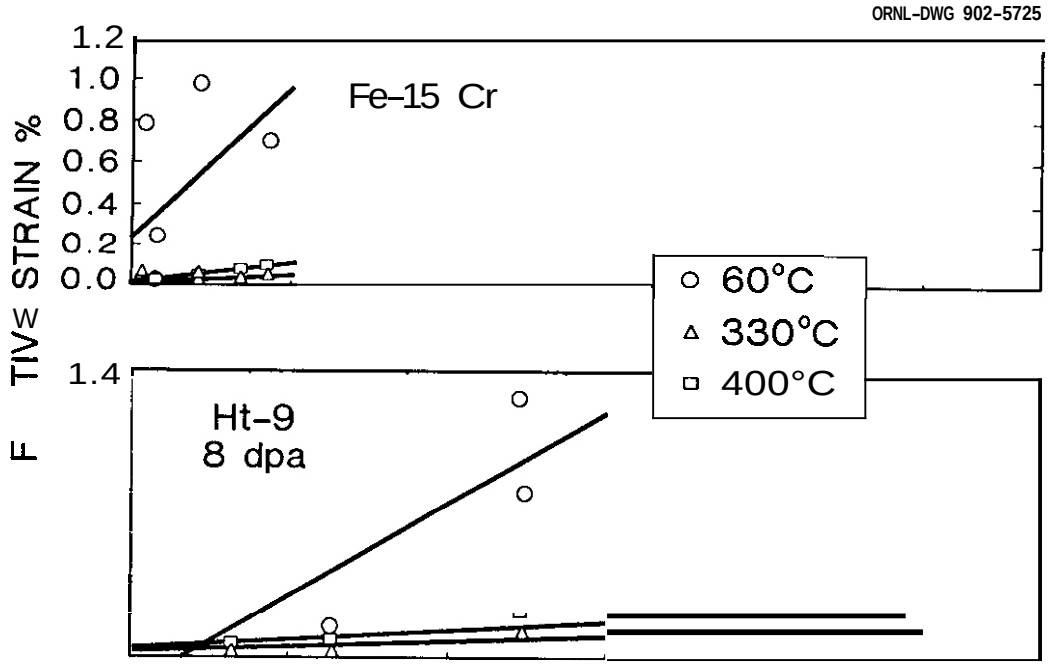

Table 1. Average creep rates for ORR-irradiated alloys in terms of effective stress and strain (MPa^{-1} dpa^{-1} × 10^{-6})

Alloy	Heat	Temperature, °C		
		60	330	400
USPCA (25% CW)	K-280	9.1–14	2.5	1.8
JPCA (SA)		5.1	1.7	3.5
316 (SA)	5316	2.2	1.4	1.4
316 (20% CW)	5316	2.2	1.3	1.3
HT-9	91353	6.3	0.35	0.56
Fe-15Cr		10.0	0.76	1.5

and for SIPA-driven climb-enabled glide we have

$$\dot{\varepsilon} = 4/9\ E/b\ (\pi L)^{1/2}\ \Omega\ D_i C_i Z_i\ , \qquad (2)$$

where $\dot{\varepsilon}$ is the creep rate, Ω is the atomic volume, L is the dislocation density, D_i is the interstitial diffusivity, C_i is the interstitial concentration, Z_i is the differential bias resulting from the preferred orientation, E is the elastic modulus, and b is the Burgers vector. The dependence on D_iC_i leads to a reduction in creep rate of about two orders of magnitude upon decreasing the temperature from 300 to 60°C. Using analytical expressions for dislocation network and loop densities that have been fit to experimental data' in Eq. (2) leads to the steady state curve plotted in Fig. 5. A large decrease in irradiation creep is predicted as temperature decreases to 60°C. This curve is based upon steady-state defect concentrations. However, at a temperature of 60°C, the time for vacancies to diffuse to sinks and reach a steady-state concentration is much longer than the time of an experiment, on the order of 100 years for the parameters used here. Thus, steady-state concentrations of vacancies and, therefore interstitials, are never reached at low temperatures. Therefore, for such low temperatures, steady-state models must be discarded. A new analysis is required based on the more fundamental point defect concentration behavior.

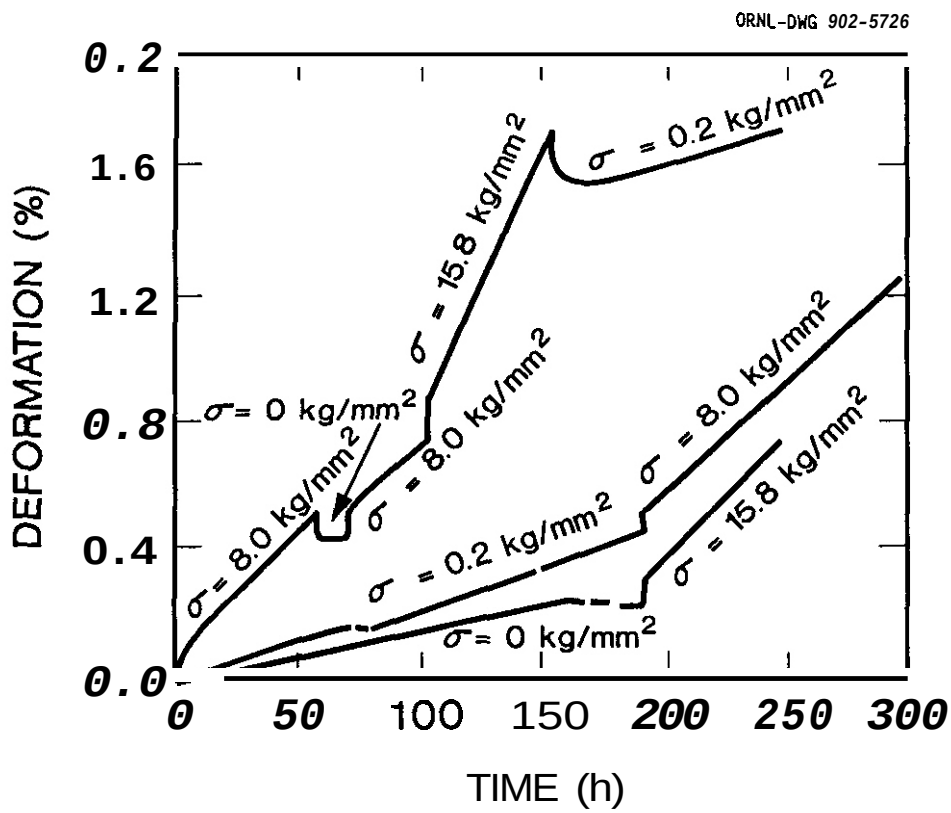

Fig. 4. Deformation in uranium under reactor irradiation at 220°C with a neutron flux of 6 × 10^{18} $n/m^2 \cdot s$. Note that deformation ceases when either stress is removed or the reactor is shut down (dashed lines). After Zaimovsky et al.[13].

The rate equations for point defect concentration are:

$$\frac{\delta C_i}{\delta t} = G - RC_vC_i - K_iC_i\ ,$$

$$\frac{\delta C_v}{\delta t} = G - RC_vC_i - K_vC_v\ , \qquad (3)$$

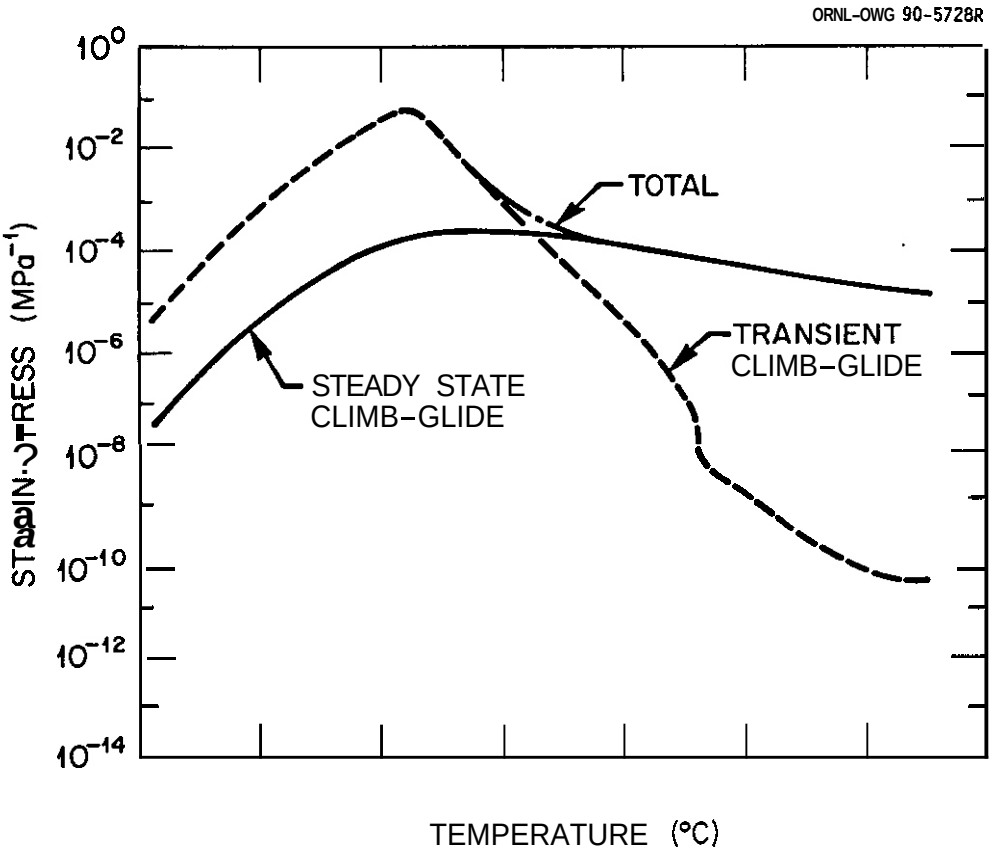

Fig. 5. Creep deformation per unit stress as a function of temperature for austenitic alloys using the conventional climb-enabled glide mdel (steady state) and using the proposed transient model. The sum of the two curves is also shown.

where G is the point defect production rate, R is the recombination coefficient, $K_{i,v} = S_{i,v}D_{i,v}$ is the rate constant for interstitial or vacancy absorption at sinks, depending upon the subscript i or v, respectively; S is the sink strength, and D is the diffusivity of interstitials or vacancies. For the steady-state case, the time derivatives were set equal to zero. The two resulting algebraic equations were then solved for C_i and C_v which were substituted into Eqs. (1) and (2). However, in the case of low temperatures, where steady-state conditions are not met, Eqs. (3) must be solved at time-dependent differential equations.

In order to make an assessment of the magnitude of low-temperature transient creep, a conservative estimate of creep rate can be made by examining point defect behavior as their concentrations approach steady state. The approach to steady state of defect concentrations is shown schematically in Fig. 6 based on Mansur.[19] The concentrations of vacancies and interstitials are equal to each other and increase at the same rate under irradiation until interstitials begin to be absorbed by sinks. This happens in a time $\tau_i = 1/K_i$, where K_i is the rate constant for loss due to absorption at sinks, which even at these low temperatures is on the order of microseconds or less. At this time, the loss rate of interstitials due to absorption at sinks balances the production rate, and a quasi-steady state is achieved with the interstitial concentration equal to G/K_i. As the vacancy concentration continues to increase, a point, τ_{R1}, is reached where recombination first becomes significant. The interstitials experience a new loss mechanism and their concentration now begins to decrease. The vacancy population continues to increase, although at a slower rate, until recombination becomes the dominant loss mechanism for defects at time τ_{R2}. Finally, at time $\tau_v = 1/K_v$, where K_v is the rate constant for absorption of vacancies at sinks, the vacancies are absorbed by sinks and this loss rate balances the vacancy production rate. At this time, both vacancy and interstitial concentrations reach steady state. It is only after this time that the theoretical models of irradiation creep previously advanced apply. At low temperatures, the time to reach steady state is far longer than the duration of the experiment. The interstitial concentration producing irradiation creep is, therefore, higher than that predicted by steady-state defect concentrations.

In the SIPA mechanism, both vacancies and interstitials are absorbed by dislocations in nearly equal numbers. There is a slight preference for interstitials to be absorbed by dislocations with Burgers vectors aligned parallel to the axis on an externally applied stress. This slight imbalance gives rise to a net climb leading to deformation in the direction of the stress and, thus to irradiation creep. However, at low temperatures, the vacancies are essentially immobile so that only interstitials are absorbed by dislocations. Without the vacancies to cancel the climb induced by the interstitials, a greatly enhanced climb rate results. Once the dislocations climb past obstacles, they are free to glide and bow out in

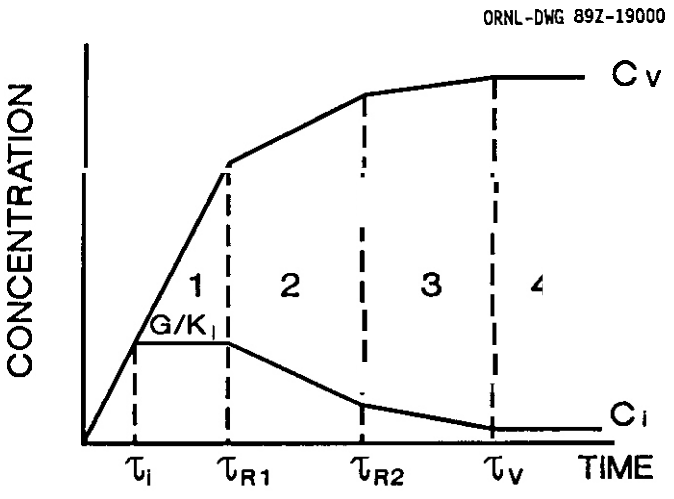

Fig. 6. Schematic representation of point defect concentrations durinu the transient followiag initiation of irradiation. After Mansur. 19

the direction of the stress resulting in irradiation creep by the climb-enabled glide mechanism. The deformation, ε_{c-g}, resulting from this mechanism is given by

$$\varepsilon_{c-g}/\sigma = (\pi L)^{1/2}/E\ \Omega/bL\ N_1 \ , \qquad (4)$$

where σ is the external stress, L is the dislocation density, Ω is the atomic volume, E is the elastic modulus, b is the Burgers vector, and N_1 is the total number of interstitials absorbed by the dislocations.' The number of interstitials absorbed, N_1 is estimated in each numbered region of Fig. 6, making the approximations given elsewhere.' The result is:

$$N_1 = G\tau_{R1} - G/K_i \ ; \qquad (5$$

$$N_2 = 0.5\ G(\tau_{R2} - \tau_{R1}) - C_i(\tau_{R2}) \ ; \qquad (6$$

$$N_3 = C_i^{ss}\ D_i S_i(\tau_v - \tau_{R2}) \ ; \qquad (7)$$

where C_i^{ss} is the steady state value of the interstitial concentration, and S_i is the sink strength for interstitials at dislocations. Substituting Eqs. (5)–(7) into Eq. (4) results in an expression for irradiation creep deformation per unit stress which is plotted in Fig. 5 together with steady-state climb glide." It is seen that the transient curve contributes primarily for low temperatures, and the steady-state curve contributes primarily for high temperatures.

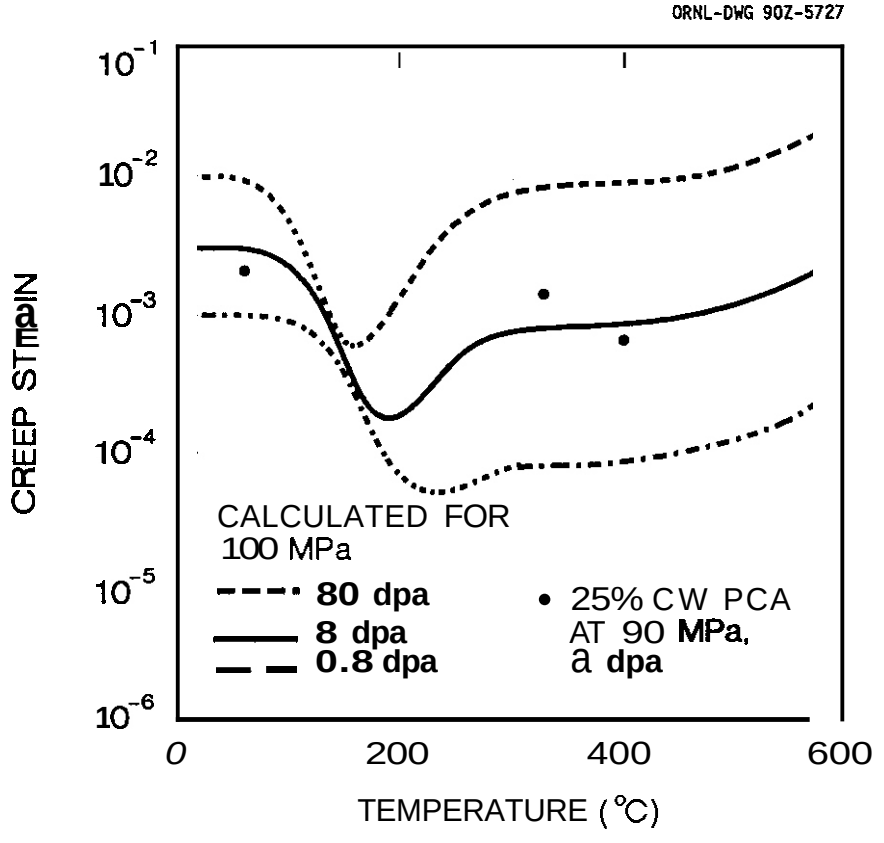

Fig. 7. Creep strain as a function of temperature using the proposed transient mechanism and numerical solution of the point defect rate equations. After Stoller et al.[20]

When the two contributions are added as in Fig. 5, irradiation creep is seen to be about the same at 60°C as above 300°C. The peak at 200°C requires further explanation. A rather primitive, although conservative, method was used to evaluate the irradiation creep deformation. A more accurate method, using a direct numerical solution to the differentia? equations for point defect concentrations, was used by Stoller et al.[20] the result of which is plotted in Fig. 7. The curve for 8 dpa agrees rather well with the data for PCA, but has a dip rather than a peak at 200°C. This discrepancy is simply the result of inaccuracies in the first method of approximation.

A similar analysis can be done for the ferritic steels investigated, and Fig. 8 shows the results using the previously described method of estimation of absorbed interstitials.[21] A qualitatively similar curve to that for austenitic stainless steels was obtained. Since there are significant uncertainties in measuring dislocation loop concentrations in the microstructures formed during low-temperature irradiations, the dislocation loop density was varied by a factor of 100 in each direction. Reducing the loop concentration made little difference, but increasing the loop concentration showed a higher level of irradiation creep at 60°C than at 300°C, which was observed experimentally. A more accurate analysis will be carried out based on the numerical solution of the defect rate equations using measured microstructural data when the actual specimens are sectioned and examined by electron microscopy.

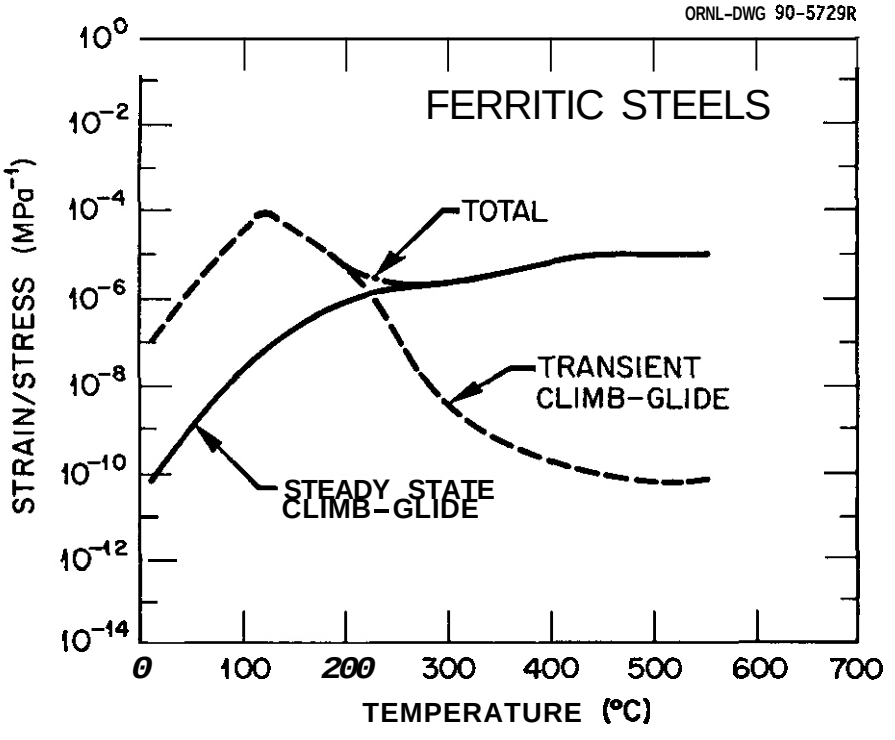

Fig. 8. Creep deformation per unit stress as a function of temperature for ferritic/martensitic alloys. Curves for the climb-enabled glide model (steady state), the proposed transient model, and the sum of the two curves are shown.

CONCLUSIONS

1. High levels of irradiation creep have been observed in austenitic and ferritic alloys at temperatures in the operating range of near-term fusion reactors such as the ITER.
2. The creep at 60°C was greater than at 330 and 400°C.
3. Low-temperature irradiation creep can be explained in terms of a new mechanism of low-temperature transient interstitial absorption.
4. The levels of irradiation creep observed in structural alloys can lead to significant deformations under primary loads and must be considered in the design of fusion reactors.

FUTURE WORK

Specimens irradiated at 200°C remain to be measured and the results analyzed. This is scheduled to be done in the next reporting period.

REFERENCES

1. R. V. Hesketh, p. 389 in Proc. on Solid State Physics Research with Accelerators, Brookhaven National Laboratory. Upton, New York (1967).
2. ITER Design Team, ITER Concept Definition (IAEA, Vienna, 1989), p. 296.
3. M. L. Grossbeck and J. A. Horak, J. Nucl. Mater. 155 6 157 (1988) 1001.
4. S. Hamada, P. J. Maziasz, M. P. Tanaka, M. Suzuki, and A. Hishinuma, J. Nucl. Mater. 155-157 (1988) 838.
5. M. P. Tanaka, S. Hamada, A. Hishinuma, and P. J. Maziasz, J. Nucl. Mater. 155-157 (1988) 801.
6. R. J. Puigh, p. 7 in Proc. of Effects of Radiation on Materials (Williamsburg, 1984), Philadelphia.
7. M. L. Grossbeck, L. K. Mansur, and M. P. Tanaka, p. 537 in: Proc. of Effects of Radiation on Materials, STP 1046, Vol. II (Andover, MA, 1989), ASTM, Philadelphia.
8. M. L. Grossbeck and J. A. Horak, Trans. ANS 55 (1987) 299.
9. J. A. Hudson, R. S. Nelson, and R. J. McElroy, J. Nucl. Mater. 65 (1977) 279.
10. R. J. Puigh, J. Nucl. Mater. 141 6 143 (1986) 954.
11. J. L. Straalsund. p. 191 in: Proc. on Radiation Effects in Breeder Reactor Structural Materials (Scottsdale, AZ, 1977), AIME.
12. S. T. Konobeevsky, N. F. Pravdyuk, and V. I. Kutaitsev, p. 433 in: Proc. on Peaceful Uses of Atomic Energy, Vol. 7 (Geneva, 1955), United Nations.
13. A. S. Zaimovsky, G. Y. Sergeev, V. V. Titova, 8. M. Levitsky, and Y. N. Sokursky, p. 566 in: Proc. 2nd Conference on Peaceful Uses of Atomic Energy, (Geneva, 1958), United Nations.
14. E. R. Gilbert, Reactor Technol. 14 (1971) 258.
15. W. G. Wolfer and M. Ashkin, J. Appl. Phys. 47 (1976) 791.
16. P. T. Heald and M. V. Speight, Phil. Mag. 29 (1974) 1075.
17. R. Bullough and J. R. Willis, Phil. Mag. 31 (1975) 855.
18. L. K. Mansur, Phil. Mag. A39 (1979) 497.
19. L. K. Mansur, Nucl. Technol. 40 (1978) 5.
20. R. E. Stoller, M. L. Grossbeck, and L. K. Mansur, in: Proc. in Effects of Radiation on Materials (Nashville, TN. 1990). ASTM (to be published).
21. M. L. Grossbeck, L. L. Horton, and L. K. Mansur, Trans. ANS 60 (1989) 295.

MICROSTRUCTURAL EXAMINATION IN FFTF IRRADIATED MANGANESE STABILIZED MARTENSITIC STEEL - Y. Kohno (University of Tokyo), A. Kohyama (University of Tokyo) and O. S. Gelles (Pacific Northwest Laboratory)[a]

OBJECTIVE

The objective of this work is to evaluate the irradiation embrittlement of manganese stabilized martensitic stainless steels in support of low activation ferritic alloy design.

SUMMARY

Transmission electron microscopy has been performed on FFTF irradiated specimens of manganese stabilized martensitic steels in order to identify the cause of irradiation-induced embrittlement. Examinations demonstrated the presence of Fe-Cr-Mn chi phase, a body-centered cubic intermetallic phase, known to be detrimental to mechanical properties.

PROGRESS AND STATUS

Introduction

Ferritic/martensitic steel is attractive for fusion applications due to microstructural stability against irradiation. HT-9 is the candidate alloy for this category, but efforts continue to provide improvements and reduce the induced radioactivity by compositional modification. As part of this effort, modified HT-9 alloys were designed. The design concept required that nickel be removed and carbon reduced to 0.1% for ductile-brittle transition temperature (DBTT) improvement, and manganese be added to compensate for austenite instability. A miniature Charpy specimen impact test program showed that these steels underwent a large shift in DBTT as a result of fast neutron irradiation at 638 K to 11.3 dpa[1,2]. Higher manganese contents increased the DBTT shift, and this DBTT degradation can be worse than that found in HT-9. Following the previous report[3], the present work is intended to inspect microstructural features in these steels in order to give insight into the mechanisms of radiation-induced embrittlement.

Experimental Procedure

The materials used were Fe-12Cr-0.1C-1.0Mo-0.2V-0.15Nb with 1.9, 3.3, 3.5, 4.7 and 6.6% Mn. Detailed chemical compositions of materials used are shown in Table 1 with alloy identification codes. Figure 1 provides a schematic comparison of the neutron fluence dependence of DBTT in two manganese stabilized steels and HT-9.[1]

Table 1

Chemical Composition of the Specimens as Supplied by the Vendor

ID	F1	F2	F3	F4	F5	HT-9
C	0.12	0.10	0.11	0.11	0.15	0.21
Mn	1.94	3.33	4.73	6.57	3.46	0.50
Si	0.12	0.12	0.10	0.10	0.11	0.21
P	0.007	0.007	0.007	0.007	0.008	0.008
S	0.005	0.005	0.005	0.006	0.006	0.003
Cr	11.95	11.80	11.79	12.00	11.90	12.10
Ni	-	0.01	-	-	-	0.57
Mo	0.98	0.96	0.96	0.96	0.97	1.03
W	-	-	-	-	0.23	0.52
V	0.25	0.21	0.25	0.20	0.26	0.33
N	0.003	0.003	0.002	0.003	0.003	0.009
Nb	0.15	0.16	0.16	0.15	0.15	-
Cu	0.01	0.01	0.01	0.01	0.01	0.04
Fe	Bal.	Bal.	Bal.	Bal.	Bal.	Bal.

(a) Pacific Northwest Laboratory is operated for the U.S. Department of Energy by Battelle Memorial Institute under Contract DE-AC06-76RLO 1830.

TEM disk specimens of these materials were irradiated in FFTF/MOTA. The irradiation conditions were 9.8 and 43.3 dpa at 693 K; 14.4 and 48.2 dpa at 793 K; and 33.8 dpa at 873 K. The irradiation conditions and the

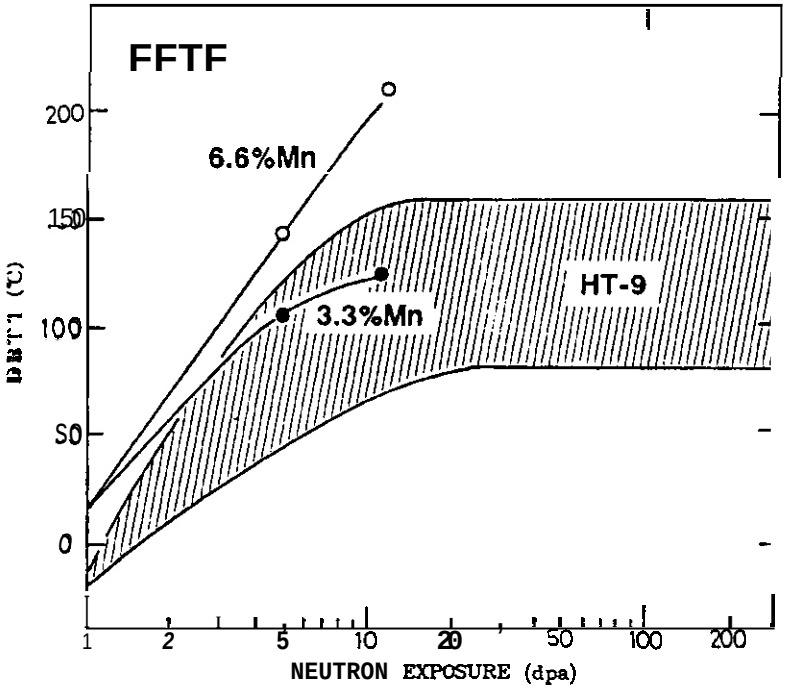

FIGURE 1. DBTT Shift of 12% Cr Martensitic Stainless Steels Irradiated at 638-693 K in FFTF/MOTA

Table 2

Summary of Irradiation Conditions and TEM Microstructural Examination

Irradiation Condition		Mn Concentration (wt%)				
		2.0	3.3	3.5	4.7	6.6
Unirr.	Unaged		*			□
	Aged					□
10 dpa	693K		*	●	●	
45 dpa		●	●	●	●	●
15 dpa	793K	*	□	□	□	□
50 dpa			*			□
35 dpa	873K		*			*

□ ● : Observation finished (● : Cavities observed)
• : To be 3-point disk bend tested followed by TEM examination.

Results and Discussion

Despite the martensite stabilization produced by manganese additions, all alloys contained delta ferrite prior to irradiation. The amount of ferrite phase was not measured quantitatively, but was estimated by metallographic examination to be less than 15% in any alloy, and it was found that the fraction of ferrite appears to decrease with manganese concentration. Cavities were observed only in specimens irradiated at 693 K to 9.8 and 43.3 dpa, but they were limited to being within the delta ferrite phase. Figure 2 shows

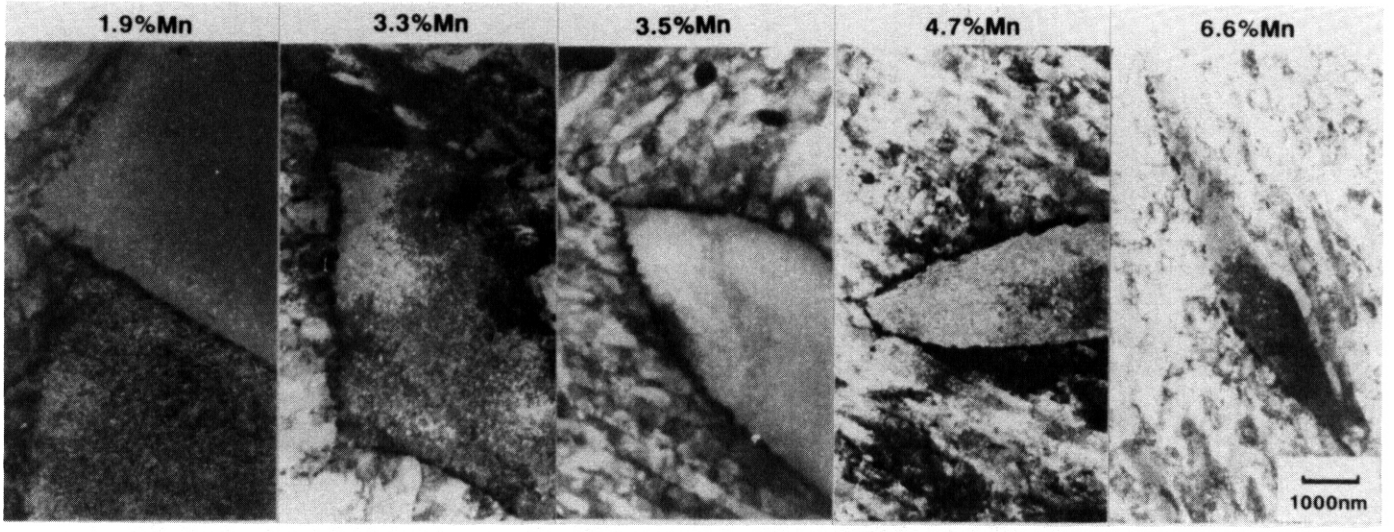

FIGURE 2. Delta-Ferrite Phase of Mn-Stabilized Steels (12C4-xMn-1Mo-Nb,V) Irradiated at 693 K to 45 dpa in FFTF/MOTA

the dependence of delta ferrite phase on manganese concentration, and also reveals cavities within the delta ferrite phase. In all alloys, the prior austenite grain boundary was poorly defined by precipitate particles, but large carbide particles could be observed. Precipitate particles following irradiation were large and clearly defined in comparison with those in the unirradiated materials, but grain boundary precipitates did not form continuous coatings. Analysis 'showed that the smaller particles were $M_{23}C_6$.

Figure 3 shows the cavity microstructure in the delta ferrite phase as a function of the manganese concentration dependence and neutron fluence dependence. Average cavity size and cavity number density decreased slightly with manganese concentration, but almost no cavities were observed in a specimen with 6.6% Mn irradiated to 9.8 dpa. Fine precipitates at high number density and with very weak contrast were observed in all irradiation conditions. The precipitate showed more clearly in ferrite grains than in martensite grains. These precipitates were also observed in irradiated 12% Cr martensitic steel, and were interpreted to be alpha prime phase. Also of note was intermetallic chi phase precipitation, which was identified along prior austenite grain boundaries in specimens with 4.7 and 6.6% Mn following irradiation at 693 K and 793 K to 14.4 dpa or more. Compositional analysis on this phase indicated Fe-16.2Cr-10.2Mn-3.0Mo-0.7Si(or W). The volume fraction of chi phase was roughly estimated to be as high as 10% in the case of 14.4 dpa/793 K irradiation. Chi phase is considered to be detrimental to mechanical properties; therefore, DBTT degradation in the materials with higher manganese concentrations can be attributed to chi phase precipitation, although there is no clear evidence that chi precipitation caused embrittlement at lower temperature.

CONCLUSION

Transmission electron microscopy has been performed on TEM disk specimens of manganese stabilized martensitic stainless steel which had been irradiated in FFTF to identify the cause of irradiation induced embrittlement. Microstructural observations of specimens irradiated at higher temperature have demonstrated the presence of Fe-Cr-Mn chi phase, a body-centered cubic intermetallic phase known to cause embrittlement. This work indicated that manganese stabilized martensitic stainless steels are prone to intermetallic phase formation, which is detrimental to mechanical properties.

FUTURE WORK

This work is completed.

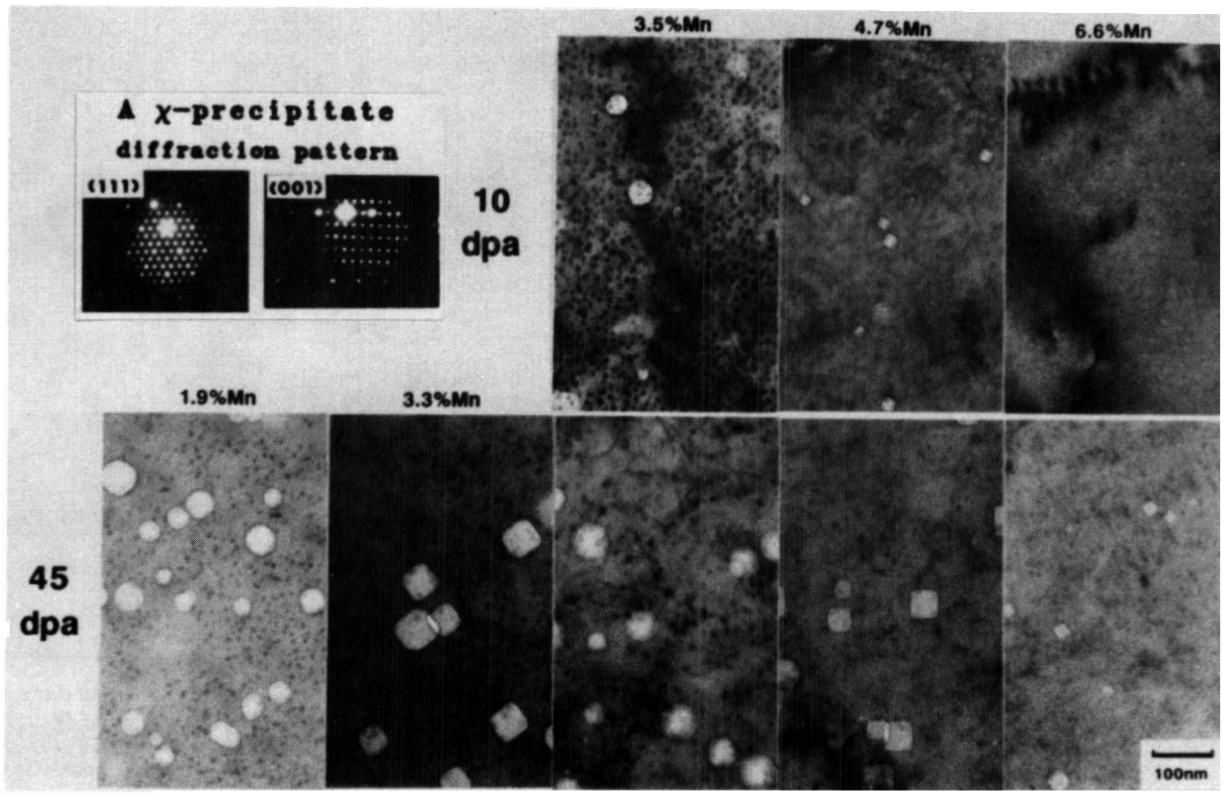

FIGURE 3. Cavity Microstructural Development in Delta Ferrite Phase of Mn-Stabilized Steels (12Cr-xMn-1Mo-Nb, V) Irradiated at 693 K to 10 and 45 dpa in FFTF/MOTA

REFERENCES

1. W. L. Hu and D. S. Gelles, "Charpy Impact Behavior of Manganese Stabilized Martensitic Steels," DOE/ER-0045/16 (1986) 140.

2. D. S. Gelles and W. L. Hu, "Radiation Eabrittlement of Manganese-Stabilized Stainless Steel," DOE/ER-0313/1 (1987) 242.

3. A. Kohyana and D. S. Gelles, "A TEM Study of Manganese-Stabilized Martensitic Stainless Steel," Annual Progress Report for FFTF/MOTA Japan-U.S.A. Collaboration (1988) 100.

NEUTRON-INDUCED SWELLING OF MODEL Fe-Cr-Mn-Ni ALLOYS AND COMMERCIAL MANGANESE-STABILIZED STEELS -
F. A. Garner, Pacific Northwest Laboratory;(a) H. R. Brager, Westinghouse Hanford Company; H. Takahashi, Hokkaido University

OBJECTIVE

The object of this effort is to determine the material and environmental factors controlling the radiation-induced evolution of reduced activation alloys.

SUMMARY

The addition of nickel to both simple and solute-modified Fe-Cr-Mn alloys leads initially to an increase in neutron-induced swelling. The addition of various minor solutes, particularly silicon, in general leads to a reduction in swelling. Depending on composition, thermomechanical condition and irradiation temperature, a wide variety of swelling behavior is observed in various commercial Fe-Cr-Mn alloys. There is some indication in the commercial alloys of massive formation of ferrite phases during irradiation at 420°C, leading to a reduction in the swelling rate.

PROGRESS AND STATUS

Introduction

Manganese-stabilized austenitic stainless steels are being considered for service as low activation structural materials for fusion devices. Although current low activation guidelines place strong limitations on the nickel content, small amounts of nickel are often included in commercial manganese-stabilized steels to assist in the stabilization of the austenite phase. An electron irradiation experiment has also suggested that addition of small concentrations of nickel will delay the onset of void swelling in Fe-Cr-Mn-Si alloys.[1] Increased nickel levels are also known to yield lower levels of swelling in many Fe-Cr-Ni based alloys.[2]

In previous studies the compositional dependence of neutron-induced swelling and phase stability for Fe-Cr-Mn ternary alloys was explored.[3-6] In the current study the swelling of Fe-Cr-Mn-Ni quaternary, solute-modified quaternary and commercial Fe-Cr-Mn alloys containing nickel was examined after irradiation in the Fast Flux Test Facility (FFTF) at temperatures in the range 420-600°C and doses as high as 75 dpa.

ExDerimental Details

The various alloys and heat treatments used in this investigation are listed in Tables 1 and 2. They were prepared as microscopy disks 3 mm in diameter by 0.25 mm in thickness. Irradiation proceeded in static sodium in FFTF at ~3 x 10^{-6} dpa s^{-1} using the Materials Open Test Assembly (MOTA) which controls the temperature to within ±5°C. Irradiation temperatures were chosen at various points between 420 and 650°C, depending on the particular set of alloys under investigation. The neutron spectrum in these experiments produces approximately 5 dpa for each 1.0 X 10^{22} n cm^{-2} (E > 0.1 MeV). The bulk swelling levels were determined using an immersion density technique accurate to ±0.16%.

Results and Discussion

The series 1 alloys described in Table 1 explore the impact of small additions of nickel to Fe-17Cr-19Mn-0.5Si alloys containing various concentrations of carbon, phosphorus and nitrogen typically found in commercial steels. Although Takahashi et al.[4] had earlier shown that nickel additions caused an extension of the incubation period of swelling during electron irradiation, Figure 1 shows that the first small amount of nickel increased the neutron-induced swelling at each of the four temperatures investigated. The microstructural origins of this behavior are currently under investigation. It is obvious, however, that the solutes incorporated in these alloys suppressed swelling compared to that of simple solute-free ternary Fe-Cr-Mn alloys.[3-5] It is well known that silicon is particularly good at suppressing swelling in many alloys.[1]

Since nickel and manganese share some similarities in their influence on phase stability but exhibit different diffusional behavior,[1] a wider range of Fe-Cr-Mn-Ni quaternary alloys was irradiated in order to gain some insight into the competitive roles played by these two elements. Figure 2 shows that, in two series of simple quaternary alloys, nickel additions usually increase swelling at first. The behavior is not monotonic, however, with either temperature or nickel content. The preliminary results of microscopy studies indicate that the increased swelling arises as a direct consequence of nickel's role in stabilizing the austenite phase against ferrite formation. The ferrite phase is well known to swell at a much lower rate than that of austenite.

(a) Pacific Northwest Laboratory is operated for the U.S. Department of Energy by Battelle Memorial Institute under Contract DE-AC06-76RLO 1830.

TABLE 1. Composition of Nickel-Bearing Alloys[a] (wt%)

Series 1[b]

Fe-16.83Cr-19.49Mn-0.03Ni-0.54Si-0.10C-0.020P-0.162N

Fe-16.59Cr-18.87Mn-1.47Ni-0.55Si-0.10C-0.019P-0.164N

Fe-16.95Cr-19.08Mn-5.90Ni-0.52Si-0.10C-0.022P-0.099N

Series 2[c]	Series 3[c]
Fe-15Cr-15Mn	Fe-10Cr-30Mn
Fe-15Cr-15Mn-5Ni	Fe-10Cr-30Mn-5Ni
Fe-15Cr-15Mn-10Ni	Fe-10Cr-30Mn-10Ni
Fe-15Cr-15Mn-15Ni	Fe-10Cr-30Mn-15Ni

(a) Annealed condition, 1030°C/0.5h/air cool
(b) All with 0.006 S, 0.05-0.07Cu and 0.01-0.03 Mo.
(c) Nominal composition.

TABLE 2. Composition of Commercial Fe-Cr-Mn Austenitic Alloys

Designation	Vendor	Condition	Composition, wt%
Nitronic Alloy 32	ARMCO	CW	18Cr-12Mn-1.5Ni-0.6Si-0.2Cu-0.2Mo-0.4N-0.1C-0.02P
18/18 Plus	CARTECH	CW, CWA	18Cr-18Mn-0.5Ni-0.6Si-1.0Cu-1.1Mo-0.4N-0.1C-0.02P
AMCR 0033	CREUSOT-MARREL	SAA,CW,CWA	10Cr-18Mn-0.7Ni-0.6Si-0.06N-0.2C
NMF3	CREUSOT-MARREL	CWA	4Cr-19Mn-0.2Ni-0.7Si-0.09N-0.02P-0.6C
NONMAG *30*	*KOBE*	SAA,CW,CWA	2Cr-14Mn-2.0Ni-0.3Si-0.02N-0.02P-0.6C

SA = 1030°C/0.5h/air cool.
CW = 1030°C/0.5h/air cool t 20% cold-work.
CWA = cold-worked condition t 650°C/1h/air cool.
SAA = 1030°C/1h/air cool t 760°C/2 h/air cool.

In general, the swelling of these quaternary alloys is somewhat lower at the higher manganese level, in agreement with the results of earlier studies on simple Fe-Cr-Mn alloys.[3-5]

Figures 3 through 6 show the swelling of the five commercial alloys (some in more than one starting condition) irradiated in this study. These alloys clearly exhibit lower swelling as a result of the addition of solutes such as Ni, Si, Mo, N, C and P. A few trends can be derived from examination of the swelling data for the commercial alloys. In general, lower levels of nickel and higher levels of silicon produce the lowest swelling alloys. Most importantly, within the dose range studied in this experiment, none of these alloys reached the 1%/dpa swelling rate characteristic of simple Fe-Cr-Mn ternary alloys[4], although the swelling rate in a number of cases was increasing rapidly. At the lower irradiation temperatures the swelling rate frequently declined strongly, a behavior also observed in simple Fe-Cr-Mn ternary alloys and attributed to the massive formation of the lower-swelling ferrite phase.[5] This behavior was most pronounced in the aged alloy conditions.

CONCLUSION

Contrary to expectations based on experience with Fe-Cr-Ni alloys and the results of electron irradiation experiments on Fe-Cr-Mn alloys, nickel additions to Fe-15Cr-15Mn and Fe-10Cr-30Mn alloys increased their swelling initially. A similar behavior was observed in Fe-17Cr-19Mn-0.5Si. Swelling decreased in general in response to additions of silicon and other typical solutes found in commercial alloys. Commercial alloys containing the lowest amount of nickel and the highest level of silicon were found to exhibit the lowest levels of swelling. There is some indication in the swelling behavior of strong phase instabilities at lower irradiation temperatures.

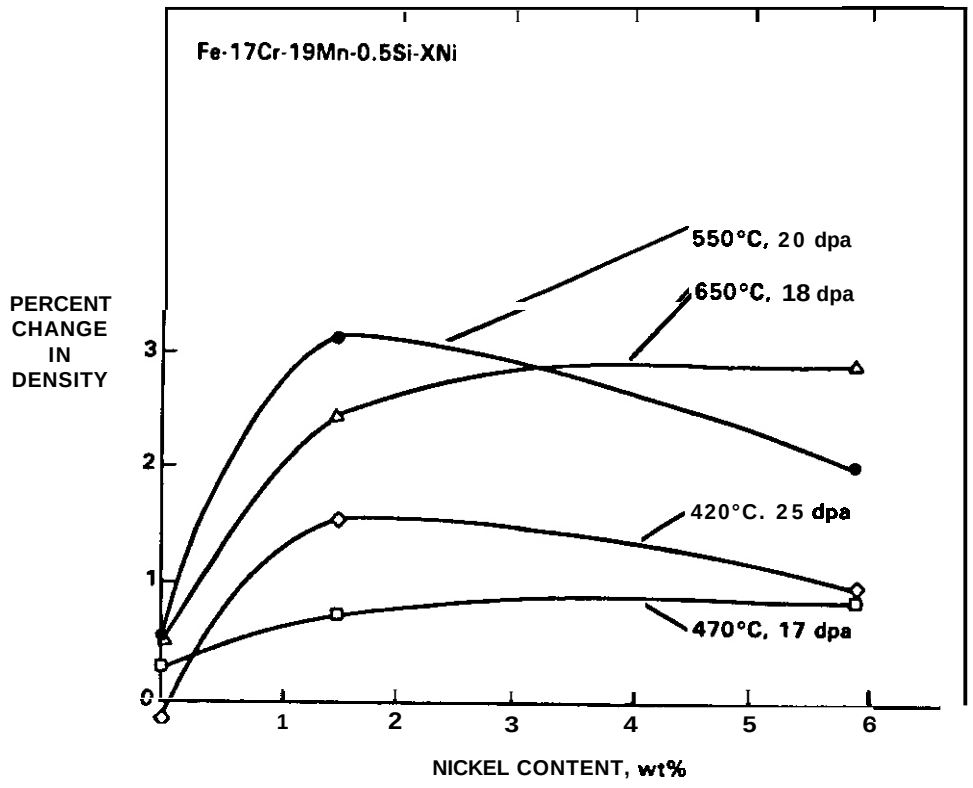

FIGURE 1. Influence of Nickel Content and Irradiation Temperature on the Swelling of Fe-17Cr-19Mn 0.5Si-XNi Alloys

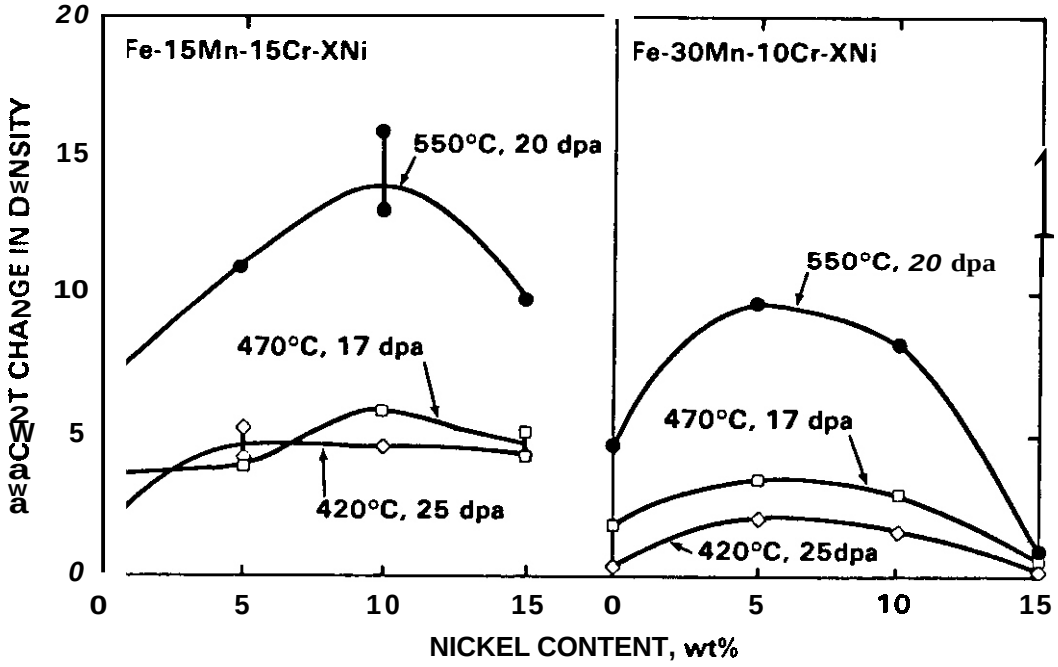

FIGURE 2. Influence of Nickel Content and Irradiation Temperature on the Swelling of Fe-15Mn-15Cr-XNi and Fe-30Mn-10Cr-XNi Alloys

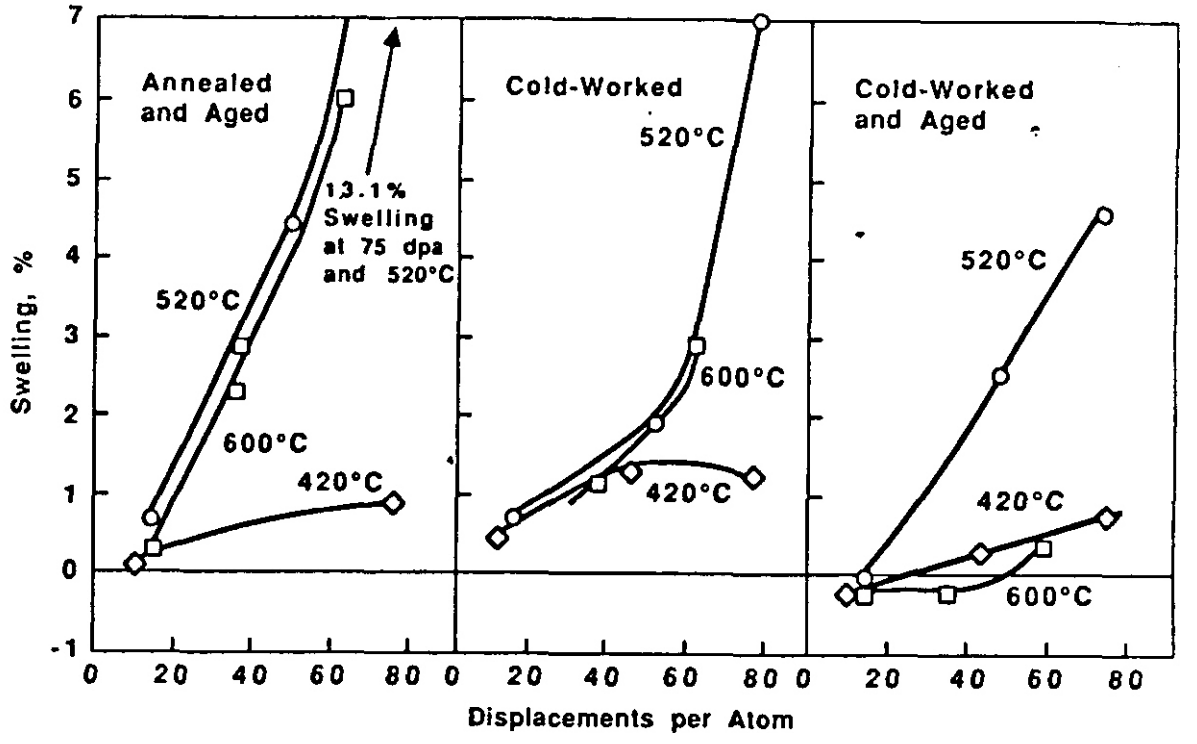

FIGURE 3. Neutron-Induced Swelling of AMCR 0033

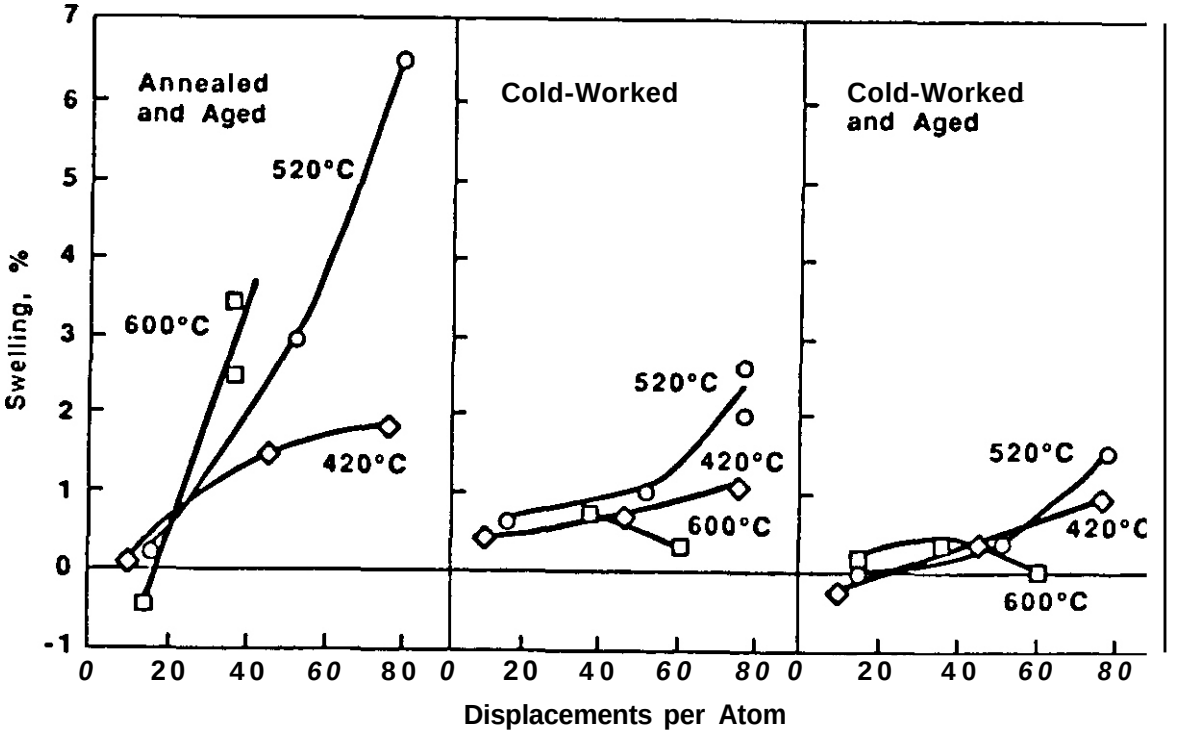

FIGURE 4. Neutron-Induced Swelling of NONMAG 30

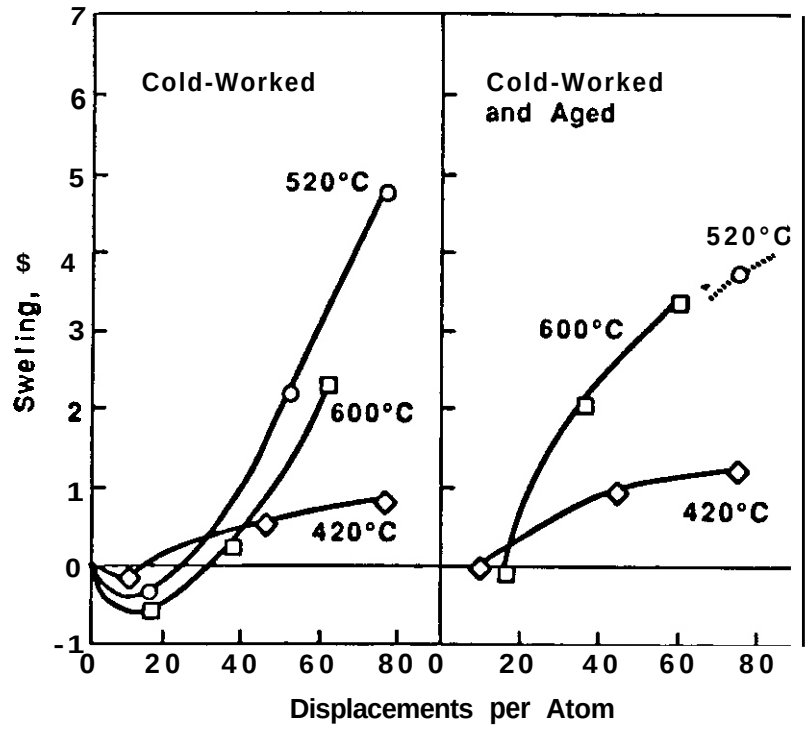

FIGURE 5. Neutron-Induced Swelling of 18/18 PLUS

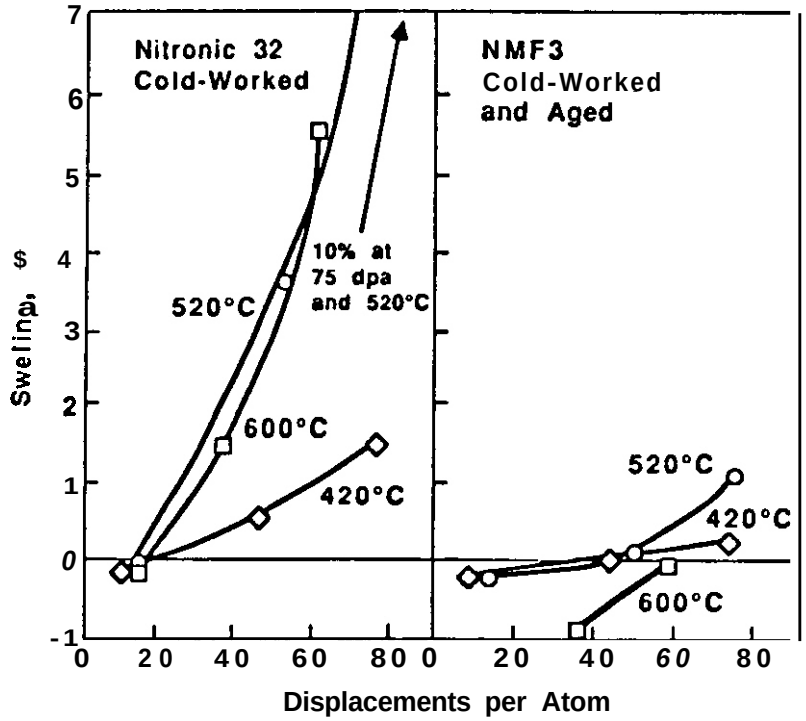

FIGURE 6. Neutron-Induced Swelling of Nitronic 32 and NMF3

REFERENCES

1. H. Takahashi, T. Takeyama, K. Tanikawa and R. Miura, J. Nucl. Mater. 133-134 (1985) 566-570.

2. F. A. Garner, J. Nucl. Mater. 122 & 123 (1984) 459-471.

3. H. R. Brager, F. A. Garner, D. S. Gelles and M. L. Hamilton, J. Nucl. Mater. 133 & 134 (1985) 907-911.

4. F. A. Garner, H. R. Brager, D. S. Gelles and J. M. McCarthy, J. Nucl. Mater. 148 (1987) 294-301.

5. F. A. Garner, F. Abe and T. Noda, J. Nucl. Mater. 155-157 (1988) 870-876.

6. J. M. McCarthy and F. A. Garner, J. Nucl. Mater. 155-157 (1988) 877-882.

THE DEVELOPMENT OF AUSTENITIC STAINLESS STEELS FOR FAST IWOUCEO-RADIOACTIVITY DECAY -- R. L. Klueh and P. J. Maziasz (Oak Ridge National Laboratory)

OBJECTIVE

Induced radioactivity in the first-wall and blanket-structure materials of fusion reactors will make these components highly radioactive after their service lifetime, leading to difficult radioactive waste-management problems. One way to minimize the disposal problem is to use structural materials in which radioactive isotopes induced by irradiation decay quickly to levels that allow simplified disposal techniques. We are assessing the feasibility of developing such austenitic stainless steels.

SUMMARY

A program is under way to develop a nickel-free austenitic stainless steel for fusion-reactor applications. Previous work on small button heats showed that an austenite-stable alloy could be obtained with a base composition of Fe-20Mn-12Cr-0.25C. To improve strength and irradiation resistance, closely controlled quantities of W, Ti, V, C, B, and P were added to this base. A large heat of this steel with the composition of the best button heat has been obtained to determine if it is possible to scale up from the small heats. The tensile properties of that heat have been found to be similar to those of the smaller heats.

PROGRESS AND STATUS

Introduction

An alloy-development program is in progress' to develop fast induced-radioactivity decay (FIRO) austenitic stainless steels to replace the high-nickel stainless steels that are among the present candidate alloys for fusion applications. These steels are designed to meet the criteria for shallow land burial of radioactive isotopes, as described in the Nuclear Regulatory Commission Guidelines 10CFR61. According to 10CFR61, Ni, N, Nb, Mo, and Cu must be minimized. For a FIRD stainless steel, manganese is to be used as a replacement for nickel.

Previous work showed that it is possible to develop a high-manganese austenitic steel with tensile properties that exceed those of type 316 stainless steel.[2,3] Initially, a base composition of Fe-20Mn-12Cr-0.25C was found to be entirely austenitic with tensile properties comparable to those of type 316 stainless steel.[2] With a series of small button heats, it was shown that the strength of the base composition could be improved by adding various alloying elements.[3] From these studies it was concluded that an alloy with a nominal composition of 20% Mn, 12% Cr, 1% W, 0.1% Ti, 0.1% V, 0.04% P, and 0.005% B, the balance iron (all compositions are in weight percent) was considerably stronger than the type 316 stainless steel in both the annealed condition and in the 20% cold-worked condition.[3]

A large heat of the new manganese steel was obtained. Tests are planned to examine the fabricability, mechanical properties, physical properties, weldability. corrosion resistance, and irradiation resistance. Tests are also planned to use this heat as a base composition for making heats to determine the optimum composition of such a high-manganese stainless steel.

Experimental Procedure

A 45-kg heat (Heat 3898) of an Fe-20Mn-12Cr-1W-0.1Ti-0.04P-0.005B alloy was obtained from Combustion Engineering, Chattanooga, Tennessee. The ingot was air-induction melted with an argon cover, after which it was cast into a 10.2 cm by 10.2 cm by 45 cm ingot. The composition of heat 3898 is given in Table 1. With one exception, the composition of this heat of material was the same as heat PCMA-21, the small (600-g) experimental heat with the best strength properties of the eight heats previously examined.[3] No vanadium was added to heat 3898, because part of the use planned for this heat was to use it as a base composition to determine the optimum level for the various alloying elements. Furthermore, the previous work indicated little effect of vanadium, and in the future this will be examined with the use of small heats.

To obtain material for the tensile specimens, a 76.2-mn-thick section was taken from the ingot and upset forged at 1050°C to a thickness of 38 to 41 mn. This material was then hot rolled to 4.75-mn-thick sheet, after which it was cold rolled to 0.76-mm-thick sheet in a series of stages. Between each stage, the steel was annealed at 1150°C. The final sheet was in a 20% cold-worked condition.

Tensile Specimens were obtained from the cold-rolled sheet. Specimens had a reduced gage section 20.3-mm long by 1.52-mm wide by 0.76-mm thick. All specimens were machined with gage lengths parallel to the rolling direction. Tensile tests were made at room temperature, 200, 300, 400. 500, and 600°C on specimens in the cold-worked condition and after two annealing treatments: 1 h at 1050°C and 2 h at 1150°C. Tests were made in vacuum on a 120-kN-capacity Instron universal testing machine at a crosshead speed of 8.5 mm/s, which resulted in a nominal strain rate of 4.2×10^{-4}/s

Results and Discussion

Figure 1 shows the microstructure of the steel in the cold-worked condition [Fig. 1(a)], after annealing 1 h at 1050°C [Fig. 1(b)], and after 1 h at 1150°C [Fig. 1(c). As can be seen, the steel contained a high inclusion content. This is presumably the result of the air-melting procedure, and a cleaner steel would result if it were electroslag remelted.

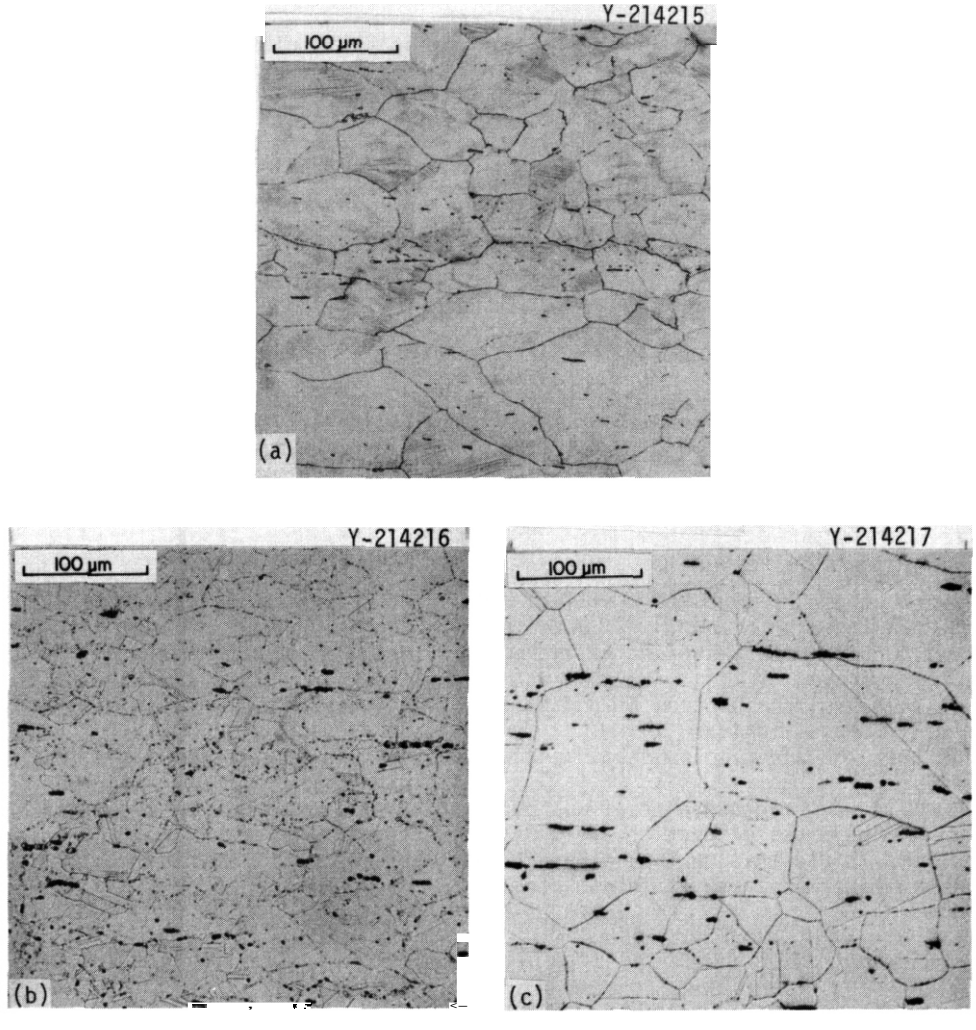

Fig. 1. Microstructure of high-manganese steel (a) 20% cold worked, (b) annealed 1 h at 1050°C, and (c) annealed 1 h at 1150°C.

Tensile data for heat 3898 are given in Table 1. Figures 2 through 7 show the tensile behavior of heat 3898 after an anneal of 1 h at 1050°C (Figs. 2 and 3), 1 h at 1150°C (Figs. 4 and 5), and in the 20% cold-worked condition (Figs. 6 and 7). For comparison, data from PCMA-21 — the strongest of the 600-g vacuum-arc melted experimental heats — are also shown on the figures. For the cold-worked Steel and the steel annealed at 1050°C, data for type 316 stainless steel are also shown for comparison. NO data were available for comparison for steel annealed at 1150°C. Note that PCMA-21 was annealed for 2 h at 1150°C.

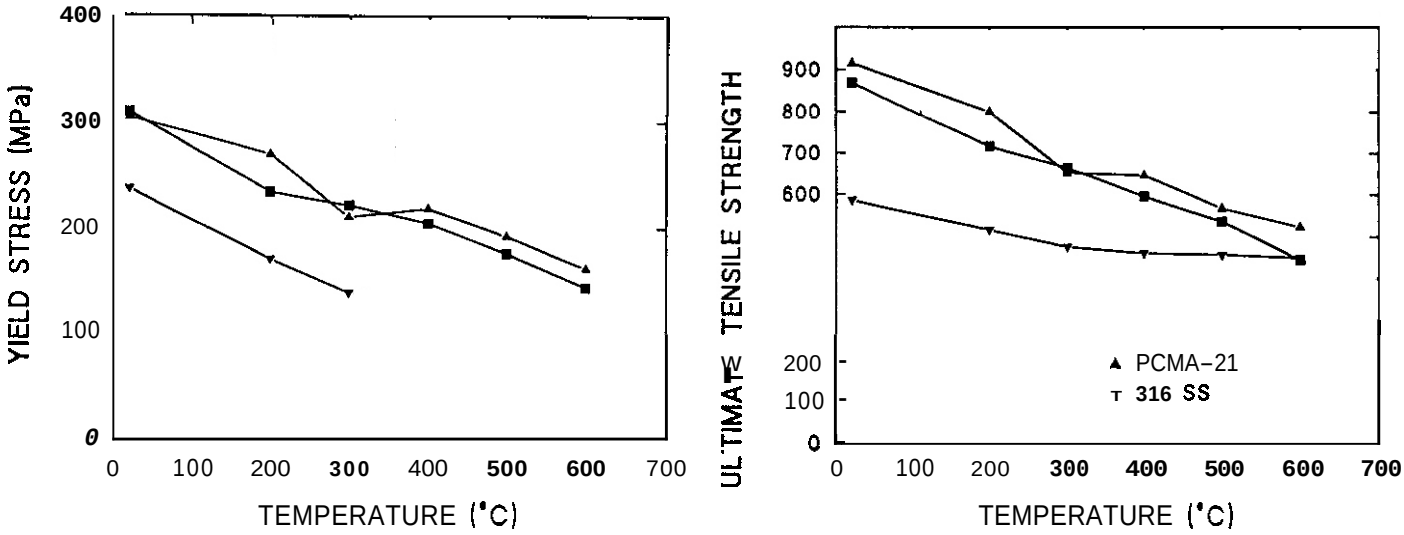

Fig. 2. (a) Yield stress and (b) ultimate tensile strength as a function of test temperature for two heats of high-manganese stainless steel and type 316 stainless steel after being annealed at 1050°C.

Table 1. Tensile Properties of 45-kg heat of high-manganese stainless steel — Heat 3898

Test Temperature (°C)	Strength, MPa		Elongation, %	
	Yield	Ultimate	Uniform	Total
	Annealed 1 h 1050°C			
21	309	885	54.7	57.5
200	211	667	49.9	52.5
300	207	654	47.5	50.4
400	195	595	41.9	45.4
500	168	540	35.3	38.4
600	138	447	30.4	34.5
	Annealed 1 h 1150°C			
21	272	838	55.6	57.0
200	192	675	61.0	64.0
300	165	607	53.5	55.6
400	156	552	45.1	48.4
500	150	512	39.1	43.6
600	130	450	33.3	36.1
	20% Cold Worked			
21	891	1080	12.6	15.0
200	797	927	8.2	10.4
300	606	844	9.5	11.8
400	625	808	10.2	13.9
500	539	716	7.6	10.5
600	458	597	6.1	8.2

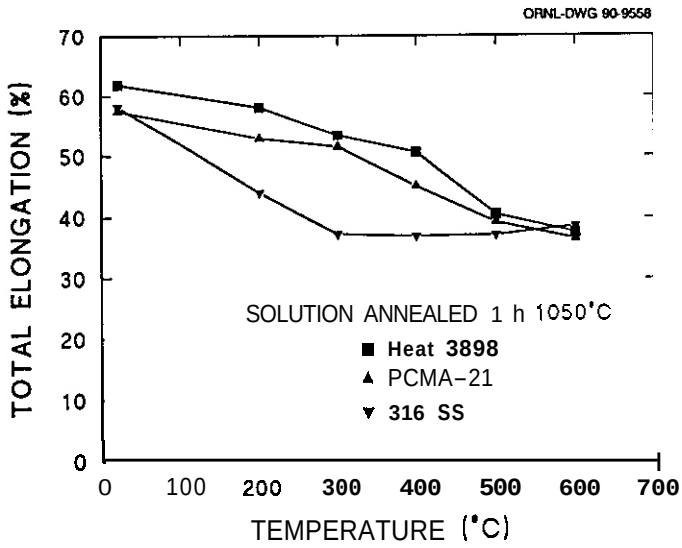

Fig. 3. Total elongation as a function of test temperature for two heats of high-manganese stainless steel and type 316 stainless steel after being annealed at 1050°C.

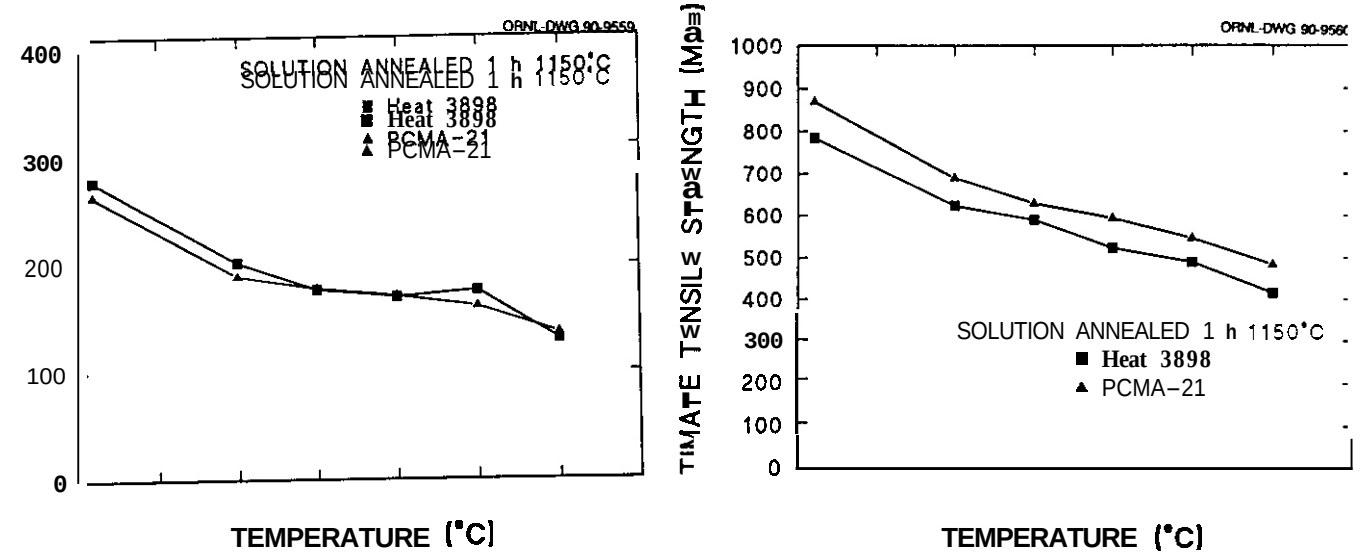

Fig. 4. (a) Yield stress and (b) ultimate tensile strength as a function of test temperature for two heats of high-manganese stainless steel after being annealed at 1150°C.

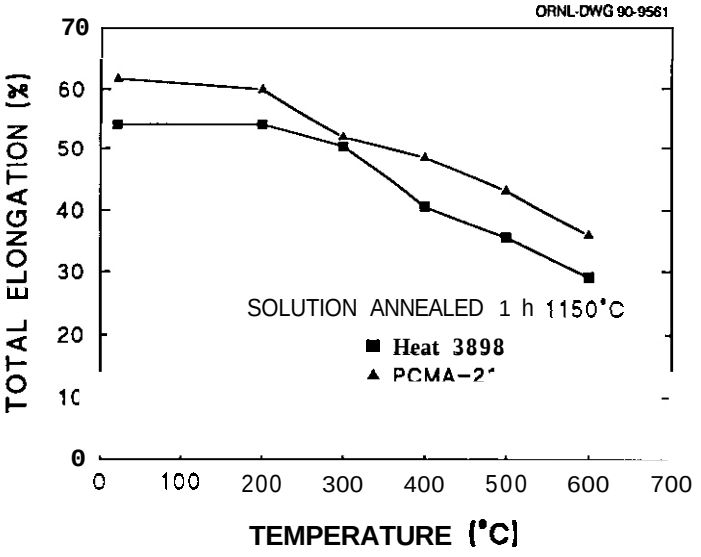

Fig. 5. Total elongation as a function of test temperature for two heats of high-manganese stainless steel after being annealed at 1150°C.

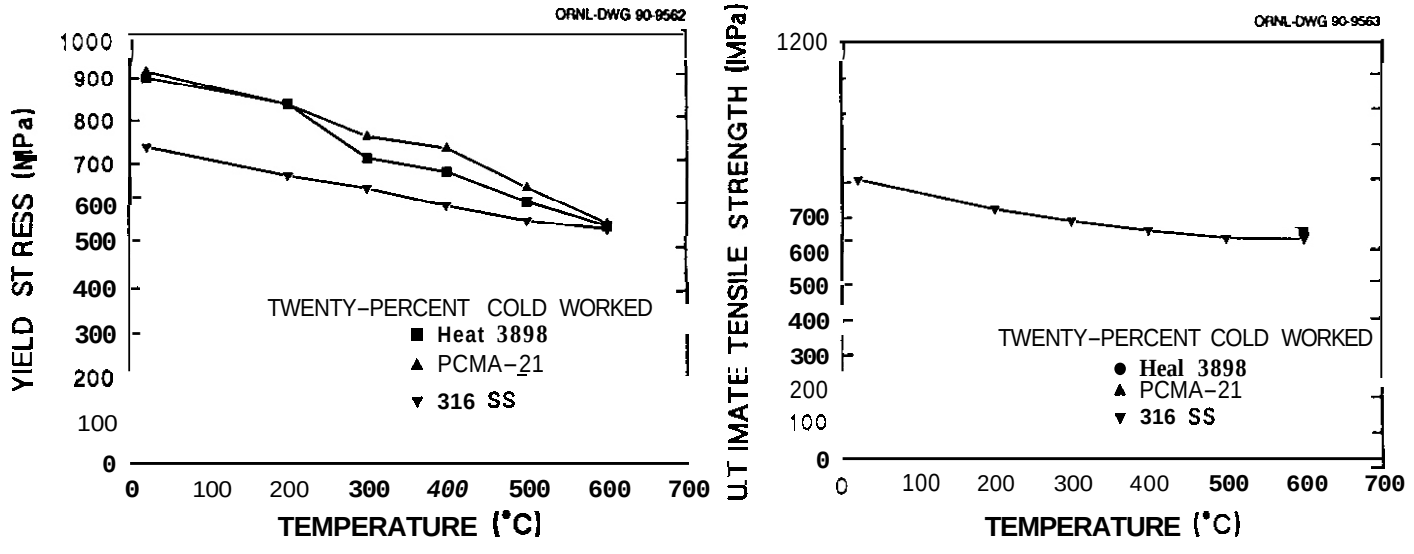

Fig. 6. (a) Yield stress and (b) ultimate tensile strength as a function of test temperature for two heats of high-manganese stainless steel and type 316 stainless steel in the 20% cold-worked condition.

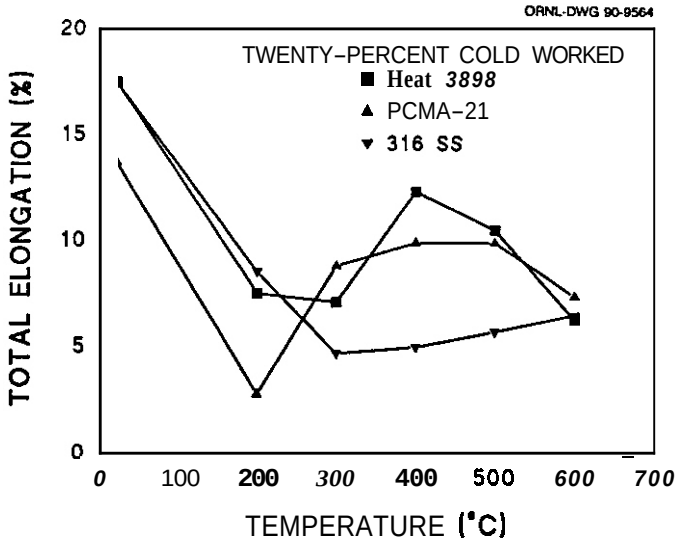

Fig. 7. Total elongation as a function of test temperature for two heats of high-manganese stainless steel and type 316 stainless steel in the 20% cold-worked condition.

The results clearly indicate that the strength and ductility of heat 3898 are comparable to those of PCMA-21. This was true despite the fact that heat 3898 contained a considerable inclusion content. This indicates that it is possible to scale up the size of the material and obtain properties comparable to those obtained from the small button heats produced by vacuum-arc melting.

SUMMARY AND CONCLUSIONS

A 45-kg air-induction melted heat of Fe-20Mn-12Cr-0.25C-1W-0.1Ti-0.04P-0.005B steel was obtained. The microstructure of 0.76-mm sheet contained a high inclusion content. However, the tensile properties of this larger heat were comparable to those of a 600-g experimental heat of similar composition.

REFERENCES

1. R. L. Klueh and E. E. Bloom, "The Development of Austenitic Steels for Fast Induced-Radioactivity Decay for Fusion Reactor Applications," Optimizing Materials for Nuclear Applications, F. A. Garner, O. S. Gelles, and F. W. Wiffen, Eds., The Metallurgical Society, Inc., Warrendale, Pennsylvania, 1985, pp. 73-85.

2. R. L. Klueh, P. J. Maziasz, and E. H. Lee, "Manganese as Austenite Stabilizer in Fe-Cr-Mn-C Steels," Mater. Sci. Enp. 102 (1988) 115-124.

3. R. L. Klueh and P. J. Maziasz, "The Development of Austenitic Stainless Steels for Fast Induced-Radioactivity Decay," Fusion Reactor Materials Semiann. Progr. Report for Period Ending March 31, 1989, DOE/ER-0313/6, pp. 227-242, Office of Fusion Energy.

6.3 Vanadium Alloys

RELATIONSHIP OF MICROSTRUCTURE AND TENSILE PROPERTIES FOR NEUTRON-IRRADIATED VANADIUM ALLOYS - B.A. Loomis and D.L. Smith (Argonne National Laboratory)

OBJECTIVE

The objective of this research is to determine the composition of a vanadium-base alloy with the optimal combination of swelling resistance, corrosion resistance, and mechanical properties in the environment of a magnetic fusion reactor.

SUMMARY

The microstructures of V-15Cr-5Ti, V-10Cr-5Ti, V-3Ti-1Si, V-15Ti-7.5Cr, and V-20Ti alloys were examined by transmission electron microscopy after irradiation at 600°C to 21-84 dpa in the Materials Open Test Assembly of the Fast Flux Test Facility (FFTF-MOTA). The microstructures of these irradiated alloys were analyzed to determine the radiation-produced dislocation density, precipitate number density and size, and void number density and size. The results of these analyses were used to compute increase of yield stress and swelling for the irradiated alloys. The computed increase of yield stress for the irradiated alloys was compared with the increase of yield stress determined from tensile tests on these irradiated alloys to allow evaluation of the influence of alloy composition on evolution of the radiation-damaged microstructure and resulting tensile properties.

PROGRESS AND STATUS

Introduction

The tensile properties and swelling for the V-15Cr-5Ti, V-10Cr-5Ti, V-3Ti-1Si, V-15Ti-7.5Cr, and V-20Ti alloys after neutron irradiation at 600°C to 87 dpa have been reported by Loomis and Smith.[1] The tensile test results show that the alloys undergo maximum irradiation hardening in the range of 25 to 50 dpa and that the V-15Cr-5Ti, V-10Cr-5Ti, and V-3Ti-1Si alloys exhibit significantly greater irradiation hardening than the V-15Ti-7.5Cr and V-20Ti alloys. The tensile test results also show that these alloys exhibit significant total elongation (8-26%) after irradiation at 600°C to 87 dpa with the V-20Ti alloy exhibiting greater (≈2x) total elongation than the V-15Cr-5Ti, V-3Ti-1Si, and V-15Ti-7.5Cr alloys. In this report, we present results of analyses based on transmission electron microscopy observations (TEM) of the irradiation damage in microstructures of these irradiated alloys. These results are used to assess the influence of alloy composition on evolution of the irradiation damage microstructure and resulting tensile properties.

Materials and Procedure

Vanadium alloys with compositions listed in Table 1 were obtained in the form of 50% cold-worked sheet with 0.3-mm thickness. Specimens for TEM were annealed at 1125°C for one h in an ion-pumped vacuum system with a typical pressure of 1.3×10^{-6} Pa. Microstructures of annealed alloys are shown in Figs. 1 and 2. The annealed, unirradiated materials had an average grain diameter of ≈30 μm and contained $\approx 10^{12}$ dislocations/m^2. The V-15Cr-5Ti, V-10Cr-5Ti, V-15Ti-7.5Cr, and V-2OTi alloys contained precipitates with 60-400 nm diameter and number density of $\sim 2 \times 10^{19}$/m^3. The V-3Ti-1Si alloy contained precipitates with 30-100 nm diameter and number density of $\sim 2 \times 10^{20}$/m^3.

Table 1. Vanadium Alloy Compositions

	Concentration (wt.%)					
Alloy	Cr	Ti	O	N	C	Si
V–15Cr–5Ti	13.5	5.2	0.119	0.036	0.050	0.039
V–10Cr–5Ti	9.2	4.9	0.023	0.003	0.010	0.034
V–3Ti–1Si	–	3.1	0.021	0.031	0.031	0.800
V–15Ti–7.5Cr	7.2	14.5	0.111	0.025	0.040	0.040
V–20Ti	–	17.7	0.083	0.016	0.038	0.048

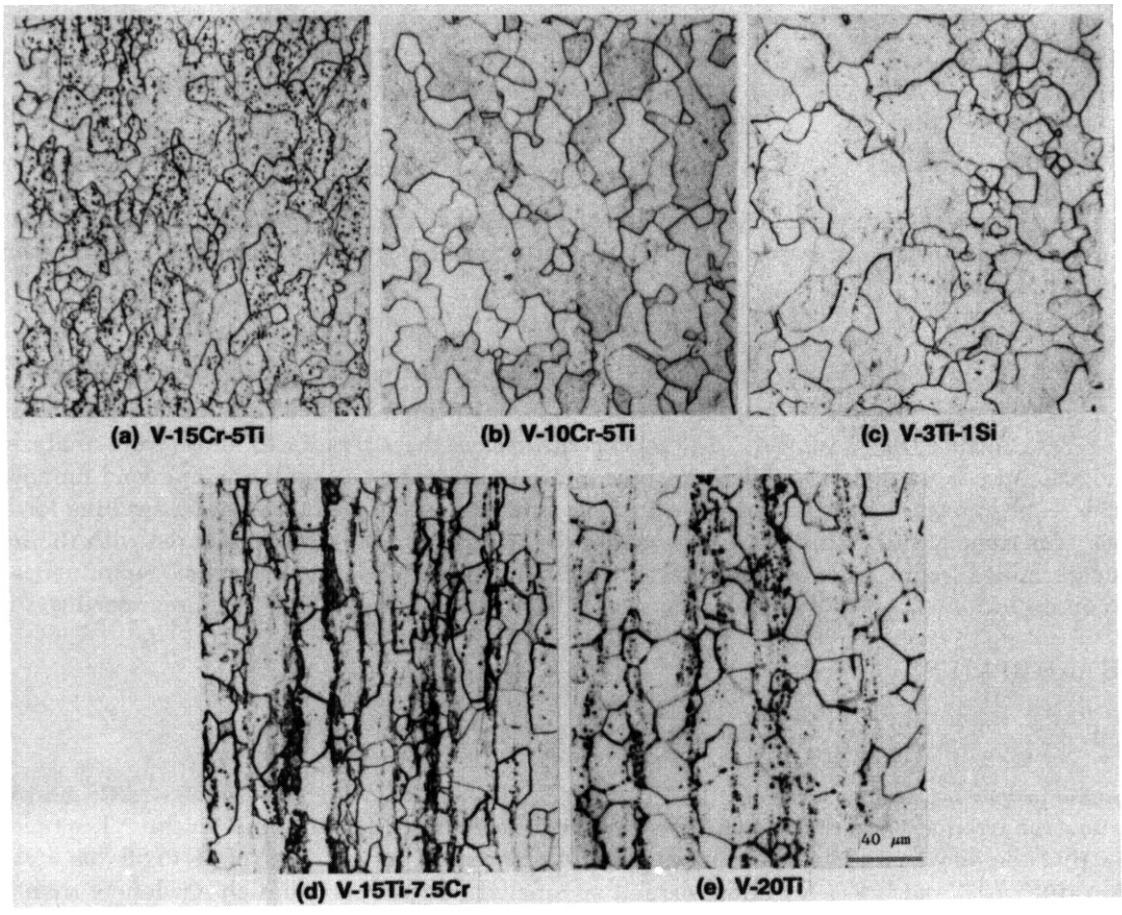

Fig. 1. Optical microstructures for vanadium–base alloys.

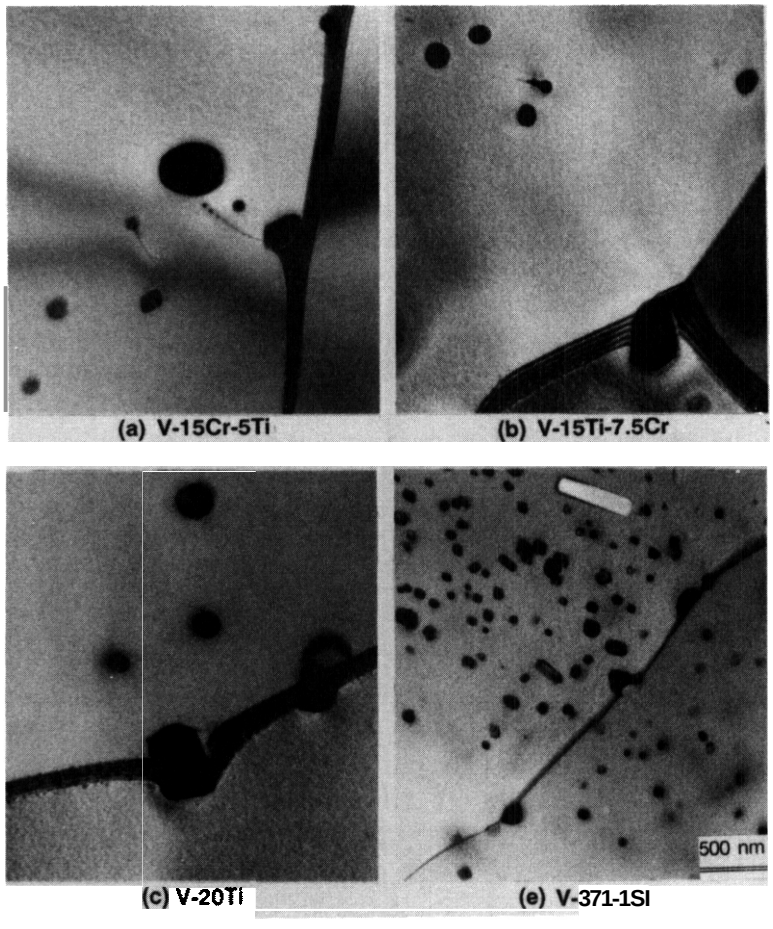

Fig. 2. TEM microstructures for vanadium–base alloys.

Specimens of the alloys for TEM were irradiated in Li-filled TZM molybdenum capsules at 600°C to neutron fluences (E > 0.1 MeV) of 3.6 x 10^{26} n/m^2 (21 dpa), 8.8 x 10^{26} n/m^2 (44 dpa), and 14.2 x 10^{26} n/m^2 (84 dpa) in the Materials Open Test Assembly during Cycles 8-10 of the Fast Flux Test Facility. Specimens irradiated to 21 dpa underwent a temperature excursion of +206°C for 50 min during Cycle 8 in the FFTF-MOTA.

Irradiated specimens (two or three for each damage level for each alloy) were prepared for TEM observation by electrochemical thinning of the specimens to perforation in a solution of 14%H_2SO_4-72% methanol-13% butyl cellosolve at -5°C. Microstructural examinations were performed on a JEOL 100CX electron microscope operating at 100 KeV. The thickness of TEM microstructures (100-200 nm) was determined from stereoscopic observations of photograph8 of microstructures.

EXPERIMENTAL RESULTS

TEM Observations and Data for Irradiated Alloys

The microstructures of alloys after irradiation at 600°C to 21, 44, and 84 dpa are shown in Figs. 3, 4, and 5, respectively. Table 2 lists the dislocation density (ρ_d), precipitate number density (N_P), precipitate average diameter (d_P), void number density (N_V), and void average diameter (d_V) determined from the microstructures for irradiated alloys. The dislocation density was determined from the equation

$$\rho_d = 2NMF/Lt, \quad (1)$$

where N was the number of dislocations intersecting a line of length L, M was the magnification, F (~1) was a factor that allowed for those dislocations out of contrast, and t was the specimen thickness.

The density of forest dislocations in the alloys increased substantially (10-30x) on irradiation to ~25 dpa but did not change significantly on additional irradiation to 84 dpa (Table 2, Fig. 6). The dislocation density in irradiated alloys was strongly dependent on alloy composition (Fig. 6). The dislocation density in V-15Cr-5Ti and V-10Cr-5Ti alloys was ≈2x the density in V-3Ti-1Si and V-15Ti-7.5Cr alloys and ≈6x the density in V-20Ti alloy.

Voids were observed in all of the irradiated alloys with void diameter and number density increasing with irradiation damage (Table 2). The V-20Ti alloy was exceptionally resistant to void formation and growth, whereas the V-15Ti-7.5Cr alloy was least resistant to void formation and growth. Voids that formed in V-3Ti-1Si and V-20Ti alloys were generally associated with precipitates formed during irradiation, whereas voids were rarely observed to be associated with precipitates in the V-15Cr-5Ti, V-10Cr-5Ti, and V-15Ti-7.5Cr alloys. The average diameter and number density of voids in the alloys increased on increasing the damage level from 44 dpa to 84 dpa. Swelling ($\Delta V/V_o$) of these irradiated alloys due to the presence of voids was computed from the N_V and d_V data in Table 2. In Table 3 and Fig. 7, these swelling values are compared with those obtained from immersion density measurements, i.e., $(D_o-D_{irr})/D_{irr}$, on these irradiated alloys.[3,4] The swelling values obtained from TEM observations and density measurements were generally in agreement except for V-15Cr-5Ti, V-10Cr-5Ti, V-3Ti-1Si, and V-20Ti specimens irradiated to 44 dpa (Table 3, Fig. 7). On the basis of the TEM observations, a density change of 1-2% for the V-15Cr-5Ti, V-10Cr-5Ti, V-3Ti-1Si, and V-20Ti alloys on irradiation at 600°C to 44 dpa must

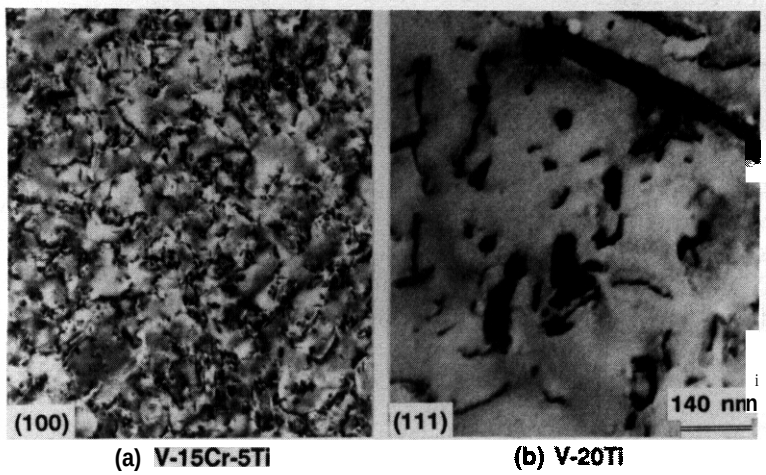

Fig. 3. Microstructures for V-15Cr-5Ti and V-20Ti alloys after irradiation at 600°C to 21 dpa in the FFTF-MOTA.

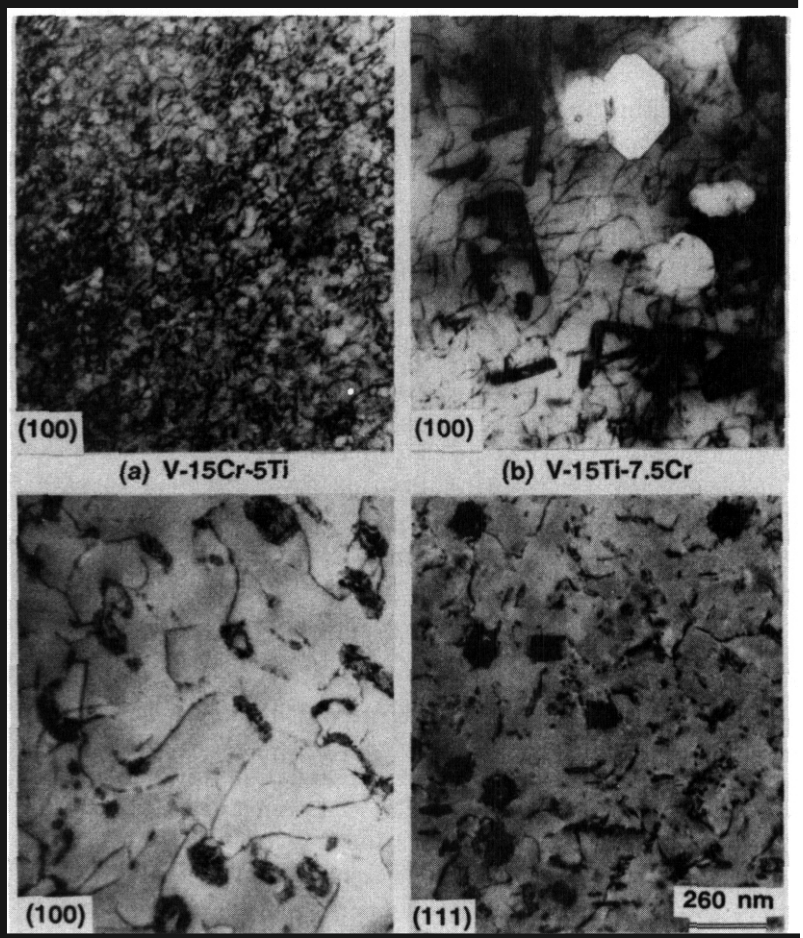

Fig. 4. Microstructures for V-15Cr-5Ti, V-15Ti-7.5Cr, V-20Ti, and V-3Ti-1Si alloys after irradiation at 600°C to 44 dpa in the FFTF-MOTA.

be attributed primarily to precipitate formation. In the case of the V-3Ti-1Si alloy specimens irradiated to 84 dpa, there were regions in the microstructures that contained a high density of relatively large voids resulting in 4.3% localized swelling.

Irradiation-produced precipitates were prominent in the microstructures of all of the irradiated alloys. The irradiation-produced precipitates were categorized, primarily on the basis of diameter, into three types (Table 2) of dim-shape precipitates. Type I precipitates were those features in the microstructures with diameters <6 nm. Type II precipitates were sited on {100} habit planes, e.g., at II in Fig. 5d, with diameter of 10-30 nm. Type III precipitates, e.g., at III in Fig. 5d, were relatively large diameter (>30 nm) and generally appeared to be strongly pinned or "wrapped with dislocations (Fig. 8). The shape of precipitates in microstructures for irradiated V-15Ti-7.5Cr alloy (Figs. 4b and 5b) was distinctly different from that in other irradiated alloys, and it was necessary to approximate the shape of these precipitates by a disc with a diameter of equivalent cross-sectional area. Also, precipitates in irradiated V-15Ti-7.5Cr alloy were transparent to the electron beam, which was not the case for precipitates in the other alloys. There was evidence in the microstructures, e.g., strain-field contrast, to lead us to tentatively conclude that the Type II precipitates were coherent with the alloy matrix, whereas Type III Precipitates were noncoherent.

Type I precipitates (features) were observed in all of the irradiated alloys. Type II precipitates were observed in V-15Cr-5Ti, V-10Cr-5Ti, and V-3Ti-1Si alloy microstructures, but were not observed in V-15Ti-7.5Cr and V-20Ti alloy microstructures. Type III precipitates were observed in microstructures of V-3Ti-1Si, V-20Ti, and V-15Ti-7.5Cr alloys, but were not observed in V-15Cr-5Ti and V-10Cr-5Ti alloy microstructures. The composition and/or crystallographic structure of the irradiation-produced precipitates in the alloys was not determined in this study.

Increase of Yield Stress

The increase of yield stress for these irradiated alloys was evaluated from the increase of shear stress ($\Delta\tau$) by use of the equation

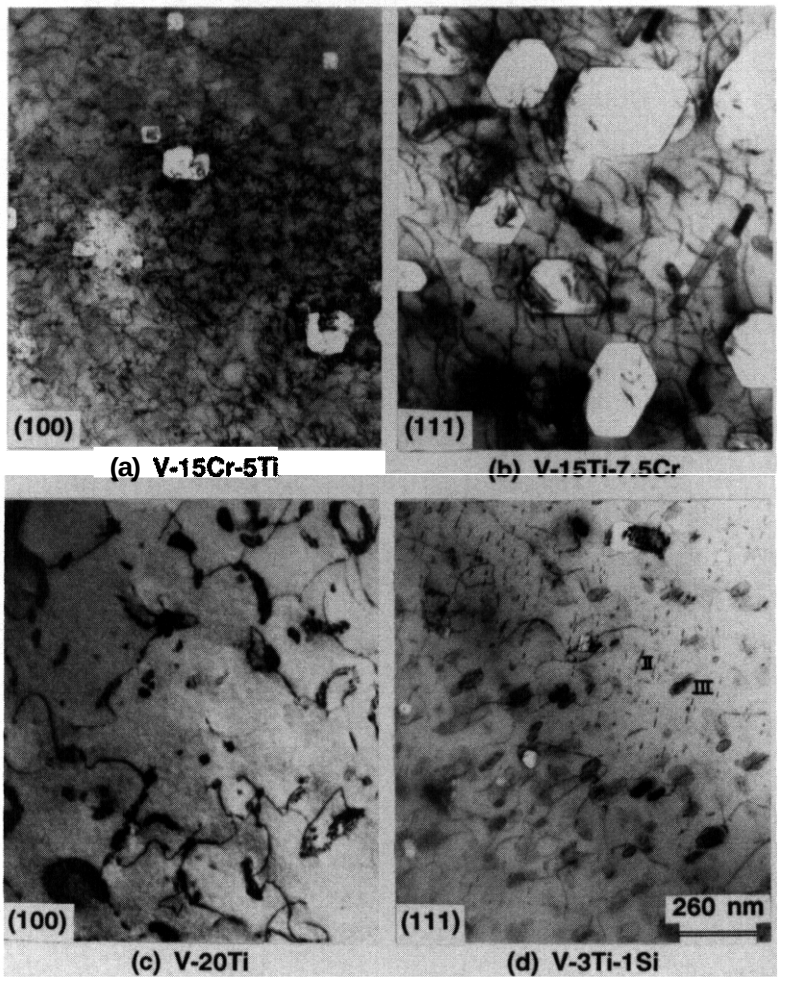

Fig. 5. Microstructures for V–15Cr–5Ti, V-15Ti–7.5Cr, V–20Ti, and V–3Ti–1Si alloys after irradiation at 600°C to 84 dpa in the FFTF–MOTA.

$$\Delta\sigma_y = \sqrt{3}\ \Delta\tau = \sqrt{3}\ (\alpha_\rho \mu b \sqrt{\rho_D} + \beta_P \mu b \sqrt{N_P d_P} + \gamma_V \mu b \sqrt{N_V d_V}).^{5-7} \quad (2)$$

In Eq. (2), α_ρ, β_P, and γ_V are the interaction parameters of gliding dislocations with forest dislocations, precipitates, and voids, respectively. In this report, we shall use α_ρ, β_P, and $\gamma_V = 0.28$.[6] Also in this equation, μ is the shear modulus and b is the Burger's vector for vanadium with values of 4.67×10^4 MPa and 0.26 nm, respectively.[6] The results of computations of the increase of yield stress that could be attributed to voids ($\Delta\sigma_V$), dislocations ($\Delta\sigma_D$), or precipitates ($\Delta\sigma_P$) in the irradiated alloys using Eq. (2) and the data in Table 2 are tabulated in Table 4. The results of these computations show that forest dislocations and precipitates created in the alloys during irradiation were the major contributors (≈90%) to the increase of yield stress. In the case of the V-15Cr-5Ti and V-20Ti alloys irradiated to 84 dpa, forest dislocations contributed ≈60% to the increase of yield stress, whereas precipitates contributed ~30%. Voids in the irradiated alloys contributed relatively small amount (<15%) to the increase of yield stress. The total increase of yield stress for irradiated alloys that was calculated by the use of Eq. (2), and the increase of yield stress determined for these irradiated alloys on tensile testing, are also listed in Table 4.[1,2] The computed increase of yield stress values ($\Delta\sigma_{TEM}$) derived from TEM observations and use of α_ρ, β_P, and $\gamma_V = 0.28$ in Eq. (2) for the V-15Cr-5Ti, V-10Cr-5Ti, and V-3Ti-1Si alloys were in good agreement with the increase of yield stress values ($\Delta\sigma_{TEN}$) determined from tensile testa (Table 4, Fig. 9). However, in the case of the V-15Ti-7.5Cr and V-20Ti alloys, the $\Delta\sigma_{TEM}$ values were substantially higher than the $\Delta\sigma_{TEN}$ values. A better agreement between the $\Delta\sigma_{TEM}$ and $\Delta\sigma_{TEN}$ values for these alloys was achieved by use in Eq. (2) of α_ρ, β_P, and $\gamma_V = 0.04$ (Table 4, Fig. 9).

Table 2. Irradiation–Produced Defect Size and Concentration

Alloy	dpa	Voids		Dislocations	Precipitates		
		d_V (nm)	N_V (m^{-3})	ρ_d (m^{-2})	Type	d_p (nm)	N_P (m^{-3})
V–15Cr–5Ti	21	12	1.4×10^{19}	3.2×10^{14}	I	4	9×10^{20}
					II	14	8×10^{21}
"	44	29	8.5×10^{18}	4.0×10^{14}	I	4	4×10^{21}
					II	14	4×10^{21}
"	84	63	1.2×10^{20}	4.8×10^{14}	I	4	3×10^{21}
					II	17	2×10^{21}
V–10Cr–5Ti	44	57	5.1×10^{18}	3.1×10^{14}	I	5	9×10^{20}
					II	15	4×10^{21}
V–3Ti–1Si	44	25	1.1x 10'9	1.5×10^{14}	I	5	lxlon
					II	IS	1x1021
					III	74	3×10^{20}
"	84	46	9.8×10^{19}	1.7×10^{14}	I	5	9×10^{20}
					II	IS	1×10^{21}
					III	52	5×10^{20}
■	84	77	1.8×10^{20}	1.2×10^{14}			
V–15Ti–7.5Cr	44	165	1.7×10^{19}	1.4×10^{14}	I	7	3×10^{19}
					III	91	8×10^{19}
"	87	177	2.6×10^{19}	1.4×10^{14}	I	7	3×10^{19}
					III	88	9 x 10'9
V–20Ti	21	22	8.7×10^{19}	7.6 x 10"	I	4	1×10^{21}
					III	58	7x1020
"	44	39	1.1x 10'9	7.6×10^{13}	I	5	5×10^{20}
					III	96	2×10^{20}
"	84	46	1.2 x 10'9	6.4×10^{13}	I	5	5×10^{20}
					III	40	2 x 1020

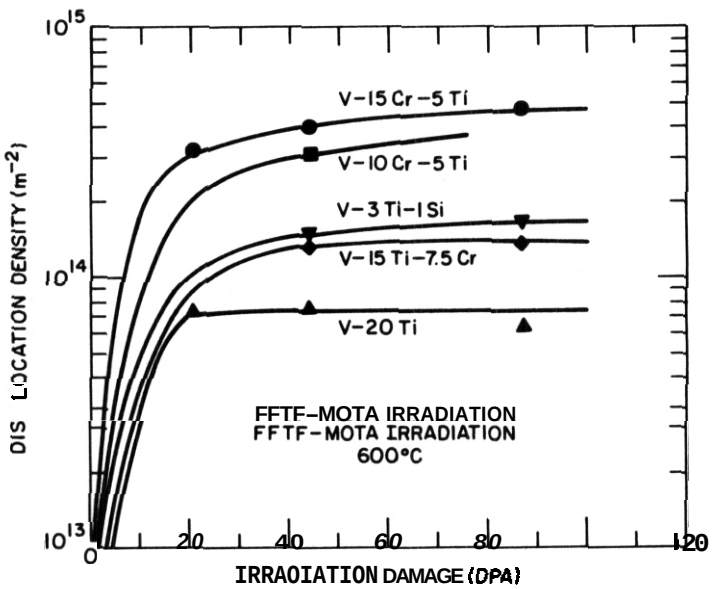

Fig. 6. Dependence of dislocation density in vanadium alloys on irradiation damage.

Table 3. Swelling of Irradiated Vanadium Alloys

Alloy	dpa	TEM $\Delta V/V_0$ (%)	Density $(D_{irr}-D_0)/D_0$ (%)
V–15Cr–5Ti	21	<0.1	0.1
	44	<0.1	0.3–1.9
	84	2.0	1.7–2.6
V–10Cr–5Ti	44	<0.1	0.7–1.8
V–3Ti–1Si	44	<0.1	0.2–0.7
	84	0.5	0.5–0.8
	84	4.3	–
V–15Ti–7.5Cr	44	4.0	2.1–4.6
	84	7.5	7.3–9.3
V–20Ti	21	<0.1	0.1
	44	<0.1	-0.1–2.1
	84	<0.1	-0.1–0.2

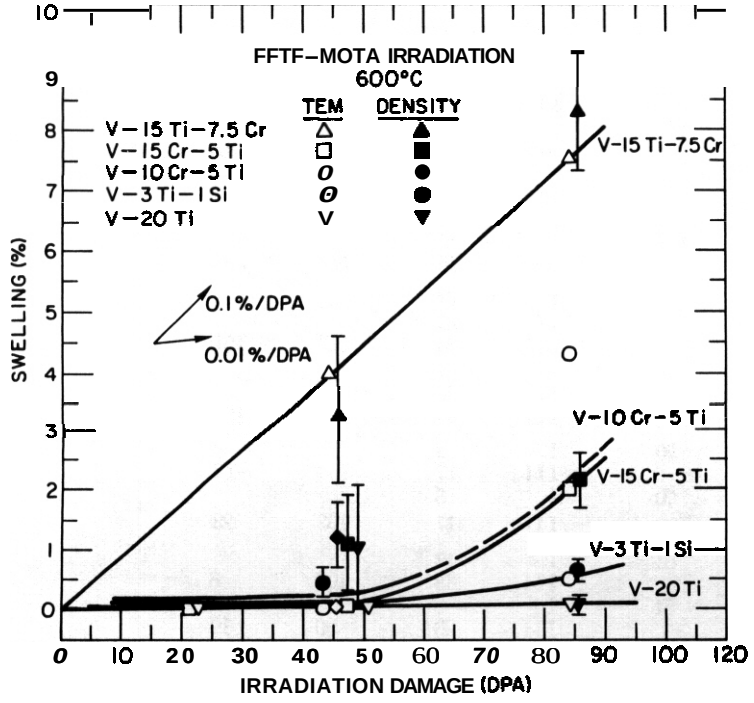

Fig. 7. Dependence of swelling of vanadium alloys at 600°C on irradiation damage.

DISCUSSION OF RESULTS

The TEM observations of microstructures in V-15Cr-5Ti, V-15Ti-7.5Cr, V-20Ti, and V-3Ti-1Si alloys after neutron irradiation at 600°C to 21-84 dpa have shown those features, i.e., forest dislocations, precipitates, and voids, that contributed to the increase of yield stress and swelling of the alloys. An evaluation of the dislocation density, precipitate number density and size, and void number density and size in the microstructures, together with computations of the increase of yield stress and swelling, has shown significant agreement with the increase of yield stress determined from tensile tests and determinations of change in density for these irradiated

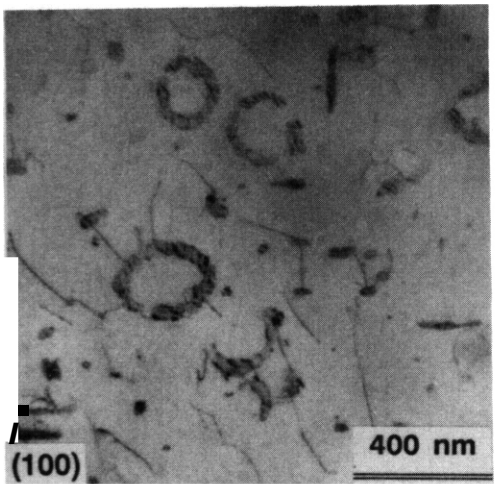

Fig. 8. Precipitates pinned or 'wrapped" with dislocations in V-20Ti alloy after irradiation at 600°C to 44 dp.

Table 4. Increase of Yield Stress for Irradiated Alloys

		TEM					
		Voids	Dislocations	Precipitates		Total	Total[1,2]
Alloy	dpa	$\Delta\sigma_V$ (MPa)	$\Delta\sigma_D$ (MPa)	Type	$\Delta\sigma_P$ (MPa)	$\Delta\sigma_{TEM}$ (MPa)	$\Delta\sigma_{TEN}$ (MPa)
Dislocation Interaction Parameter = 0.28							
V–15Cr–5Ti	21	2	105	I	11		
				II	62	180	179
"	44	3	118	I	24		
				II	44	189	221
"	84	17	129	I	20		
				II	34	200	170
V–10Cr–5Ti	44	3	104	I	13		
				II	46	166	150
V–3Ti–1Si	44	3	72	I	13		
				II	26		
				III	28	142	151
"	84	13	77	I	12		
				II	26		
				III	30	158	150
V–15Ti–7.5Cr	44	lo	70	I	3		
				III	17	100	–17
"	84	13	70	I	3		
				III	17	103	23
v–2oTi	21	8	51	I	12		
				III	38	109	8
"	44	4	51	I	9		
				III	26	90	lo
"	84	4	47	I	9		
				III	17	77	2
Dislocation Interaction Parameter = 0.04							
V–15Ti–7.5Cr	44	1	lo	I	1		
				III	2	14	–17
"	84	2	lo	I	1		
				III	2	15	23
V–20Ti	21	1	7	I	2		
				III	5	15	8
"	44	1	7	I	1		
				III	4	13	10
"	84	1	7	I	1		
				III	2	11	2

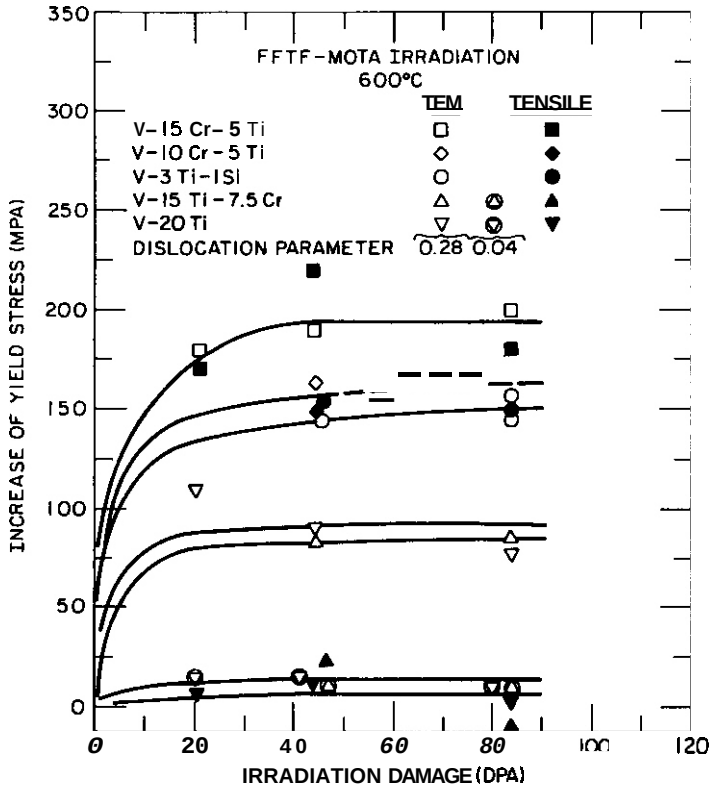

Fig. 9. Dependence of increase of yield stress for vanadium alloys irradiated at 600°C on irradiation damage.

alloys. A significant result obtained from these analyses and computations was the contributions of forest dislocations, precipitates, and voids to the increase of yield stress. In the case of the V-15Cr-5Ti and V-20Ti alloys irradiated to 84 dpa, forest dislocations contributed ~60% to the increase of yield stress, whereas precipitates contributed ~30%. Voids in the irradiated alloys contributed a relatively small amount (<15%) to the increase of yield stress.

It is generally recognized that production of forest dislocations. precipitates, and voids in a material on irradiation are inextricably related and that increase of yield stress (0.2% strain) for an irradiated material is determined by initiation of dislocation glide and by the resistance presented to dislocation movement through these microstructural "barriers." However, it is our view that the composition of radiation-produced precipitates and the crystallographic compatibility, i.e., coherency or noncoherency, of the radiation-produced precipitates with the alloy lattice basically governs evolution of the alloy microstructures and the forest dislocation density on irradiation. We have tentatively concluded on the basis of the TEM observations that Type II radiation-produced precipitates in V-3Ti-1Si, V-15Cr-5Ti, and V-10Cr-5Ti alloys were coherent with the alloy lattice, whereas Type III precipitates in V-3Ti-1Si, V-20Ti, and V-15Ti-7.5Cr alloys were noncoherent. The experimental results obtained by Bohm suggest that precipitates in unirradiated V-3Ti-1Si, V-15Cr-5Ti, and V-10Cr-5Ti alloys should be coherent in the alloy lattice, whereas precipitates in the V-20Ti alloy should be noncoherent with the alloy lattice.[8] Also, Loomis et al. have shown clear evidence, i.e., strain-field contrast in TEM microstructures, for coherent precipitates in ion-irradiated V-5Ti and V-15Cr-5Ti alloys.[9] Type I precipitates are expected to be coherent with the alloy lattice because of their small size. It might be expected in the absence of other contributing factors that the forest dislocation density in the irradiated alloys would be essentially equivalent because, for a given radiation damage level, the number of vacancy and interstitial defects produced in the irradiated alloys in the present study was similar and the number density of dislocations in the alloys before irradiation can be assumed to have been nearly equal. This was not the case, however, because it was determined that the dislocation density in the V-15Cr-5Ti alloy was ≈2x the density in V-3Ti-1Si and V-15Ti-7.5Cr alloys and ≈6x the density in V-20Ti alloy, even though the forest dislocation density in the irradiated alloys obtained a saturation level at 20-40 dpa irrespective of their dislocation density. Therefore, we suggest that the difference in observed density of forest dislocations in the alloys and consequently their different irradiation hardening, i.e., increase of yield stress, is attributable to coherence or noncoherence of irradiation-produced precipitates in the alloys.

The V-15Cr-5Ti, V-10Cr-5Ti, V-3Ti-1Si, and V-20Ti alloys were resistant to void formation and growth during neutron irradiation ($\Delta V/V_o < 0.1\%/dpa$). Loomis et al. attributed the inhibition of void formation in V-Ti and V-Ti-Cr alloys on ion irradiation to the formation of Ti_3O precipitates that can incorporate vacancy defects in the precipitate structure of this titanium oxide.[9] Vacancy-0-Ti complexes are believed to form during irradiation, diffusing and agglomerating into Ti_3O precipitates. Experimental evidence confirming this mechanism of inhibition of void swelling may have been observed by Ohnuki, et al.[10] in TEM microstructures (Fig. 8) for neutron-irradiated V-10Ti alloy. It is suggested that a temperature excursion of +206°C (50 min duration) during irradiation at 600°C to 14 dpa rendered visibility to vacancy clusters in the titanium oxide precipitate that would otherwise not be visible. The exceptional resistance to void swelling during neutron irradiation of V-20Ti alloy ($\Delta V/V_o < 0.01\%/dpa$) in comparison to V-3Ti-1Si and V-15Cr-5Ti alloys may be attributed to the higher solubility of oxygen in the V-20Ti alloy.[11] The exceptionally high void swelling of the V-15Ti-7.5Cr alloy is believed due to the composition and/or crystallographic structure of the irradiation-produced precipitates that did not incorporate vacancy defects.

The effect of neutron irradiation on ductility, i.e., uniform and/or total elongation, of the neutron-irradiated vanadium alloys is essentially understandable in consideration of the results obtained from analyses of the TEM microstructures and computations of increase of yield stress. The increase of yield stress values (Fig. 9, Table 4) for the irradiated alloys suggests that the effect of neutron irradiation on ductility of V-15Ti-7.5Cr and V-20Ti alloys should be less than for the V-3Ti-1Si, V-15Cr-5Ti, and V-10Cr-5Ti alloys. If uniform elongation data for the irradiated alloys are considered, this is indeed the case except for the V-15Ti-7.5Cr alloy irradiated to 87 dpa.[1] The low ductility in this latter case is attributed to the inability of the tensile specimen to withstand crack propagation in a matrix containing large-diameter voids ($\Delta V/V_o \approx 8\%$). These results suggest that vanadium alloys can undergo void swelling of 54% without significant impact on the tensile properties during neutron irradiation.

CONCLUSIONS

Analyses of TEM microstructures for V-15Cr-5Ti, V-10Cr-5Ti, V-15Ti-7.5Cr, V-20Ti, and V-3Ti-1Si alloys after neutron irradiation at 600°C to 21-84 dpa, together with computations of the increase of yield stress from these analyses, have shown that forest dislocations and radiation-produced precipitates are major contributors to the increase of yield stress determined for these alloys on tensile testing.

The irradiation hardening of neutron-irradiated V-Ti and V-Ti-Cr alloys is dependent on Ti concentration that may be attributed to coherence or noncoherence of radiation-produced precipitates.

The inhibition of void swelling of neutron-irradiated V-Ti and V-Ti-Cr alloys by Ti may be attributed to formation of titanium oxide superstructures that can incorporate vacancy defects. V-Ti and V-Ti-Cr alloys can undergo void swelling of 4% without significant impact on tensile properties.

FUTURE WORK

The composition and crystallographic structure of precipitates in unirradiated and neutron-irradiated V-Ti, V-Ti-Cr, and V-Ti-Si alloys will be determined from TEM observations and use of EDXS and EELS techniques.

REFERENCES

1. B. A. Loomis and D. L. Smith, "Tensile Properties for Neutron-Irradiated Vanadium Alloys," Fusion Reactor Materials Semiannual Progress Report for Period Ending September 30, 1989, DOE/ER-0313/7, Oak Ridge National Laboratory, Oak Ridge, TN, pp. 203-209.

2. B. A. Loomis, A. B. Hull, and D. L. Smith, "Evaluation of Low-Activation Vanadium Alloys for Use as Structural Material in Fusion Reactors," Proceedings of the Fourth International Conference on Fusion Reactor Materials, December 4-8, 1989, Kyoto, Japan.

3. B. A. Loomis and D. L. Smith, "Swelling of Neutron-Irradiated Vanadium Alloys," Fusion Reactor Materials Semiannual Progress Report for Period Ending March 31,1989, DOE/ER-0313/6, Oak Ridge National Laboratory, Oak Ridge, TN, pp. 339-345.

4. B. A. Loomis, D. L. Smith, and F. A. Gamer, "Swelling of Neutron-Irradiated Vanadium Alloys," Proceedings of the Fourth International Conference on Fusion Reactor Materials, December 4-8, 1989, Kyoto, Japan.

5. F. A. Gamer, M. L. Hamilton, N. F. Panayotou, and G. D. Johnson, J. Nucl. Mater. 103 & 104 (1981) 803.

6. J. Moteff, D. J. Michel, and V. K. Sikka, in: Defects and Defect Clusters in BCC Metals and Alloys, Nuclear Metallurgy, Vol. 18, Ed. R. J. Arsenault (National Bureau of Standards, Gaithersburg, MD, 1973) p. 198.

7. B. A. Loomis, B. J. Kestel, and D. L. Smith, J. Nucl. Mater. 155-157 (1988) 1305.

8. H. Bohm, "Strengthening Mechanism in Vanadium-Titanium Alloys," Proceedings of Second International Conference on the Strength of Metals and Alloys, Vol. 1, August 30-September 4, 1970, Pacific Grove, CA, American Society of Metals, pp. 341-345.

9. B. A. Loomis, B. J. Kestel, and S. B. Gerber, "Solute Segregation and Microstructural Evolution in Ion. Irradiated Vanadium-Base Alloys," Proceedings of 13th International Symposium on Radiation-Induced Changes in Microstructure. June 23-25, 1986, Seattle, WA, Part 1, pp. 730-742.

10. S. Ohnuki, D. S. Gelles, B. A. Loomis, F. A. Gamer, and H. Takahashi, "Microstructural Examination of Simple Vanadium Alloys Irradiated in the FFTF/MOTA," Fusion Reactor Materials Semiannual Progress Report for Period Ending September 30, 1989, DOE/ER-0313/7, Oak Ridge National Laboratory, Oak Ridge, TN, pp. 177-189.

11. K. H. Kramer, J. Less-Common Met. 21 (1970) 365.

6.4 Copper Alloys

STRENGTH AND FATIGUE OF DISPERSION-STRENGTHENED COPPER — T. J. Miller (Auburn University), S. J. Zinkle (Oak Ridge National Laboratory), and B. A. Chin (Auburn University)

OBJECTIVE

To measure the tensile and fatigue properties of a commercial high-conductivity dispersion-strengthened copper alloy over the temperature range of 20 to 600°C in order to assess its suitability for fusion applications.

SUMMARY

The tensile and fatigue properties of cold-worked copper and a commercial Cu-Al_2O_3 dispersion-strengthened alloy were measured at temperatures between 25 and 600°C. The GLIDCOP Al-15 alloy, which contains 0.15 wt % Al in the form of Al_2O_3 particles, exhibited a significantly higher tensile and fatigue strength than copper under all test conditions. The mechanical properties of this alloy appear to be suitable for high-strength, high-conductivity alloy applications in fusion reactors.

1. Introduction

High-strength, high-conductivity copper alloys have a number of potential applications in magnetic fusion reactors. The unique combination of high electrical conductivity and high strength makes this class of materials an ideal choice for high-field normal conducting magnets. In addition, their strength and high thermal conductivity are well suited for high heat flux applications such as the structural material for divertors or limiters. The anticipated operating environment includes temperatures from 77 to 725 K, stresses of 200 MPa or higher, and desired fatigue lifetimes up to 10^5 cycles. Oxide dispersion-strengthened copper is preferred over precipitation-strengthened copper for most fusion applications due to its superior void swelling resistance' and its high softening (recrystallization) temperature. The useful operating temperatures for most precipitation-strengthened coppers is limited to <300°C due to radiation-enhanced recrystallization effects.[2,3] Another advantage associated with the high recrystallization temperature of dispersion-strengthened copper is that brazing can be performed without a degradation in strength.'

GLIDCOP Al-15 is a commercially available[5] dispersion-strengthened copper produced from a dilute copper-aluminum powder (0.15 wt % Al) that has been internally oxidized and hot extruded, resulting in small (~10 nm diameter) particles of A1203 in a pure copper matrix. The room temperature electrical and thermal conductivity of A1-15 is ~92% that of pure copper.[5] Dispersion-strengthened copper has been selected for the toroidal field magnets of the proposed Compact Ignition Tokamak (CIT), and is the reference copper alloy for the International Thermonuclear Experimental Reactor (ITER) divertor assembly.

This report describes the tensile and fatigue properties of GLIDCOP Al-15 from room temperature to 600°C in order to assess the suitability of this alloy for the proposed CIT and ITER applications. Measurements were also made on 10% cold-worked copper for comparison.

2. Experimental Procedure

Tensile and fatigue tests were performed on miniature sheet tensile specimens corresponding to the SS-1 geometry.[6] The SS-1 specimen has an overall length of 44.5 mm and a gage section that is 20.3 mm long, 1.52 mm wide, and 0.76 mm thick. Pure copper sheet specimens obtained from Johnson Matthey were cold rolled from 2.5 to 0.84 mm and then re-crystallized by annealing in air at 400°C for 1 h. The sheet was then cold rolled an additional 10% to produce a final thickness of 0.76 mm and specimens were machined into the SS-1 geometry. The GLIDCOP Al-15 was obtained in extruded bar form which had been directionally cold worked (~90%) and was coated with a copper cladding due to the extrusion process. The cladding was removed using electrodischarge machining (EDM) and sheets were cut using the same process. SS-1 specimens were then machined from the sheets with the gage length parallel and transverse to the cold-worked direction.

Tensile tests were conducted in a vacuum chamber on a 120 kN Instron, closed loop, servo-hydraulic materials test machine at a crosshead speed of 0.0085 mm/s. Tests were performed at temperatures ranging from ambient to 600°C. The specimens were held at the test temperature for 0.5 h before the start of the test.

A commercial fatigue machine was modified at Auburn University' to test miniature sheet specimens in a pure bending mode. The basic concept of the apparatus is a cantilever beam with a cyclic load applied to the free end. Strain gages attached to the machine produce a signal which is used to calculate the stress at the surface from the bending moment. All of the fatigue specimens failed at the axial position corresponding to the maximum calculated stress.

Longitudinal specimens for fatigue testing were mechanically polished and then electropolished using a 67% methanol–33% nitric acid solution to produce a defect-free surface. This is an important step for fatigue tests since surface flaws are a source of crack initiation which may result in shorter fatigue life. The specimens were tested in a plane bending mode using a constant strain amplitude during the test (minimum to maximum stress ratio of R = 0) and a cycle frequency of 10 Hz. Elevated-temperature fatigue tests were performed at 600°C in flowing argon gas. For the 600°C fatigue tests, the initially applied maximum stress exceeded the yield stress for fatigue lifetimes up to 1.5 × 10^6 cycles. It was assumed for these hi'gh-temperature specimens that thermal creep associated with the plastic deformation caused the specimens to bend to a new equilibrium position near the midpoint of the deflection range (i.e., the stress ratio changed to R = -1). All tests performed in the future will be set up with a stress ratio of R = -1 to avoid this complication.

3. Results and Discussion

3.1 Tensile Tests

The yield strength versus temperature results for both copper and GLIDCOP are shown in Fig. 1. The GLIOCOP specimens were tested in both the longitudinal and transverse directions. The strength in the two directions was comparable (Fig. 1). The room temperature yield strength of GLIDCOP (330 MPa) was higher than that of copper (210 MPa), and remained higher at all temperatures. The GLIOCOP yield strength decreased gradually with temperature, whereas the pure copper had a more abrupt decrease in the curve at around 400°C. This is due to the recrystallization of copper.[8] After recrystallization, the strength of copper is very low compared to its original (room temperature) value. This limits structural applications for copper to temperatures which do not exceed the recrystallization temperature. GLIDCOP, on the other hand, does not recrystallize until temperatures near the melting temperature since the alumina particles inhibit dislocation nmvement.[4,5]

The ultimate tensile strength versus temperature for copper and GLIDCOP is shown in Fig. 2. Again, the GLIDCOP shows greater strength at all temperatures. Tensile tests performed on GLIDCOP along the transverse axis produced results close to that of the cold-worked direction (Fig. 2), indicating that there is little effect of directionality on the tensile properties.

The elongation to failure of the GLIOCOP specimens was –16% at all temperatures. The corresponding total elongation in the copper specimens varied from –20% at room temperature to –50% at 600°C. where the increased ductility at high temperatures may be attributed to recrystallization effects. The uniform elongation of the GLIDCOP decreased from 10%to –2.5% as the test temperature increased from 25 to 600°C.

3.2 Fatigue Tests

The results of the room temperature fatigue tests are shown in Fig. 3, where the data are plotted in the form of maximum applied tensile stress (S) versus the number of cycles to failure (N). Both S/N curves exhibit the typical shape expected for nonferrous materials,[9] where the fatigue strength decreases gradually with increasing cycles but does not reach a true fatigue limit. The fatigue strength in the low

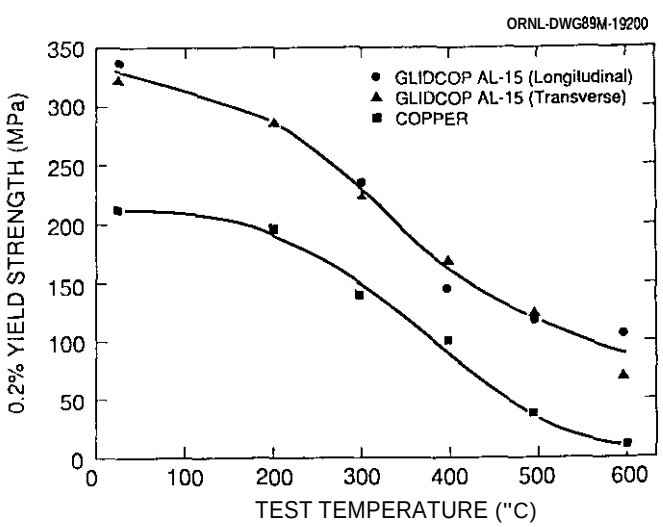

Fig. 1. Yield strength of copper and GLIDCOP Al-15 copper alloy.

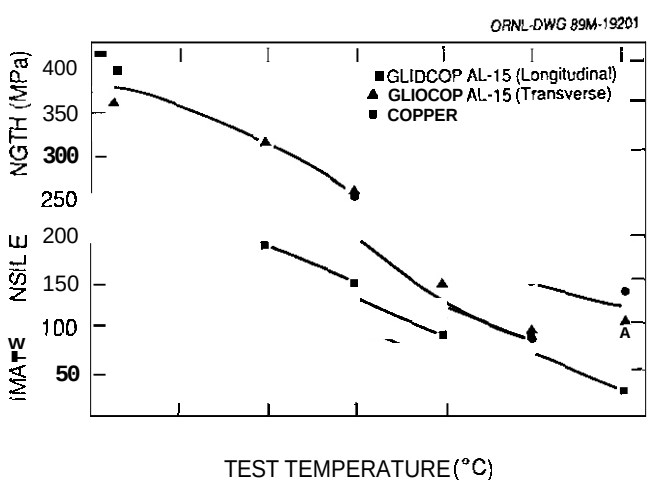

Fig. 2. Ultimate tensile strength of copper and GLIDCOP Al-15 copper alloy.

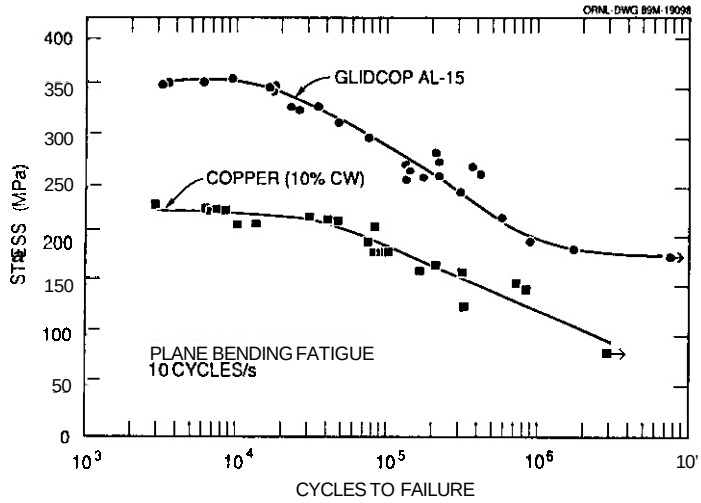

Fig. 3. Fatigue strength of copper and GLIOCOP A1–15. Specimens machined in the longitudinal direction.

cycle ($<10^4$ cycles) regime was nearly constant, which is due to the application of stresses that exceed the uniaxial yield strength — the corresponding failure stress is intermediate between the yield and ultimate strength of the material. It is evident from Fig. 3 that the room temperature fatigue properties of GLIDCOP A1–15 are clearly superior to those of copper. The fatigue strength at 10^5 cycles (the design limit for applications in CIT and ITER) is 290 MPa for GLIDCOP versus 190 MPa for copper. The fatigue life of GLIDCOP at an applied stress of 200 MPa is ~10^6 cycles, which is an order of magnitude higher than the copper fatigue life.

Figure 4 compares the S/N curves of GLIDCOP at room temperature and 600°C. As expected, the fatigue strength is reduced by a substantial amount at elevated temperatures — the fatigue strength at 10^5 cycles is ~115 MPa. It is clearly evident that the fatigue life decreased rapidly when the applied stress exceeded the vield strenoth (330 and 90 MPa, respectively, for testing at 25 and 600°C).

The fracture surfaces of selected specimens were examined with a scanning electron microscope. All of the fracture surfaces showed evidence of considerable ductility, and there were no major differences in the topography of the room temperature and 600°C specimens.

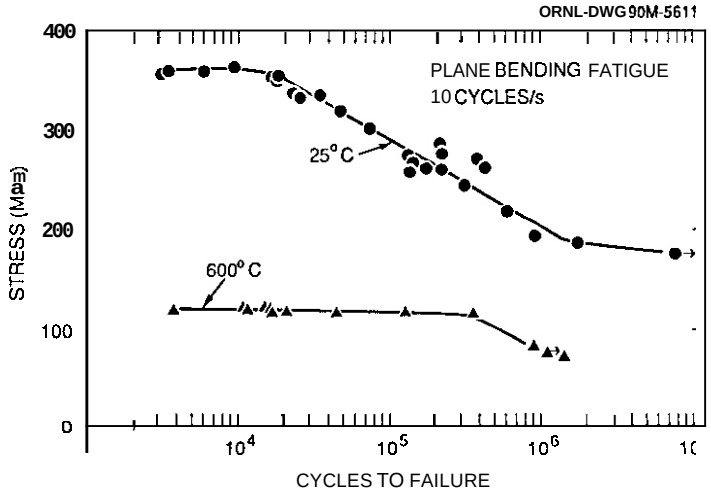

Fig. 4. Fatigue strength of longitudinal GLIDCOP A1–15 specimens at room temperature and 600°C. The 600°C results assume R = -1 and therefore represent a lower bound for the actual fatigue strength.

3.3 Comparison with Literature Results

The tensile and fatigue properties of copper have been studied extensively, and the present results for copper are in good agreement with these studies. For example, the measured fatigue strength of copper at 10^6 cycles was 110 MPa which agrees with the literature value.[9,10] There have been a number of studies performed on dispersion-strengthened copper that have demonstrated its superior mechanical properties compared to copper, particularly at high temperatures.[11,12] Unfortunately, most of these studies utilized a rather coarse dispersion and are therefore not directly applicable to GLIDCOP which contains a high density of small particles. Comparison with the limited amount of elevated temperature tensile data that has been obtained on GLIDCOP copper alloys[4,5,13,14] shows good agreement with the present results (i.e., the shapes of the tensile strength versus temperature curves are similar). Slight quantitative differences between the different studies may be attributed to different cold-work levels in the alloys.[5]

There is only one known measurement of the fatigue properties of GLIDCOP A1–15, which was performed by the manufacturer at room temperature[5] on 94% cold-worked rod. Their measurements, obtained in a cantilever beam rotating-bending mode at a frequency of 167 cycles/s, showed uniformly higher fatigue strength (by 15 to 20%) compared to the present results. Other studies have shown that the rotating bending fatigue test can overestimate the fatigue strength due to dynamic hysteresis effects' which cause the true stress to be less than the nominal stress. More likely, the fatigue stress differences may be due to the higher starting yield strength of the GLIDCOP in the previous study (470 vs 330 MPa due to a higher amount of cold work). The higher frequency associated with the previous study (167 vs. 10 Hz) should also produce a higher measured fatigue strength.' There are no known previous fatigue measurements of GLIOCOP at elevated temperatures. Further tests with a stress ratio of R = -1 are needed to confirm the present results.

4. Summary and Conclusions

Measurements on the tensile and fatigue properties of GLIDCOP A1-15 dispersion-strengthened copper indicate that this alloy shows good mechanical stability in the temperature range of 25 to 600°C. The measurements indicate that GLIDCOP A1-15 is suitable for many of the proposed applications in fusion reactors requiring high-strength, high-conductivity materials (including CIT and ITER). Applications which demand very high strengths may require the use of higher strength $Cu-Al_2O_3$ alloys, such as GLIDCOP A1-25 or Al-60 (0.25 and 0.6 wt % Al, respectively).

FUTURE WORK

The tensile and fatigue properties of GLIDCOP specimens brazed with conventional and induction furnaces will be measured and evaluated.

Acknowledgments

The GLIDCOP A1-15 alloy was supplied by the Fusion Energy Division at ORNL. Partial support for this study was provided by the Oak Ridge Associated Universities NERA graduate student research participation program. Experimental assistance was provided by N. H. Rouse and E. L. Ryan.

References

1. H. R. Brager and F. A. Garner, in: Effects of Radiation on Materials, Fourteenth Int. Symp., ASTM STP 1046, eds., N. H. Packan, R. E. Stoller. and A. S Kumar, American Society for Testing and Materials, Philadelphia, 1989, pp. 599–604.
2. S. J. Zinkle, G. L. Kulcinski, and L. K. Mansur, J. Nucl. Mater. 141-143 (1986) 188.
3. M. Apello and P. Fenici, J. Nucl. Mater. 152 (1988) 348.
4. J. J. Stephens, R. J. Bourcier, F. J. Vigil, and D. T. Schmale, Sandia National Laboratory Report, SAND88-1351 (September 1988).
5. A. V. Nadkarni, in: High Conductivity Copper and Aluminum Allays, eds., E. Ling and P. W. Taubenblat (TMS-AIME, New Vork, 1984) p. 77.
6. R. L. Klueh, Nucl. Engr. Design/Fusion 2 (1985) 407.
7. R. H. Wong, M.S. thesis, Mechanical Engineering Department, Auburn University (1986).
8. G. E. Dieter, Mechanical Metallurgy, 2nd ed. (McGraw-Hill, New York, 1976) p. 239.
9. N. E. Frost, K. J. Marsh, and L. P. Pook, Metal Fatigue (Oxford University Press, New Vork, 1974).
10. C. Laird, Met. Trans. A B (1977) 851.
11. M. H. Lewis and J. W. Martin, Acta Met. 11 (1963) 1207.
12. R. L. Graham, O. A. Edge, and D. C. Moore, J. Inst. Metals 99 (1971) 81.
13. S. J. Zinkle, ADIP Semiann. Prog. Rept., DOE/ER-0045/16 (March 31, 1986), p. 163.
14. J. E. Synk and K. Vedula, Mat. Sci. Technol. 3 (1987) 72.

UNUSUAL TENSILE AND FRACTURE BEHAVIOR OF PURE COPPER AT HIGH LEVELS OF NEUTRON-INDUCED SWELLING -
K. R. Anderson, University of Illinois; F. A. Garner, Pacific Northwest Laboratory;(a) J. F. Stubbins, University of Illinois

SUMMARY

The most common measures of ductility are uniform and total elongation and reduction of area. Pure copper in the unirradiated state exhibits large amounts of both measures of ductility along with a serpentine glide fracture morphology. After irradiation at 411-414°C with fast neutrons to 34 or 50 displacements per atom (dpa), the tensile and fracture behavior change greatly. Significant uniform elongation is retained but the reduction of area is very small.

Such a unilateral shift between macroscopic measures of ductility is unusual. The fracture surface is also unusual and reflects not only the influence of the large swelling levels attained during irradiation but also the distribution of swelling near grain boundaries. The unique fracture mode in highly voided copper appears to enhance susceptibility to crack propagation and sudden failure without necking, even though the material exhibits a significant level of uniform elongation prior to failure.

OBJECTIVE

The object of this effort is to provide data on the performance of copper alloys during irradiation at high temperatures.

PROGRESS AND STATUS

Introduction

Copper alloys are candidates to serve as high heat flux components in future fusion energy devices. In this role they must be exposed to large levels of neutron displacement damage and temperatures as high as ~500°C under some conditions. Since copper and most of its alloys do not maintain sufficient mechanical strength at such high temperatures, this requires the use of innovative designs or development and use of new copper alloys.

To address this need a series of both exploratory and focused irradiation experiments were conducted by Pacific Northwest Laboratory on a wide variety of copper alloys in the Materials Open Test Assembly (MOTA) to 16-100 dpa.[1-3] This device operates in the Fast Flux Test Facility (FFTF) in Richland, WA. These studies confirmed the conclusion of several earlier low fluence (≤15 dpa) studies conducted at 385°C in EBR-II[4,5] that internally oxidized dispersion strengthened copper-alumina alloys retained much of their strength and were very resistant to void swelling.

However, some proposed designs envision that diverters might be constructed from relatively pure copper, supported by a network of components constructed from dispersion strengthened alloys. The pure copper is not resistant to swelling, however, and there is some concern that void swelling will change its thermal conductivity and mechanical properties. To address this possibility, the swelling, tensile properties and fracture behavior of pure copper were studied using specimens irradiated at 411-414°C in FFTF to doses of 5.6 and 8.2 X 10^{26} n/m^2 (E>0.1MeV) or 34 and 50 dpa, respectively.

ExDerimental Details

Two types of specimens were utilized in this study. Miniature tensile specimens and 3mm TEM disks were fabricated from 0.01 in. thick sheet of marz grade copper (99.999%) using a commercial hand operated press and conventional tool steel die sets. The dimensions of the miniature tensile specimens are shown in Figure 1. The punching operation sometimes produced a slight deformation burr on the specimen edge which was subsequently removed by lightly sanding on 600 grit SiC grinding paper. Both specimen types were permanently identified by laser engraving with both a material and irradiation code. Codes were placed on the tabs of the miniature tensile specimens and on the circumference of one face of the TEM disks. Laser engraving constituted the final step in the specimen fabrication process prior to annealing in argon at 450 for 15 minutes. Some specimens were also aged at 420°C for 1026 hrs. to ascertain whether significant changes in tensile properties would result purely from the high temperature exposure. While this is an important consideration for solute-bearing or cold worked alloys, it was not anticipated that much change would occur in already fully annealed copper.

(a) Pacific Northwest Laboratory is operated for the U.S. Department of Energy by Battelle Memorial Institute under Contract DE-AC06-76RLO 1830.

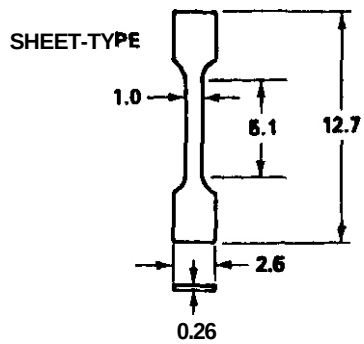

FIGURE 1. Dimensions (in mm) of Miniature Tensile Specimens

Specimens were irradiated in several sealed helium-filled subcapsules at 1.5 x 10^{-6} dpa/s with the temperature actively controlled within ±5°C. After irradiation, density measurements were conducted on two identical TEM specimens at each irradiation condition using an immersion density technique with an accuracy of ±0.16% volume change.

The tensile properties of unirradiated, thermally aged and irradiated miniature tensile specimens were determined at room temperature using a screw-driven precision horizontal tensile testing frame specifically designed for testing miniature sheet type specimens.[6] The properties determined were the 0.2% offset yield strength, ultimate tensile strength, fracture strength, uniform elongation, and total elongation. Prior to testing, the thickness of each specimen was measured using a micrometer. The error associated with the thickness measurement was f0.0025 mm. All testing was performed at room temperature (24°C) at a crosshead velocity of 2.4 x 10^{-6} m/sec which corresponds to a strain rate of 4.1 x 10^{-4} sec^{-1} for these miniature specimens.

Fractography was performed using a JEOL JSM 35C scanning electron microscope (SEM). Fracture surfaces required examination soon after tensile testing due to rapid formation of an oxide layer which obscured detail at magnifications over approximately 1000x. This was determined by comparing the resolution obtainable on new fracture surfaces, and that of slightly oxidized fracture surfaces.

Results

Swelling and tensile properties of the various specimens tested are listed in Table 1. Tensile curves are shown in Figure 2. Prior to irradiation, copper exhibited tensile properties which would be expected for a nominally pure FCC metal. It possessed an ultimate tensile strength of 170 MPa combined with a large uniform and total elongation. As shown in Figure 3 the reduction of area of the specimens was nearly 100%. The fracture surfaces, shown in Figure 4 were composed of wavy slip steps and ripples characteristic of a serpentine glide failure mechanism. Surprisingly, there were significant differences in the tensile behavior of the annealed and the aged specimens, with different yield strengths, hardening curves, uniform elongation and especially total elongation. The reasons for this difference in behavior have not yet been determined.

After irradiation, significant changes did occur in the mechanical properties and fracture morphology, as shown in Figures 5-8. These changes arise primarily from the strong influence of void swelling, which was -18% at 34 dpa and -29% at 50 dpa. Both the yield and ultimate tensile strengths were found to decrease whereas the fracture strength increased greatly with increasing displacement damage. Surprisingly, the uniform elongation remained large but the reduction of area was almost 0%. as shown by the fracture surfaces in Figures 5 and 7.

The fracture morphology on a microscopic scale is unusual and reflects the influence of the high void swelling levels attained in these specimens. Note in Figure 5, and even more distinctly in Figure 8, that the fracture surfaces appear to be composed of two distinct types of regions. These are somewhat irregular transgranular surfaces with dimples of one size distribution and also relatively flat regions whose surfaces are populated by what appears at first glance to be much larger dimples. (As we will show later, these are grossly deformed voids). As swelling increases the latter type of region becomes more dominant. Note also that occasionally there are abrupt changes in the level of these flat surfaces. The grain boundary areas were found to be denuded of voids and where they were parallel to the tensile axis of the specimen the grain boundary regions were distorted to form "knife-edge" ridges which extended well above the fracture surface.

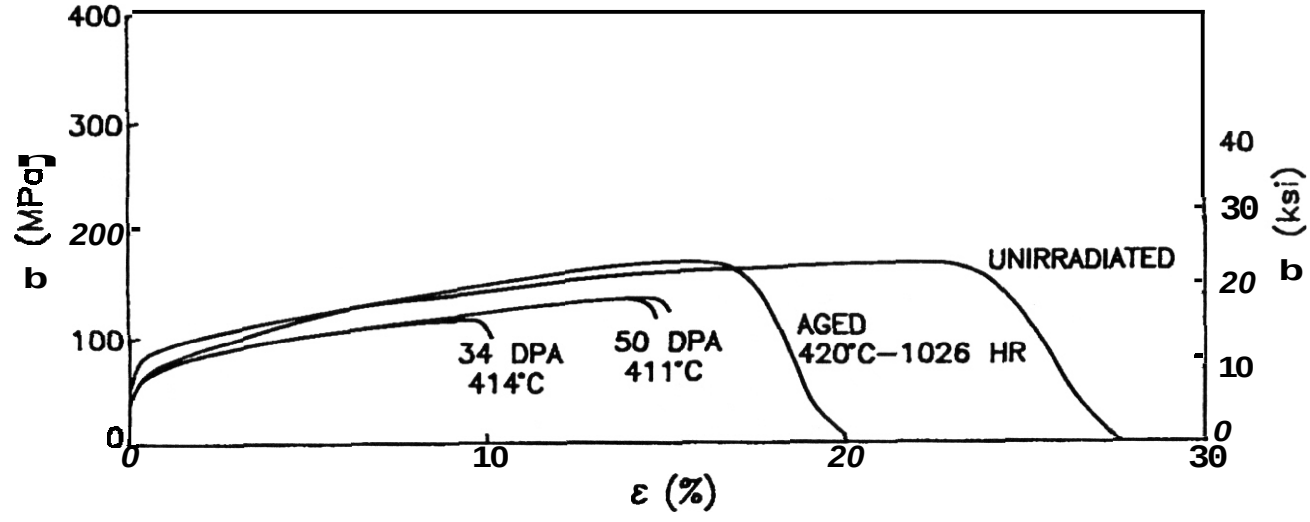

FIGURE 2. Tensile Behavior Observed in this Study, Showing Significant Uniform Elongation Combined with an Extreme Loss in Necking Ability Following Irradiation

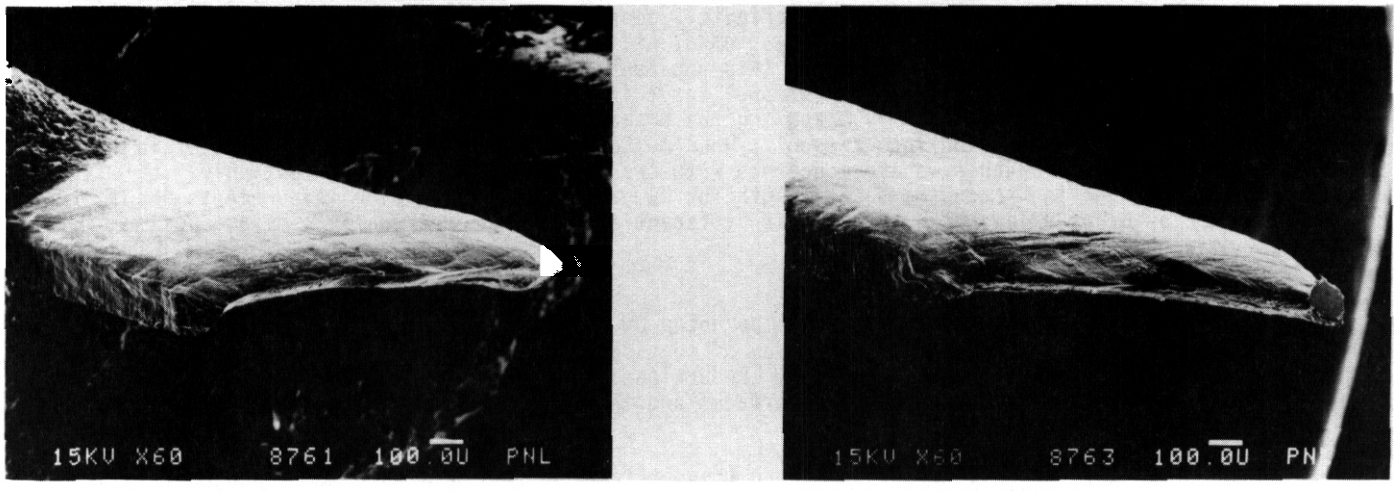

FIGURE 3. Both Fracture Surfaces of an Unirradiated Copper Specimen Showing -100% Reduction of Area

The flat regions observed on the fracture surfaces might be mistaken for transgranular fracture caused by flow localization. However, when looking at the extreme vertical microplastic deformation present in the material between voids, (shown in Figure 8), it is obvious that the singularly crystallographic, flat cleavage morphology associated with flow localization is not present. The large faceted features on this surface arise from deformation of the material between voids, where the boundary of each void is drawn out until it meets that of its neighbors, producing a honeycomb appearance of the fractured void array surface. One undistorted face of each original void is usually visible in the bottom of each honeycomb segment. These void faces are always parallel to the overall flat fractured surface.

On both the planar surfaces and the rougher transgranular surfaces SEM observation of fractured voids showed the void shape to be the same as that determined by English and coworkers' using transmission electron microscopy: octahedrons bounded by (111) planes having substantial (110) planar truncations. Observation of the base, walls, and fracture lips of the honeycomb units on several planar fracture surfaces leads to the conclusion that the void arrays fractured parallel to (111) planes.

TABLE 1

Swelling and Average Tensile Properties of Miniature Copper Specimens

Condition	Yield Strength (0.2% offset) MPa	Ultimate Tensile Strength MPa	Fracture Strength MPa	Uniform Elongation (%)	Total Elongation (%)	Swelling' ΔV/Vo,%
Unirradiated	74.7	170.6	4.5	23.2	29.0	0
Aged 420°C, 1026 hrs.	70.5	170.6	2.1	16.7	20.8	0
34 dpa, 414°C	64.0	116.1	103.4	9.7	10.1	17.1, 18.3*
50 dpa, 411°C	63.0	131.2	119.7	14.7	15.0	28.3, 30.2*

+ % swelling = (% density change)/[(1-% density change)].
* Density measurements. were made on two separate TEM specimens and demonstrate a moderately small amount of variability in measured swelling.

Discussion

Within the limited accuracy of these small specimens, the tensile data suggest that the yield strength might, and the ultimate tensile strength most definitely does drop with accumulated swelling. Conventional wisdom would suggest that both swelling and the ~0.4% of nickel and ~0.15% of zinc formed at SO dpa by transmutation should strengthen the materials. This apparent drop arises primarily due to the decrease in the load-bearing area due to swelling. For 29% swelling this corresponds to an ~18% increase in area. Nine percent was already taken into account by measuring the actual specimen thickness, leaving another nine percent in width that was not taken into account. When measuring strength, it is not important to measure the increased gauge length because we are concerned with cross sectional area. Interestingly, it is also not important to measure the increased gauge length for comparisons of elongation measurements. This is due to a consequence of Barba's law which states that different-sized but geometrically similar specimens will yield the same elongation values.

The observed decrease in reduction of area was also noted by Livak and coworkers,[4,8] although it was not as prominent at the lower dose levels of 3 and 15 dpa of that study where swelling was 1.8% and 6.8%. respectively. The pronounced loss of macroscopic reduction in area is compensated on a microscopic scale by an exceptional reduction of area between void surfaces and in the unvoided material adjacent to grain boundaries.

The mechanisms producing the observed behavior are thought to arise not only as a consequence of large levels of void swelling but also as a consequence of its distribution. It is well known that in irradiated pure metals such as copper and nickel that there is usually a zone denuded of voids and dislocation loops on both side of grain boundaries, reflecting the efficiency of such boundaries in absorbing both the vacancies and interstitials produced during irradiation. There is also a tendency for the denuded zone to be bounded by a zone of enhanced swelling relative that of the matrix. A recent example is shown in the work of Zinkle and Farrel1.[9]

Thus the interior of grains are strengthened by irradiation and surrounded first by zones that have larger levels of voidage and therefore less load-bearing area between voids. This zone is then surrounded by a very soft zone next to a grain boundary. This very soft zone is the material that first yields in the tensile test. The stress at which these grain boundary zones yield is probably the same for both unirradiated and irradiated materials. When the zone of larger voids is oriented with respect to the stress axis so as to inactivate the primary slip system, the remaining ligaments between voids become very small. Failure initiates on one side of the grain boundary, although the fracture path sometimes leaps either across the denuded zone, or to a different parallel void array, thereby producing a change in level on the otherwise planar fracture surface. When the fracture surface attempts to cross intervening grains an irregular transgranular fracture surface results with less overall deformation of the voids on that surface.

It has been shown that void swelling of pure copper at 32-34 dpa is reduced from ~30% to ~1.5% when the irradiation temperature is 529°C instead of 414°C.[10] Therefore it is expected that the unusual fracture behavior observed here will not develop as quickly at temperatures well above 400°C. Zinkle and Farrell have shown, however, that void swelling in copper occurs in a temperature regime reaching as low as ~182°C.[9]

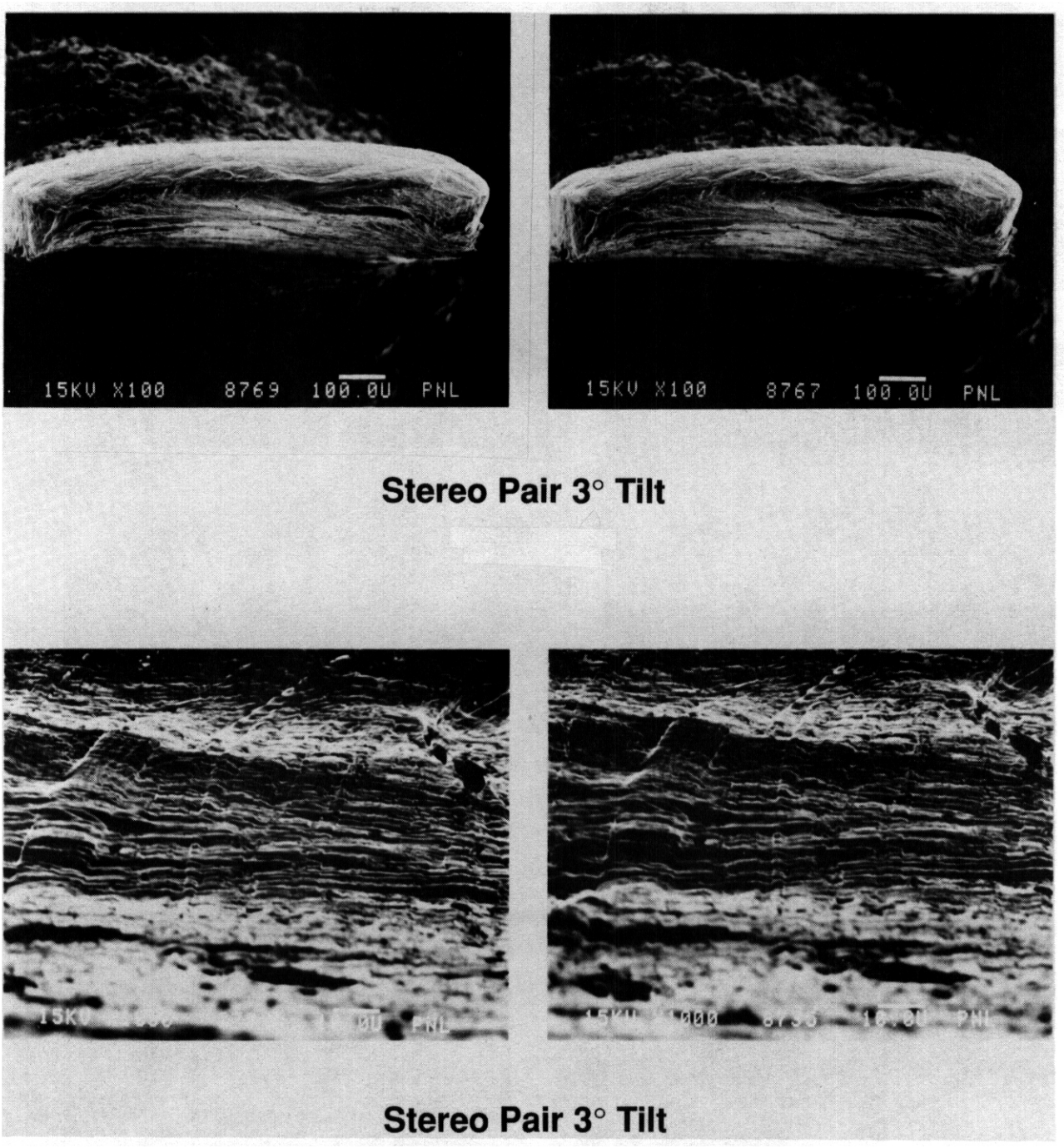

FIGURE 4. Fracture Surface of Unirradiated Copper, Showing Wavy Slip and Ripples Characteristic of a Serpentine Glide Fracture Mechanism

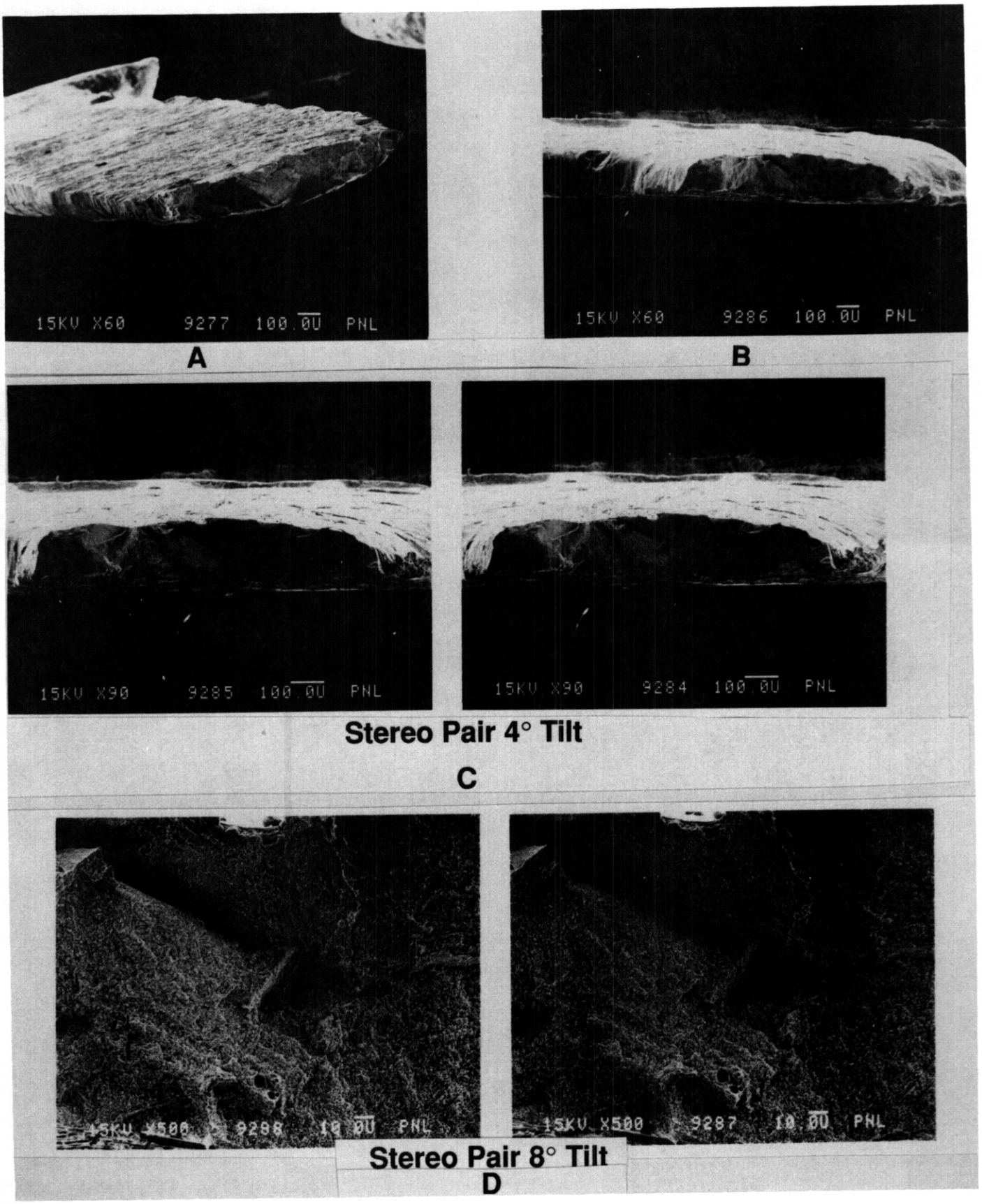

FIGURE 5. Fracture Surfaces of Copper Irradiated at 414 ± 5°C to 34 dpa. The swelling level is ~18%

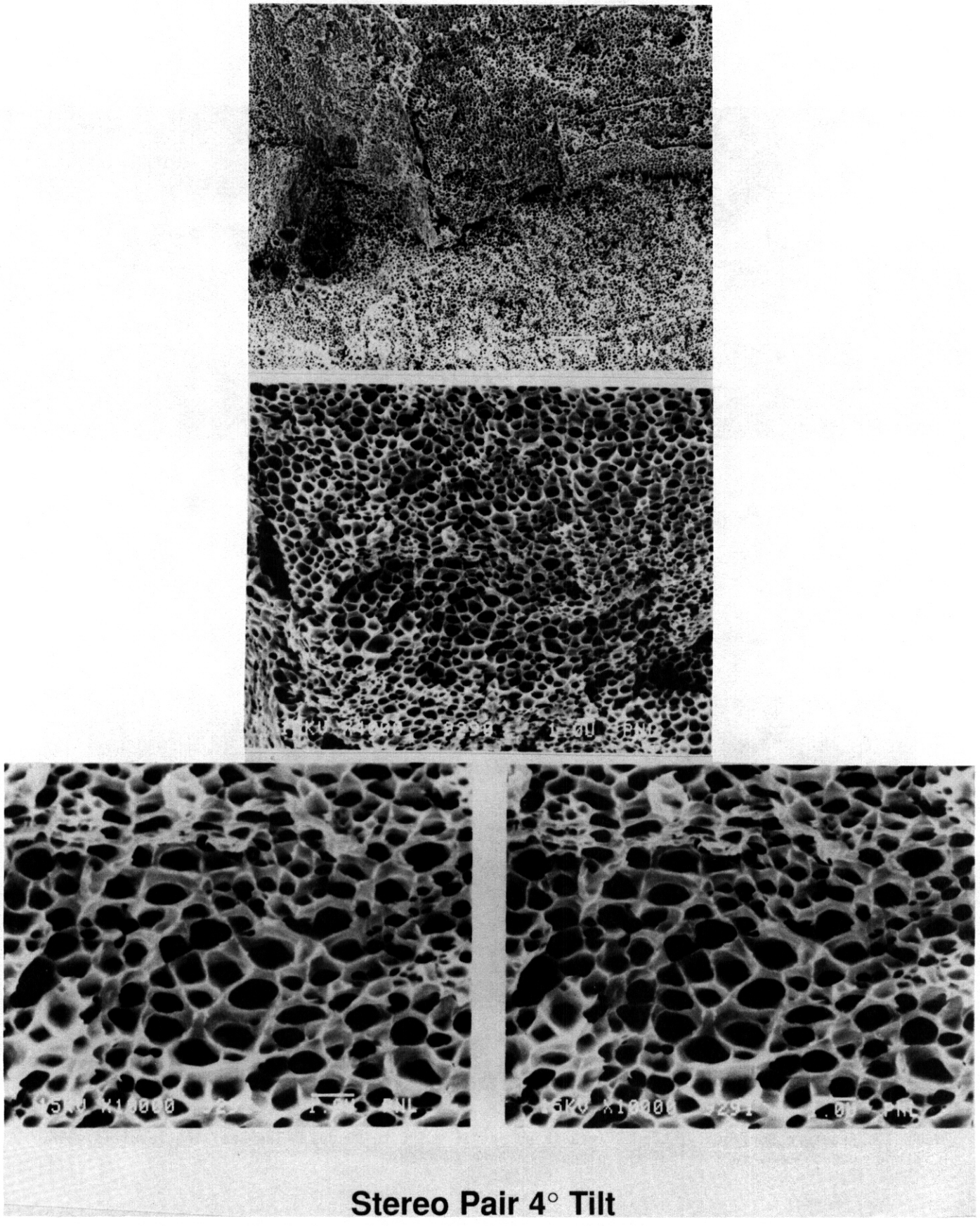

FIGURE 6. Higher Magnification Fractographs of 34 dpa Specimens

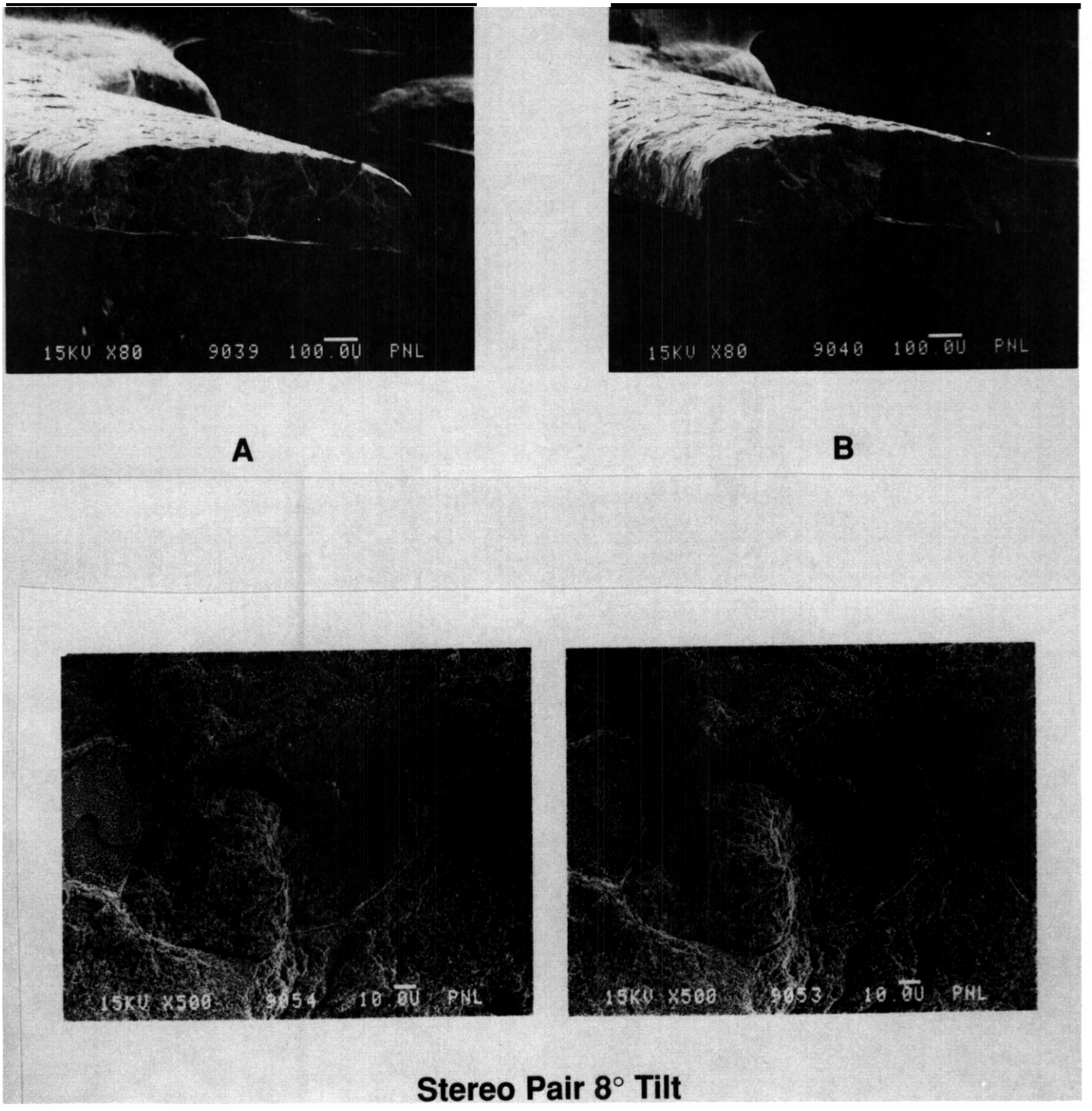

FIGURE 7. Fracture Surfaces of Copper Irradiated at 411 ± 5°C to 50 dpa. The swelling level is ~29%. Note in 7c the sudden jumps in level of the planar fracture surfaces.

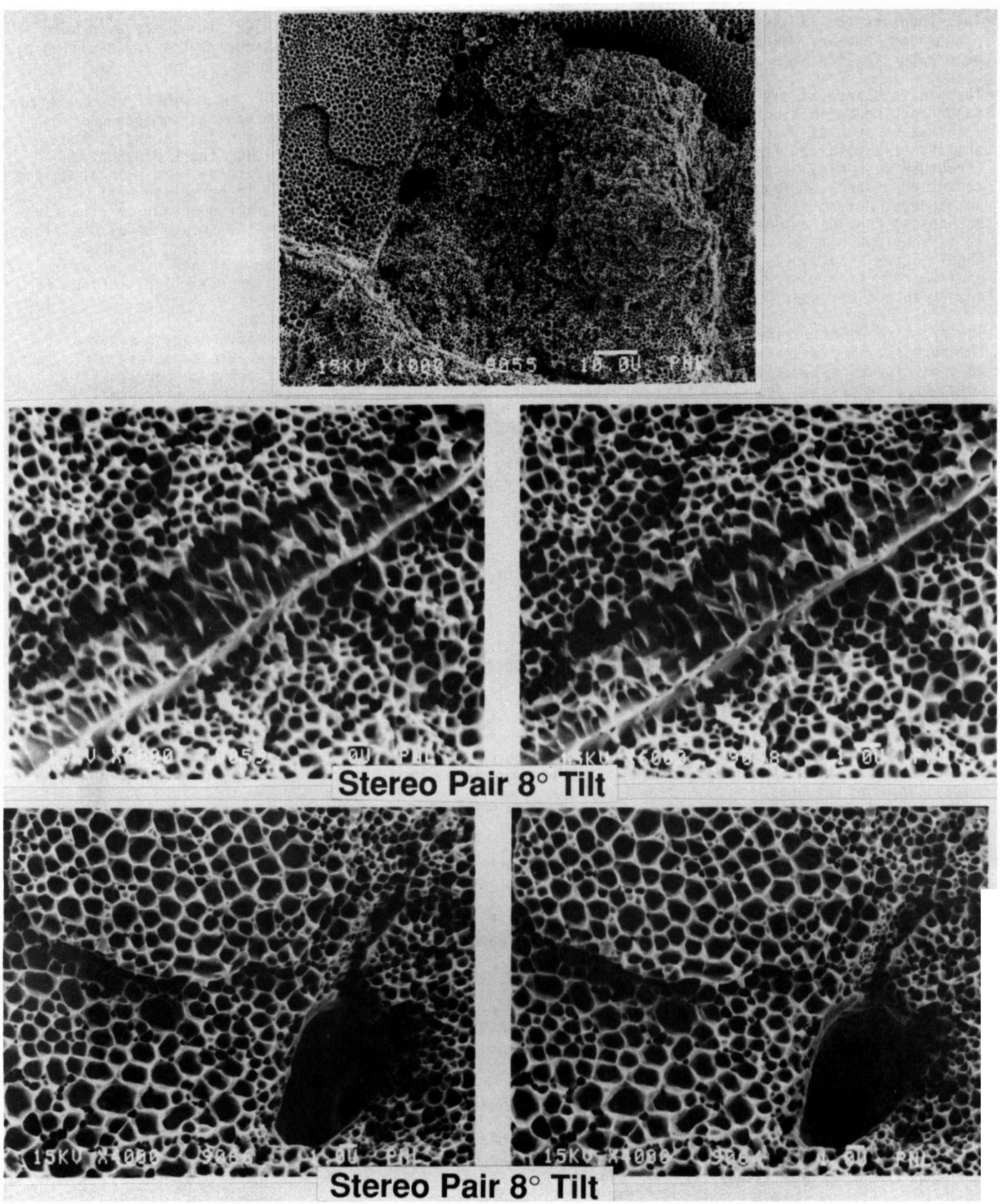

FIGURE 8. Higher Magnification Fractographs of 50 spa Specimens. Note two different types of fracture surface, each with different size void-like features. Note both jumps in planar fracture surfaces and "knife-edge" distortion of void-free zones at grain boundaries.

This suggests that a similar behavior will occur at temperatures well below 400°C. It may be even more pronounced, however, since denuded zones generally decrease in width at lower temperatures and swelling may be greater for the same damage level (dpa).

There exists several distinct ideas of what constitutes ductility in metals.[11,12] In general, there are two major working definitions of ductility. The first is the ability of a metal to undergo homogeneous deformation such as that encountered in rolling or other metal forming operations. The second is the ability of a metal to flow plastically under localized loading; primarily involving crack propagation (fracture mechanics) considerations. The two most common measures of ductility are uniform elongation and reduction of area of specimens during a tensile test. Uniform elongation tends to correlate well with homogeneous deformation whereas reduction of area shows good correlation with crack propagation (fracture mechanics) considerations. Most metals tend to exhibit nearly equal amounts of both measures of ductility. It is very unusual for a metal to exhibit one measure of ductility without also exhibiting the other. In highly irradiated copper, however, there exists a substantial uniform elongation combined with an extremely minimal reduction of area. This unusual combination of properties has several important implications for copper in nuclear applications.

The practice of utilizing copper, or solid solution strengthened copper alloys, as a brazing material for the more swelling-resistant dispersion strengthened coppers may not be advisable. Interfacial joints, such as those formed by brazing, are typically the weakest part of any component. Placing copper or solid solution strengthened copper at this inherently weak interface will exacerbate the problems normally encountered with brazed joints. Having irradiated, highly voided, crack-prone copper at an already weak interface is thus not a good idea. The volumetric expansion of an irradiated brazed copper joint, due to void swelling, may in itself be large enough to induce compressive loading on the joined components. This is particularly important in brazing alloys containing small amounts of silver. Silver additions have been shown to accelerate the neutron-induced swelling of copper.[1,10]

CONCLUSIONS

Highly voided copper exhibits unusual tensile behavior and fracture morphology, with its most prominent feature being a substantial decrease in reduction of area at fracture. Fracture mechanics considerations must be thoroughly investigated when unalloyed copper is employed in high temperature radiation environments. The fracture mechanism producing this behavior appears to be a result not only of the high levels of swelling produced at high neutron-induced displacement doses and high temperatures, but particularly of the influence of its distribution especially in the vicinity of grain boundaries.

ACKNOWLEDGMENTS

This work was supported by the U.S. Department of Energy under Contract DE-AC06-76RLO-1830. The participation of K. R. Anderson and J. F. Stubbins was sponsored by the Northwest College and University Association for Science.

REFERENCES

1. H. R. Brager, H. L. Heinisch and F. A. Garner, J. Nucl. Mater., 133-134 (1985) 675.

2. F. A. Garner, M. L. Hamilton, K. R. Anderson, J. F. Stubbins, B. N. Singh, A. Horswell and W. F. Sommer, Fusion Reactor Materials Semiannual Progress Report DOE/ER-0313/6, March 31, 1989, pp. 351-356.

3. H. R. Brager and F. A. Garner, in Effects of Radiation on Materials: 14th International Symposium (vol. 11) ASTM STP 1046, N. H. Packan, R. E. Stoller and A. S. Kumar, Eds. American Society for Testing and Materials, Philadelphia, 1990, pp. 599-604.

4. R. J. Livak, H. M. Frost, T. G. Zocco, J. C. Kennedy and L. W. Hobbs, J. of Nucl. Mater., Vol. 141-143 (1986), pp. 160-162.

5. R. J. Livak, T. G. Zocco and 1. W. Hobbs, J. of Nucl. Mater., Vol. 144 (1987) 121-127.

6. N. F. Panayotou, S. D. Atkin, R. J. Puigh and 8. A. Chin, "Design and Use of Nonstandard Tensile Specimens for Irradiated Materials Testing", in The Use of Small-Scale Specimens for Testing Irradiated Materials, ASTM STP 888 (1986), pp. 201-219.

7. C. A. English, B. L. Eyre and J. W. Muncie, Phil. Maa. A, Vol. 56, no. 4 (1987), pp. 453-484.

8. R. J. Livak, T. G. Zocco and J. C. Kennedy, in ADIP Semiannual Proaress Report, DOE/ER-0045/14, (1985), pp. 152-160.

9. S. J. Zinkle and K. Farrell, J. Nucl. Mater. 168 (1989) 262.

10. F. A. Garner, H. R. Brager and K. R. Anderson, accepted for publication in J. Nucl. Mater. as part of proceeding of the Fourth International Conference on Fusion Reactor Materials.

11. G. E. Dieter, Ductility, ASM, ed. H. W. Paxton, (1968). pp. 1-30.

12. G. E. Dieter, Mechanical Metallurgy, Second Edition, McGraw - Hill, New York, 1976, pp. 10-11, 333-334.

6.5 Environmental Effects on Structural Alloys

COMPATIBILITY BETWEEN VANADIUM–BASE ALLOYS AND FLOWING LITHIUM: PARTITIONING OF HYDROGEN AT ELEVATED TEMPERATURES - A. B. Hull, O. K. Chopra, B. Loomis, and D. Smith (Argonne National Laboratory)

OBJECTIVE

A major concern in fusion reactor design is possible hydrogen–isotope–induced embrittlement of structural alloys in the neutron environment expected in these reactors. The objective of this study was twofold: to examine the extent of H partitioning between vanadium alloys and flowing lithium and to provide experimental data for the development of an analytical model that will predict the effect of nonmetallic elements on the stability of vanadium alloys in lithium.

SUMMARY

Hydrogen fractionation occurs between lithium and various refractory metals according to a temperature-dependent distribution coefficient, K_H, that is defined as the ratio of the hydrogen concentration in the metallic specimen to that in the liquid lithium. In the present work, K_H was determined for pure vanadium and several binary (V–10Cr, V–15Cr, V–5Ti, V–15Ti, V–20Ti, V–30Ti) and ternary alloys (V–10Cr–5Ti, V–15Cr–1Ti, V-15Cr–5Ti, V–3Ti–0.5Si), and the commercial Vanstar 7 (V–10Cr–3Fe–1Zr). Hydrogen distribution studies were performed in an austenitic steel forced-circulation lithium loop. Equilibrium concentrations of hydrogen in vanadium–base alloys exposed to flowing lithium at temperatures of 350 to 550°C were measured by inert gas fusion techniques and residual gas analysis. Thermodynamic calculations are consistent with the effect of chromium and titanium in the alloys on the resultant hydrogen fractionation. Experimental and calculated results indicate that K_H values are very low; i.e., the hydrogen concentrations in the lithium-equilibrated vanadium-base alloy specimens are about two orders of magnitude lower than those in the lithium. Because of this low distribution coefficient, embrittlement of vanadium alloys by hydrogen in lithium would not be expected.

PROGRESS AND STATUS

Introduction and Background

Vanadium alloys such as V-5Cr-5Ti, V-5Ti, V-5Ti-1Si, and V-20Ti are attractive candidates for use as structural materials in fusion reactor blankets because of their excellent resistance to neutron radiation damage, low induced radioactivity, high strength at elevated temperatures, and favorable thermophysical properties.[1] On the basis of extensive testing, they appear to exhibit the best combination of strength, ductile-brittle transition temperature (DBTT), swelling rate, and lithium dissolution rate for a structural material in a fusion reactor. Resistance to hydrogen embrittlement is another key issue; one potential contributor to hydrogen pickup is the transfer of hydrogen from the reactor coolant and breeder to the structural material.

Molten lithium has been proposed as both a coolant and breeder material because of its excellent heat transfer and tritium breeding characteristics. Local corrosion phenomena and mass- and interstitial-element transfer rates depend on the difference between the chemical activity of the alloy constituents in the structural material and that of lithium.[2]

Understanding the parameters that affect the solubility and diffisivity of tritium in liquid lithium is important for evaluating the permeation and inventory of tritium in the blanket and for optimizing the tritium extraction process. Additionally, the issue of hydrogen-isotope-induced embrittlement is a major question for all structural alloys exposed to both the neutron environment expected in a fusion reactor and a lithium reactor coolant. In this paper, experimental data on the partitioning of hydrogen between lithium and candidate vanadium alloys are summarized and the significance of the experimental results for the fusion reactor environment is discussed.

Experimental Procedures

The compositions of the vanadium-base alloys in Table 1 were selected primarily because of their low neutron activation. Most of these alloys have been investigated with respect to compatibility with a lithium reactor coolant,[2,3] yield strength before and after irradiation,[4] swelling resistance,[5] ductile-brittle transition temperature,[6,7] and resistance to hydrogen, helium, and irradiation embrittlement.[1,8,9]

Table 1. Chemical Composition of Vanadium and Vanadium–base Alloys

Nominal[a] Composition	ANL I.D.	Melt[b] No.	Concentration (wt.%) Cr	Ti	Concentration (wppm) H	O	N	C	Si	S	Fe
V	BL-19	V6	---	---	<5.0	1101	161	360	-		
V-10Cr	BL-35	ANL 35	9.5	...		340	45	120	<50	-	410
V-15Cr	BL5	ANL 5	14.1	...	15.0	330	69	200	<50	-	570
V-10Cr-5Ti	BL-43	ANL 206	9.2	4.9	<5.0	230	31	100	340	20	170
V-15Cr-5Ti$_1$	BL-23	CAM834	12.9	5.9	9.0	400	490	280	1230	50	420
V-15Cr-5Ti$_2$	BL-24	ANL 101	13.5	5.2	33.6[c]	1190	360	500	390	<30	520
V-15Cr-5Ti$_3$		ANL 274			50.0	810	138	230	-		
V-15Cr-5Ti$_4$	v 4	ANL 282	14.9	5.25							500
V-15Cr-1Ti	BL-26	ANL 26	14.1	1.0		560	86	140	<50	-	650
V-3Ti-0.5Si$_1$	BL-42	WI 8505		3.1	65.3[c]	580	190	140	5400	90	190
V-3Ti-0.5Si$_2$	BL-27	ORNL 10837	---	3.1	8.0	210	310	310	2500	120	380
V-5Ti	BL-46	TWC 831		4.6		300	53	85	160	10	
V-15Ti	BL13	ANL 13	---	14.4	-	1580	370	440	205	-	6300
V-20Ti$_1$	BL15	CAM832	---	17.7	16.0	830	160	380	480	<10	390
V-20Ti$_2$	Inv#144	ANL 215	---				-	-			
V-30Ti	Inv#5	-	---			1300	-	-			
V-10Cr-3Fe-1Zr	BL-28	CAM837	9.0	---		275	520	640	-	-	32000

[a]Analyses were performed by the Analytical Department of the Teledyne Wah Chang Albany Co.
[b]Due to material scarcity, it was not always possible to work with well-characterized material, thus necessitating use of four different melts of V-15Cr-5Ti, for example. In such cases, "-" indicates insufficient information, while "---" indicates element not present.
[c]Hydrogen analyses were performed by residual gas analysis [9].

In the current study, hydrogen fractionation was investigated utilizing a diversity of specimen types and test conditions. Specimens examined included corrosion coupons,[2] tensile specimens,' and specimens designed specifically for this study with approximate dimensions of 19 x 10 x 0.9 mm. The specimens were either mechanically polished or left in "as received condition4 before exposure to lithium.

The hydrogen distribution tests were conducted in a forced-circulation lithium loop, using three test vessels and a secondary cold-trap purification system, constructed of Type 304 stainless steel. A description of the lithium test facility has been presented previously.[10] The quantity of lithium in the loop was –20 L, and the lithium was recirculated at –1 L/min from the high-temperature to the low-temperature test vessel. As shown in Table 2, the cold trap was maintained at 220-202°C (23°C above the freezing temperature of lithium).

Table 2. Lithium Loop Operating Conditions for Various Hydrogen Distribution Testa

Test Run	Loop Temperature (°C) Test Vessel	Equilibration Vessel	Supply Vessel	Cold Trap
6	538	482	410	208
8	482	427	426	213
10	500	452	425	208
13	400	345	350	221
15	482	412	398	202
17	480	403	392	220
20	463	360	355	206
21	545	503	450	215

During Tests 6 and 8 (Table 3), the hydrogen partial pressure in lithium (P_{H_2}) was monitored by a hydrogen activity sensor consisting of an alpha-iron membrane immersed in liquid lithium in the supply vessel.8 The ion pump was valved out and the hydrogen was allowed to diffuse into the manifold until equilibrium was attained. Equilibrium pressure was measured with a dual–range ionization gauge.8 The hydrogen concentration was determined both from the hydrogen activity meter and by yttrium equilibration procedures. Lithium samples, withdrawn from the equilibration vessel and filtered through 5–μm metal frits, were analyzed for nitrogen, carbon, and trace metals. The carbon concentration was determined by the acetylene evolution method,[11] and nitrogen concentration was determined by micro-Kjehldal nitrogen combustion.[12] Trace metals were determined by inductively coupled plasma atomic emission spectroscopy. The procedure for lithium sampling and analysis has been described in more detail elsewhere.[13]

Following exposure, the lithium was removed from the specimens by immersion in liquid NH_3 or in an alcohol mixture containing 50% ethyl alcohol and 50% methyl alcohol chilled to 5-10°C. This chemical dissolution procedure was strictly observed to avoid the introduction of hydrogen into the specimens.[9] The hydrogen content in the specimens following lithium exposure was determined by one of three analytical methods(Table 4). Residual gas analysis (RGA) was the analytical technique preferred for hydrogen determination[8,9] because of its nondestructive nature. Total hydrogen in the specimens after exposure to the lithium was determined from the P_{H_2} in the gaseous constituents that were evolved on heating a specimen at a rate of 15°C/min from 25 to 1000°C. The P_{H_2} was determined by a quadrapole, partial-pressure, residual gas analyzer mounted in an ion-pumped vacuum system. The temperature of a specimen during heating was determined with a recording infrared pyrometer. The hydrogen concentration in the lithium-exposed specimens was also determined by the combustion technique in a purified argon environment at Teledyne Wah Chang with a LECO Model RH-1 Hydrogen Determinator with 0.1–μg resolution (Analytical Technique 2, Table 4). Hydrogen analyses were also performed at Argonne National Laboratory using both vacuum fusion and inert gas fusion techniques. In both of the latter analytical techniques, the reference specimens were standardized with National Bureau of Standards calibrations.

Table 3. Chemical Composition of Lithium at Time of Test Runs

Test Run	Lithium Flow Age[a] (x 10,000h) Begin Test	Lithium Sample	Nonmetallic Concentration (wppm) Nonmetallic N[c]	C[d]	H[e]	Metallic[b] Fe	Ca	Cr	Mo	Ti	V
As Received[f]			100	-[g]		10	300	5			<5
6	4.5617	5.1384	26	11	118						
8	5.8800	5.9844	23	55	90	79	50	49	146	80	
10	6.9756	6.980	167[h]	119	100	6690	67	1730	78	147	<20
13	7.1040	7.0400	136	84	105						
E	7.3835	7.2994	88	57	110	102	310	30	10	40	<5
17	7.8257	7.8229	1912[i]	47	140	44	209	E	<10	64	<10
20	8.4231	8.4088	225	13	120	48	146	<10	<10	108	<10
21	8.4259	8.4088	225	13	135	48	146	<10	<10	108	<10

[a]Time since operation of the FFTL-3 loop commenced in 1980.
[b]Analysis by inductively coupled plasma atomic emission spectroscopy.
[c]Nitrogen in lithium determined by micro-Kjehldal nitrogen combustion technique [12].
[d]Carbon in the lithium was determined by the acetylene evolution method [11].
[e]Hydrogen in lithium in Tests 6 and 8 was determined by H meter and substantiated by yttrium equilibration [8]; in Tests 10-21, hydrogen was determined by the yttrium equilibration method.
[f]Information provided by lithium supplier, LITHCO.
[g]The "-" indicates insufficient information rather than absence of element.
[h]Increase in most elements can be attributed to extended time period at high temperatures (Test 6).
[i]Argon cover gas purifier (gettering furnace) malfunctioned, and ingress of air into cover gas system caused a high N concentration.

Table 4. Hydrogen Concentration in Vanadium-base Alloys after Exposure to Flowing Lithium

Specimen Identity	Test No.	Exposure Conditions: Temp (°C)	Exposure Conditions: Time (h)	Exposure Conditions: H in Li[c] (wppm)	Hydrogen in Alloy (wppm)	K_H[a]	Analytical Method
V	6	482	1508	118	3	0.025	3
	8	427	405	90	7	0.078	3
	17	403	234	140	2.8	0.020	2
	20	360	24	120	8	0.067	2
	20	463	24	120	11	0.09	2
	21	503	42	135	4.7	0.035	2
	21	545	42	135	3.4	0.025	2
V-10Cr	a,	463	24	lal	7	0.058	2
	21	503	42	135	6	0.044	2
	21	545	42	135	6	0.044	2
V-10Cr-5Ti	15	482	3400	110	4.3	0.039	1
V-15Cr	17	403	234	140	3.3	0.023	2
	a,	463	21	120	5	0.042	2
	21	503	42	135	3	0.022	2
	21	545	42	135	4.7	0.035	2
V-15Cr-1Ti	I3	400	72	105	5.8	0.055	3
	17	403	234	140	6	0.043	2
V-15Cr-5Ti$_1$[d]	8	482	1992	90	7	0.078	3
V-15Cr-5Ti$_2$	6	538	1384	118	2	0.017	3
	6	482	1618	118	1	0.008	3
	6	538	794	118	3.	0.025	3
	10	500	2,	100	0.3	0.003	1
	15	482	3400	110	7.7	0.070	1
V-15Cr-5Ti$_3$	I3	400	24	105	2.2	0.021	1
V-15Cr-5Ti$_4$		403	234	140	2.2	0.016	2
V-3Ti-0.5Si$_1$	10	500	25	100	6.7	0.067	1
	13	400	24	105	3.6	0.034	1
	a,	463	24	120	6	0.050	2
	21	503	42	135	7	0.052	2
	21	545	42	135	6	0.044	2
V-3Ti-0.5Si$_2$	15	482	3400	110	4.7	0.043	1
V-5Ti	a,	463	24	120	4.6	0.038	2
	21	503	42	135	4.3	0.032	2
	21	545	42	135	4.2	0.031	2
V-15Ti	20	463	24	120	6	0.05	2
	21	503	42	135	4.8	0.036	2
	21	545	42	135	3	0.022	2
V-20Ti$_1$	6	482	619	118	8	0.068	3
	15	482	3400	110	6	0.054	1
	17	403	234	140	3.2	0.023	2
	17	403	234	140	2.7	0.019	3
V-20Ti$_2$	20	463	24	120	9	0.075	2
	21	503	42	135	7	0.052	2
	21	545	42	135	6	0.044	2
V-30Ti	20	463	24	120	18	0.15	2
	21	503	a	135	16	0.1185	2
	21	545	42	I35	10	0.074	2
V-10Cr-3Fe-1Zr	6	538	590	118	6	0.051	3

[a] The distribution coefficient, KH, is defined as the ratio of the hydrogen concentration in the Li-exposed alloy tu that in the Li [3,14].

[b] Analytical methods are as follows: (1) residual gas analysis [9]; (2) inert gas fusion, Teledyne Wah Chang Co.; and (3) vacuum and inert gas fusion, Argonne National Laboratory Analytical Chemistry.

[c] The uncertainties in the values of the concentration of hydrogen in the lithium, as determined by the hydrogen activity meter and/or yttrium equilibrations, are ± 25%.

[d] Refer to Table 1 for explanation of subscripts 1, 2, 3, 4.

Results and Analysis

Lithium hydride (LiH) is the solid phase in equilibrium with saturated solutions of hydrogen in lithium. As can be seen in Fig. 1, the calculated solubility of hydrogen in lithium[8,14] increases uniformly with temperature.

The high solubility of hydrogen in yttrium can be used to provide an independent determination of the hydrogen concentration in the lithium. Yttrium samples were exposed to lithium in the loop at temperatures of 408 to 538°C. The concentration of hydrogen in the yttrium specimens, determined by vacuum fusion analysis, was used in conjunction with calculated distribution coefficients to determine the hydrogen concentration in lithium. The concentrations are plotted in Fig. 1 as a function of both the cold-trap temperature and the exposure vessel temperature. The results show that, to a first approximation, the cold-trap temperature had a significant effect in controlling the upper limit of hydrogen in the system. As can be seen in Fig 1, the hydrogen concentrations determined by yttrium exposure show good agreement with the solubility curve at the temperature of the cold trap for each test (Table 2).

Hydrogen will fractionate between lithium and various refractory metals as a function of temperature. A distribution coefficient, K_H, can be defined as the ratio of the hydrogen concentration in the metallic alloy to that in the liquid lithium:

$$K_H = C_M / C_{Li} \qquad (1)$$

where C_M and C_{Li} are concentrations (wt.%) of hydrogen in the metal and lithium, respectively, at constant P_{H_2}. The calculated distribution of hydrogen among various refractory metals and liquid lithium is shown in Fig. 2 as a function of temperature.[8,14] At 500°C, a hydrogen concentration of 100 wppm in lithium will establish hydrogen concentrations of ~3000 wppm in yttrium, 10 wppm in titanium, 0.3 wppm in vanadium, and <0.0001 wppm in chromium.

The experimentally determined hydrogen distribution coefficients from yttrium equilibrations (Fig. 2) exhibit good correspondence with the predicted results. The K_H values for vanadium, shown as open circles in Fig. 2 and as closed circles in Figs. 3-5, exhibit variations that can be attributed to the diversity of specimen types and test conditions. For comparison, distribution coefficients obtained from tests at 600°C[13] are included in Figs. 2-5. The higher values of K_H in tests 8 and 20 can be attributed to the specimen cleaning method observed in test 8 and the short equilibration time in test 20. At temperatures of <400°C, the lithium equilibration period should be >>24 h.

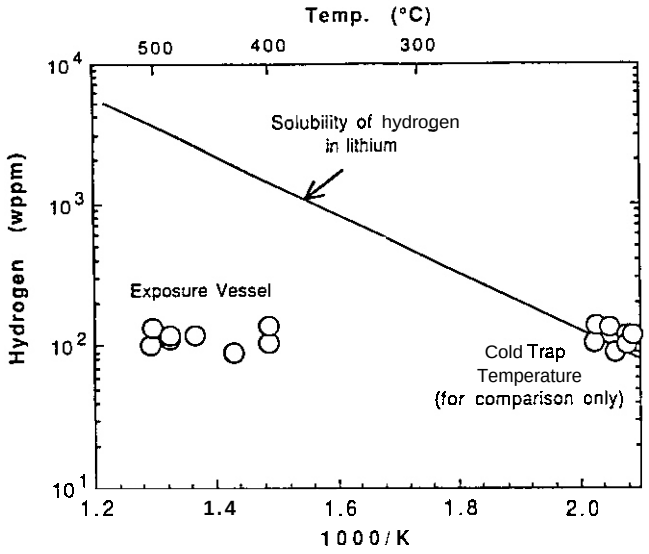

Fig. 1. Solubility of hydrogen in liquid lithium.

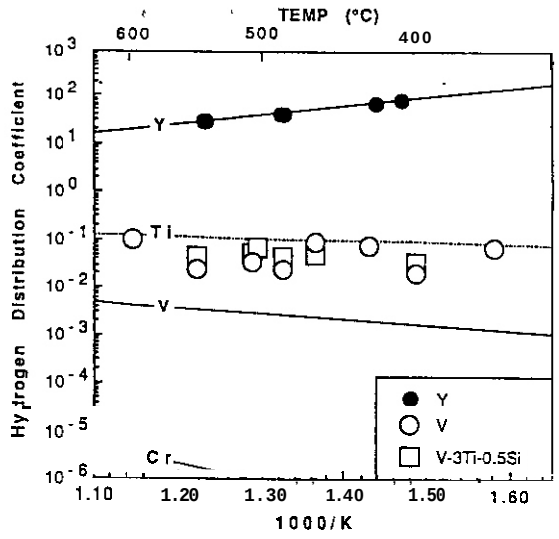

Fig. 2. Temperature dependence of equilibrium distribution coefficients of hydrogen between vanadium and V–3Ti–0.5Si and lithium. Lines indicate calculated values for different pure metals.

The K_H values for the V-3Ti-0.5Si alloy at 500°C were based on hydrogen concentrations obtained by both RGA and inert gas fusion techniques (Table 4), and the results are in good agreement.

The results for the ternary V-Cr-Ti system in Table 4 and Fig. 3 from tests 6, 10, 13, 15, and 17 exhibit a fair degree of scatter in the experimentally determined K_H values. The three values in Fig. 3 for the V-15Cr-5Ti alloy from test 6 at temperatures of 538 and 482°C follow the trend of decreasing K_H as the temperature decreases.

An effect of Ti or Cr in the binary V-Ti and V-Cr alloys on K_H is consistent with the calculated curves (Fig. 2), i.e., the value of K_H increases with the concentration of Ti at all temperatures (Fig. 4) and decreases with an increase in the concentration of Cr (Fig. 5).

CONCLUSIONS

1. The results from the hydrogen analyses (Table 4) suggest that the hydrogen isotope inventories in V-Ti, V-Cr, and V-Ti-Cr structural materials would not be substantially different.
2. Because the distribution coefficient for hydrogen in vanadium and vanadium-base alloys is much less than one ($\sim 10^{-2}$), hydrogen embrittlement as a result of somewhat higher hydrogen concentrations in lithium would not be expected.
3. The tritium concentration in lithium of a fusion reactor is expected to be <1 wppm or <1% of that in our lithium loop (~100 wppm),[15] thus the results obtained in this study indicate that tritium pickup by vanadium alloys in the reactor structure will not be significant.
4. The low hydrogen levels in vanadium-base alloys exposed to flowing lithium in this study were shown to produce good residual ductility.[1]

FUTURE WORK

Experiments are planned to extend the temperature range of these tests and to examine more closely the alloys V-3Ti-1Si, V-5Cr-5Ti, V-10Ti, and V-7Cr-5Ti.

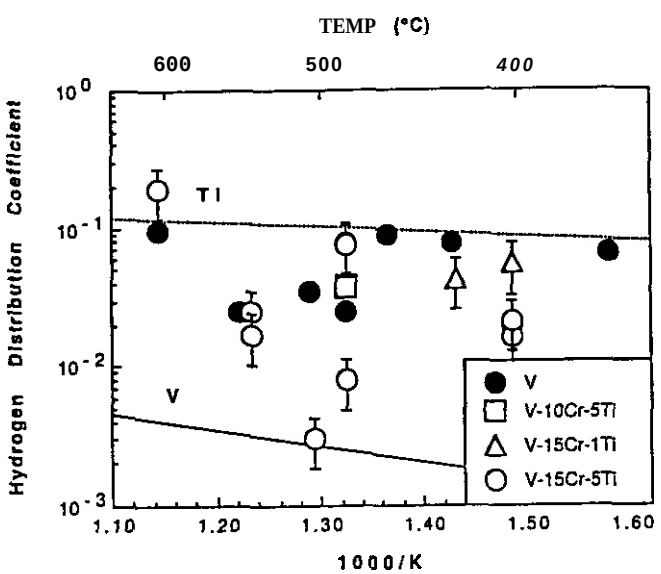

Fig. 3. Temperature dependence of equilibrium distribution coefficients of hydrogen between selected ternary vanadium alloys and lithium. Lines indicate calculated values for pure metals.

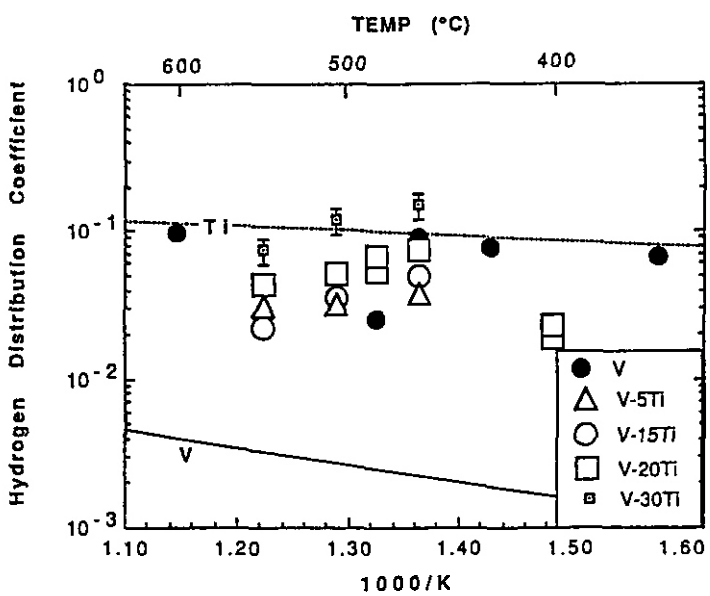

Fig. 4. Effect on hydrogen distribution coefficients of titanium concentration in binary vanadium alloys.

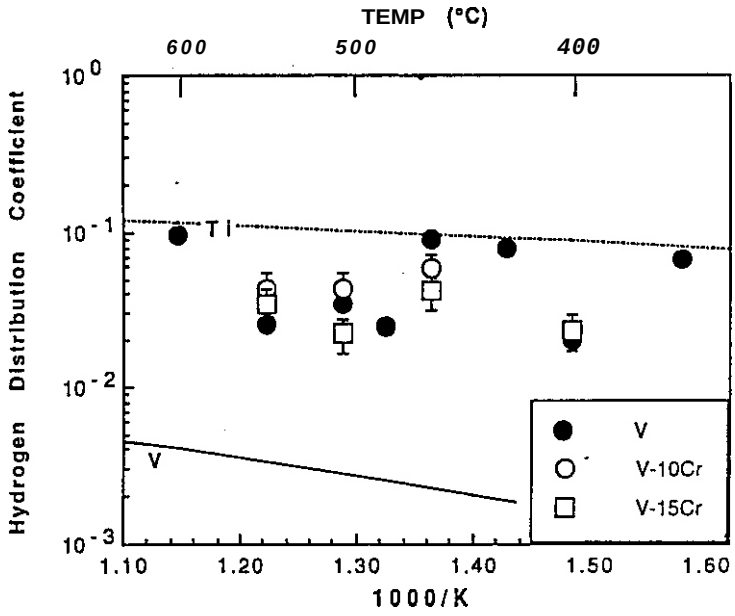

Fig. 5. Effect on hydrogen distribution coefficients of chromium concentration in binary vanadium alloys.

REFERENCES

1. B. A. Loomis, A. B. Hull, and D. L. Smith, in: Proc. 4th Intl. Conf. on Fusion Reactor Materials, Dec. 4-8, 1989, Kyoto, Japan.

2. O. K. Chopra and D. L. Smith, J. Nucl. Mater. 155-157 (1988) 683.

3. O. K. Chopra and A. B. Hull, Fusion Tech. 15, 303-308 (1989)

4. B. A. Loomis, R. H. Lee, D. L. Smith, and J. R. Peterson, J. Nucl. Mater. 155-157 (1988) 631.

5. B. A. Loomis, D. L. Smith, and F. A. Gamer in: Proc. 4th Intl. Conf. on Fusion Reactor Materials, Dec. 4–8, 1989, Kyoto, Japan.

6. B. A. Loomis, B. J. Kestel, B. D. Edwards, and D. L. Smith, in: Fusion Reactor Materials, Semiannual Progress Report for Period Ending September 30, 1988, DOE/ER-0313/5, Oak Ridge National Laboratory, Oak Ridge, TN (April 1989), p. 242.

7. B. A. Loomis and D. L. Smith in: Proc. Proc. 4th Intl. Conf. on Fusion Reactor Materials, Dec. 4-8, 1989, Kyoto, Japan.

8. A. B. Hull, O. K. Chopra, B. A. Loomis, and D. L. Smith, Fusion Tech. 15 (1989) 303.

9. B. A. Loomis, A. B. Hull, O. K. Chopra, and D. L. Smith, in: Fusion Reactor Materials, Semiannual Progress Report for Period Ending March 31, 1988, DOE/ER-0313/4, Oak Ridge National Laboratory, Oak Ridge, TN (Aug., 1988), p. 160.

10. O. K. Chopra and D. L. Smith, J. Nucl. Mater. 133& 134, 861 (1985).

11. R. M. Yonco and M. I. Homa, J. Nucl. Mater. 138, 117 (1986).

12. L. M. Melnick, L. L. Lewis, and B. D. Holt, Determination of Gaseous Elements in Metals, John Wiley and Sons, NY (1974), p. 392.

13. D. L. Smith, R. H. Lee, and R. M. Yonco, Proc. 2nd Intl. Conf. on Liquid Metal Technology in Energy Production, U. S. Dept. of Energy Report CONF-800401-P1 (1980) p. 272.

14. K. Natesan and D. L. Smith, Nucl. Technol. 22, 138 (1974).

15. D. L. Smith, et al., Fusion Reactor Blanket Shield Design Study, Argonne National Laboratory Report ANL/FPP-79-1 (1979).

OEPOSITION BEHAVIOR OF AUSTENTIC STAINLESS STEEL IN MOLTEN Pb-17 at. % Li - P. F. Tortorelli (Oak Ridge National Laboratory1

OBJECTIVE

The purpose of this work is to Characterize the corrosion of candidate or model fusion materials by slowly flowing lithium and Pb-17 at. % Li in the presence of a temperature gradient. Dissolution and deposition rates are measured as a function of alloy composition, exposure time, temperature. and additions to the liquid metals. These measurements are combined with microstructural analyses of the specimen surfaces to establish mechanisms and rate-controlling processes for the corrosion and mass transfer reactions. determine the suitability of particular materials for service in specific liquid metal environments, and provide input into fusion materials development.

SUMMARY

The mass transfer of type 316 stainless steel in Pb-17 at. % ti was studied using a thermal convection loop operating at a maximum temperature of 500°C to generate mass change and surface composition data as a function of time and loop position. Oata analysis indicated that particles suspended in the flowing liquid metal (particularly those containing nickel1 probably played a significant role in overall transport and deposition. There was also some evidence of physical detachment of deposits. The deposition of chromium (but not nickel1 correlated with the temperature dependence of solubility. as did previous weight change results from a study of ferritic (Fe-Cr) steels in nonisothermal Pb-17 at. % Li. Oue to the influence of particulate matter in the liquid metal and deposit detachment, mass transfer prediction for austenitic (Fe-Cr-Ni) steels in Pb-17 at. % Li should be more complicated than that for Fe-Cr steels.

STATUS AND PROGRESS

With all liquid metals under nonisothermal conditions. deposition of dissolved species constitutes at least as serious a concern as material thinning. and. in recent years, greater attention has been given to deposition processes in molten Pb-17 at. % Li (hereafter denoted as "Pb-17Li").[1-5] The accumulation of deposits can lead to flow restrictions that increase pumping power requirements and decrease heat transport. In nuclear applications. deposition of radioactive species outside the primary reactor area can necessitate increased shielding and remote maintenance. Therefore, deposition-relevant data for type 316 stainless steel (as a model austenitic alloy) exposed in a loop circulating Pb-17Li between 500 and 370 to 400°C has been analyzed as a function of time and compared to what is known about deposition in the Fe-Cr alloy/Pb-17Li loop system.

Net weight changes for type 316 stainless steel coupons positioned around the interior of a Pb-17Li thermal convection loop (TCL) are shown in Fig. 1 for three different specimen sets exposed for 698. 4500. and 10.000 h. (Descriptions of the experimental procedures and the 10.000 h weight change data were reported previously.)[3,6] In all cases. the mass of material dissolved from the coupons was much greater than the amount deposited on specimens and the total transported mass increased with increasing time. However. compared to the weight losses. there was little increase in weight gains between 4500 and 10,000 h for the coupons in the vertical cooled ("cold") leg of the TCL. The AT of the type 316 stainless steel loop decreased during the course of these experiments. presumably due to localized accumulation of deposits that impeded the flow of the liquid metal. Therefore. the comparison of the longer term data in Fig. 1 reflects a changing cold leg temperature profile. Accordingly, Fig. 2 shows the 4500 and 10.000 h weight change data plotted against cold leg specimen temperature rather than position in the TCL. For further comparison, Fig. 2 includes previously reported 10.000 h data[3] for Fe-12Cr-1MoVW steel exposed to Pb-17Li in a ferritic steel TCL under similar conditions.

The nature of the process(es) that led to net weight gains was characterized by microscopic examination of the surfaces of cold leg specimens exposed for several thousand hours. As described previously,[3,7] deposition was not uniform across the exposed surfaces: individual or clustered deposits were sometimes observed and the deposit number and size densities were not always constant across a particular coupon. In several cases. 'detachment' of deposits was noted. particularly for the 10,000 h specimens, which had large deposit-free areas at the lower temperatures.[3,7] As shown in Fig. 1, weight gains were also measured for the specimens positioned at the bottom of the TCLs heated vertical (hot) leg and deposits were observed on the 4500 h specimen in this location. (The equivalent 10.000 h specimen was not examined). Relative to those observed on the cold leg coupons, these deposits were small and less numerous. in agreement with the small weight increase measured for this specimen (Fig. 1).

ORNL-DWG 89-11758

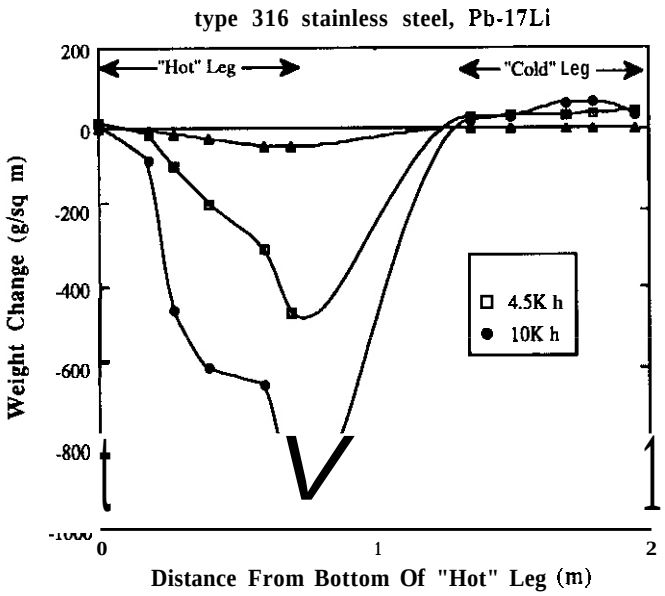

Fig. 1. Weight change versus loop position for type 316 stainless steel specimens in a Pb-17 at. % Li thermal convection loop operating between 500 and 370 to 400°C. (Distance is measured in direction of liquid metal flow.)

ORNL-DWG 89-11759

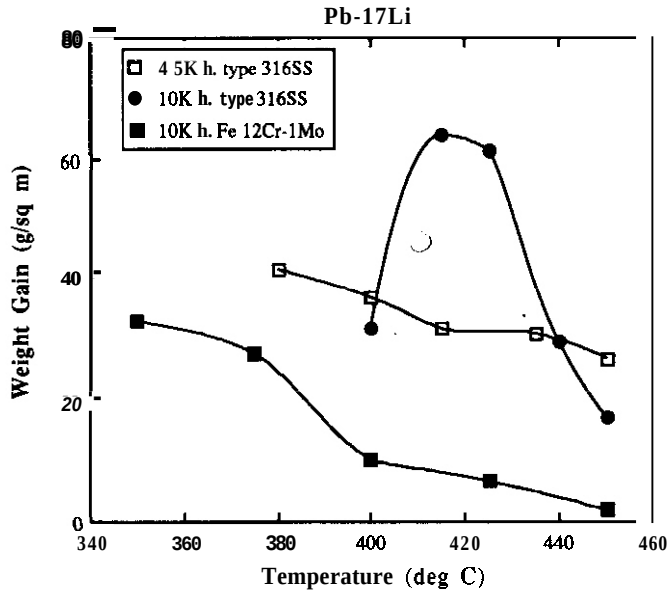

Fig. 2. Weight gain versus temperature for type 316 stainless steel specimens in the cooled vertical leg of a Pb-17 at. % Li thermal convection loop operating between 500 and 370 to 400°C.

Energy dispersive x-ray (EDX) analysis was used in conjunction with scanning electron microscopy to determine the composition of the observed deposition products. Results for the cold leg specimens exposed for 4500 and 10.000 h are summarized in Table 1. which contains average compositions determined from a number of deposits of a particular type observed in cross section. A distinct dependence of deposit composition on loop position, as previously reported based only on the 10.000 h data,[3] was observed for both exposure conditions. The agreement between the deposit compositions measured for coupons exposed for 4500 h and those for the 10.000 h surfaces was excellent for the C4 and C5 specimen positions: in all cases the average composition was Fe-7Cr-(2-3)Ni (wt %). At lower temperatures. the deposits were a combination of two or more of Fe-7Cr-(2-3)Ni (A. in Table 1), Fe-(32-50)Ni-(11-25)Cr (B), Fe-(33-35)Cr-2Ni (C), and Fe-(50-70)Cr-2Ni (D), as shown in Table 1. (When multiple compositions are shown. they are listed in probable order of abundance). Although there were some compositional differences between the two exposure times. a predominance of Cr-rich deposits were observed at lower temperatures for both specimen sets. Type A deposits were found on the 4500 h specimens in the C6 and CJ positions (see Table 1). but such products were completely absent from the surfaces of the corresponding 10.000 h specimens (even when such were analyzed normal to the surface rather than in cross section[3,7]). Another difference between the two sets of results was the point at which nickel-enriched deposits (type B) appeared: such deposits were observed farther up the cold leg (at a higher temperature) in the longer term loop experiment. This is also evident in Fig. 3. where surface-averaged concentrations of Fe, Cr. and Ni are plotted versus cold leg loop position. With the caveat that these average values could be somewhat misleading because more than one type of deposit was found on some of the surfaces, these plots clearly illustrate the general trend of increasing Cr/Fe with decreasing temperature and the nickel enrichment at intermediate cold leg temperatures. There was no apparent clustering of deposits of like compositions in the cases where there was more than one deposit type.

The compositions of selected specimen surfaces along part of the heated loop section were also determined by EDX analysis. Surface-averaged compositions for these specimens are shown in Fig. 4. The deposits formed on the specimen exposed for 4500 h at the bottom of the heated vertical ("hot") leg (net weight gain) were A type: their average composition was Fe-8Cr-2Ni-1Si. As reported previously,[3,6] specimens at the maximum temperature position (500°C) suffered preferential dissolution of nickel and chromium. In fact, as shown in Fig. 4, many of the hot leg specimens that experienced weight losses were depleted in these elements relative to the starting concentrations of the steel. However, the plot for the 4500 h set [Fig. 4(a)] showed a maximum in surface nickel concentration at an intermediate temperature, while the specimens between 460 and 420°C exhibited surface nodules of pure Mo.

Table 1. Average composition of mass transfer deposits on type 316 stainless steel coupons in cold leg of Pb-17 at. % thermal convection loop for two exposure periods

Loop position	3900 h		10,008 h	
	Temperature[a] (°C)	Composition[b]	Temperature[a] (°C)	Composition[b]
c4	460	A	460	A
c5	440	A	445	A
C6	420	A,C,D	430	B,D
c7	395	(A,B,D)[c]	415	D,B
C8	370	D,C,B	400	D,B

[a]Approximate.

[b]Compositions determined by energy dispersive x-ray analysis. Multiple average compositions Shown when distinct types of deposits were observed. Listed in decreasing order of apparent abundance when multiple compositions are reported except where noted otherwise Concentrations are in wt %.

A: Fe-(7-10)Cr-(2-3)Ni
B: Fe-(32-50)Ni-(11-25)Cr
C: Fe-(33-35)Cr-2Ni
D: Fe-(50-70)Cr-2Ni

[c]Approximately equal abundance.

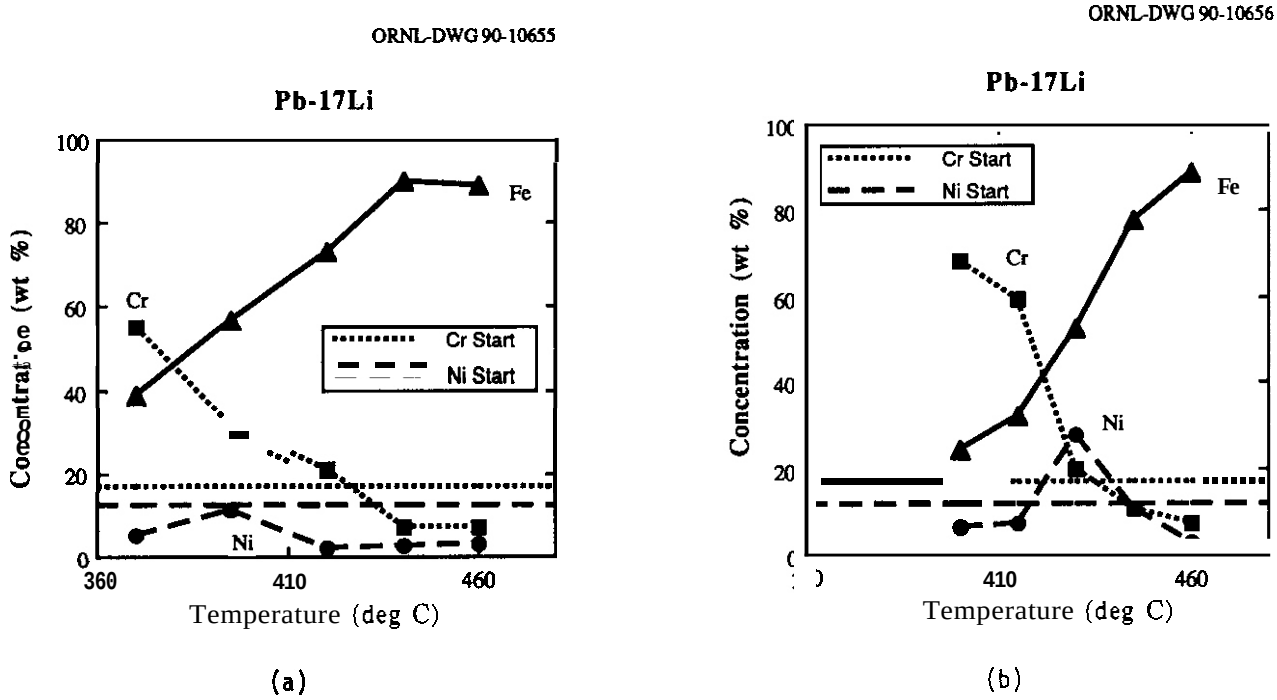

Fig. 3. Elemental concentration versus position in the cooled vertical leg for type 316 stainless steel specimens in a Pb-17 at. % Li thermal convection loop operating between 500 and 370 to 400°C for 4488 h. Concentrations determined by energy dispersive x-ray analysis. (a) 4488 h. (b) 10,008 h. (Horizontal lines represent starting concentrations of chromium and nickel.)

ORNL-DWG 90-10657

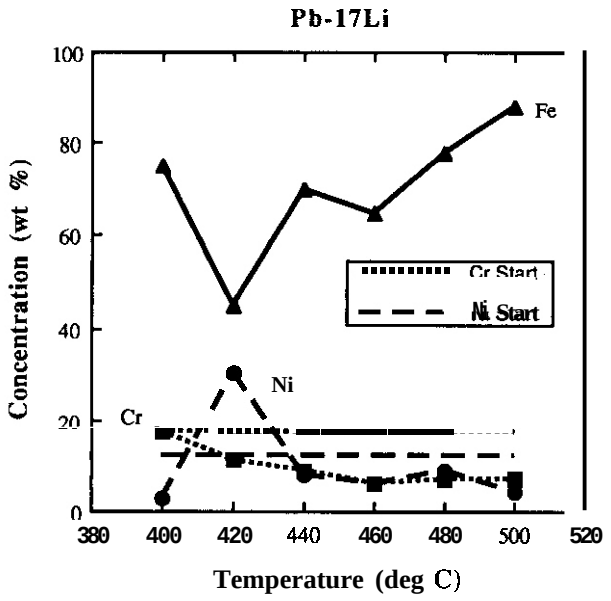

(a)

ORNL-DWG 90-10658

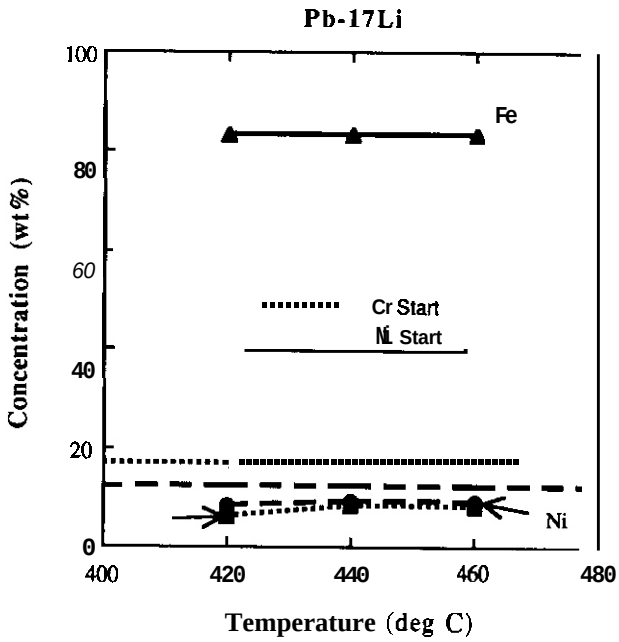

(b)

Fig. 4. Elemental concentration versus position in the heated vertical leg for type 316 stainless steel specimens in a Pb-17 at. % Li thermal convection loop operating between 500 and 370 to 400°C for 10,008 h. Concentrations determined by energy dispersive x-ray analysis (a) 4488 h. (b) 10,008 h. (Horizontal lines represent starting concentrations of chromium and nickel.)

Under equilibrium. steady-state conditions. the net flux. J_i, of element i from or to a specimen exposed to molten Pb-17Li at loop position r can be expressed as

$$J_i(r) = k_i^z(r)[C_i^o(r) - C_i(r)] \quad (1)$$

where k_i^z is the effective rate constant for dissolution (z=s) or deposition (z=p) of element i. C_i^o is the solubility of this element in the Pb-17Li, and C_i is the local concentration of element i in the liquid metal. (C_i^o and k_i^z are dependent on temperature. which is a function of r.) Normally. in the higher temperature region of the loop $C_i^o > C_i$ and dissolution occurs ($J_i > 0$, weight losses are measuredl. while in the colder part of the circuit $C_i^o < C_i$ and weight is gained from deposition on the solid surfaces. Such solubility-driven transport can be monitored by measurements of weight changes ($\Sigma \int J_i dt$) of coupons arrayed around the loop. which typically produce mass transfer profiles such as those shown in Fig. 1. While Eq. (1) yields a qualitative understanding of corrosion and mass transfer in this and other liquid metal systems. it cannot. in many cases, explain the quantitative aspects of deposition caused by additional kinetic and thermodynamic factors, such as interactions among solutes and reactions with impurities in the liquid metal or solid. As shown below. this solubility-based approach does not predict many of the features of the present mass transfer profiles.

Figure 1 shows that while substantial mass was lost from the hot zone specimens during each loop experiment. much less material per unit area was deposited on the cold leg specimens. Furthermore. this large imbalance between the measured weight losses (Δm^S) and gains (Δm^p) increased as a function of exposure time. (The total coupons weight gains and losses for the three expoiure periods are listed in Table 2.1 This discrepancy between Δm^S and Δm^p could be explained if deposition in the TCL was preferentially occurring on loop walls Or in parts of the loop not containing specimens. However, it is interesting to note that in a recent mass transfer study of austenitic steel in Pb-17Li,[4] in which the total amount of deposited mass was determined by destructive examination of loops and physical removal of deposition products from all surfaces. the total dissolved mass was still significantly greater (by a factor of 1.5-2) than the total mass gain from deposition. Such findings tend to indicate that the present observation of an imbalance between Δm^S and Δm^p may not be just due to the failure of cold leg coupons to accurately reflect the appropriate amount of deposited material. instead. it seems likely that there might be particles of solutes in the Pb-17Li. in support of this argument, Borgstedt et al.[5] have reported concentrations of Fe, Cr. and Ni in Pb-17Li above their respective solubility limits. Suspended particles can continue to remain in the liquid metal until they agglomerate to a size where plugging may occur. Therefore, indications of a flow restriction (decreasing AT with time) in the type 316 stainless steel Pb-17Li TCL of the present study do not necessarily indicate that solubility-driven deposition was occurring outside of the area covered by the coupons.

Table 2. Total measured weight changes for specimens exposed in Pb-17Li thermal convection loops

	Measured weight loss (mg)	Measured weight loss (mg)
316 SS, 700 h	42	1
316 SS, 4488 h	1051	65
316 SS, 10,008 h	2673	74

The formation of particles in the liquid metal may well be related to an inefficient andlor sluggish deposition process(es). The growth of deposits requires registry with the underlying surface and if such is not possible, or is somehow disrupted during the initial stages of deposition. supersaturation and/or particle formation can occur and be maintained.[8] Previously reported observations of small deposits in definite patterns on some of the 10,000 h surfaces[3,7] may indicate that deposition on the coupons was retarded in this way. While both supersaturation and particle formation would lead to reduced deposition fluxes [based on Eq. (1)], only the former condition would also inhibit dissolution unless the particles dissolved in the hot zone. Therefore, on the basis of the large imbalance in weight gains and losses and the relatively large dissolution area. it can be concluded that the liquid metal was not just greatly supersaturated in the present case.

Poor deposit adhesion can also contribute to the observed discrepancy between Δm^s and Δm^p. Oetachment of deposition products can occur during exposure to the liquid metal (a source of particulate matter). during cooling after specimen removal from the loop, and/or during the specimen cleaning process.[6] Observations of delamination of the deposit layer[7] lend some validity to a contribution of deposit detachment to lover weight gains. Furthermore. the significant amount of deposit-free surface areas on the lower temperature coupons of the 10,000 h specimen set[7] is indicative of poor adhesion - a phenomenon that should be more prevalent at longer times when deposited layers become relatively thick.

The above consideration of the overall weight change data and general surface morphologies indicate three possible contributions to the discrepancy between the amounts of mass dissolved and deposited: heterogeneous. localized deposition in loop areas not covered by coupons. homogeneous particle nucleation in the molten Pb-17Li, or physical removal of deposits from cold leg coupons. Allowing for all these possibilities, a mass balance for the loop would yield

$$\Delta m^s \approx \Delta m^p + \Delta m^f + \Delta m^d + \Delta m^r + \Delta m^n \qquad (2)$$

where Δm^s and Δm^p are as defined above. Δm^f is the mass of particles that formed from solute released from coupons and stayed suspended in the Pb-17Li, Δm^d is that of detached deposits suspended in the liquid metal, Δm^r is the contribution of deposits removed during cooling or specimen cleaning, and Δm^n is the mass associated with nonproportional deposition in areas of the loop not monitored by coupons. In order to gain a better understanding as to the relative importance of these processes in controlling mass transfer and deposition, the cold leg weight change profiles and surface chemistry data is analyzed in some detail below.

As can be seen in Fig. 2. the weight gain profile for the 10,000 h specimen set is distinctly different from that after 4500 h. In the dissolution regime, $C_i^o - C_i > 0$, and. for a given time. J_i and measured weight losses should normally increase with increasing temperature. as can be noted in Fig. 1 for the three exposure periods. When $C_i^o - C_i < 0$, deposition should occur. In many of these cases. weight gains increase as the temperature decreases and a weight change profile like that shown in Fig. 2 for the 4500 h specimen set is measured. However. if the two functions that determine the magnitude of J_i ($|C_i^o - C_i|$ and k_i^p) vary oppositely with respect to temperature, it is also possible that a maximum in the weight gain versus loop temperature curve, such as shown in Fig. 2 for the 10,000 h set. would result. In view of the 4500 h data, this possibility is considered highly unlikely - the functional dependence of $|C_i^o - C_i|$ or k_i^p on temperature should not be different for the two loop experiments. Therefore. it appears that the 10.000 h data cannot be explained on the basis of such competition between factors that influence J_i, which was one of several possibilities suggested when only the 10.000 h data was considered.)

If the physical removal of deposits from cold leg surfaces occurred, it could also explain the differences between the 4500 and 10,000 h deposition data. The shape of the cold leg profile for the 10.000 h coupons (see Fig. 2) could have resulted from a loss of previously deposited material that reached a critical thickness for detachment. The observation that the cold leg coupon surfaces in the two extended loop experiments showed similarities in surface composition trends is consistent with a process of initially equivalent deposition profiles: in general, as shown in Table 1 and Fig. 3. iron was the principal deposited element at higher temperatures of the cold legs. and chromium was dominant at the coldest loop positions. Some of differences in the composition data between the two experiments - for example, the appearance of Fe-Ni nodules at a higher temperature for the 10,000 h set . could possibly be explained by detachment of such deposits at lower temperatures. but the observation of type A (Fe-low Cr) deposits on lower temperature coupons in the 4500 h experiment is not consistent with such an argument. On the other hand, if suspended particles contributed to the mass transfer process. it is entirely possible to have deposition of particles rich in Ni anywhere in the loop,[9] particularly at longer times when their density and size in the liquid would be much greater. Further evidence for such deposition was revealed by the hot leg surface composition data for the 4500 h coupons [see Fig. 4(a)]: a maximum in nickel concentration was also observed despite an overall decrease in weight. If these increases in surface nickel concentrations are due to the influence of Ni-containing particles in the Pb-17Li, the deposition rate is not governed by solubility considerations. but rather by hydrodynamic factors and sticking coefficients. The EOX data appear to be consistent with the role of particulate matter in the transport of Ni around the loop and thus affirm a contribution of such particles to the discrepancy between measured weight gains and losses

The same TCL was used for the exposures of the three type 316 stainless steel specimen sets to Pb-17Li and. previously. had circulated lithium for over 10.000 h. Therefore, a large fraction of the loop's heated section, originally type 316 stainless steel. was already significantly depleted in nickel when fresh specimens were inserted. The presence of a low-nickel loop surface relative to the composition of the coupons created a possible driving force for transport of dissolved nickel to the loop wall of the hot leg. Such a process could increase the contribution of Δm^n [Eq. (2)] to the observed imbalance in measured weight losses and gains. However, this situation never seemed to have an effect on dissolution rates in lithium or Pb-17Li.[6,10] Furthermore, as shown in Fig. 4, nickel was deposited on some hot leg coupons after 4500 h and also was found on cold leg coupons after 10,000 h (Fig.3, Table 1). Thus, it does not appear that the concentration gradient between hot leg specimens and loop wall had a dominant influence on mass transport. A more important factor may be that, as successive specimens sets were exposed to the Pb-17Li, deposits were already present on the loop wall in the colder part of the TCL. Therefore, deposit nucleation on this surface could have been favored over that on the fresh coupons during exposure of a later specimen set. If this was the case. a nonproportional partitioning of deposits to the loop wall (Δm^n) could contribute to the mass imbalance and. as observed in the present experiments, this difference would increase with increasing time as deposition in the cold zone increased with successive exposures.

While nickel transfer around the loop appeared to be 'irregular". the surface-averaged cold leg composition data (Fig. 3) revealed that the chromium concentration increased monotonically with decreasing temperature. In both the 4500 h and 10,000 h experiments. the chromium concentration profiles appeared to show behavior expected for a solubility-driven deposition process since, at a given time, the amount of deposited chromium. Δm_{Cr}^p, increased with decreasing C_{Cr}^o as predicted by Eq. (1):

$$\Delta m_{Cr}^p = \int J_{Cr} dt = \int k_{Cr}^p [|C_{Cr}^o - C_{Cr}|] dt \qquad (3)$$

assuming C_{Cr} is constant around the loop. in view of the monotonic behavior of the cold leg chromium concentration with temperature and the preferential dissolution of chromium in the hot leg,[3,6] two mass transfer balance points can be defined as being those loop positions where $J_{Cr} = 0$. These points delimit the area of chromium dissolution relative to that for its deposition. The balance points can he determined from the data shown in Figs. 3 and 4 by noting the loop position (temperature) at which the surface composition curves intersect the horizontal line representing the starting surface concentration of Cr in the alloy.[11] For the 4500 h experiment. they are about 415 and 425°C for the hot and cold legs. respectively. Under the assumption that the elemental fluxes (J_i) are independent of each other (that is. the activity of chromium at the interface is not strongly affected by changes in the relative concentrations of the other elements).

$$J_{Cr}(T_b) = 0 = k_{Cr}^z(T_b)[C_{Cr}^o(T_b) - C_{Cr}] \qquad (4)$$

and, therefore,

$$C_{Cr} = C_{Cr}^o(T_b) \qquad (5)$$

where T_b is the loop temperature at the balance point in either the hot (T_h) or the cold leg (T_c) Because solubility is normally a single-valued function of temperature, Eq. (5) indicates that if the balance point temperatures are unequal, C_{Cr} cannot be constant around the loop. However, from the 4500 h data, $T_h \approx T_c$ within the accuracies of the surface composition and temperature measurements. These results are therefore consistent with a constant C_{Cr} and, as mentioned immediately above, with solubility-driven chromium deposition as described by Eq. (1). Furthermore, referring to Fig. 3, it can be noted that T_c is approximately the same (within 10°C) for the 4500 and 10,000 h profiles. In view of Eq. (5), this finding implies that C_{Cr} has reached an equilibrium. steady-state value. which is characteristic of solubility-driven transport as described by Eq. (1). (However. a constant C_{Cr} can also be possible with particle transport.)

Based on the above considerations. it can be concluded that there is an important homogeneous particle nucleation contribution to overall mass transfer of type 316 stainless steel in Pb-17Li thermal convection loops. The influence of particle formation in nonisothermal liquid metal systems has been recognized for many years,[9] and as already noted. a role of particulate matter in determining mass transport in Pb-17Li has been suggested or implied by the results of others.[4,5] While the present results indicate that the particles contain substantial amounts of nickel. it is not necessary that all of them are nickel-rich or Fe-Ni. Some may contain chromium in significant concentrations, but. because such particles neither redissolved (as evidenced by continual chromium depletion for the hot zone specimens and $T_h \approx T_c$, see above) nor attached themselves to loop coupons (no irregularities in the chromium profiles). they do not influence the measured quantities except for their contribution to the imbaiance in overaii weight lasses and gains. On the other hand. the nonmonotonic mass transfer profiles for Ni (Figs. 3 and 4) may mask some solubility-driven deposition of this element. However, the relativeiy low concentration of nickel found on many of the cold leg surfaces and the observations that nickel-rich deposits tended to deposit over chromium-enriched ones (that is. chromium came out of solution earlier than nickel1 indicate that this type of transport for nickel was quite limited.

Referring to Eq. (2), the above analyses of the cold leg coupon data for the 4500 and *10.000* h specimen sets cannot definitively show that any of the possible contributions to the mass imbalance (particles. detachment, nonproportional deposition) are negligible. Despite the complication of a possible concentration driving force for preferential deposition on the loop wall in the extended exposure experiments, the present data and the results of others[4,5] strongly support a role of particle transport in this Pb-17Li system. This finding is particularly compelling in view of the work of Flament et al.,[4] in which $\Delta m^n = 0$, and a definite mass imbalance was still measured. There was also direct evidence of some particle detachment either during exposure or after specimen removal. As mentioned above. in the former case. such release of deposits can then be treated as an additional source term for particles in the liquid metal.

Previous work3 concluded that, in contrast to the type 316 stainless system, solubility-driven deposition was the most *important* factor for mass transfer of a Fe-12Cr-1MoVW steel exposed to Pb-17Li in a ferritic steel TCL under similar conditions. Figure 2 shows the differences in cold leg mass gain profiles between these two steel systems: increasing weight gains with decreasing temperature were measured in the Fe-12Cr-1MoVW steel experiment 110,076 h). There was some discrepancy between measured weight gains and losses. but it was much smaller than what was observed for type 316 stainless steel. Cold leg deposits in the ferritic steel loop were type A (Fe-8Cr). This mass transfer behavior of the Fe-12Cr-1MoVW steel is similar to much of what was observed in the 4500 h austenitic steel experiment with respect to chromium transport (compare the cold leg mass change profiles shown in Fig. 4). In this way. the results for the ferritic system support many of the present findings. Furthermore, the observation of a mass imbalance in the Fe-Cr experiment (also reported for a ferritic steel/Pb-17Li loop system[4]) may indicate that. as discussed above. particles involving chromium may form, but are not manifested in a way that is amenable to the type of measurements and analyses of the previous and present studies. If this is the case, mass transfer prediction for ferritic steels in Pb-17Li may not be as straightforward as it would normally seem when a solubility-controlled process is dominant. (Indeed. for both steels, if particles could "float' in Pb-17Li, mass transport becomes increasingly complex.)[12] However, the present results do show that even apart from the complications of preferential dissolution and nonuniform surface recession[3,6] (not observed for the ferritic steels). predictive capability for modeling, and control of. mass transport in lead-lithium will be more difficult for austenitic (Fe-Ni-Cr) alloys than for Fe-Cr steels.

CONCLUSIONS

1. Particles played a role in overall transport in thermally convective Pb-17Li. The irregular movement of nickel around the loop was associated with particle formation and attachment to solid surfaces

2. While some chromium transport may have involved particles, the surface composition data showed that deposition of chromium was primarily controlled by a solubility driving force. This finding agreed with results from a previous study of a Fe-Cr steel in nonisothermal Pb-17Li. A balance point analysis indicated that a steady-state chromium concentration in the Pb-17Li was achieved.

3. Physical detachment of deposits (during or after exposure) contributed to the significant differences in measurements of dissolved and deposited masses.

4. The analysis was complicated by the possible influence of preferential deposition on the thermal convection loop wall due to differences in composition between it and the specimens.

5. Due to the influence of particles and lack of good deposit adhesion. as well as the effects of preferential dissolution, mass transfer prediction for austenitic (Fe-Cr-Ni) steels in Pb-17Li should be more complicated than that for ferritic (Fe-Cr) steels.

FUTURE WORK

Any further work in this area will concentrate on research regarding the use of specific surface reactions on steels in Pb-17 at. % ti to inhibit mass transfer in nonisothermal systems.

REFERENCES

1. 2. Peric. G. Drechsler. G. Frees, and H. U. Eorgstedt. pp. 522-1 - 522-7 in Proc. Fourth Int'l Conf. on Lig. Metal Eng. and Technol., Vol. 3. Societe Francaise d'Energie Nucleaire. 1988.

2. M. Broc. P. Fauvet, T. Flament. A. Terlain. and J. Sannier. pp. 527-1 - 527-10 in Proc. Fourth Int'l Conf. on Lig. Metal Eng. and Technol., Vol. 3. Societe Francaise d'Energie Nucleaire. 1988.

3. P. F. Tortorelli. pp. 528-1 - 528-10 in Proc. Fourth Int'l Conf. on Lio. Meta1 Ena. Technol. Vol. 3, Societe Francaise d'Energie Nucleaire. 1988.

4. T. Flament, A. Terlain. and J. Sannier, to be published.

5. H. U. Borgstedt et al., to be published.

6. P. F. Tortorelli and J. H. DeVan, J. Nucl. Mater. 141-143 (1986) 592-598.

7. P. F. Tortorelli. 'Thermal Gradient Mass Transfer in Ferrous Alloy Pb-17 at. % Li Systems." pp. 279-287 in Fusion Reactor Mater. Semiannl. Prog. Rep. March 31. 1987, DOE/ER-0313/2, September 1987.

E. O. F. Kammerer et al.. Trans. AIME 212 (1958) 20-25.

9. L. F. Epstein. "Static and Dynamic Corrosion and Mass Transfer in Liquid Metal Systems." Liquid Metals Technol., Chem. Eng. Prog. Symp. Ser. 20, 53 (1957) 67-81.

10. P. F. Tortorelli and J. H. DeVan, pp. 81-88 in Proc .3rd Int'l. Conf. on Liquid Metal Eng. and Technol., Vol. 3, The British Nuclear Energy Society. 1985.

11. P. F. Tortorelli. J. H. DeVan, and J. E. Selle, pp. 13-44 - 13-54 in Proc. Second Int'l Conf. on Liouid Metal Technol. in Enerav Production, USDOE report. CONF-800401-P2, 1980.

12. J. H. DeVan, Oak Ridge National Laboratory, to P. F. Tortorelli. Oak Ridge National Laboratory. private communication. January 1990.

RAOIATION-INDUCE0 SENSITIZATION OF PCA UNDER SPECTRALLY TAILORED IRRADIATION CONDITIONS — T. Inazumi (Japan Atomic Energy Research Institute, assigned to ORNL) and G.E.C. Bell (Oak Ridge National Laboratory)

OBJECTIVE

The objective of this work is to evaluate radiation-induced sensitization of PCA under a simulated fusion reactor environment by the electrochemical potentiokinetic reactivation (EPR) test technique and obtain data relevant to the International Thermonuclear Experimental Reactor (ITER).

SUMMARY

The degree of sensitization of 25% cold-worked PCA irradiated at 60, 200, 330, and 400°C up to 7 dpa under spectrally tailored conditions in the ORR-MFE-6J/7J experiments was evaluated by the electrochemical potentiokinetic reactivation (EPR) test technique on miniaturized TEM disk-type specimens. Irradiation at 60°C to 7 dpa did not affect the reactivation behavior of PCA. The reactivation charge of PCA was increased by the irradiation at 200, 330, and 400°C, as compared with unirradiated control specimens, and increased with increasing irradiation temperature. Post-EPR examination of the specimen surfaces showed grain boundary etching for the specimen irradiated at 400°C, but not for the specimens irradiated at 330°C and below. This indicates that the intergranular stress corrosion cracking (IGSCC) susceptibility associated with chromium depletion along grain boundaries was not increased by the irradiation at temperatures below 330°C to this damage level. Localized attack across the grain faces was observed for all the specimens irradiated at 200, 330, and 400°C, which suggests the occurrence of localized sensitization in the grain interior. The investigation of the possibility of the localized sensitization in grain interiors and its effects on the corrosion behavior is in progress.

PROGRESS AND STATUS

Introduction

The sensitization of PCA irradiated at 420°C to 9 dpa in FFTF/MOTA was detected by the EPR test technique using miniaturized specimens.[1,2] The increased reactivation charge and resulting grain boundary etching indicated the occurrence of radiation-induced sensitization, and suggested the increased susceptibility of this material to IGSCC in a high-temperature water environment. However, in fusion reactors. the irradiation environment will be different from that in FFTF. In ITER, for example, the design temperatures in normal service condition for water-cooled components are 50 to 200°C.[3] The damage rate is lower and the He:dpa ratio is higher compared with those in FFTF. The degree of radiation-induced sensitization is expected to be less because of the decreased mobility of vacancies and interstitials at lower temperatures, but, on the other hand, the lower damage rate will work toward compensating the effect of temperature decrease,[4] and the higher helium generation may affect radiation-induced segregation (RIS).[5]

A spectrally tailored experiment (MFE-6J/7J) in the Oak Ridge Research Reactor (ORR) was recently completed after reaching the damage level of 7 dpa.[6] In this experiment, the damage rate and He:dpa ratio of materials were maintained at values typical of ITER first wall and blanket designs.

In the present study, radiation-induced sensitization was evaluated for the PCA irradiated in the spectrally tailored experiment at temperatures including the design temperature range for ITER.

Experimental

Material — The material used in this study was PCA with the chemical composition shown in Table 1. Disk-type specimens, 3 mn in diameter by 0.25 mm thick, were prepared from the 25% cold-worked sheet of PCA. The specimens were irradiated at 60, 200, 330, and 400°C to 7 dpa in the ORR.

Table 1. Chemical composition of PCA (wt %)

C	Si	Mn	P	S	Ni	Cr	Mo	Ti	Fe
0.05	0.4	1.8	0.01	0.003	16.2	14.0	2.3	0.24	bal

EPR Test — A detailed description of the testing system was given elsewhere.[7,8] The single-loop EPR tests were performed at the test conditions shown in Table 2. The reactivation charge was calculated using total tested area[1,2] to determine the degree of sensitization.

Table 2. EPR test conditions

Solution	0.5 M H_2SO_4 + 0.01 M KSCN
Temperature	30°C
Passivation	2 min at +200 mV vs SCE
Reactivation scan	3 V/h

Surface Examination — Observation of the specimen surfaces after EPR testing was carried out with an optical microscope and SEM to examine the morphology of sensitization. Surface observation was also carried out for the specimen irradiated at 200°C after EPR testing was interrupted during the reactivation process to examine the relationship between increase in reactivation current and development of etching structures on the specimen surface.

Results

EPR Test — Reactivation curves for irradiated and unirradiated specimens are shown in Fig. 1. Compared with the unirradiated specimen, the peak current density was increased by irradiation at temperatures above 200°C. The increase in the current density was larger at higher irradiation temperatures. Irradiation at 60°C did not have any effects on the reactivation behavior.

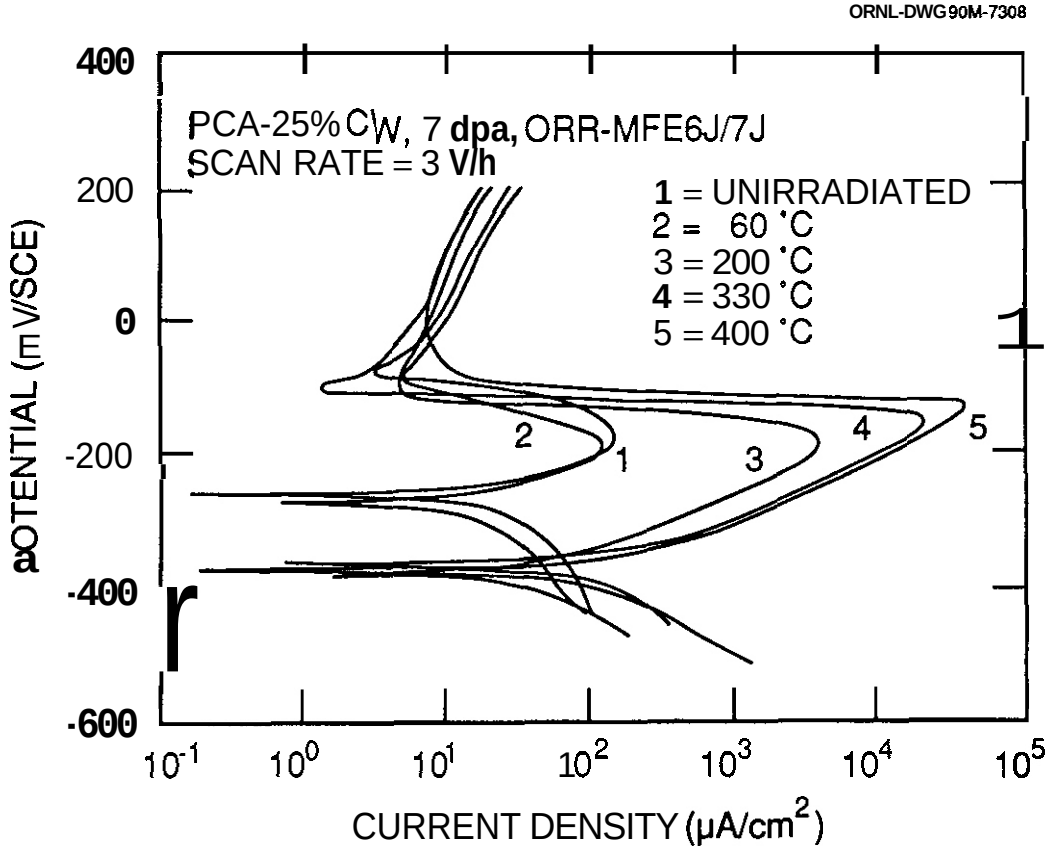

Fig. 1. Reactivation curves of PCA.

The calculated Pa values of the irradiated specimens are shown as a function of irradiation temperature in Fig. 2. There was no effect of radiation on the Pa value at 60°C. The Pa value was increased by the irradiation at above 200°C as compared with the unirradiated specimen. At an irradiation temperature of 200°C, the Pa value was more than an order of magnitude higher than that of the unirradiated specimen. The Pa value increased with increasing irradiation temperature. The Pa value at 400°C was an order of magnitude higher than that at 200°C.

Surface Examination — Optical micrographs of the irradiated specimen surfaces after EPR testing are shown in Fig. 3. The fine scale etching across grain faces appeared for the specimens irradiated at above 200°C. The density of the etching increased with increasing irradiation temperature. The grain boundary etching was observed only in the specimen irradiated at 400°C. Etching along slip lines was also observed in the 400°C specimen.

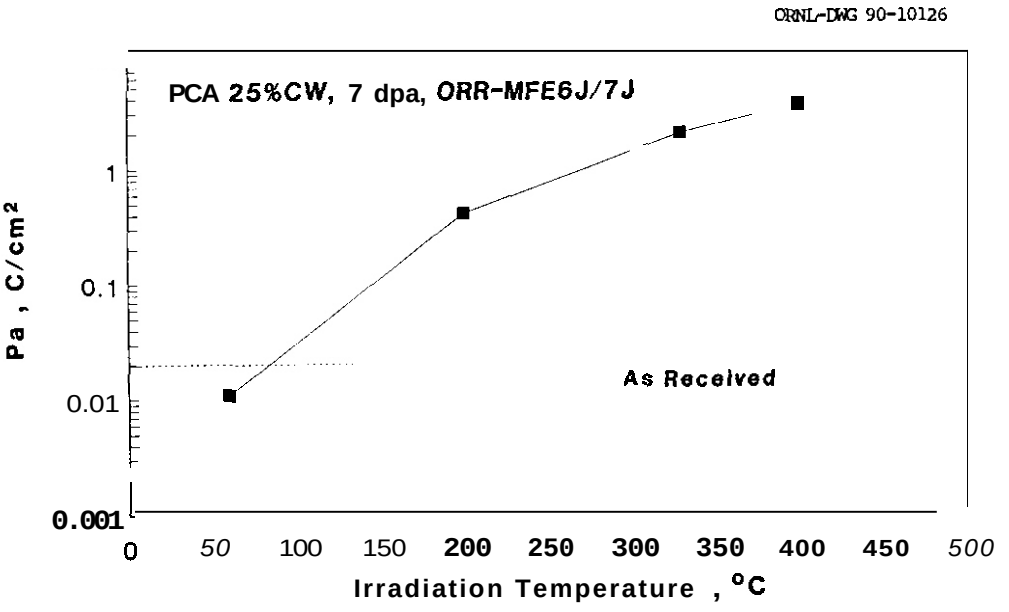

Fig. 2. Effect of irradiation temperature on Pa value of PCA.

SEM micrographs of the surface of the specimens irradiated at 200 to 400°C are shown in Fig. 4. Oiscontinuous grain boundary etching was found at the irradiation temperature of 400°C. At the irradiation temperatures of 200 and 330°C. grain boundary etching was not observed, and only grain face etching was found. In the specimen irradiated at 200°C, the grain face etching took the form of pitting-type corrosion. The pits varied in size, ranging from less than 0.2 μm to 2 um. Some of the pits appeared to have coalesced. The original smooth surface remained intact between the pits. At the irradiation temperature of 330°C. the specimen surface showed dimple-shape corrosion across the grain face. The dimple diameters ranged from 0.2 μm to 1 μm. Similar dimple-shape corrosion was observed on the grain face of the 400°C specimen, but the individual dimples were not as clear as those at 330°C.

The microstructural changes in the surface of the specimen irradiated at 200°C during the reactivation process are shown in Fig. 5. No etching was observed at the Flade potential. The density of the etching increased with increasing current density from half way to the peak and saturated at the peak current density.

Discussion

At the irradiation temperature of 200°C. which is in the range of the design operation temperatures of ITER, the Pa value was increased by more than an order of magnitude as compared with the unirradiated condition, but grain boundary etching was not found on the specimen surface after EPR testing. This indicates that the IGSCC susceptibility of the PCA was not increased by the irradiation at this temperature. However, the pitting-type etching was observed on grain faces after EPR testing. As shown in the changes in etching structure of the specimen surface during the reactivation process (Fig. 5), it is clear that the increase in the reactivation current of the specimen irradiated at 200°C can be related to the development of the fine grain face etching. Since the EPA test detects the instability of passive films, the etching suggests the occurrence of localized sensitization in grain interiors. Such a localized sensitization in grain interiors may become the initiation sites of transgranular stress corrosion cracking (TGSCC) and/or may increase the general corrosion rate.

The radiation-induced segregation (RIS) to the defects formed in grain interiors during irradiation, such as dislocation loops and voids, were examined for PCA irradiated at 420°C in FFTF/MOTA.[9] Both dislocation loops and voids were found to be depleted in chromium. The pitting-type etching on grain faces observed in this study may be attributed to such RIS to defects. As shown in Fig. 4, the density of the etching on grain faces increased and the attack became more severe with increasing irradiation temperature. This temperature dependence supports the mechanism of the localized sensitization by RIS where the degree of chromium depletion is determined by mobility of vacancies and interstitials. Grain boundary sensitization was not observed at temperatures of 330°C and below, which indicates that chromium depletion at grain boundaries by RIS was less than that in defects in grain interiors at lower temperatures. This may be explained by shorter diffusion distance of vacancies and interstitials to defects in grain interiors rather than to grain boundaries. The effect of the difference in diffusion distance could be pronounced at lower temperatures due to decreased mobility of vacancies and interstitials.

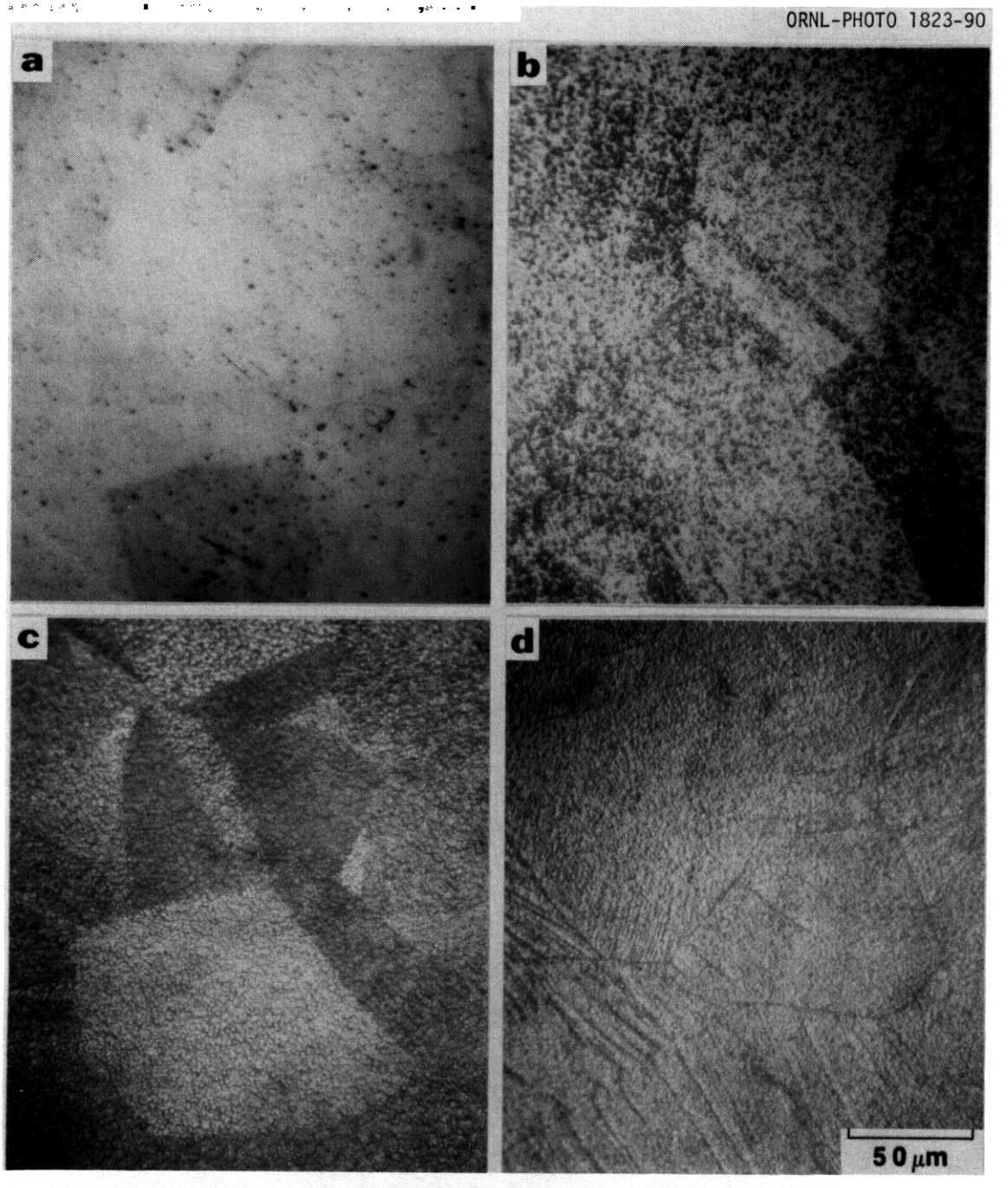

Fig. 3. Optical micrographs of irradiated PCA after EPR testing. Specimens were irradiated at (a) 60°C; (b) 200°C; (c) 330°C; (d) 400°C.

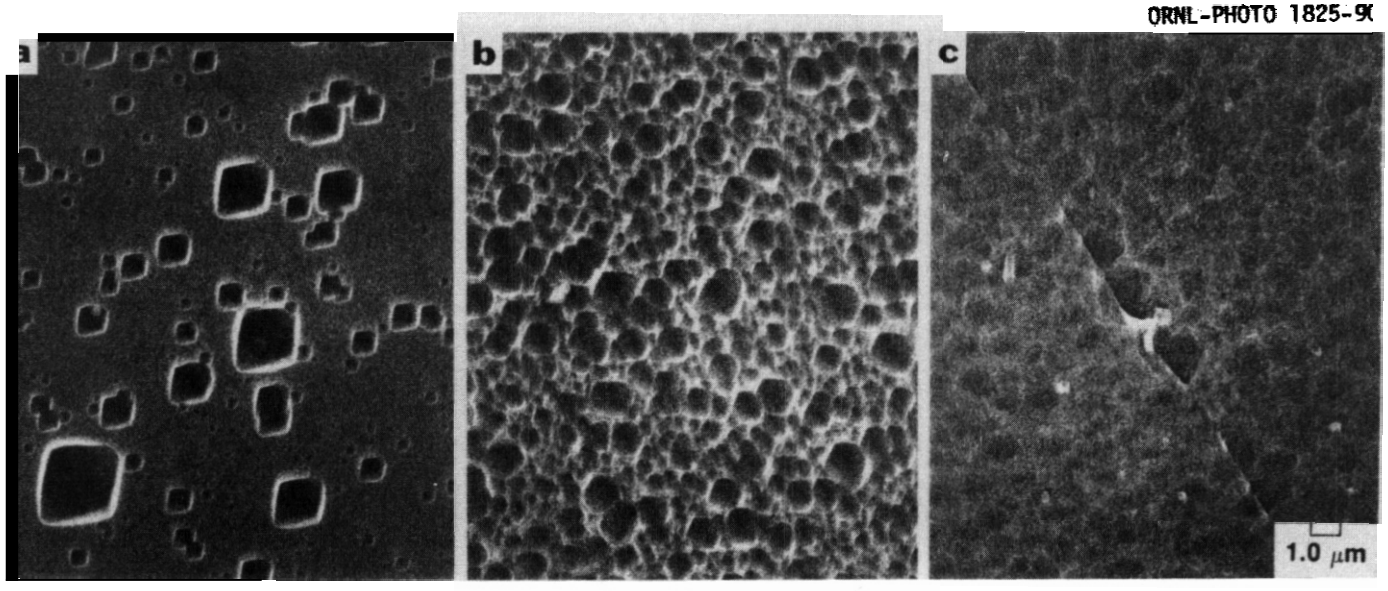

Fig. 4. SEM micrographs of irradiated PCA after EPR testing. Specimens were irradiated at (a) 200°C; (b) 330°C; (c) 400°C.

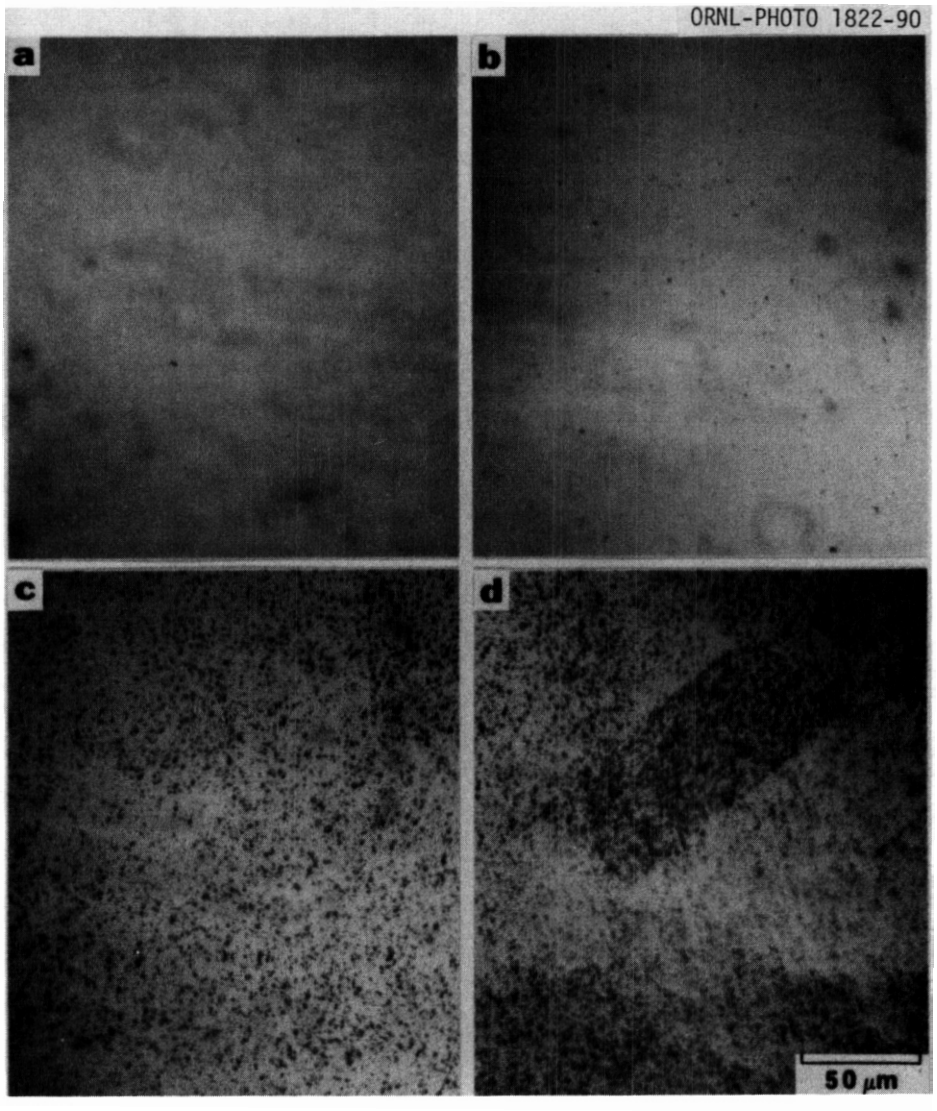

Fig. 5. Optical micrographs of PCA irradiated at 200°C. EPR testing was interrupted at (a) Flade potentfal; (b) 1/2 peak; (c) peak; (d) –100 mV from peak.

Figure 6 shows the comparison of the reactivation curves (scan rate = 6 V/h) of PCA from this spectrally tailored experiment in ORR (400°C, 7 dpa, 1.8 × 10^{-7} dpa/s, He:dpa:14) and from the irradiation in FFTF/MOTA (420°C, 9 dpa, 9 × 10^{-7} dpa/s, He:dpa:0.4). The specimens from both irradiation conditions showed similar reactivation curves. Although the Flade potential was higher for the specimen from FFTF, the degree of sensitization can be considered to be similar for both irradiation conditions. The definitive answer for the effect of each irradiation parameter is not yet possible from this comparison. However, since the difference in dose rate may compensate the difference in temperature[4] and RIS saturates between 5 to 10 dpa (ref. 10), this comparison may reflect the difference in He:dpa ratio. Therefore, the similar reactivation behavior in both irradiation conditions suggests that He:dpa ratio does not strongly affect the radiation-induced sensitization of this material.

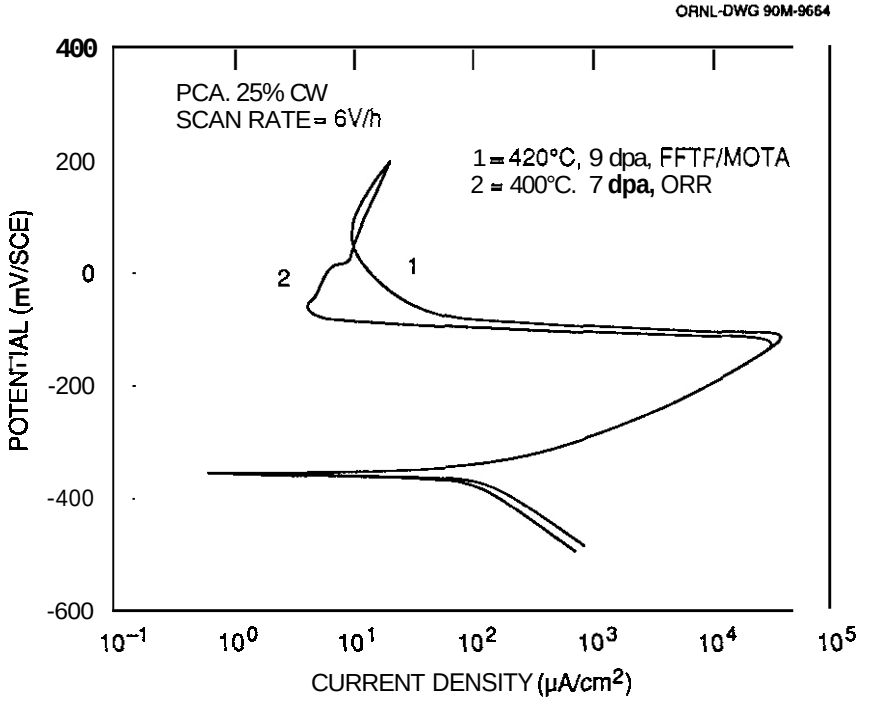

Fig. 6. Comparison of reactivation curves in different irradiation conditions.

Conclusions

The degree of radiation-induced sensitization in 25% cold-worked PCA irradiated at 60 to 400°C to 7 dpa under spectrally tailored conditions in ORR-MFE 65/75 was evaluated by the EPR test technique using miniaturized specimens. The following conclusions were obtained.

1. The irradiation at 60°C up to 7 dpa did not affect the electrochemical properties of PCA as measured by the EPR test technique.
2. The reactivation charge was increased by the irradiation at 200 to 400°C as compared with that of the unirradiated specimen.
3. The reactivation charge increased with increasing irradiation temperature.
4. Grain boundary sensitization was observed for the specimen irradiated at 400°C, which may lead to increased susceptibility of PCA to IGSCC.
5. Localized attack of grain faces was observed far the specimens irradiated at 200 to 400°C after EPR testing, which suggested the occurrence of localized sensitization in grain interiors.

FUTURE WORK

Fundamental electrochemical measurements will be carried out to examine the possible effects of the localized sensitization in grain interiors on the corrosion behavior of PCA. EPR measurements will be continued on alloys with different compositions to evaluate the effects of alloy composition on susceptibility to radiation-induced sensitization.

REFERENCES

1. T. Inazumi and G.E.C. Bell, Fusion Reactor Materials (Semiannual Progress Report), DOE/ER-0313/7, Office of Fusion Energy (September 1989), pp. 235–41.
2. T. Inazumi, G.E.C. Bell, E. A. Kenik, and K. Kiuchi, Corrosion (to be published).
3. U.S. ITER Nuclear Group, ITER and Blanket Work Package Report, ANL/FPP/88-1, 1988.
4. P. R. Okamoto and L. E. Rehn, J. Nucl. Mater. 83 (1979) 2–23.
5. S. Ohnuki, H. Takahashi, and R. Nagasaki, J. Nucl. Mater. 155–157 (1988) 823–27.
6. L. R. Greenwood, Fusion Reactor Materials (Semiannual Progress Report), DOE/ER-0313/6, Office of Fusion Energy (March 1989), pp. 23–25.
7. T. Inazumi and G.E.C. Bell, Fusion Reactor Materials (Semiannual Progress Report), DOE/ER-0313/6, Office of Fusion Energy (March 1989), pp. 373–77.
8. T. Inazumi, G.E.C. Bell, and K. Kiuchi, J. Nucl. Mater. (Proceedings of ICFRM-4, Kyoto, Japan), to be published.
9. E. A. Kenik, T. Inazumi. and G.E.C. Bell, J. Nucl. Mater. (to be submitted).
10. J. M. Perks, A. D. Marwick, and C. A. English, Radiation-Induced Sensitization of Stainless Steels (Proc. of Symp. held at Berkeley Nuclear Laboratories, Sept. 23, 1986), CEGB, 1987, pp. 15–34.

7. SOLID BREEDING MATERIALS

The FU8R-1B Irradiation Experiment - Tritium Release and Physical Stability of Solid Breeder Materials

O. D. Slagle, G.W. Hollenberg, and D.L. Baldwin, Pacific Northwest Laboratory(a)

OBJECTIVE

The purpose of this work is to evaluate the performance of candidate ceramic breeding materials for use in a fusion blanket. This evaluation is specifically aimed at characterizing the behavior of materials in a neutron flux.

SUMMARY

The FU8R-18 irradiation experiment in E8R-II has provided important information on the irradiation behavior of candidate lithium solid breeder materials in a high energy neutron spectrum. The solid breeder materials include Li_2O, $LiAlO_2$, Li_2ZrO_3, Li_8ZrO_6 and Li_4SiO_4 pellets and $LiAlO_2$ spheres. The irradiation behavior of the materials was characterized for the temperature range from 400 to 900°C. The amount of tritium retained by the solid breeder materials, as well as sweiling and physical stability, was determined for specimens removed after the first period of irradiation.

$LiAlO_2$, Li_2ZrO_3, and Li_8ZrO_6 exhibited excellent dimensional stability during irradiation while the dimensional stability of Li_2O was found be dependent on the microstructure. The amount of retained tritium is compared to similar closed capsule experiments and extends the data to burnups as high as 1.6 X 10^{21} at/cc.

PROGRESS AND STATUS

Introduction

The FU8R-18 high fluence irradiation experiment of solid breeder materials has completed the first period of irradiation in the E8R-II Reactor. The purpose of the experiment was to evaluate the performance of candidate solid breeder materials for use in a fusion blanket.[1] Describing the irradiation behavior of a solid breeder during operation involves the release of tritium, the change in chemical properties that affect the release of tritium, and the physical stability of the solid breeder itself.

There were two primary objectives of the FUBR-1B experiment: 1) characterize the irradiation behavior of a number of solid breeder materials with different microstructures in the temperature range of from 400 to 900°C and 2) define the behavior of large diameter pellets of solid breeder materials with the associated large temperature gradients. The primary purpose of this paper is to present the observations and measurements made on the small diameter solid breeder specimens which provide data on the effect of microstructure on the irradiation behavior. The as-irradiated physical condition, dimensional changes, and lithium transport observations made on the large diameter specimen have been described by Slagle and Hollenberg.[2]

Experiment Design

The irradiation was carried out in the E8R-II reactor, and the specimen design has been described previously.[1] Specimen columns were 1 cm in diameter and consisted of 4 pellets with a total length of 5 cm. The design temperatures were 450, 650 and 850°C. A cerium getter tab in the plenum of each subcapsule reduced tritiated water to tritium and hence facilitate the diffusion of tritium out of the stainless steel subcapsule.

The first insertion of the FU8R-18 experiment was removed from the reactor after 341.5 EFPD. A description of the solid breeder pellets and the irradiation temperatures is given in Table 1. Three different types of Li_2O pellets were studied. Type 1 is a low density variation of the Type 2 or reference microstructure, while Type 3 is a large grain variation of the reference microstructure. Also included in the pellet matrix were large grained $LiAlO_2$, Li_8ZrO_6, Li_2ZrO_3, and Li_4SiO_4, and two subcapsules without getter tabs containing a Type 2 - Li_2O and small grain $LiAlO_2$. In addition to the pellet specimens one subcapsule contained 35 micron diameter spheres of $LiAlO_2$.

ExDerimental Results

After irradiation, the pins were neutron radiographed, the diameter of the sample region characterized by profilometry, and the plenum gas analyzed. No measurable distortion of the capsule wall was found. In

---

(a) Pacific Northwest Laboratory is operated for the U.S. Department of Energy by Battelle Memorial Institute under Contract DE-AC06-76RLO 1830.

Table 1.

Grain Size, Density and Irradiation Temperature of the Pellets in the FUBR-1B First Insertion. Those specimens irradiated in capsules with no getter tabs are designated as (NG).

Specimen Type	Density	Grain Size (microns)	Irradiation Temperature (°C)
Li_2O			
Type 1 (Low density)	60	4	420,360(NG),800
Type 2 (Reference)	80	4	420,360,820
Type 3 (Large grain)	82	80	420.820
$LiAlO_2$			
Large grain	80	35	820(2)
Small grain	78	<<I	420(NG)
Li_2ZrO_3	87	2	550
Li_8ZrO_6	80	3	610
Li_4SiO_4	79	2	450

those capsules containing getter tabs, the remaining tritium was less than a factor of 10^{-8} of the total tritium produced, thus confirming the efficiency of the getter design.'

The goal burnup for the ^6Li in the solid breeders was 4%. The burnup was determined from the amount of helium released to the plenum. The average burnup was determined to be 4.4 ± 1.8%. Variations in fractional burnups are attributed to the axial position of the subcapsule in the pin and position of the pin relative to the core center.

The specimens were removed from the subcapsule, and the ease with which this was effected was an indication of the swelling/interaction of the specimen with the capsule. The $LiAlO_2$, Li_8ZrO_6, and Li_2ZrO_3 specimens, and two Li O specimens fell out of the cladding intact. The Li_2O specimens which fell out were the Type 2 specimens frradiated at 630 and 820°C. The LiAlO spheres irradiated at 650°C were dark brown and poured freely from the capsule. The Li_4SiO_4 pellets felf out but were fragmented. The remaining Li_2O, along with the $LiAlO_2$ with no getter, were firmly wedged in the cladding, and the cladding had to be slit to remove them.

The diametral changes occurring during irradiation for the three different types of Li_2O pellets are given in Table 2. In most cases, whole pellets were not available to obtain length measurements. In general, all of the specimens increased in diameter during irradiation except for the Type 2, reference specimen, irradiated at 820°C. It is to be noted that the two specimens with the least swelling, Type 2 at 630 and 820°C, are also the only Li_2O specimens that fell out of the clad.

Figure 1 is a comparison of the postirradiation condition of the Li_2O ,specimens listed in Table 2. The Type 2 and 3 specimens irradiated at 420°C have a dark inner core, while the Type 1 specimen irradiated at the same temperature does not. At an irradiation temperature of 630°C, the dark inner core does not occur for the Type 2 specimen, while at highest irradiation temperature of 820°C this dark inner core does not occur for any of the Li_2O specimens.

$LiAlO_2$, Li_8ZrO_6, and Li_2ZrO_3 were dimensionally stable during the irradiation and decreased in the range from 0.0 to 0.25% for all dimensions. This substantiates the previous observations at lower burnups of on the dimensional stability of $LiAlO_2$ and Li_2ZrO_3 reported by Hollenberg.[3] No dimensional measurements were made on the Li_4SiO_4 specimens because these pellets did not survive the irradiation intact.

Two subcapsules were irradiated without getter tabs. One subcapsule contained Li_2O irradiated at 630°C and the other contained LiAlO, irradiated at 420°C. The Li_2O pellets have an outer ring of black discoloration, similar to the center discoloration seen in the pellets in Figure 1. The pellets had decreased in length or "hot pressed" during the irradiation to give density increases in the range of 3-11%. The $LiAlO_2$ specimens were removed as fragments after irradiation. These specimens had a dark inner core similar to that found in the Type 2 and 3 LiO_2 irradiated at 420°C.

Table 2.

Percent Diametral Changes in the Three Types of Li_2O at the Different Irradiation Temperatures

	Irradiation Temperature (°C)		
	420	630	820
Type 1	2.80%		2.58%
Type 2	3.86%	2.52%	-1.98%
Type 3	3.95%		3.90%

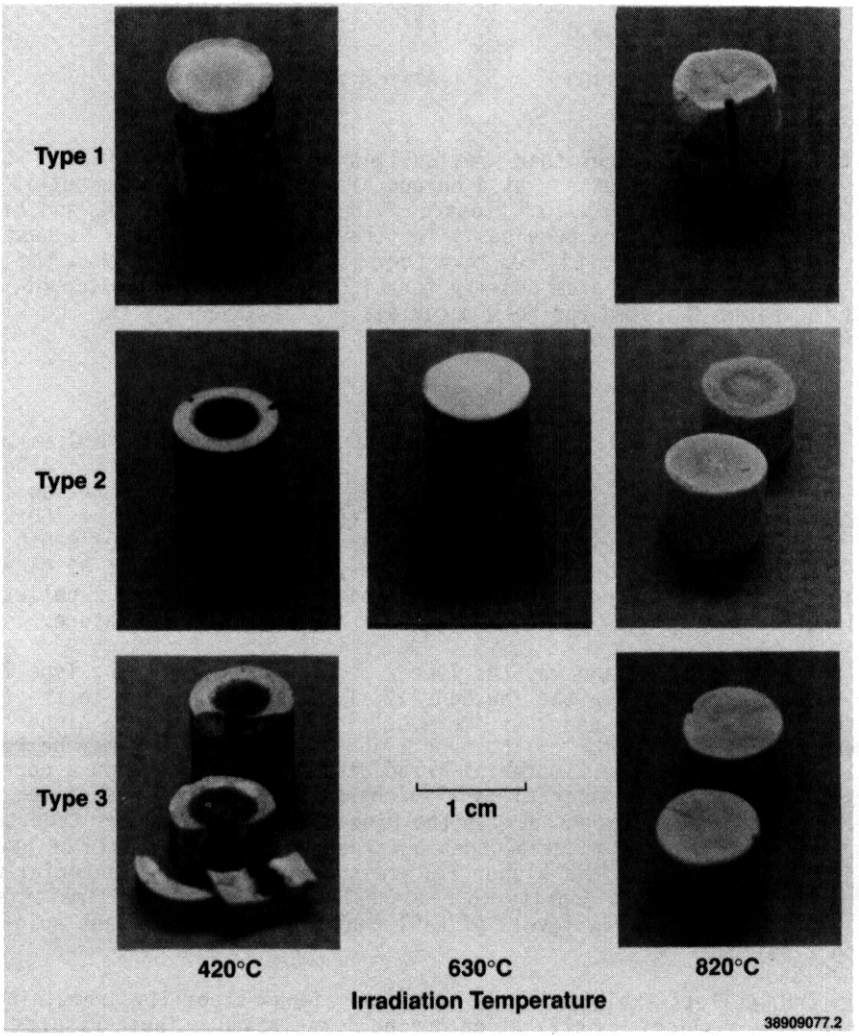

FIGURE 1. As-Irradiated Li_2O Pellets as a Function of Microstructure (Type 1, 2 and 3) and Irradiation Temperature

The amount of retained tritium was determined for selected specimens using the method described previously by Baldwin and Hollenberg.[4] The results are given in Table 3 along with the calculated burnups. The amounts of tritium retained are given both in the form of percent of the total generated and as atoms/cc retained.

Tritium retention data for the previous closed capsule experiments have indicated that the retained tritium, in terms of at/cc, increases with increasing burnup and decreases with increasing temperature.[1] The

Table 3.

Results of Retained Tritium in FUBR-1B Specimens. (1) and (2) denote type of Li_2O.

Material	Irrad. Temp.	Burnup (10^{21}) (at/cc)	Retained Tritium (%)	Retained Tritium (10^{19}) (at/cc)
$Li_2O(1)$	800	1.35	0.3	0.41
$Li_2O(2)$	820	1.61	0.33	0.53
$LiAlO_2$	820	1.02	2.0	2.04
Li_2ZrO_3	550	1.4	0.64	0.90
Li_8ZrO_6	610	1.27	1.22	1.55
Li_4SiO_4	450	1.67	7.02	11.72

present data are for burnups which are larger than previously reported. The retained tritium for Li_2O is less than that found for comoarable temperatures at a burnup of 1.1 x 10^{20} atoms/cc but is in good agreement with that found for the lower burnup of 0.4 x 10^{20} atoms/cc. The results for $LiAlO_2$ and Li_2ZrO_3 are equivalent to the tritium retention reported previously for these materials at the highest burnups of 0.5 and 0.95 x 10^{20} atoms/cc, respectively.. The Li_8ZrO_6 fnventory is somewhat larger than-the previous Li_2ZrO_3 inventory. However, if the higher lithium atom density for Li_8ZrO_6 is taken into account, then the retained tritium per lithium atom is nearly the same for both materials. The inventory for the Li_4SiO_4 is nearly identical to the inventory found at the lower burnup.

Discussion

The dimensional changes for Li_2O given in Table 2 indicate that the decrease in the diameters for the Type 2 pellets irradiated to 820°C, is in contrast to the increase or swelling found for the other specimens. This difference in dimensional change can possibly be related to the microstructure of the as-irradiated pellets. The Type 1 and 2 pellets were hot pressed to the desired density at a temperature of 700°C, with little grain growth. The Type 3 pellets were fabricated by cold pressing and sintering at 800°C. Grain growth was induced by introducing LiOH into the starting powder to give a final grain size of 80 microns. Because of their relatively low fabrication temperature and small grain size, the Type 1 and 2 pellets would be more likely to undergo additional sintering when heated above their fabrication temperature.

There is the additional problem of explaining why the Type 2 pellet shrinks and the Type 1 does not. One possible explanation is that the porosity in the low density, Type 1, material is in the form of larger, more stable pores than the type 2 material and thus, more difficult to sinter to a higher density. Alternatively, the difference in the behavior of the type 1 and type 2 materials may be related to their difference in appearance in Figure 1. Type 2 material irradiated at 450°C has a dark core while type 1 material does not. This darker appearing material is also characteristic of the specimens irradiated with no getter where larger T_2O pressures are expected. If the higher density materials tend to retard the release of T_2O compared to the low density material then a larger T_2O pressure could be present in the center of the type 2 and type 3 pellets, This higher T_2O pressure in the type 2 material would form LiOT, a sintering aid for Li_2O,[6] and could effect a density increase relative to the type 1 material. Considering the long times involved (365 days), even low levels of LiOT could play a significant role in the densification of the Type 2 pellet.

The $LiAlO_2$, Li_8ZrO_6, and Li_2ZrO_3 pellets exhibited excellent dimensional stability, remaining intact during irradiation and undergoing only a slight densification during irradiation. These results can be compared to the previous results for LiAlO and Li_2ZrO sumnarized by Hollenberg.[1] As found in the present experiment, Li_2ZrO_3 had previously remained intact at temperatures from 500 to 900°C. The present observation of the 80% TD $LiAlO_2$ specimens remaining intact differs from the previous results, where lower density $LiAlO_2$ specimens irradiated above 700°C fragmented during irradiation. The primary difference is that the previous specimens had a grain size less than 1 micron while the present specimens have a grain size of 35 microns. Typically finer grain size results in higher strength so that the reduction in grain size, by itself, does not explain the difference in behavior. Determining the difference in behavior will require a more extensive characterization of the microstructures.

CONCLUSIONS

The results of the FUBR-1B irradiation give additional insight into the irradiation behavior of a variety of solid breeder materials irradiated to burnup values as high as 1.9 x 10^{21} at/cc. The following are the primary conclusions:

1. $LiAlO_2$ and Li_2ZrO were dimensionally stable at the higher burnups, reaffirming the results found at lower burnups. In addition, Li_8ZrO_6, which had not previously been characterized with respect to its irradiation behavior, was also Bound to be dimensionally stable.

2. The tritium inventory for Li_2O at the higher burnups was lower than expected, while the inventory for both $LiAlO_2$ and Li_2ZrO_3 are in good agreement with previous data. Li_8ZrO_6, although having a slightly larger inventory than Li_2ZrO_3, appears to be a viable breeder candidate.

3. The microstructure of Li_2O can play a major role in the tritium release behavior. This is particularly evident in the appearance of the material at temperatures from 400-600°C. However, the interdependence of tritium release and microstructure can also influence the dimensional stability at higher temperatures.

FUTURE WORK

Work will continue on obtaining tritium retention data for the reminder of the small diameter specimens. Microstructural characterization of these specimens is also planned to further define the differences between the outer lighter colored regions and the center darker core regions.

REFERENCES

1. G. W. Hollenberg, R. C. Knight, P. J. Densley, L. A. Pember, C. E. Johnson, R. B. Poeppel and L. Yang, J Nucl Mater 141-143 (1986) 271-274.

2. O. D. Slagle and G. W. Hollenberg, presented at the American Ceramic Society Meeting, Indianapolis, Ind, April 24-25, 1989, PNC-SA-16870.

3. G. W. Hollenberg, in Advances in Ceramics, Vol 25 edited by I. J. Hastings and G. W. Hollenberg, The American Ceramic Soc, Westerville, Ohio, 1989.

4. D. L. Baldwin and G. W. Hollenberg, J Nucl Mater 141-143 (1986) 305.

5. G. W. Hollenberg and D. L. Baldwin, J Nucl Mater 133-134 (1985), 242-245.

6. D. S. Applegate and R. B. Poeppel, in Advances in Ceramics, Vol 25 edited by I. J. Hastings and G. W. Hollenberg, The American Ceramic Soc, Westerville, Ohio, 1989.

DESORPTION CHARACTERISTICS OF THE $LiAlO_2$-H_2-H_2O (g) SYSTEM - A. K. Fischer and C. E. Johnson (Argonne National Laboratory)

OBJECTIVE

The objective is to describe the kinetics of desorption of H_2O (g) and H_2 from the surface of ceramic tritium breeders with data that allow the characteristics of tritium release to be predicted by designers and modelers.

SUMMARY

Temperature programed desorption (TPD) measurements have started on the $LiAlO_2$-H_2 system. The sensitivity of the mass spectrometer that will detect the peaks was shown to be adequate for the measurements. Blank experiments to characterize the behavior of the stainless steel sample tube in the measurements have revealed the evolution of N_2 from the steel, a process facilitated by H_2. It is necessary to stabilize the sample tube so that it does not augment or distort the TPD peaks. The behavior of an unstabillzed tube was demonstrated by means of a simulated TPD run. Stabilization consists of treating the tube with 990 ppm H_2 in helium at high temperature until undistorted simulated TPD runs are obtained. A $LiAlO_2$ sample was loaded in the apparatus: it came from the same batch of material that was used in an EXOTIC test. Prolonged drying of the sample in a He-H_2 stream is necessary, a finding that has important implications for many earlier reports on measurements of tritium release from irradiated samples where it was not demonstrated that the sample was adequately dry or that the apparatus did not affect the data.

PROGRESS AND STATUS

Introduction

Temperature programed desorption (TPD) is a wel1-developed technique for providing data that describe the energetics and kinetics of desorption of gases from the surfaces of solids.[1] The TPD spectra also provide more qualitative comparisons of the release of adsorbates under different conditions. In the fusion power program, the interest centers on the evolution of H20 (g) and H_2 (g) from ceramic tritium breeders.

In the previous report, rough TPD spectra for the $LiAlO_2$-H_2O system were presented: these were derived from what were essentially shakedorn runs for the then-new apparatus. Since then, because programmatic interest is strong for data to understand the behavior of H_2 with breeders, the effort was shifted to provide data for the $LiAlO_2$-H_2 system. In the earlier work on the TPD of H_2O, it was demonstrated that spurious and distorted peaks in the TPD spectra could be introduced by interactions of the stainless steel tubing holding the sample with both H_2 and H_2O (g). It was necessary, therefore, to determine conditions for stabilizing the tube walls for the TPD of H_2. Without these blank experiments, subsequently measured TPD curves would be of questionable validity.

Sensitivity Determinations

In the course of the demonstration of tube stability, measurements were made of the sensitivity of the mass spectrometer detector system for H_2 TPD peaks. Readings for successive dilutions of H_2 in helium indicated that a gas containing approximately 7 vppm H_2 could be distinguished easily from the baseline. Simultaneous mass spectrometer readings and electrolytic trace moisture monitor readings indicated that H_2O peaks at the tenths of 1 vppm level are detectable. These sensitivities are expected to be adequate for the needed measurements.

Detection of Gaseous N_2

A new finding from the blank experiments with the empty sample tube is that a gaseous species of 26 amu appears, especially when H_2 is present. It was shown that this species corresponds to N_2 and that it probably originates in the steel of the sample tube: it is not an impurity in the gases nor does it come from an air leak. It is known that release of nitrogen from iron (denitriding) is much more rapid if the gas phase contains H_2 than if it does not.[2] The observed behavior is consistent with this background.

The significance of the nitrogen for the desorption of H_2 and H_2O from a ceramic breeder is that it is possibly a coadsorbent, but the effect of this is not yet clear. In the empty tube experiments, the N_2 appears at levels that are comparable to the level of evolved H_2O. As the measurements with $LiAlO_2$ continue, it will be important to look for correlations between TPD peaks and the N_2 levels. It is possible that there might be a connection with an unpublished report claiming apparently good release of tritium with a purge gas passed through hot titanium, though at the moment it appears reasonable that those observations reflected the effects of unsuspected additions of hydrogen, though nitrogen could have been involved, too.

Work supported by the U.S. Department of Energy, Office of Fusion Energy, under contract Y-31-109-Eng-38,

Stabilization of Stainless Steel Tube for TPD Measurements

In the present measurements of the TPD of H_2 from $LiAlO_2$, pure helium will be passed through the $LiAlO_2$ sample while the temperature rises linearly with time. The sample will have been equilibrated immediately before with a known partial pressure of H_2. If H_2 adsorbs on $LiAlO_2$, the desorption steps will consist of increments of H_2 coming off the sample and passing through the sample tube and apparatus tubing to the mass spectrometer for detection. It is important to establish that there are no or negligible interactions between the H_2 and the tubing, or that they can be compensated for. One approach is to treat the tube with the $He-H_2$ mixture to the point where subsequently a pulse of H_2 in pure helium will pass unaffected. In this condition, the tube is said to be stabilized. In order to test the effectiveness of the stabilization process, a series of simulated TPD runs with the empty tube was performed. In such a run, a series of TPD peaks was simulated by introducing into the system a square wave spike of 5 min duration of He-990 ppm H_2 every 100°C at temperatures from 200 to 700°C; the temperature ramp rate was 5.5°C/min.

In Figure 1, the traces for H_2 and H_2O are shown, together with the temperature ramp, for an unstabilized tube. The tube was treated with pure helium at 200°C overnight. The 200, 300, 400, and 500°C spikes show a fairly gradual upward trend for H_2. However, the distinctly higher H_2 spikes for 600 and 700°C show the effect of interactions that augment the H_2 level. The reason is suggested by the H_2O trace which is assumed to originate from reduction of surface oxide by H_2 and from the recombination of adsorbed OH groups. After a decline from the level of H_2O in the 200°C spike, the H_2O level was essentially constant for the 300, 400, and 500°C spikes. The increase at 600°C suggests that the migration of surface OH leading to recombination and evolution of H_2O as well as its reduction by the steel, yielding H_2, is increasingly activated at higher temperatures. Figure 2 shows the simultaneous N_2 trace: this gas is being evolved at essentially the same level during the spikes and at an enhanced rate compared to the rate with pure helium.

After several treatments and TPD simulations, a final one was performed. Here, 990 ppm H_2 in helium was passed through the tube at 667°C overnight. The simulated TPO spectrum is shown in Figure 3. The spikes for H_2 and H_2O are nearly uniform in height, though increasing a little at higher temperature. Reduction of oxide to H_2O is still going on when H_2 is introduced. The readings from the electrolytic water analyzer were low, reaching approximately 1 ppm at the peaks and dropping as low as 0.2 ppm. Though the tube is not ideally stable, the present state will be taken to represent a practical and provisional level of stabilization toward H_2 spikes up to a temperature of approximately 660°C. When the tube is loaded with

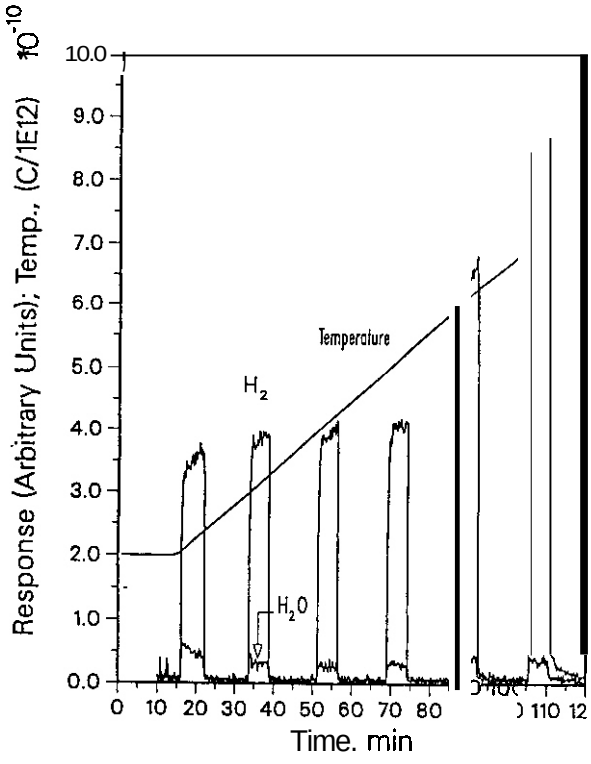

Figure 1. Simulated TPO spectrum for unstabilized stainless steel sample tube without a sample. Gas phase alternates between pure helium and helium with 990 ppm H_2. Evolved H_2O is shown.

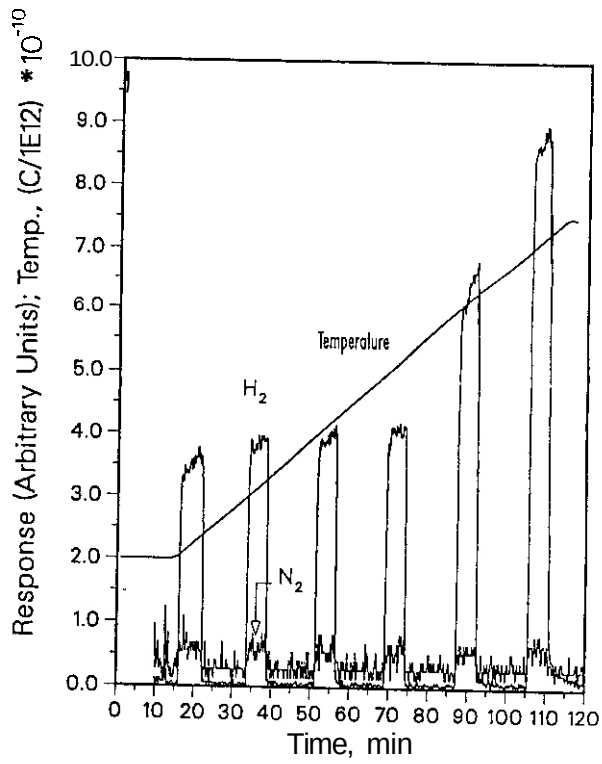

Figure 2. Simulated TPD spectrum same as for Figure 1 but showing level of evolved N_2.

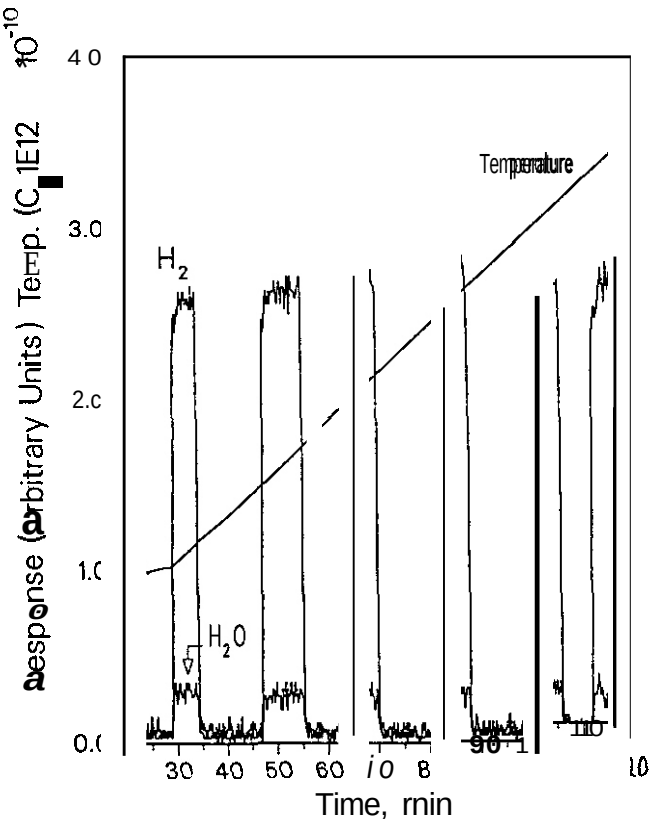

Figure 3. Simulated TPO spectrum for a stabilized stainless steel tube. H_2O level is shown.

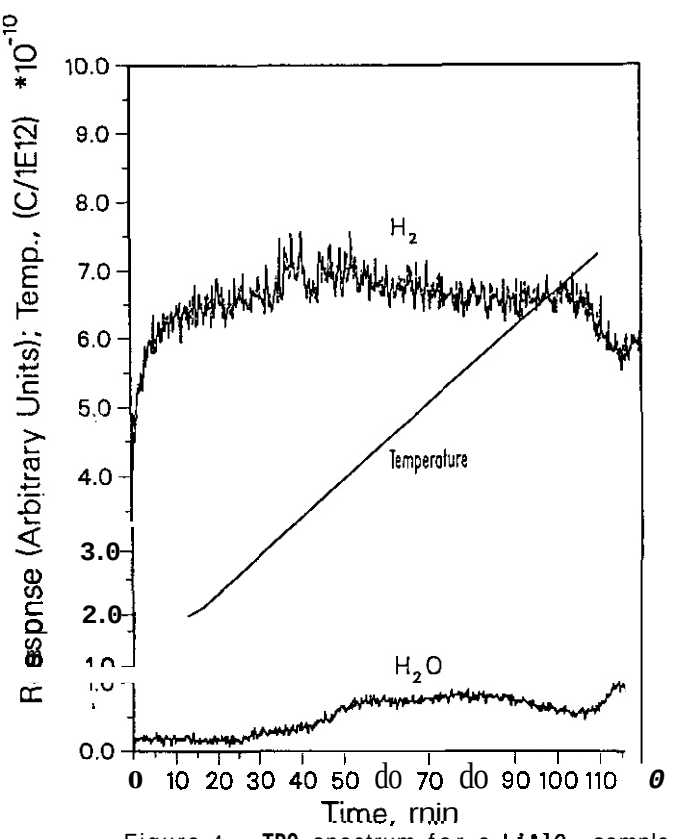

Figure 4. TPO spectrum for a $LiAlO_2$ sample that is incompletely dry. Gas phase supplied to the sample is helium with 990 ppm H_2.

sample, treatment with H_2 will be repeated until reproducible TPD spectra are obtained, at which time it will be assumed that a condition of tube stability will again have been achieved. The appearance of the peaks relative to these simulated ones will also affect how much correction to consider.

TPD Measurements on $LiAlO_2$-H_2

The same sample tube that was used for the above blank and stabilization experiments was loaded with 0.52 g of $LiAlO_2$ that was prepared at Saclay, France. This material is a portion of that which was supplied for the EXOTIC V experiment. In its preparation it had been sintered at 1100°C and before being bottled for the present study it was heated at 800°C for 1 hr. A drydown period was entered after the sample was loaded. During this time, the sample was first heated to 200°C in pure helium for 1.5 hr, then in 990 ppm H_2 in helium at 300°C for 65 hours. Early in the 300°C period, the water analyzer recorded 110 ppm H_2O in the evolved gas. At the end of this time, the H_2O level was down to 0.55 ppm and declined further to 0.20 ppm when the sample was cooled to 200°C in preparation for a TPO run. This TPD run was for background information on a sample known not to be very dry yet in a tube known not to be stabilized yet. The temperature ramp was programmed to run from 200 to 750°C at 5.5°C/min. The result is shown in Figure 4. Considerable diffuse evolution of H_2O is still continuing, on an overall level at approximately 30 ppm. Between approximately 650 and 700°C, the H_2O evolution declines before rising again. This is like the extensive H_2O evolution that was observed earlier in the work on adsorption and desorption of H_2O. The H_2 trace being higher than it would be for the 990 ppm H_2 alone shows the effects of the reaction of the considerable amount of residual H_2O with the steel. At this stage, of course, part of the evolved water can also originate from oxide on the steel. No CO_2 was detected in the evolved gases so that the Saclay material appears to be free of carbonate.

An important though probably unpopular comment to make from this observation of extensive evolution of H_2O from material that is "dry" by everyday standards is that reports of tritium release measurements from irradiated samples often do not indicate that the samples were dried even as well as this one was, and which still is not dry enough to produce reproducible TPO, i.e., kinetic data. Nor has the stability of the apparatus been demonstrated in published reports. For example, in one case it was stated that the samples were stored in air before and after irradiation with no indication of steps to clean the sample. Yet. reports abound with bewildering comparisons of tritium release performance, i.e., the kinetics of release, when what must be addressed for a sound basis for comparison is not only the condition of the sample, but also the impact from the tubing of the apparatus which often is much more extensive than that in the apparatus for the present study. It has come to our attention that M. Briec at Grenoble has started to consider the possible rule of line effects in some of the irradiation work done there.

FUTURE WORK

After completion of experimental measurements and analysis of the data on the desorption of H_2 from $LiAlO_2$, measurements of desorption of H_2 from Li_2ZrO_3 will start. Further elucidation of the behavior of hydrogen isotope species will be gained by measurements of the effect of protium on desorption of deuterium: with the mass spectrometric detection system, this will require a change to argon as the sweep gas so that interference can be avoided from helium at 4 amu, where D_2 would also appear.

REFERENCES

1. J. L. Falconer and J. A. Schwarz, "Temperature--Programmed Desorption and Reaction: Applications to Supported Catalysts," Catal. Rev. - Sci. Eng., 25 (1983) 141.

2. J. D. Fast, "Interaction of Metals and Gases," Vol. 2, pp. 236 ff.

8. CERAMICS

HELIUM-ASSISTED CAVITY FORMATION IN ION-IRRADIATED CERAMICS — S. J. Zinkle (Oak Ridge National Laboratory) and S. Kojima (Nagoya University, Nagoya, Japan)

OBJECTIVE

To examine the microstructural changes in ceramic insulators following irradiation at fusion-relevant He/dpa levels.

SUMMARY

Polycrystalline specimens of spinel ($MgAl_2O_4$) and alumina (Al_2O_3) were irradiated at room temperature and 650°C with either dual- or triple-ion beams in order to investigate the effects of simultaneous displacement damage and helium implantation on cavity formation. The cavities in alumina were aligned along the direction of the c-axis, with diameters ranging from <2 to 10 nm. The cavities in spinel were preferentially associated with dislocation loops and were of similar size as the cavities in alumina. Catastrophic amounts of cavitation were observed at the grain boundaries in spinel when the displacement damage level exceeded a critical value (~20 dpa) in the presence of a fusion-relevant (~60 appm/dpa) helium environment.

PROGRESS AND STATUS

Introduction

There has been a number of studies on the microstructural changes associated with particle irradiation of ceramics.[1-13] However, there is only a limited amount of information available at conditions relevant for fusion reactors,[5-7] where both displacement damage and helium gas generation will occur. The high energy neutrons associated with fusion reactors produce large quantities of helium and hydrogen in low-Z ceramic materials compared to fission neutron irradiations. For example, the helium generation rates per unit damage in Al_2O_3 at a fusion reactor first wall and in a fission reactor have been calculated to be 60 and 5 appm/dpa, respectively.[14]

2. EXPERIMENTAL DETAILS

Stoichiometric polycrystalline (30 μm grain size) specimens of alpha-alumina and spinel ($MgAl_2O_4$) were obtained from GE Lucalox and Ceradyne, Inc., respectively. The alumina contained 0.25 wt % MgO as a sintering aid and the major chemical impurities (wt ppm) in spinel were: Li (1000), Fe (200), Ga (70), Ca (60), and Si (30). Mechanically polished specimens were simultaneously irradiated with helium and heavy ions using procedures that are described in detail elsewhere.[10] In all cases, the helium implantations were performed using a $^4He^+$ beam that was continuously ramped in energy between 200 and 400 keV to produce a uniform helium concentration at depths between 0.5 and 1.0 μm. The spinel specimens were simultaneously irradiated with He^+ and 2.0 MeV Al^+ beams. The Al_2O_3 specimens were simultaneously irradiated with He^+, 2.0 MeV Al, and 1.44 MeV O^+ beams. The calculated EDEP-1 (ref. 15) ion ranges for these conditions are 1.30 μm for the Al^+ beam in spinel, and 1.18 μm for both the O^+ and Al^+ beams in Al_2O_3. Previous studies have shown that the actual ion ranges in these two ceramics are ~15% higher than the calculated values.[7,12]

Table 1 summarizes the experimental conditions for the transmission electron microscope (TEM) specimens irradiated in this study. The depth-dependent displacements per atom (dpa) damage levels associated with the ion irradiations were determined from EDEP-1 (ref. 15) calculations and using a displacement energy of 40 eV (refs. 10,16). The damage and helium per displacement values (He/dpa) were calculated at the center of the helium implantation region (0.7 μm depth) where the damage rate is approximately 45% that of the peak damage rate. The midrange damage flux was $\sim 1 \times 10^{-3}$ dpa/s for all of the irradiations. One of the spinel specimens (Table 1) was preimplanted with 2700 appm He and then irradiated with dual Al^+ and He^+ beams to a moderate damage level in order to study the effect of high helium concentrations in the absence of high damage levels.

Following the irradiation, each specimen was glued face-to-face to a polished spinel or alumina disk using controlled pressure in a Teflon-padded vise. The glued sandwich was sectioned, mechanically dimpled, and ion milled using a 6 kV Ar beam until perforation in order to produce a cross-section specimen suitable for TEM observation.

Table 1. Ion Irradiation Conditions for TEM Study

Material	Temperature (°C)	Helium Concentration (appm)	Midrange Damage Level (dpa)	Midrange He/dpa
$MgAl_2O_4$	650	3900	26	150
$MgAl_2O_4$	650	3700	5	730[a]
Al_2O_3	650	540	7	70
Al_2O_3	25	810	13	60
Al_2O_3	25	190	22	9

[a]Includes 2700 appm preimplanted helium concentration.

3. RESULTS

3.1 Spinel

Small cavities were observed at depths corresponding to the helium-implanted region (0.6 to 1.1 μm). As shown in Fig. 1, the cavities were preferentially associated with dislocation loops (in this case loops on $(\bar{1}11)$ and $(\bar{1}01)$ planes are shown nearly edge-on). The mean cavity diameter in the helium-implanted region was ~3 nm. The cavity density was ~1 × $10^{23}/m^3$ for the high-dose spinel specimen, and ~1 × $10^{22}/m^3$ in the low-dose specimen that was preimplanted with helium.

The grain boundaries were dramatically affected by the helium coimplantation when the midrange displacement dose was higher than a critical dose of ~20 dpa. Examples of the grain boundary cavitation are shown in Figs. 2 and 3. Extensive grain boundary cavitation is apparent from the surface to an irradiated depth of 1.5 μm. The width of the cavitation zone was ≈0.15 μm for the specimen irradiated to 26 dpa. Subsurface cracks emanating from the grain boundary cavity are also visible in Fig. 3. These cracks presumably developed during the postirradiation specimen preparation (pressure gluing stage), although it is also possible that they were initiated during the irradiation. TEM examination of grain boundaries in a specimen implanted with a comparable amount of helium but irradiated to a dose of only 5 dpa showed only limited cavitation at the boundary.

3.2 Alumina

Cavity formation was concentrated at depths of 0.2 to 1.1 μm, which is close to the helium implantation depths. Grain boundaries did not exhibit any appreciable amounts of cavity formation. The details

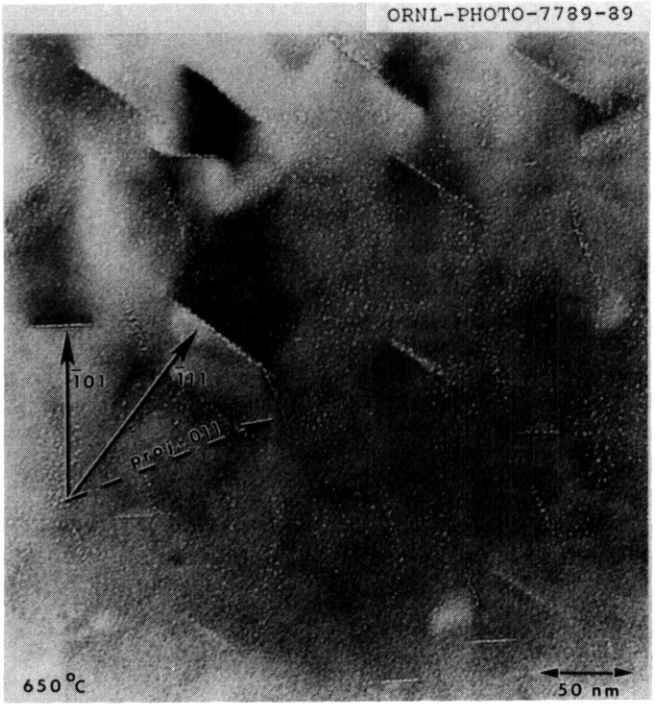

Fig. 1. Cavity microstructure in a helium-implanted region of spinel showing preferential association of cavities with dislocation loops. The specimen was irradiated at 650°C to a midrange damage level of 26 dpa and an implanted helium level of 3900 appm.

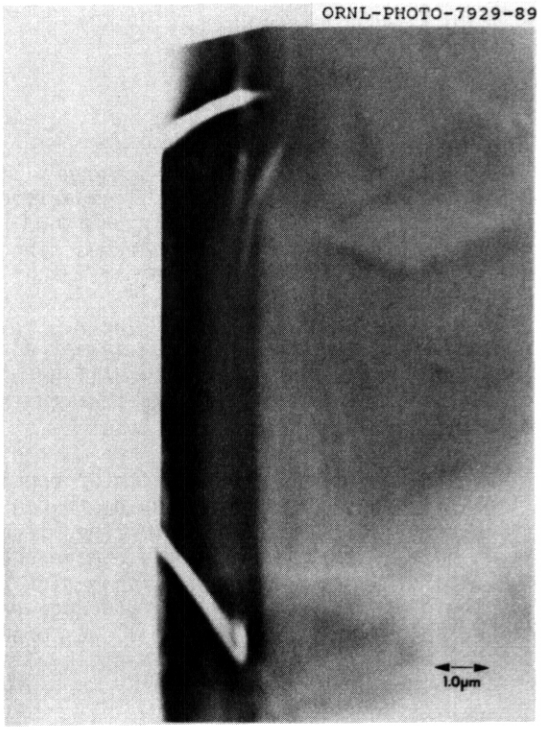

Fig. 2. Low-magnification cross-section TEM photograph showing extensive cavitation in the irradiated portion of two inclined grain boundaries in spinel (same irradiation conditions as Fig. 1).

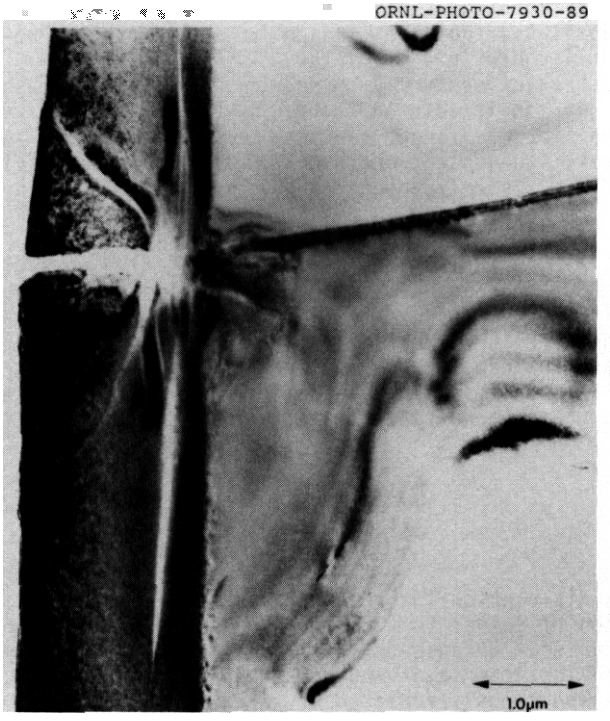

Fig. 3. Grain boundary cavitation and subsurface cracking in an irradiated spinel specimen.

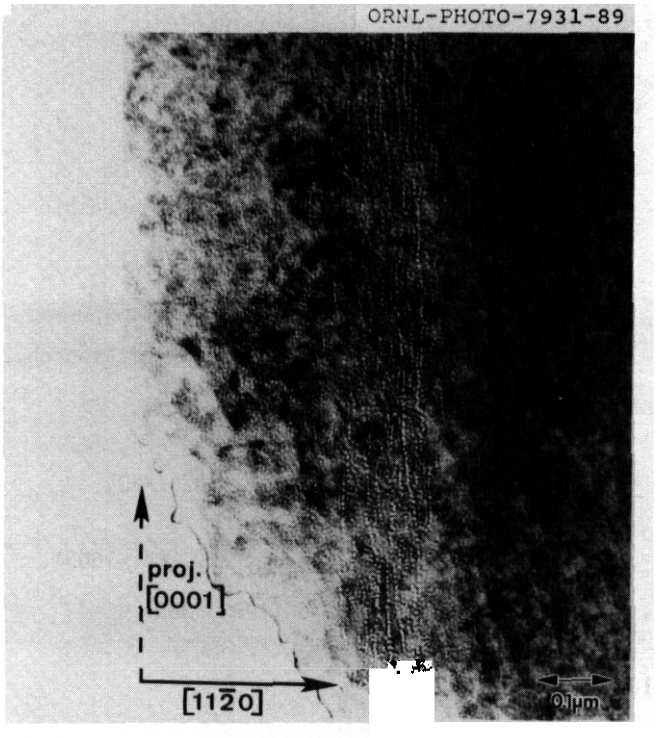

Fig. 4. Cavities aligned along the c-axis in Al_2O_3 irradiated at 25°C to a midrange damage level of 22 dpa and a helium concentration of 210 appm. The projection is tilted ~10 deg from the c-axis to show the alignment along [0001].

of the matrix cavity size and density depended on the irradiation conditions. Small cavities with a diameter <2 nm were observed throughout the cavitated region. In addition, it was generally observed that a larger sized (d ~ 5 nm) population of cavities developed in a band of ~0.25 μm width centered at a depth of ~0.9 μm. The Al_2O_3 specimen irradiated at 25°C to a midrange damage of 13 dpa (60 appm He/dpa) exhibited only the 2 nm cavity size throughout the cavitation region. The density of the "large" cavities was ~$2 \times 10^{22}/m^3$ for specimens irradiated to either 7 dpa at 650°C (70 appm He/dpa) or 22 dpa at 25°C (9 appm He/dpa). The density of "small" cavities was ~$1 \times 10^{23}/m^3$ for all irradiation conditions studied.

In agreement with previous irradiation studies,[1,4,5,8,13] the cavities in alumina were aligned along the c-axis. Figure 4 shows an example of this cavity alignment for an Al_2O_3 specimen irradiated at 25°C to a midrange damage level of 22 dpa (9 appm He/dpa). Irradiation at 650 and 25°C to 7 and 13 dpa, respectively, at He/dpa ratios of ~70 resulted in only a slight amount of cavity alignment along the c-axis. This suggests that high doses (~20 dpa) may be required at these temperatures to form an ordered void array or that the alignment process is sluggish in the presence of fusion-relevant (high) levels of helium per unit damage. Irradiation of Al_2O_3 at temperatures above 700°C produces c-axis alignment of cavities for doses as low as 1.5 dpa.[5,8]

DISCUSSION

Previous fission neutron[8,9,13] and single ion[10–12] irradiation studies of spinel have not reported any cavity formation in the grain interiors unless the irradiating ion was an inert gas." The present study shows that matrix cavity formation in spinel can be induced during irradiation if sufficient quantities of helium are present. The matrix swelling levels observed in this study ($\Delta V/V$ ~ 0.1%) are too low to be of practical engineering concern for fusion reactor applications. However, the swelling behavior under different irradiation conditions (temperature, damage rate) needs further investigation.

The grain boundaries in spinel experienced catastrophic cavitation when irradiated at a fusion-relevant He/dpa ratio (Figs. 3, 4). Grain boundary cavitation was not observed in single-ion irradiated material.[11-13] Fission neutron irradiation studies have found that planar arrays of small voids form at a distance of ~6 nm from the grain boundary following irradiation to 23 dpa at 825°C.[8,13] In the present study, spinel specimens irradiated to a dose of 5 dpa at 650°C exhibited elongated or disk-shaped cavities at a distance of ~3.5 nm on both sides of grain boundaries. These cavities presumably grow and coalesce with increasing displacement dose to produce the 0.15 μm grain boundary cavitation zone observed in the specimen irradiated to 26 dpa. This suggests that polycrystalline spinel is unacceptable for many fusion reactor applications and that single crystals must be used.

Cavity formation in A1203 was observed in specimens irradiated at both 25 and 650°C, and did not appear to be strongly influenced by a change in the He/dpa ratio from the fission to fusion rate. Previous studies have reported cavity formation in A1203 for irradiation temperatures >600°C.[2,5,6,8,13,17] The bimodal size distribution of cavities visible in the present study may be due to helium effects as suggested by Lee et al.[5] They observed "small" cavities in ion-irradiated A1203 specimens that had been either helium preimplanted or nonimplanted. An additional set of "large" cavities was only observed in specimens that had been preimplanted with helium. However, the depth range over which the bimodal cavity distribution was observed in the present study ($\Delta X \approx 0.25$ μm) is only about one-half of the calculated width for the 0.2 to 0.4 MeV He^+ implantation in Al_2O_3.

Both A1203 and $MgAl_2O_4$ exhibited similar amounts of matrix cavitation ($\Delta V/V \approx 0.1\%$) following irradiation at fusion-relevant conditions. There is no clear difference between the cavity microstructures of A1203 following irradiation at fission and fusion He/dpa rates — cavities form easily in A1203 even in a low-helium (or zero helium[5]) environment. For spinel, helium appears to play an active role in promoting cavity formation, and fusion-relevant He/dpa rates can induce catastrophic grain boundary cavitation. Due to the difficulty of matrix cavity formation in spinel, cavities are formed preferentially at structural discontinuities such as dislocation loops and grain boundaries that act as strong interstitial point defect sinks.

5. CONCLUSIONS

Cavity formation in spinel occurs preferentially at dislocation loops and grain boundaries following irradiation at fusion-relevant He/dpa ratios. Irradiation of spinel to a dose of 26 dpa at 650°C caused complete cavitation at all of the irradiated grain boundaries. Because of this effect, only single crystal specimens should be considered for fusion reactor applications involving damage levels above 1 dpa. A bimodal distribution of cavities was observed in Al_2O_3 specimens irradiated at 25 and 650°C, with no large differences apparent between irradiation at fission and fusion He/dpa ratios. The amount of matrix cavity swelling was small (~0.1%) for all of the irradiated spinel and alumina specimens.

Acknowledgments

The specimens for this study were supplied by P. F. Becher and F. W. Clinard, Jr.. and prepared by C. P. Haltom, J. W. Jones, and A M Williams. The nultiple-beam ion irradiations were performed by S. W. Cook and M. B. Lewis. We thank Frances Scarboro for typing the manuscript.

REFERENCES

1. F. W. Clinard. Jr., J. Nucl. Mater. 85686 (1979) 393.
2. F. W. Clinard, Jr. and L. W. Hobbs. in Physics of Radiation Effects in Crystals. R. A. Johnson and A. N. Orlov, eds. (Elsevier. Amsterdam, 1986), pp. 387–471.
3. C. W. White et al., Mat. Sci. Reports 4 (1989) 41–146.
4. L. W. Hobbs, J. Am. Ceram. Soc. 62 (1979) 267–78.
5. W. E. Lee, M. L. Jenkins, and G. P. Pells, Phil. Mag. A 51 (1985) 639.
6. Y. Katano, H. Ohno, and H Katsuta. J. Nucl. Mater. 155-157 (1988) 366.
7. S. J. Zinkle, in Mat. Res. Soc. Symp. Proc. Vol. 128, eds.. L. E. Rehn et al. (MRS, Pittsburgh, 1989). p. 363.
8. F. W. Clinard. Jr., G. F. Hurley, and L. W. Hobbs. J. Nucl. Mater. 1086109 (1982) 655.
9. C. A. Parker et al., J. Nucl. Mater. 1336134 (1985) 741.
10. S. J. Zinkle. J. Am. Ceram. Soc. 72 (1989) 1343.
11. P. A. Knight, M. L. Jenkins, and G. P. Pells, Mat. Res. Soc. Symp. Proc., Vol. 152 (MRS, Pittsburgh, 1989). p. 135.
12. S. J. Zinkle and S. Kojima, Nucl. Instr. Methods B 46 (1990) 165.
13. T. E. Mitchell and R. A. Youngman, 7th Int. HVEM Conf., eds., R. M Fisher et al., LBL-16031, CONF-830819 (1983), p. 163.
14. R. J. LaBauve, R. J. Livak, and F. W. Clinard, Jr., Adv. Ceramic Mater. 3 (1988) 353.
15. J. Manning and G. P. Mueller. Comput. Phys. Commun. 7 (1974) 85.
16. N. M. Ghoniem and S. P. Chou. J. Nucl. Mater. 155-157 (1988) 1263.
17. T. Shikama and G. P. Pells, Phil. Mag. A 47 (1983) 369.

IN SITU MEASUREMENTS OF DIELECTRIC PROPERTIES IN ALUMINA - R. E. Stoller, R. H. Goulding, and S. J. Zinkle (Oak Ridge National Laboratory)

OBJECTIVE

This work has been undertaken in support of the near-term research and development needs of CIT.

SUMMARY

A series of experiments have been planned to measure the dielectric properties of alumina in the presence of ionizing and displacive irradiation.

PROGRESS AND STATUS

Introduction

Ion cyclotron resonance heating (ICRH) has been proposed as a major heating source for CIT and ceramic vacuum windows are a critical component of ICRH systems.[1] It is important that these windows remain transparent to the radio frequency (rf) energy, in part because excessive heating due to rf power absorption could lead to their mechanical failure. The rf power absorbed in these ceramics is proportional to the so-called loss tangent. The loss tangent, tan δ is defined as the ratio of the imaginary part to the real part of the dielectric constant, tan $\delta = \varepsilon''/\varepsilon'$. Typical values for the loss tangent in unirradiated ceramics of interest to the fusion program are from 10^{-4} to 10^{-3}, with 10^{-3} being near the maximum tolerable value without modification of present designs.

Experimental Plans

Postirradiation measurements have shown that ionizing and displacive irradiation can increase the value of the loss tangent.[2-6] There is also some evidence that the amount of the increase is dependent on the neutron spectrum.[2] However, there have been no relevant measurements of dielectric properties during irradiation. There is some concern that the losses may be higher during irradiation because of the higher density of charge carriers that will exist. In addition, the validity of postirradiation measurements is called into question by data that shows significant levels of recovery of the loss tangent at room temperature following proton irradiation.[4] In order to address these concerns, a series of irradiation experiments have been planned to measure the dielectric properties of typical ceramics in situ.

The experiments call for the use of two facilities. The first is the Gamma Irradiation Facility (GIF) of the High Flux Isotope Reactor (HFIR) at the Oak Ridge National Laboratory. The GIF uses spent HFIR cores as a source of gamma radiation. Decay of fission products in the spent cores leads to an ionizing damage rate of 10^8 rad/h, which is comparable to that expected in the CIT. The HFIR-GIF provides a relatively large radiation volume that can be easily accessed. The active radiation volume is a cylinder about 40 cm long with a radius of 5.71 cm. The gamma heating in this facility has been measured using a thermocouple welded to a stainless steel test piece. The peak temperature measured was about 120°C. Such a low temperature should have no impact on the hardware used in these experiments. However, the temperature will be monitored since the resistivity of the copper cavity is temperature dependent.

Since the HFIR spent cores do not provide a component of displacive irradiation, the TRIGA reactor at the University of Illinois will be used to obtain data on the influence of a mixed (i.e., displacive plus ionizing) irradiation environment. A beam tube with a 15.2 cm inner diameter that runs adjacent to the TRIGA core will be used for these experiments. Like the HFIR-GIF, the transverse beam tube in the TRIGA provides a large, accessible test volume. When the TRIGA is operated in a pulsed mode, both the displacive and ionizing damage rates are near those in the CIT. The peak damage rates are 1.8×10^{-7} dpa/s (displacive) and 200×10^8 rad/h (ionizing). The use of appropriate shielding materials in the TRIGA experiments will permit the ratio displacive to ionizing radiation to be varied in order to examine the relative importance of both components.

The dielectric measurements will be made using a capacitively loaded resonant cavity. The initial set of experiments in the HFIR will measure the loss tangent at 100 MHz. The geometry of the TRIGA will provide more flexibility in the cavity dimensions; this will permit probing lower frequencies. The dimensions of a prototype cavity that has been built to bench-test the design are shown in Fig. 1. The cavity method is well suited to measurement of the loss tangent because the power dissipation in the ceramic relative to the balance of the experimental apparatus is maximized. In addition, losses in the feed line can be accounted for without the need for prior calibration, which would be extremely difficult

type N connector

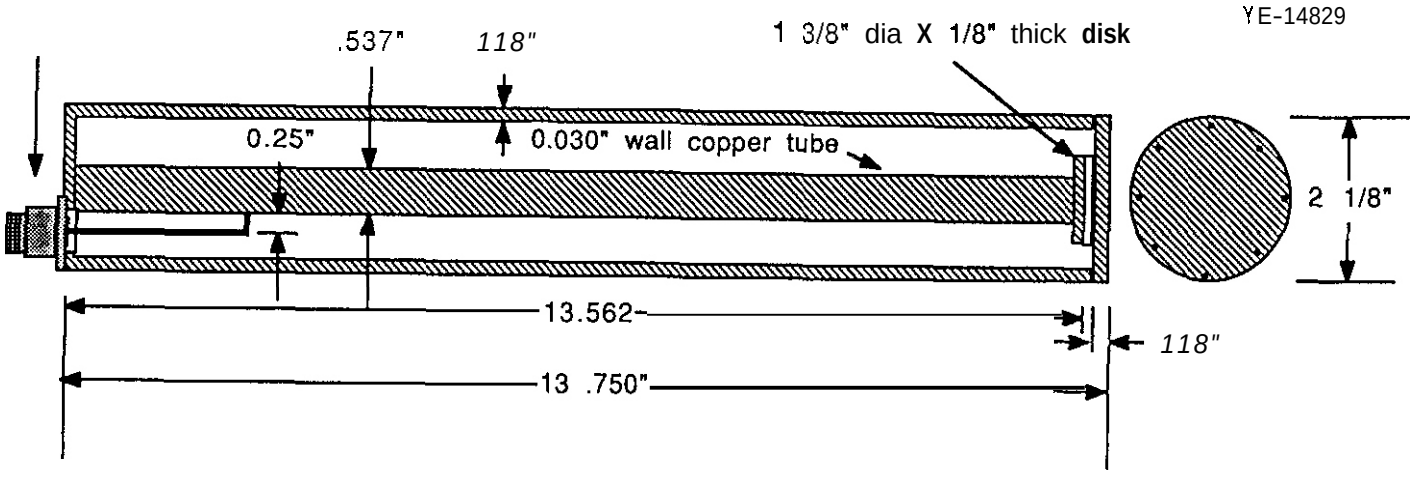

Fig. 1. Design of prototype resonant cavity for in situ dielectric measurements.

to accomplish in situ. The loss tangent can be measured by determining the cavity quality factor, Q which is the ratio of the stored energy to the energy dissipated per rf field period. The loss tangent is given by the equation:

$$\tan\delta = \left(\frac{\beta\ell}{\sin(2\beta\ell)} + \frac{1}{2}\right)\left[\frac{1}{Q} - \frac{1}{Q_0}\right], \qquad (1)$$

where β is equal to the angular frequency divided by the speed of light, ℓ is the length of the coaxial cavity center conductor, Q is the quality factor with the ceramic in place, and Q_0 is the quality factor at the same frequency when the ceramic is absent. Both of the Q values in Eq. (1) refer to the so-called "unloaded Q," for which only the energy stored and dissipated in the cavity itself are taken into account. They can be determined by measuring the ratio of the reflected to transmitted power as a function of frequency over a 1 MHz range centered at the resonant frequency of the cavity. Relative changes in the real part of the dielectric constant can also be measured using the resonant cavity technique with an accuracy of 1/Q, or less than 1% for the highest values of the loss tangent expected here.

Alumina (Al_2O_3) is a prime candidate material for use in rf heating systems. Therefore, the initial measurements will focus on this material. The experimental matrix includes the use of oriented single-crystal sapphire and commercial-grade polycrystalline alumina. The commercial products have been obtained from two different vendors. Since postirradiation measurements have shown a significant influence of impurities,[3,4] the commercial products include several different purity levels.

Experimental Schedule

The HFIR is in the process of ascending to full power following an extended outage. The current schedule at the HFIR should make a fully spent core available for the initial measurements in June, 1990.

REFERENCES

1. R. H. Goulding, F. W. Baity, P. L. Goranson, D. J. Hoffman, P. M. Ryan, D. J. Taylor, and J. J. Vugo, "ICRF Antenna Design for CIT and ALCATOR C-MOD," Radio Frequency Power in Plasmas, Eighth Topical Conference, A.I.P. Conf. Prof. No. 190, American Institute of Physics, New York, 1989, pp. 250-253.
2. J. L. Scott, F. W. Clinard, Jr. and F. W. Wiffen, J. Nucl. Mater. 133 & 134 (1985) 156-163.
3. G. P. Pells and G. J. Hill, J. Nucl. Mater. 141-143 (1986) 375-381.
4. S. N. Buckley and P. Agnew, J. Nucl. Mater. 155-157 (1988) 361-365.
5. G. P. Pells, J. Nucl. Mater. 155-157 (1986) 67-76.
6. H. M. Frost, "Millimeter-Wave Properties of Neutron-Irradiated Ceramics for RF-Window MFE Applications," Eighth Annual Progress Report On Special Purpose Materials for Magnetically Confined Fusion Reactors, DOE/ER-0113/5, National Technical Information Service, Springfield, Virginia, March, 1986, pp. 11-16.

CERAMICS FOR FUSION PROGRAM RESEARCH MATERIALS INVENTORY — Roger E. Stoller (Oak Ridge National Laboratory)

OBJECTIVE

The purpose of this work is to maintain a standard set of ceramic reference materials for use in the U.S. Fusion Reactor Materials research program.

SUMMARY

A stock of commercial, polycrystalline alumina with four different levels of purity (0.94, 0.976, 0.995, and 0.998) has been added to the Fusion Reactor Materials inventory. The material is in the form of 3/4 in. (0.998) and 1 in. (0.94) diameter rods and 2 in. by 2 in. bars (0.976 and 0.995).

PROGRESS AND STATUS

Introduction

Since experiments involving ceramic materials are becoming increasingly important, work has begun on assembling a standard set of ceramic reference materials for use by the U.S. Fusion Reactor Materials research program. The first materials have been added to this inventory.

Materials Added to Inventory

Coors Ceramics Company and the WESGO Division of GTE Products have both donated a stock of commercial, polycrystalline alumina with two different purity levels. The two grades of alumina obtained from Coors are designated AD-94 and AD-998 with nominal purities of 0.94 and 0.998, respectively. The WESGO material carries the designations of AL-300 and AL-995 for 0.967 and 0.995 pure alumina. Samples of all four materials will be analyzed to determine the impurity content in greater detail. The Coors material is in the form of 3/4 in. (AD-998) and 1 in. (A-94) diameter rods. Ten 12-in.-long rods of both materials were donated. The AL-300 and AL-995 are in the form of hard-fired, 2 in. × 2 in. × 15 in. bars. One bar of each grade has been obtained from WESGO.

Requests for material from this inventory should be directed to R. E. Stoller at the Oak Ridge National Laboratory. The request should include a description of the intended use and the amount of material required. Reports of research utilizing these materials that are published in the open literature should acknowledge the donation by Coors Ceramics and/or WESGO.

DISTRIBUTION

1–16. Argonne National Laboratory, 9700 South Cass Avenue, Argonne, IL 60439

M. C. Billone	P. A. Finn	B. A. Loomis
P. E. Blackburn	A. K. Fischer	R. F. Mattas
O. K. Chopra	A. B. Hull	L. A. Niemark
R. G. Clemmer	C. E. Johnson	D. L. Smith
D. R. Diercks	F. Kassner	S. W. Tam
		H. Wiedersich

17. Argonne National Laboratory, EBR-II Division, Reactor Materials Section, P.O. Box 2528, Idaho Falls, ID 83403-2528
D. L. Porter

18. Auburn University, Oepartment of Chemical Engineering, 201 Ross Hall, Auburn, AL 36849
B. A. Chin

19–34. Battelle-Pacific Northwest Laboratory, P. O. Box 999, Richland, WA 99352

M. D. Freshley	M. L. Hamilton	J. M. McCarthy
F. A. Garner (5)	H. L. Heinisch	B. D. Shipp
D. S. Gelles	G. W. Hollenberg	O. D. Slagle
L. R. Greenwood	R. H. Jones	J. L. Straalsund

35–36. Carnegie Institute of Technology, Carnegie-Mellon University, Schenley Park, Pittsburgh, PA 15213
W. M. Garrison, Jr. J. C. Williams

37. Department of Energy, Richland Operations Office, Federal Bldg., MS A590, Richland, WA 99352
Paul Pak

38. EG&G Idaho, Inc., Fusion Safety Program, P.O. Box 1625, Idaho Falls, ID 83415-3523
D. F. Holland

39–42. General Atomics, P.O. Box 85608, San Diego, CA 92138

J. Baur	D. I. Roberts
T. A. Lechtenberg	K. R. Schultz

43. General Dynamics Corporation, 5001 Kearny Villa Road, San Diego, CA 92138
T. L. Cookson

44. Georgia Institute of Technology, School of Textile Engineering, Atlanta, GA 30332
D. S. Tucker

45. Grand Canyon University, Department of Natural Science, 3300 W. Camelback Rd., Phoenix, AZ 85017
W. A. Coghlan

46. Hokkaido University, Faculty of Engineering, Kita 13, Nishi 8, Kita-ku, Sapporo 060, Japan
Professor Heishichiro Takahashi

47-50. Japan Atomic Energy Research Institute, Tokai Research Establishment, Tokai-mura, Naka-gun, Ibaraki-ken 319-11, Japan
Dr. Tatsuo Kondo Or. Akimichi Hishinuma (3)

51. Kyushu University, Research Institute for Applied Mechanics, 6-1, Kasuga-Koen, Kasuga-Shi, Fukuoka-Ken 816, Japan
Professor Takeo Muroga

52–54. Lawrence Livermore National Laboratory, P.O. Box 808, Livermore, CA 94550

E.C.N. Dalder	J. Perkins
M. Guinan	

55–63. Los Alamos National Laboratory, P.O. Box 1663, Los Alamos, NM 87545

J. L. Anderson	D. J. Dudziak	C. O. Kise
L. D. Caudill	H. M. Frost	R. Liepens
F. W. Clinard	G. Hurley	T. Zocco

64. Manlabs, Inc.. 231 Erie Street, Cambridge, MA 02139
O. Tognarelli

65. Massachusetts Institute of Technology, Department of Metallurgy and Materials Science. Cambridge, MA 02139
L. Y. Hobbs

66. Massachusetts Institute of Technology, 138 Albany Street. Cambridge, MA 02139
O. K. Harling

67-68. Massachusetts Institute of Technology. Room 13-4069, Cambridge, MA 02139
N. J. Grant — K. C. Russell

69–70. Massachusetts Institute of Technology. Plasma Fusion Center Headquarters, Cambridge, MA 02139
H. D. Becker — O. B. Montgomery

71. McDonnell-Douglas Astronautics Company, East, 0922242, Bldg. 92, P.O. Box 516. St. Louis, MO 63166
J. Y. Davis

72–73. Nagoya University, Institute of Plasma Physics, Furo-Cho, Chikusa-ku. Nagoya 464-01, Japan
Professor Akira Miyahara — Or. Chusei Namba

74. Nagoya University, Department of Nuclear Engineering, Furo-Cho, Chikusa-ku, Nagoya 464-01, Japan
Professor Mitchio Kiritani

75–76. National Institute of Standards and Technology, Boulder, CO 80302
F. R. Fickett — M. B. Kasen

77. National Materials Advisory Board. 2101 Constitution Avenue, Yashington, OC 20418
K. M. Zwilsky

78-79. National Research Institute for Metals, Tsukuba Branch, Sengen, Tsukuba-shi, Ibaraki-ken 305, Japan
Dr. Masatoshi Okada — Or. Haruki Shiraishi

80. Naval Research Laboratory, Yashington, DC 20375
J. A. Sprague

81–121. Oak Ridge National Laboratory, P.O. Box 2008, Oak Ridge, TN 37831

Central Research Library
Document Reference Section
Laboratory Records Department (2)
Laboratory Records—RC
Patent Section
D. J. Alexander
C. C. Baker
J. Bentley
E. E. Bloom
D. N. Braski
T. O. Burchell
S. O. Frey
R. H. Goulding
M. L. Grossbeck
T. Inazumi
E. A. Kenik
R. L. Klueh
Eal Lee
A. W. Longest
L. K. Mansur
P. J. Maziasz
T. C. Reuther
T. K. Roche
A. F. Rowcliffe (10)
R. L. Senn
J. Sheffield
L. Snead
R. E. Stoller
K. R. Thoms
P. F. Tortorelli
S. J. Zinkle

122–123. Princeton University, Princeton Plasma Physics Laboratory, P.O. Box 451. Princeton, NJ 08540
H. Furth — Long-Poe Ku

124. Rensselaer Polytechnic Institute, Troy. NV 12181
D. Steiner

125. Rockwell International Corporation, NA02, Rocketdyne Division, 6633 Canoga Avenue, Canoga Park, CA 91304
D. W. Kneff

125–127. Sandia National Laboratories, P.O. Box 5800. Albuquerque, NM 87185-5800
M. J. Davis — Y. B. Gauster

128–129. Sandia National Laboratories, Livermore Oivision 8316, Livermore, CA 94550
Y. Bauer — Y. G. Yolfer

130. San Diego State University, Mechanical Engineering Dept., San Diego, CA 92182-0191
L. D. Thompson

131. Tohoku University, Institute for Materials Research, Katahira 2.1-1, Sendai 980, Japan
Professor Hideki Matsui

132. Tohoku University, Institute for Materials Research, Orai Branch, Oarai, Higashi-Ibaraki-gun, Ibaraki-ken 311-13, Japan
Professor Hideo Kayano

133. Tohoku University, Department of Nuclear Engineering, Tohoku University, Aoba, Aramaki, Sendai 980, Japan
Professor Katsunori Abe

134–135. University of California, Department of Chemical and Nuclear Engineering, Santa Barbara, CA 93106
G. E. Lucas
G. R. Odette

136–138. University of California, Department of Chemical, Nuclear and Thermal Engineering, Los Angeles, CA 90024
M. B. Abduo
R. W. Conn
N. M. Ghoniem

139. University of Michigan, Department of Nuclear Engineering, Ann Arbor, MI 48109
T. Kamnash

140. University of Missouri, Department of Nuclear Engineering, Rolla, MO 65401
A. Kumar

141. University of Tokyo, Department of Materials Science & Technology, 2641 Yamazaki Noda City, Chiba Prefecture 278 Japan
N. Igata

142–143. University of Tokyo, Department of Nuclear Engineering, 3-1, Hongo 7-Chome, Bunkyo-ku, Tokyo 113 Japan
Professor Shiori Ishino (2)

144–145. University of Tokyo, Department of Materials Science, 3-1, Hongo 7-Chome, Bunkyo-ku, Tokyo 113, Japan
Professor Akira Kohyama
Professor Yutaka Kohno

146. University of Wisconsin, Nuclear Engineering Dept., 1600 Johnson Drive, Madison, WI 53706
G. L. Kulcinski

147–152. Westinghouse Hanford Company, P. O. Box 1970, Richland, WA 99352
H. R. Brager
A. M. Ermi
G. D. Johnson
F. M. Mann
R. J. Puigh
R. L. Simons

153. Department of Energy, Oak Ridge Operations Office, P.O. Box 2001, Oak Ridge, TN 37831
Assistant Manager for Energy Research and Development

154–159. Department of Energy, Office of Fusion Energy, Washington. DC 20585
S. E. Berk
M. M. Cohen
N. A. Davies
R. J. Dowling
R. E. Price
F. W. Wiffen

160–208. Department of Energy, Office of Scientific and Technical Information, Office of Information Services, P.O. Box 62, Oak Ridge, TN 37831
For distribution as shown in DOE/TIC-4500, Distribution Categories UC-423 (Magnetic Fusion Reactor Materials) and UC-424 (Magnetic Fusion Energy Systems)